# PARTICLE PERCOLATION IN BLOCK CAVING MINES

By

**Mohd Hazizan Mohd Hashim**

A thesis submitted in fulfilment
of the requirements for the degree of
Doctor of Philosophy

THE UNIVERSITY OF NEW SOUTH WALES

SCIENTIA

MANU ET MENTE

SYDNEY • AUSTRALIA

School of Mining Engineering
The University of New South Wales
Sydney, Australia
July 2011

PLEASE TYPE

**THE UNIVERSITY OF NEW SOUTH WALES**
**Thesis/Dissertation Sheet**

Surname or Family name: **MOHD HASHIM**

First name: **MOHD HAZIZAN**

Other name/s:

Abbreviation for degree as given in the University calendar: **PhD**

School: **SCHOOL OF MINING ENGINEERING**

Faculty: **FACULTY OF ENGINEERING**

Title: **PARTICLE PERCOLATION IN BLOCK CAVING MINES**


**Abstract 350 words maximum: (PLEASE TYPE)**

Knowledge of particle percolation impacts on both the economics and safety of cave mining operations. Nevertheless, very little research has focused on particle percolation in block or sub-level caving mines. The aim of this thesis is to study the percolation of fine particles in highly angular particle assemblies similar to caved rock, using physical and discrete element numerical models.

In the first stage the magnitude and distribution of shear strain resulting from isolated draw was measured using scaled physical models (1:100) on 13.20 mm crushed basalt aggregate. Digital images of marker particles were taken after each draw cycle and the changes in shear strain were calculated.

In the second stage, a Shear Cell for Percolation of Geomaterials (SCPG) was designed for angular rock particles. Percolation tests were carried out for ideal media consisting of steel spheres (4.00 mm), glass spheres (4.00, 5.00, 6.00, 15.75 mm) and plastic spheres (4.00 mm) and highly angular crushed basalt aggregate (2.86, 4.05, 5.21, 6.18, 13.20 mm). Key combinations of fine and bed-matrix particles were tested to quantify the effect of strain rate, particle diameter ratio, density and shape. Of the parameters tested, percolation was most influenced by particle diameter ratio, shape and strain rate, while density had the least effect. To explore the mechanisms controlling percolation across the range of tested particle shapes and sizes, a dimensionless percolation rate (DPR) relation was derived using the method of Bridgwater et al. (1978).

In the third stage selected SCPG experiments were numerically simulated using Particle Flow Code in Three Dimensions (PFC3D). Due to the limitations of PFC3D, particle shapes and sizes were simplified and all other parameters were kept as similar to the measured parameters as possible. Results from the physical SCPG experiments on angular particles were simulated using clump logic. The results were compared to corresponding numerical and physical experiments on mono-spherical particles with the same equivalent spherical diameter as the angular particles. The PFC3D results had broad agreement with the SCPG physical experiments showing that percolation is predominantly affected by particle shape and the ratio of fine and bed-matrix particle sizes.




........................ Signature ........................ Witness ........ 12/12/2011 Date



**FOR OFFICE USE ONLY**

Date of completion of requirements for Award:

**THIS SHEET IS TO BE GLUED TO THE INSIDE FRONT COVER OF THE THESIS**

**ORIGINALITY STATEMENT**

'I hereby declare that this submission is my own work and to the best of my knowledge it contains no materials previously published or written by another person, or substantial proportions of material which have been accepted for the award of any other degree or diploma at UNSW or any other educational institution, except where due acknowledgement is made in the thesis. Any contribution made to the research by others, with whom I have worked at UNSW or elsewhere, is explicitly acknowledged in the thesis. I also declare that the intellectual content of this thesis is the product of my own work, except to the extent that assistance from others in the project's design and conception or in style, presentation and linguistic expression is acknowledged.'

Signed ……………………………………………………..............

12/12/2011

Date ……………………………………………………................

**COPYRIGHT STATEMENT**

‘I hereby grant the University of New South Wales or its agents the right to archive and to make available my thesis or dissertation in whole or part in the University libraries in all forms of media, now or here after known, subject to the provisions of the Copyright Act 1968. I retain all proprietary rights, such as patent rights. I also retain the right to use in future works (such as articles or books) all or part of this thesis or dissertation.

I also authorise University Microfilms to use the 350 word abstract of my thesis in Dissertation Abstract International (this is applicable to doctoral theses only).

I have either used no substantial portions of copyright material in my thesis or I have obtained permission to use copyright material; where permission has not been granted I have applied/will apply for a partial restriction of the digital copy of my thesis or dissertation.'

Signed ……………………………………………

Date ……………………12/12/2011………………..

**AUTHENTICITY STATEMENT**

‘I certify that the Library deposit digital copy is a direct equivalent of the final officially approved version of my thesis. No emendation of content has occurred and if there are any minor variations in formatting, they are the result of the conversion to digital format.’

Signed ……………………………………………..

Date ……………………12/12/2011………………..

# DEDICATION

To my devoted beloved family

and

particularly my father in law, the late Ismail Melan who left us

during the preparation of this dissertation.

# ACKNOWLEDGEMENTS

I would like to express my sincere appreciation and gratitude to following persons and organisations for providing assistance and guidance during the research and writing of this thesis:

**Dr Glenn Sharrock**, my principal supervisor, for his guidance, academic and technical support throughout the research. This dissertation could not have been accomplished without his expert guidance, great encouragement, and strong support at all levels during the completion of this dissertation.

**Dr Serkan Saydam**, my co-supervisor, for his technical support, encouragement and for providing valuable comments and suggestions on my work.

**Ministry of Higher Education Malaysia (MOHE)** and **Universiti Sains Malaysia (USM)**, for the scholarship and financial support under the Academic Staff Training Scheme (ASTS).

**Mr John Everett**, who installed and acquired necessary instrumentation of the electronic circuit for the Shear Cell for Percolation of Geomaterials (SCPG) device, **Mr Paul Gwynne** for providing technical advice during the physical experiment tests and **Mr Allen Roberts** for construction of the shear cell.

Staff members of the School of Mining Engineering and postgraduate colleagues, for their individual help and encouragement and for providing both resources and friendship during my time with the school. My appreciations are also extended to my friends and my fellow graduate students for their help and company for the duration of the study.

Finally, the deepest appreciation is reserved for my mother and family especially to my beloved wife and our little daughter whose love, understanding, caring and providing emotional support in which sustained me throughout this research. I deeply cherish the life with them.

# ABSTRACT

Knowledge of particle percolation impacts on both the economics and safety of cave mining operations. Nevertheless, very little research has focused on particle percolation in block or sub-level caving mines. The aim of this thesis is to study the percolation of fine particles in highly angular particle assemblies similar to caved rock, using physical and discrete element numerical models.

In the first stage the magnitude and distribution of shear strain resulting from isolated draw was measured using scaled physical models (1:100) on 13.20 mm crushed basalt aggregate. Digital images of marker particles were taken after each draw cycle and the changes in shear strain were calculated.

In the second stage, a Shear Cell for Percolation of Geomaterials (SCPG) was designed for angular rock particles. Percolation tests were carried out for ideal media consisting of steel spheres (4.00 mm), glass spheres (4.00, 5.00, 6.00, 15.75 mm) and plastic spheres (4.00 mm) and highly angular crushed basalt aggregate (2.86, 4.05, 5.21, 6.18, 13.20 mm). Key combinations of fine and bed-matrix particles were tested to quantify the effect of strain rate, particle diameter ratio, density and shape. Of the parameters tested, percolation was most influenced by particle diameter ratio, shape and strain rate, while density had the least effect. To explore the mechanisms controlling percolation across the range of tested particle shapes and sizes, a dimensionless percolation rate (DPR) relation was derived using the method of Bridgwater et al. (1978).

In the third stage selected SCPG experiments were numerically simulated using PFC3D$^{TM}$. Due to the limitations of PFC, particle shapes and sizes were simplified and all other parameters were kept as similar to the measured parameters as possible. Results from the physical SCPG experiments on angular particles were simulated

using clump logic. The results were compared to corresponding numerical and physical experiments on mono-spherical particles with the same equivalent spherical diameter as the angular particles. The PFC results had broad agreement with the SCPG physical experiments showing that percolation is predominantly affected by particle shape and the ratio of fine and bed-matrix particle sizes.

# LIST OF ABBREVIATIONS

| | |
|---|---|
| AC/DC | Adaptive Continuum/ Discontinuum Code |
| BCF | Block Cave Fragmentation |
| COR | Coefficient of Restitution |
| CPF | Cumulative Percentage Mass Passing of Fine Particles |
| DEM | Discrete Element Method |
| DPR | Dimensionless Percolation Rate |
| EZ | Extraction Zone |
| IEZ | Isolated Extraction Zone |
| IMF | Incremental Percentage Mass of Fine Recovered |
| IMZ | Isolated Movement Zone |
| ISZ | Isolated Stagnant Zone |
| LHD | Load-Haul-Dump Truck |
| MOHE | Ministry of Higher Education Malaysia |
| MZ | Movement Zone |
| PFC | Particle Flow Code |
| PFC2D | Particle Flow Code in Two Dimensions |
| PFC3D | Particle Flow Code in Three Dimensions |
| PSSC | Primary Segregation Shear Cell |
| PSSC-II | Primary Segregation Shear Cell II |
| REV | Representative Elementary Volume |
| RFID | Radio Frequency Identification |
| UNSW | University of New South Wales |
| USM | Universiti Sains Malaysia |
| SCPG | Shear Cell for Percolation of Geomaterials |
| SSA | Simple Shear Apparatus |
| SZ | Stagnant Zone |

# TABLE OF CONTENTS

## TABLE OF CONTENTS

**CHAPTER 3**

**SHEAR CELL FOR PERCOLATION OF GEOMATERIALS – DESIGN AND EXPERIMENTAL METHOD**

**CHAPTER 4**
**MATERIAL PROPERTIES AND CHARACTERISATION**

**CHAPTER 5**
**PERCOLATION EXPERIMENTS ON IDEALISED MATERIALS AND CRUSHED BASALT**

# LIST OF FIGURES

# LIST OF TABLES

# CHAPTER 1: INTRODUCTION

## 1.1 BACKGROUND

Over the past decade caving methods, sometimes referred to as “unsupported methods” (Brown 2003), have emerged as important and become the underground bulk mining methods of choice (Chitombo 2010). Examples of caving methods include block caving (BC), sub-level caving (SLC) and long wall mining. It is anticipated that block caving will continue to grow in importance as more massive lower grade ore deposits are mined, and to extend the life and viability open-pit mines as they reaching their economic mining depth.

Block cave mining is a method in which a large block of massive ore is undercut causing the ore to break under its own weight due to gravitational forces. The caved ore is then recovered through drawpoints[1]. The block caving technique can be classified by two processes; the extraction of small caved rocks created initially by blasted and the fracture of compact material located in the upper layers due to the stress propagation generated by the extraction process.

[1] Drawpoint refers to the excavated structure on the extraction or production level through which the caved rock is loaded and removed from the cave.

Block caving method provides the bulk mining of large and relatively low-grade ore bodies to be mined with low cost and high recovery. As a result, this method is becoming more common worldwide especially in the large-scale extraction of massive steeply dipping ore bodies with large vertical continuity (e.g., Cadia East, Australia; Northparkes, Australia; San Manuel, USA; Palabora, South Africa and Freeport, Indonesia). The method may also sometimes be implemented to convert open-pit operations to underground operations.

On the other hand, the *gravity flow*[2] of caved rock is a critical component of a block cave and sub-level caving which significantly influences the economics of the operation. Drawing from other disciplines, it is known that granular materials consist of particles of varying sizes, densities and/or shapes, and that segregation occurs during shaking or transport (Gray and Thornton 2005). Segregation is defined as the phenomenon whereby a flowing granular mass consisting of particles with diverse physical properties becomes spatially inhomogeneous (Rosato and Blackmore 2000).

Segregation is commonly classified based on its mechanism (Tang and Puri 2004). A total of thirteen segregation mechanism have been identified and summarised as follows: push-away, trajectory, displacement, rolling, percolation, sieving (or sifting), impact, angle of repose, embedding, air current, fluidization, agglomeration and diffusion (or concentration-driven displacement) by de Silva at el. (2000). “Percolation segregation” or referred as “percolation” during the course of this thesis (illustrated in Figure 1.1) was selected for the present thesis due to its applicability to the block caving mines (i.e., gravity flow of caved rock, conveying, transportation and associated issues in economic and safety of caving mines).

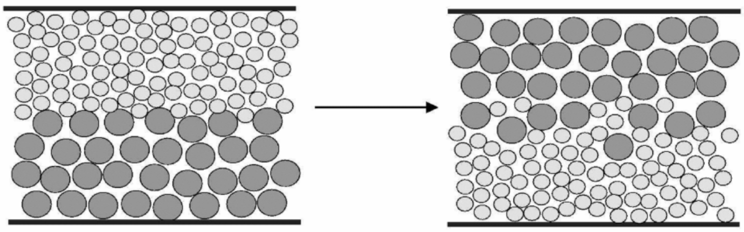

Figure 1.1: Percolation segregation (after Li 2005)

[2] Gravity flow of caved rock is the process by which ore/fragmented rock/broken material mass flow/moves under the influence of gravity.

Several researchers have recognised percolation as an important mechanism in segregation (Bridgwater et al. 1969; Tanaka 1971; Bridgwater and Ingram 1971; Drahun and Bridgwater 1983; Mosby et al. 1996a; de Silva et al. 2000; Duffy and Puri 2002; Tang 2004). Percolation of fine particles occurs when mixtures of particles with different sizes are exposed to perpendicular shear deformations and paralleled gravity force (Duffy and Puri 2002). During shear, fine particles are exposed to the void structure of the coarse matrix, allowing fine particles to find and drop through suitable voids in the coarse particle layer (Johanson et al. 2005). Whenever a mixture of particles of different sizes is disturbed in such a way to rearrange the particles, percolation of fine particles can occur.

In block and sub-level caving mines, segregation can arise from percolation induced by gravity (Mosby et al. 1996b). In view of this, particles resulting from fine *fragmentation*[3] generated in the cave column (Lewis and Clark 1964) have the potential to rapidly move downward and be drawn earlier than coarser fragments (Laubscher 2000; Pierce 2004). Implications of this phenomenon are that the potential exists for fine waste to enter drawpoints and mix up into the pit thus reducing the concentration of mineralisation in the caved ore (Laubscher 2000).

The above circumstances may cause preferential draw if fine waste and/or induced hang-ups and cavity problems exist near the drawpoints (i.e., hardening process of the percolated fines through the coarse particles). Hang-ups near drawpoints may also become a major problem and increase the operating cost due to secondary blasting processes and thus significantly impact mine operation and profitability (Baiden et al. 2008).

Percolation of fine particles during the gravity flow of caved rock is also significant as the fines influence the shape of the extracted volume, and hence affect the overall recovery and dilution[4] (Just and Free 1971; Kvapil 1982; Chen 1997;

[3] Fragmentation refers to the process or results of caving, blasting and drawing process of initially in situ rock mass, ore or mineralise.

[4] Dilution is generally defined as the quantity or percentage of waste rock (generally related to unwanted lower grade ore) in relation to the volume of ore extracted at drawpoints.

Pretorius 2007; Castro and Trueman 2008). With regard to this, Pakalnis et al. (1995) reported that uncontrolled dilution may have a major impact on economic viability of one mining operation and can contribute to ore losses of up to 20%. This finding was also supported by Wellmer et al. (1998) who found that dilution problem in mines generally varies between 5-30%.

Other forms of percolation exist. For example Chambers (2008) noted that once surface subsidence occurs, water can percolate down through the caved rock and may convey some disintegrated heavy minerals (e.g., mercury, lead and zinc) which may result in contamination of groundwater and/or surface water. In addition, Beus et al. (1999) identified several potential safety problems relating to the ore and waste rock hang-ups such as structural failures, blocked gates, water flow and air blasts. Also, percolation of fine particles from ground water transport is a key factor in mud rushes.

Nevertheless, despite the potential significant effect of fines percolation on block caves (i.e., dilution, preferential draw, safety hazard, hang-up problem, economical of caving operational), there is very little research devoted to percolation in mining applications. Most work on percolation has emerged in chemical and/or powder applications (e.g., Bridgwater et al. 1969, 1978, 1985a; Bridgwater and Ingram 1971; Scott and Bridgwater 1975, 1976; Cooke et al. 1978; Cooke and Bridgwater 1979; Drahun and Bridgwater 1983; Duffy and Puri 2002).

Moreover, efforts to understand the percolation mechanism are made more difficult since most of the previous studies have focused on mono-size distributions of spherical particles (i.e., spherical glass, sphere sand) and/or narrow distributions of particle sizes. In addition, mono-sphere media was employed by many researchers due to the fact that most of the numerical methods still represent granule and highly angular shaped particles as circular discs in 2D or spheres in 3D. The use of mono-size particle and/or narrow distribution may not be relevant to caved rock created in block caving mines, consisting of highly angular shapes and wide size distribution.

In view of the above point, Yenge (1980) noted that the use of other material such as sand could not satisfactorily described mining problem due to dissimilar conditions (i.e., particles sizes and boundary) and thus, may not be analogous to caved rock. Therefore, the use of materials such as crushed aggregates which more closely represent caved rock has advantages over the sand particles thus provided similarity to the caved rock which is essential towards better understanding of percolation in caving mines. Nevertheless, some limitations and difficulties arise from the use of highly angular particles mainly related to the experimental difficulties, measurement techniques on the bed structure and scale-up uncertainties (Matveev et al. 2006).

Alternatively, it is generally agreed that in addition to physical models, numerical models are powerful and versatile (Campbell 1989; Savage and Dai 1993; Rosato and Kim 1994; Pierce et al. 2003) and offer an alternative method to study the gravity flow of caved rock. Nevertheless, these are still developing and rely heavily on the assumption that circular discs in two dimensions (2D) and/or sphere in three dimensions (3D) which in practice are far removed from the actual highly angular shape of caved rock. It is noteworthy that although numerical methods and computer technology have advanced significantly over the last 20 years some key factors restrict the application of numerical methods in the modelling of caved rock flow.

The first limitation is the number of particles. For instance the Discrete Element Method (DEM)[5] which, depending on a number of factors such as model duration, particle stiffness and mass, at present is limited to around 500,000 particles for standard desk-top computers or 10,000,000 for high performance computers. Accordingly within this particle limitation, it is not possible to fully represent a complete mine consisting of a large number of highly angular shapes and sizes similar to caved rock. In particular these limits restrict 3D modelling. The second is the particle shape. Angular particle shapes are possible, at the cost of run time, and a reduction in the total number of particles. The third is particle stiffness, which reduces the critical time step,

[5] Discrete Element Method (DEM) (or sometimes referred as a Distinct Element Method) is run in such way that the contact forces were compute and resulting Newtonian dynamics of individual particles in an assembly and provides insight into the microstructure of the granular assemblies. In particle flow this method is favoured over other numerical methods due to its ability to embrace rotational degrees-of-freedom as well as enduring contacts

thereby reducing the number of particles which can be practically simulated (Beus et al. 1999).

In summary, particle percolation in cave mines, which is influenced by factors such as particle shape, size, density and transport properties (i.e., shear strain) is an important mechanism to consider. As full scale tests are only now been performed and have limitations, (i.e., can take years to complete), physical and numerical models provide a method to improve the understanding of percolation mechanisms of caved rock. Given that sole application of numerical models is not sufficient towards reliable results and applications, validation of these methods through physical models is required.

For these reasons, this thesis has focused on the application of both approaches; physical modelling and discrete element numerical modelling, to provide insight into the mechanisms and parameters controlling percolation of fine particles in the block caving mine environment.

## 1.2 RESEARCH OBJECTIVES AND HYPOTHESES

The main objective of this thesis is to study percolation of fine particles[6] in a matrix of coarser "bed" particles[7] under induced gravity flow in controlled experimental conditions. The knowledge gained from this experimental work is further complemented by the development of a numerical model aimed at providing a link between physical modelling results and practical applications.

In this context, a number of key motivations exist for improving our understanding of fine particle percolation and to achieve this goal, the thesis tested two hypotheses:

[6] The term "fine particles" refers to granular media which are relatively smaller than the matrix of larger or coarser bed particles.

[7] The term "larger or coarser particles" are refers to granular media which are relatively large and used as the bed-matrix during percolation tests.

*Hypothesis One -* ***"Particle shape and size significantly influence the percolation of fine particles in bed matrices of highly angular aggregates."***

*Hypothesis Two -* ***"Discrete element models incorporating clump representations of angular particles provide different percolation estimates than spherical mono-size particles."***

## 1.3 RESEARCH APPROACH

Although the study of particle percolation has emerged and continued for more than 50 years (especially in chemical engineering and/or associated engineering disciplines), there is essentially no validated theory developed for large scale systems such as those encountered in block caving mines. Efforts to understand these systems are restricted by data limitations, where even relatively basic parameters such as fragmentation cannot be easily measured or modelled.

As a result, further research is required to understand the mechanisms of fine particle percolation and, in particular, percolation rates. In answering this problem statement, a contribution is made into three major aspects:

- design and fabrication of a new simple shear cell rig to determine the quantitative relations of highly angular shapes of particles percolation to physical properties such as particle diameter ratio, shape, density, strain effect, and particle size distribution of the coarse bed-matrix media;
- development of a numerical model using discontinuum methods (DEM approach) to simulate, replicate and validate granular flow as a possible means of linking experimental results to mine scale; and
- assessment of shear-strain under isolated draw in a controlled 2D scaled physical model.

In summary, the research method involves three stages (Figure 1.2). The first stage focuses on the material characterisation of both spherical (*ideal media*[8]) and highly angular particles (*crushed aggregate media*[9]).

The second stage was conducted using a new physical model called the ***Shear Cell for Percolation of Geomaterials*** **(SCPG)** which was designed and constructed specially for percolation studies on angular rock fragments with geometric similitude to those typically found in the block caving mines. Prior to the construction of the SCPG, an assessment of shear strain under isolated draw in controlled Type-A Kvapil models were conducted to provide insights into the magnitude of strain around the *draw zone*[10] of a single drawpoint in a block caving mine.

Data from the shear strain assessment (i.e., shear strain magnitude) was then incorporated as test parameters for the percolation study using the SCPG. It is noteworthy that the SCPG is different to other experimental test rigs due to its ability to study the percolation of fine particles using both ideal and crushed aggregate media under controlled shear strain conditions.

In the third stage the results of SCPG experiments were used to calculate parameters defining the *dimensionless percolation rate* (DPR). These parameters were used to validate numerical models of the SCPG by means of the *Particle Flow Code in Three Dimensions* (PFC3D™)[11] software (Itasca 1999, 2005b, 2008b). This required the development of new numerical models with special emphasis on non-spherical shapes similar to caved rock (i.e., clump particles). Similarly, the magnitude of shear strain and material properties from stage one formed the foundation for the numerical stage, in order to generate numerical similitude to the SCPG experiments.

[8] Ideal media refers to material that is experimentally and practically easy to control, and is often represented by circular discs in 2D and/or spheres in 3D for the ease of numerical modelling (i.e., glass spheres, steel spheres and spherical sands).

[9] Crushed aggregate media refers to highly angular basalt aggregates that provide reasonable geometric and density similitude to the caved rock.

[10] Draw zone refers the zone of caved rock that will eventually channel to a particular drawpoint during progressive draw events.

[11] PFC3D™ software is based on the Discrete Element Method (DEM) approach which employs an explicit time-stepping algorithm and captures many elements of the micro-mechanics of granular media.

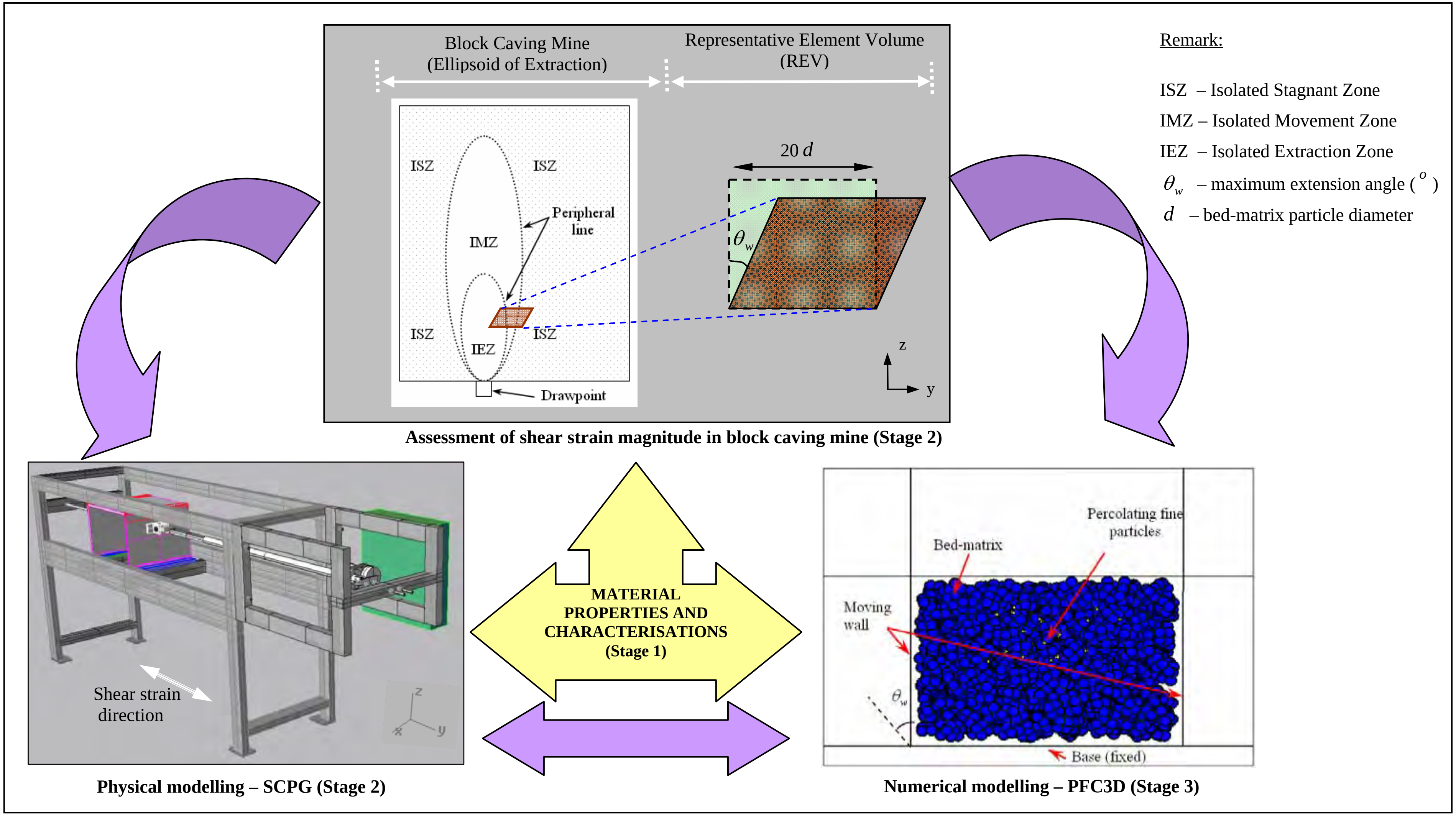


Figure 1.2: Research methodology - concept diagram showing the project stages and REV method employed for the study of rock percolation.

Since, in practice, it is almost impossible to represent and achieve all the necessary conditions for full similitude (i.e., kinematics and dynamics), the *Representative Elementary Volume* (REV) (Bear 1972) was adopted as a guide in predicting their effective properties (Kanit et al. 2003). In line with above point, the REV size can be associated with a given precision of the estimation of the required overall property and the number of realisations of a given volume ($V$) of microstructure that one is able to consider (Kanit et al. 2003).

Campbell and Bridgwater (1973), Scott and Bridgwater (1975, 1976) and Bridgwater et al. (1978, 1985b) carried out a series of experiments in which the aim was to isolate the effect of a shear field as a cause of percolation/segregation. They concluded that the width of the zone in which percolation occurred was varying from 5 to 15 particle diameters ($15d$). This suggested that to achieve reliable results, a significantly wider and large size shear box apparatus is required. As a result, this thesis employed a minimum $20d$ for the REV purposes in both the physical models and numerical simulations.

In the present research, the REV concept has been employed in various stages including the percolation test using SCPG (Chapter 3 and 5), numerical modelling in PFC3D™ (Chapter 6) and shear strain assessment by the mean of Type-A Kvapil Model (Section 3.4).

## 1.4 THESIS OUTLINE

This thesis comprises seven chapters. A brief summary covering the contents of each chapter is given below:

**Chapter 1** (Introduction) is an overview of the background, hypothesis, objectives and methodology.

**Chapter 2** (Literature Review) firstly presents a review of gravity flow in block caving mines. This is followed by detail review of similitude related to the percolation study approaches which includes the physical, full scale and numerical modelling. At the end of the chapter, a summary of literature and research directions for percolation studies for caving mines is presented.

**Chapter 3** (Shear Cell for Percolation of Geomaterials – Design and Experimental Method) describes in detail the design and fabrication of an apparatus for the investigation of fine particle percolation in a matrix of coarse angular aggregate. This chapter also presents the experimental aspects, results and discussions on the shear strain magnitude assessment for the case of a Type-A Kvapil Model of an isolated drawpoint, representing a block caving mine. The results from the assessment provide estimates of the strain rate and total shear strain needed in the SCPG experiments.

**Chapter 4** (Material Properties and Characterisation) describes the material properties and characterisations of two different types of media used in the percolation experiments namely: ideal media and crushed aggregate media. Some key material properties and characterisation tests used in this chapter include particle size distribution, shape and shape factor, particle density and shear box test.

**Chapter 5** (Percolation Experiments on Idealised Materials and Crushed Basalt) presents results and analysis of physical model experiments conducted using the SCPG. This includes a discussion on each of the parameters including: the effect of strain rate ($\dot{\gamma}$), particle diameter ratio ($d_p / d_b$), particle shape, particle density ratio ($\rho_p / \rho_b$) and the assessment of dimensionless percolation rate (DPR).

**Chapter 6** (Numerical Simulation: Validation and Analysis) presents the replication and validation of the SCPG simulation model using PFC3D™. The aim of this chapter is to explore the strengths and limitations of discrete element numerical modelling of percolation mechanisms. This is followed by the development of a new numerical model with emphases on the use of clump logic to represent highly angular shape particles, representing caved rock.

**Chapter 7** (Conclusions and Recommendations for Future Research) is a discussion on the findings, summarises the major conclusions of this thesis and provides recommendations and directions for future work.

## 1.5 PUBLISHED PAPERS

The following peer reviewed papers containing extracts of this thesis were prepared and published during the period of research:

- Hashim, MHM, Sharrock, GB and Saydam, S 2008, 'A review of particle percolation in mining', in Y Potvin, J Carter, A Dyskin and R Jeffrey (eds), *Proceeding First Southern Hemisphere International Rock Mechanics Symposium (SHIRMS)*, 16-19 September 2009, Perth, Australia, Australian Centre for Geomechanics, Perth, vol. 1, pp. 273-284.

- Hashim, MHM and Sharrock, GB 2009, 'Numerical investigation of the effect of particle shape on percolation', in *43rd U.S. Rock Mechanics Symposium and Fourth U.S.-Canada Rock Mechanics Symposium (ARMA 2009)*, 28 June-1 July 2009, Asheville, North Carolina, U.S., American Rock Mechanics Society (ARMA), North Carolina, ARMA09-034 (CD-ROM), paper no. 34, 8 p.

- Sharrock GB and Hashim, MHM 2009, 'Disturbed gravity flow in block caving', in *43rd US Rock Mechanics Symposium and Fourth U.S.-Canada Rock Mechanics Symposium (ARMA 2009)*, 28 June-1 July 2009, Asheville, North Carolina, U.S., American Rock Mechanics Society (ARMA), North Carolina, ARMA09-070 (CD-ROM), paper no. 70, 12 p.

- Hashim, MHM and Sharrock, GB 2010, 'Quantification of shear-strains in a 2D block cave scaled physical model', in *ISRM International Symposium - 6th Asian Rock Mechanics Symposium*, 23-27 October 2010, New Delhi, India, Paper ARMS6-2010-025, New Delhi, CBIP-ISRM, 9 p., accessed 3 May 2011, <http://www.onepetro.org>.

- Hashim, MHM and Sharrock, GB 2012, 'Effect of size distribution in percolation of fine particles', in 6*th International Conference and Exhibition on Mass Mining (MassMin 2012)*, 11-13 June 2012, Sudbury, Canada. (Abstract accepted, paper in progress).

# CHAPTER 2:
# LITERATURE REVIEW

## 2.1 INTRODUCTION

This chapter evaluates the literature relevant to the gravity flow of caved rock and percolation of fine particles in caving mines. Section 2.2 discusses the gravity flow of caved rock in a caving mine followed by a detailed description on the methods employed to understand the mechanisms of gravity flow (Section 2.3). Section 2.4 presents a review on the similitude of scaled physical models.

A detailed discussion on the percolation of fine particles is presented in Section 2.5 with emphasis on the fundamental aspects of percolation and selected works on percolation studies. Finally, Section 2.6 presents discussions and conclusions on the literature review and summarises research directions towards better understanding of percolation in caving mines.

## 2.2 GRAVITY FLOW IN CAVING MINES

Cave mining refers to all mining methods where the orebody is caved naturally (by the action of gravity) after undercutting (Laubscher 1994) and/or trough assisted caving (e.g., blasting) in which the caved material is recovered through drawpoints. Examples of cave mining include block caving, panel caving, inclined drawpoint caving and front caving (Laubscher 1994). Even though the gravity flow (Brown 2003) of caved rock has been studied for almost a decade its mechanisms are still far from understood (Campbell 1990; Hutter and Rajagopal 1994; Brown 2003; Brady and Brown 2004).

In line with above point, Rustan (2000) noted that the theory of flow of fine particles within the coarse blasted rock (particularly in SLC) were generally not understood and asserted that such particles' properties (i.e., shape, size, size distribution and relative density) are most important factors determining the characteristics of bulk solids during storage and flow. Figure 2.1 illustrates a typical layout of block caving mine.

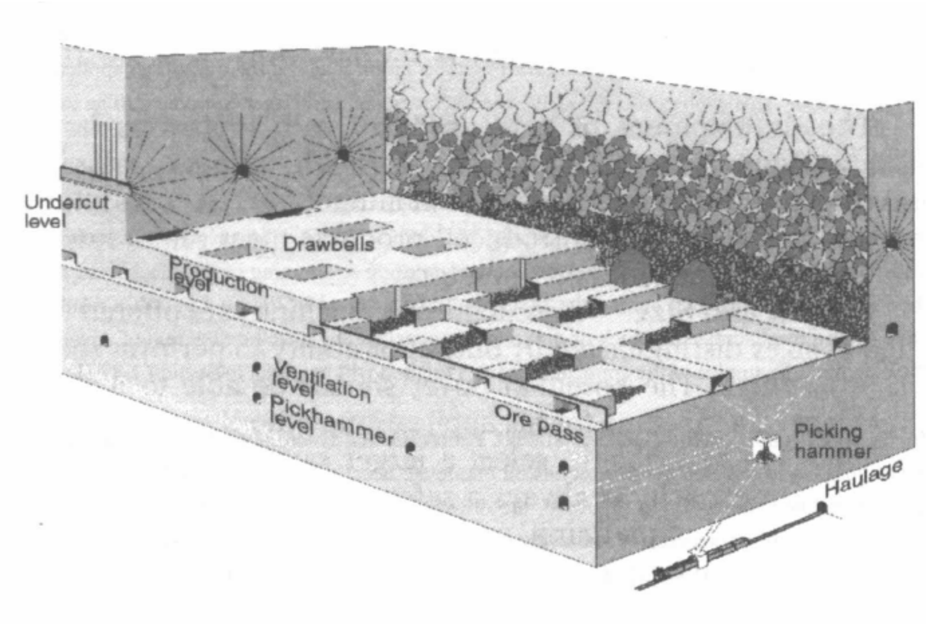


Figure 2.1: Typical diagram of block caving mine (after Hamlin 2001).

Understanding gravity flow of caved rock is crucial to the success of caving operations (Guest 2007) with respect to the fact that almost all caved rock consists of particles of varying sizes, densities and/or shapes. The differences in particle properties predominantly display a range of behaviour and unique characteristics upon handling process and difficult to model (Jaeger et al. 1996). For instance, under certain conditions, a granular material can flow like a fluid (Campbell 2006), or a frictional assembly of particles. With regards to this, Hutter and Scheiwiller

(1982) noted that such rapid gravity flow mechanisms are hard to adequately describe because of experimental and analytical difficulties.

In practice, gravity flow has a direct impact on the efficiency of the caving method (e.g., Just and Free 1971; Chen 1997; Pretorius 2007; Trueman et al. 2008) and this is known to affect the overall recovery and dilution ingress (Hashim et al. 2008). The relatively poor understanding of gravity flows of caved rock is currently an area of concern in the industry (Melo et al. 2006, 2007).

## 2.3 PHYSICAL AND NUMERICAL MODELS OF GRAVITY FLOW IN BLOCK CAVING

A comprehensive and detailed discussion and review on selected aspects of gravity flow and percolation in mining applications is presented by several authors (Peters 1984; Chen 1997; Gustafsson 1998; Rustan 2000; Power 2004; Halim 2004; Hashim et al. 2008; Sharrock 2008).

As a result of limited understanding of this area, the control of fines percolation, dilution and ore recovery are made more difficult. In this section, three main methods employed in gravity flow of caved rock in block caving mine are reviewed and discussed, namely: *full-scale tests*, *scaled physical models* and *numerical models.*

### 2.3.1 Full Scale Tests

Efforts to collect full scale data are fundamental. The key advantage of using the full scale tests in gravity flow studies is that scalability issues can be avoided and real outcomes measured. Nevertheless, it is worth highlighting that almost all existing tests have focused on SLC mines, while to the author’s knowledge, there is no published full scale test documented on block caving mines except by Brunton et al. (2012) at the Ridgeway Deeps Block Cave (RWD), Australia.

One drawback in full scale tests lies within the difficulty and limited access to the ore body prior to mining operations. This often delays the progress of the experiment and collection of the results (Castro 2006). Other drawbacks of full scale tests are the relatively high costs and extremely time consuming nature of testing (Sandstrom 1972; Just 1981). One clear example of this issue was reported by Alvial (1992) who made an attempt to run a partially full scale test in a block caving geometry using old tyres as markers in the extraction zone of El Teniente Mine, Chile. He reported that only 19 markers were recovered at the drawpoints of the mine within 10 years. No conclusion was published due to very limited results collected at the end of his experiment.

There are around seven published full scale tests into the study of the flow of caved rock in caving mines, and these predominantly concern SLC mines (Table 2.1). In these full scale tests, large numbers of individual markers are placed within the experimental production rings. As the markers move towards the drawzone, the coordinate of each recovered marker at certain tonnage drawn is recorded and plotted.

However, since all full scale tests were carried out within specific geometries with regards to that caving mine, often all the results were only specific to that mine and for this reason generalisation of the results on flow of caved rock in block caving mines is doubtful (Halim 2004). Additionally, this method of monitoring flow does not describe any mechanisms of flow except time taken and general direction of flow.

Table 2.1: List of published full scale gravity flow marker trials in sub-level and block caving mines.

| Location | Markers recovered | Mining Method | Researcher(s) |
|---|---|---|---|
| Grängesberg, Sweden | Approximately 70% | SLC | Janelid (1972) |
| He-Pei, China | Approximately 60% | SLC | Chen and Boshkov (1981); Rustan (2000) |
| El Teniente Mine, Chile (partially full scale test) | 19 markers over 10 years (no conclusion been made) | BC | Alvial (1992) |
| Kiruna, Sweden | Approximately 30% | SLC | Gustafsson (1998); Quinteiro et al. (2001) |
| Perseverance, Australia | Approximately 53% | SLC | Hollins and Trucker (2004) |
| Ridgeway, Australia | 56% (primary) 75% (secondary) | SLC | Brunton (2008) |
| Ridgeway Deeps Block Cave, Australia | Approximately 80% | BC | Brunton et al. (2012) |

Nevertheless, work is underway to develop smart markers[12]. One example is the *Smart Marker System* which can be tracked within the cave (Elexon Electronics 2009) as illustrated in Table 2.2. Alternatively, smart markers would provide data to allow real time adaptation of draw schedules, and vastly improve the knowledge base of gravity flow. One advantage of this method is the markers path will be recorded and hence the effect of mine geometry such as block height and draw point spacing can be studied which is not the case with conventional markers (i.e., tyre and plastic tube). Full scale marker trial tests are however underway at a number of mines including Ridgeway Deeps Block Cave in Cadia Valley, Australia.

[12] Elexon Electronics refers the Smart Markers as "*….blast resistant, long-life Radio Frequency Identification (RFID) devices that are placed in the ore body of sub-level or block cave mines. The Smart Marker System automatically detects, logs and time stamps Smart Markers as they are extracted with ore at the production level. It collects installation and extraction data in real time*".

Table 2.2: Schematic flow of the smart marker system application (after Elexon Electronics 2009).

| Illustration | Process | Description |
|---|---|---|
|  | Installation | Readers are installed above locations where the Load-Haul-Dump (LHD), extracting ore and Smart Markers likely to travel. Smart Markers are then activated and installed in the ore body, or are 'fed' to the cave |
| 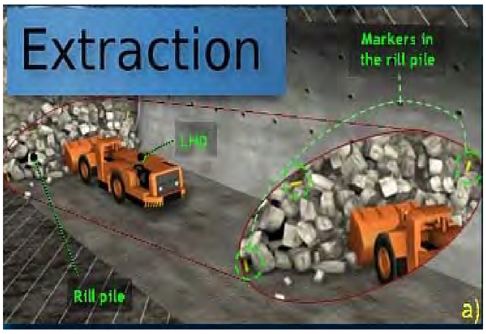 | Extraction | After installation, Smart Markers flow with the ore to the drawpoint.<br><br>The LHD vehicle loads ore and any Smart Markers into its bucket. |
|  | Detection | Readers mounted to the 'back' (ceiling) of the mine automatically detect Smart Markers in the LHD bucket (allowing the draw point to be established). Reader data is then transferred to the surface via network or Bluetooth download to a Scanner. |
| 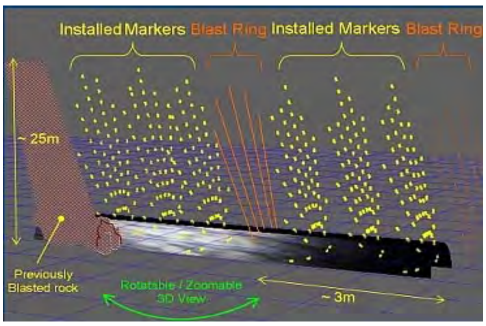 | Analysis | Underground rock flow analysis begins as soon as Smart Markers are automatically detected. Graphical tools and/or analysis tools were then used to analyse the data. |

It is apparent that in the study of gravity flow in sub-level and block caving mines, full scale tests have received very limited attention. However, any attempt to improve the collection of flow data is valuable toward in moving better understanding in the real practice environment of caving mine operation.

### 2.3.2 Scaled Physical Modelling

Scaled physical modelling was one of the earliest methods employed to simulate gravity flow of caved rock. In general, scaled physical modelling of block caving mines can be referred to the physical copy or replication of a specific block caving mine. Examples of comprehensive description on significant modelling studies concentrating on the *Isolated Extraction Zone* (IEZ)[13] descriptions is available by Sharrock (2008) and presented in Appendix A.

In ideal circumstances, a properly designed physical model or laboratory model "*should behave in all respects like a controlled (usually miniature) version of prototype*" (Hughes 1993). Sterrett (2002) noted that "*Scale modelling that is based on the principle of physical similarity is a method for predicting the behaviour of certain quantifies in a specific, complex situation*".

According to Schuring (1977), the scale reproduction of a physical model provides some advantages as follows:

- ability to analytically perform any experimental works with empirical information;
- scale models permit transformation of one system to manageable proportions of required systems to be conducted;
- shorten experimentation period; and
- promote a deeper understanding of the phenomenon under investigation.

[13] Isolated Extraction Zone (IEZ) refers to an extraction zone isolated from other extraction zones/level as a result of drawing from an isolated drawpoint.

The significance of choice of scale in physical modelling work has been addressed by a number of authors. With regards to this, Langhaar (1951) stated that the use of scale models are necessary, based on the fact that physical quantities can be fully described by the fundamental laws of mechanics. Nevertheless, very little research has been conducted on the impact of scale on model accuracy. Most physical models of block caves have been conducted at either scales of 1:100, 1:30 or 1:20.

In general much of the published work has concluded that larger scale models are better (Janelid 1972; Sandstrom 1972; Power 2004). However, given the materials handling difficulties and subsequent length of experiments (McMurray 1976; Just 1981), it is more effective to conduct experiments at a smaller scale, if they can be demonstrated to provide results comparable to those of larger scale physical models.

Castro (2006) and Castro et al. (2006) employed a three-dimensional (3D) scaled physical model to study flow in block caving using gravel as the model media. The model had dimensions of 3.5 m (length) x 2.5 m (width) x 3.3 m (height). The physical model could hold approximately 55 tonnes of aggregate as shown in Figure 2.2. He then repeated the experiments previously undertaken at 1:30 scale by Power (2004). Using a 1:100 scaled 3D physical model, Castro (2006) reported findings that contradicted Power’s assertion on the effect of particle size on draw width. He also found that there was no significant distortions between scales on the extraction zone and reported that results from a 1:100 model could be used to obtain those in a 1:30 scale. These findings offer the possibility for extrapolation from 1:100 scale to full scale of a caving mine and by far in contradiction with previous assertion that greater scale may produce more reliable results than smaller scale.


Figure 2.2: Large 3D Julius Kruttschnitt Mineral Research Centre (JKMRC) physical model (after Castro et al. 2006).

In view of the above findings, it is concluded that there is still room for further improvement to the effectiveness of the scale models in understanding gravity flow. Large scale physical models may be expected to produce better results and more closely represent the actual caving mine but at the same time increase the material handling requirements and limit the overall dimension of the caving mine that can be modelled.

Hence, it is concluded that there is potential for small scale models, perhaps using centrifuges to achieve force similitude, to provide more reliable data. Therefore, quantitative work and validation on the effect of scale within the physical models are still required. Nevertheless, efforts to improve the understanding in gravity flow of caved rock still motivated and performed on two types of media: sand grains (e.g., Kvapil 1965a, 1965b, 1992; Janelid and Kvapil 1966; Marano 1980; Heslop and Laubscher 1981) or gravel models (e.g., Janelid 1972; Peters 1984; Power 2004; Castro 2006).

#### *2.3.2.1 Sand models*

The use of sand materials in early experiments allowed small scale models of large systems to be run but at the cost of model similitude (Section 2.4). Another reason to the use of sand models is the ability of sand to behave alternately as a “liquid-like” or as a “solid-like” material to the response of external forces on a different time scale (Barker 1994). For example, the sand particles have greater mobility, and hence tend to behave as a “liquid” based on its ability to flow out of a smooth-sided hopper or even when it is moving down towards an inclined chute. Conversely, sand particles tend to behave as a “solid” as it forms into a pile or when it is confined to a container. During this stage they will externally support applied stresses with a minimum deformation.

Accordingly, some work on the sand models is still relevant and has initiated many important findings. Kvapil’s ellipsoid theory (Kvapil 1965a, 1965b, 1992; Janelid and Kvapil 1966) is one of the best examples of a sand model that is still used as a design guideline in some SLC mines around the world. Using a 2D Type A – Classic Gravity Flow Model, Kvapil (1965a) constructed a simple sand model that has a vertical axis of the gravity flow. The front wall is constructed of glass. This model intersects with the centre of an extraction opening located at the bottom of the bin while it was filled with layered black and white sand. As the opening slot at the bottom of the bin was opened, the sand flowed out, generating certain phases as illustrated by Figure 2.3.

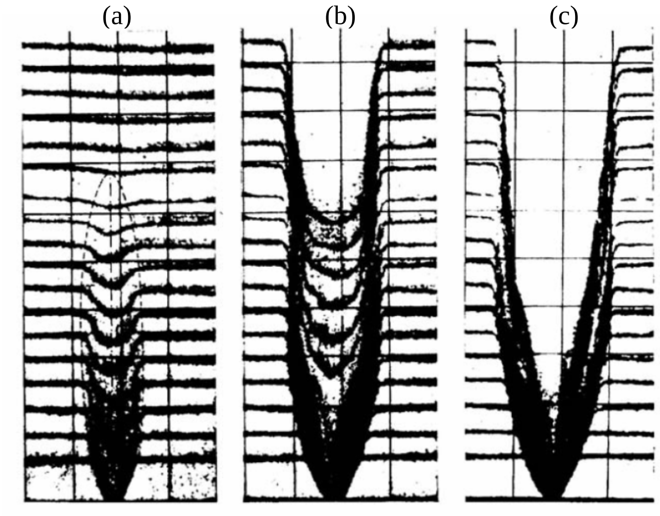


Figure 2.3: Kvapil Type A – 2D Classic Gravity Flow Models (after Kvapil 1965a). Note: (a) Early draw stages (b) Intermediate draw stages (c) Prior to the draw stage.

Subsequent to this work, Kvapil proposed the concept of “ellipsoid of motion” to describe the geometry of granular flow (i.e. caved rock) and used terms of *ellipsoid of loosening* and *ellipsoid of extraction* to describe two types of flow volume in an ellipsoid of motion. The ellipsoid of loosening can be referred to the limiting outline that defines the original location of material that has been drawn from an outlet (or draw point) at any given point. While the ellipsoid of extraction referred to as the limiting outline that describes the boundary between stationary material and that which has moved from its original location at a given extracted mass (or extracted material with volume $V_c$) as illustrated in Figure 2.4.

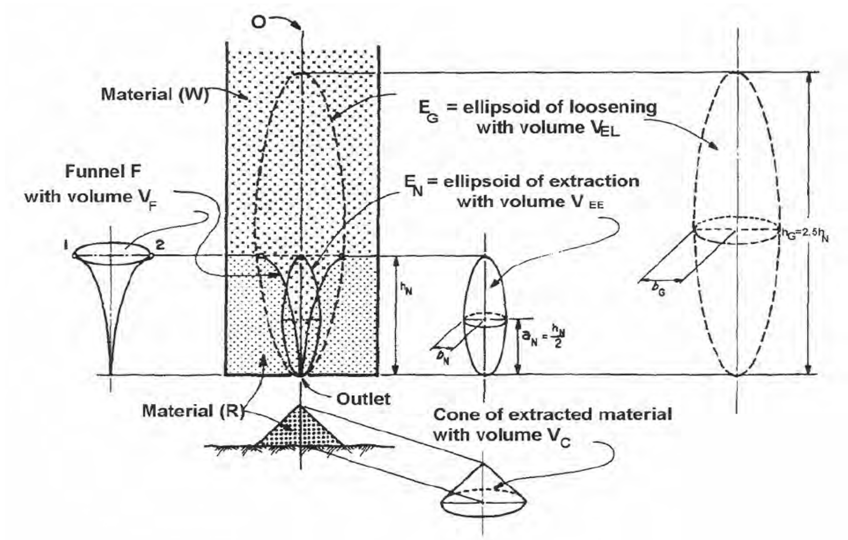


Figure 2.4: The ellipsoid theory (after Kvapil 1992).

Kvapil also concluded that the eccentricity of the ellipsoid of motion was a function of particle size where the finer the sands the model had, the slimmer and more elongate were the ellipsoid of motion be (Kvapil 1965a) as illustrated in Figure 2.5. In addition, Kvapil also noted that the ellipsoid's eccentricity is depends on a number of factor such as particle size, ellipsoid's height, discharge rate, shape and form of the fragment, percentage of fines, sand and clay, moisture content and the magnitude, distribution and direction of external loads and forces (Kvapil 2004). Later, based on the ellipsoid theory, Janelid and Kvapil (1966) published a paper that proposed general design rules for the design of sub-level layouts that is widely used as a design guideline in many SLC mines.

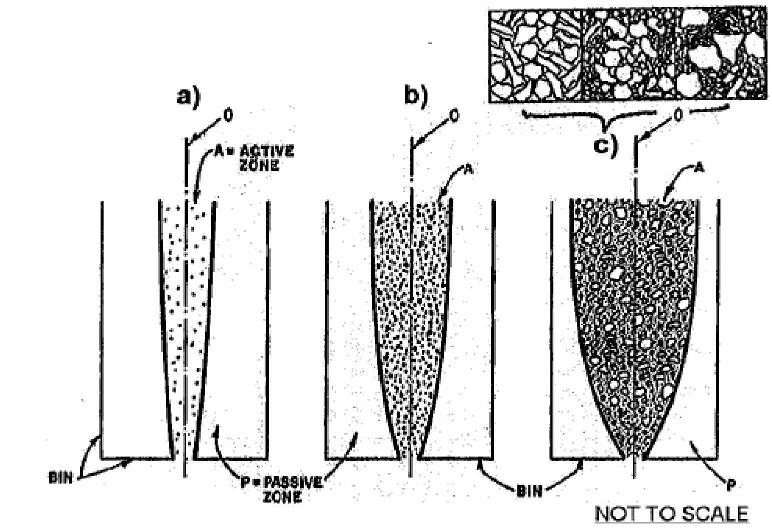


Figure 2.5: The width of the gravity flow stream as a function of material type (after Kvapil 2004). Note: (a) Very fine material (b) Granular material (c) Coarse material.

However, the validity of Kvapil's ellipsoid theory did receive some argument from other sand modellers. Marano (1980) and Laubscher (2000) used a 3D sand model which was specifically built to investigate interactive drawing of adjacent drawpoints. It was found that the shape of the body of motion resembles a cylinder with cone shape at the base thus conclude that the ellipsoid theory does not model the flow accurately. However, this conclusion appeared to be questioned as there was no detailed explanation on how the deduction was made based on the model experiments.

Some major drawbacks in sand models were reported such as inaccuracy of measuring the zone extracted material (Halim 2004), the shape effect, low friction angle and scalable issue. It is noted that unlike gravel, sand grains are more spherical than the actual block in caved rock. The caved rock is better represented by crushed gravel (Campbell 1990). Furthermore, the lower friction angle of sand compared to that of gravel significantly affects the draw width (Janelid 1972). On the other hand, it is also found that the sand particles when scaled up do not resemble the actual fragmentation of caved rock due to the fact that most current block caving mines have very coarse caved ore (Halim 2004) compared to fine and rounded particles.

#### *2.3.2.2 Gravel models*

Gravel offers closer geometric similarity with a caved rock but the feasible model size is restrained by the geometric scale factor, which is has a maximum value of 1:20 (Janelid 1972) and/or 1:30 scale (Power 2004). In contrast, there is evidence that reliable results may be obtained using a 1:100 scale model (Castro 2006).

Subsequent to development of ellipsoid theory by Kvapil (1965a, 1965b), Janelid (1972) carried out experiments in a 3D model of a 1:20 scale against the full scale test done at Grängesberg mine in Sweden. The test was run using gravel generated by the crushed ore from Grängesberg mine. It was found that the breadth and depth of the flow were almost identical. In view of this, Janelid (1972) attributes those finding was due to the less packed and more moveable material used in the model. It is worth highlighting that no general rules for the flow of caved rock were formulated due to the fact that the model was built specifically for that mine.

Peters (1984) built a 2D gravel model with a dimension of 4.5 m (height) x 3.6 m (length) and 0.5 m (width) to investigate the effect of particles size and drawpoint width on the size and shape of the zone of drawn material for a single drawpoint condition. He found that the draw envelope is not affected by the particle size which contradicted Kvapil’s ellipsoid theory and later the conclusion was challenged by Power (2004).

Subsequent to Peters (1984) studies, Power (2004) built a large scale 3D gravel model with a dimension of 2.2 m (length) x 2.1 m (width) x 3.3 m (height) at a scale of 1:30. The model was used to study the effect of particle sizes to the draw zone width. Power's model results demonstrated that particle size does affect draw width. For instance, Power found that the coarse particles will yield wider draw zone than fine ones (such as in sand models). This finding accords with Kvapil's (Kvapil 1965a) and Nedderman's (Nedderman 1995) research. With regard to the differences between his findings to the Peters' results, Power postulated that this is due to the 2D nature of the physical model and 3D nature of the full scale.

Similarly objective to the Janelid's experiments (Janelid 1972), Power (2004) conducted and compared the results of a 3D gravel model at a 1:30 scale against his full scale test employed by himself at the Ridgeway SLC Mine, Australia. It was found that the results were directly scalable with the exception of the depth of the draw zone. It is interesting to highlight that based on a 1:30 scale or greater as a general guideline, Power concluded that there was evidence to suggest that if the scale of the physical model was large enough, it may be possible to produce better results than with the smaller scale model. This was later challenged by Castro (2006) as previously discussed in Section 2.3.2.

### 2.3.3 Numerical Models

Numerical models have proven to be a powerful tool in the investigation of granular flows (Campbell 1989; Savage and Dai 1993; Rosato and Kim 1994; Pierce et al. 2003). Since the costs of construction and time constraints relative to the immediate needs of an active mine often limit the usefulness of physical modelling (McNearny and Barker 1998), the numerical models offer an alternative method to study gravity flow of caved rock.

If the characteristics of the in-situ material, mining geometries and in-situ stresses are well understood, the numerical modelling can be used to predict the geometry and behaviour of various aspects of caving mines. In view of this, the numerical modelling can be divided into three approaches: the *continuum mechanics methods*, *discontinuum mechanics methods* and *hybrid/coupled continuum-discontinuum codes*.

#### *2.3.3.1 Continuum mechanics methods*

In continuum mechanical methods, granular materials are treated as continua. Continuum methods are concerned with the mechanical behaviour of a granular media that behaves as a fluid (Tardos 1997; Karlsson et al. 1999) or a solid on the macroscopic level (Spencer 1980). These physical properties are then represented by tensors and expressed in coordinate systems for computational convenience. One assumption on this method is that the material properties of the ensemble may be represented by continuous functions so that the medium may be divided infinitely without losing any of its intrinsic properties (Ng et al. 2008).

Some continuum theories adopt a complex mathematical approach and are limited to the representation of spherical shape particles. Although these models are partially successful in capturing some characteristics of the flow, they do not incorporate information on the particle micro-mechanics, which influence the material parameters (Christakis et al. 2002).

This is crucial as these findings are needed to model the various interactions between different particles or particles with their surrounding environment. As a result, they are not able to simulate processes that are of great importance in mining applications (i.e., hopper filling/emptying, ore handling and conveying), where these interactions lead to phenomena such as particle size segregation (Christakis et al. 2002) that potentially lead to dilution problem in an ore draw zone.

Aranson and Tsimring (2001) developed a continuum description of partially fluidized granular flows based on the hydrodynamic equation for the flow coupled with the other parameter equation. The method was able to describe the transition between a flowing and statics component of the arbitrary system in thin granular layer on inclined planes with rough bottom. Several important features were also reported including the structure of the stability diagram, the triangular shape of downhill avalanches at small inclination angles, and the sphere on shape of uphill avalanches for larger angles.

There is some discrepancy in the reliability of continuum mechanics in representing granular flow. For instance, Rycroft et al. (2009) noted that recent work on granular materials may suggest inapplicability of continuum law in revealing inhomogeneities at the particle level such as force chains and slow cage breaking. While some of the continuum mechanic methods may be able to capture some mechanisms involved in caved rock, such methods lack sufficient theoretical understanding and accordingly still need to be validated through the experimentation (Castro 2006).

#### *2.3.3.2 Discontinuum mechanics methods*

Discontinuum mechanics and the associated problem of discontinuous boundaries has been given a vast attention recently. Some examples of program based on this method are *Particle Flow Code* (PFC) (Cundall and Strack 1979a), *Discontinuous Deformation Analysis* (DDA) (Shi 1988) and *Cellular Automata* (CA) (Baxter and Behringer 1991).

Cellular automata consists of a regular and repetitive arrangement of an array of similar cells which allowed it to have a finite and discrete set of possible states. Based on the rules that depend only on the local neighbourhood state, the cell state in the arrangement is updated simultaneously in space at discrete time intervals.

An early application of 3D cellular automata to caving is documented in Sharrock (1999). The method has subsequently been calibrated to a large scale physical modelling tests, marker trials data, and anecdotal evidence of flow at a large number of sub-level and block caving operations. Percolation has been included as a model parameter, but these models rely on assumptions from previous work in chemical and civil engineering. As a consequence, further development and validation from actual caving and targeted experimental studies is required.

On the other hand, Particle Flow Code in Three Dimensions (PFC3D$^{TM}$) (Itasca 1999, 2005b, 2008b) which employs an explicit time-stepping algorithm is one of the finest examples of DEM model and was first introduced by Cundall and Strack (1979a). It offers several advantages including the ability to simulate a wide variety of caved rock situations, inter-body attraction laws and arbitrary geometries and allows a more detailed study of the micro-mechanics of the granular assemblies (Jing and Hudson 2002; Ng 2005).

In general, DEM was run in such a way that the contact forces were computed and resulted in Newtonian dynamics of individual particles in an assembly (Itasca 2005b). As a result, the distribution of shear and normal force, rotation, velocity and displacement are determined in two dimensions for each particle. Significant progress has been developed in DEM method since its first introduction. Table 2.3 summarised the significant DEM computer codes developed for granular flow modelling.

Unlike some other numerical methods, DEM can also be run in parallel processing which means that it can be run faster at a greater number of particles using a cluster of core-processors (Hancock et al. 2010). However, it has been argued that some drawback arise with regard to a number of particles and particle shape limitations (Beus et al. 1999) especially when modelling the large scale systems (Hogue and Newland 1993) and in many cases remains unvalidated.

Fraige et al. (2008) and Powrie et al. (2005) noted that modelling non-uniform shapes in DEM becomes essential for better understanding of granular material behaviour. Based on quarter-symmetry PFC3D$^{TM}$ simulations, Pierce et al. (2003) were able to prove that the particle shape (and size) significantly influences the flow of particles in the *Isolated Draw Zone* (IDZ)[14] .

[14] Isolated Draw Zone (IDS) refers to a draw zone isolated from other draw zones as a result of drawing from an isolated drawpoint.

Table 2.3: Examples of DEM computer codes (after Akram and Sharrock 2009).

| Year | Author/s | Computer code | Dimension |
|---|---|---|---|
| 1978 | Cundall (Cundall 1974) | RBM | 2D |
| 1978 | Cundall (Cundall 1978) | BALL | 2D |
| 1979 | Cundall and Strack (Cundall and Strack 1979b) | TRUBALL | 2D |
| 1985 | Cundall-Itasca | UDEC | 2D |
| 1985 | Bagster and Kirk (Bagster and Kirk 1985) | Model Heap | 2D |
| 1986 | Corkum (Ting et al. 1989) | DISC | 2D |
| 1987 | Cundall | PFC2D/PFC3D | 2D/3D |
| 1988 | Cundall (Cundall 1988) | 3DEC | 3D |
| 1988 | Walton (Walton et al. 1988) | 3DSHEAR | 3D |
| 1989 | Bathurst and Rothenburg (Bathurst and Rothenburg 1989) | GLUE | 2D |
| 1989 | Williams and Pentland (Williams and Pentland 1989) | Unnamed code | 3D |
| 1989 | Taylor and Preece (Taylor and Preece 1989) | DMC | 2D |
| 1989 | Ng (Ng 1989) | CONBALL | 2D |
| 1990 | Ghaboussi and Barbosa (Ghaboussi 1990) | BLOCKS3D | 3D |
| 1991 | Ng and Dobry (Ng and Dobry 1991) | CONBALL | 3D |
| 1991 | Hakuno and Yamamoto (Hakuno and Yamamoto 1991) | Unnamed code | 2D |
| 1992 | Rothenburg and Bathurst (Rothenburg and Bathurst 1991) | ELLIPSE2D | 2D |
| 1992 | Mishra and Rajmani (Mishra and Rajamani 1992) | 2DMILL | 2D |
| 1993 | Cleary (Clearly 1993) | Unnamed code | 2D |
| 1994 | Hill and Zheng (Hill and Zheng 1994) | Granular | 2D |
| 1995 | Donz´e and Magnier | YADE | 3D |
| 1996 | Muller (Muller 1996) | Discs-Polyhedra | 2D |
| 1996 | Kovestsky | Unnamed code | 3D |
| 1997 | Xu and Yu (Xu and Yu 1997) | ELLIPSE3D | 3D |
| 1997 | Lin and Ng (Lin and Ng 1997) | Unnamed code | 3D |
| 1997 | Hustrulid and Brown (Hustrulid 1997) | Parallel DEM | 2D |
| 1999 | Sharrock (Sharrock 2003) | 2DFLOW and 3DFLOW Distributed DEM (disc) | 3D |
| 2000 | CSIRO – Muhlhaus | FASTDISC | 2D |
| 2001 | ELFIN | Coupled FEM – DEM | 3D |
| 2002 | CSIRO - Cleary | Parallel code–spheres, discs | 3D |
| 2006 | ACcESS MNRF | ESYS_Particle | 3D |
| 2007 | DEM Solutions Ltd. | EDEM | 3D |
| 2008 | (Weatherley 2009) | ESYS, High performance parallel code - spheres | 3D |

Despite the fact that particle shape is known to affect the flow properties of caved rock, most DEM computer codes still represent granule and highly angular shapes as circular discs in 2D or spheres in 3D (Sakakibara et al. 2008). The main reason for the ongoing use of discs and spheres is reduced contact detection time and this allows significantly shorter processing time for discs and spherical particles, as compared to non-uniform particles (Campbell 1990; Clearly and Sawly 2002; Fraige et al. 2008).

At present, most numerical methods are limited to relatively small number of particles and generally limited to spherical particles. Existing DEM computer codes running on high performance computers, at best deal with in the order of 10 milion particles of spherical shape while by contrast, CA methods can deal with as many as 100 million particles. It is postulated that within the above particle limit, representation of a large number of highly angular shaped and size distribution of an actual caved rock is by far comparatively inadequate.

Sharrock and Hashim (2009) estimated that nearly 300 billion angular 3D particles are required to numerically replicate a full volume of a 1 mm - 5 mm highly angular particles into 2.5 m (height) x 1.2 m (width) x 1.2 m (length) of a simply scaled physical model. Therefore, based on current computer technology, a full representation of the complexities of even a relatively simple scaled physical model cannot as yet be achieved with confidence.

#### *2.3.3.3 Hybrid/Coupled continuum-discontinuum methods*

The hybrid or coupled continuum-discontinuum methods are combinations of both input parameters of the particles and continua. In this manner, hybrid codes run as stand alone computer codes with a possibility of element transformation of granular (or continuum method) into discontinua (or discontinuum method) and vice versa.

One example of the hybrid codes is found in a study of the evaluation of damage-induced permeability conducted by Fabian et al. (2006) called *Adaptive Continuum/ Discontinuum Code* (AC/DC). In principle AC/DC is operating based on the use of a periodic discontinuum “base brick” of PFC (Itasca 2003) for which more or less simplified continuum equivalents are derived. AC/DC code can dynamically select the appropriate “brick” type to be used according to the level of deformation in each part of the model.

In the case of rock damage caused by excavation, the discontinuum models are used in which the particles were assemblies and the breakage of bond under stress were performed and recorded. Since a large part of most models experiences minimum rate of strain, an accurate description of such post-peak behaviour and large-strain were not required. Thus, a large model frequently can be separated into a strongly strained “core” area to be represented by a discontinuum and a peripheral area for which the continuum zones would be adequate as illustrated by Figure 2.6.

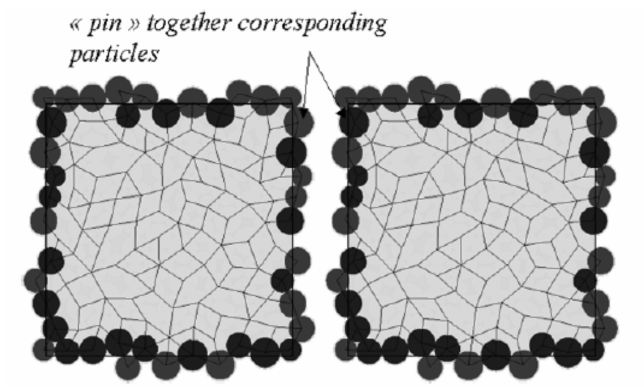


Figure 2.6: Particle configurations in AC/DC hybrid “base brick” (after Fabian et al. 2006). The code was run by creating a discontinuum model in zones where damage is happening or likely to happen and a continuum model elsewhere.

Saiang (2009) performed coupled analysis using the continuum and coupled continuum–discontinuum methods to study the behaviour of the blast-induced damage zone around the tunnel. Discontinuum methods of DEM namely PFC2D (Itasca 2008a) were employed to simulated the inner segment of the model, while the outer segment was simulated using the FLAC (Itasca 2005a).

In this study, FLAC was selected as a server while PFC2D as a client to simulate contact establishment between the two codes. On the other hand, synchronization of the cycling in both codes was performed simultaneously in order to determine the actual displacements of the blast-induced damage zone around the tunnel. During the process, a series of walls is created in PFC2D while at the same time each wall was corresponded to a single surface segment of a FLAC zone as shown in Figure 2.7.

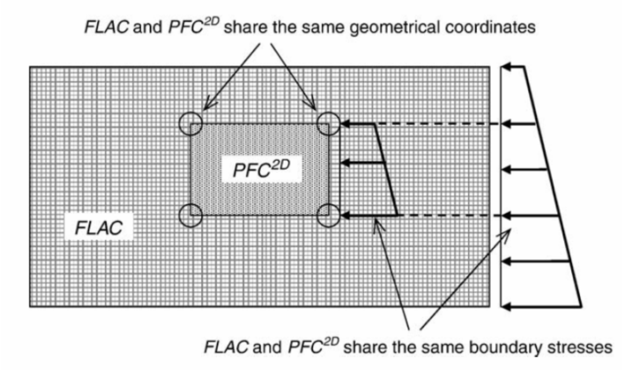


Figure 2.7: Illustration of the important features for coupling of FLAC and PFC2D (after Saiang 2009). Inner segment of the model is modelled by PFC2D, while the outer segment was simulated using FLAC.

However, since most hybrid codes are still under development, some limitations occurred due to ongoing calibration requirements, coupled with intensive computational demands whilst running codes. Nevertheless, given the ongoing advancement of computer technology, hybrid codes have a potential to overcome some limitations that arise from discontinuun and continuum methods.

### 2.3.4 Summary

Based on a detailed review of methods to simulate gravity flow in block caving, it is concluded that no one method is capable of producing reliable results towards better understanding of gravity flow in block caving.

Physical modelling is still relevant and appears to be a potential for changes to industry standards but have to deal with the appropriate scale, costs of construction and time constraints relative to the immediate needs of an active mine. While it is no doubt best to obtain percolation data from full scale tests, these are expensive, time consuming and the parameters of interest are difficult to measure thus resulting in limitations to further interest to the researcher.

On the other hand, numerical modelling has proven to be a powerful tool for this purpose especially in providing insight into the micromechanics of caved rock interactions. However, these remain largely unvalidated due to the lack of reliable data. Moreover, all numerical methods rely heavily on computing speed and time especially when modelling the large-scale systems with complex particles with highly angular shape.

As this cannot be achieved with current methods and technologies, results from numerical model are perhaps best compared on the basis of mechanistic and non-qualitative analysis and validated with both physical models and/or full scale test data.

## 2.4 SIMILITUDE

In order to accurately represent actual full scale environments, similitude to similar conditions is necessary if useful results are to be produced. Hughes (1993) noted "*Similitude is achieved when all major factors influencing reactions are in proportion between prototype and model, while those factors that are not in proportion throughout the modelled domain are so small as to be insignificant to the process*".

Castro et al. (2006) proposed six criteria to achieve suitable similitude between the two scale models of caved rock:

- geometrical similitude for the whole block dimensions, drawpoint dimensions, particle size distribution and particle shape;
- the gravity ($\lambda_g$) and bulk density ($\lambda_\rho$) in the two models must be the same;
- the scale of stresses must be the related to that of length, ($\lambda_\sigma = \lambda_\tau = \lambda_l$);
- the wall friction angle ($\phi_w$) should be similar to the internal friction angle ($\phi$);
- the time taken or timing of event ($\lambda_t$) must be related to the square root of the length scaling factor ($\lambda_l$) (or $\lambda_t = \lambda_l^{1/2}$); and

- the residual friction angles ( $\lambda_{\phi_r}$ ) in which its refer to the material's constant under shear must be the same.

In order to generate reliable results, there are three conditions which must be met to achieve similitude between a scaled model and a full-scale environment: the *dynamic similitude*, *kinematic similitude* and *geometric similitude* (Schuring 1977).

### 2.4.1 Dynamic Similitude

Understanding the dynamics of caved rock in caving mines is essential since most granular material handling systems behave unpredictably (and in some cases are irreproducible) (Goldhirsch 1999). Dynamic similitude refers to the scaling forces such as the compaction, vertical stress and horizontal stress within the model. This means that the ratio between forces acting on both particles and boundaries in the model and full-scale situation must be constant (Halim 2004) and this makes it far more complex than geometric and/or kinematic similitude.

It is worth highlighting that it is almost impossible to achieve full dynamic similitude using a scaled-down physical model (Pöschel et al. 2001) as one cannot scale all the forces on a particle in the physical model. As yet there is no evidence nor any published article that reports that anyone has been able to achieve full dynamic similarity in the physical models of caved rock.

Nevertheless as the draw rate is expressed as tons/day, two parameters that can be scaled down are mass and time; respectively. With regards to this, Castro (2003) suggested that the draw rate is probably one parameter of dynamic similitude in caving model that is possible to be scaled down with physical models with following equations:

#### *2.4.1.1 Mass scale factor*

Mass, $m$ (kg) is the product of the density, $\rho$ (kg/m³) and volume, $V$ (m³) and can be expressed as

$$m = \rho V = \rho L^3$$

$$\rho = \frac{m}{L^3} \quad \text{(Equation 2.1)}$$

Where $L$ = length

By scaling the $L$ by a factor $k$,

$$m' = \rho'(kL)^3$$

$$\rho' = \frac{m'}{(kL)^3} \quad \text{(Equation 2.2)}$$

where $m'$ = mass scale, $\rho'$ = density scale

If the rock type is similar for both the model and the mine, the density is equal

$$\rho = \rho' \quad \text{(Equation 2.3)}$$

Therefore, substituting Equation 2.1 and Equation 2.2 into Equation 2.3, given the mass scale, $m'$

$$\frac{m}{L^3} = \frac{m'}{(kL)^3}$$

$$m' = k^3 m \quad \text{(Equation 2.4)}$$

The mass scale factor is $k^3$.

#### *2.4.1.2 Time scale factor*

In order to ensure that the particle acceleration is analogous in both the full scale operation and within the scaled model, the time scale factor can be derived from the acceleration formula:

$$a = \frac{l}{t^2} \quad \text{(Equation 2.5)}$$

Where $a$ = acceleration (m/s$^2$), $l$ = travel distance (m), $t$ =time (s)

Since acceleration experienced by the particle must be the same in both full scale operation, $a_{actual}$ and within the scaled model, $a_{scaled}$ therefore

$$a_{actual} = a_{scaled}$$

$$\frac{l_{actual}}{t_{actual}^{\;2}} = \frac{l_{scaled}}{t_{scaled}^{\;2}}$$

$$\left(\frac{t_{scaled}}{t_{actual}}\right)^2 = \frac{l_{scaled}}{l_{actual}} \qquad \text{(Equation 2.6)}$$

By scaling the $\frac{l_{scaled}}{l_{actual}}$ by a factor of $k$

$$k = \left(\frac{t_{scaled}}{t_{actual}}\right)^2 \qquad \text{(Equation 2.7)}$$

If the time scale, $t'$ be expressed as

$$t' = \frac{t_{scaled}}{t_{actual}} \qquad \text{(Equation 2.8)}$$

Therefore, substituting Equation 2.7 and Equation 2.8 into Equation 2.6,

$$k = (t')^2$$

$$t' = \sqrt{k} \qquad \text{(Equation 2.9)}$$

The time scale factor is $\sqrt{k}$ .

### 2.4.2 Kinematic Similitude

Kinematic similitude is described as ensuring the motion and acceleration of a particle in the model is similar to that experienced in a full scale block cave. According to Hudson et al. (1979), kinematic similitude can be achieved when the ratio between the components of all vectorial motion for the scaled model is the same for all particles at all time.

Further, it is worth noting that although it is impossible to realistically archive full dynamic similitude in the physical modelling, some authors have assumed that this would not have enough of an impact on the kinematic similarity that might counteract the effectiveness of the physical model (Power 2004). These circumstances can be best addressed by minimising any dynamic dissimilarity that may arise during modelling of physical models.

### 2.4.3 Geometric Similitude

Geometric similarity refers to the length aspects of the model in which the vertical and horizontal scales are the same (Hughes 1993). In other words, geometric similitude ensures that all elements of the model have the same shape as in the full-scale situation. Some authors have stated that a reasonable approximation of geometric similitude can be achieved in scaled physical models (Power 2004; Halim 2006). Nevertheless these claims may be argued since most of the work presented still could not adequately represent real caved rock fragmentation sizes (Laubscher 1994) thus far removed from the real caved fragmentation sizes. A detailed discussion on this is presented in Section 4.4.1.

Parameters such as particle size, shape and distribution can be scaled with minimal difficulty. This also applies to the size, shape and orientation of drawpoints which can be designed to a desired scale. The significant demonstration of useful results achieved by modelling a particular process at the appropriate scale conditions to achieve geometric similitude are shown by work of Peters (1984), Power (2004) and Halim (2006).

Based on scalable calculation of an average rate of draw using load-haul-dump (LHD) equipment that operates in most of the block caving mines, Castro (2006) proposed a scaled set of instantaneous draw rates at different geometrical scales as shown in Table 2.4.

Table 2.4: Draw rates for different scales (after Castro 2006).

| Geometric scale factor ( $\lambda_L$ ) | Mine effective draw rate (Q, t/hr) | Mine instantaneous draw rate (t/day) | Draw scale factor ( $\lambda_Q$ ) | Model instantaneous draw rate (kg/hr) | Model effective draw rate (kg/day) |
|---|---|---|---|---|---|
| 1:30 | 200 - 300 | 100 - 600 | 2.03E-04 | 40 - 60 | 20 - 122 |
| 1:50 | 200 - 300 | 100 - 600 | 5.66E-05 | 11 - 17 | 6 - 34 |
| 1:100 | 200 - 300 | 100 - 600 | 1.00E-05 | 2 - 3 | 1 - 6 |

It is noteworthy to highlight that several factors have been assumed in generating Table 2.4:

- the media is non-cohesive and moving slowly under the influence of gravity;
- the media is heterogeneous but isotropic;
- interstitial fluid dynamics are not considered;
- breakage mechanisms are not considered; and
- the model is 3D without special weak boundaries.

Given this simplified and idealised model of caved rock, the applicability of these draw rates for scaling similitude is still questionable. Nevertheless, the work indicates that it is possible to at least scale down one parameter of dynamic similitude with geometric similitude as demonstrated in Castro's work.

### 2.4.4 Summary of Similitude in Scaled Physical Models of Caving

Based on current achievements in the physical and numerical studies, full similitude of a scale physical model with regard to a caving operation has not been firmly established and requires more study. As achieving full similitude is almost impossible, attempts to minimise the effect of dissimilarities within the scale model is essential especially in relation to those referring to the dynamic similitude and/or kinematic similitude.

## 2.5 PERCOLATION OF FINE PARTICLES IN BLOCK CAVING MINES

### 2.5.1 Introduction

The flow of caved rock is a critical part of a block caving and SLC mining operations (Cleary and Sawley 2002; Brown 2003; Guest 2007; Castro and Trueman 2008). Caved rock consists of particles of varying sizes, densities and/or shapes is exposed to segregation during gravity flow (Gray and Thornton 2005). In some cases, the segregation will have significant influence on economics of the operation (previously discussed in Section 1.1) due to the physical and mechanical properties differences (Jha et al. 2008) of caved rock.

There is very little research devoted to percolation in mining applications. Most of the work on percolation has emerged in powder or chemical applications and an understanding of the percolation of particle mechanisms in caving is still emerging. Segregation is defined as a phenomenon whereby a flowing granular mass consisting of particles with diverse physical properties becomes spatially inhomogeneous (Rosato and Blackmore 2000). Segregation has been classified differently depending on variables of preferences for instance where there exist differences in the size, density, shape, composition and structure (Hogg 2003). However, the most commonly used classification approach appears to be "segregation mechanisms" (Tang and Puri 2004).

Table 2.5 describes all the mechanisms of segregation identified by previous researchers (Mosby et al. 1996a; de Silva et al. 2000) that occur in processing and handling of granular solids while Figure 2.8 illustrates mechanisms of segregation. Segregation phenomena can arise from percolation induced by gravity flow and vibration (Mosby et al. 1996b).

Ottino and Khakhar (2000) noted that differences in particle properties may induce segregation upon handling and other processes. Enstad (2001) noted that percolation, displacement, diffusion segregation and agglomeration segregation are usually not active during filling of heaps but which may be active and important in other situations (i.e., ore extraction).

Percolation segregation is the most dominant mechanism during conveying, storage, flow and mixing process (Jha and Puri 2010) which generally can take place in mining operations. A review of percolation of caved rock in the SLC and block caving is discussed in the next section.

Table 2.5: Mechanism and description of segregation (adapted after Mosby et al. 1996a and de Silva et al. 2000).

| Mechanism | Description | Cause |
|---|---|---|
| Angle of repose | Different components are sequentially filled onto a heap while the lower angle of repose component flows towards the edges of a heap. | Angle of repose |
| Embedding | Larger or denser particles to penetrate a layer on the surface of a heap at its apex, and become locked there. | Inertia |
| Air current | A mechanism caused by handling regimes (i.e., in the present of air flow) which carry fine particles and deposits them far away from the deposition point. On the other hand the coarse particles remain close to the deposition point. | Air current entrainment |
| Rolling | Large or rounded particle roll down the surface of a heap in formation. | Rolling |
| Sieving | Movement of smaller particles downward through a rolling or sliding layer of large particle. Also referred as “sifting”. | Rolling, sliding layer |
| Percolation | Movement or falling of small particles through gaps between larger particles due to shearing. Although might be similar to sieving, it does not require the larger particles to being a flowing layer. | Vibration, local shear planes and gravitational forces |
| Fluidization | The lighter particles form a 'fluidized' layer and make only coarse particles able to penetrate the fluidized fines while the finer particles remain in the top layer. | Fluidization, density |
| Trajectory | Reducing in the speed of smaller particles during free flight due to the difference between large and small particles in air drag and body forces such as gravity and deceleration. | Air drag and inertia |
| Impact | Particle with higher coefficient of restitution bounce off a heap surface. | Bouncing |
| Displacement | Larger particles rise to the surface of a mixture of large and small particles in stage due to the vibrations. Were also related to percolation (Enstad 2001). | Vertical vibration |
| Push-away | Heavier particles falls on the apex of the heap push-away lighter while equivalent sized particles move towards the edges of the heap. | Density |
| Agglomerate | Very fine particles to formed larger aggregates whereas the other components continue as single particles. Usually this effect is active when there is some moisture present. | Agglomeration |
| Diffusion | Higher mobility in fine particles than that of large particles, leading them to concentrate in zones. Also referred as “concentration driven displacement”. | Diffusion, concentration of displacement |

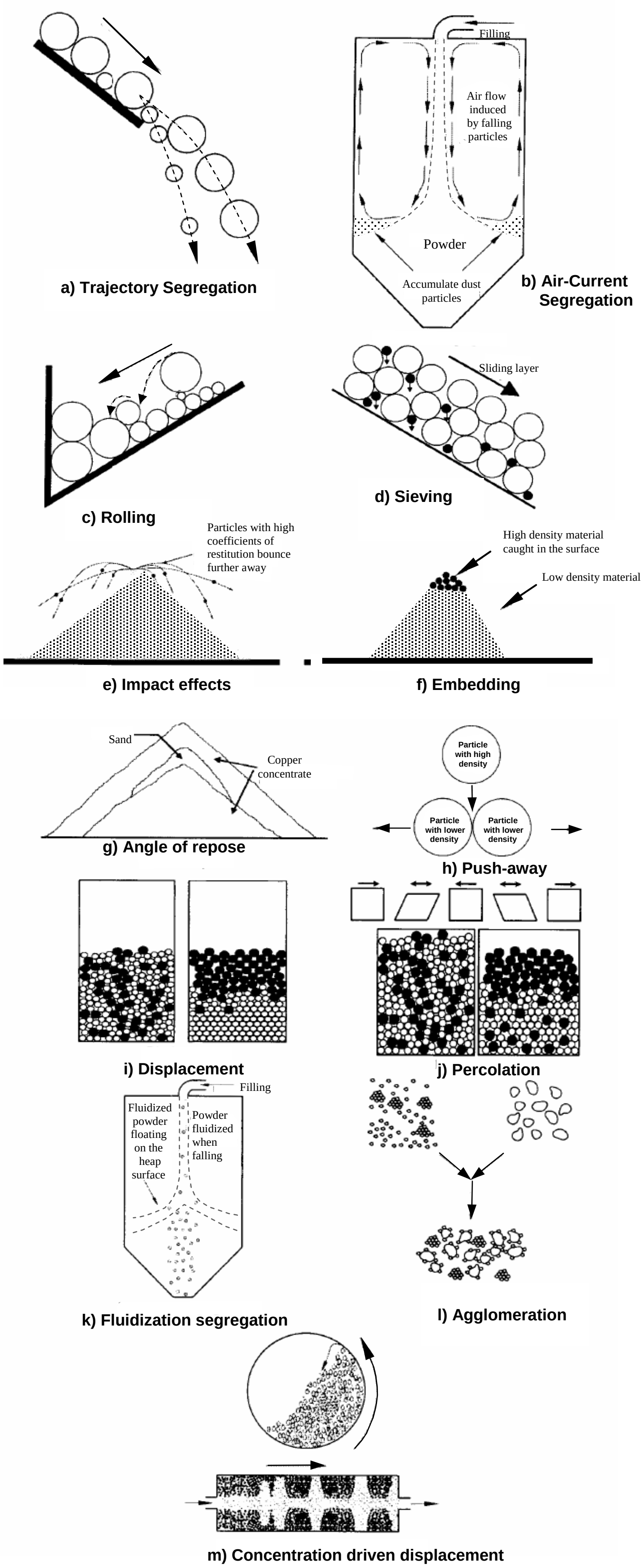


Figure 2.8: Mechanisms of segregation (after de Silva et al. 2000).

### 2.5.2 Percolation of Fine Particles

One key aspect of gravity flow that is imperfectly understood is the percolation of fine particles. The study of particle percolation has been employed in various contexts especially in chemical and powder applications (Bridgwater et al. 1969, 1978, 1985a, 1985b; Bridgwater and Ingram 1971; Scott and Bridgwater 1975, 1976; Cooke et al. 1978; Cooke and Bridgwater 1979; Drahun and Bridgwater 1983; Foo and Bridgwater 1983; Bridgwater 1995). Percolation has been recognised as an important mechanism in segregation (Bridgwater et al. 1969; Tanaka 1971; Mosby et al. 1996b; de Silva et al. 2000; Duffy and Puri 2002).

Percolation of fine particles (or sometimes referred as interparticle percolation) (Scott and Bridgwater 1975; Cooke et al. 1978) occurs in mixtures of different particle sizes as illustrated in Figure 2.8j. When such assemblies are subjected to shear strains and/or volumetric deformation and gravitation force, fine particles percolate through interstitial gaps (Williams 1976; Mosby et al. 1996b; Vallance and Savage 2000; Duffy and Puri 2002; Johanson et al. 2005).

Percolation can also occur whenever a mixture of particles of different sizes are disturbed in such a way to rearrange the particles (Axe 1995). Disturbance can arise from the existence of shear within the mass, caused, for example, by stirring or by pouring the particles into a heap or even when a mixture is shaken (Williams 1976).

It is interesting to highlight that all the previous studies have resulted in essentially the same finding. These studies concluded that both the diameter ratio of coarse to fine particles, and the associated density ratio, significantly affects the rate of percolation of fine particles during a shearing process. Nevertheless, the finding may only be applicable to the chemical and powder applications.

In sub-level and block caving mines, segregation phenomena can arise from percolation induced by gravity and vibration (Mosby et al. 1996b). This phenomenon significantly affects the flow characteristics of ore in ore pass systems

(Hadjigeorgiou and Lessard 2007), dilution and eventually the efficiency of the caving method (Chen 1997; Pretorius 2007).

In view of this, others factors such as particle shape, size, and transport properties (i.e., shear strains) within the fragmented rock mass are perhaps the most important factors to be considered in study of percolation mechanism in caving mine. As full scale test may be too expensive to be achieved, physical and numerical models provide a reproducible way to provide understanding of percolation mechanisms of caved rock.

### 2.5.3 Mechanism of Percolation

According to Bridgwater (1994) and Cooke et al. (1978), a dimensional analysis of percolation velocity ($u$) for a small sphere percolating through larger spheres can be written as Equation 2.10:

$$\frac{u}{\dot{\gamma} d_b} = \frac{\bar{y}}{\gamma d_b} = f\left(\frac{d_p}{d_b}, R_b, R_p, \frac{\sigma}{E_b}, \frac{E_p}{E_b}, \frac{d_b \rho_b g}{E_b}, \frac{d_b \dot{\gamma}^2}{g}, \frac{\rho_p}{\rho_b}, \mu_b, \mu_p\right) \quad \text{(Equation 2.10)}$$

Where:

- $u$ = mean downward velocity of percolating particle (m/s);
- $\bar{y}$ = mean distance percolate (m);
- $\dot{\gamma}$ = strain rate ($s^{-1}$);
- $\gamma$ = shear strain (dimensionless);
- $d_p$ and $d_b$ = the percolating and matrix of coarse bed particle diameters respectively (m);
- $R_b$ = shape factor for the matrix of coarse bed particles, indicating the modification of the production of holes due to deviation from spherical shape of the matrix of coarse bed particles;
- $R_p$ = shape factor for the percolating material, indicating the modification in the utilisation of holes due to deviation from spherical shape of the percolating material;

- $E_p$ and $E_b$ = Young's modulus of the percolating particle and the matrix of coarse bed particle respectively (N/m²);
- $\sigma$ = normal stress on the top surface of the cell (kg/ms²);
- $g$ = acceleration due to gravity (m/s²); and
- $\rho_p$ and $\rho_b$ = the percolating and matrix of coarse bed particle densities respectively (kg/m³).

Bridgwater (1994) found that the significance of the various dimensionless groups in Equation 2.10 can be defined as follows:

- $d_p/d_b$ is the ratio of percolating particle to matrix of coarse bed particle diameter or a measure of the utilisation of holes in the deforming large particles by small particles;
- $\sigma / E_b$, the ratio of normal stress to Young's modulus for the matrix of coarse bed particles ($E_b$) is a measure of the loss of free space due to the deformation of matrix of coarse bed particles due to normal stress;
- $E_p / E_b$, the ratio of Young's modulus of percolating and matrix of coarse bed particles, is a measure of the loss of mobility of percolating due to deformation under stress. The influence of $E_p / E_b$ under applied stress is slight (Cooke et al. 1978);
- $d_b \rho_b g / E_b$ where $\rho_b$ denotes density of the matrix of coarse bed particles and $g$ the acceleration due to gravity, is a measure of deformation of a matrix of coarse bed particles under its own weight and may be negligible;
- $d_b \dot{\gamma}^2 / g$ is a measure of the ratio of the time for particle to fall through a gap to the lifetime of the gap under acceleration due to gravity ($g$);
- $\rho_p / \rho_b$, the ratio of percolating to matrix of coarse bed particle density, is a measure of the microscopic force seeking to open the space between matrix of coarse bed particles. An increase in $\rho_p / \rho_b$ will slightly raises $u / \dot{\gamma} d_b$ up by 24% (Cooke et al. 1978; Bridgwater et al. 1985a);
- $\mu_b$, the dynamic coefficient of friction of matrix of coarse bed particles, is included as a measure of the frictional properties within the matrix of coarse bed particles; and

- $\mu_p$, the dynamic coefficient of friction between matrix of coarse bed and percolating particles, is included as a measure of the frictional properties between the matrix of coarse bed particles and percolating particles.

Bridgwater (1994) also noted that the voidage of the matrix of coarse bed particles is not included in Equation 2.10 as it is deemed to be a dependent variable. The voidage is set by the conditions of stress, with the matrix of coarse bed particles being at the critical state because of the application of sufficient strain.

Cooke et al. (1978) found that the dimensionless factor of $u / \dot{\gamma} d_b$ slightly decreases as normal stress rises while $u / \dot{\gamma} d_b$ was also increased at low strain rates. On the other hand, Bridgwater et al. (1978) postulated that if the diameter ratio of particle-to-matrix of coarse bed ($d_p / d_b$) are between $0.269 \leq d_p / d_b \leq 0.673$ the $u / \dot{\gamma} d_b$ the ratio significantly decreased. In accordance to this, Johanson et al. (2005) found that if the fines are less than one-third the size of coarse particles and free flowing, they may percolate through the coarse matrix of particles resulting in sifting (or sieving) segregation.

Additionally, Equation 2.11 was developed by Bridgwater and his team (Bridgwater et al. 1978; Bridgwater 1994) to assess the relationship between the dimensionless percolation rate ($\bar{y} / \gamma d_b$) or $u / \dot{\gamma} d_b$ relative to diameter ratio ($d_p / d_b$). The negative exponential relationship with diameter ratio indicates that as the size of the fine particles approaches that of the coarse particle, which requires an increasingly greater amount of shear strain for percolation to occur (Pierce 2004).

$$\frac{\bar{y}}{\gamma d_b} = \frac{u}{\dot{\gamma} d_b} = k_1 \exp\left[ -k_2 \frac{d_p}{d_b} \right] \qquad \text{(Equation 2.11)}$$

Where:

- $\bar{y}$ is defined as the mean percolation distance travelled by percolating particles in given strain (mm);
- $u$ is defined as the mean downward velocity of percolating particle (mm/s);
- $\gamma$ is shear strain (dimensionless) while $\dot{\gamma}$ is defined as strain rate ($s^{-1}$);

- $\bar{y}/\gamma d_b$ is measure by the most probable distance in bed particle diameters that an isolated percolating particle is expected to drop/travel when subjected to $\gamma$ =1.0 or 100% (Bridgwater et al. 1978; Pierce 2004, 2010);
- $u/\dot{\gamma} d_b$ is measure by the mean downward velocity of percolating particle, $\bar{u}$ when subjected to the rate of strain ($\dot{\gamma}$) (Bridgwater et al. 1978);
- $k_1$ and $k_2$ are two arbitrary constants that were found to be equal to 20 and 8 respectively (Pierce 2004); and
- $d_p/d_b$ is the ratio of percolating particle to matrix of coarse bed particle diameter or a measure of the utilisation of holes in the deforming large particles by small particles.

### 2.5.4 Factors Affecting Percolation

Scott and Bridgwater (1975) studied the rate of percolation of small particles in a simple shear cell in which the bed is subjected to uniform shear strain. By reversing the direction of movement of the cell, unlimited strain can be applied. They found that differences in particle size were the most significant cause of percolation. They showed that the percolation velocities observed could be explained in terms of the diffusion equation.

Based on replication of physical experiments by Bridgwater et al. (1978), Pierce (2004) used PFC3D™ to study a series of shear tests of coarse and fine spherical particles in caved rock. He noted that for particles that are smaller than the minimum interstices between larger particles, percolation can occur spontaneously while particles that are larger than the minimum interstices may only percolate if the bed is disturbed in some way (e.g., through shearing).

Table 2.6 shows a number of control parameters on percolation rate highlighted by Bridgwater et al. (1978), Drahun and Bridgwater (1983) and Pierce (2004). It was reported in these studies that at shear strain rates below 0.4 $s^{-1}$, percolation rates are sensitive to the particle diameter ratio. On the other hand, percolation velocity is less affected when the strain rate ($\dot{\gamma}$) is above 0.4 $s^{-1}$ as this increases the interception between the particles. Such at the high interception between the particles, the gaps that form between coarse particles will have less possibility for a longer opening thus decreasing the probability of a fine particle to pass through an underlying gap.

Table 2.6: Parameters controlling percolation rate.

| Description | Comment |
|---|---|
| Particle diameter ratio | Largest effect compared to other controlling parameters. |
| Rate of strain | Percolation rates increase until $\dot{\gamma}$ =0.4 s $^{-1}$ and reduces above 0.4 s $^{-1}$. |
| Normal stress | An increase in the normal stress reduces the percolation velocity. |
| Particle density | Higher density particles percolate faster than lower density particles (applied to the similar shape and size particle). |
| Material properties | Particles with low elastic modulus percolate faster than higher elastic modulus. |
| Surface properties | Smooth and shiny surfaces percolate faster than rough and scratched surfaces. |
| Shape properties | Rounded shape percolate faster than angular shape. |
| Wall effects | Smaller particles percolated more rapidly at the wall than in the matrix of coarse bed. |

Pierce (2004) numerically replicated and simulated Bridgwater's et al. (1978) simple shear apparatus and found that in general, materials with greater density and lower elastic modulus exhibit higher percolation rates. Johanson et al. (2005) noted that if particle shapes are different, then the internal friction angles of individual components may be different, resulting in angle of repose segregation.

### 2.5.5 Previous Studies on Percolation

Percolation has been the subject of a large number of publications on either physical or numerical modelling. On the other hand, to the author's knowledge, there is no significant record of research output across full scale tests, which was probably due to the high cost and difficulty in measuring specific mechanism such as shear strain in actual caving mine.

#### 2.5.5.1 Physical modelling

Percolation mechanisms in powder applications have been extensively studied by Bridgwater and his co-authors (Bridgwater et al. 1969, 1978, 1985a, 1985b; Bridgwater and Ingram 1971; Scott and Bridgwater 1975, 1976; Cooke et al. 1978; Cooke and Bridgwater 1979; Drahun and Bridgwater 1983). During this period, Bridgwater and his team performed a number of experiments to provide insight into fundamental processes controlling the distribution of components in a free flowing powder and/or of agglomerates in a cohesive one. Later, this was reviewed and expanded by Savage (1987) and Bridgwater (1994, 1995).

During the 1970's, Bridgwater and his co-authors built a number of devices to investigate percolation rates that was primarily developed for testing soils (Scott and Bridgwater 1975; Bridgwater et al. 1978). The end result was a *Simple Shear Apparatus* (SSA) called Mark IA, IB, IIA, IIB, III, IV and V that induced percolation (Table 2.7).

Table 2.7: Principal features of the SSA models built by Bridgwater and his co-authors (after Bridgwater et al. 1978).

| Device | Dimension (L x W x H) (mm) | Bed-matrix particle diameter, $d_b$ (mm) | Base | Drive | Maximum shear strain ($\gamma_{\max}$) |
|---|---|---|---|---|---|
| Mark IA | 250 x 250 x 220 | 13x13x12 | Plane | Hand | 1.68 |
| Mark IB | 250 x 250 x 220 | 13x13x12 | Fixed hemispheres | Hand | 2.00 |
| Mark IIA | 362 x 355 x 220 | 19x19x12 | Fixed hemispheres | Motor | 2.18 |
| Mark IIB | 362 x 355 x 220 | 19x19x12 | Hemispheres plus prongs | Motor | 2.18 |
| Mark III | 354 x 355 x 246 | 19x19x12 | Rotating spheres | Motor | 2.18 |
| Mark IV | 70 x 70 x 55 | 12x12x9 | Fixed hemispheres | Hand | 2.00 |
| Mark V | 354 x 355 x 246 | 19x19x12 | Rotating spheres | Hydraulic | 2.18 |

Figure 2.9 shows one simple shear apparatus (Mark IIA) developed by Bridgwater and his team that operated by moving a bed of particles in a back and forth direction. In this type of simple shear apparatus, the location of the shear box rotation-pivot

was set at the centre of the upper side wall (along the z-axis). Tang (2004) noted that implication of the centre-pivoted motion is likely to create a *dead zone*[15] (Duffy 2001) and produces unlimited shear strain. A detailed discussion on this topic is presented in Chapter 3.

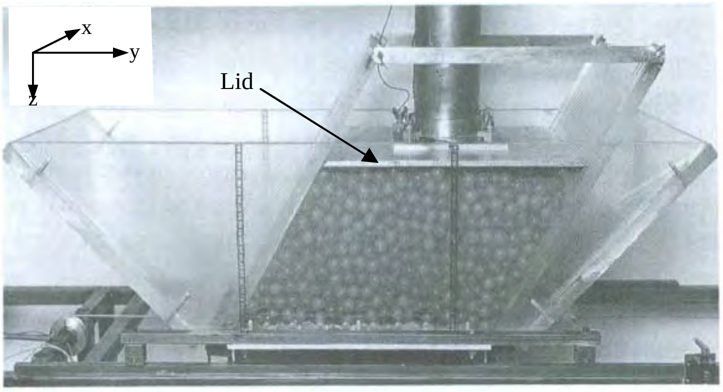


Figure 2.9: The Simple Shear Apparatus (SSA) (after Bridgwater 1994). Note that the SSA imparts principal motion by moving a bed of particles in a back and forth in the y-axis direction with a single tube at the centre of the upper side wall (z-axis) in which the fine percolating sphere was entering the hole in the lid one at a time.

By moving a bed of particles in a back and forth motion along the y-axis direction, creates a uniform strain which enables the percolation rate to be found without recourse to exhaustive sampling or cine photography (Scott and Bridgwater 1975). By using this apparatus, a bed of coarse particles was sheared so that its shape changed from a rectangular to a parallelogram (Figure 2.10) and thus analogous to a *failure zone* (Scott and Bridgwater 1975; Cooke and Bridgwater 1979). The failure zone is defined as a thin layer (or gaps) between two groups of particles, in which there is considerable motion (Bridgwater and Ingram 1971). For instance, in a failure zone, a binary mixture of large and small particles may deform permitting the rapid passage of small ones through it.

[15] Dead zone is defined as the phenomenon at which the shear motion experience by material within the shear box is in a minimum state (in some cases close to zero) along the axis line (x, y or z-axis).

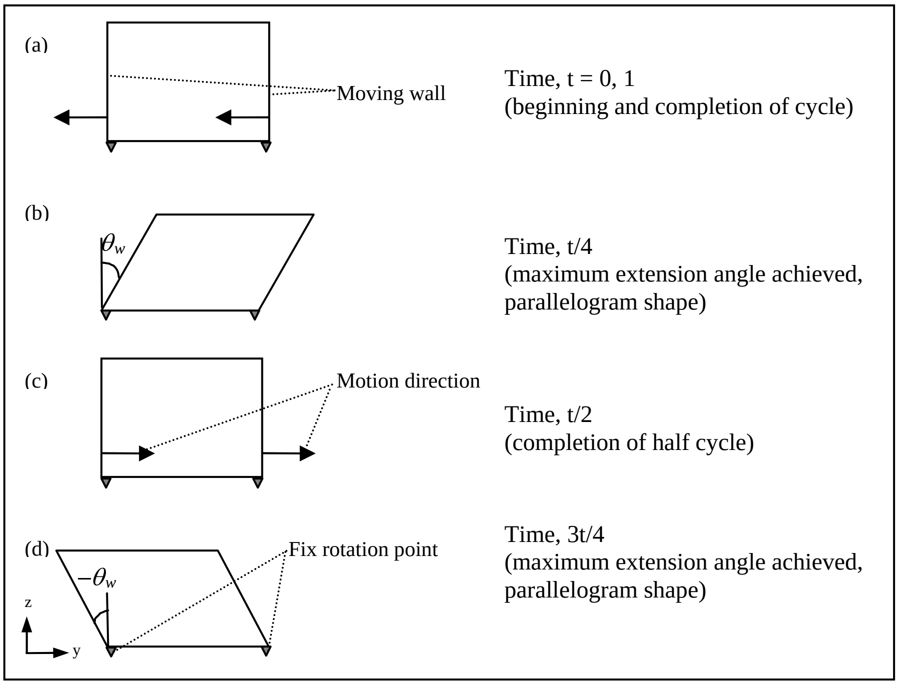


Figure 2.10: Motion imparted to particles by the SSA (adapted after Cooke et al. 1978). Note that position of moving walls at half-stroke intervals is shown.

Percolation rates were established by measuring the mean time taken for particles fed from the top of the cell to transverse the cell and fall out at the bottom. Percolation rates were then measured from the slope of the linear relation found between residence time and bed height, thus eliminating end effects (Cooke and Bridgwater 1979). The linear relationship also implies that the behaviour of the material in the cell is independent of position and that the percolation velocities deduced are true material properties (Cooke et al. 1978).

Through a series of experimental works, Scott and Bridgwater (1975) found that percolation rates depend mainly on total strain, the relative sizes of large and small particles and also on rate of strain. It is also postulated that percolation rates are found to increase with increasing shear rate and decreasing size of the smaller particles. Nevertheless, most of the work done by Bridgwater and his team focused on powder systems and its application to mining scale granulates remain to be undertaken.

Johanson et al. (2005) built a simple shear box with a dimension of 130 mm (length) x 130 mm (width) x 50 mm (height) to measure the magnitude of sieving segregation occurring in matrix of bed particles (sand grains) as shown in Figure 2.11. This design was similar to one attributed to Scott and Bridgwater (1976) and Stephens and Bridgwater (1978a, 1978b) for measurement of a single particle through a matrix of bed particles assembly of material.


Figure 2.11: Front-view of simple shear box apparatus by Johanson et al. (2005).

By using this simple shear box device, the total shear strain ($\gamma_{total}$) is computed from the maximum extension angle ($\theta_w$) of the side walls as illustrated in Figure 2.10. The number of cycles ($N$) given by Equation 2.12 :

$$\gamma_{total} = 4N\tan(\theta_w) \qquad \text{(Equation 2.12)}$$

A complete shear cycle consists of starting with the end walls perfectly vertical (Figure 2.10a) and moving the bottom plate left until the moving wall forms an angle with the vertical of $\theta_w$ (Figure 2.10b). Once this maximum extension is achieved, the strain direction is reversed and strain is continued until the maximum extension angle $-\theta_w$ is reached (Figure 2.10c and Figure 2.10d). Finally the bottom piston is moved to the position where the end walls are completely vertical and another cycle is started (Figure 2.10a) (Johanson et al. 2005).

It is concluded by this experiment that sieving segregation can be modelled as a velocity dispersion term that depends on total strain and the available void space. However, the use of sand particles (350 μm materials sandwiched between two layers of 1650 μm sand) employed in this study may not represent the actual cave mining environment. Campbell (1990) asserted that caved rocks resulting from crushing or caving are generally highly angular. Since sand particles are more spherical than angular, the finding of Johanson et al. (2005) may not be consistently reliable when applied to caving mining.

With regard to above point, Yenge (1980) noted that the flow of caved rock could not be described satisfactorily by theories developed for the flow of other materials (such as sand) because the particles sizes, discharges rates and boundary conditions in the mining problem were not analogous to those of other cases. Nevertheless, the simple shear box apparatus used in this work has shown a potential approach to differentiate between the angle of repose segregation or percolation process.

Hsiau and Shieh (1999) constructed a 2D shear cell device (Figure 2.12) with adjustable lower wall velocity. This shear cell operated based on similar principles to an annular shear cell (sometimes referred as ring shear cell or rotational shear box). Glass spheres with a mean diameter of 3 mm were used as granular materials. Image processing technology and a particle tracking method were employed to measure the average and fluctuation velocities in the streamwise and the transverse direction.

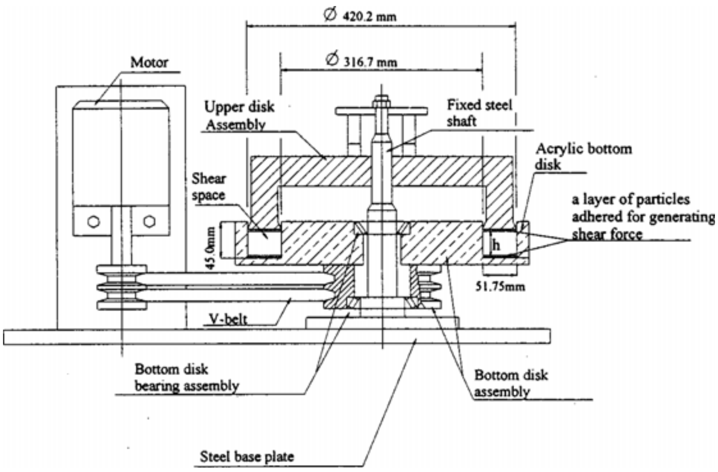


Figure 2.12: Two-dimensional annular shear cell with adjustable lower velocity (after Hsiau and Shieh 1999).

It was found that the diffusive displacement of tracking particles were the highest in the high-shear region and significantly decreased with the rate of shear imposed. However, since the experiments were limited to being 2D, it could not genuinely represent actual percolation in a typical mining scenario. In addition to the above drawback, because of the visualisation limitation, only the flows adjacent to the inner surface of the bottom disk could be recorded and analysed while the walls need to be cleaned and polished before each experiment to reduce the wall friction effect.

In view of above drawback in annular shear cell, the U.S. Pharmacopeia (n.d.) found that due to its design, the annular shear cell was also not able to generate a uniform shearing of the powder bed (i.e., material on the outside of the annulus is sheared more than material in the inner region). Another setback is the construction is too heavy, which was disadvantageous for tests at low stresses and no possibility to perform wall friction tests (i.e., bulk solid sample test) (Schulze 2003).

The annular shear cell may be practical for powder test applications (or particles with diameter less than 5 mm) with relatively small sample sizes (generally less than 2 kg). However, given the appropriate sample size and its mass (i.e., in mining study), the application of annular shear test is not applicable. Even if a very large shear annular shear cell is used in order to test coarse particles (the standard annular shear cell has a diameter of about 50 mm), it is difficult to get an even distribution of normal stresses and shear stresses in the shear zone (Schwedes and Schulze 1990; Schwedes 2003).

Although it is possible for the annular shear cell to generate very large shear strains compared to the translational type of shear tester (i.e., simple shear apparatus), the applicability of this type of shear tester is not relevant to caving problems since in the large scale of current block caving mine (more than 100 m in height) a low magnitude of shear strain is anticipated (Hashim and Sharrock 2010). A detail discussion of this topic is presented in Section 3.4.

Given the above limitations, it is apparent that the simple shear cell demonstrates some advantages over the annular shear cell. Firstly, the simple shear cell allows a large quantity of sample to be tested and secondly is more relevant to the modelling of coarse particles (i.e., 5 - 20 mm rock aggregate) which is significant in particle shape effect studies.

Subsequent to their work using a vertically oriented shear tester device, Duffy and Puri (2002) designed the *Primary Segregation Shear Cell* (PSSC). The PSSC was capable of applying up to 25% strain by changing the cam connected to a variable speed motor. The effects of size ratio, strain, cycle speed and bed depth on particle percolation were evaluated. It is postulated that size ratio is the most dominant variable affecting the percolation rate of fines through a bed of coarse particles.

However, since this work used a mixture of spherical glass shapes, the particles did not represent the shape of caved rock. Glass spheres are probably a reasonable approximation for the sand particles, which, although angular on the surface, are still roughly spherical in shape and become more so as collisions break off any protuberances.

Later, Tang (2004) upgraded and built a second generation of the *Primary Segregation Shear Cell II* (PSSC-II) as shown in Figure 2.13. Some new features was introduced in PSSC-II such as selection of shear motion along the x-axis in order to avoid a close to zero energy around the dead/central zone of the cell as been experienced by PSSC (shear motion along the z-axis) (Duffy and Puri 2000). The PSSC-II dimension was also slightly larger than the previous PSSC with a dimension of 150 mm (length) x 63 mm (width) x 100 mm (height).

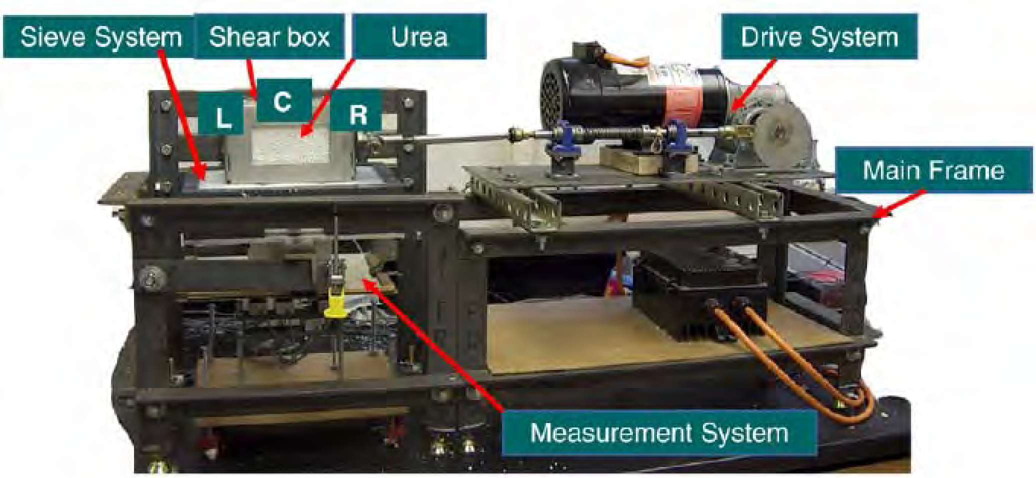


Figure 2.13: Primary segregation shear cell of generation two (PSSC-II) (after Jha and Puri 2009).

Jha and Puri (2009) then used the PSSC-II to study time-dependent percolation segregation in binary mixtures of particulate materials with two different materials; urea (spherical particles) and potash (angular particles). It was found that for both potash and urea, percolation of fines during shear motion predominantly decreased with decrease in size ratio. Jha and Puri (2009) also commented that percolation segregation of fine particles was dependent on size, shape and density.

Nevertheless, it is not known if these findings are applicable to caved rock. Several factors such as the reliability of relatively small cell size which is not specifically built for scaleable purposes and the type of particulate material used in the study. In addition, some limitations to the physical properties of the particulate material (with regards to the urea and potash particles) used in the study was found to be far removed from the nature of caved rock.

#### *2.5.5.2 Numerical modelling*

In addition to physical testing, the potential of numerical methods such as DEM to replicate the mechanisms involved in shear-induced percolation are promising. The DEM approach offers significant opportunities in visualizing and understanding the mechanisms of percolation as it provides insight into the microstructure of the caved rock.

Based on the replication of physical experiments by Bridgwater et al. (1978), Pierce (2004) used PFC3D$^{TM}$ to study a series of shear tests of coarse and fine spherical particles in caved rock. In addition, this work considered two-particle clumps and a shear box in the vertical shearing direction rather then the horizontal direction as carried out by Bridgwater et al. (1978). It was concluded that the vertical shearing direction did not have a significant influence on percolation rate and generally produced similar results to the horizontal direction. Nevertheless, since this work only introduced two-particle clumps to study the effect of shape on percolation rate, and significantly higher number of particles (i.e., six-particle clumps or higher) is a pre-requisite for modelling caved rock.

It is also indicated by Pierce (2004) that percolation rate is not significantly influenced by shearing direction while reducing the strain rate significantly increases the percolation rate of fine particles. However, several other shapes are required for the tests before final conclusions are drawn since this work are only limited to two-clump particles (spherical versus two-particle clumps) only.

Subsequent to this, Hashim and Sharrock (2009) used PFC3D$^{TM}$ and numerically extended the work conducted by Bridgwater et al. (1978) and Pierce (2004) with a larger shear cell. The shear cell was approximately twice the size of Bridgwater's simple shear apparatus and Pierce's PFC3D$^{TM}$ shear cell. In order to better represent the shape factors of actual caved rock, the particles had similar shapes factors to caved rock. By introducing two more complex shapes; cylinders and cuboids it was found that the percolation rate is predominantly affected by particle shape and the size ratio of the percolation and matrix particles. However, data from physical models and/or full scale tests are required to validate these results. It is worth highlighting that it is one of the aims of this thesis to validate and develop a new numerical model based on the PFC3D$^{TM}$ with emphasis on more complex non-spherical granular material and sizes for percolating study of caved rock in caving mine which is explored in Chapter 6.

Hancock et al. (2010) implement parallel DEM code known as *ESyS-Particle* which is capable of running on supercomputers to study block caving flow around an isolated drawpoint including fines percolation. The mono-sphere particles and/or particle clusters was generated by bonding two spheres together. It was reported that the ESyS-Particle are discretionally within the range of those results from previous studies on caving flow dynamics with exception to the Castro 3D large physical model (Castro 2006).

Of all the above numerical works employed in the study of percolation, it is concluded that numerical models are still developing and in most of the cases, remain unvalidated in studies on caved rock (or partially validated by using previous physical model data on ideal materials). More over, sphericity (i.e., circular discs in 2D or sphere particles in 3D) has been assumed in most studies for many reasons in numerical modelling as it is easy (in theoretical work and computer simulations) to detect a collision of circular particles, as particles are in contact whenever their centre are two radii apart (Campbell 1990) thus reduced contact detection time.

## 2.6 SUMMARY AND RESEARCH DIRECTION

In summary, an improved knowledge of gravity flow of caved rock and associated percolation mechanisms has very general application in caving mines (e.g., block caving, sub-level caving, back-fill method), minerals processing, geology, civil engineering and other fields such as chemical, powder and pharmaceutical. Most recent physical experiments emerging from the chemical and powder applications, have shown that both the diameter ratio of coarse to fine particles and the associated density ratio significantly affects the percolation rate of fine particles during shearing. Although these studies are comprehensive, they concentrate only on the percolation of mono-size shaped particles (i.e., spherical glass, sphere sand) and/or narrow distributions of particle sizes or shapes not applicable to caving.

Publications on percolation in caving are extremely limited, and hence research is required to identify the percolation mechanisms and to develop an improved understanding on the factors controlling fines percolation in angular rock particles. On the other hand, apart from physical modelling, numerical modelling has proven to show promising results in the field of fine particles percolation. However the use of numerical modelling remains largely unvalidated due to the lack of reliable data from physical models and/or full scale tests. Nevertheless since full scale tests for block caves are only now being undertaken, numerical models are usually validated through physical models.

In view of the above points, particle shape, size, density and transport properties such as shear strains and strain rates within the caved rock are perhaps the most important factors to be considered in future numerical and physical modelling studies on caving.

Given to the above concerns, this thesis aims to explore shape and size effects on the percolation of fine particles in a bed-matrix of coarse aggregates under controlled experimental conditions. In order to achieve this goal, both spherical (ideal media) and highly angular particles (crushed aggregate media) were studied using a new physical model called the Shear Cell for Percolation of Geomaterials (SCPG). Other parameters such as particle size distribution, particle shape, density and transport properties (i.e., shear strain and strain rate) were studied. This knowledge is a step towards better understanding of percolation mechanism in coarse angular media, and hence caved or fragmented rock.

Apart from the use of the SCPG, this thesis also aims to take steps towards an improved understanding of the impact of particle shape and size on percolation rate, through the application of DEM. In line with the above objective it is also hypothesised that for percolation studies on caved rock, DEM approaches using non-spherical shape particles excel over the spherical mono-size particles. Accordingly, DEM models were developed using non-spherical particle shapes representing caved rock with up to six particle spheres clumped together in order to behave as a single bonding particle.

Numerical particles were then tested in conditions similar to the integrated data from the SCPG and 1:100 scaled Type-A Kvapil Models for shear strain assessment (Hashim and Sharrock 2010) to study the validity of the PFC3D$^{TM}$ simulations. A detailed discussion on the experimental results, key features of the SCPG and Type-A Kvapil Model assessment is explored and presented in Chapter 3 and 5 respectively.

Both approaches (physical and numerical modelling) offer the potential to improve cave drawpoint layouts in the future. Moreover an improved knowledge of percolation in caving mines is essential towards identify and avoid dilution hazards, optimise ore recovery towards safe and optimization of caving mine operation.

# CHAPTER 3:
# SHEAR CELL FOR PERCOLATION OF GEOMATERIALS – DESIGN AND EXPERIMENTAL METHOD

## 3.1 INTRODUCTION

This chapter presents a detailed description of the design and fabrication of a Shear Cell for Percolation of Geomaterials (SCPG) for the investigation of fine particle percolation in a bed-matrix of coarse angular aggregates similar to caved rock. A detailed description and key features of the SCPG and parameters required for the percolation study in block caving are described within the first and second sections of this chapter. Finally, a comprehensive summary of the experimental procedures and methodology is presented in the last section.

## 3.2 A SHEAR CELL FOR PERCOLATION OF GEOMATERIALS

Given the limited attention and published work in percolation studies on coarse angular materials similar to caved rock, a new apparatus to investigate the fine particles percolation in the bed-matrix of highly angular aggregate was designed and fabricated as shown in Figure 3.1.

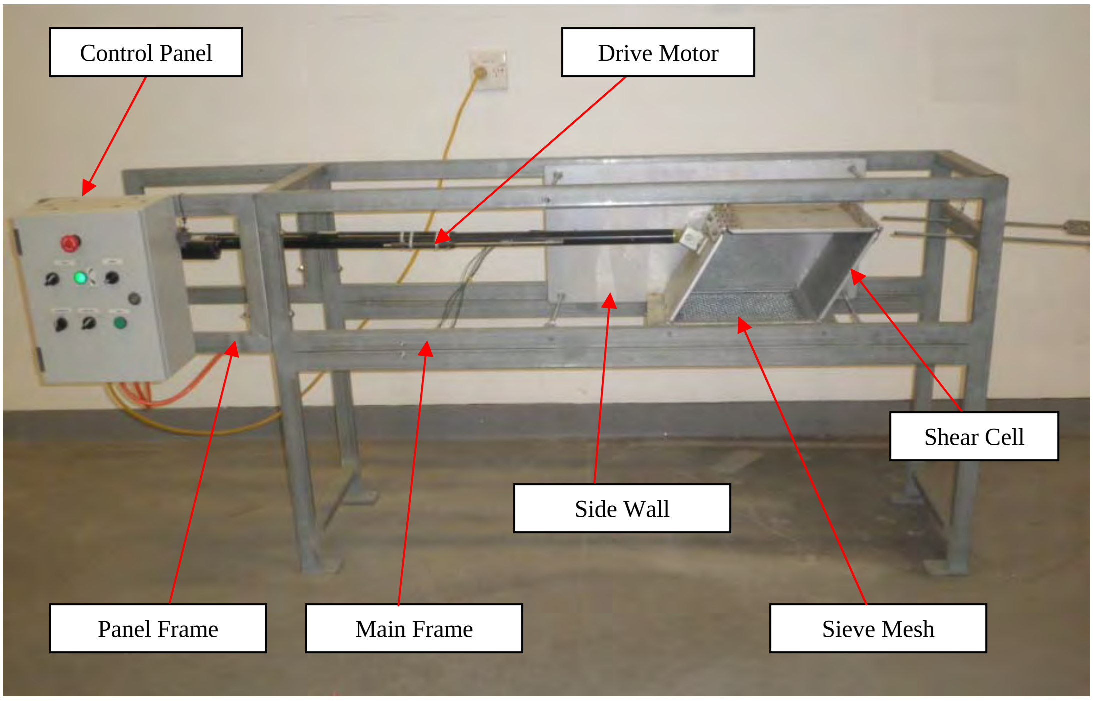


Figure 3.1: Shear Cell for Percolation of Geomaterials. Note the front side wall was removed to provide apparent view of shear cell and sieve mesh.

Some of the SCPG key features that distinguish it from previous simple shear cells are:

- unlike the previous tools that largely employed for powder applications, the SCPG was the first apparatus that was designed and fabricated specifically for percolation studies of coarse angular rock fragments with shapes similar to caved rock;
- currently, SCPG is believed to be among the largest of its kind used for the percolation studies (with a loaded mass of approximately 75 kg). This distinguished the SCPG from the others percolation apparatus which generally small in size and with limited capacity (less than 5 kg loaded mass);
- the SCPG also introduced more complex and highly angular shape aggregate as bed-matrix particles. This characteristic is important and differs considerably from other research that tends to use a mono-size sphere particle (i.e., glass spheres, rounded sand) as bed-matrix particles. In addition to this, glass spheres were also used in order to generate comparative results within the ideal and crushed aggregate media. The use of highly angular coarse media is to better represent caved rock in caving mines;

- the SCPG is also capable of quantifying percolation of fine particles with different particle size distributions, shape, strain rate and density. In addition to this, the percolation process can be observed (i.e., in the ideal bed-matrix) and visually recorded in real time during the course; and
- the SCPG is also capable of producing lower strain rate (0.01 $s^{-1}$) with the use of a sphere screw type linear actuator motor. Such motor drive system has the advantage of generating the least vibration over ring-worm motor systems (employed by most researchers).

Accordingly, the SCPG was designed specifically to study the effect of strain rate ($\dot{\gamma}$), particle diameter ratio ($d_p / d_b$), shape and density for ideal and crushed aggregate media under controlled experimental conditions. A detailed discussion of the above parameters is presented in Chapter 5.

## 3.3 DESIGN REQUIREMENTS AND KEY FEATURES

The SCPG has four main components namely: the *main frame*, *drive system*, *shear box* and *sieving and measurement system*. A computer-aided drawing program (Rhinoceros®) was utilised during design process and the key features of each component are summarised in the following sections.

### 3.3.1 The Main Frame

The main frame is made of 35 mm x 50 mm RHS steel tubing (Figure 3.2) that has been cut and fixed together to form a robust and stiff support for the overall systems. It was divided into two sections: the *shear cell frame section* and the *control panel frame section*. The shear cell frame section was used for not only providing enough space for the measurement system but also supporting the shear cell and sieving system. On the other hand, the control panel frame section was designed for supporting the drive system and can be disengage depending on the motor drive dimensions (i.e., actuator length). Both frame sections were connected and fixed using four M10 thread rods and nuts.

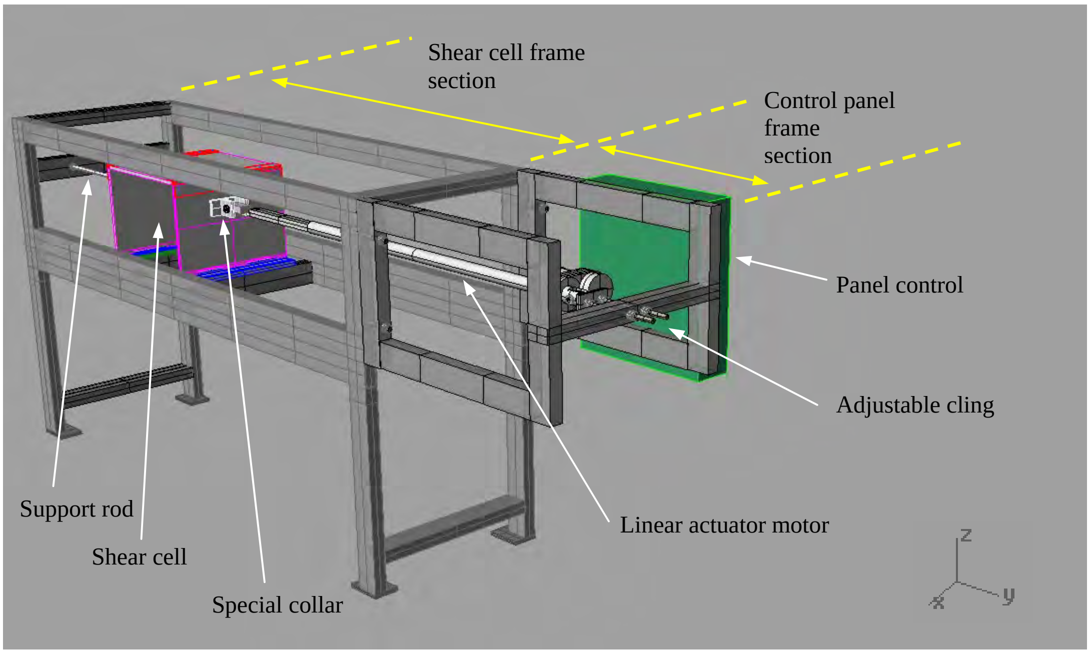


Figure 3.2: SCPG main frame and drive system. Note the side walls were hidden to provide clear view of shear cell.

Overall, the main frame consist of 1720 mm (length) x 550 mm (width) x 1100 mm (height) and 550 mm (length) x 550 mm (width) x 400 mm (height) for the control panel frame section. Each leg of the main frame can be fixed to the floor to prevent vibration.

In general the main frame should be:

- stable and strong to support the overall systems;
- constantly stable under motion and minimizing any vibrations; and
- provide sufficient space for the operation and routine maintenance of the measurement system.

### 3.3.2 The Drive System

The drive system features a linear actuator motor set, a special collar to join the self aligning rod clevis of the linear actuator to the shear cell wall and the adjustable cling for the rear clevis of the linear actuator. The drive system should:

- produce enough power and motion to meet the kinetic energy required for the bed-matrix media and shear cell;
- meet required variations in strains and strain rates;
- provide adjustable and controllable strain and strain rate;
- be easy to maintain; and
- produce minimum vibration and shock energy to the overall system.

#### *3.3.2.1 Linear actuator and auto-switch system*

The linear actuator used in this study is a heavy duty industrial sphere screw actuator series IJ35524600N supplied by Motion Technologies Pty. Ltd., Australia. The motor provides a maximum lift tube stroke to 600 mm and has power requirements of 24V/20A. It can hold up to 12kN static capacity with a maximum load at approximately 3.5 kN (the total mass of the shear cell and bed-matrix is approximately 200 kg). Some important features of the linear actuator include the motor, self alignment rod clevis, inner lift tube, outer lift tube and gearing system as illustrated in Figure 3.3.

A linear actuator system was chosen because it generates the least vibration compared to the other types of motors (i.e., worm-ring disk). Tang (2004) highlighted that one drawback of using the ring-worm disk type in his PSSC-II test rig was the relative position of cam with the respect to the linear guide must be reset following the adjustment of the drive bar on the paddle (the drive bar and the drive wall connector) when different strains are required which in practical terms is time consuming and may lead to prone step error.

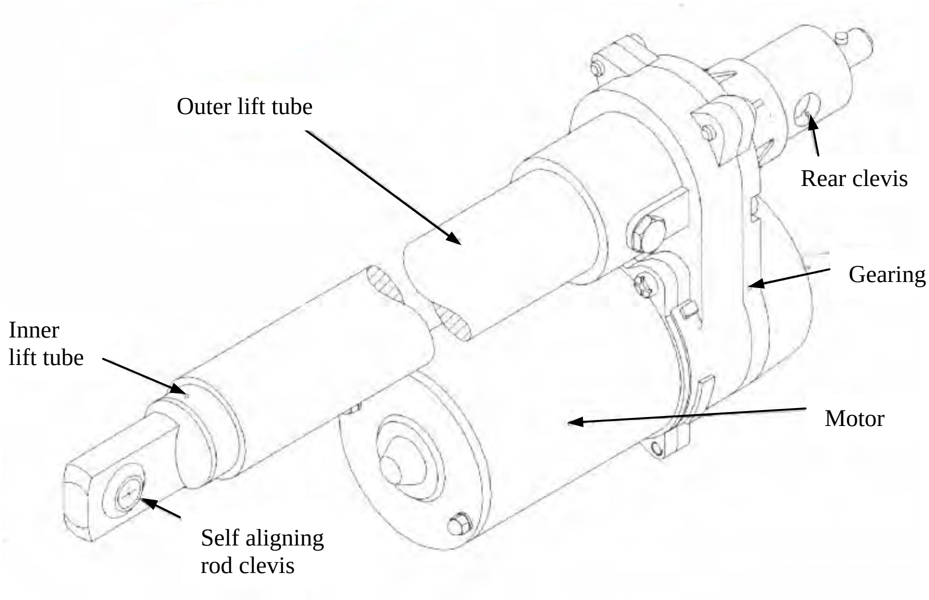


Figure 3.3: The linear actuator features and components (after Motion Technologies Pty. Ltd. 2010).

Conversely, given that the maximum extension angle ($\theta_w$) of the drive walls must be ensured to consistently change from a rectangular to a parallelogram and thus analogous to a failure zone (Cooke and Bridgwater 1979), an automatic switch system has been introduced in the SCPG. Basically, the control switch will automatically drive the motor toward the maximum value of $\theta_w$. Once the required $\theta_w$ value is achieved, the switch system will change into opposite direction until the cycles are completed. The automatic switch controller button needs to be reset each and every time the new test is run.

### *3.3.2.2 Special collar design*

A special "collar" was designed to join the self-aligning rod clevis of the linear actuator and the drive wall of the shear cell (Figure 3.4). By using this design, no adjustment to the position of the linear actuator inner and outer tube needed to be made during the entire operation; thus generating the least amount of vibration whilst producing relatively low levels of noise during the operation.

Figure 3.4: A special collar designed to join the self aligning rod clevis of the linear actuator to the shear cell wall.

#### *3.3.2.3 Adjustable cling*

An adjustable cling (Figure 3.2) was designed as a link to join the rear clevis of the actuator motor and the main frame. One of the advantages of this design is that it provides flexibility for motor alignment according to the motor size and dimension (if required).

### 3.3.3 The Shear Cell

The shear cell is the most crucial part of SCPG and was designed to meet the following operational requirements:

- provide quick loading and unloading of test materials;
- be able to transfer the energy uniformly to the test material during shearing;
- allows fast configuration of the collection pan with respect to the shear cell;
- strong and robust to accommodate the variations shear strain magnitude during the tests; and
- be able to provide the required shear strain motion such that the percolation could be simulated.

The shear cell was designed with dimensions: 355 mm (length) x 355 mm (width) x 250 mm (height) and was amongst the largest, apart from the Simple Shear Apparatus of Bridgwater et al. (1978) built for powder application study which had dimensions of 355 mm (length) x 354 mm (width) x 246 mm (height). Principally the shear cell of the SCPG comprises of 10 mm (thick) galvanised plate that differed from the SSA (Bridgwater 1994) which was made of Perspex. The use of galvanised plate provided advantages over other types of material (i.e., Perspex cell). Unlike the Perspex which is easily damaged and bent, the galvanised plate acted as a robust and rigid wall. These features make the SCPG capable of running highly angular media (e.g., crushed aggregate) which is essential in representing close similarity of caved rock in caving mine.

Both of the drive and the end wall of the SCPG were connected together with the upper wall by at the top and connected by the heavy duty stainless steel hinge and tightened using the hexagonal nuts as illustrated by Figure 3.5. On the other hand, the bottom parts of the drive and the end wall were designed resembling the hinge with 6 mm opening in the centre and connected with a 5 mm stainless pin allows free movement in the y-direction.

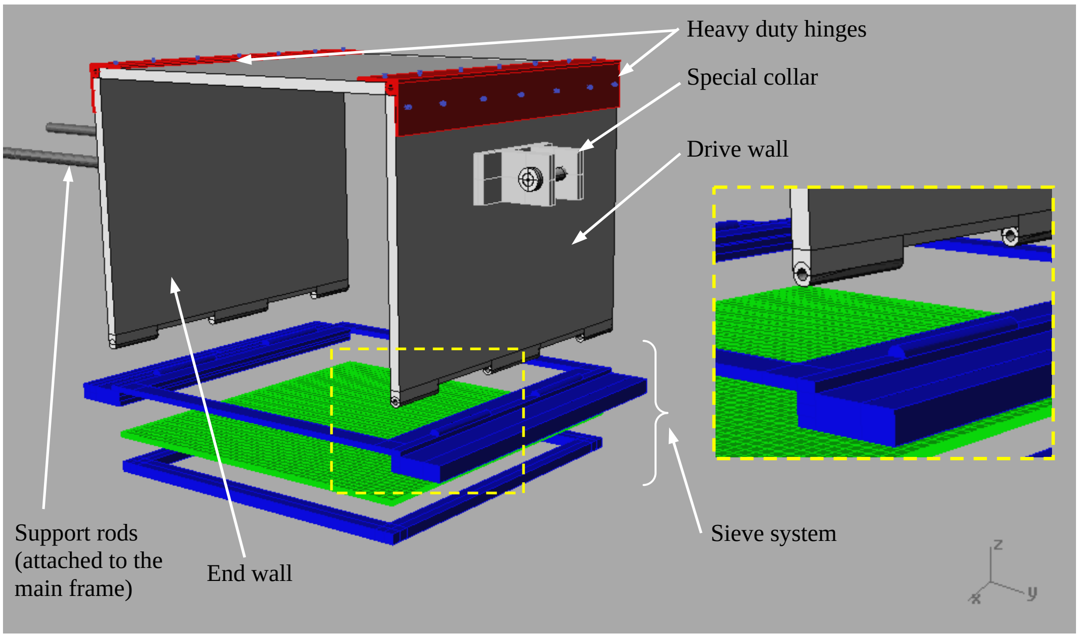


Figure 3.5: The shear cell perspective. Enlargement (yellow dash box) show the design of the shear cell base which is hinged with a 5 mm pin connector.

The shear cell drive wall also consists of a “special collar” attached on the drive wall and was designed to connect the self aligning rod clevis motor and drive wall. The end wall were designed to be attached with support rods (Figure 3.2) which provided an extra support to the end wall during the material loading and unloading (i.e., the drive wall is pre-supported by the linear actuator inner lift tube during the loading).

#### *3.3.3.1 Determination of the maximum extension angle ($\theta_w$)*

Apart form the strain rate ($\dot{\gamma}$), the maximum extension angle ($\theta_w$) is considered as the key parameter in the percolation study. The total shear ($\gamma_{total}$) in the shear cell is computed from the maximum extension angle ($\theta_w$) of the moving walls (drive wall and end wall) as illustrated in Figure 2.10. A complete shear cycle ($N$) consists of starting with the end walls perfectly vertical and moving the side wall in the y-axis direction until the end wall forms an angle with the vertical of $\theta_w$. Once this maximum extension is achieved, the strain direction is reversed and strain is continued until the maximum extension angle $-\theta_w$ is reached (the $-\theta_w$ value denoted as an opposite direction thus $\theta_w = |-\theta_w|$. Finally the side wall is moved to the position where the end wall is completely vertical and a new cycle is started given the total shear strain ($\gamma_{total}$) as Equation 3.1:

$$\gamma_{total} = 4N\tan(\theta_w) \qquad \text{(Equation 3.1)}$$

Based on the shear cell dimension, in order to achieve 100% shear strain (or $\gamma$=1.0) (Bridgwater et al. 1978; Pierce 2004) the shear cell needed to be sheared at a maximum of 45º in each direction. However it was found that shearing the cell to a maximum angle of 45º reduced the cell volume by around 25% from the initial volume (Figure 3.6b), thus reducing the percolation during each cycle. In addition, the adoption of a maximum shear angle of 45º results in interaction of fine particles/marker with the wall (i.e., wall effect) as projected by the vertical travel course shown in Figure 3.6b. In order to overcome this problem, the maximum angle of 26.5º was adopted which significantly increased the shear cell volume by up to

90% from the original volume thus minimised the potential of particle-wall interaction as illustrated in Figure 3.6c.

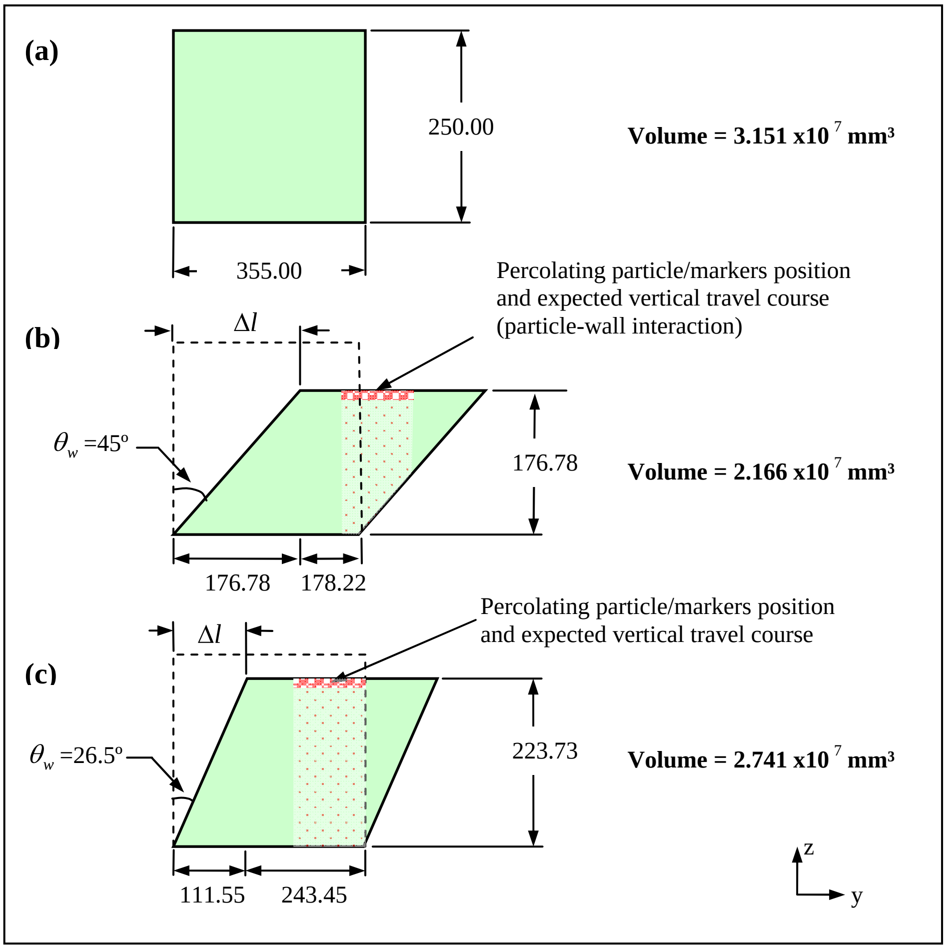


Figure 3.6: Determination of shear cell maximum extension angle ( $\theta_w$ ), deformation length ( $\Delta l$ ) and volume. Note that all dimensions in millimetres unless specified.

Figure 3.7a demonstrates that it is impracticable to achieve a large effective area at $\theta_w$=45º while shearing the box at $\theta_w$=26.5º creates approximately 132 mm length available for percolation (Figure 3.7b). In view of this, an effective area is defined as the area of which the percolating particles will have higher potential to the percolation during shear. This is consistent with the definition of failure zone (described previously in Section 2.5.3.1) by Scott and Bridgwater (1976) and Cooke and Bridgwater (1979). Apparently, the failure zone was considered as 10 times the particle diameter (Campbell and Bridgwater 1973; Scott and Bridgwater 1975; Bridgwater et al. 1978) and thus given the failure zone width of around 158 mm for the 15.75 mm glass sphere and 132 mm for the 13.20 mm basalt aggregate. Based on geometrical calculations and the shear cell dimensions, it is concluded that $\theta_w$=26.5º provides the best balance and this value was adopted for all experiments.

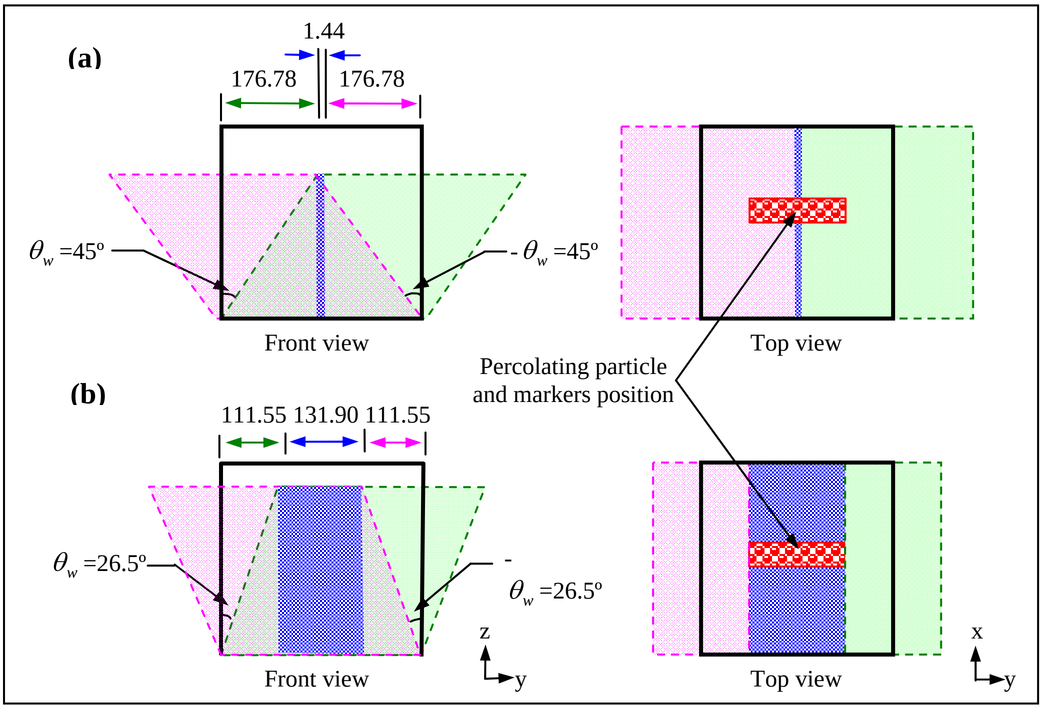


Figure 3.7: Determination of effective area (blue colour) for fine particles and marker position. Note: i) Shear cell in back direction (magenta) and front direction (green).

ii) The deformation length ($\Delta l$) of the shear cell is denotes by the green double arrow (front direction) and magenta double arrow (back direction).

iii) All length dimensions in millimetres unless specified.

In practice, shearing the box at $\theta_w$=26.5º makes the calculation of $N$ cycles easy. For instance, in order to produced $\gamma_{total}$=400% (or $\gamma_{total}$=4.0), the box was required to completed eight shear cycles compare to other angle (i.e., $\theta_w$=30º which required the shear cell to completed 6.93 cycles which convincingly impractical). In view of above point, Equation 3.2 was derived in order to calculate the total shear strain ($\gamma_{total}$) at $\theta_w$=26.5º.

$$\gamma_{total} = 8N\tan(\theta_w) \qquad \text{(Equation 3.2)}$$

### *3.3.3.2 Selection of shear motion and strain rate ($\dot{\gamma}$)*

There are three possible principal motion directions for the shear cell namely: x-axis, y-axis or z-axis. With regard to this, all three principal motion directions are expected to experience a dead zone as illustrated by Figure 3.8.

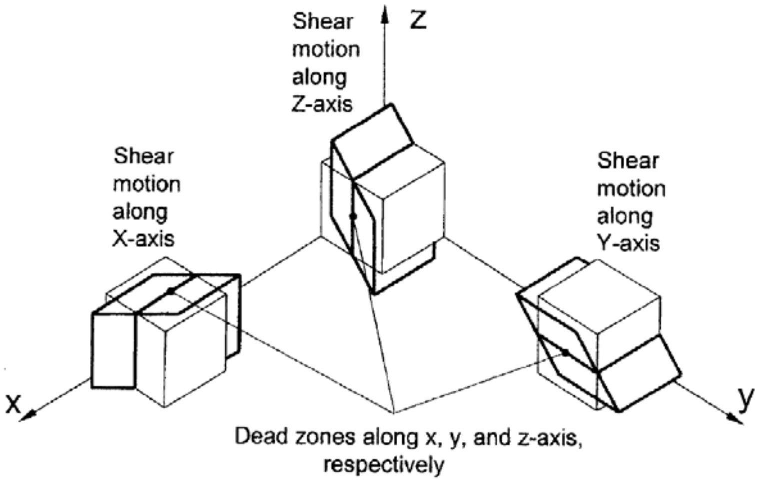


Figure 3.8: Schematic of three primary spatial shear motions (after Tang 2004).

Some drawbacks were noted by Scott and Bridgwater (1976) and Tang (2004) in each of the motion directions and are presented in Table 3.1. Table 3.2 summarises published works attributed to the specific apparatus designed by respective researchers.

Table 3.1: Principal motion direction and its drawback (after Scott and Bridgwater 1976 and Tang 2004).

| Principal motion directions | Drawbacks |
|---|---|
| Along the x-axis | - set back relative to the motion between the stationary screen/sieve (located at the bottom) shear cell and the four moving wall which may result in fine particles falling outside from the pan collection system. |
| Along the y-axis | - particles close to the bottom of the shear cell may receive negligible energy from two moving sidewalls. |
| Along the z-axis | - energy in the dead zone (i.e., central zone) is close to zero.<br>- the motion constraint along with the large damping impedes the efficient transfer of energy to the material occupying the dead zone.<br>- the diffusion coefficient of particles significantly lower with the increased bed-matrix height. |

Table 3.2: Significant physical modelling studies on percolation using simple shear cells.

| Author(s)/Date | Principal shear strain motion directions | Cell dimension (L x W x H) and particles diameter | Remark |
|---|---|---|---|
| Bridgwater et al. (1969, 1978, 1985a, 1985b);<br>Bridgwater and Ingram (1971);<br>Scott and Bridgwater (1975, 1976);<br>Cooke et al. (1978);<br>Cooke and Bridgwater (1979);<br>Drahun and Bridgwater (1983) | Along the y-axis | - Mark IA and IB (250 x 250 x 220 mm)<br>- Mark IIA and IIB (362 x 355 x 220 mm)<br>- Mark III and V (354 x 355 x 246 mm)<br>- Mark IV (70 x 70 x 55 mm)<br>- spherical sphere range from 2.35-37.20 mm | - test were conducted using a single percolating particle at a time<br>- some of the percolating particles interacted with the side and base walls (wall effect)<br>- wedging problem arise near the corners and the hold-up of percolating spheres<br>- work focused on powder systems |
| Johanson et al. (2005) | Along the y-axis | - 130 x 50 x 130 mm<br>- sand particles (0.35-1.65 mm) | - to measured the magnitude of sifting segregation occurring in bed-matrix<br>- work focused on powder systems |
| Duffy and Puri (2002) | Along the z-axis | - 100 x 50 x 100 mm<br>- mixtures of glass spheres materials; powder mixture | - shear motion energy was not uniformly transferred across the powder mixture<br>- work focused on powder systems |
| Tang (2004) | Along the x-axis | - 100 x 63 x 100 mm<br>- binary of glass spheres; mash poultry feed | - work focused on powder and agricultural applications |
| Hsiau and Shieh (1999) | Streamwise - horizontal direction (x-axis);<br>Transverse - vertical direction (y-axis) | - consists of rotating bottom disk (outside diameter 450 mm x 45 mm thick and a stationary upper disk)<br>- 3 mm glass spheres as granular media | - work focused on rheology study |
| Shear Cell for Percolation of Geomaterials (SCPG) | Along the y-axis | - 355 x 355 x 250 mm<br>- 4.00, 5.00, 6.00 mm of variety shape of glass spheres; 2.86, 4.05, 5.21, 6.18, 13.20 mm highly angular aggregates | - effect of coarse angular rock fragments and ideal media studied<br>- work focused on caved rock |

Principally, the strain in the region of the bed-matrix and fine percolating particles needs to be uniformly dispersed and its magnitude is found from the end wall movement. In view of above points, Bridgwater (1994) asserts that although the strain that could be applied in one direction was limited by practical considerations, it is still acceptable that the direction of straining could be reversed repeatedly thus generating failure zones. With respect to above points and in consideration of the least effected shear cell motion principal direction (Table 3.1 and Table 3.2), the SCPG was designed to adhere to the principal motion along the y-axis direction to overcome the low energy problem during shearing.

Additionally, Pierce (2004, 2010) numerically replicates Bridgwater et al. (1978) simple shear apparatus and extended the works by shifting the shearing direction from horizontal (y-axis) to the vertical (z-axis). Accordingly, Pierce (2004, 2010) found that the impact of vertical shearing direction had no significant influence on percolation rate and generally produced similar results to that in horizontal direction.

With regards to the risk of less energy received by the particles close to the bottom of the shear cell as noted in Table 3.1, an attempt to capture the movement of the bed-matrix medium at the bottom part of the SCPG were made by positioning three different colours of glass sphere at the bottom centre of the shear cell for the case of an ideal bed-matrix (15.75 mm glass sphere). The three glass spheres were used as the marker and were positioned at the bottom of the shear cell in order to observe the horizontal movement (along the y-axis) during shear. Figure 3.9-3.11 shows that the movement of the glass spheres at the bottom in the back and forth direction during the shearing was occurred hence proven the ability of the SCPG to overcome low energy transfer problem that may occur at the bottom part of the shear cell along the y-axis direction.

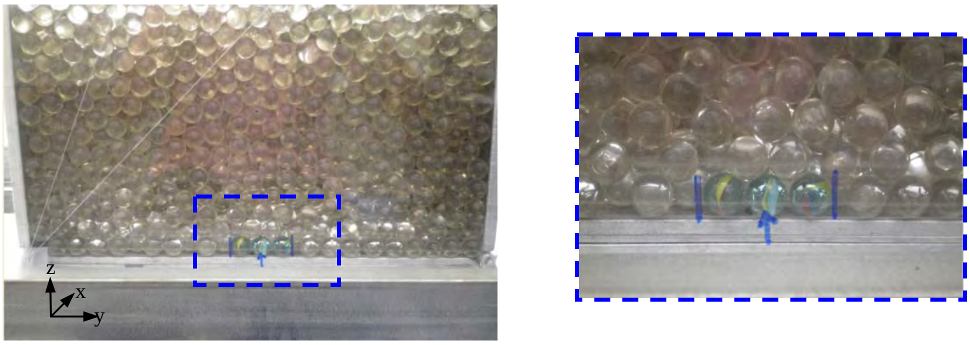


Figure 3.9: Position of three different glass spheres colour at the centre of the bottom part of shear cell prior to the shearing (left) and the enlargement of the blue square (right). Note that the blue arrow is the centre.

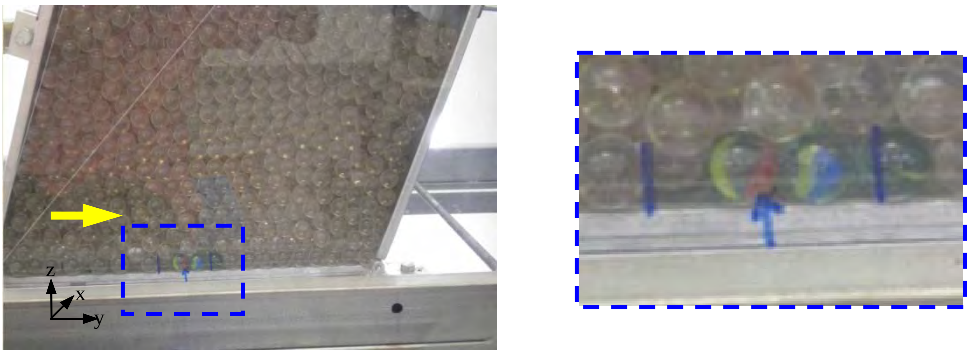


Figure 3.10: Position of three different glass spheres colour during the forth direction of the shear (left) and the enlargement of the blue square (right). Note that the yellow arrow shows the direction of movement of the glass spheres.

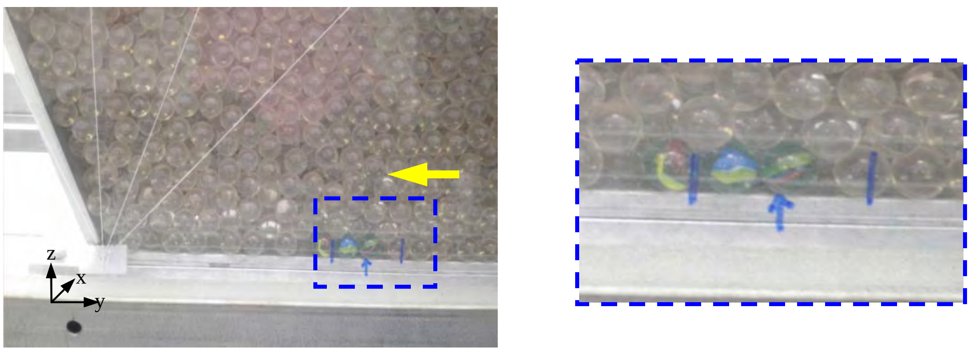


Figure 3.11: Position of three different glass spheres colour during the back direction of the shear (left) and the enlargement of the blue square (right). Note that the yellow arrow shows the direction of movement of the glass spheres.

An attempt was made to measure the distribution of shear strain within the cell using 2.86 mm basalt aggregate as percolating fine particles in the matrix of 15.75 mm glass spheres and 13.20 mm basalt aggregate (coarse bed-matrix). The results and discussion of the calibration test is presented in Section 5.2.

Based on the observations for both ideal (15.75 mm glass sphere) and crushed aggregate media (13.20 mm basalt aggregate) as a bed-matrix in the shear cell, it was found that the SCPG was able to overcome low energy magnitude at the bottom part of the shear cell (along the y-axis). On the other hand, the strain rate must be set to adequately develop a uniform shear strain at particular motor speed without significant vibrations. For this purpose the strain rates of 0.01, 0.02, 0.03 and 0.04 mm per mm/s (or $s^{-1}$) were chosen.

Given that there is no published work devoted to assessing the magnitude of shear strain (i.e., physical model and full scale test) in scaled physical models, a preliminary assessment was required toward appropriate assumption of strain magnitude in block caving mines. Despite some development in numerical analysis (i.e., Pierce et al. 2003; Pierce 2004; Hancock et al. 2010) most of the works do not represent actual rock particle shapes due to the nature of the discs in 2D or spheres in 3D (Sakakibara et al. 2008). Therefore, it is concluded that further efforts are required to develop reliable results, especially in order to replicate large scale tests with realistic caved rock fragmentation and marker data for calibration. Nevertheless an attempt to assess shear strain magnitudes in an isolated drawpoint (representing a block caving mine) by the means of 1:100 scaled Type-A Kvapil Model (Hashim and Sharrock 2010) is presented in Section 3.4.

#### *3.3.3.3 Observation wall or sidewall*

The SCPG observation wall used two 1100 mm (length) x 350 mm (height) x 20 mm (thick) clear Perspex glass as front panel to provide clear viewing and visual image recording of marker flow during drawing for the ideal media tests. However, the use of clear Perspex glass is impractical for the crushed aggregate media since the highly angular shape quickly damages the glass surface. Therefore, for the case of crushed aggregate media, the Perspex glass was replaced by 10 mm thick galvanised plate. The observation wall (or sidewall for the galvanised plate) were fixed using four M10 tread rods and can be adjusted to ensure that the both side wall closely parallels to the shear cell thus prevent fine particles from leakage through the gaps as illustrated in Figure 3.12.

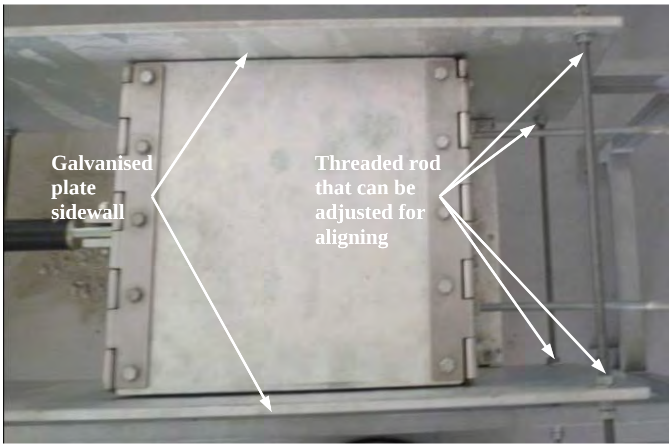


Figure 3.12: The adjustable side wall (galvanised plate) for the crushed aggregate media used in the test rig.

### *3.3.3.4 Selection of pivot position*

The dead zone effect can be shifted to the wall vicinity near the pivot location by placing the pivot on the drive wall rather than at the centre of shear cell. With regards to this, Tang (2004) noted that the use of centre-pivoted motion (i.e., Bridgwater et al. 1978; Johanson et al. 2005) should be avoided since this may produces limited shear strains and a dead zone (Duffy 2001) along the centre of axis-motion.

As the shear cell of the SCPG is attached by side-pivoted collar on the upper part of the drive wall (Figure 3.5), the dead zone along the y-axis is anticipated to be shifted to the wall vicinity where the pivot is located thus remove the dead zone effect on the centre of the shear cell. Tang (2004) also asserted that geometrically, side-pivoted motion can achieve twice the maximum strain compared to the centre-pivoted motion during the shear.

### 3.3.4 The Sieving and Measurement System

The sieving and measurement system is comprised of a sieve mesh, collection pan and weighing scale. Some key features of the sieving and measurement system include:

- provide effective separation of the percolated and sieved fines from which the accumulated particles were collected for the weighing;
- provide a rigid support for the bed-matrix and fine particles during the test which accumulated at the lower portion of the mixture;
- be simple to operate and isolated from motion components;
- prevent fine particles from leakage (pan collector); and
- resist rapid wear that may induced by the motion of bed-matrix used for the tests.

#### *3.3.4.1 Sieve mesh*

The sieving system, shown in Figure 3.13 comprised of reinforced stainless steel wire mesh and supported by the two frames namely: the 5 mm thick upper mesh frame and 10 mm thick lower mesh frame (Figure 3.5). The wire mesh was placed between the upper and lower mesh frame and fixed by nine M10 hexagonal nuts at the bottom part of the shear cell.

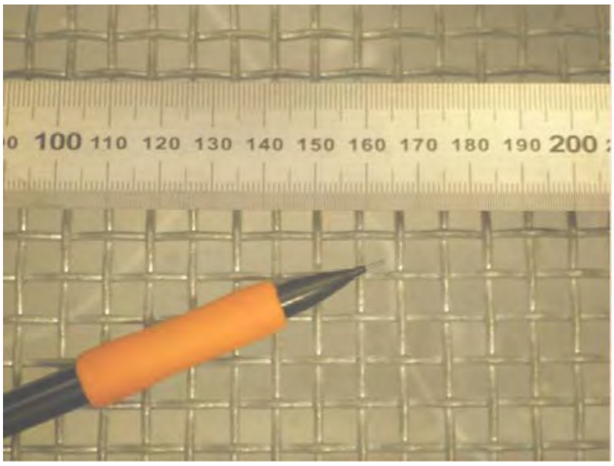


Figure 3.13: The 6.75 mm aperture stainless steel wire mesh.

The sieving system was designed to ensure that it was easier to be removed and at the same time was robust enough to support the mass load of bed-matrix during the test. In addition, sieve mesh should also have a resistance from rapid wear and tear. For these kinds of purposes, 2.00 mm diameter of stainless steel wire mesh was chosen and attached using hexagonal screws while the collection pan was placed at the bottom part of the mesh.

In view of the above, the screen size also needs to be large enough so that the fine particles drop freely through the opening during shear. In order to achieve the required condition, a 6.75 mm sieve aperture was selected and was also kept for all tests to maintain consistent results.

#### *3.3.4.2 Collection pan*

The collection pan (Figure 3.14) comprises of 5 x 5 compartments with an overall size of 350 mm x 350 mm. All 25 compartments were built from plastic with dimensions of 50 mm x 60 mm while the gaps between the collection pan and the load cell platform were approximately 5 mm. A transparent plastic were chosen for a better visual of the percolated fine particles and markers all the way through the bottom direction of the pan collection as shown in Figure 3.14.


Figure 3.14: Side view of collection pan.

Alternatively, the collection pan can be removed easily without affecting the shear cell. In order to simplify the dropped fine particles collected at the small compartment, a detachable compartment made up by plastic were created for each of the collection pan compartments. All small compartment was also numbered (Figure 3.15) in order to ease recording and identification of markers. The small compartments are able to retain a maximum of 60 gram of percolated particles before overflow.


Figure 3.15: The collection pan and numbered compartments.

Due to the nature of SCPG test mechanism, it is postulated that the shear cell will have a tendency to simulate two types of segregation mechanism: sieving and percolation (refer to Section 2.5.1). With regard to this, percolation segregation is expected to occur in the central region of the shear cell while the sieving segregation is projected to occur near the side wall zones as illustrated in Figure 3.16b.

With regards to the above point, sieving segregation may be considered as a further development or extension of percolation segregation (Tang 2004). During the motion of the side walls, a large magnitude of high motion energy generated around the side walls produces enough energy required for the smaller particles to move downward through a rolling or sliding layer of coarse particle (i.e., sieving mechanism) (Mosby et al. 1996a; de Silva et al. 2000).

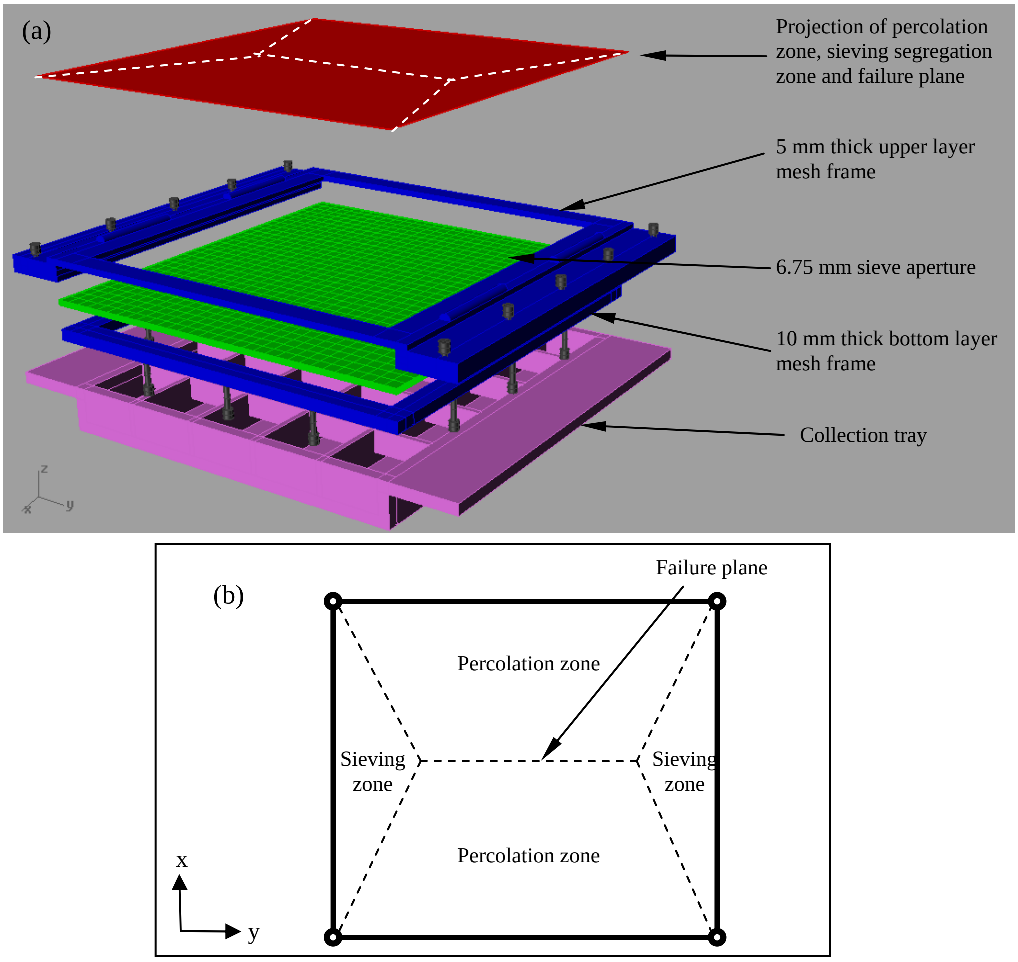


Figure 3.16: A schematic of the percolation and sieving segregation zones in the shear cell. Note: (a) Perspective view of sieving system (b) Schematic view of sieving system.

By moving a bed of particles in a back and forth direction during the test, the centre region of the shear cell is expected to experience only a small degree of deformation, thus generating a uniform slow motion and localised shear plane along the centre region. During the test, the fine particles will fall through gaps between the coarse particles due to uniform shearing and gravitational forces (i.e., percolation mechanism) (Mosby et al. 1996a; de Silva et al. 2000).

It is significant to highlight that although the process might be similar to sieving mechanism, it does not require the larger particles to being a flowing layer. This is the main reason to distinguish between the sieving segregation (occurs near the side walls) and percolation segregation (occurs along the centre of region of the shear cell).

In the case of nearly free-flowing material, it is expected that most fine particles are collected in the centre of the pan collector compartments (denoted by the pale blue colour; compartment 12-14 respectively) as shown in Figure 3.17. By contrast, a relatively small quantity of fines particles will be accumulated within the surrounding compartments from the centre of the pan collector (illustrates by yellow colour; compartment 6-10,11,15,16-20 respectively) while the smallest amount of fine particle are expected to dropped into the outer compartments (light green colour; compartment 1-5 and 20-25 respectively).

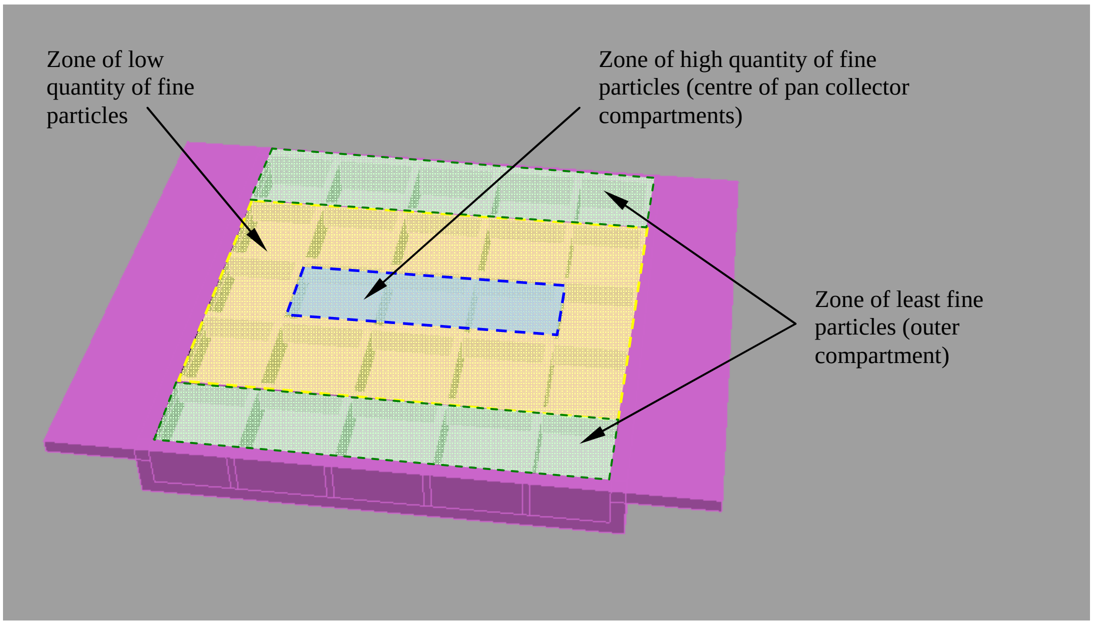


Figure 3.17: Schematic of the probable zone of high quantity (pale blue), low quantity (light yellow) and lowest amount (light green) of fine particles to be collected at the collection pan compartments.

### *3.3.4.3 Weighing scale*

Two types of electronic scales were used for weighing. The large scale with an accuracy of ±0.01 kg (August-Sauter D7470) was used for the bed-matrix (15.75 mm glass sphere and 13.20 mm crushed basalt aggregate) weight measurement while a smaller scale size was chosen for fine percolating particles mass (Mettler AE260 Delta Range) with an accuracy of ±0.1 grams.

### 3.3.5 Accessories and Tools for the SCPG

The accessories and tools for running SCPG includes: a spoon for deposition of coarse materials, a spatula to level the coarse bed surface, collection pan and small basket for unloading coarse particles, brush, standard sieves (10.00 mm and 2.36 mm respectively), stainless steel ruler, stop watch, digital SLR camera and tripod.

## 3.4 SHEAR STRAIN ASSESSMENT - SCALED PHYSICAL MODELLING

The SCPG physical and numerical experiments presented in Chapters 5 and 6 require estimates of both the total shear strains and strain rate. This experiments discussed in this section aim to use 1:100 scaled Type-A Kvapil Model (Kvapil 1965a, 1965b) to make estimates of these parameters:

- assess of the magnitude of shear strain in the region of the Isolated Movement Zone (IMZ), Isolated Extraction Zone (IEZ), Isolated Stagnant Zone (ISZ) and the centre of movement for the case of an isolated drawpoint, representing a block caving mine; and
- the shear strains were used to guide the selection of strain rate and total shear strains in the SCPG experiments in Chapter 5.

It worth noting that there is no published work on actual experiments exists on the shear strain magnitude around the drawpoint region of actual block caving mines. McNearny and Abel (1993) commented that apparently little theoretical or actual knowledge of draw is available in the case of block caving mine and surprisingly, to date, this statement is still true. As a result, based on the author's knowledge, there is no test documented or published with regards to the shear strain assessment in the block caving mines from physical models or full scale tests.

### 3.4.1 Terminology

Various authors have defined terms describing the shape formed by material flow within the cave during the extraction processes. In the shear strain assessment, the author used the terminology defined in Halim (2004). The *Extraction Zone* (EZ) is an approximately ellipsoidal shape (Kvapil 1965a) as is the shape formed by the material drawn from the drawpoint at any given point in time.

As this material moves down, the surrounding material subsidies and loosens. This zone of loosened material is defined as the *Movement Zone* (MZ) while the remaining stationary material located outside the limit ellipsoid, beyond the MZ periphery, is defined as the *Stagnant Zone* (SZ). When these flow zones are acting in isolation, as is the case when drawing from a single drawpoint, they are referred to as *Isolated Extraction Zone* (IEZ), *Isolated Movement Zone* (IMZ) and *Isolated Stagnant Zone* (ISZ) respectively. On the other hand, the *peripheral line* is described as an imaginary layer that separating two different zones as shown in Figure 3.18 and Figure 3.19 respectively.

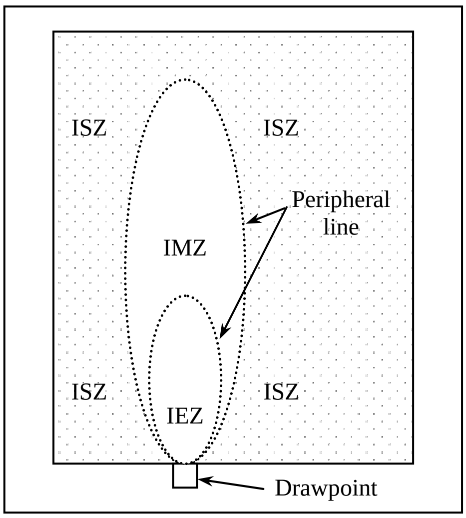


Figure 3.18: Definition of IEZ, IMZ and ISZ.

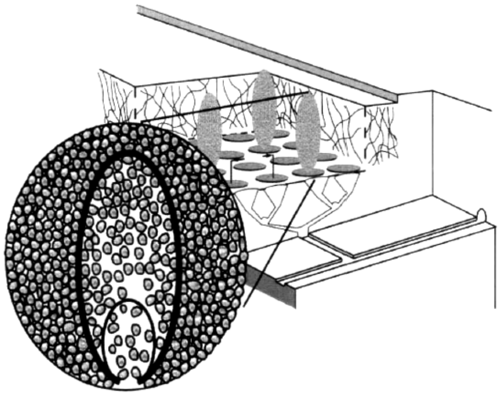

Figure 3.19: Schematic distribution of drawpoints employed in the block caving method. The ellipsoidal shapes on top of several hoppers intend to mimic the distribution of EZ's. Zoom view schematises the loosening zone (limited by the thicker line) and the IEZ (thin line) (after Melo et al. 2006).

### 3.4.2 1:100 Scaled Type-A Kvapil Gravity Flow Model

Type-A Kvapil Model (previously discussed in Section 2.3.2.1) was chosen to gain an initial understanding of the distribution and magnitude of shear strain and strain rates. Typically, the main reason for selecting such a model is due to the ability to view the flow of particles and associated movement zones.

A description of such models is advanced by Kvapil as follows:

- Type-A Kvapil Model are performed on a very simple vertical glass model using horizontal layers in which its modelled a gravity flow movement in 2D;
- the model characterised by having a vertical axis of the gravity flow that intersects the centre of an extraction opening located on the bottom of the model. The extraction opening in the model has minimum dimensions and yet is sufficiently large for a fluent and uninterrupted flow of material; and
- the model must be horizontally layered filling (the layers can be of different thickness and/or colour) in order to observe the gravity flow movement. However, the horizontal layered filling was not used in current experiment and replaced by the coordination of marker sets in a systematic way for the shear strain assessment.

It worth noting that Type-A Kvapil Models have certain limitations relating to sidewall effects which occur through the interaction of particles and walls. Nevertheless, given the lack of previous studies to quantify shear strain on coarse rock fragments, a Type A model is the appropriate place to begin. Future models will consider full three-dimensional, bell geometry, continuous particles refilling method and strain fields in which the shear strain magnitude is assessed and compare to the Type-A Kvapil Model.

The model dimensions (1.0 m length x 0.13 m width x 1.0 m height) were designed to represent an isolated drawzone with actual dimensions 100 m (length) x 13 m (width) x 100 m (height) at 1:100 scale. The selection of 1:100 scale allows a reasonable height and width to be simulated according to the fact that the scaled model does not directly affect the relationship between the draw height and draw width (Janelid 1972; Castro 2003; Power 2004; Halim 2006). The finding was generated based on 3D scaled model while it is still remains unvalidate with the 2D scaled model. In light of the above fact, Castro (2006) conducted research on the influence that a change in geometric scale has on the extraction zone and reported that results from a 1:100 model could be used to obtain those in a 1:30 scale. In addition, a 1:100 scale allows more realistic block cave dimensions to be modelled without the need for extremely large physical models which would be difficult for measuring shear strains.

The media used for the physical modelling tests was a 14.00 mm crushed basalt aggregate supplied by BC Sands, Sydney. This material has $d_{50}$ =13.20 mm and were used as the filling media and marker particles which represent a geometric similitude of 1.32 m fragmented rocks at 1:100 scale. The use of non-cohesive gravel is currently considered the best method to represent angular material found in block caves (Power 2004). A complete description of media characterisation and physical properties used for the tests is presented in Chapter 4.

A set of four markers in a rectangle pattern at approximately 50 mm spacing were used for the measurement of shear strains as shown in Figure 3.20. Each of the marker sets were divided into six horizontal levels and were positioned at an approximately row spacing of 150 mm and column spacing of 100 mm. A total of 128 markers with different colours and numbering codes for identification were used in the tests. These markers were selected randomly from the rock population used in the modelling experiments, in an attempt to minimise any bias in their flow. Each of the markers were washed, dried, spray-painted with a different colour according to their column and numbered for ease of identification and visual image recording.

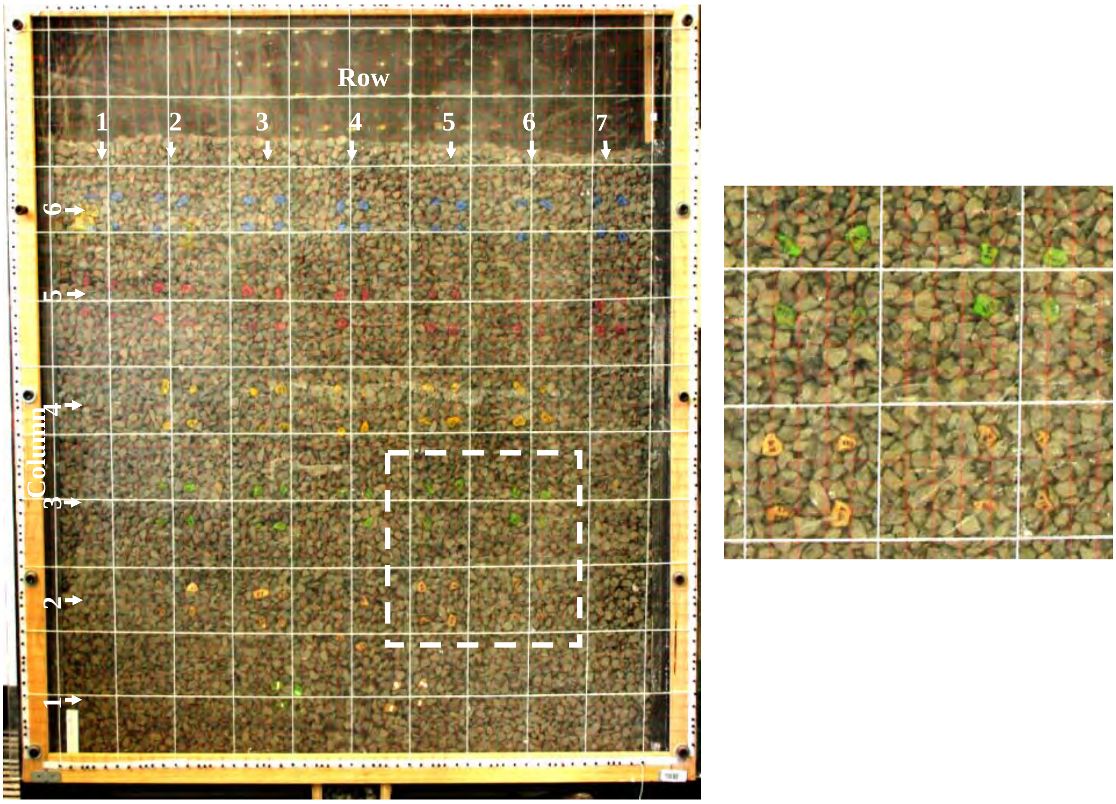


Figure 3.20: 1:100 scaled physical model of Type-A Kvapil Model (left) and the enlargement of the white square (right).

An attempt to achieve kinematic similitude was made by drawing material from the model in quantised amounts (approximately 400 gram per draw), with the interval between each draw event sufficiently long to simulate a realistic uniform draw scenario, rather than simulating continuous flow. Kvapil (1965a) suggested that provided the overall draw material had good activity, it was unimportant if all points were drawn simultaneously or successively. Supporting this, Heslop and Laubscher (1981) suggested that in practice it is not essential that drawpoints be worked simultaneously provided that the interaction of stress fields was maintained. Therefore in order to prevent asymmetric draw and to approximate 2D flow, the aggregate was drawn from both front and back faces of the model in small amounts of 200 grams to reach the 400 grams strain measurement intervals.

Typically, the model was designed to be capable of filling from both above and by lying the model down and removing the front panel and separated by three components namely: the main frame, rear and front panel and drawpoint and filling system.

#### *3.4.2.1 Main frame*

The main frame composed two rectangular frames that has been cut and weld together onto the base piece of aluminium. An extra piece of aluminium was bolted across the top of the model to retain accurate dimensions and can be remove before the test. Two long pieces of the metal (1180 mm length) were added to the base and connected using corner brackets and bolts.

#### *3.4.2.2 Rear and front panel*

A 20 mm thick clear Perspex window was used as front panel to provide clear viewing and visual image recording of marker flow during drawing. A 100 mm x 100 mm rectangular white string (larger coordinate scale) and 20 mm x 20 mm rectangular red string (smaller coordinate scale) was attached to the front panel using bolts as shown in Figure 3.20. Both rectangular string are use as a coordinate system during the test and also provide a guide for the marker positioning.

On the other hand, the rear plate was made of a 30 mm ply board spray painted black and attached to the top and bottom side panels using small blocks of wood. This system allows for the rear plate to be moved and adjusted according the required width. The rear panel was also raised from the base plate by a height of 60 mm to allow for the drawpoint system. The black painted ply board was chosen as it would provide a clear contrast to the medium during loading and was suitably rigid to provide load force support induced by the aggregate during the tests.

#### *3.4.2.3 Drawpoint and filling system*

The drawpoints were created using 18 mm thick ply board and were connected by corner brackets as shown in Figure 3.21 for easy removal. The width chosen for the model drawpoint is similar to a drawbell width (100 mm model or 10 m full scale) based on seven times the nominal particle size of the bed-matrix medium as recommended by Nedderman (1992). No specific drawbell shape was used in this study. The reasoning for this decision is that the main objective of the study was to assess the shear strain without directly associating the results to any specific caving mine designs. Even so, previous studies indicate that the IEZ is not significantly influenced by the drawbell as indicated in Castro's work (Castro 2006) and in his personal correspondence with Power (Power 2003 cited in Castro 2006). Nevertheless, these results are inconclusive and say nothing about the effects of drawbell on shear strains and more work is needed.

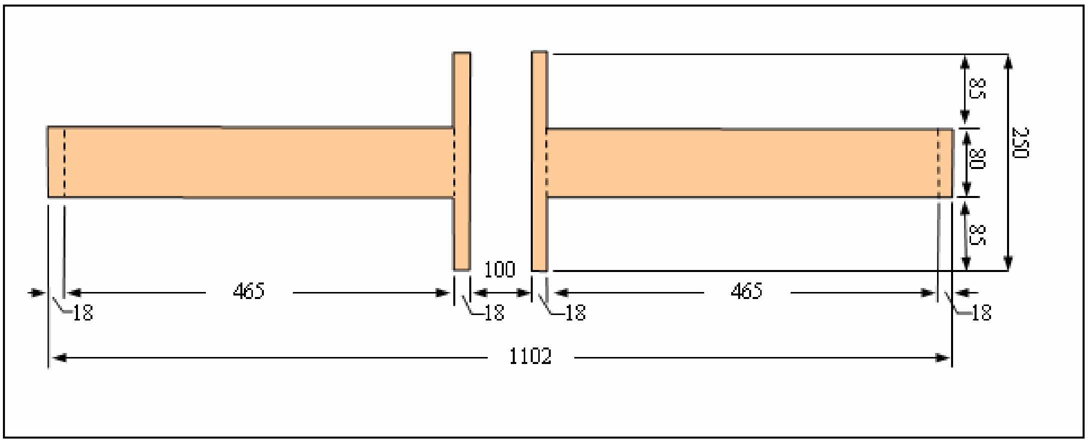


Figure 3.21: Drawpoint design (dimensions in millimetres).

Side panels were custom fit and attached to the main frame using bolts at the top and bottom of the panels. These were then removed, spray painted black and cut into 200 mm height while the top and bottom pieces being fixed to the main frame. The removable side panels also enabled filling from the sides for both markers and aggregates.

### 3.4.3 Experimental Method

#### *3.4.3.1 Loading the model*

The procedure for loading the model is as follows:

i. The front and back drawpoint were blocked using small blocks of metal.
ii. With only the top and bottom side panels in place the bed-matrix medium was loaded into the model.
iii. Upon reaching the designated level (approximately 20-25 mm from the level), a piece of wood with dimensions approximately matching the models width and depth was used to level the medium. This was done from the sides, loading or removing rocks by hand as appropriate
iv. A set of four markers were positioned as a rectangle pattern (approximately 50 mm spacing) adjacent to the Perspex glass surface while the numbered on the marker's surface were positioned towards the front panel for ease of identification and visual image recording.
v. A thin layer of bed-matrix aggregates were loaded onto the markers as a wedge to ensure the marker were not shifted during the filling of the next level of bed-matrix medium.
vi. The adjacent sets of markers were positioned at a column spacing of approximately 100 mm within the same level. The process was repeated until all the designated rectangle patterns within the column were positioned accordingly.
vii. The model was then filled with the bed-matrix medium up to the preferred level and the steps (ii) to (vi) were repeated until all the markers were positioned accordingly and the model was fully loaded.

#### *3.4.3.2 Drawing from the model*

The procedure for drawing from the model is as follows:

i. The small blocks metal at the front and back of the drawpoint were removed.
ii. A scoop was inserted into the rill to create a 45 degree angle with the base plate as shown in Figure 3.22. A fixed volume container of aggregates (approximately

400 gram) was extracted for each draw i.e., ±200 gram each from both the front and back faces of the model in order to prevent asymmetric draw and to approximate 2D flow. The cumulative mass drawn, draw number were recorded and a still image was taken of the model flow.

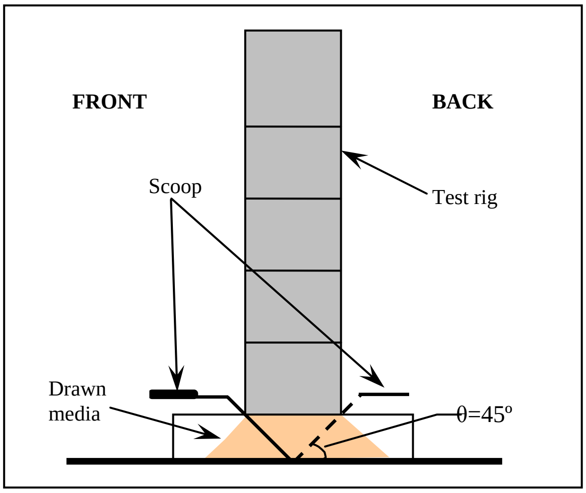


Figure 3.22: Diagram of drawing method

iii. The drawn aggregates were tipped into a shallow container and hand sorted for marker(s) that are removed from the model.
iv. Markers were identified and recorded against the draw number and were isolated into the storage boxes.
v. The remaining bed-matrix medium removed from the model was restored to the storage bins.
vi. Steps (ii) to (v) were then repeated on the back and front alternately and any observations or alterations in the experimental set up were recorded.

### 3.4.4 Method of Analysis

All the initial coordinates of the markers were individually recorded and each set are marked by its colour and coordinate. The following nomenclature was introduced for the ease of identification and analysis while illustration of the nomenclature is given in Figure 3.23:

- the first segment identifies the colour of the marker;
- the second segment refers to the column number; and
- the third segment denotes the row number.

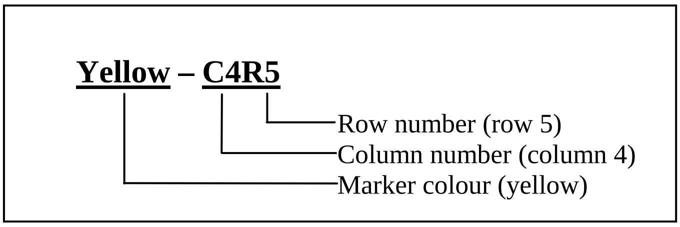


Figure 3.23: Nomenclature for the marker identification

Each of digital images taken at the end of each draw event were analysed and illustrated using the Rhinoceros® computer aided drawing program. Incremental shear strain ($\gamma_{inc}$) in relation to the draw number was then calculated using Equation 7.1 and defined as displacement of one surface with respect to another divided by the distance between them. On the other hand, the global shear strain ($\gamma_{global}$) [Equation 7.2] is defined as total displacement of one surface with respect to another divided by the distance between them. The shear strain magnitude in the Isolated Movement Zone (IMZ), Isolated Extraction Zone (IEZ), Isolated Stagnant Zone (ISZ) and the centre of movement are then plotted in a moving average graph of incremental shear strain versus draw number.

$$\gamma_{inc} = \frac{\Delta\ell}{H} = \tan\theta_{inc} \text{ (dimensionless)} \qquad \text{(Equation 7.1)}$$

$$\gamma_{global} = \frac{\Sigma L}{H} = \tan\theta_{global} \text{ (dimensionless)} \qquad \text{(Equation 7.2)}$$

Where, as shown in Figure 3.24:

- $\Delta\ell$ is the deformation in the $x$-direction (mm);
- $\Sigma L$ is the total deformation in the $x$-direction (mm);
- $H$ is the original length (mm); and
- $\theta_{inc}$ and $\theta_{global}$ is angle the sheared line makes with its original orientation.

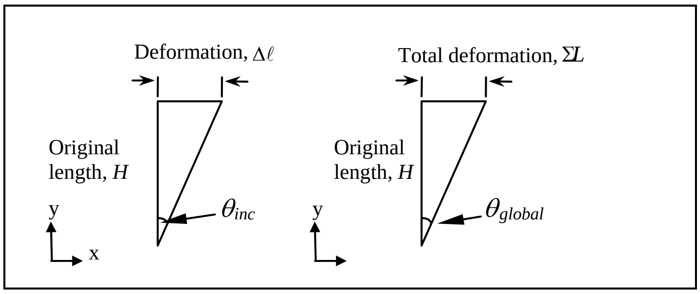


Figure 3.24: Shear strain diagram. Note: (a) Incremental shear strains (b) Global shear strains.

### 3.4.5 Results and Discussions

#### *3.4.5.1 Off-axis shear strains in the IMZ and IEZ*

Off-axis shear strains in the IMZ and IEZ were represented by the markers along rows 3 and 5 respectively (as shown in Figure 3.20). Figure 3.25 illustrates an example of significant changes experienced by Red-C3R5 marker set from initial stage (before draw) until final (after 57 draw event) using Rhinoceros®. Figure 3.25b shows that the Red-C3R5 marker set has transformed from an initial rectangular shape to rhomboid shape after 57 draw events.

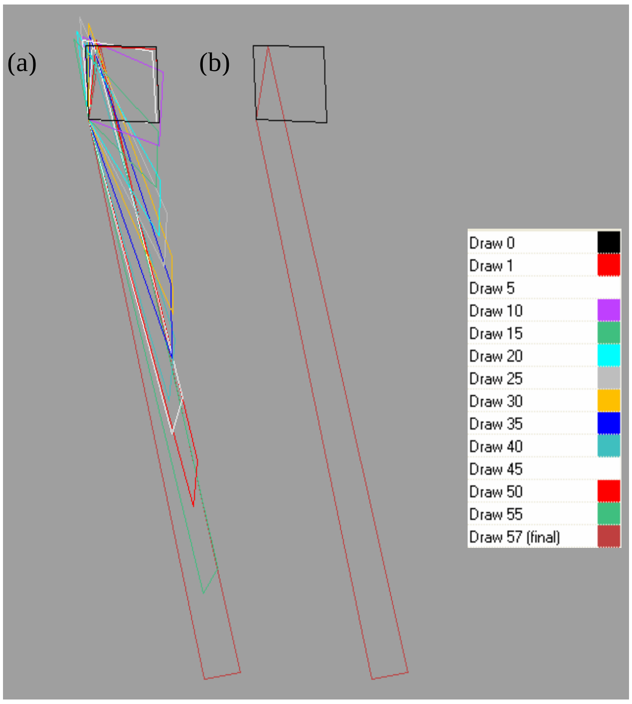


Figure 3.25: Illustration of Red-C3R5 marker set shape during the test using the Rhinoceros® programme. (a) “Incremental shear strains” at each draw increment (b) “Global shear strains” from initial position (black colour line) and final shape prior draw (red colour line). The layer colours show the marker shape transformation at each draw increment.

A draw event versus incremental shear strain graph for the IMZ and IEZ were plotted from the initial equilibrium stage (before draw) until the marker sets were removed through the drawpoint (Figure 3.26). The moving average interval was the mean of three readings. The graph represents the Gold-C2R5, Green-C3R5, Yellow-C4R5 and Red-C5R5 marker sets respectively.

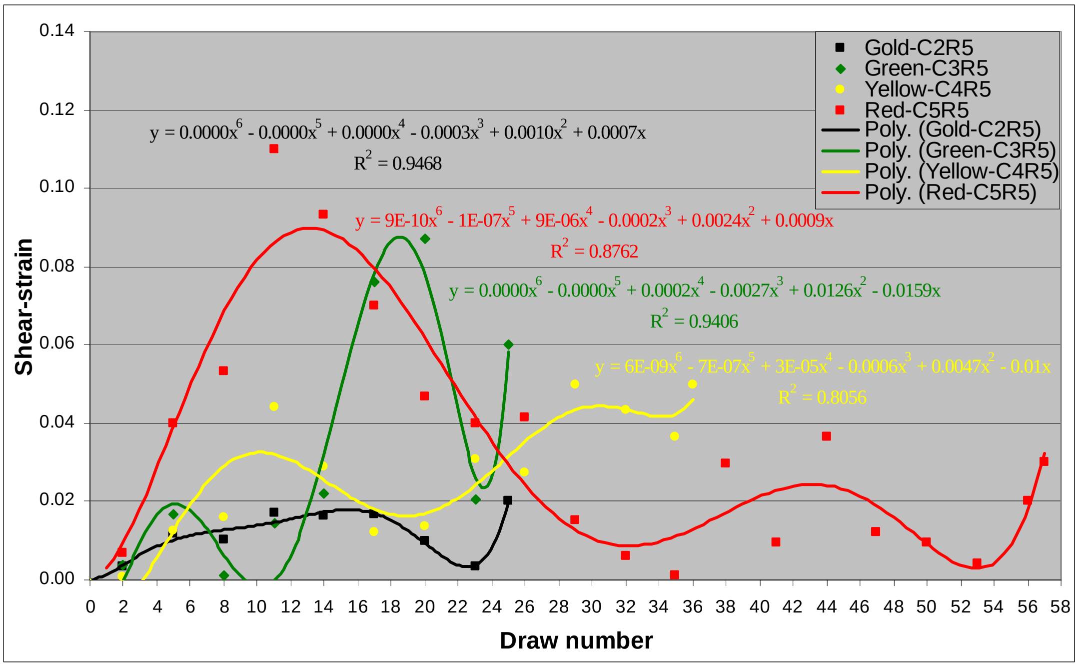


Figure 3.26: Draw number versus incremental average of shear strain around the IMZ and IEZ.

This plot shows that while the shear strain magnitude in the IMZ and IEZ varies significantly, some common patterns are present. For example Figure 3.26 illustrates that two moving average maxima points occur for each of the marker sets, and these points are explained through consideration of the marker encountering the IMZ and IEZ transition point (e.g., within the IMZ-IEZ peripheral boundary).

During the drawing processes, markers travel down towards the drawpoint while at the same time the ellipsoid of IMZ grows larger. For the duration of these processes, the shear strains are constantly increasing until reaching the first maxima point. This is followed by a significant reduction in shear strain as more uniform downward movement occurs towards the drawpoint. A similar pattern is observed as the markers enter the IEZ boundary, which is the second maxima point.

Figure 3.27 shows the movement of the red marker set (Red-C5R5), as it approaches the ISZ – IMZ boundary. It was apparent that at draw number 12, the red marker set has completely moved to the IMZ as illustrated by the first maxima point in Figure 3.26.

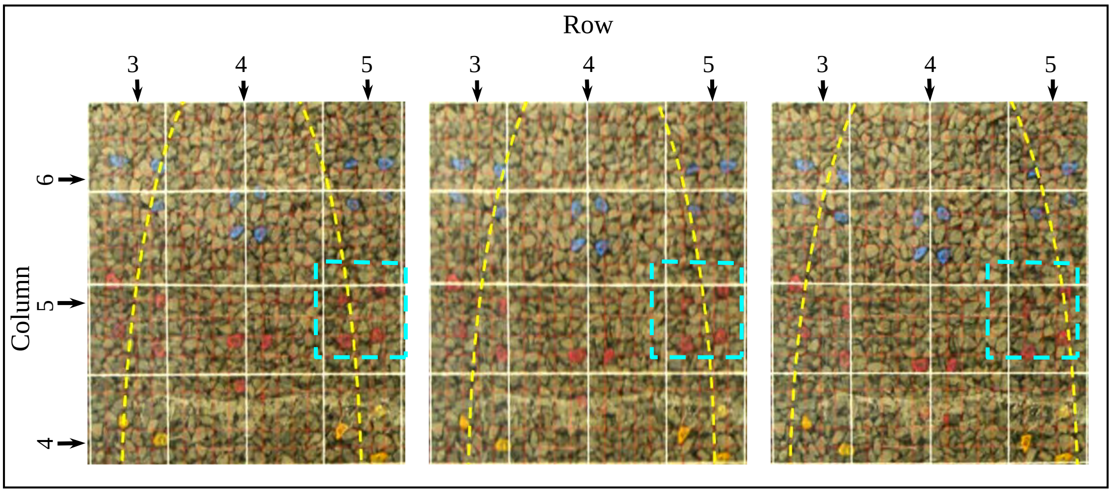


Figure 3.27: Mobilisation of the red marker set Red-C5R5 (turquoise square) downward to the IMZ periphery (yellow dashed line) as the IMZ zone grows. Note that draw number 10 (left), number 11 (middle) and number 12 (right).

Based on the measured data, the incremental shear strain at IMZ and IEZ is in the order $0.01 \leq \gamma_{inc} \leq 0.10$ in which the magnitude was highest along the ISZ-IMZ boundary (represent by the yellow dashed line; Figure 3.27 and maxima in the polynomial fit; Figure 3.26). The significantly higher magnitude of shear strain at the ISZ-IMZ boundary shows that the marker sets temporary experiences a rapid movement as it shifts from the stagnant position (in ISZ) into moving aggregates in the IMZ. The similar observation was also recorded within the IMZ-IEZ boundary as the marker set instantly transits from the IMZ into IEZ during draw.

It is also interesting to note that the marker sets experience high incremental shear strains near the drawpoint, just prior to being removed from the model, as illustrated by the end of graph in Figure 3.26. This can be explained by the rapid horizontal flow movement during the final draw increments. As a result, shear strains were found to be high near the drawpoint, where removal of confining stress occurs due to drawing (Hashim and Sharrock 2010).

### 3.4.5.2 Shear strain along the central axis

The shear strains along the central axis (illustrated by row 4 in scaled physical model) showed similar patterns to the off-axis results; draw event relations for selected Blue-C6R4 and Yellow-C4R4 set markers are shown in Figure 3.28. However, the marker sets along the central axis experience lower magnitudes of shear strain as compared to those off-axis near the IMZ.

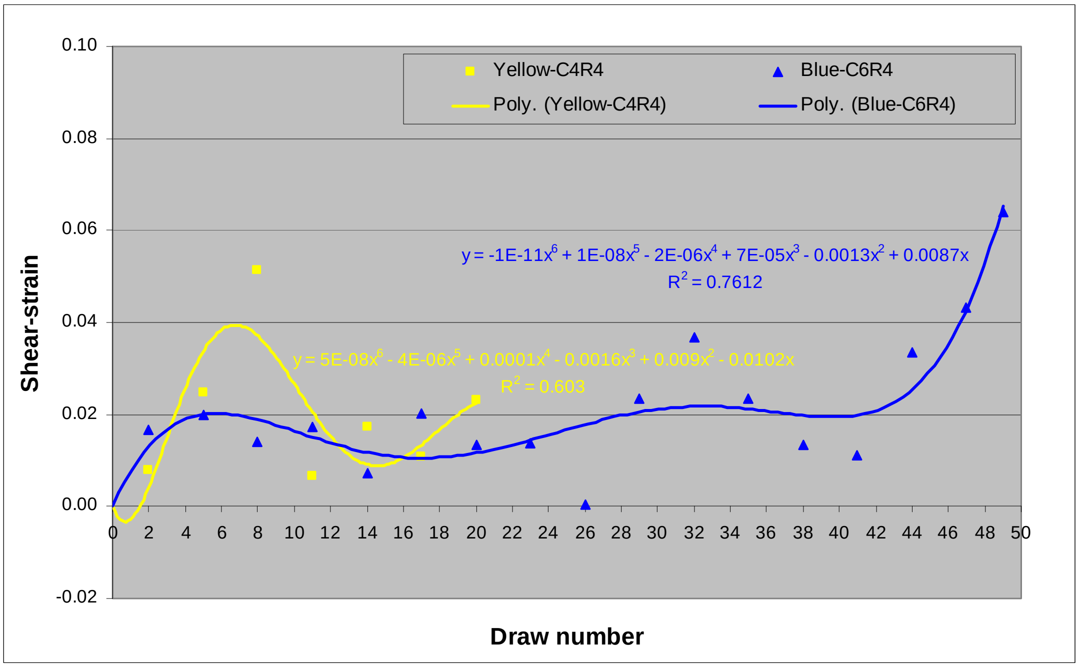


Figure 3.28: Draw number versus incremental average of shear strain along the centre of movement.

A graph of shear strain along the central axis (Figure 3.28) suggests that the Yellow-C4R4 marker set entered the IMZ as early first draw (represented by first yellow maxima). The second maxima occurred at the draw number seven (approximately 2800 grams of drawn mass) as the markers entered the IEZ. Similar pattern were also observed for the Blue-C6R4 marker sets as it mobilized downward to the IMZ periphery shown in Figure 3.29.

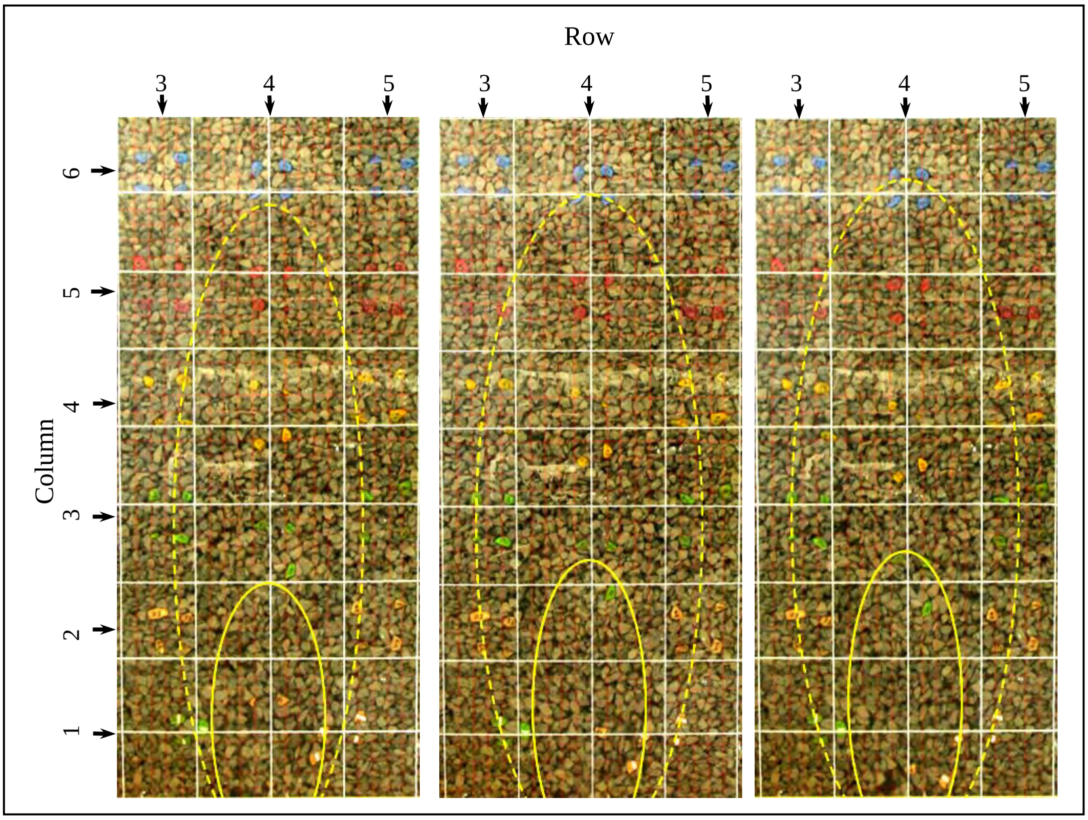


Figure 3.29: Mobilisation of the Blue-C6R4 marker set downward to the IMZ periphery (yellow dashed line) and IEZ periphery (yellow line). Note that draw number 4 (left), number 5 (middle) and number 6 (right).

By projecting the first and second maxima, the maximum shear strain values along the centre of movement were found to be relatively low (≤ 0.05). Once again, the shear strains were higher at the end of drawing processes as shown in Figure 3.28.

The low incremental shear strain values along the central axis as compared to the off-axis shear strains in the IMZ and IEZ are expected since in general, the marker sets along this path experience mainly vertical translation (straight down to the drawpoint) during each draw event (Hashim and Sharrock 2010). It was also found that the low shear strains occur along the centre of movement as shown in Figure 3.30b. Note that in this region strains are mostly volumetric.

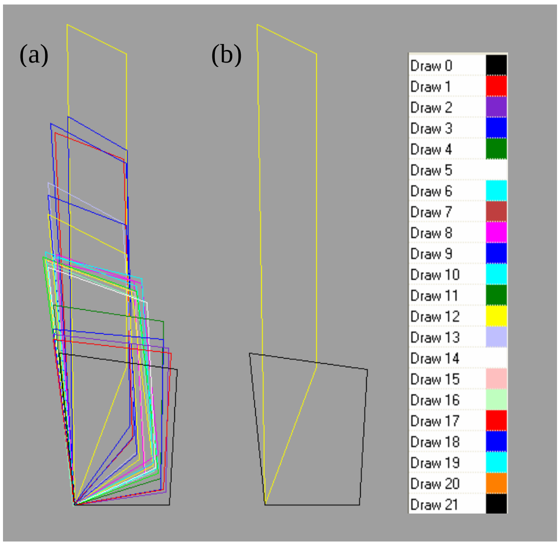


Figure 3.30: Illustration of Yellow-C4R4 marker set shape during the test using the Rhinoceros® programme. Note: (a) "Incremental shear strains" at each draw increment (b) "Global shear strains" from initial position (black colour line) and final shape prior draw (red colour line). The layer colours show the marker shape transformation at each draw increment.

On another note, the patterns (but not the magnitudes) of shear strain, recorded in Figures3.26 and 3.28, generally agree with PFC3D simulations by Pierce (2004). Pierce (2004) conducted numerical simulation to examine the role of shear-induced inter-particle percolation in preferential downward migration of fine fragments in caved rock. In this work it is noted that the central axis of the stagnant zone and the movement zone centre experience lower shear strains in comparison to the significantly higher off axis shear strains as illustrated in Figure 3.31. The primary objective of this study was to numerically model the percolation experiments undertaken by Bridgwater et al. (1978) on mono-sized particles.

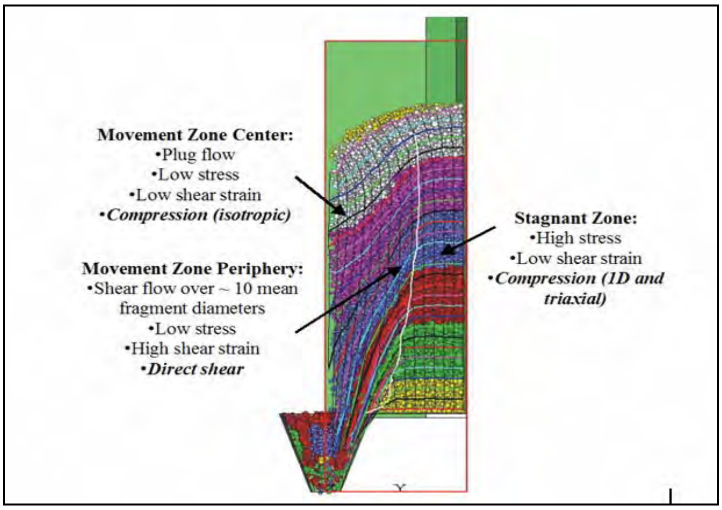


Figure 3.31: Typical illustration of PFC3D results conducted by Pierce (2004).

### *3.4.5.3 Shear strain in the ISZ*

The incremental shear strains in the ISZ were found to be persistently below the threshold of measurement ($\gamma_{inc} \approx 0$) for the entire process as illustrated in Figure 3.32. It is hypothesised that elastic shear strain exists around the ISZ. Nevertheless, based on DEM modelling by Pierce (2004), aggregates (and marker sets) are expected to experience high horizontal stresses around the ISZ.

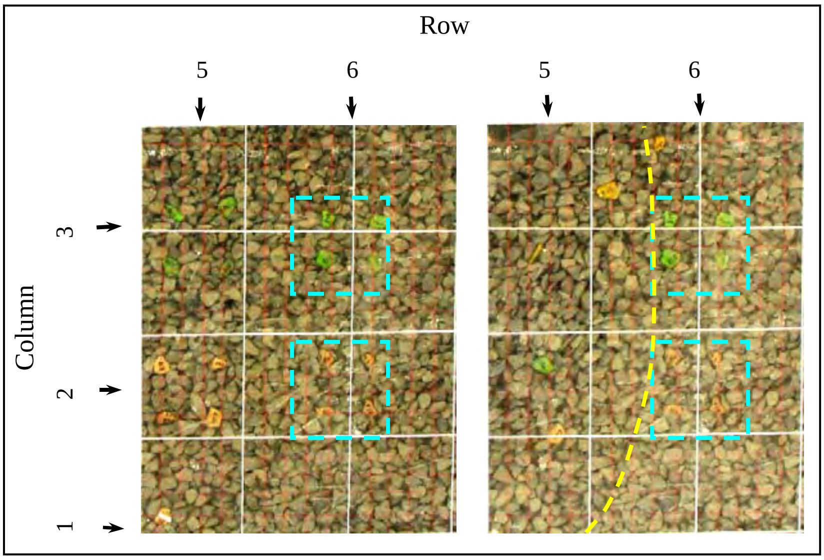


Figure 3.32: Position of Gold-C2R6 and Green-C3R6 and set markers (turquoise square) in IZS that remain unchanged while the IMZ is represented by yellow dashed line. Note that left picture was at initial (before draw) and right picture was at final draw.

Pierce (2004) reports that as both the IMZ and IEZ grow, high horizontal stresses initiate the deviatoric stress within aggregates (and marker sets) around the ISZ. At this stage, the aggregate and marker sets in the IMZ began to mobilise thus reducing the size of the ISZ.

### 3.4.6 Conclusions

A 1:100 scaled Type-A Kvapil Model was employed to assess the shear strain experienced in an isolated drawpoint, representing a block caving mine. Figure 3.33 illustrates the magnitude of shear strain in the region of the Isolated Movement Zone (IMZ), Isolated Extraction Zone (IEZ), Isolated Stagnant Zone (ISZ) and the centre of movement. The results indicate that the magnitude of incremental shear strain along the central axis of the movement zone was lower compared to off-axis, in the IMZ and IEZ respectively.

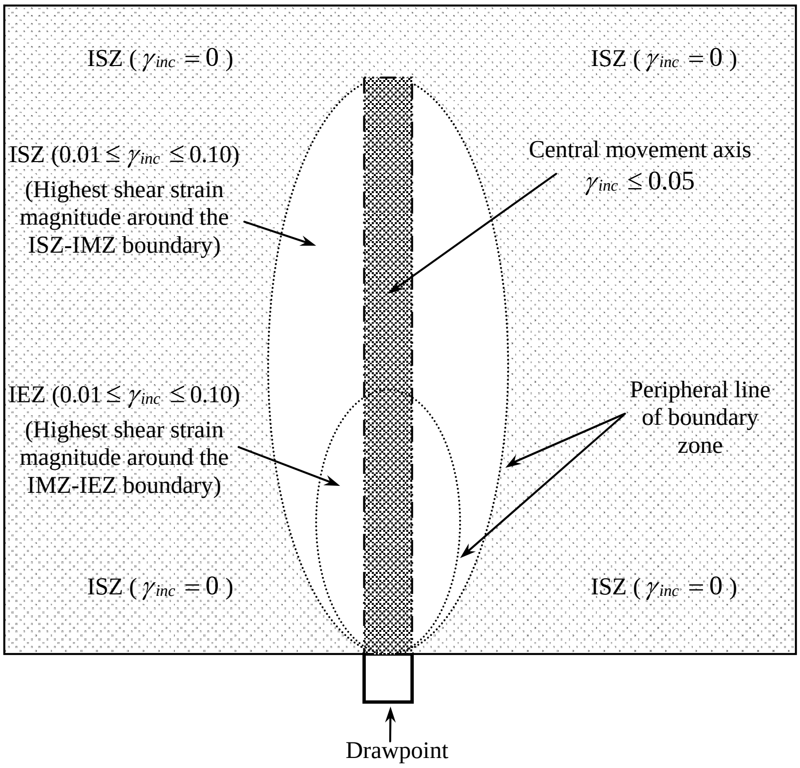


Figure 3.33: Magnitude of shear strain in IEZ, IMZ, ISZ and the centre of movement.

As the work is based solely on two dimensional modelling, a three dimensional scaled model is recommended for future work. In addition, simultaneous filling methods during the draw should also be introduced while an interactive draw condition is recommended to provide confirmation of these results. Nevertheless this assessment helps quantify the magnitude of shear strain experienced around an isolated drawpoint in a block caving mine.

## 3.5 SUMMARY OF SHEAR CELL FOR PERCOLATION OF GEOMATERIALS

A Shear Cell for Percolation of Geomaterials was designed and constructed for the percolation studies on coarse angular aggregates with shape factors similar to caved rock. It is believed that this test rig is the first to be introduced for percolation of fine particles in a coarse rock particle bed-matrix. The SCPG was used to quantify particle diameter ratio effect, strain effect, shape effect, density effect and size distribution effect for percolation of fine particles.

The SCPG was designed, fabricated and devised to produce reproducible results with standard procedures in order to contribute towards new understanding of the percolation of fine particles in the ideal and crushed aggregate media. The key features of the works lies within the efficiency of the SCPG system to ensure that all the tests are delivered to a high standard in a practical time frame.

Principally, the SCPG uses similar mechanism employed by Scott and Bridgwater (1976) and Stephens and Bridgwater (1978a, 1978b) for measurement of a single particle through a bed-matrix (as previously discussed in Section 2.5.5.1). This was done by shearing the shear cell so that its shape changed from a rectangular to a parallelogram thus analogous to a failure zone (Cooke and Bridgwater 1979). By using such a mechanism, the SCPG is capable to achieve a uniform strain which enables the percolation rate to be found without recourse to exhaustive sampling or cine photography.

Some key features that distinguish the SCPG is it ability to carry out higher amount of fine particles and introduction of highly angular aggregates with attributes similar to caved rock. These characteristics differ considerably from other research that use spherical fine particles and/or rounded aggregate (i.e., rounded sand) as a bed-matrix in their percolation studies. The use of highly angular media such as gravel aggregate is expected to produce results more relevant to caved rock.

The experimental design, results and discussion of percolation experiments are documented in Chapter 5 while a validation and development of new numerical model based on PFC3D™ is presented in Chapter 6.

# CHAPTER 4: MATERIAL PROPERTIES AND CHARACTERISATION

## 4.1 INTRODUCTION

This chapter describes the material properties of two different types of media used in the percolation experiments: ideal media and crushed aggregate media. Some key material properties and characterisation tests used in this chapter include particle size distribution, shape and shape factor, particle density, porosity, void ratio and shear box testing.

It is worth highlighting that the use of 13.20 mm basalt aggregate (crushed aggregate media) as bed-matrix in the SCPG is a key feature distinguishing this research from earlier scholarship on mono-size spherical particles. Accordingly, the shape and surface friction of crushed rock aggregate closely resembles real caved rock than the mono-size spherical particles (e.g., glass spheres). Characterisation tests were also undertaken for both ideal media and crushed aggregate media such as glass spheres, fine basalt aggregates, plastic spheres and steel spheres according to its appropriateness with regards to the nature of percolation tests.

## 4.2 MODEL MEDIA

The media used for physical modelling experiments of shear-strain assessment and simple shear cells must comply or best closely appropriate geometric similitude. On the other hand, it is also necessary to consider an appropriate material that provides better control and handling yet produces reliable results. With regards to this, two types of test media: ideal media and crushed aggregate media were selected for this research.

### 4.2.1 Ideal Media

An ideal media such as spherical glass, metal spheres (i.e., steel sphere) or spherical sands provides better control in terms of experimental practice and results that are easy to analyse. Moreover, spherical media was employed by many researchers due to the fact that most of the numerical methods still represent granule and highly angular shapes particles as circular discs in 2D or spheres in 3D (Sakakibara et al. 2008). It is interesting to highlight that the use of glass spheres in segregation tests has received a relatively large amount of publications (e.g., Bridgwater et al. 1969; Cooke et al. 1978; Cooke and Bridgwater 1979; Hsiau and Shieh 1999; Duffy and Puri 2002; Johanson et al. 2005; Jha and Puri 2009).

Tang (2004) noted that the use of ideal media employed by many researchers is related to the fact that glass spheres offer a number of practical features such as ideal shape (spherical), size range diversity, high flow-ability and economical factor (available at reasonable cost commercially). However, results from the use of ideal media cannot readily be applied in industrial applications and in most cases, are far removed from real world application.

For the purpose of this research, glass spheres of various shapes (spherical, cubical, cylindrical and bi-conical shape), steel spheres (spherical) and plastic spheres (spherical) were selected as ideal media. Table 4.1 summarized overall characterisation and test parameter of the ideal media used in the SCPG while Figure 4.1 shows the materials used as the ideal media in this thesis.

Table 4.1: Characterisation and test parameter for ideal media.

| Media | Shape | Test parameter for percolation study | Characteristic tests |
|---|---|---|---|
| 15.75 mm glass sphere | Spherical | As a bed-matrix particle | Particle density and volumetric;<br>Particle shape and shape factor;<br>Void ratio and porosity |
| 6.00 mm glass sphere | Spherical | Diameter ratio effect | |
| 5.00 mm glass sphere | Spherical | Diameter ratio effect | |
| 4.00 mm glass sphere | Spherical | Diameter ratio effect;<br>Strain effect;<br>Density effect;<br>Shape effect | |
| 4.75 mm steel sphere | Spherical | Density effect | |
| 4.00 mm plastic sphere | Spherical | Density effect | |
| 4.00 mm bi-conical glass | Bi-conical | Shape effect | |
| 4.00 mm cylindrical glass | Cylindrical | Shape effect | |
| 4.00 mm cubical class | Cubical | Shape effect | |

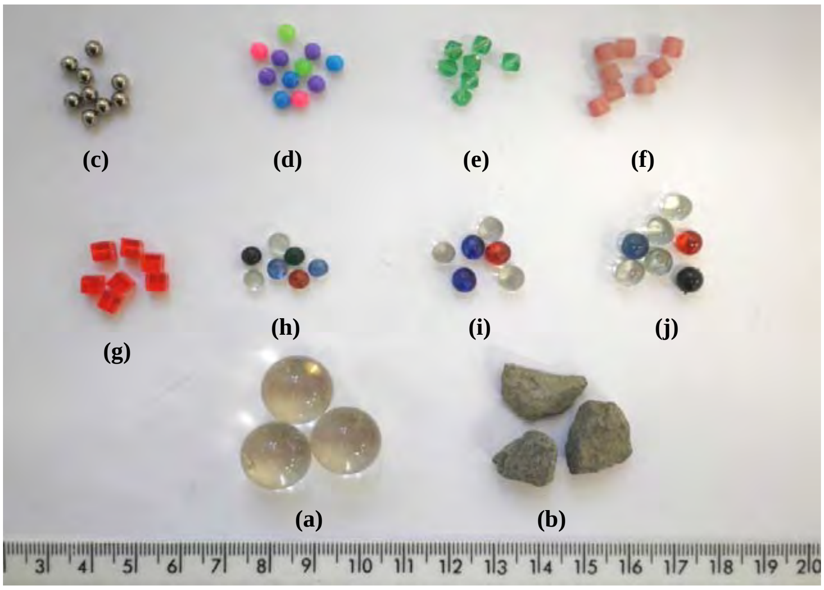


Figure 4.1: Ideal particles used in the study and comparison between the bed-matrix of (a) 13.20 mm crushed basalt aggregate (b) 15.75 mm glass sphere (c) 4.00 mm steel sphere (d) 4.00 mm plastic sphere (e) 4.00 mm bi-conical glass (f) 4.00 mm cylindrical glass (g) 4.00 mm cubical class (h) 4.00 mm glass sphere (i) 5.00 mm glass sphere (j) 6.00 mm glass sphere.

The selection criterion was based on the ready availability of modelling materials and the similitude features of the natural granular aggregates. For instance, glass spheres provide close density to the crushed basalt aggregate in the diameter ratio, strain and shape effect tests for the percolation study. The selection of the spherical particles (glass spheres) to model the ideal media was also in order to evaluate the capability of the DEM code (PFC3D$^{TM}$) to build the same geometry of the particles in the DEM simulations (Chapter 6). In addition, the selection of an ideal media (spherical shape) is necessary to test the hypothesis on the size and shape effect between the non-spherical (i.e., particle clumps) and mono-sphere particles in Chapter 6.

### 4.2.2 Crushed Aggregate Media

An aggregate media such as angular aggregates[16] (ASTM D653-04 2005), crushed rock or gravel[17] (ASTM C125-03 2005) is difficult to measure and characterise but the results provide similar representation of the shape, density and surface friction to caved rock characteristic and properties. For instance, granular aggregate or crushed rock may engage far more complex properties and experimental procedures than glass spheres or sand particles.

Basalt aggregate, sometimes referred as Blue Metal was chosen to represent crushed aggregate media, was purchased from BC Sands, Sydney. Several size aggregates were considered as the crushed aggregate media range from 7, 10, 14 and 20 mm size. With respect to the selection of suitable crushed aggregate size, the 7 mm aggregate size was considered too small to be used as bed-matrix (e.g., the sieve aperture is 6.75 mm). Geometrically, a nominal 10 mm aggregate size was also not suitable for the percolation tests (e.g., the largest fine percolating particle size is 6.18 mm) and might not produce a satisfactory correlation between the particle diameter ratio ($d_p/d_b$) tests while the 20 mm aggregates size was also removed for this thesis due to its larger size.

[16] Angular aggregate is defined as an aggregate or the particles of which process well-defined edge formed the intersection of roughly planar faces.
[17] Gravel is defined as a coarse aggregate resulting from natural disintegration and abrasion of rock or processing of weakly bond conglomerate.

As a result, 14.00 mm aggregate was adopted as the nominal bed-matrix in the SCPG. The selection of 14.00 mm basalt aggregate (later referred as $d_{50}$ =13.20 mm through the thesis) was also based on its geometrical properties. In line with the geometrical properties, Castro (2006) asserted the significance geometrical properties (i.e., particle's size, distribution and shape) have on the gravity flow of caved rock. In addition, the 13.20 mm basalt aggregate offered the closest diameter with the 15.75 mm glass sphere (ideal media) used in this thesis.

It must be noted also that the 13.20 mm basalt aggregates used in the SCPG was used for the shear strain assessments presented in Section 3.4. This media was employed to ensure that a good correlation between the shear strain assessment (Type-A Kvapil Model) and percolation test (SCPG rig) existed. Alternatively, the 13.20 mm basalt aggregates represent a geometric similitude of 1.32 m fragmented rocks at 1:100 scale and 0.40 m at 1:30 scale.

On the other hand, the fine percolating particles for the crushed aggregates (2.86, 4.05, 5.21 and 6.18 mm) were composed using the sieve of 7 mm aggregates purchased separately. Each of the fine percolating particles was washed, dried, spray-painted with a different colour according to their sizes for ease of identification and visual image recording.

A full characterisation and physical properties is discussed in detail within this chapter while Table 4.2 and Figure 4.2 depict the basalt aggregates used in this thesis. It should be highlighted that since the main objective of the thesis was to study the percolation of granular aggregates, any size lower than 2.36 mm are removed in the tests since it was considered as coarse sand (ASTM C125-03 2005). Furthermore, due to the fact that the sand particles tend to behave (and become) more spherical than angular, any representation of sand particle in mining problem may not be consistently reliable (Yenge 1980).


Figure 4.2: Crushed aggregates media used in the study and comparison between the bed-matrix of (a) 13.20 mm crushed basalt aggregate (b) 15.75 mm glass sphere (c) 2.86 mm (d) 4.05 mm (e) 5.21 mm (f) 6.18 mm.

Table 4.2: Characterisation and test parameters for crushed aggregate media.

| Media | Shape | Test parameter for percolation study | Characteristic tests |
|---|---|---|---|
| 13.20 mm basalt aggregate | Highly angular | As a bed-matrix particle | Direct shear test;<br>Particle density and volumetric;<br>Particle shape and shape factor;<br>Void ratio and porosity |
| 6.18 mm basalt aggregate | Highly angular | Diameter ratio effect | Particle density and volumetric;<br>Particle shape and shape factor;<br>Void ratio and porosity |
| 5.21 mm basalt aggregate | Highly angular | Diameter ratio effect | Particle density and volumetric;<br>Particle shape and shape factor;<br>Void ratio and porosity |
| 4.05 mm basalt aggregate | Highly angular | Diameter ratio effect;<br>Strain effect;<br>Density effect;<br>Shape effect | Particle density and volumetric;<br>Particle shape and shape factor;<br>Void ratio and porosity |
| 2.86 mm basalt aggregate | Highly angular | Diameter ratio effect | Particle density and volumetric;<br>Particle shape and shape factor;<br>Void ratio and porosity |

## 4.3 SAMPLING PROCEDURE

An accurate sampling according to standard preparation is significant in order to obtain reliable results before any test could be carried out. Samples must be as close as possible to represent the average properties of the batch on which the tests are undertaken (BS EN 932-1:1997 1997).

According to ASTM Committee E-29 on Particle and Spray Characterization (1998), bulk samples can be reduced to appropriate sample sizes for testing by using a riffling method (using a *riffle box*[18]) or by coning and quartering method (normally involves shovelling for a large pile of samples). Alternatively, the riffling method is only appropriate for a dry material while coning and quartering can be used to reduce a dry or wet/damp material down to quantity which can be further prepared. The coning and quartering method (Figure 4.3) was selected for sampling preparation based on time considerations due to the large amount of basalt aggregates.

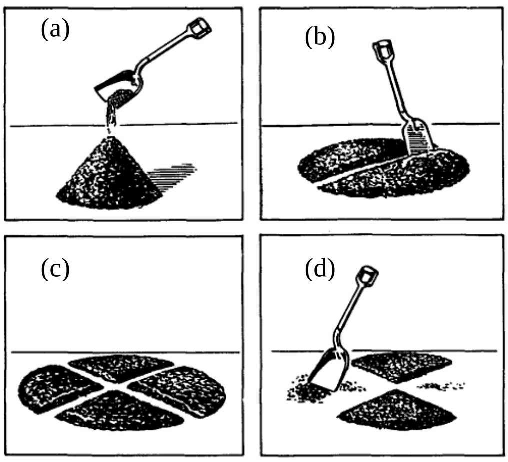


Figure 4.3: Coning and Quartering method (after ASTM Committee E-29 on Particle and Spray Characterization 1998). Note: (a) Piling (b) Flattening (c) Slicing (d) Rejecting.

[18] Riffle box is an apparatus that consists of an even number of chutes discharging in alternate directions. The material is passed through the riffle box and which divides the material into two portions. One of these portions is then removed while the other portion is passed through the riffle box again. The process repeated until the sample has been reduced to the required size.

In the coning and quartering method, a shovel is used to mix the aggregates to form a cone by pouring the gravel into the centre of a cone. In order to ensure that the aggregates are scattered down the cone uniformly, the cone is turned over three times and then flattened by pressing the flat surface of the shovel on the top of the cone (referred as flat cone).

The flat cone was then split equally into quarters and any two opposite quarter are discarded. The process repeated for the remaining two quarters until the sample has been reduced to the required size for testing (i.e., sieving test). Horwitz (1990) noted that if the process is performed only once, coning and quartering is no more efficient than taking alternate portions and discarding the others.

## 4.4 MATERIAL CHARACTERISTIC TESTS

### 4.4.1 Particle Size Distribution

Only 13.20 mm crushed basalt aggregate was selected for the particle size distribution test. The reason to this was due to the fact that all the ideal media used in this thesis generally composed by a constant singular mono-size particles (i.e., 15.75 mm glass sphere). On the other hand, fine percolating crushed aggregate media (6.18, 5.21, 4.38, 2.86 mm basalt aggregates) was predetermined using the nearest standard sieve size interval available as shown in Table 4.3.

Table 4.3: Fine percolating crushed particles median sieve size.

| Media | Sieve size interval | Median sieve size |
|---|---|---|
| 6.18 mm aggregates | 5.66 mm and 6.70mm | 6.18 mm |
| 5.21 mm aggregates | 4.75 mm and 5.66 mm | 5.21 mm |
| 4.05 mm aggregates | 3.35 mm and 4.75 mm | 4.05 mm |
| 2.86 mm aggregates | 2.36 mm and 3.35 mm | 2.86 mm |

Since there are only two nearest sieve size interval available for each of the fine particles sieve test, no size distribution graph is available (i.e., for the 4.05 mm aggregates, only two closest standard sieve sizes were available: 3.35 mm and 4.75 mm). Therefore, the median sieve size between the two closest size intervals were selected as the fine crushed aggregate media size (Equation 4.1) in the percolation tests as presented in Table 4.3.

$$\text{Fine aggregates diameter } (d_p) = \frac{d_{upper} + d_{lower}}{2} \qquad \text{(Equation 4.1)}$$

Where:

- $d_{upper}$ = upper sieve size (mm); and
- $d_{lower}$ = lower sieve size (mm).

The test for the particle size distribution (13.20 mm basalt aggregate) was conducted according to ASTM standard (ASTM D422-63 2007) by means of a sieve test. A sieving test is a method of dividing up a material into size fractions by passing it through sieves with a series of decreasing sieve apertures. Sieves size are selected to cover the entire range of the particle sizes present in the representative sample. The quantity of representative samples on each sieve is then measured and the results were used to generate a particle size distribution chart.

Particle size distribution tests on 13.20 mm basalt aggregate were conducted using a 30 kg representative sample by the coning and quartering method. The sieving test was done by taking small increments (approximately 2-3 kg/sieve) until the entire representative sample were finished. The sieve analysis test results are presented in Table 4.4 while the cumulative particle size distribution of 13.20 mm basalt aggregate is shown in Figure 4.4a.

Table 4.4: Particle size distribution test of the 13.20 mm crushed basalt aggregate.

| Particle size (mm) | Retained mass (g) | Cumulative passing (%) | Distribution (%) |
|---|---|---|---|
| >22.4 | 0.00 | 100.00 | 0.00 |
| 22.4 | 0.00 | 100.00 | 1.87 |
| 19.00 | 561.32 | 98.13 | 6.51 |
| 16.00 | 1,959.14 | 91.62 | 39.06 |
| 13.20 | 11,752.64 | 52.56 | 24.23 |
| 11.20 | 7,288.23 | 28.33 | 12.78 |
| 9.50 | 3,843.05 | 15.55 | 7.13 |
| 8.00 | 2,147.76 | 8.42 | 2.75 |
| 6.70 | 827.11 | 5.67 | 2.28 |
| 5.60 | 684.35 | 3.39 | 1.59 |
| 4.75 | 479.67 | 1.80 | 1.07 |
| 2.36 | 321.41 | 0.73 | 0.73 |
| <2.36 | 219.09 | 0.00 | 0.00 |
| Total | 30,083.77 | | 100.00 |

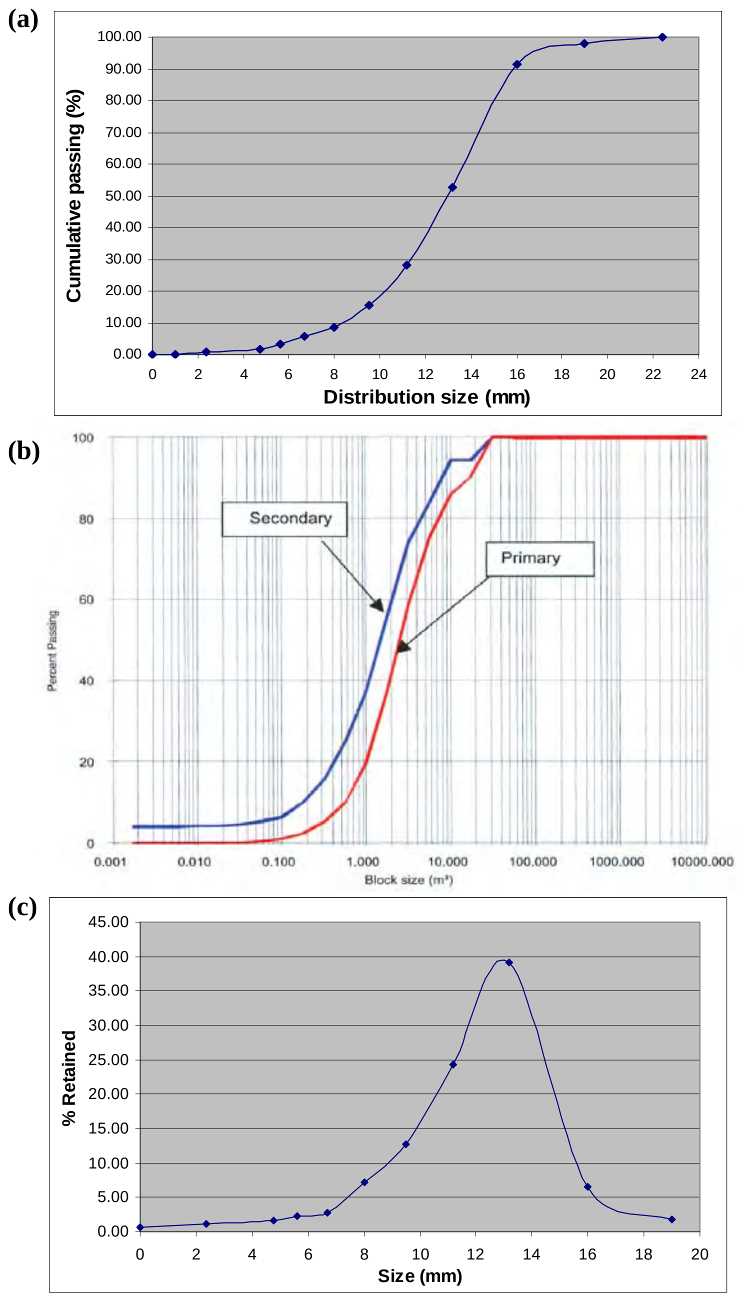


Figure 4.4: Comparison of particle size distributions. Note: (a) Cumulative passing of 13.20 mm basalt aggregate used in this thesis (b) Typical distribution of primary and secondary fragmentation of rock mass after being drawn through 100 m vertically using BCF program (after Brown 2003) (c) Particle size distribution of 13.20 mm crushed basalt aggregate used in this thesis.

The particle size distribution of the crushed basalt aggregates was compared to that of the typical distribution of primary and secondary fragmentation of rock mass after being drawn through 100 m vertically generated by *Block Cave Fragmentation* (BCF) (Figure 4.4b). BCF is a program developed to estimate the size of rock fragments and currently the most widely used method of assessing *in situ*, primary and secondary fragmentation in caving mine operations (i.e., block caving, panel caving) (Brown 2003). However, since BCF relies on a simplified technique for determining *in situ* block sizes and empirical rules to predict how the blocks would reduce in size in a draw column (Esterhuizen 1994 cited in Brown 2003), it is necessary to compare the particle size distribution with available real data in block caving mine.

Figure 4.4c shows that the 13.20 mm basalt aggregate used in this thesis is positively skewed towards coarse particles. It is concluded that the 13.20 mm aggregate consist of high frequency of coarser size classes, while finer particles (e.g., <7.00 mm) cover a wide range of sizes at lower frequency per size class. This proportion provides the 13.20 mm aggregate as a wide distribution of particle sizes.

It is worth highlighting that although the particle size distribution of crushed aggregate media used in this thesis represents a wide distribution, it is not in full agreement with Laubscher's real caved rock fragmentation data (Laubscher 1994). Analogous to this finding is generally most of the crushed aggregates produced in the quarrying process (i.e., crushing and screening) could not adequately represent real caved rock fragmentation. This assertion is factual since most of the aggregates products were classified according to the specific mesh size (i.e., 7, 10, 14 and 20 mm) hence limit its particle size distribution.

Subsequently, the above finding was also extended to the previous particle size distribution used by Power (2004) and Castro (2006) in their respective caved rock flow works and mono-sphere particles employed by Bridgwater et al. (1978) for percolation study. It was found that the particle size distributions employed by above researchers are far removed from the Laubscher's real caved rock fragmentation data as illustrated in Figure 4.5. In addition, the mono-size distribution of 15.75 mm glass spheres in SCPG and 19 mm phenolic resin in Bridgwater et al. (1978) (mono-size) were also included in Figure 4.5 to provide a comparison between wide and mono-size distribution.

Nonetheless, the size distribution of 13.20 mm aggregate used in this thesis was found to fit within the Laubscher's fine, medium and coarse cave fragmentation size distribution.

In contrary, both the Power's and Castro's size distribution only fit within the medium and coarse cave fragmentation size distribution as illustrated in Figure 4.5.

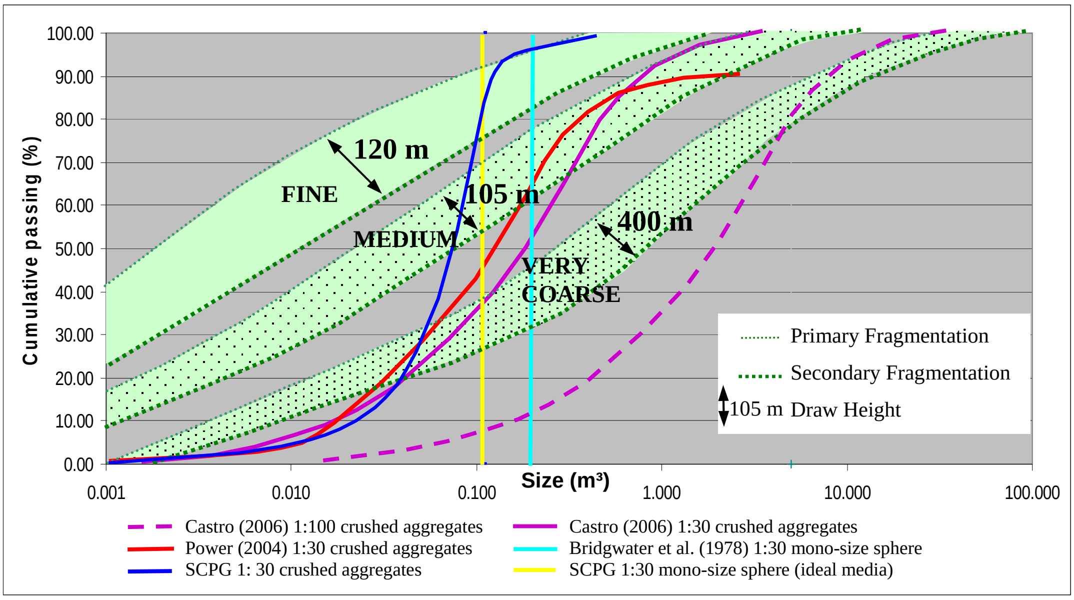


Figure 4.5: Comparison of caved fragmentation size distribution used in particle flow study (adapted and updated after Laubscher 1994).

An implication to the above finding is although most of previous work on particle flow of caved rock claimed to represent wide distribution of particle sizes, it is still cannot genuinely represent an actual real caved rock fragmentation in block caving mine. Nevertheless, it is noted that any attempt to characterise and work with a wider particle size distribution is difficult while a narrow distribution usually provides an ease of experimental control and analysis.

Therefore, it is essential to test the effect of percolation of fine particles in real caved rock distribution in which it can reflect the actual cave mine environment. Nonetheless, the real caved rock distribution effect is not been tested in this thesis due to time restrictions and experimental practicality. For instance, to realistically represent 1:100 scaled medium caved rock fragmentation, it is estimated that 75% of particles sizes used as the bed-matrix are composed by <6.70 mm aggregates. Accordingly, experimental control is difficult and impractical since a large quantity of fines (<6.70 mm) is expected to accumulated in the small compartment of the pan collector and overflow it (i.e., the sieve mesh opening for SCPG was designed at 6.75 mm). Although this problem can be overcome by reducing the sieve mesh aperture (e.g., 2.36 mm), this would require significant changes in fine/marker sizes (e.g., 2 mm) and thus be different to the experimental designs and test parameters employed in SCPG.

### 4.4.2 Particle Density, Volume, Porosity, Voids Ratio and Approximate Young's Modulus

Particle density and volume of both ideal and crushed aggregate media were obtained by using an Archimedes test on approximately 30 particles from each media sub-type. Table 4.5 summarises the volumetric particle solid densities, porosity, voids ratio and approximate Young's modulus of material used in this thesis while complete table of the summary is presented in Appendix B.

Table 4.5: Summary of mean particle density, volume, porosity, voids ratio and approximate Young's modulus of ideal and crushed aggregate media.

| Material | | Density, $\rho$ (g/cm³) | Volume, $V$ (cm³) | Porosity, $\eta$ | Voids ratio, $\varepsilon$ | Approximate Young's modulus, $E$ (GPa) |
|---|---|---|---|---|---|---|
| Crushed Aggregate Media | 13.20 mm aggregate | 2.76 | 0.79 | 0.36 | 0.57 | 50 - 100 |
| | 6.18 mm aggregate | 2.74 | 0.06 | 0.36 | 0.57 | 50 - 100 |
| | 5.21 mm aggregate | 2.73 | 0.04 | 0.37 | 0.58 | 50 - 100 |
| | 4.05 mm aggregate | 2.74 | 0.02 | 0.36 | 0.57 | 50 - 100 |
| | 2.86 mm aggregate | 2.75 | 0.01 | 0.37 | 0.58 | 50 - 100 |
| Ideal Media | 15.75 mm glass sphere | 2.49 | 2.06 | 0.40 | 0.67 | 50 - 90 |
| | 6.00 mm glass sphere | 2.53 | 0.12 | 0.40 | 0.66 | 50 - 90 |
| | 5.00 mm glass sphere | 2.54 | 0.07 | 0.39 | 0.65 | 50 - 90 |
| | 4.00 mm glass sphere | 2.52 | 0.04 | 0.40 | 0.66 | 50 - 90 |
| | 4.00 mm steel sphere | 7.72 | 0.03 | 0.13 | 0.15 | 200 |
| | 4.00 mm bi-conical glass | 2.45 | 0.04 | 0.41 | 0.69 | 50 - 90 |
| | 4.00 mm cylindrical glass | 2.40 | 0.05 | 0.42 | 0.71 | 50 - 90 |
| | 4.00 mm cubical class | 2.48 | 0.07 | 0.40 | 0.68 | 50 - 90 |
| | 3.90 mm plastic sphere | 0.97 | 0.03 | N.A. | N.A. | 2 |

### 4.4.3 Particle Shape, Equivalent Spherical Diameter ($D_s$) and Particle Shape Factor ($r_v$)

Given the fact that the shape of crushed aggregate is significant in percolation studies (Cooke et al. 1978), an attempt to classify the ideal and crushed aggregate medias' particle shape, equivalent spherical diameter ($D_s$) and its shape factor, $r_v$ was made. The particle shape dimensions (i.e., length, width and depth) were determined using a calliper (±0.01 mm accuracy) as illustrated by Figure 4.6 while the average of these three dimensions ($d_m$) is determine by Equation 4.2.

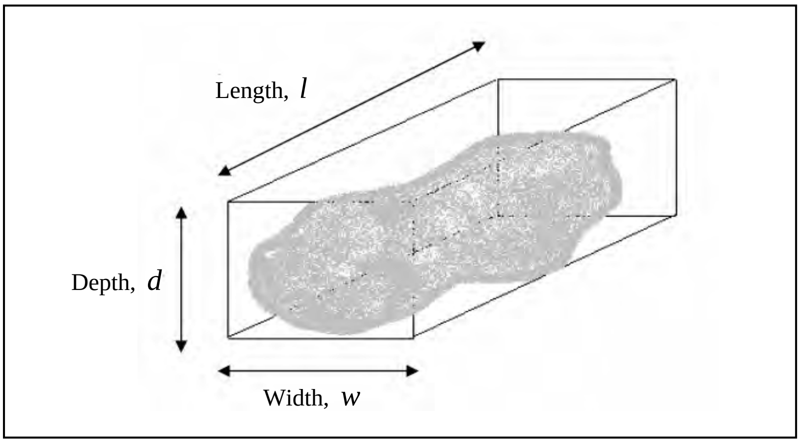


Figure 4.6: The principal dimensions of an aggregate particle (adapted after Erdoğan 2003).

$$d_m = \frac{l+w+d}{3} \qquad \text{(Equation 4.2)}$$

Table 4.6 summarised the particle shape tests of both ideal and crushed aggregate media used in the tests (a complete test data can be referred in Appendix B). Based on the Table 4.6, the relative mean aspect ratio for the 13.20 mm basalt aggregates is approximately (15.51:13.25:10.18) while the standard deviation was relatively narrow at 2.46:2.30:1.98 respectively.

It is also found that the flakiness ratio ($l/w$) of the crushed basalt aggregates were found to be low with a median ratio of $l/w$ =1.20 while for the elongation ratio ($l/d$) was significantly higher at $l/d$ =1.56 and normally distributed. These values broadly show that the crushed basalt aggregates used in this study can be described as bulky in nature. In view of this, the bulky media is defined as a particle that has relatively similar values in all three dimensions and was typically formed from the mechanical, crushing and blast actions (i.e., quarrying process).

These finding were extended in the case of the 6.18, 5.21, 4.05 and 2.86 mm basalt aggregates (represent percolating fine particles) and was found to have similar patterns (normally distributed) for both the standard deviation and mean aspect ratio. In the alternative, all the ideal media used in this thesis has shown constant value in both flakiness ratio ($l/w$) and elongation ratio ($l/d$) respectively (i.e., $l/w \approx l/d \approx 1.0$).

In view of the fact that the granular materials (i.e., caved rock) are rarely composed of perfectly spherical particles, Nedderman (1992) has recommended the use of the equivalent spherical diameter ($D_s$) method. Generally the $D_s$ is defined as the diameter of the sphere having the same volume as the particle (Equation 4.3) where $V$ is the volume of the particle

$$D_s = \left(\frac{6V}{\pi}\right)^{1/3} \qquad \text{(Equation 4.3)}$$

On the other hand, Marsal (1973) noted that direct measurements of gravelly materials (coarse aggregates) may show some differences between the nominal diameter of sieve opening (or aperture) and the average particle diameter of aggregates ($d_m$). This argument was deduced due to the fact that the range of sizes in the fraction merely depends on the size of the next smaller sieve. According to above assertion, it is significant to determine the particle shape factor ($r_v$), as given by Equation 4.4 where $V$ denoted as volume of the particle while $d_m$ is defined as average particle diameter.

$$r_v = \frac{6V}{\pi . d_m^{\ 3}} \qquad \text{(Equation 4.4)}$$

A summary of the equivalent spherical diameter ($D_s$) and the particle shape factor ($r_v$) of material used in this thesis were presented in Table 4.6.

Table 4.6: Mean value and standard deviation of particle shape test, mean diameter value ($d_m$), equivalent spherical diameter methods ($D_s$) and the particle shape factor ($r_v$) for ideal and crushed aggregate media used in the tests.

| | Material | Length, $l$ (mm) | Width, $w$ (mm) | Depth, $d$ (mm) | $l/w$ | $l/d$ | $d_m$ (mm) | $D_s$ (mm) | $r_v$ |
|---|---|---|---|---|---|---|---|---|---|
| Crushed Aggregate Media | 13.20 mm aggregate | 15.51 (2.46) | 13.25 (2.30) | 10.18 (1.98) | 1.20 (0.08) | 1.56 (0.21) | 12.90 (2.14) | 11.48 (2.02) | 0.77 (0.05) |
| | 6.18 mm aggregate | 6.26 (0.46) | 4.97 (0.57) | 4.24 (0.56) | 1.23 (0.12) | 1.44 (0.19) | 5.15 (0.45) | 4.83 (0.42) | 0.84 (0.02) |
| | 5.21 mm aggregate | 5.43 (0.49) | 4.37 (0.46) | 3.44 (0.47) | 1.27 (0.11) | 1.57 (0.23) | 4.38 (0.49) | 4.08 (0.36) | 0.81 (0.02) |
| | 4.05 mm aggregate | 4.18 (0.37) | 3.34 (0.48) | 2.88 (0.42) | 1.19 (0.20) | 1.43 (0.25) | 3.43 (0.36) | 3.19 (0.36) | 0.81 (0.07) |
| | 2.86 mm aggregate | 3.22 (0.32) | 2.56 (0.43) | 1.95 (0.47) | 1.24 (0.17) | 1.60 (0.39) | 2.55 (0.35) | 2.41 (0.34) | 0.84 (0.09) |
| Ideal Media | 15.75 mm glass sphere | 15.76 (0.06) | 15.75 (0.05) | 15.73 (0.09) | 1.00 (0.00) | 1.00 (0.00) | 15.74 (0.06) | 15.78 (0.03) | 1.01 (0.01) |
| | 6.00 mm glass sphere | 6.10 (0.10) | 6.04 (0.08) | 6.03 (0.10) | 1.00 (0.02) | 1.01 (0.01) | 6.04 (0.08) | 6.16 (0.09) | 1.07 (0.03) |
| | 5.00 mm glass sphere | 5.11 (0.11) | 5.05 (0.09) | 5.02 (0.10) | 1.01 (0.01) | 1.02 (0.02) | 5.05 (0.09) | 5.03 (0.10) | 1.00 (0.06) |
| | 4.00 mm glass sphere | 4.12 (0.09) | 4.05 (0.07) | 4.00 (0.11) | 1.01 (0.03) | 1.03 (0.03) | 4.06 (0.07) | 4.02 (0.09) | 0.97 (0.09) |
| | 4.00 mm steel sphere | 4.00 (0.00) | 4.00 (0.00) | 4.00 (0.00) | 1.00 (0.00) | 1.00 (0.00) | 4.00 (0.00) | 4.00 (0.00) | 1.00 (0.00) |
| | 4.00 mm bi-conical glass | 4.20 (0.07) | 4.15 (0.05) | 4.00 (0.03) | 1.05 (0.01) | 1.02 (0.02) | 4.12 (0.04) | 4.06 (0.03) | 0.95 (0.02) |
| | 4.00 mm cylindrical glass | 4.20 (0.06) | 4.15 (0.06) | 4.15 (0.06) | 1.01 (0.01) | 1.01 (0.01) | 4.16 (0.06) | 4.58 (0.05) | 1.34 (0.02) |
| | 4.00 mm cubical class | 4.22 (0.06) | 4.15 (0.05) | 4.11 (0.06) | 1.01 (0.01) | 1.02 (0.01) | 4.17 (0.05) | 5.08 (0.09) | 1.80 (0.13) |
| | 4.00 mm plastic sphere | 4.00 (0.00) | 4.00 (0.01) | 3.97 (0.00) | 1.00 (0.00) | 1.01 (0.01) | 3.99 (0.00) | 3.94 (0.00) | 0.96 (0.00) |

On the other hand, the equivalent spherical diameter methods ($D_s$) (Nedderman 1992) shows a significantly lower value of 11.48 mm compared to the average diameter value, $d_m$ value of 12.90 mm for the coarser crushed aggregate (13.20 mm basalt aggregates). It was also found that the difference of $D_s$ and $d_m$ are varied in the case of fine percolating crushed aggregate media while for ideal media closely approximated each of the values.

The difference between $D_s$ and $d_m$ were relatively typically predetermined by the $r_v$ value. For instance, the significant difference of $D_s$ and $d_m$ value for 4.00 mm cubical glass shape (ideal media) is directly proportional to its large $r_v$ value ($r_v$ >1.81) while this contradict for the 4.00 mm steel sphere (ideal media) with the discrepancy was found to be zero ($r_v$ =1.0) as shown in Table 4.6.

Figure 4.7 illustrates the Marsal's shape factor used particles shape classification. Principally, Marsal (1973) has classified the particle shape based on the shape factor, $r_v$ as a function of the ratio $d/d_m$. In this chart, plate or plate like particles have small values lie between Curves 1 and 2 (0.2< $r_v$ <0.4) while rod shape particles fall on Curve 2 ($r_v$ =0.43; i.e., cylindrical glass). On the other hand, prismoidal fragments of rock have shape factors smaller than or equal to those corresponding to Curve 3 (0.5< $r_v$ <0.8) whereas spherical particles (i.e., glass spheres, steel sphere, spherical plastic sphere) have a value of $r_v$ close to unity.

Based on the Marsal's shape factor classification chart in Figure 4.7, it was indicates that the crushed aggregate media (13.20, 6.18, 5.21, 4.05 and 2.86 mm) used in the tests merely consists of prismoidal particles with sharp edges. On the other hand, an ideal media such as the spherical materials (4.00, 5.00, 6.00 mm glass spheres, 4.00 mm plastic sphere and 4.00 mm steel sphere) were found to fall on the edge of Curve 3 with the $r_v$ close to unity. It was also found that the 4.00 mm bi-conical glass fall in the vicinity of the edge of Curve 3 (revolution ellipsoids) which can be classified as close to spherical shape.

However the cylindrical and cubical glass tests show a higher $r_v$ value ($r_v$ >1.0) thus broadly disagree with the Marsal's shape factor classification. One possible reason to this can be related to the fact that the Marsal's shape factor classification only deal with low depth/mean diameter ratio, $d/d_m$ particles (i.e., rods, mortar and glass plates). Figure 4.7 clearly shows that the Curve 2 (cylinders) only resembled by the $d/d_m$ < 0.625 thus make the cylindrical glass used in the test ($d/d_m$ =1.01) differed from the Curve 2 (cylinders). In addition, the significantly lower $d/d_m$ < 0.250 value represents Curve 1 (square plates) generated by the mortar and glass plates used in Marsal's shape factor classification are far less than the cubical glass used in the test ($d/d_m$ = 0.99).

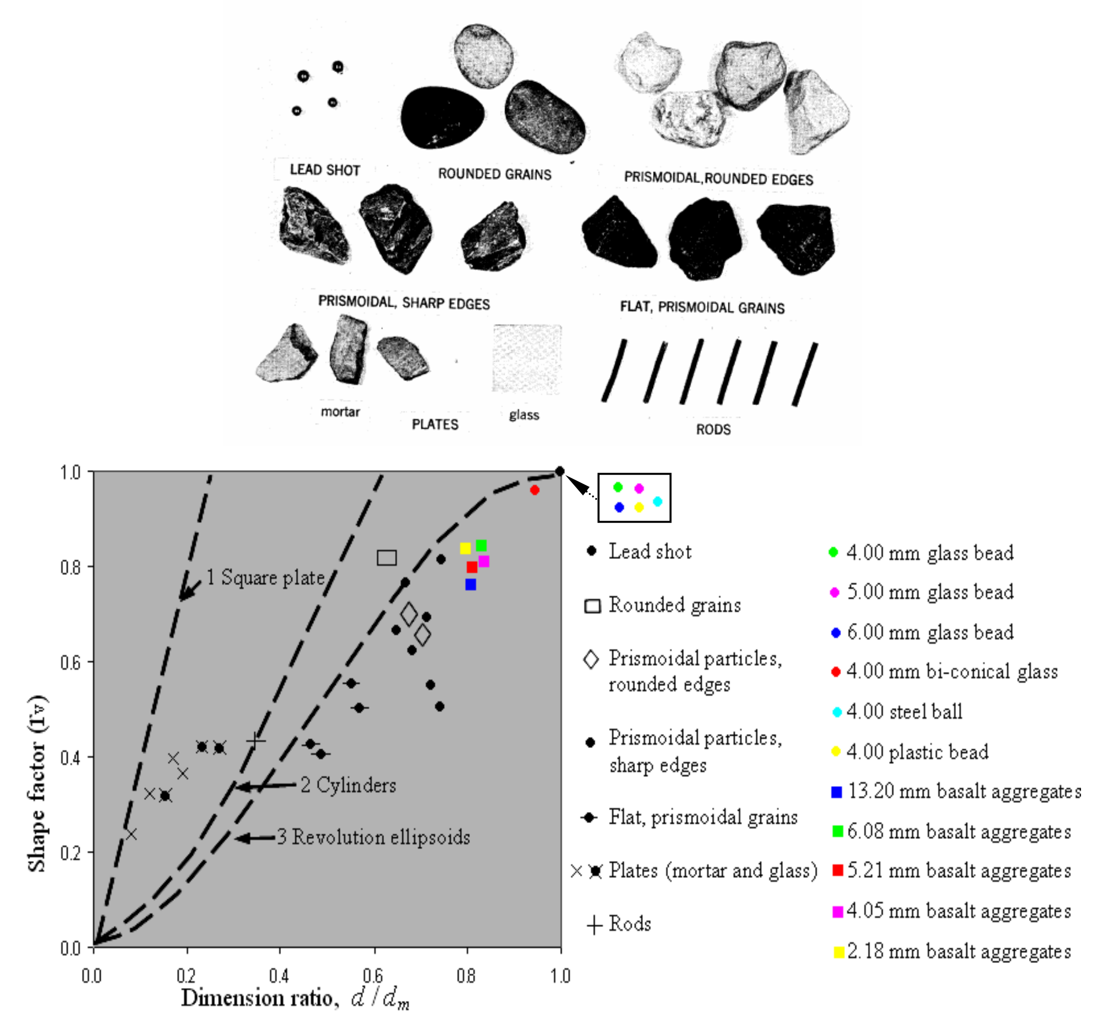


Figure 4.7: Marsal's shape factor classification chart (adapted and updated after Marsal 1973).

Note: (i) Type of particle tested (upper) and shape factor for several types of particles according to their shape (lower).

(ii) Theoretical Curves 1, 2 and 3 for square plates, cylinders and ellipsoid respectively are used as reference marks in this chart.

### 4.4.4 Shear Strength

Shear box testing was undertaken for the 13.20 mm basalt aggregates using a 305 mm x 305 mm heavy duty shear box with a depth at approximately 150 mm. In the line of the large shear box used for the tests, ASTM D3080-98 (2000) recommended that the minimum initial representative sample thickness of the direct shear box shall be greater than six times the maximum particle diameter and 10 times the maximum particle diameter for the shear box width. Apparently, direct shear testing was first employed by Coulomb in 1776 (Lamb and Whitman 1969).

Principally, the shear strength test was used to determine the friction angle, angle of dilation and friction angle of the basalt aggregates.

Terzaghi et al. (1996) listed some advantages over alternative testing methods such as:

- the test sample required can be relatively small (i.e., 100 mm x 100 mm) or very large (i.e., 305 mm x 305 mm);
- direct shear test is simple and relatively easy to operate; and
- the sample can be made to shear in a prescribed plane or zone.

Some disadvantages of the shear box test include uncertainty in interpretation of the results due to non-uniformity of the stresses and strains that occur across the shear surface, and throughout the sample thickness (Nakao and Fityus 2008).

The procedure of the test is as follows:

i. An appropriate amount of representative sample was prepared and the mass were recorded (approximately 45 kg/test) to determine a bulk density of the sample used in the large shear box.
ii. A normal force was then applied to the sample and the initial reading of the dial gauge and calibration values was recorded.
iii. All the required strength characteristics including shear stresses, horizontal or shear displacements and vertical dilations were monitored against each value of normal stress during the tests at required intervals time until the specimen failed.
iv. The data were then transferred to normal and shear stresses as per the equipment’s calibration data sheet.
v. The steps (i) to (iv) were repeated for at least three different normal forces.

The shear box tests were conducted at normal stresses of 100, 200 and 400 kPa respectively. A summary of these tests was presented by the Table 4.7 and Figure 4.8 respectively.

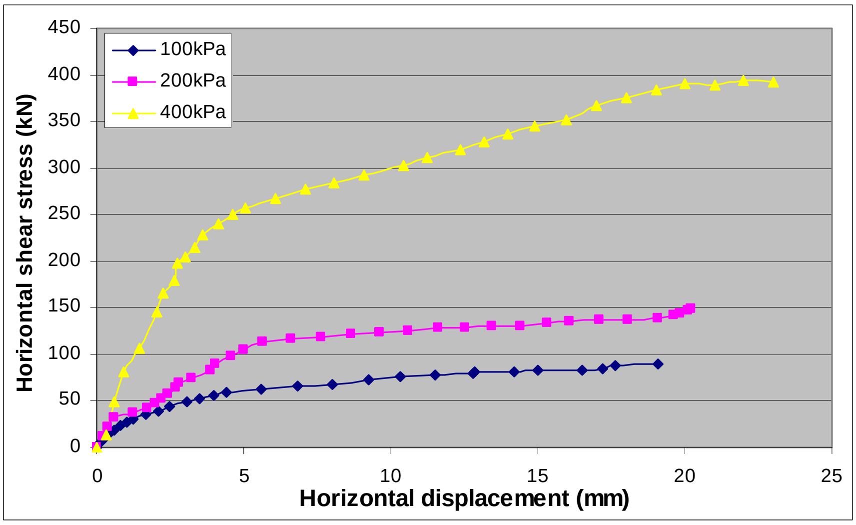


Figure 4.8: Shear displacement versus shear stress for different values of normal stress.

Table 4.7: Direct shear box testing result.

| Test sample | Normal stress at failure, $\sigma_{nf}$ (kPa) | Shear stress at failure, $\tau_f$ (kPa) | Dilatancy angle, $\upsilon$ (°) |
|---|---|---|---|
| 1 | 105.72 | 83.18 | 2.86 |
| 2 | 212.61 | 137.10 | 1.85 |
| 3 | 429.61 | 388.52 | 2.72 |

The Mohr-Coulomb linear failure criterion was then plotted and shown in Figure 4.9. The angle of friction ($\phi$) for the 13.20 mm basalt aggregates were then calculated using Equation 4.5 and was found to be $\phi$=49°.

$$\phi = \tan^{-1}\left(\frac{\sigma_{nf}}{\tau_f}\right) \qquad \text{(Equation 4.5)}$$

Where

- $\sigma_{nf}$ is the normal stress at failure (kPa); and
- $\tau_f$ is the shear strength at failure (kPa).

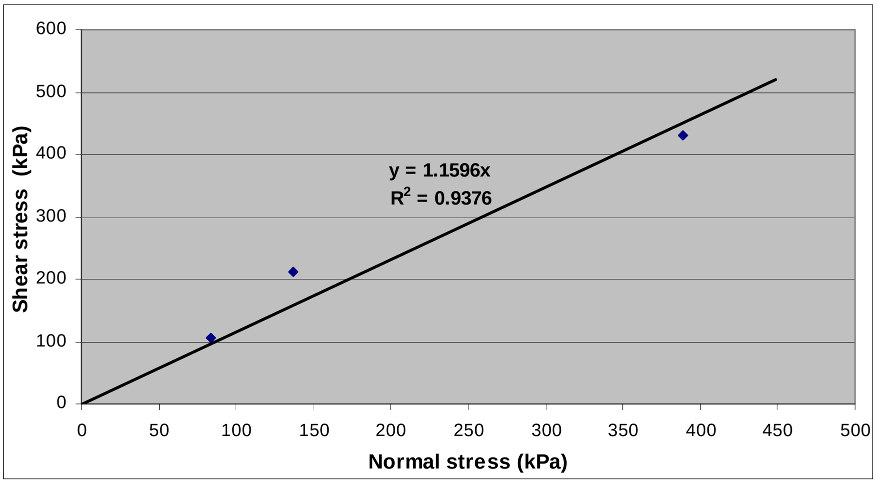


Figure 4.9: Mohr-Coulomb shear failure criterion plot.

In view of Mohr-Coulomb shear failure plot, Castro (2006) noted that generally this type of plot gives good estimates of residual friction for large normal stresses but it does not consider the effect that dilatancy has on shear strength at low confinement. In most cases, most of the sample could experience dilatancy when it is exposed to the shear strain as illustrated in Figure 4.10.

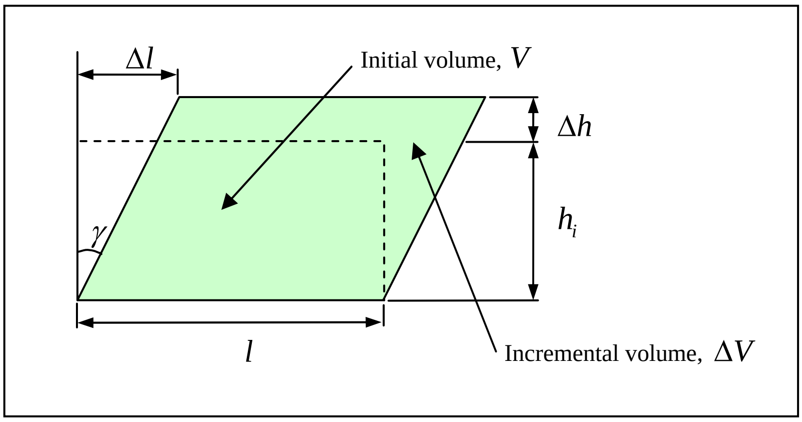


Figure 4.10: Schematic of shear-strain in two dimensions.

Equation 4.6 and 4.7 were used to calculate the dilatancy angle ($\upsilon$) and the apparent angle of friction ($\phi'$) respectively.

$$\upsilon = \tan^{-1}\left(\frac{\varepsilon_v}{\varepsilon_\gamma}\right) = \tan\left(\frac{\Delta H / H}{\Delta L / L}\right) \qquad \text{(Equation 4.6)}$$

Where:

- $\Delta H$ and $\Delta L$ are the total horizontal and vertical deformation during shear respectively (mm);
- $H$ and $L$ are the original height and length of sample respectively (mm);
- $\varepsilon_v$ is the volumetric strain and given by $\varepsilon_v = -\Delta V / V = -\Delta h / h_i$; and
- $\varepsilon_\gamma$ is the shear strain and given by $\varepsilon_\gamma = -\Delta l / l$.

$$\phi' = \tan^{-1}\left(\frac{\sigma_{nf}}{\tau_f}\right) \qquad \text{(Equation 4.7)}$$

Where:

- $\sigma_{nf}$ is the normal stress at failure (kPa); and
- $\tau_f$ is the shear strength at failure (kPa).

Angle of dilatancy ($\upsilon$) can also be determine using the experimental data (i.e., measured at the shear box) (Abriak and Caron 2006). This were done by measuring the vertical displacement at both sides of the point at which the normal force being applied to determine the change in height with shear ($\Delta h$). The shear strain against the volumetric strain were then plotted to determine the angle of dilatancy as shown in Figure 4.11.

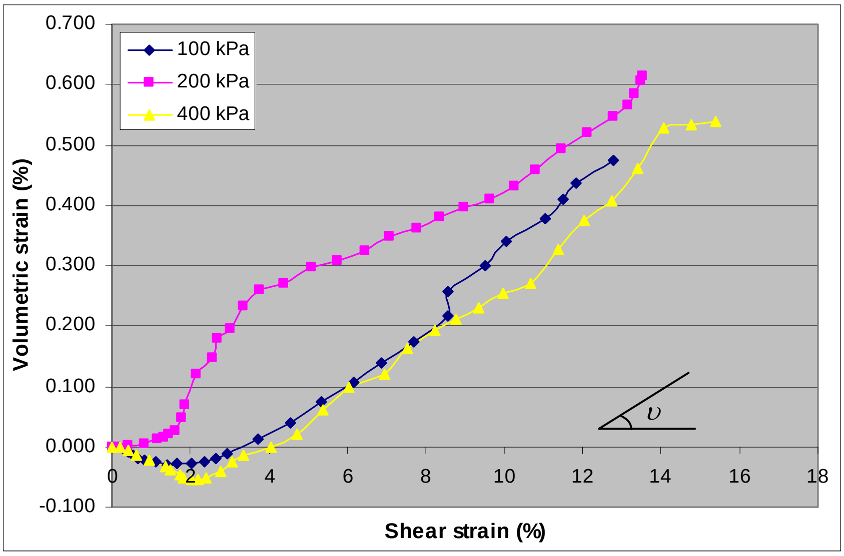


Figure 4.11: Determination of the angle of dilatancy from experimental data.

Table 4.8 present the results of mean apparent friction angle, dilatancy angle and the residual friction for the 13.20 mm basalt aggregates used in the test. Any increment within the $\upsilon$ mean that the granular sample volume increased during the shear (i.e., the granular mass dilated). The residual friction angle ($\phi_r$) of basalt aggregates was then calculated using Equation 4.8 given the mean value of residual friction angle, $\phi_r$ = 35.2º. This value was found to be within the guidelines by Hoek and Bray (1981) and Wyllie (1999).

$$\phi_r = \phi' - 0.8\upsilon \qquad \text{(Equation 4.8)}$$

Where:

- $\phi_r$ and $\phi'$ is the residual friction angle and apparent friction angle respectively; and
- $\upsilon$ is the dilatancy angle.

Table 4.8: Summary of direct shear test result.

| Test sample | Normal stress at failure, $\sigma_{nf}$ (kPa) | Shear stress at failure, $\tau_f$ (kPa) | Apparent friction angle, $\phi'$ (º) | Angle of dilation, $\upsilon$ (º) | Residual friction angle, $\phi_r$ (º) |
|---|---|---|---|---|---|
| 1 | 105.72 | 83.18 | 38.3 | 3.0 | 35.5 |
| 2 | 212.61 | 137.10 | 32.8 | 1.9 | 31.0 |
| 3 | 429.61 | 388.52 | 42.1 | 2.7 | 39.4 |
| Mean | | | 37.7 | 2.5 | 35.2 |
| Standard deviation | | | 4.68 | 0.61 | 4.22 |

## 4.5 CONCLUSIONS

This chapter documents the material properties and characterisation of the ideal and crushed aggregate media used in this thesis. It was concluded that although the 13.20 mm basalt aggregates has a wide size distribution, and presents similar patterns to the BCF program, it still could not adequately represent real caved rock fragmentation sizes as proposed by Laubscher (1994). These findings were extended to other particle flow works in caving mines and it was found that the particle size distribution used in previous works also far removed from real-world caved fragmentation sizes.

It is important to note that none of particle size distributions were presented for the fine percolating basalt aggregates (6.18, 5.21, 4.05, 2.86 mm) since there are only two nearest sieve size interval available for each of the fine particles sieve test. Nevertheless, all the fine percolating basalt aggregate sizes were classified based on the median sieve size between the two closest size intervals of each percolating basalt aggregates.

The particle density tests showed that generally all the material was classified within the appropriate range of density for caved rock. It is noted that the glass medium (i.e., $\rho$ =2.49 g/cm$^3$) appeared to have the closest density to basalt aggregates (i.e., $\rho$ =2.76 g/cm$^3$). The shear box test was also employed for the basalt aggregates. It was found that the mean value of residual friction angle ($\phi_r$) for basalt was 35.2º. This value was found to be set within the guidelines by Hoek and Bray (1981) and Wyllie (1999).

The particle shape tests conducted on the crushed aggregate media (basalt aggregates) found that the flakiness ratio ($l/w$) and elongation ratio ($l/d$) were normally distributed and can be classified as "bulky". All ideal media tested had constant values of both flakiness ratio and elongation ratio analysis ($l/w \approx l/d \approx 1.0$).

In view of above findings, Cleary (2008) asserts the importance of modelling at least the primary aspects of shape which are the aspect ratios in the principal directions of the particle and some measure of whether it is rounded or angular/blocky. It was further observed by the Marsal's shape factor classification chart that crushed aggregate media merely consists of prismoidal particles with sharp edges. By contrast, spherical and bi-conical shape materials were found to fall within the edge of Curve 3 with the $r_v$ close to unity with the exception of cubical and cylindrical shaped materials.

All the known and derived parameters of the above tests are used in the percolation tests using the SCPG (Chapter 5), numerical modelling in PFC3D$^{TM}$ computer code (Chapter 6) and shear strain assessment by the mean of 1:100 scaled Type-A Kvapil Model (Section 3.4).

# CHAPTER 5:
# PERCOLATION EXPERIMENTS ON IDEALISED MATERIALS AND CRUSHED BASALT

## 5.1 INTRODUCTION

The aim of this chapter is to describe the physical experiments to investigate percolation using the Shear Cell for Percolation of Geomaterials (SCPG). This work follows from Chapter 3 which described the design and fabrication of the SCPG and Chapter 4, the characterisation of test materials. Accordingly, the effect of strain rate ($\dot{\gamma}$), particle diameter ratio ($d_p / d_b$), shape and density for ideal and crushed aggregate media were tested under controlled experimental conditions. This chapters aims seek to prove or disprove the hypotheses that particle shape and size play a significant role in percolation of fine particles in the matrix of highly angular large/coarse aggregates.

The work in this chapter is organised as follows. Section 5.2 and 5.3 presents the methodology and parameters used. This is followed by Sections 5.4 and 5.5 in which the results are analysed and presented. Finally, in Section 5.6, all results are analysed into dimensionless percolation variables which take account of the similarity of all experiments. The results are then used to study the strengths and limitations of DEM numerical simulations in Chapter 6.

## 5.2 METHODOLOGY

### 5.2.1 Background

The experimental techniques were designed to measure the affect of strain rate ($\dot{\gamma}$), particle diameter ratio ($d_p / d_b$), shape and density on fine particle percolation. Alternatively, the percolation of fine particles in the matrix of highly angular large/coarse aggregates was quantified by two parameters: the "cumulative % mass passing of fine particles (CPF)" and; the dimensionless percolation rate (DPR).

The CPF is defined as the cumulative percentage mass passing of fine particles recovered ($C_m$) over the total mass ($m$) of fine particles used in the test (Equation 5.1).

$$\text{CPF} = \frac{C_m}{m} \text{ x } 100\% \qquad \text{(Equation 5.1)}$$

The dimensionless percolation rate (DPR) is used to assess the relation between the dimensionless percolation rate ($\bar{y} / \gamma d_b$ or $u / \dot{\gamma} d_b$) relative to particle diameter ratio and is denoted by Equation 5.2.

$$\frac{u}{\dot{\gamma} d_b} = \frac{\bar{y}}{\gamma d_b} = k_1 \exp\left[-k_2 \frac{d_p}{d_b}\right] \qquad \text{(Equation 5.2)}$$

Where:

- $\bar{y}$ is defined as the mean percolation distance travelled by percolating particles in given strain (mm);
- $u$ is defined as the mean downward velocity of percolating particle (mm/s);
- $\gamma$ is shear strain (dimensionless) while $\dot{\gamma}$ is defined as strain rate ($s^{-1}$);
- $u / \dot{\gamma} d_b$ is measure by the mean downward velocity of percolating particle ($u$) when subjected to the rate of strain;
- $k_1$ and $k_2$ are two arbitrary constants that were found to be equal to 20 and 8 respectively; and
- $d_p / d_b$ is the ratio of percolating particle to bed-matrix particle diameter or a measure of the utilisation of holes in the deforming large particles by small particles.

The arithmetic mean of the repeated experiments for each of the four test parameters ($\dot{\gamma}$, $d_p / d_b$, particle shape and density) were plotted against on CPF graph and a third order polynomial was fitted to each data set. Additionally, the CPF and DPR results will be compared with the physical observation and digital images taken during the tests.

### 5.2.2 Standard Operating Procedure for SCPG

#### *5.2.2.1 Preliminary setting*

Prior to the tests, all the systems such as sieving and shear cell alignment need to be properly adjusted and fixed correctly (i.e., the shear cell is in parallel position and the automatic switch controller was preset to a designated strain rate).

#### *5.2.2.2 Loading procedure*

The procedure for loading the model is as follows:

i. The end wall plate of the shear cell is fastened with two treaded M10 rod in constrain the cell during loading.

ii. All the hexagonal nuts on the drive wall plate side are unbolted while the top plate wall of the shear cell is tilted on the end wall plate as shown in Figure 5.1.

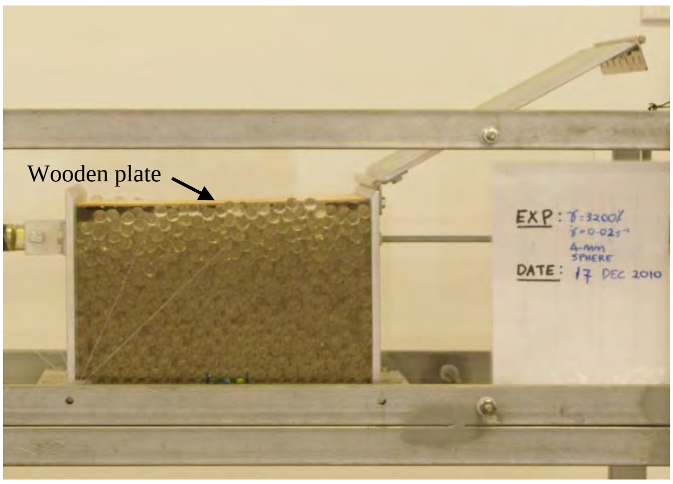


Figure 5.1: Typical example of loading process for II series. Note that the top plate wall of the shear cell is tilted on the end wall plate while the bed-matrix is levelled by wooden plate at approximately 220 mm height.

iii. The matrix of coarse bed particles (15.75 mm glass sphere or 13.20 mm crushed basalt aggregate) is carefully loaded into the box using a small bucket located at a constant height to ensure random positioning of particles.

iv. Upon reaching the designated level (220 mm height) and mass, a piece of wood with dimensions approximately matching the models width and length was used to level the medium. At 220 mm height the shear cell having an approximately 75 kg of mass at full capacity.

v. A designated mass of fine particles are placed on the top of the coarse bed particles, at the centre of the shear cell (i.e., y-axis) on a masking board with internal dimensions 60 x 180 mm (Figure 5.2). This will result in avoiding the wall effects of the percolating fine particle with the side, drive and end walls respectively. It is worth highlighting that this problem was identified in early physical experiments by Bridgwater et al. (1978). On the other hand, a different set of coloured percolating fine particle coordinates are aligned to the centre of small compartments 12, 13 and 14 as shown in Figure 5.2 (left).


Figure 5.2: The masking plate used for fine particle configuration with an opening diameter of 60 mm x 180 mm at the centre [right]. Note that the opening dimension of the wooden plate was the same size as the three adjacent small compartments located at the centre of pan collector (compartment numbers 12, 13 and 14) [left].

vi. The mask is removed and replaced by a thick wooden plate with a central opening and a normal load is placed on the top of the wooden plate.

vii. The top wall of the shear cell was then re-attached with the drive wall and all hexagonal nuts are fastened. The support rods are then removed.

#### *5.2.2.3 Testing*

The procedure for testing is as follows:

i. The auto run switch button is pressed and stopped every 100% strain intervals for the first complete cycle (one complete cycle equals is 400%). Following the first completed cycle, the test is only paused at the end of each subsequent complete cycle (400% strain) until the required $\gamma_{total}$ is achieved.

ii. During the interval test pause, any fine particles collected and dropped into the small pan collector compartments were weighted while parameters such as run time duration, total strains ($\gamma_{total}$) and the spatial distribution of fine particles on the collection pan is recorded. Any markers collected are recorded against the compartment number, run time duration and $\gamma_{total}$.

iii. The procedure (i) and (ii) is repeated and any observations in the experimental set up are recorded.

iv. Each test is repeated three times in order to find the average reading of mass passing of fine particles recovered.

#### *5.2.2.4 Emptying the shear cell*

The procedure for emptying the model is as follows:

i. The motor is switched off and the threaded rods are attached back to the end side wall.

ii. The hexagonal nuts are loosened and the top wall of the shear cell was tilted on the end wall plate.

iii. Using the 10.00 mm sieve, the matrix of coarse bed particles is carefully sieved and then restored to the storage bins. The remaining fine particles and markers collected are restored to the storage compartments.

### 5.2.3 Configuration of Fine Particles

Four possible initial configurations for the fine particle/markers in the shear cell were considered, as illustrated in Figure 5.3.

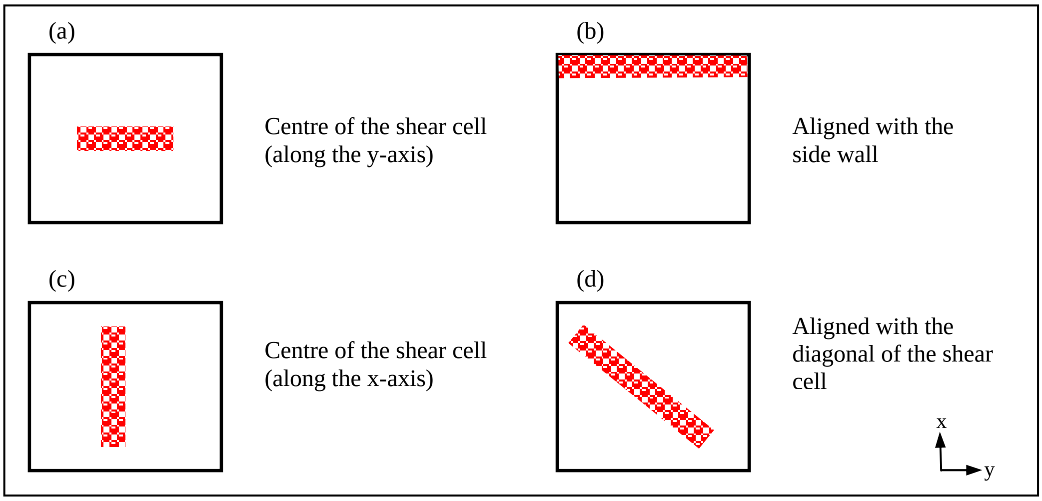


Figure 5.3: Plan view showing the configuration of the fine particles/markers position.

The initial position of the fine particles/markers is important toward reproducible and reliable results. The centre of the shear cell (y-axis) option (Figure 5.3a) was selected based on several considerations:

- ability to minimise (or prevent) interaction with the side walls (Perspex glass and galvanised plate), end wall and drive wall (Figure 5.3b);
- facilitate and enhance the percolation potential as the energy generated by the drive wall is uniformly distributed along the y-axis (as shown in Section 3.3.3.2);
- particles placed near the wall vicinity (Figure 5.3b) may significantly experience higher sieving segregation potential while configuration along the x-axis (Figure 5.3c) might produce a narrow zone of low strains (dead zone effect) thus limiting percolation; and
- configuration by aligning with the diagonal of the shear cell may potentially experience both sieving segregation and low energy distribution (Figure 5.3d). Some of the percolating fine particles may interact with the wall vicinity (wall effect) and risk of leakage at the model base may occur.

It is worth noting that the use of a side wall constructed from Perspex glass or galvanised plates does not cause a wall effect to the percolating fine particles during the tests. This is based on the fact that the fine particles are positioned far enough from the wall edges (approximately 90 mm from the drive and end wall edges and 145 mm from the both side walls). This minimises the wall effects of the percolating fine particle with the side, drive and end walls respectively. Similarly, it is worth highlighting that this problem was identified in early physical experiments by Bridgwater et al. (1978).

### 5.2.4 Granular Materials – Fine and Coarse Matrix

A total of four combinations (or series) of fine and coarse matrix particles were generated from the ideal media (identified as *I*) and crushed aggregate media (identified as *B*). For instance, percolating fine particle of 4.05 mm basalt aggregate in the bed-matrix of 15.75 mm glass sphere are referred as *BI series*. In other words, the first alphabet denoted as a fine percolating particles material type while the second alphabet denoted as a coarse material type.

Complete identification codes for the binary series of material used in the tests are shown in Table 5.1.

Table 5.1: Testing configurations of fine and coarse matrix particles - identification codes.

| Series of media | Type of media | | Identification code |
|---|---|---|---|
| | Fine Material | Bed-matrix | |
| Ideal-Ideal | Glass spheres; Plastic sphere; Steel spheres | Glass sphere | II |
| Crushed aggregate -Ideal | Basalt aggregates | Glass sphere | BI |
| Ideal-Crushed aggregate | Glass spheres; Plastic sphere; Steel spheres | Basalt aggregates | IB |
| Crushed aggregate - Crushed aggregate | Basalt aggregates | Basalt aggregates | BB |

## 5.3 EXPERIMENTAL CHARACTERISATION

### 5.3.1 Selection of Total Shear Strain ($\gamma_{total}$) and Strain Rate ($\dot{\gamma}$)

It is known from previous studies that critical parameters for the SCPG are: the total shear strain ($\gamma_{total}$) and; strain rate ($\dot{\gamma}$), and hence these parameters need to be carefully selected. For example, if $\gamma_{total}$ is set too low, most of the fine particles might not be collected while a high value may not be practical due time constraints.

Preliminary tests investigated the precision and accuracy of SCPG and also served to determine the maximum shear strain required to achieve completion of the experiments. Experiments were deemed to be complete when a significantly lower mass percentage of fines were collected (CPF <1%) for three consecutive shear strain cycle (i.e., each complete cycle comprised of 400% shear strain). These tests showed that the required run time (or total shear strain, $\gamma_{total}$) for the II and BI series was achieved within $\gamma_{total}$=3200%. Conversely, for the IB and BB series, a significantly lower percentage of percolated fine particles were collected after $\gamma_{total}$=3200% which required higher total shear strains and much longer run times. For instance, a preliminary test for the IB series required $\gamma_{total}$>10,000% to achieve similar results to the II series, which was deemed impractical.

Moreover, such at lower shear strain rates, a longer time is needed (i.e., total run time for the $\dot{\gamma}$=0.01 $s^{-1}$ test is four times slower than at $\dot{\gamma}$=0.04 $s^{-1}$). For example, approximately 8 hours or $\gamma_{total}$>10000%, was required to complete an IB series test at $\dot{\gamma}$=0.01 $s^{-1}$. Therefore, for the IB and BB series, the total shear strain was extended to $\gamma_{total}$=4800% which provides adequate results within practical time limitations. As a result, the strain rate was designed at 0.01, 0.02, 0.03 and 0.04 $s^{-1}$ respectively to conform to the shear strains estimated from scaled physical models of isolated extraction zones, presented in Section 3.4.

Overall, a total of 152 tests were performed using the SCPG with a minimum of three repetitions of each test. On average each test took 3-5 hours to complete which included loading, shearing, measurement of recovered mass of fine particles, digital imaging, documentation, emptying and cleaning.

### 5.3.2 Parameters Tested

There are four main parameters to be tested namely:

- effect of shear strain ($\gamma_{total}$);
- effect of particle diameter ratio ($d_p / d_b$);
- effect of particle shape; and
- effect of particle density.

It has been postulated by other researchers that percolation is predominantly controlled by the $d_p/d_b$ and $\dot{\gamma}$ (e.g., Bridgwater et al. 1969, 1978, 1985a, 1985b; Bridgwater and Ingram 1971; Scott and Bridgwater 1975, 1976; Cooke et al. 1978; Cooke and Bridgwater 1979; Drahun and Bridgwater 1983; Duffy and Puri 2002; Pierce 2004; Tang 2004). This conclusion is relevant to mono-size assemblies of spherical particles. However, there have been no efforts to see if similar controls exist for highly angular rock particles, or wide distributions of highly angular rock particles. This work is considered necessary toward better understanding of percolation mechanisms in caving mines. A summary of all parameters tested in the present research is shown in Table 5.2.

Table 5.2: Summary of test parameters and particle types used in the SCPG.

| Test parameter | Code | $\gamma_{total}$ (%) | $\dot{\gamma}$ ( $s^{-1}$ ) | Percolating particle | Coarse bed-matrix |
|---|---|---|---|---|---|
| Particle diameter ratio effect | II | 3200 | 0.04 | 4.00, 5.00 , 6.00 mm glass spheres | 15.75 mm glass sphere |
| | BI | | | 2.86, 4.05, 5.21,6.18 mm basalt aggregate | 15.75 mm glass sphere |
| | IB | 4800 | | 4.00, 5.00 , 6.00 mm glass spheres | 13.20 mm basalt aggregate |
| | BB | | | 2.86, 4.05, 5.21,6.18 mm basalt aggregates | 13.20 mm basalt aggregate |
| Strain rate effect | II | 3200 | 0.01, 0.02, 0.03, 0.04 | 4.00, 5.00 , 6.00 mm glass spheres | 15.75 mm glass sphere |
| | BI | | | 2.86, 4.05, 5.21,6.18 mm basalt aggregates | 15.75 mm glass sphere |
| | IB | 4800 | | 4.00, 5.00 , 6.00 mm glass spheres | 13.20 mm basalt aggregate |
| | BB | | | 2.86, 4.05, 5.21,6.18 mm basalt aggregates | 13.20 mm basalt aggregate |
| Particle shape effect | II | 3200 | 0.04 | 4.00 mm glass sphere, cubical glass, cylindrical glass, bi-cone glass | 15.75 mm glass sphere |
| | BI | | | 4.05 mm basalt aggregate | 15.75 mm glass sphere |
| | IB | 4800 | | 4.00 mm glass sphere, cubical glass, cylindrical glass, bi-cone glass | 13.20 mm basalt aggregate |
| | BB | | | 4.05 mm basalt aggregate | 13.20 mm basalt aggregate |
| Particle density effect | II | 3200 | 0.04 | 4.00 mm plastic sphere, 4.00 mm glass sphere, 4.00 mm steel sphere | 15.75 mm glass sphere |
| | BI | | | 4.05 mm basalt aggregate | 15.75 mm glass sphere |
| | IB | 4800 | | 4.00 mm plastic sphere, 4.00 mm glass sphere, 4.00 mm steel sphere | 13.20 mm basalt aggregate |
| | BB | | | 4.05 mm basalt aggregate | 13.20 mm basalt aggregate |

#### *5.3.2.1 Effect of strain rate*

The strain rate effect was investigated for fine particles consisting of 4.00 mm glass spheres and 4.05 mm basalt aggregate in a bed-matrix of 15.75 mm glass spheres and 13.20 mm basalt aggregate respectively. The selection of 4.00 mm glass spheres and 4.05 mm basalt aggregate as percolating particles was to provide a close approximation to the other data sets (i.e., 5.00 mm glass sphere and 5.21 mm basalt aggregate).

A maximum shear strain rate magnitude of $\dot{\gamma}$=0.04 s$^{-1}$ was chosen for all tests due to time constraints and additional lower strain rates magnitude (i.e., $\dot{\gamma}$=0.01, 0.02 and 0.03 s$^{-1}$) were introduced to study the effect of strain rate.

#### *5.3.2.2 Effect of particle diameter ratio*

The effect of particle diameter ratio is investigated within a range of different $d_p/d_b$ as follows:

- II ($d_p/d_b$=0.25, 0.32 and 0.38);
- BI ($d_p/d_b$=0.18, 0.26, 0.33 and 0.39);
- IB ($d_p/d_b$=0.30, 0.38 and 0.46); and
- BB ($d_p/d_b$=0.22, 0.31, 0.39 and 0.47)

The percolating particles selected were 4.00, 5.00, 6.00 mm glass spheres and 2.86, 4.05, 5.21, 6.18 mm basalt aggregates. The bed-matrix is 15.75 mm glass spheres and 13.20 mm basalt aggregate. Since in practice, the diameter of the percolating particle depends on the coarse matrix diameter, availability of the ideal media in market and the available size of standard testing sieves, the final $d_p/d_b$ may vary slightly. For instance, the II series tests using the 4.00 mm glass sphere in 15.75 mm glass sphere given the $d_p/d_b$=0.25 while for the BB series tests using the 4.05 mm basalt aggregate in 13.20 mm basalt aggregates given the $d_p/d_b$=0.31.

In practice, fine particles should also be easily seen (i.e., brightly coloured) and identified when drawn and also be easy to hand-paint and numerically label (as markers). In addition, other factors such as suitable wire mesh aperture size with regard to the SCPG sieve system should also be considered.

#### *5.3.2.3 Effect of particle shape*

It is worth highlighting that although the particle shape is known to significantly affect percolation rate, only a small number of publications exist in this area and are predominantly focused on chemical and/or powder applications. With regards to the above point, five particle shapes were introduced in this thesis: the spherical, cubical, cylindrical, bi-conical (4.00 mm fine ideal media) and angular shape (4.05 mm fine crushed basalt).

#### *5.3.2.4 Effect of particle density*

The particle density effect test was carried out to study the effect between the denser and lighter particles. Particle density tests were conducted at $\dot{\gamma}$=0.04 $s^{-1}$ with spherical particles (4.00 mm diameter). Nevertheless, the introduction of 4.05 mm crushed basalt aggregate was made in order to provide insight into the effect of particle shape and density. This is to different to previous percolation studies on density effect conducted by previous researchers (Section 2.5.5).

## 5.4 GENERAL OBSERVATIONS

It was observed that for the BB and IB series, minor breakage of the coarse particles contacts occurred near the vicinity of shear box wall. This is the result of the 13.20 mm basalt aggregate which are characterised as prismoidal particles with sharp edges (Section 4.4.3), leading to a small quantity of chippings and rock dust during shearing process. This was expected since the use of highly angular and wide distributions of particle sizes promotes higher attrition to the sharp asperities of the basalt aggregate compared to spherical mono-size particle such as 15.75 mm glass sphere.

Less than 1% rock dust (by mass) was generated mainly near the side wall of the shear box. This material accumulated in the edges of the pan collector compartments (Figure 5.4). The relatively small quantity of rock dust generated near the wall does not affect the percolation of fine particles at the centre of shear box where the measurements were collected. Additionally, in view of the fact that the particles used are dry and the experiments were conducted in the low humidity conditions, moisture effects are expected to be slight and not affecting the dust.

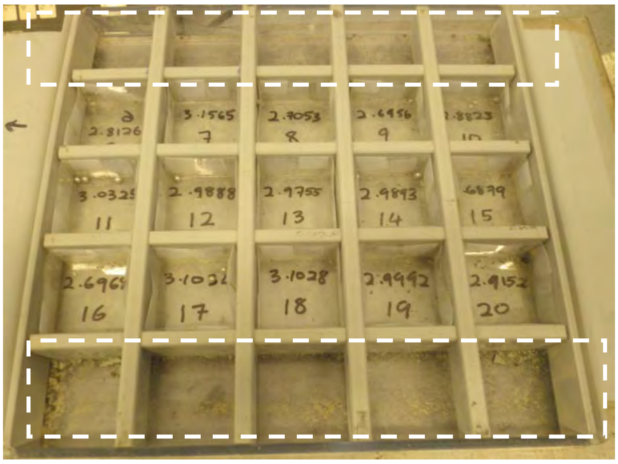


Figure 5.4: Fine dust and aggregate attrition generated near the side wall and collected in the outer cells of the collector compartment (white boxes).

It is worth highlighting that since the SCPG employed a manual weighing system it offered some advantages over the automatic mass balance system used by others such as Tang (2004). Alternatively, the small compartment of pan collector can be separated in which the rock dust and chipping can be removed out before the weighing thus provide a higher precision results than the automatic weighing system.

An attempt to study the horizontal travel distance of fine marker particles through the percolation mechanism was made by placing nine coloured markers at the top of bed-matrix (simultaneously with the fine particles as shown in Figure 5.5c). The fine marker particles were aligned with the central axis of the small collection compartment (numbers 12, 13, 14; Figure 5.5d). It was found that after the test, some of the recovered markers had travelled as far as a single compartment distance (each compartment consist of 50 mm x 60 mm in dimension). For instance, the blue marker was originally positioned adjacent to compartment 14 before the test and was recorded to fall in compartment 15 at $\gamma_{total}$=3200% as shown in Figure 5.5e.

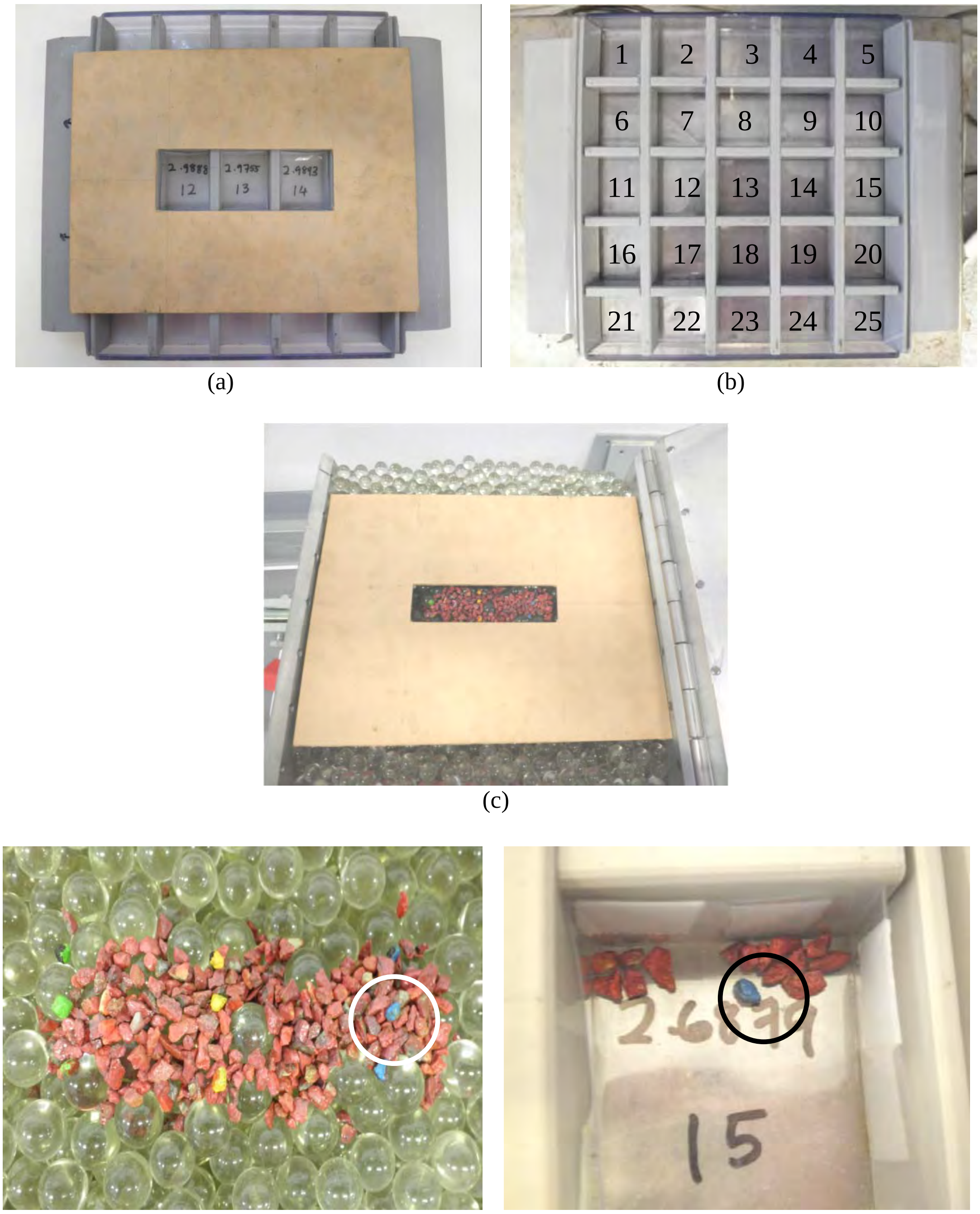


(a) (b) (c) (d) (e)

Figure 5.5: Marker trial, horizontal percolation study. (a) Masking plate, the opening dimension of the plate is the same as the three compartments at the centre of pan collector (b) Compartments number nomenclature (c) Initial configuration of fine particles and markers on the top of bed-matrix (d) The blue marker positioned adjacent to compartment 14 [white circle] (e) Example of blue marker position [black circle] recovered in compartment 15.

It is noteworthy that a small number of fine particles (particularly 6.18 mm basalt aggregate) were trapped at the 6.75 mm sieve mesh as shown in Figure 5.6. One explanation relates to the particle orientation during shearing. It is apparent that although all the 6.18 mm basalt aggregate has passed the 6.75 mm sieve (Section 4.4.1), some of the aggregate has a maximum dimension greater than the mesh aperture (previously presented in Section 4.4.3). As a result the orientation and rearrangement of particles during shearing may result in the capture of particles in the sieve. This circumstance is rare and affects a small number of particles (< 0.5% by mass). This did not happen for the other materials tested in this thesis.

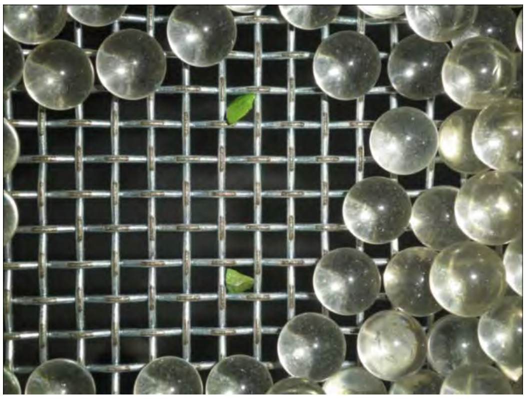

Figure 5.6: Example of 6.18mm basalt aggregate trapped at the 6.75 mm sieve mesh due to the particle orientation during shearing.

All test results were reproducible. Figure 5.7 shows a typical calibration plot for volumetric fine particle mass versus cumulative percolating fines collected. The results have a linear relation which indicates that the shear motion energy was uniformly transferred across the material in the shear cell. The calibration tests also demonstrate that the SCPG is able to generate consistent results with reasonable precision and accuracy required for quantification of the four parameters. These results agree with those of Bridgwater (1994) who asserts that "…*the key facts to emerge from the percolation study on the use of simple shear apparatus are that the data are reproducible, systematic with independent variables and independent of the amount of the material in the cell*".

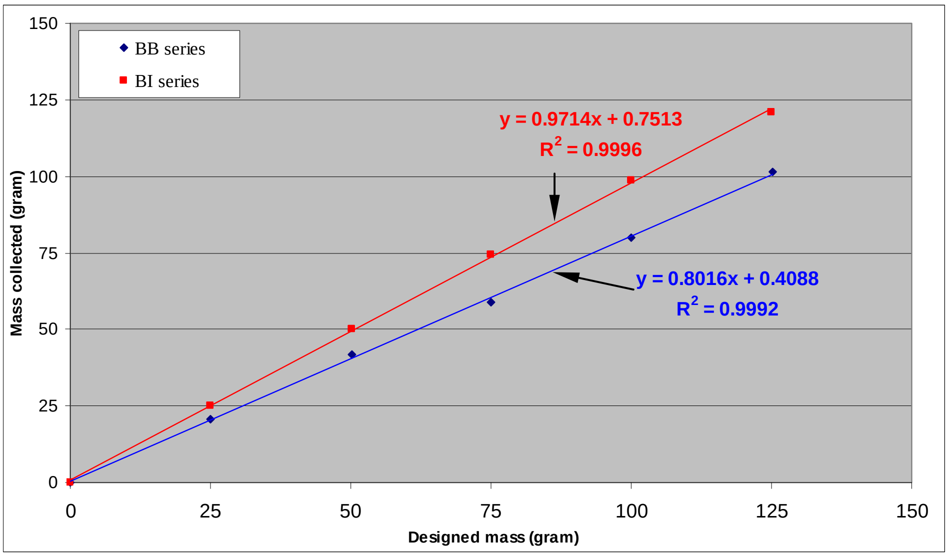


Figure 5.7: Volumetric fine particle mass versus mass of cumulative percolating fines collected at $\dot{\gamma}$ =0.04 s$^{-1}$. Note that for BI series ($d_p/d_b$ = 0.22, $\gamma_{total}$ =3200%) while BB series ($d_p/d_b$ =0.18, $\gamma_{total}$ =4800%).

## 5.5 RESULTS AND DISCUSSIONS

A total of four parameters are presented within the following sections including:

- effect of shear strain;
- effect of particle diameter ratio;
- effect of particle shapes; and
- effect of particle density.

### 5.5.1 Effect of Strain Rate

#### *5.5.1.1 Overview of results and general observations*

A total of 48 tests were performed for the effect of strain rate which were carried at $\dot{\gamma}$ =0.01, 0.02, 0.03 and 0.04 s$^{-1}$ respectively. A complete listing of results is found in Appendix C1 while Table 5.3 summarises these tests.

Table 5.3: Test designed for investigation of the effect of strain rate.

| Series | Percolating fine particles | Coarse bed-matrix | Strain rate ($s^{-1}$) | Controlled experimental conditions |
|---|---|---|---|---|
| II | 4.00 mm glass sphere | 15.75 mm glass sphere | 0.01; 0.02; 0.03; 0.04 | Particle diameter ratio; Particle density; Normal stress; Particle shape; Shear strain |
| BI | 4.05 mm basalt aggregate | | | |
| IB | 4.00 mm glass sphere | 13.20 mm basalt aggregate | | |
| BB | 4.05 mm basalt aggregate | | | |

All tests were conducted under controlled experimental conditions as follows:

- particle diameter ratio:
  - 4.00 mm (fine particle) and 15.75 mm (coarse particle) glass sphere represent ideal media (i.e., $d_p / d_b$ =0.25);
  - 4.05 mm (fine particle) and 13.20 mm (coarse particle) basalt aggregate represent crushed aggregates media (i.e., $d_p / d_b$ =0.31); and
  - Both fine and coarse particles were chosen due the fact that it provided closest proximity with each other compare to the other sets (as discussed previously in Section 5.3.2.2).
- normal stress, $\sigma_n$ =0.9 kPa. It is worth highlight that the effect of normal stress is considerable small and in most cases are negligible (Scot and Bridgwater 1976; Bridgwater et al. 1978; Cooke et al. 1978);
- shear strain, $\gamma_{total}$ =3200% for the II and BI series and $\gamma_{total}$ =4800% for the IB and BB series;
- particle shape. Two type of particle shapes; 4.00 mm glass sphere (represent ideal media) and 4.05 mm basalt aggregate (represent crushed aggregate media) were selected since it provides the closest size with each other; and
- particle density. The selection of 4.00 mm glass sphere ( $\rho$ =2.52 g/cm³) and 4.05 mm basalt aggregate ( $\rho$ =2.74 g/cm³) provides the closest density with 15.75 mm glass sphere ( $\rho$ =2.49 g/cm³) and 13.20 mm basalt aggregate ( $\rho$ =2.76 g/cm³).

The following observations were noted during the tests:

- percolation mass was found to increase with increasing shear strains;

- percolation mass is the highest at $\dot{\gamma}$=0.04 $s^{-1}$ relative to the strain rate;
- percolation of fine particles was controlled by the bed-matrix properties during shearing especially for the IB and BB series; and
- the CPF in bed-matrix of crushed aggregate media (basalt aggregate) was significantly lower than that of ideal media (glass sphere).

In order to provide ease of identification and analysis of the effect of strain rate all tests in Sections 5.5.1.2, 5.5.1.3, 5.5.1.4 and 5.5.1.5, are presented with reference to the following nomenclature given in Figure 5.8, and described as follows:

- the first segment identifies the series type of binary mixture of media used in the test; and
- the second segment refers to the strain rate.

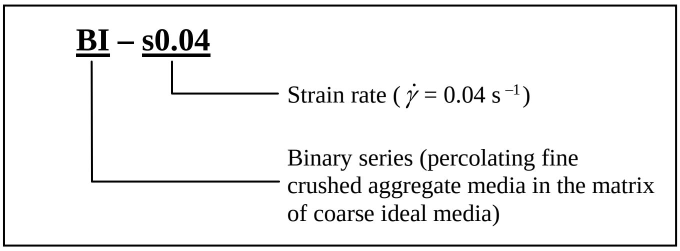


Figure 5.8: Nomenclature used in the effect of shear rate tests.

Figure 5.9 presents the results of four different series (II, BI, IB and BB) at various strain rates ($\dot{\gamma}$=0.1, 0.02, 0.03 and 0.04 $s^{-1}$). It was observed for the II and BI series that as $\dot{\gamma}$ increases, CPF increases by 3-15%. By contrast in the IB and BB series, CPF increased by 3-5%. This finding suggests that percolation is controlled by the bed-matrix in both ideal and crushed aggregate media.

Alternatively, the higher CPF shown in II and BI series than the IB and BB series can be partially explained by the higher porosity and void ratio of 15.75 mm glass sphere used as bed-matrix compare to the 13.20 mm basalt aggregate. For instance the porosity and void ratio of 15.75 mm glass sphere were found to be $\eta$=0.40 and $\varepsilon$=0.67 respectively while slightly lower for the 13.20 mm basalt aggregates ($\eta$=0.36 and $\varepsilon$=0.57).

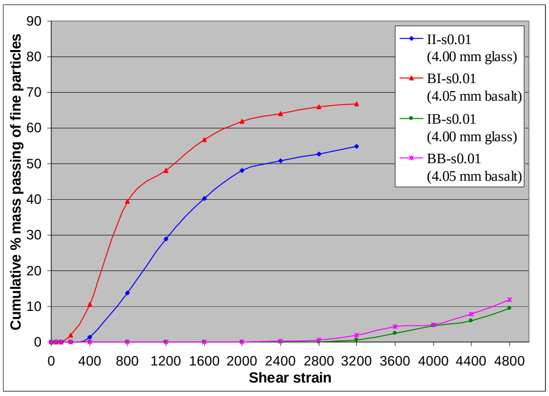


a) $\dot{\gamma} = 0.01\ s^{-1}$

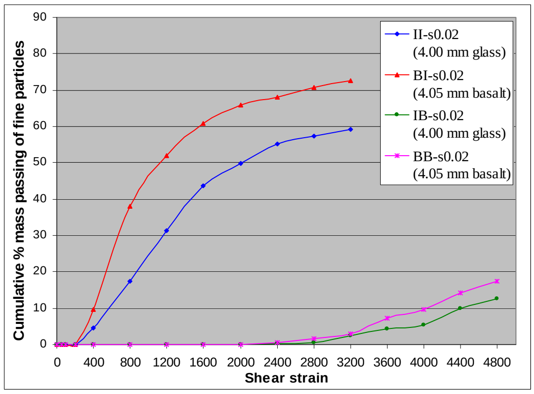


b) $\dot{\gamma} = 0.02\ s^{-1}$

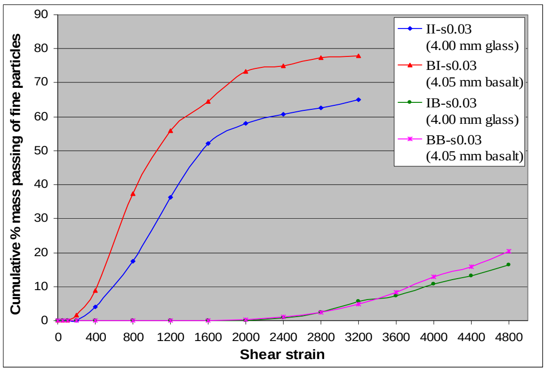


c) $\dot{\gamma} = 0.03\ s^{-1}$

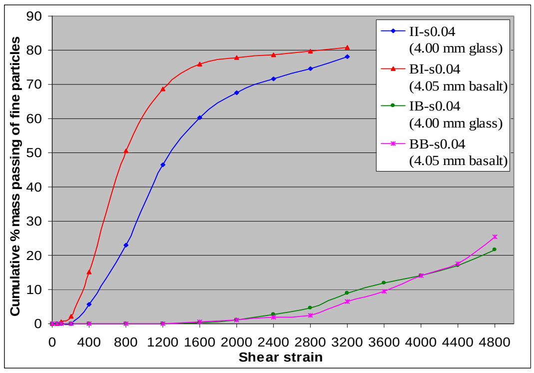


d) $\dot{\gamma} = 0.04\ s^{-1}$

Figure 5.9: Comparison of the shear strain versus cumulative % mass passing of fine particles (CPF) at different strain rate. Note that the percolating fine particles used are 4.00 mm glass sphere and 4.05 mm basalt aggregate while the coarse matrix used are 15.75 mm glass sphere and 13.20 mm basalt aggregate respectively. The plots were generated by the mean of three readings.

On the other hand, comparison of CPF values in similar bed-matrix tests (i.e., II and BI series) also found that the fine crushed aggregate media (4.05 mm basalt aggregate) has a higher percolation than fine ideal media (4.00 mm glass sphere). Alternatively, it is hypothesised that the particle shape of both the fine and bed-matrix impacts on the CPF. This hypothesis is discussed in detail in Section 5.5.3.

The results of strain rate effect in percolation are discussed in the following sections, in the following order:

- Fines: Ideal media; Bed-matrix: 15.75 mm glass spheres (II series);
- Fines: Crushed basalt; Bed-matrix: 15.75 mm glass spheres (BI series);
- Fines: Ideal media; Bed-matrix: 13.20 mm crushed basalt (IB series); and
- Fines: Crushed basalt; Bed-matrix: 13.20 mm crushed basalt (BB series).

### *5.5.1.2 Fines: Ideal media; Bed-matrix: 15.75 mm glass (II series)*

A total of 12 tests were carried out for the II series (i.e., three tests for each strain rate). A typical set of results obtained are shown in Figure 5.10. It is deduced that the percolation of fine particles is controlled by strain rate and increases with shear strain. It was observed that the CPF increased between 5-15% for each of the strain rates tested (0.01, 0.02, 0.03 and 0.04 $s^{-1}$).

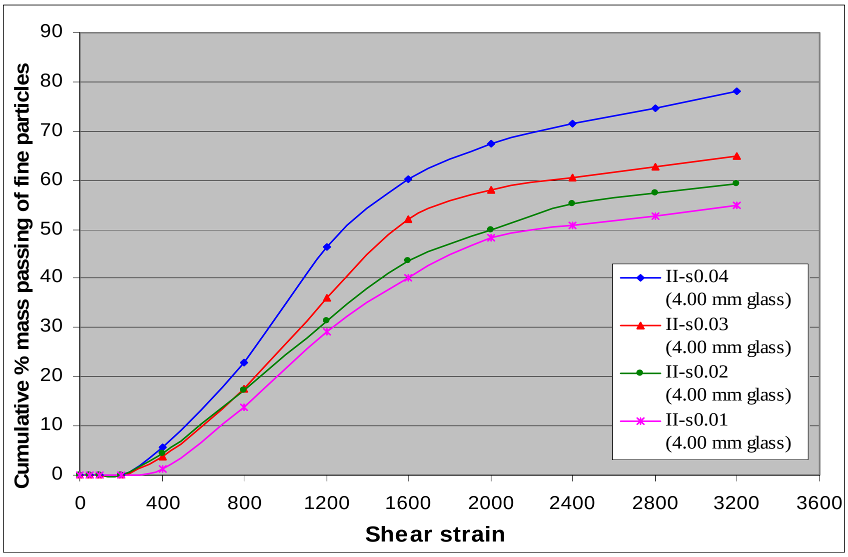


Figure 5.10: Mean shear strain versus cumulative % mass passing of fine particles (CPF) for the II series. The bed-matrix is 15.75 mm glass sphere.

In view of the above finding, the potential of the fine particles to travel through the voids of bed-matrix can be describe by the increase of the particle mobility. With regards to this, Scott and Bridgwater (1975) conducted some experiments on the effect of strain rate and concluded that percolation potential increases with increasing strain rate. Accordingly, they also postulated that the increase in percolation potential was subjected to the increase in particle mobility and decreasing size of the fine particles.

In order to provide a comparison of results, a third order of polynomial was used to model the relation: *shear strain* versus *incremental mass % of recovered fines* (IMF) as shown in Figure 5.11.

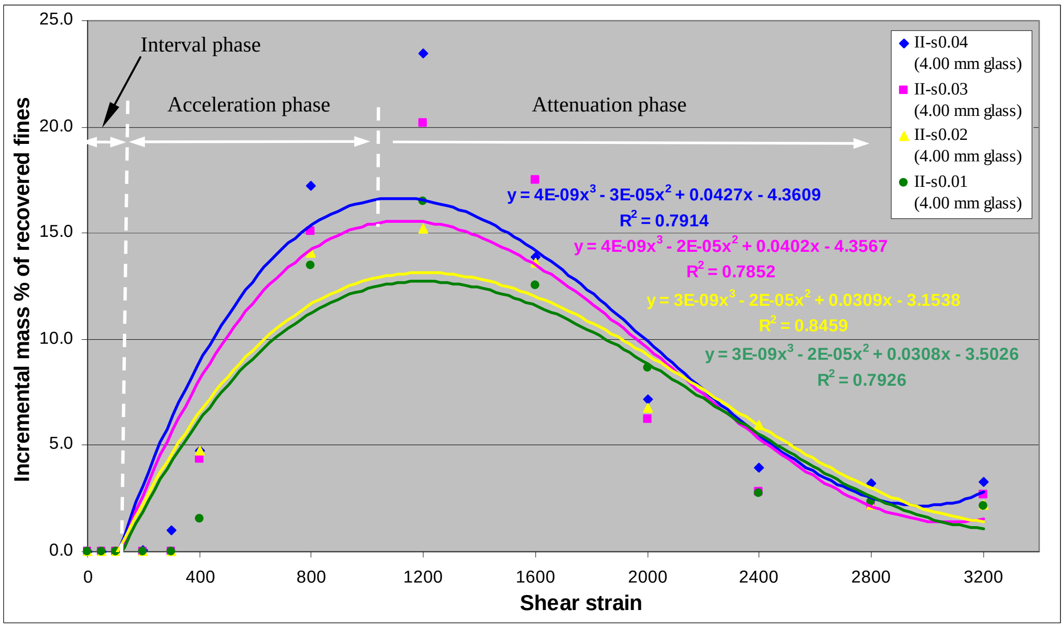


Figure 5.11: Shear strain versus incremental mass % of recovered fines (IMF) in II series. Note that the equation and R² value denoted by the same colour while the bed-matrix is 15.75 mm glass sphere. The third order of polynomial fit was generated by the mean of three readings.

Figure 5.11 shows that percolation in the II series can be categorised into three different phases namely: the *interval phase*, *acceleration phase* and *attenuation phase*.

- the interval phase is the period from commencement of the experiment until the first arrival of a fine particle. In general, the interval phase is controlled by the percolation potential to pass the void gaps during shearing;
- the acceleration phase is the period in which a group of fine particles passed the void gaps within the bed-matrix and are recovered in the collection compartments (illustrated by a rapid increment of fine particles mass). During this period, the % mass of fine particles recovered continuously increases until it reaches the maxima. At the maxima, most of the freely travelling fine particles (without being captured or detained within the void gaps) have passed through the bed-matrix; and
- following the maxima, the attenuation phase starts. For the duration of this phase, some of fine particles began to fill or partially fill void gaps in the bed-matrix and are captured or detained. The accumulation of the fine particles reduces the potential for percolation (depicted by the decreased and/or constant magnitude of IMF). Nevertheless, it is still possible for

percolation to increase provided that some of the detained fine particles were able to find sufficient gaps to percolate.

Figure 5.11 illustrates that as the percolation reaches its maxima (approximately $\gamma_{total}$ =1200%), percolation significantly decreases. One possible explanation is that the higher percentage of fines to fill or partially fill the void in the bed-matrix of both 15.75 mm glass spheres. Arteaga and Tüzün (1990) assert that void filling by the fine particles is one of the main reasons that significantly reduced the probability of fine particle to percolate within the gaps fractions bed-matrix during percolation.

The above observation can also be further explained by considering the packing of a binary mixture (i.e., fine percolating particle in a bed-matrix). According to Ketterhagen et al. (2008), for such binary mixture of sizes, the void fractions will decrease with increasing of the fines mass fraction that fill the void gaps. As the fines fraction continues to increase, less interstitial volume is available for percolating fines to pass through thus limiting the percolation. This observation is shown by the Figure 5.12.

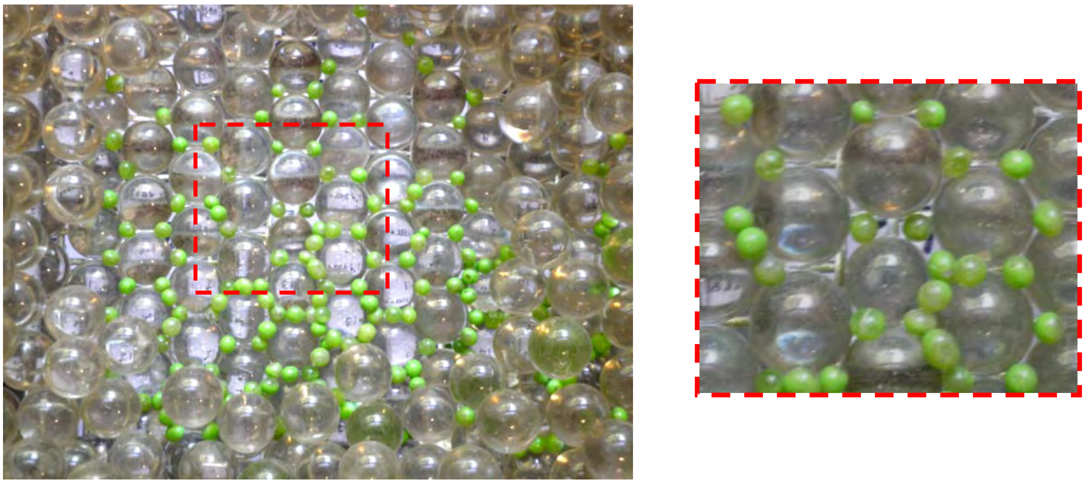

Figure 5.12: Example of condition in which the fine particles filled or partially filled pores/void fractions (red dashed line enlargement) in the bed-matrix at approximately 10 mm height above the base of the SCPG mesh after shearing. Note that 4.00 mm glass sphere (green) in the bed-matrix of 15.75 mm glass sphere.

### *5.5.1.3 Fines: 4.05 mm crushed basalt; Bed-matrix: 15.75 mm glass (BI series)*

A total of 12 tests were carried out for the BI series (i.e., three tests for each strain rate); the results are presented in Figure 5.13. A key finding is that the percolation of 4.05 mm fine basalt aggregate increased with strain rate much the same as ideal media.

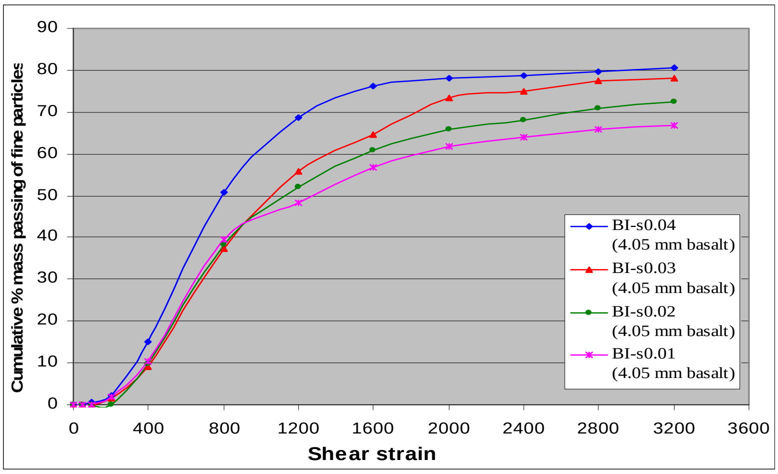


Figure 5.13: Mean shear strain versus cumulative % mass passing of fine particles (CPF) for the BI series. The bed-matrix is 15.75 mm glass sphere.

It is surprising to note that for the BI series, each of the strain rate (0.01, 0.02, 0.03 and 0.04 $s^{-1}$) tested shows that the peak of CPF were slightly higher (5-15%) than in the II series (Section 5.5.1.2). This finding may at first seem to contradict previous assertions (e.g., Massol-Chaudeur et al. 2002; Lebron and Robinson 2003) which postulate that more rounded (or spherical) particles generally percolate (and segregate) faster than angular particles due to the fact of its higher flowability. Nevertheless, the significantly higher percolation in BI series than the II binary mixture suggests that the shape effect may have a significant impacted on percolation. It also needs to be remembered that angular particles are not described by a single dimension and for this reason the equivalent spherical diameter may not be the best method of categorising particle size for these tests.

It was hypothesised in Section 1.2 that particle shape plays a significant role in percolation of fine particles in a matrix of highly angular coarse aggregates under gravity and shearing. The above hypothesis is consistent with that obtained by Tang and Puri (2007) and Jha et al. (2008) who experimentally compared spherical (i.e., glass sphere, urea) and angular shaped (i.e., mash poultry feed, potash) effect relative to the segregation and percolation potential. However, it is worth noting that rock fragments are far more angular than the mash poultry feed and potash used by above researchers.

Accordingly, Tang and Puri (2007) and Jha et al. (2008) found that after certain shear strains, the angular shaped particles excel over the spherical one. Furuuchi and Gotoh (1992) noted that spherical particles do not always percolate faster than irregular shape particles even if it is the same size. They postulated that this phenomenon occurred because the downward velocity of percolating particles are mainly influenced by the drag coefficient, particle mass and projected area in the percolating direction.

The third order of polynomial model (Figure 5.14) shows the BI series has a similar pattern to II series, up to a point. However, unlike the II series which generally completed the attenuation phase at approximately $\gamma_{total}$ = 3000%, the BI series ended slightly earlier (i.e., $\gamma_{total}$ =2800%) and is followed by the second acceleration phase. This suggests that after $\gamma_{total}$ =2800% it is more likely that some of the detained fine basalt particles have re-oriented sufficiently to pass through the void gaps.

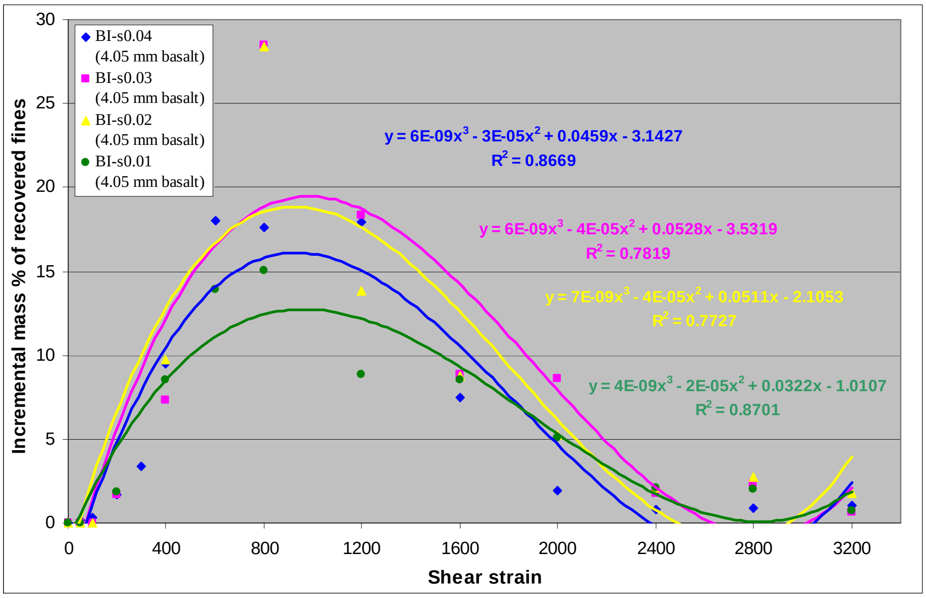


Figure 5.14: Shear strain versus incremental mass % of recovered fines (IMF) in BI series. Note that the equation and R² value denoted by the same colour while the bed-matrix is 15.75 mm glass sphere. The third order of polynomial fit was generated by the mean of three readings.

#### *5.5.1.4 Fines: 4.00 mm glass; Bed-matrix: 13.20 mm crushed basalt (IB series)*

For IB series, a total 12 tests were performed for the 4.00 mm glass sphere (percolating fine particles) and 13.20 mm basalt aggregate (bed-matrix) (i.e., three tests for each strain rate). It was observed that more shear strain is needed ($\gamma_{total}$=4800%) due to the longer residence time required for fine particles to travel within the bed-matrix which typically started only after $\gamma_{total}$=2000% (Figure 5.15).

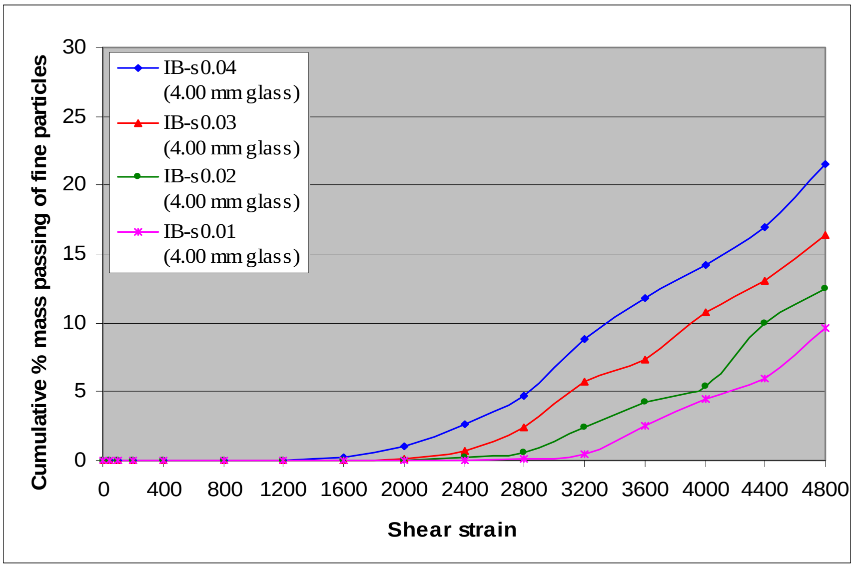


Figure 5.15: Mean shear strain versus cumulative % mass passing of fine particles (CPF) for the IB series. The bed-matrix is 13.20 mm crushed basalt.

The percolation in IB series is also controlled by the bed-matrix (13.20 mm basalt aggregate) during shearing which is shown by the low CPF compared to the II and BI series. This suggests that the surface properties and particle shape of the bed-matrix of highly angular basalt may have an impact to the percolation potential of fine particles. Matveev et al. (2006) investigated the downstream flow of fine granular through the fixed reactor bed and concluded that the average filtration velocity was primarily influenced by the character of the surface of the spheres constituting the bed.

Quantitatively, the percolation of fine particles in the IB series reduced by almost 70% as compared to the II and BI series at $\gamma_{total}$=3200%. Alternatively, this finding indicates that the results from ideal media (i.e., mono-size shaped particles) may not adequately be used for the real world applications especially to the block caving mines. For instance, caved rock consists of highly angular shapes and wide size distribution sizes far removed from ideal media.

Using a third order polynomial model (Figure 5.16) to $\gamma_{total}$=4800% it was found that only two phases were recorded; the interval and acceleration phases. This suggests that higher shear strains are required to measure all three phases as noted in Section 5.5.1.2 and Section 5.5.1.3. Nevertheless, at shear strains higher than $\gamma_{total}$>4800% were not conducted due to the limitations previously discussed in Section 5.3.1. Nonetheless, it is postulated that at significantly higher shear strains ($\gamma_{total}$>4800%), CPF increases linearly with increases in strain rate until it reach the maxima and is followed by an attenuation phase in which the percolation potential is reduce during this phase.

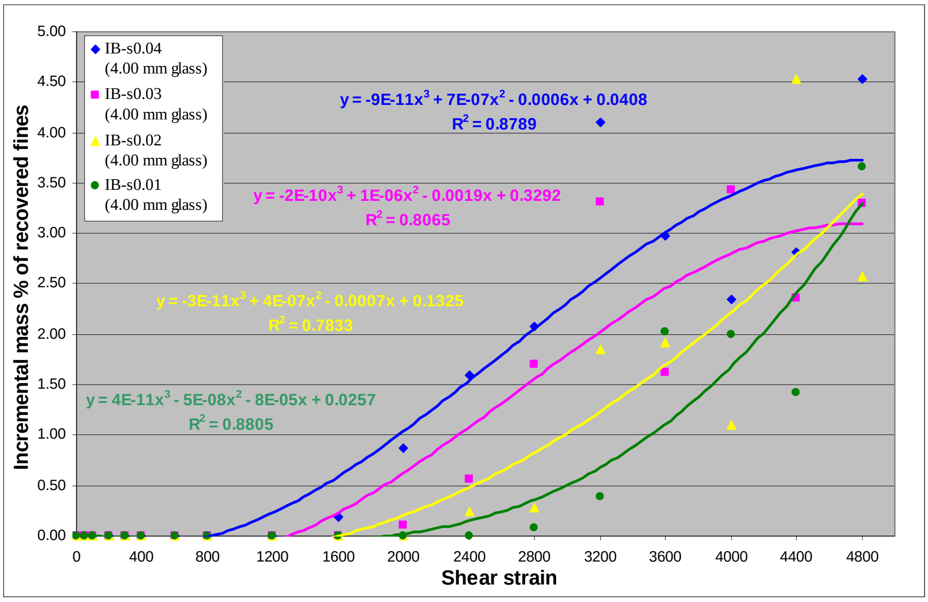


Figure 5.16: Shear strain versus incremental mass % of recovered fines (IMF) in IB series. Note that the equation and R² value denoted by the same colour while the bed-matrix is 13.20 mm crushed basalt. The third order of polynomial fit was generated by the mean of three readings.

#### *5.5.1.5 Fines: Crushed basalt; Bed-matrix: 13.20 mm crushed basalt (BB series)*

A total of 12 tests were performed for the BB series in which 4.05 mm basalt aggregate was used as the percolating fine particles in a matrix of 13.20 mm basalt aggregate. Similar to the IB series, higher shear strains were required to complete each test.

Figure 5.17 presents typical CPF results for the BB series for four strain rates (0.01, 0.02, 0.03 and 0.04 $s^{-1}$). It is concluded that the percolation of fine granulate particles in the coarse angular aggregate is increases linearly with strain rate and shear strains. Similarly to the IB series, the use of highly angular aggregate significantly reduced the CPF by up 85% at $\gamma_{total}$ =3200% compared to the II and BI series tests.

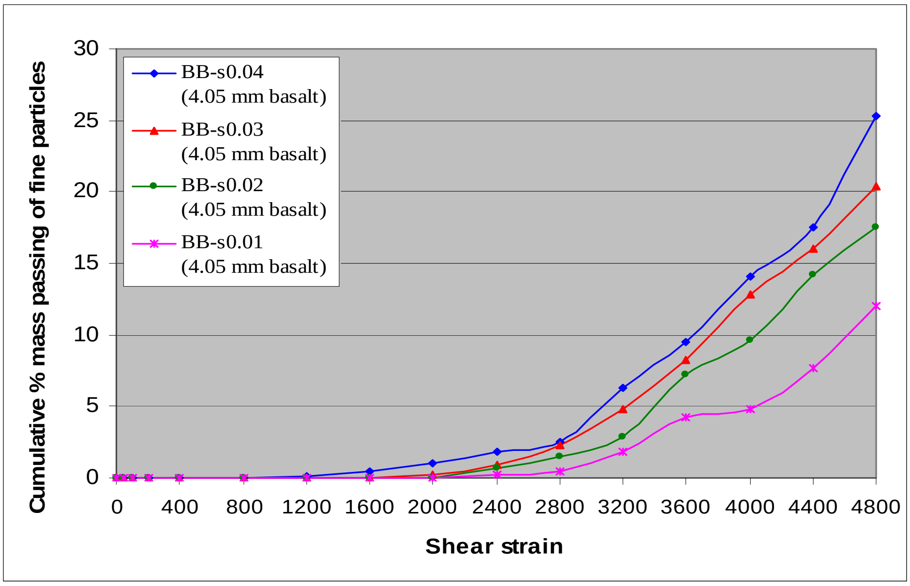


Figure 5.17: Mean shear strain versus cumulative % mass passing of fine particles (CPF) for the BB series. The bed-matrix is 13.20 mm crushed basalt.

However, it was found that at $\gamma_{total}$ =4800%, the IMF in the BB series exceeded that of the IB series by 5%. Once again this suggests that the physical properties of basalt aggregate such as particle shape and void ratio is more significant than other parameters such as particle density and strain rate. The significantly lower CPF is illustrated by the third order of polynomial model (Figure 5.18) in only the interval and acceleration phases are present. It is postulated that the percolation potential increases linearly with strain rate in the following order of BB-s0.01 to BB-s0.02 to BB-s0.03 to BB-s0.04 respectively.

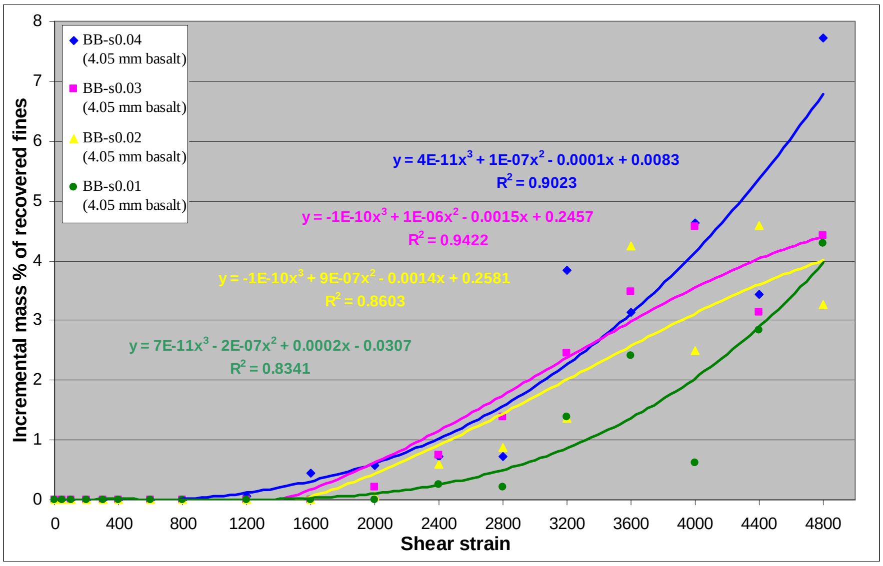


Figure 5.18: Shear strain versus incremental mass % of recovered fines (IMF) in BB series. Note that the equation and $R^2$ value denoted by the same colour while the bed-matrix is 13.20 mm crushed basalt. The third order of polynomial fit was generated by the mean of three readings.

### *5.5.1.6 Summary*

It is concluded that percolation is significantly effected by strain rate. Previous studies on percolation asserted that the percolation rate increases proportionally with of strain rate until $\dot{\gamma}=0.4\ s^{-1}$ (e.g., Bridgwater et al. 1978; Bridgwater 1994). On the other hand, percolation rate is less affected when the strain rate is above 0.4 $s^{-1}$ as these increase the “interactions” such as collisions between small and large particles. At the high strain rates, the gaps between coarse particles are open for less time thus decreasing the probability of a fine particle to pass through an underlying gap. Nevertheless, since the SCPG employed a significantly lower strain rate ($\dot{\gamma}<0.04\ s^{-1}$) to replicate the low shear strain magnitude in block caving mine, such “interaction” phenomenon is postulated to be less significant.

Results on percolation of fine particles in bed-matrix of 15.75 mm glass spheres demonstrated the significant effect of strain rate on percolation. However, it was found that the CPF in the bed-matrix of 13.20 mm basalt aggregate was much lower than that of ideal media (15.75 mm glass sphere). This finding implies that the results of studies from chemical, powder and agricultural applications (e.g., Bridgwater and co-authors; Duffy and Puri 2002; Jha et al. 2008) are not applicable to coarse angular media encountered in caving mines. It was also found that the CPF increased linearly with shear strain and was controlled by the bed-matrix properties (i.e., particle shape and size).

### 5.5.2 Effect of Particle Diameter Ratio

#### *5.5.2.1 Overview of results and general observations*

A total of 42 tests were performed to investigate the particle diameter ratio effect including tests on 4.00, 5.00 and 6.00 mm glass spheres and 2.86, 4.05, 5.21 and 6.18 mm basalt aggregates as percolating fine particles. 13.20 mm basalt aggregate and 15.75 mm glass sphere were used as the bed-matrices. It is worth noting that a strain rate of 0.04 $s^{-1}$ was selected as previously discussed. A full listing of results is found in Appendix C2 while Table 5.4 summarises the testing parameters and configurations.

Table 5.4: Test series for investigation of the effect of particle diameter ratio on percolation.

<table>
<tr><th>Series</th><th>Particle diameter ratio</th><th>Percolating fine particles</th><th>Coarse bed-matrix</th><th>Controlled experimental conditions</th></tr>
<tr><td rowspan="3">II</td><td>0.25</td><td>4.00 mm glass sphere</td><td rowspan="7">15.75 mm glass sphere</td><td rowspan="14">• Strain rate (0.04 $s^{-1}$);<br>• Particle density;<br>• Normal stress (0.9 kPa);<br>• Particle shape;<br>• Shear strain (3200% for the II and BI series and 4800% for the IB and BB series)</td></tr>
<tr><td>0.32</td><td>5.00 mm glass sphere</td></tr>
<tr><td>0.38</td><td>6.00 mm glass sphere</td></tr>
<tr><td rowspan="4">BI</td><td>0.18</td><td>2.86 mm basalt aggregate</td></tr>
<tr><td>0.26</td><td>4.05 mm basalt aggregate</td></tr>
<tr><td>0.33</td><td>5.21 mm basalt aggregate</td></tr>
<tr><td>0.39</td><td>6.18 mm basalt aggregate</td></tr>
<tr><td rowspan="3">IB</td><td>0.30</td><td>4.00 mm glass sphere</td><td rowspan="7">13.20 mm basalt aggregate</td></tr>
<tr><td>0.38</td><td>5.00 mm glass sphere</td></tr>
<tr><td>0.45</td><td>6.00 mm glass sphere</td></tr>
<tr><td rowspan="4">BB</td><td>0.22</td><td>2.86 mm basalt aggregate</td></tr>
<tr><td>0.31</td><td>4.05 mm basalt aggregate</td></tr>
<tr><td>0.39</td><td>5.21 mm basalt aggregate</td></tr>
<tr><td>0.46</td><td>6.18 mm basalt aggregate</td></tr>
</table>

The following observations were noted during the tests:

- CPF is predominantly affected by the particle diameter ratio of percolating and bed-matrix particles;

- percolation of fine particles was controlled by the bed-matrix properties during shearing especially for the IB and BB series; and
- the CPF in bed-matrix of crushed aggregate media (basalt aggregate) was significantly lower than that of ideal media (glass sphere).

In this section, the results of particle diameter ratio effect in percolation are presented as follows:

- Fines: Ideal media and crushed basalt; Bed-matrix: 15.75 mm glass spheres (II and BI series); and
- Fines: Ideal media and crushed basalt; Bed-matrix: 13.20 mm crushed basalt (IB and BB series).

### *5.5.2.2 Fines: Ideal media and crushed basalt; Bed-matrix: 15.75 mm glass spheres (II and BI series)*

The following nomenclature was used for the ease of identification and analysis of the effect of diameter ratio test in Sections 5.5.2.2 and Section 5.5.2.3 (Figure 5.19):

- the first characters identify the series type of binary mixture of media used in the test; and
- the second segment refers to the particle diameter ratio ($d_p / d_b$).

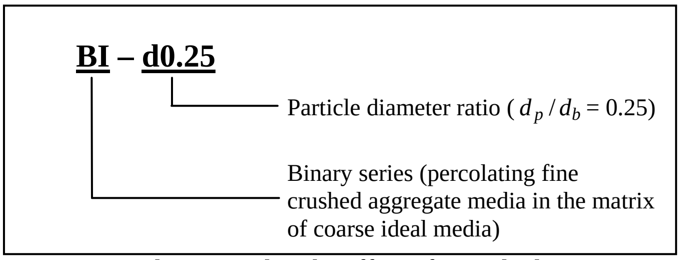


Figure 5.19: Nomenclature used in the effect of particle diameter ratio tests.

Figure 5.20 presents CPF for the II and BI series. It was found that the BI-d0.18 series (2.86 mm basalt fines in 15.75 mm glass spheres) provided the highest percolation rate; almost all the fine particles (CPF = 98.98%) were recovered at $\gamma_{total}$ =800%.

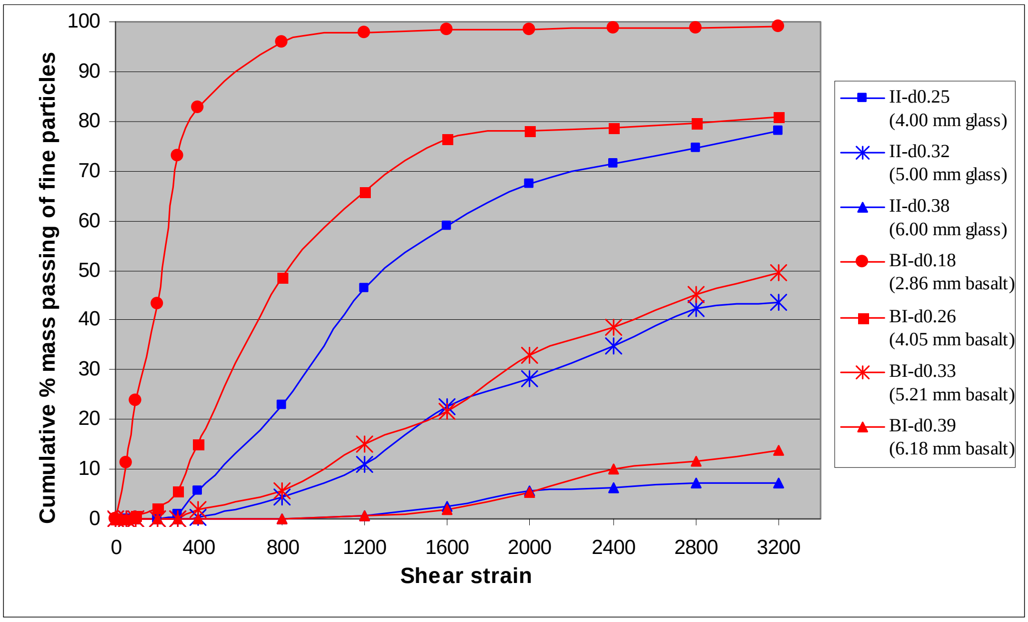


Figure 5.20: Mean shear strain versus cumulative % mass passing of fine particles (CPF) for the II and BI series. The bed-matrix is 15.75 mm glass sphere.

In comparison to this finding, Robinson and Friedman (2002) found that when the void gaps of the small particles is less than about one-third of the gap fraction formed between the large particles, percolation may occur. In line with this, Robinson and Friedman (2002) postulated that this phenomenon may arise provided that the fine particles are adequately small to fit between the pores created by the large particles.

The above finding is also supported by Johanson et al. (2005) who found that for free flowing fines, if the fines are less than one-third the size of coarse particles, they may percolate through the coarse matrix of particles. In addition to the above finding, Hogg (2009) noted that in general, gravitational forces promote a net downward motion of the smaller particles which can readily pass through the void gaps of the bed-matrix.

It is also observed that as $d_p / d_b$ increases, percolation of fine particles becomes more prevalent as shown in the II-d0.38 and BI-d0.39 series (CPF=7.26% and 13.75% at $\gamma_{total}$=3200% respectively). This suggests that as the fine particle size increases, the probability of smaller particles filling the void gaps and passing through the bed-matrix decreased thus reduced the CPF.

Alternatively, the above phenomenon can be linked to Ketterhagen et al. (2008) simulation works on the effects of particle properties and hopper geometry. It was noted that as the quantity of fine particles in the voids of bed-matrix are increased, substantially reduced interstitial volume is available for percolating fines. As the quantity of fine particles is increased, the void fraction reaches a minimum point where the percolation is capped as shown by the stagnant graph of BI-d0.18 (after $\gamma_{total}$ >1200%) in Figure 5.20.

It is interesting to highlight that typically all fine crushed aggregates media (basalt aggregates) have been shown to produce higher CPF than ideal media (glass sphere) for each of the case of closest $d_p / d_b$ ratio (i.e., II-d0.25 and BI-d0.26; II-d0.32 and BI-d0.33). This finding may be associated to the shape effect based on the fact that the packing of an aggregate is dependent also on the shape of the aggregate particles (Kwan and Mora 2001). Alternatively, it can be deduced that for the similar or closest particle sizes, the shape effect of basalt aggregate (i.e., flakiness and elongate shaped) might significantly contributed to the increases in percolation than the spherical shaped of similar particles size. This hypothesis is discussed in detail in Section 5.5.3.

Theoretically, an attempt to calculate the possible number of fine particles that may pass through the void gaps of a single-staggered bed-matrix were employed using the Rhinoceros® computer aided drawing program. Alternatively two types of sphere packing were selected: the *cubical packing* (represent the least densely of all possible single-staggered packing type) and the *hexagonal packing* (represent the densest of all possible single-staggered packing). Both spherical packing types were illustrated in Figure 5.21 and Figure 5.22.

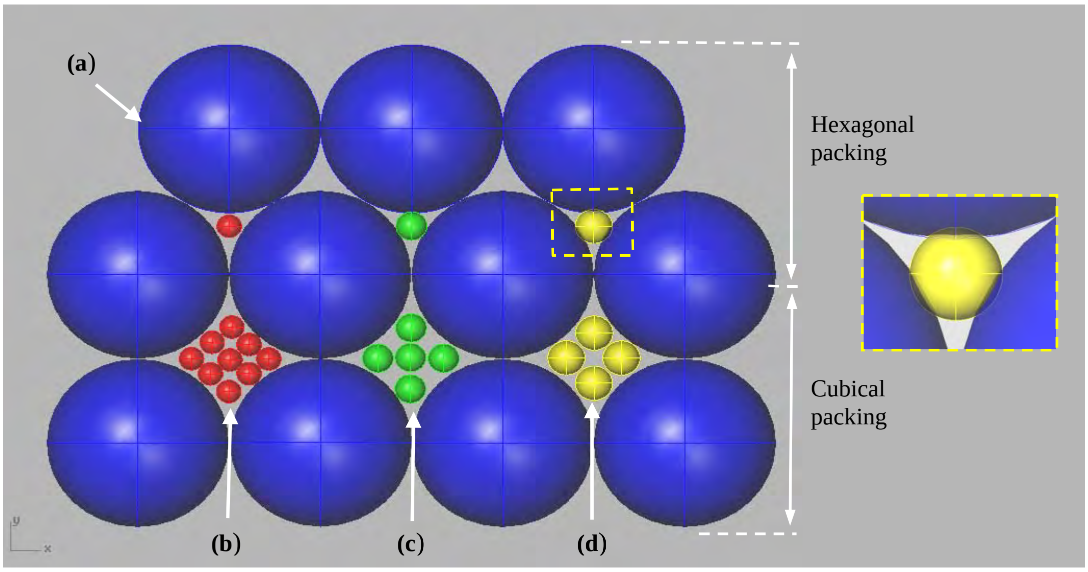


Figure 5.21: Theoretical number of percolating fine particle in cubical and hexagonal packing and the enlargement of the yellow dashed square packing for the particles diameter ratio effect in II series (drawn to scale).

Note: (a) 15.75 mm glass spheres ( $D_s$ = 15.78 mm) [blue colour]
(b) 4.00 mm glass spheres ( $D_s$ = 4.05 mm) [red]
(c) 5.00 mm glass spheres ( $D_s$ = 5.03 mm) [green]
(d) 6.00 mm glass spheres ( $D_s$ = 6.16 mm) [yellow].

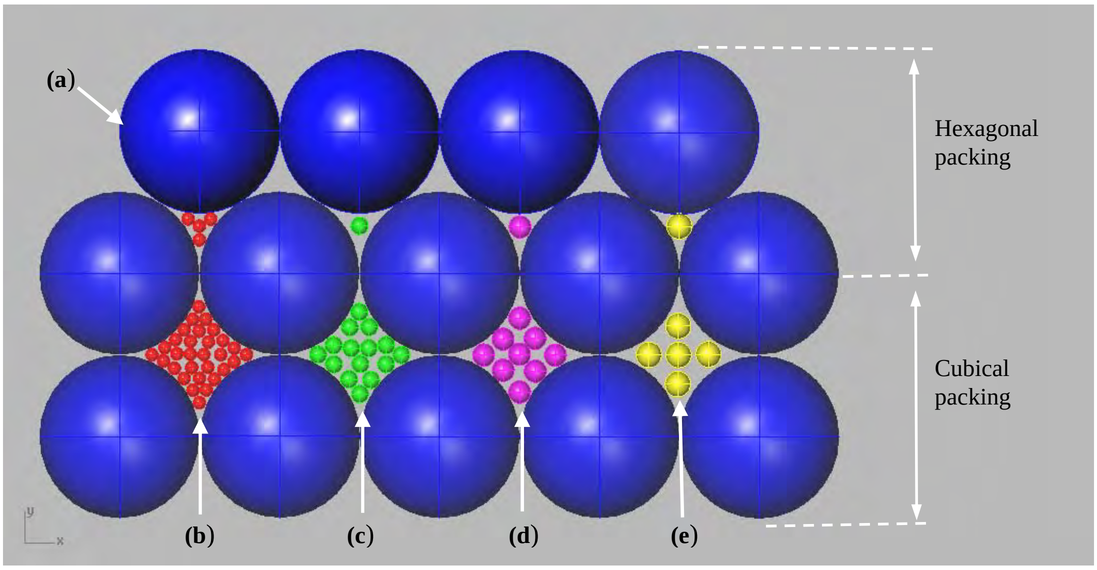


Figure 5.22: Theoretical number of percolating fine particles in cubical and hexagonal packing for the particles diameter ratio effect in BI series (drawn to scale).

Note: (a) 15.75 mm glass spheres ( $D_s$ = 15.78 mm) [blue colour]
(b) 2.86 mm basalt aggregate ( $D_s$ = 2.41 mm) [red]
(c) 4.05 mm basalt aggregate ( $D_s$ = 3.19 mm) [green]
(d) 5.21 mm basalt aggregate ( $D_s$ = 4.08 mm) [magenta]
(e) 6.18 mm basalt aggregate ( $D_s$ = 4.83 mm) [yellow]

It worth noting that the equivalent spherical diameter method ($D_s$) (Nedderman 1992) previously discussed in Section 4.4.3 was used for both ideal and crushed aggregate media as this provides a method to compare each media type. Figures 5.21 and 5.22 show that the 2.86 mm basalt aggregate ($d_p / d_b$ =0.18) provides the highest number of fine particles passing through the voids of bed-matrix in cubical and hexagonal packing (a maximum of 30 and four particles can simultaneously pass through the void gap respectively). By comparison, for the 6.00 mm glass sphere ($d_p / d_b$ =0.38) only four in cubical packing and one in hexagonal packing can pass freely through the void gap.

Although this estimation method is different to the actual condition during the test, it provides some idea of the correlation between $D_s$ and potential for fine particles to pass through the void gaps. Moreover, this method provides a meaningful method to explain the significant higher percentage of small particles (i.e., 2.86 mm basalt aggregate) available to move within the 15.75 mm bed-matrix (Figure 5.20).

White and Walton (1937) theoretically calculated several potential packing configurations of spherical particles and found that the cubical packing fill a theoretical void space of 47.64% as compared to 39.55% for hexagonal packing. White and Walton (1937) also found that the use of very fine filler in the remaining voids will reduce the voids by up to 3.9%. On contrary, the use of spherical particles does not appear to reduce the porosity but other irregular shape (i.e., cylindrical shaped) would reduce the porosity below that possible with spheres provided its sufficiently arranged.

Alternatively such combinations of cubical, hexagonal packing (single-staggered) and/or any packing types (i.e., double-staggered, pyramidal, tetrahedral) in spherical particles configurations significantly fills the void gaps thus reducing the potential for fine particle percolation. This phenomenon was clearly observed in the II series as presented in Figure 5.23.

Figure 5.23: Cubical and hexagonal packing configurations in II series after shearing. Note that 4.00 mm glass spheres (green colour) are located at approximately 80 mm above the base of the SCPG mesh.

Figure 5.24 shows the comparison between the 15.75 mm glass sphere packing before and after the shearing. It is obvious that after a period of shearing, the random packing arrangement of 15.75 mm glass sphere has significantly altered and is more uniformly packed (shown by the triangle shape in Figure 5.21). This shows that after several periods of shearing, the potential of fine particles to pass through the void gaps decreased due to the changes in the packing from random to hexagonal packing. According to this, Duffy and Puri (2002) noted that cubical packing is usually unstable compared to the other types of packing (e.g., orthorhombic, hexagonal) which is generally more stable but require tapping or vibration to attain the theoretical configurations.

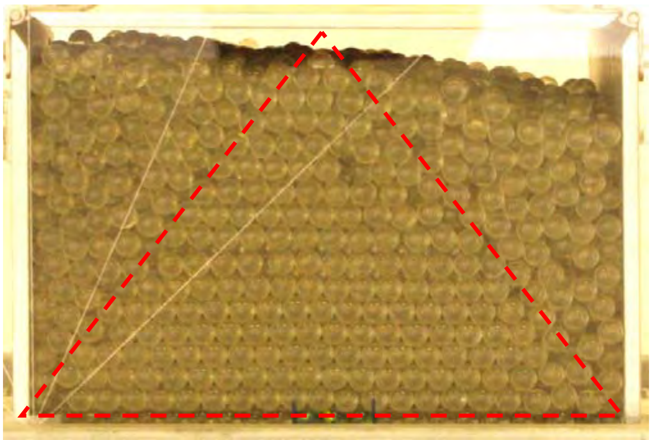

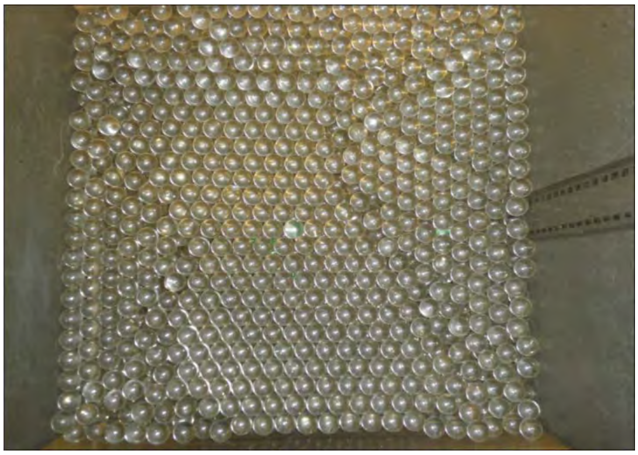

Figure 5.24: Comparison of 15.75 mm glass sphere packing before shear (upper picture), prior shearing ($\gamma_{total}$ =3200%; centre picture) and top view of the bed-matrix after test at approximately 100 mm above the base of the SCPG mesh (lower picture). Note that the hexagonal packing is denoted by the red dashed line.

Figure 5.25 is a plot of shear strain versus incremental mass % of fine recovered (IMF) with a third order of polynomial model fitted for both the II and BI series. The polynomial model shows that for the BI-d0.18, the acceleration phase was rapid, occurring simultaneously as the shearing started suggested that most of the fines particles spontaneously percolated through the void gaps of bed-matrix. The similar pattern also takes place to the II-d0.25 and BI-d0.26 series, but at a lower acceleration rate. On the other hand, the interval, acceleration and attenuation phases for higher $d_p/d_b$ ratios (i.e., II-d0.32, II-d0.38, BI-d0.33 and BI-d0.39) occurred at significant slower rates than the lower $d_p/d_b$ ratio.

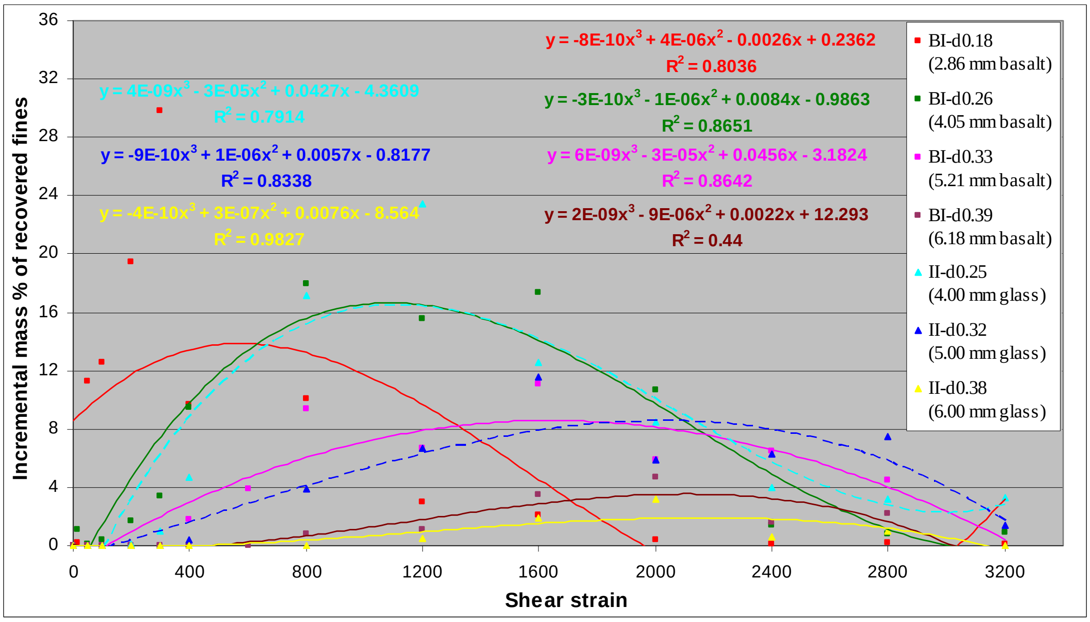


Figure 5.25: Shear strain versus incremental mass % of recovered fines (IMF) in II and BI series. Note that the equation and R² value denoted by the same colour while the bed-matrix is 15.75 mm glass sphere. The third order of polynomial fit was generated by the mean of three readings.

It was observed that after $\gamma_{total}$ =800%, the BI-d0.18 series reached maxima and followed by the attenuation stage. During this stage, it is deduced that most of the fines began filling the void gaps. As this process continues, less interstitial volume is available for percolating fines to pass freely through the void gaps of bed-matrix thus the percolation becomes stagnant and restricted. However, after $\gamma_{total}$ =3000%, the fines percolation of BI-d0.18 series began to increase suggesting that during this period, most of the detained fine particles may have rearranged and found sufficient gaps to pass through the bed-matrix in which the significant increased in percolation were observed. These finding accords with Bridgwater (1994) which commented on the probability of particles orientation during shearing can significantly increase the potential for percolation.

#### 5.5.2.3 *Fines: Ideal media and crushed basalt; Bed-matrix: 13.20 mm crushed basalt (IB and BB series)*

Figure 5.26 shows the CPF for IB and BB series. The graph shows that longer residence times were needed for the fine particles to travel through the matrix of crushed aggregate media (13.20 mm basalt aggregate). This finding is contradicted with the finding in II and BI series (Section 5.5.2.2) by which the percolation of the fine particles were significantly higher at lower shear strain. This demonstrated that for the IB and BB series, the bed-matrix predominantly affects the percolation of fine particles. Tang and Puri (2004) noted that series of size and shape differences may lead to increase of the potential fine particles to pass through the void gap of coarse particles which was reflected by the higher percentage of percolation in BB series than the nearest $d_p/d_b$ set (i.e., IB-d0.30 and BB-d0.31) illustrated in Figure 5.26.

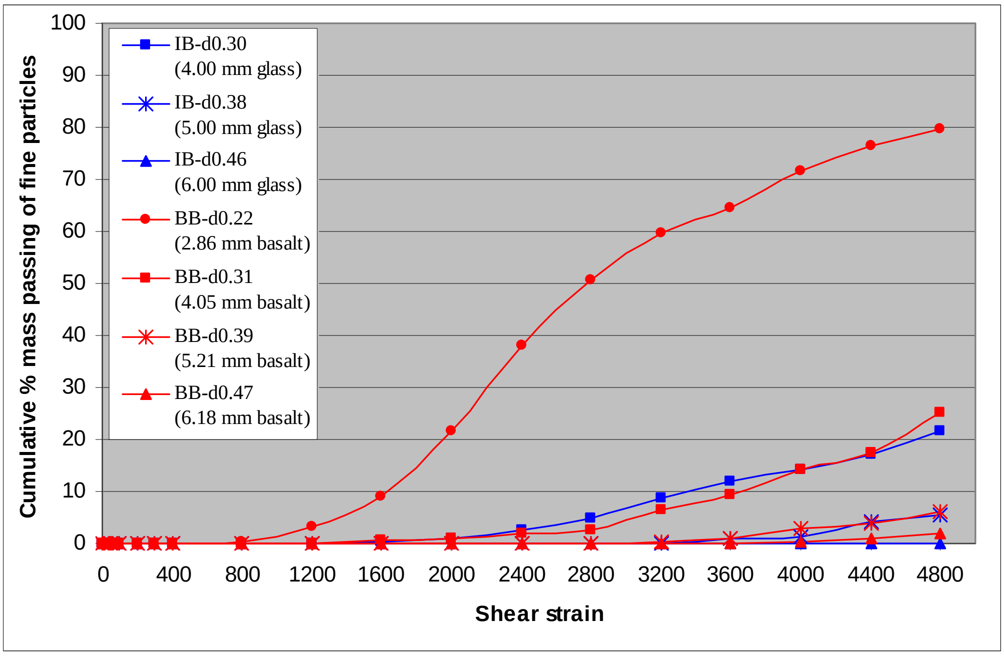


Figure 5.26: Mean shear strain versus cumulative % mass passing of fine particles (CPF) for the IB and BB series. The bed-matrix is 13.20 mm crushed basalt.

It was also found that the higher $d_p/d_b$ ratio, the longer residence time required thus producing lower CPF. For instance, after $\gamma_{total}$=4800% both the highest $d_p/d_b$ (i.e., IB-d0.46 and BB-d0.47) were found to percolate the least (CPF=0% and 1.78% respectively) compared to the others diameter ratio. This value is comparatively low against the lower $d_p/d_b$ (i.e., BB-d0.22) with CPF=79.63%. This finding agrees with Matveev et al. (2006) who found that larger particles will travel over longer distances due to some possible resistance (i.e., bounce off the spheres of the matrix) thus increases their residence time.

Once again, the above phenomenon can be further described by considering the equivalent spherical diameter methods ($D_s$) as illustrated in Figures 5.27 and 5.28. Although the 2.86 mm basalt aggregate ($d_p/d_b$=0.18) provides the highest number of fine particles passing through the voids of bed-matrix in hexagonal packing (one particle; Figure 5.27) and cubical packing (four particles; Figure 5.28), it still notably lower than in the BI series. Whilst, for other basalt aggregates (4.05, 5.21 and 6.18 mm), it clearly shows that only single particles may possibly pass the voids at a time within the cubical packing and none for the hexagonal packing. This suggested that practically, the potential of larger $d_p/d_b$ ratio to pass the interstitial gaps are statically low thus explained the lower CPF of (IB-d0.30, IB-d0.38, IB-d0.46, BB-d0.31, BB-d0.39, BB-d0.47) in Figure 5.26.

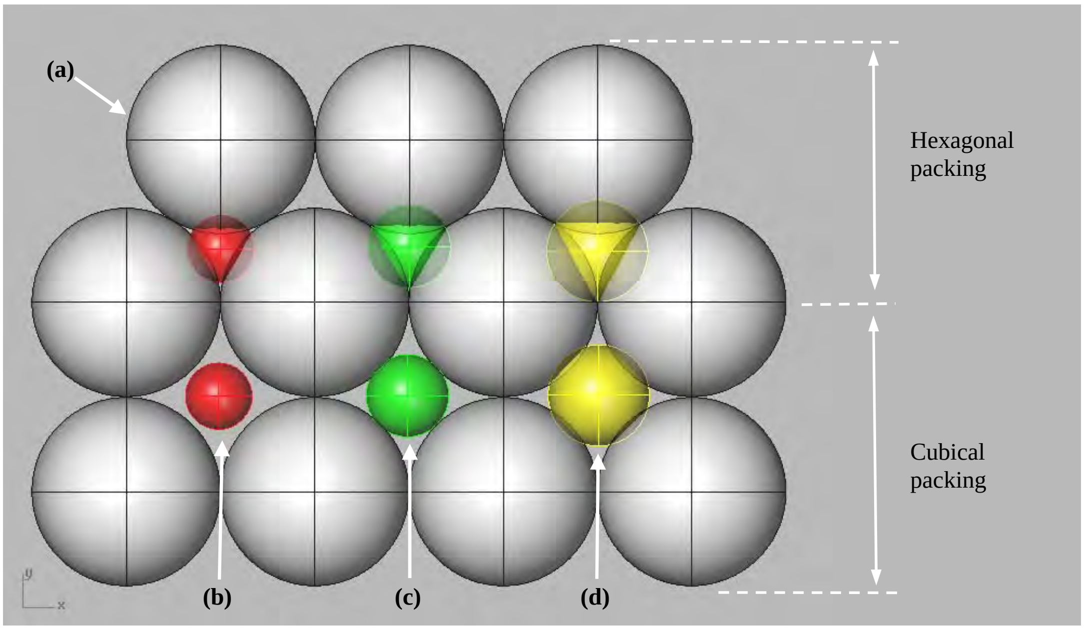


Figure 5.27: Theoretical number of percolating fine particle in cubical and hexagonal packing for the particles diameter ratio effect in IB series (drawn to scale).

Note: (a) 13.20 mm basalt aggregate ($D_s$ = 11.48 mm) [gray colour]
(b) 4.00 mm glass sphere ($D_s$ = 4.05 mm) [red]
(c) 5.00 mm glass sphere ($D_s$ = 5.03 mm) [green]
(d) 6.00 mm glass sphere ($D_s$ = 6.16 mm) [yellow]

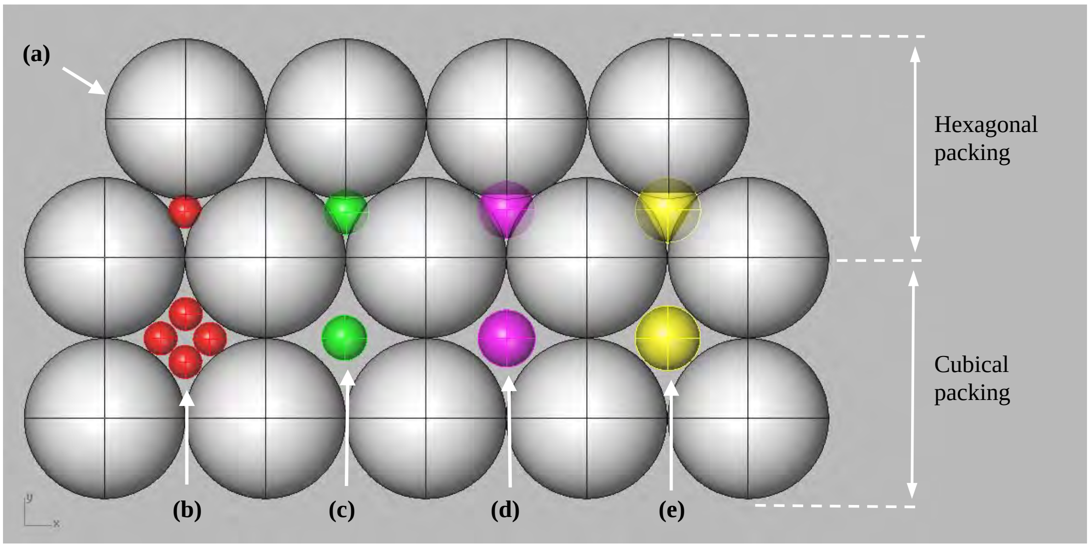


Figure 5.28: Theoretical number of percolating fine particle in cubical and hexagonal packing for the particles diameter ratio effect in BB series (drawn to scale).

Note: (a) 13.20 mm basalt aggregate ( $D_s$ = 11.48 mm) [gray colour]
(b) 2.86 mm basalt aggregate ( $D_s$ = 2.41 mm) [red]
(c) 4.05 mm basalt aggregate ( $D_s$ = 3.19 mm) [green]
(d) 5.21 mm basalt aggregate ( $D_s$ = 4.08 mm) [magenta]
(e) 6.18 mm basalt aggregate ( $D_s$ = 4.83 mm) [yellow]

Meanwhile, the slightly higher CPF were observed within the three closest sets of series (i.e., IB-d0.30 and BB-d0.31; IB-d0.38 and BB-d0.39; IB-d0.46 and BB-d0.47 respectively). It is postulated that these differences also resulted from particle shape effects. For example, 5.00 mm glass sphere in 13.20 mm basalt aggregate (IB-d0.38) only produce CPF=5.49% which slightly lower than the closest set of 5.21 mm basalt aggregate in 13.20 mm basalt aggregate (BB-d0.39; CPF=6.02%).

In view of the higher percolation percentage in the BB-d0.22 series, it was postulated that the probability for a small particle to encounter a void large enough and to enter the void region is greater than that for a big particle. This is in accord with Stephens and Bridgwater (1978b) and Foo and Bridgwater (1983) which found that the smaller particles will tend to percolate faster than large particles toward the regions of largest solids fraction because the voids are typically smaller in such regions while larger particles cannot enter and remain in the region of smaller solids fraction. Nevertheless, for the case of assemblies with similar particle diameter ratios, others physical properties such as particle shape, density, particle surface (i.e., rough or smooth) can influence the percolation of fine particles.

Figure 5.29 exemplifies polynomial fit for the effect of particle diameter ratio in IB and BB series. It is clearly shown that the BB-d0.22 series has the higher percolation potential at the earlier stage than others series. Unlike other series which experiences the interval phase at the beginning of shearing, the BB-d0.22 series has a very short interval phase. This can be proven by the rapid increment of polynomial fit in the BB-d0.22 while for the IB-d0.30 and BB-d0.31 moderate short interval phase was observed. On the other hand, the IB-d0.38, BB-d0.39 and BB-d0.47 shows the longer interval phase before began to enter the acceleration phase.

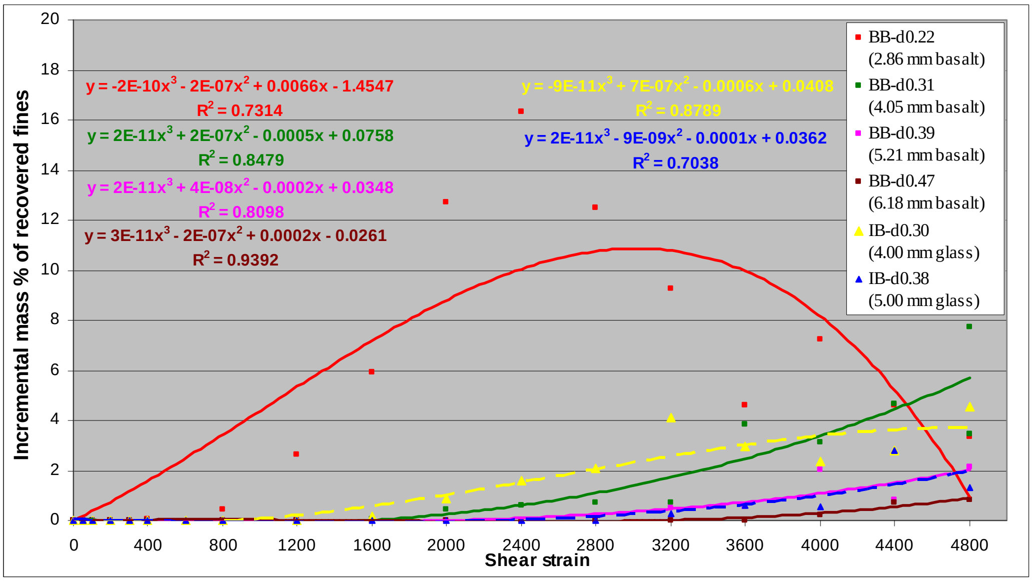


Figure 5.29: Shear strain versus incremental mass % of recovered fines (IMF) in IB and BB series. Note that the equation and R² value denoted by the same colour while the bed-matrix is 13.20 mm crushed basalt. The third order of polynomial fit was generated by the mean of three readings. The IMF for IB-d0.46 (6.00 mm glass) was not included since the value was found to be zero for the entire shearing.

After reaching its maxima (approximately $\gamma_{total}$ =3000%), the percolation potential decreases suggesting that the increase of fine particles to fill or partially fill void in the bed-matrix began to take place (shown by significant drop in the plot). Shinohara et al. (1972) conducted a study of size segregation using the percolation model and postulated that the smaller, more angular and denser particles has a higher ability to pass through the void gaps of bed-matrix and this follow by filling of the voids of the stationary layer with the separated particles. By contrast, the IB and BB series, the acceleration phase was still developing and progressing slowly, suggesting that a longer time is required before the maxima peak of percolation is reached.

Additionally, it is suggested that for the IB and BB series, the percolation of fine particles is controlled by the type of bed-matrix used (i.e., 13.20 mm basalt aggregate). This was clearly the case for higher $d_p / d_b$ ratio, in terms of the potential of large fine particles (i.e., IB-d0.38, BB-d0.39 and BB-d0.47) to percolate which was found to be generally lower than in the II and BI series probably due to the lower ratio of sufficient void gaps in the 13.20 mm basalt aggregate. It can be therefore postulated that significantly lower void gaps may result in bridging and mechanical interlock of fines (Jha et al. 2008) thus implied the significant affect of $d_p / d_b$ ratio and the packing bed of coarse particles matrix have in particle percolation.

#### *5.5.2.4 Summary*

The results show that particle diameter ratio has a significant effect on the percolation of fine particles in a coarse bed-matrix. It was shown that the larger the particle diameter ratio between the fine and matrix of coarse bed particles, the lower the CPF. This finding agrees with published work by previous researchers.

The study also found that percolation of fine particle increases proportionally with shear strain. On the other hand, for the range of test conditions considered (i.e., constant normal stress, strain rate, total strain, and limited particle shapes) it was shown that percolation is also controlled by the bed-matrix type (i.e., IB and BB series).

Alternatively, the particle diameter ratio effect for crushed aggregate media was investigated. These results provide improved estimates of percolation for coarse angular rock fragments similar to those found in block caving mines. For instance, the work is a step towards improved estimates of percolation rates for fine particles in block caves.

### 5.5.3 Effect of Particle Shape

#### *5.5.3.1 Overview of results and general observations*

A total of 30 tests were performed to investigate the effect of particle shape which includes the spherical, cubical, cylindrical and bi-conical (represent fines ideal media) and granular (crushed aggregate). Table 5.5 summarises the parameters tested during the particle shape experiments. A complete listing of results is found in Appendix C3.

Table 5.5: Test designed for the effect of particle shape.

| Series | Particle shape parameter | Percolating fine particles | Coarse bed-matrix | Controlled experimental conditions |
|---|---|---|---|---|
| II | Spherical | 4.00 mm glass sphere | 15.75 mm glass sphere | • Particle diameter ratio;<br>• Strain rate (0.04 $s^{-1}$);<br>• Normal stress (0.9 kPa);<br>• Particle density;<br>• Shear strain (3200% for the II and BI series and 4800% for the IB and BB series) |
| | Cubical | 4.00 mm glass cube | | |
| | Cylindrical | 4.00 mm glass cylinder | | |
| | Bi-conical | 4.00 mm glass bi-cone | | |
| BI | Angular | 4.05 mm basalt aggregate | | |
| IB | Spherical | 4.00 mm glass sphere | 13.20 mm basalt aggregate | |
| | Cubical | 4.00 mm glass cube | | |
| | Cylindrical | 4.00 mm glass cylinder | | |
| | Bi-conical | 4.00 mm glass bi-cone | | |
| BB | Angular | 4.05 mm basalt aggregate | | |

The following observations were noted during the tests:

- particle shape affects percolation; and
- the CPF in bed-matrix of crushed aggregate media (basalt aggregate) was significantly higher than that of ideal media (glass sphere) in both the bed-matrix.

Some observations were recorded for the 4.05 mm basalt aggregate. Generally it was found that the flattest basalt particles (i.e., higher flakiness ratio, $l/w$) percolated faster than the longer one (i.e., higher elongate ratio, $l/d$). A typical example of these particles is shown in Figure 5.30. This observation can be related to the higher potential of flat shaped particles to oriented and sufficiently pass through the void gaps within the bed-matrix than more elongate shaped particles. With regards to this, Furuuchi and Gotoh (1992) observed that the particle residence time significantly increases as particle elongation increases, due to the longer time to orientate and pass through the mesh aperture.

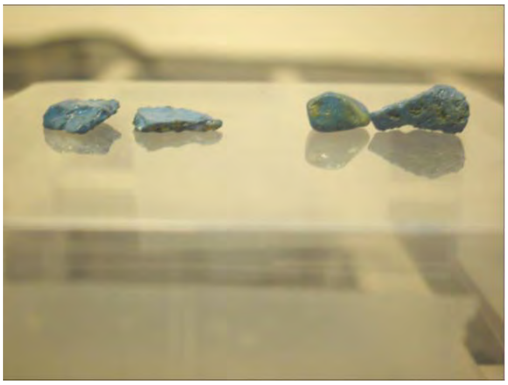

Figure 5.30: Comparison of particles shape of 4.05 mm basalt aggregate collected at $\gamma_{total}$ < 1200% [left] and prior to the end of the shearing at $\gamma_{total}$ = 3200% [right]. Note that for the left particles $l/w \geq 1.5$, $l/d \leq 1.6$ while the right particle has $l/w \leq 1.1$, $l/d \geq 1.6$.

Nevertheless, it was also demonstrated that spherical particles (glass spheres) percolated faster than the elongated shape particles (i.e., highly elongated basalt aggregate). Meloy et al. (1985) and Clark and Meloy (1988) used a stack of 20 identical sieves called "sieve-cascadograph" to measure the shape distribution of particles and concluded that the residence time of spherical particles in the stack is much less than that of elongated ones. The present work broadly agrees with this finding, as shown in Figure 5.30.

Moreover, by studying the transition zone of higher aspect ratio particles ($l/w$ and/or $l/d$), Abbaspour-Fard (2005) qualitatively recognised that more arching occurred as the aspect ratio of particles increases. The finding suggests that the higher aspect ratio particles may interlock among each others during the particle movement than the spherical (asymmetric particles).

In general, the results of particle shape effect in percolation were presented as follows:

- Fines: Ideal media and crushed basalt; Bed-matrix: 15.75 mm glass spheres (II and BI series); and

- Fines: Ideal media and crushed basalt; Bed-matrix: 13.20 mm crushed basalt (IB and BB series).

### *5.5.3.2 Fines: Ideal media and crushed basalt; Bed-matrix: 15.75 mm glass spheres (II and BI series)*

Figure 5.31 presents the particle shape results of both the II and BI series. It is apparent that the granular shapes (4.05 mm basalt aggregate) have a significantly higher CPF (80.73%) follow by spherical (78.01%), bi-conical (71.27%), cylindrical (69.87%) and cubical (60.53%). Initially, the higher CPF shown by the spherical shaped particles than others ideal media (i.e., cubical, bi-conical and cylindrical) is expected. Cleary (1999) reported that elongated particles can produce flow rates up to 30% lower than circular particles and also might alter the flow patterns during the motion. In addition, Cleary (1999) found that the flow rates of particles decrease by up to 28% for highly blocky or highly angular particles.

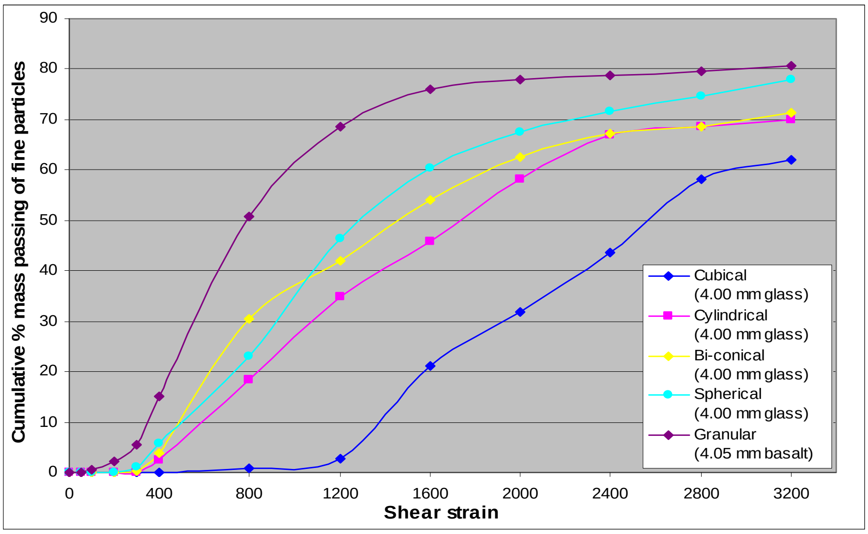


Figure 5.31: Mean shear strain versus cumulative % mass passing of fine particles (CPF) for the II and BI series. The bed-matrix is 15.75 mm glass sphere.

However, it is surprising to note that the angular shaped particles (basalt aggregate) were shown to have higher percolation than the spherical shape particles (ideal media). This finding confirmed that the shape effect is significant in contrast to works on mono-size and ideal media in which they postulated that the effect of particle shape is insignificant (e.g., Scott and Bridgwater 1975; Lebron and Robinson 2003).

In fact, the experimental results shown in Figure 5.31 elucidate the effect of particle shape in particle percolation. The results agree with Johansson (1996) who found that mixtures with different particle shapes (i.e., binary of irregular fine particle in spherical coarse matrix) are easier to segregate than those with mono-size and/or shaped particles. Experiments undertaken by Makse (1997, 1999) found that for particles of the same size, cubic grains tend to segregate near the top of the pile while the rounded grains segregate near the bottom. However, rounded grains may also roll down more easily than cubic grains, as shown in Figure 5.32.

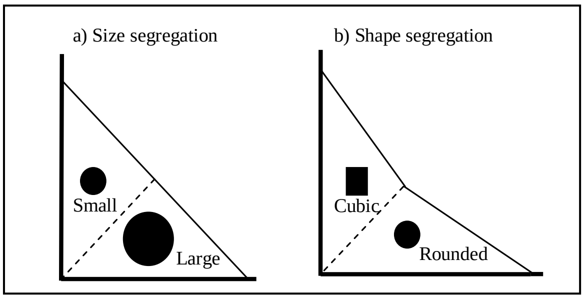


Figure 5.32: Two segregation effects due to the diversity of particles size and shape (after Makse 1997).

Figure 5.32a shows that large particles tend to segregate at the bottom of the pile compared to the smaller particles since large grains roll down more easily on top of small grains than small grains roll on top of large grains. Figure 5.32b illustrates that more rounded particles tend to segregate at the bottom of the pile compared to the more cubical particles. Makse (1997, 1999) also postulated that since larger particles generally have more cubical shape than the smaller particles, this may lead to granular stratification especially for the case of series of both size and shape segregation.

Figure 5.33 illustrates the theoretical number of percolating fine particles in cubical and hexagonal packing for the particles shape effect by considering the equivalent spherical diameter methods ($D_s$). It is clearly shown that the basalt aggregate provided the highest number of fines that simultaneously pass the void gaps of the

15.75 mm glass sphere than others particles shaped. Apparently, the basalt aggregate (granular shaped) also had the largest void penetration ratio (Figure 5.33b) which can be associated to the highest CPF in Figure 5.31.

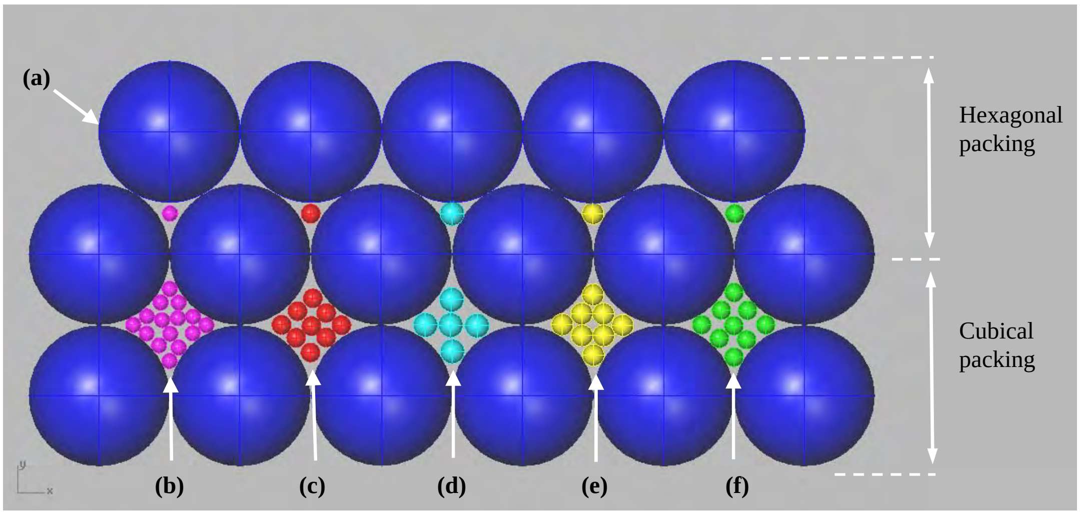


Figure 5.33: Theoretical number of percolating fine particle in cubical and hexagonal packing for the particles shape effect for II and BI series (drawn to scale).

Note: (a) 15.75 mm glass sphere ( $D_s$ = 15.78 mm) [blue colour]
(b) 4.05 mm basalt aggregate ( $D_s$ = 3.19 mm) [magenta]
(c) 4.00 mm bi-conical glass ( $D_s$ = 4.06 mm) [red]
(d) 4.00 mm cubical glass ( $D_s$ = 5.08 mm) [turquoise]
(e) 4.00 mm cylindrical glass ( $D_s$ = 4.58 mm) [yellow]
(f) 4.00 mm glass sphere ( $D_s$ = 4.02 mm) [green]

Figure 5.34 illustrates the third order of polynomial fit for the II and BI series. It is clearly observed that the angular (4.05 mm basalt aggregate) and spherical shaped particles (or closely sphere such as bi-conical) were found to accelerate more rapidly (acceleration phase) at the beginning of shearing than cylindrical and cubical shaped particles. This was followed by the cylindrical shaped particles which particularly began with the short interval phase and slowly accelerated through the shearing process. On the contrary, the cubical shaped particles have shown the longest interval phase and slower acceleration phase than others particle shape.

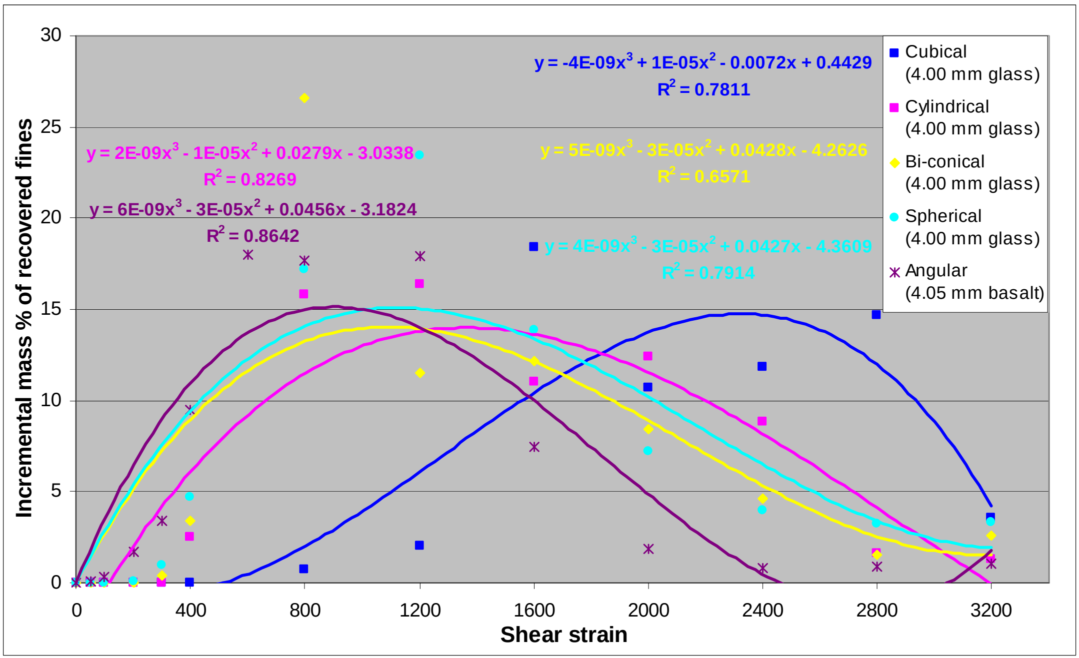


Figure 5.34: Shear strain versus incremental mass % of recovered fines (IMF) in II and BI series. Note that the equation and $R^2$ value denoted by the same colour while the bed-matrix is 15.75 mm glass sphere. The third order of polynomial fit was generated by the mean of three readings.

In view of the slow percolation potential of particle shape, Gögüs et al. (2001) studied the effect of regularly shaped particles (cylindrical, cubic, wedge-shaped prisms and box-shaped prisms) have on the settling behaviour and fall velocity of angular particles and observed that:

- cubic particles generally did not follow the centreline of the settling column while they were falling, and in addition to tipping and sliding, they rotated all the time following a helical path;
- box-shaped prisms of small thickness followed almost the centreline of the settling column with oscillation about the shortest axis and little sliding. As the thickness increased so that the smallest surface approached that of a square, prisms started rotating around the longest (approximately horizontal) axis and descended along a non-vertical and frequency helical path;
- cylindrical particles appeared to fall like the box-shaped prisms of square base with rotation about any axis. The path followed by them was also non-vertical and helical; and
- wedge-shaped prisms followed an almost vertical path along the centreline of the settling column having the largest surface area perpendicular to the motion of particle. Only a small amount of oscillation was observed.

Accordingly, the above finding of this section seem logical and can be correlated to the lower CPF of cubical and cylindrical shaped particles as shown in Figure 5.31.

### *5.5.3.3 Fines: Ideal media and crushed basalt; Bed-matrix: 13.20 mm crushed basalt (IB and BB series)*

Generally, there is agreement that the effect of particle shape is smaller in comparison with the size ratio effect, $d_p / d_b$ (e.g., Drahun and Bridgwater 1983; Bridgwater 1994). Nevertheless, although the above assumptions look relatively comprehensive, they only concentrated on the percolation of mono-size shaped particles (i.e., glass sphere, sphere sand) and/or narrow distribution of particle sizes.

Figure 5.35 presents a set of results for the effect of particle shape on percolation of fine particles in the matrix of granular coarse bed (13.20 mm basalt aggregate). It is observed that a much longer time is required before the percolation increases. Generally, after $\gamma_{total}$=4800%, the granular shaped particle have the highest CPF (25.29%) followed by spherical (21.50%), bi-conical (21.12%), cylindrical (20.83%) and cubical (6.45%). This suggests high shear strains are needed for the fine particles to pass the highly angular bed-matrix (basalt aggregate) than spherical bed-matrix (15.75 mm glass sphere).

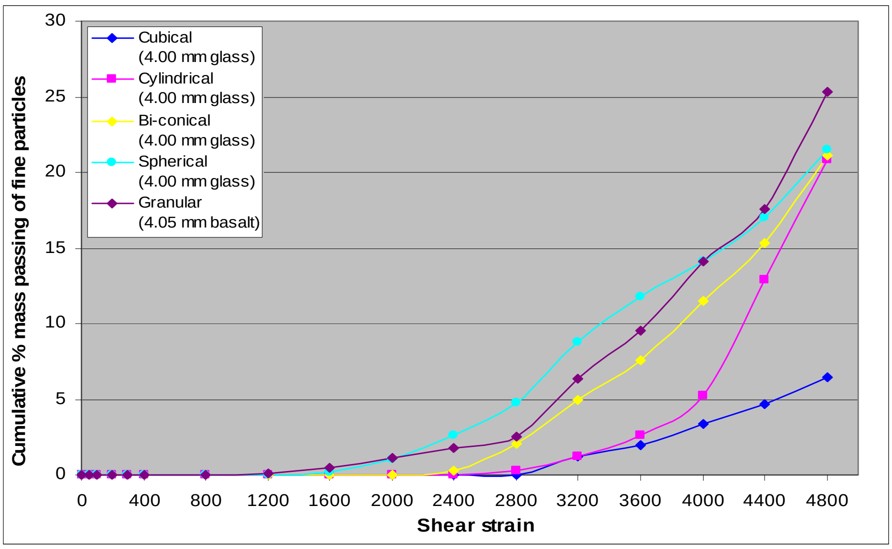


Figure 5.35: Mean shear strain versus cumulative % mass passing of fine particles (CPF) for the IB and BB series. The bed-matrix is 13.20 mm crushed basalt.

Nevertheless, the significantly higher CPF of granular and spherical shaped compared to the cubical and cylindrical shaped is generally in agreement Tang et al. (2003) cited in Tang and Puri (2004). Particularly, by using the PSSC-II apparatus, Tang et al. (2003) found that segregation (which included the percolation mechanism) is significantly higher for a binary mixture of irregular-spherical fine and coarse particles than when using both spherical shaped coarse and fine particles.

Kwan and Mora (2001) studied the effect of shape on packing of aggregate particles and concluded that the shape factor and the convexity ratio are the most important parameters affecting the packing of aggregate. This assertion is shown by the lower CPF in the matrix of coarse particles (13.20 mm basalt aggregate). For the IB and BB series, the shape of bed-matrix (highly angular) are predominantly affected the percolation than the II and BI series (spherical shaped of bed-matrix). This suggests that particle shape has a significant impact on the geometry packing of bed-matrix which limits fine particles to fill in and pass through the void of bed-matrix thus slowing percolation. Jaeger and Nagel (1992) assert that the rigidity and flow characteristics of a granular material are determined by the geometry packing of its constituent particles in which the granular particles tend to form a disordered structure.

Consequently, Abbaspour-Fard (2005) numerically investigated the role of particle shape on matrix of coarse bed particle behaviour of particles and found that the size of the homogenous densely packed area was generally increasingly smaller in beds of particles of higher aspect ratio (i.e., basalt aggregate). Based on the numerical simulation results, Abbaspour-Fard (2005) also concluded that the change of particle shape from spherical to non-spherical had a greater effect on the packing structure of the particle bed than an increasing in the aspect ratio of non-spherical particles. This finding evidently supports the significant higher CPF in spherical shape (15.75 mm glass sphere) than the angular shaped of bed-matrix (13.20 mm basalt aggregate).

It is also interesting to note that spherical shaped particles have higher percolation during early shearing (until $\gamma_{total}$=4000%) than angular shaped particles, however after a certain period of shearing, it was found that the CPF of fine angular particles was significantly higher than the spherical shaped particles. Some possible explanations are advanced as follows:

- during shearing, particles began to rearrange and oriented. At this stage, the spherical shaped particles are expected to have higher mobility than angular particles which allowed fast penetration through the void packing of the highly angular bed-matrix (13.20 mm crushed basalt);
- at $\gamma_{total}$ =4000%, the void packing of highly angular bed-matrix were forming a more stable packing resulted in lower percolation potential for the spherical shaped particle thus the percolation become stagnant (or minimise);
- for the angular shaped particles, the re-orientation and particle rearrangement is postulated to begin at the initial shearing. During this stage “interlocking” of the fine particles and void packing of coarse particles is likely to occur thus minimise the percolation potential of the fine particles later in the test. Ridgway and Rupp (1971) noted that generally the angular shaped particles should lock together better than spherical shaped particles; and
- once particle orientation and rearrangement was complete, the cumulative effect of shape and density with size was more dominant than size alone (Jha et al. 2009).

The above conclusion is also supported the by considering the equivalent spherical diameter methods ($D_s$) in cubical and hexagonal packing as depicted by Figure 5.36. Based on theoretical hexagonal packing drawing (Figure 5.36) of possible number of fine particles that may freely pass through the void gaps of coarse aggregates, it is demonstrates that all fine particles remain in the bed-matrix. Tang (2004) noted that the fine particle fall-path is principally determined by the failure zone pathway (or void gaps). Therefore, it is hypothesised that without the packing arrangement that creates large void gaps and permits the rapid passage of smaller particles through the bed-matrix, the chances of the fine particle percolating is low.

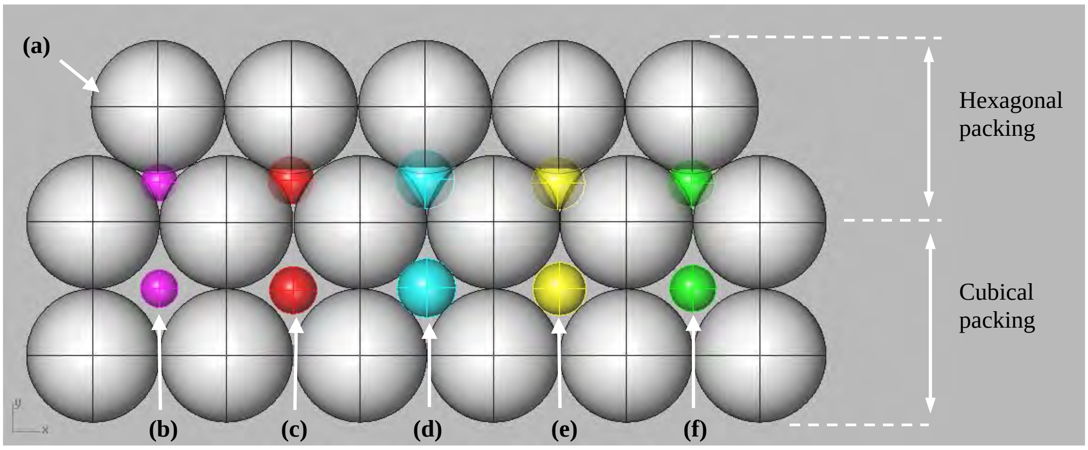


Figure 5.36: Theoretical number of percolating fine particles in cubical and hexagonal packing for the particles shape effect for BB and IB series (drawn to scale).

Note: (a) 13.20 mm basalt aggregate ( $D_s$ = 11.48 mm) [grey colour]
(b) 4.05 mm basalt aggregate ( $D_s$ = 3.19 mm) [magenta]
(c) 4.00 mm bi-conical glass ( $D_s$ = 4.06 mm) [red]
(d) 4.00 mm cubical glass ( $D_s$ = 5.08 mm) [turquoise]
(e) 4.00 mm cylindrical glass ( $D_s$ = 4.58 mm) [yellow]
(f) 4.00 mm glass sphere ( $D_s$ = 4.02 mm) [green]

Nevertheless, unlike the IB and BB series, fine particles can still percolate through the bed-matrix of crushed aggregate provided that the fines can rearrange and oriented in such the way it can pass the void gaps in the bed-matrix. This is confirmed by the higher CPF of fine crushed basalt (granular shaped) at $\gamma_{total}$ =4800% than other type of shapes (i.e., spherical, cubical, cylindrical) shown in Figure 5.35.

In view of above finding, Yi et al. (2001) listed several possible reasons that might enhance the probability of higher percolation in the bed-matrix of granular shaped particles as follows:

- the irregularly shaped particles can readily lodge in the interstitial void spaces; and
- the void spaces formed from irregularly shaped coarse particles are larger than those for spherical-shape particles.

A typical observation of void gaps filling and penetration by granular shaped particles is shown in Figure 5.37.

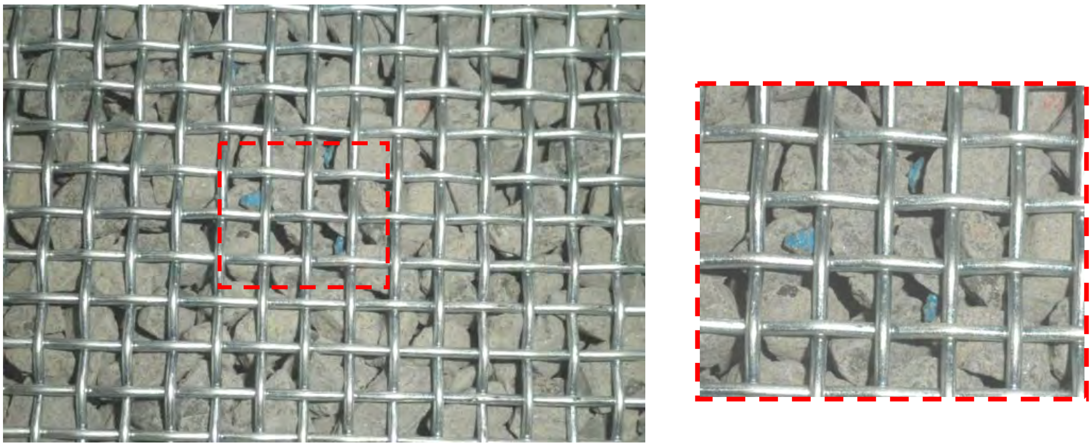

Figure 5.37: Example of condition in which the fine particles filled or partially filled pores/void fractions (red dashed line enlargement) within the bed-matrix near the sieve mesh of SCPG during shearing. Note that 4.05 mm basalt aggregate (blue) in the bed-matrix of 13.20 mm basalt aggregate.

A third order polynomial model for the shape effect on percolation of fine particles in IB and BB series is presented in Figure 5.38. It is concluded that the percolation of fine particles in the IB and BB series were found to be slower than that of the II and BI series (i.e., longer interval phase). It was also found that at the early stage of shearing, the spherical particles percolated faster than the granular shaped particles. The significant higher percolation shown in the spherical particles at the early stage lies within the greater mobility of spherical (or rounded) particle than highly angular particles (Makse 1997, 1999).

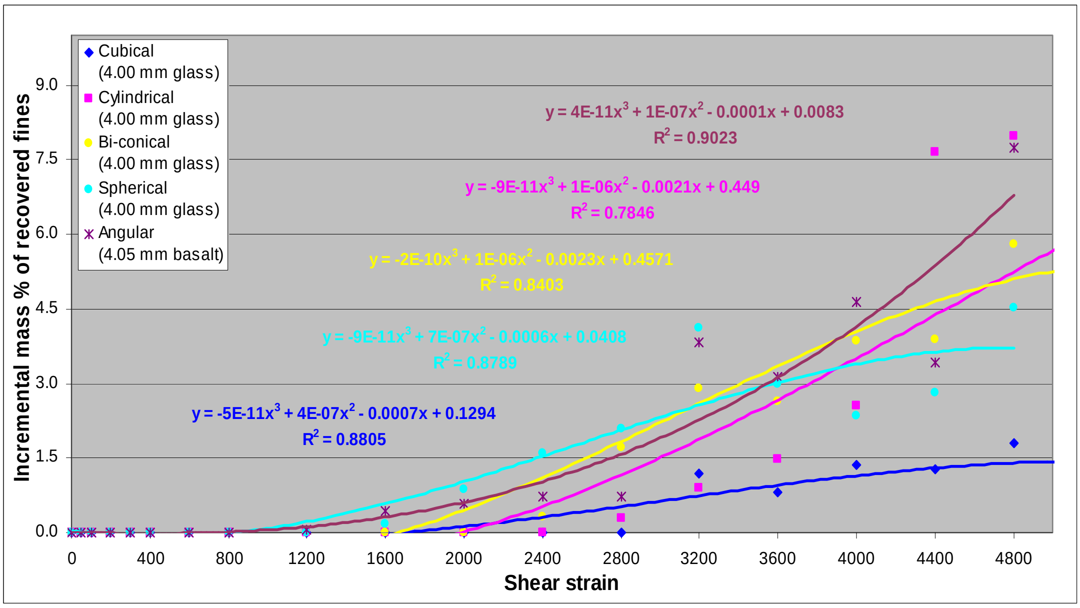


Figure 5.38: Shear strain versus incremental mass % of recovered fines (IMF) in IB and BB series. Note that the equation and R² value denoted by the same colour while the bed-matrix is 13.20 mm crushed basalt. The third order of polynomial fit was generated by the mean of three readings.

On the other hand, similarly to that observed in the II and BI series, it was found that after a certain period of time (i.e., $\gamma_{total} > 3600\%$), the angular shaped particles have a higher degree of percolation. This suggests that for the binary mixtures of both angular shaped particles, the interlocking between the angular shaped fine particles and the angular coarse voids packing are greater than that the binary of spherical-angular shaped (i.e., spherical fine in coarse angular particles).

During early shearing, the higher mobility of spherical, or near spherical fines promotes the finer particles to rapidly fill (or partially fill) the larger void gaps and pass through it. After some period of shearing (and time), some of the voids are saturated and interlock as the coarse angular shaped particles oriented and rearranged hence minimising the void gaps ratio. For this period, the percolation rate is stagnant and less spherical fine shaped particles were available to pass the void gaps (depicted by the moderate increment plot in Figure 5.38).

The significantly higher mobility and higher percolation rate of fine spherical particles can also be related to the smooth surface properties. However, this effect is generally small and slight. Bridgwater et al. (1978) and Bridgwater (1994) noted that experimentally, the effect of surface roughness of both fine and coarse particles was found to be insignificant.

Conversely, in both series of fine and coarse angular shaped (i.e., angular; fine 4.05 mm basalt) particles will spontaneously rearranged and oriented since the beginning of shearing in which the interlocking and arching of the binary mixtures increases (Bexter et al. 1989) thus make the percolation slower. After a period of time (and shearing), the higher amount of angular fines started to filled the void gaps. As the amount of angular fines recovered increases with time (and shearing), some of the detained fine particles were pushed over and pass the void gaps by the action of gravitational force, strain and continued filling by fine particles at the upper level. During this period a significant increase was observed and illustrated by the steep increment of particle distribution in Figure 5.38.

In accordance to the above explanation, Shinohara (1979) asserts that for binary mixtures of irregular-spherical shaped particles, angular particles penetrate into the layer of spherical particles only at the moment of the latter layer's expansion under shear stress that occurs continuously during the flow process.

#### *5.5.3.4 Summary*

Shape is one of the most difficult features to define (Hu and Stroeven 2006). It is worth highlighting that although large amounts of published work exist on spherical and/or mono-size shaped particles, data on angular shaped particles are extremely limited. Previous percolation studies found that the effect of particle shape is small and insignificant for bed matrices of spherical particles. While this is true for mono-sphere particles, the use of highly angular particles in this thesis contradicts previous assertions that effect of particle shape on percolation is small. By contrast, the results of the present study show that the effect of particle shape in both the percolating fine and bed-matrix aggregate is significant. This finding implies that the results from ideal media (i.e., spherical shaped particles) cannot be used for real world applications involving coarse rock fragments such as block caving.

In block caving, the caved rock consists of highly angular shaped particles and wide size distributions. The assumption that ideal media with equivalent spherical diameters similar to caved rock has the same percolation characteristics as caved rock appears to be incorrect. In conclusion, it was demonstrated that particle shape is significant thus proving the hypothesis that particle shape plays a significant role in percolation of fine particles in matrices of highly angular large/coarse aggregates.

These findings also indicate that shape factor is important in any percolation study for rock particles. Moreover, future numerical and physical experiments should consider particle shapes and size distributions similar to actual caved rock.

### 5.5.4 Effect of Particle Density

#### *5.5.4.1 Overview of results and general observations*

A total of 32 tests explored the effect of particle density on percolating fine particles in a matrix of coarse particles. Table 5.6 summarised the material properties used in the density effect of fine percolating particles. A complete listing of results is found in Appendix C4.

Table 5.6: Test designed for the effect of particle density.

| Series | Particles density ratio ( $\rho_p / \rho_b$ ) | Percolating fine particles | Coarse bed-matrix | Controlled experimental conditions |
|---|---|---|---|---|
| II | 1.01 | 4.00 mm glass sphere | 13.20 mm basalt aggregate | • Particle diameter ratio;<br>• Strain rate (0.04 $s^{-1}$ );<br>• Normal stress (0.9 kPa);<br>• Particle shape;<br>• Shear strain (3200% for the II and BI series and 4800% for the IB and BB series) |
| | 0.39 | 4.00 mm plastic sphere | | |
| | 3.10 | 4.00 mm steel sphere | | |
| BI | 1.10 | 4.05 mm basalt aggregate | | |
| IB | 0.91 | 4.00 mm glass sphere | 15.75 mm glass sphere | |
| | 0.35 | 4.00 mm plastic sphere | | |
| | 2.80 | 4.00 mm steel sphere | | |
| BB | 0.99 | 4.05 mm basalt aggregate | | |

It was observed that denser particles are recovered in the zone of high quantity of fine particles (centre of the pan collector; denoted by compartment number 12-14) as shown in Figure 5.39a. This finding agrees with Holmes (1934) and Syskov and Lyan (1960) cited in Tang and Puri (2004) which showed that denser particles accumulate near the centre and are surrounded by less dense particles while they are discharged and/or free-fall at a certain height. By contrast, a significantly larger amount of less dense particles (i.e., plastic spheres) were collected in the centre of pan collector (compartment 12-14) and vicinity of the centre of pan collector (compartment 6-10, 11, 15, 16-20 respectively; Figure 5.39b)

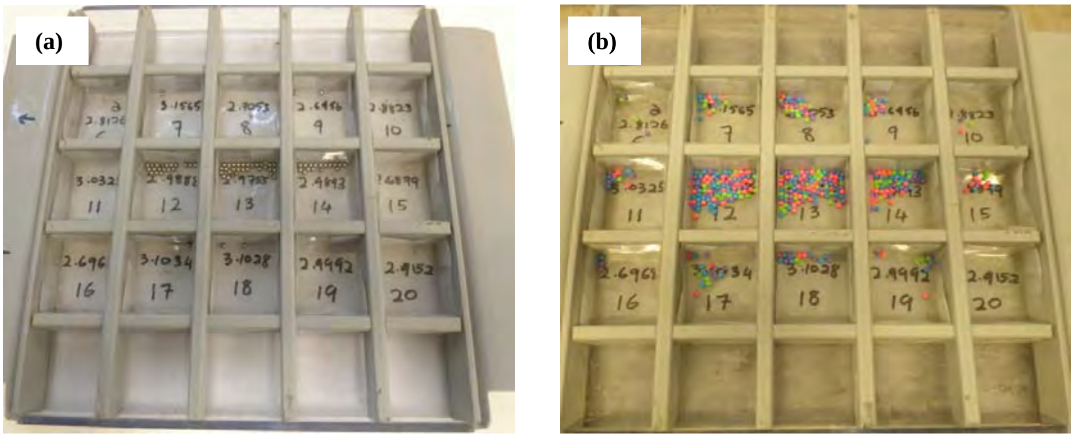


Figure 5.39: Typical examples of density effect concentration in the pan collector compartments in ideal media of coarse aggregate (15.7 mm glass sphere) at $\gamma_{total}$ =3200%. Note: (a) Large quantity of 4.00 mm steel sphere (denser particles) in centre of pan collector (b) Large amount of 4.00 mm plastic sphere (lighter particles) in centre of pan collector and surrounding.

The following classification was used for the ease of identification and analysis of the effect of particle density within the Section 5.5.4.2 and 5.5.4.3 respectively while illustration of the nomenclature is given in Figure 5.40:

- the first segment identifies the series type of binary mixture of media used in the test; and
- the second segment refers to the fine–matrix of coarse bed particles density ratio.

**BI** – **b1.10**

Fine particle/matrix of coarse bed particledensity ratio ( $\rho_p$ / $\rho_b$ = 1.10)

Binary series (percolating fine crushed aggregate media in the matrix of coarse ideal media)

Figure 5.40: Nomenclature for the effect of particle density.

In general, the results of particle density effect in percolation were presented as follows:

- Fines: Ideal media and crushed basalt; Bed-matrix: 15.75 mm glass spheres (II and BI series); and
- Fines: Ideal media and crushed basalt; Bed-matrix: 13.20 mm crushed basalt (IB and BB series).

#### 5.5.4.2 *Fines: Ideal media and crushed basalt; Bed-matrix: 15.75 mm glass spheres (II and BI series)*

Differences in particle density are known to affect the fine particle percolation (e.g., Bridgwater et al. 1985a, 1985b; Cooke et al. 1978; Duffy and Puri 2002) in which might be anticipated from potential energy considerations (Hogg 2009). In view of above points, Hogg (2009) noted that density effect can be explained by the force (gravitational) acting on a particle may affect by both size and density which relatively permitting ability to penetrate a bed of particles.

In an event of fairly compact systems that consist of similar size but different density of fine particles, the fines with higher density might modestly receive advantage to percolate faster through the coarse bed of matrix during vibration and/or shearing. Nevertheless, it is generally agreed that the effects are usually considerably smaller than those due to size differences (e.g., Campbell and Bridgwater 1973; Scott and Bridgwater 1975; Bridgwater 1994; Vallance and Savage 2000).

The above statement may be largely true for the case of both fine and bed-matrix of mono-sized particles (spherical shaped); however, the effect of particle density in such of a mixture of various particle shapes (e.g., spherical fine particles in angular shape of bed-matrix or vice versa) is still largely unproven and tested.

Figure 5.41 shows the CPF within the ideal media of bed-matrix (15.75 mm glass sphere). It is interesting to note that although there are significant differences in the CPF magnitude at low shear strains, all the fine materials converge to a common CPF (in the order of 76% to 80%) after $\gamma_{total}$=3200%. This finding broadly agrees with Cooke et al. (1978) who found that denser particles (steel) percolate faster than less dense particles (acrylic resin, plastic).

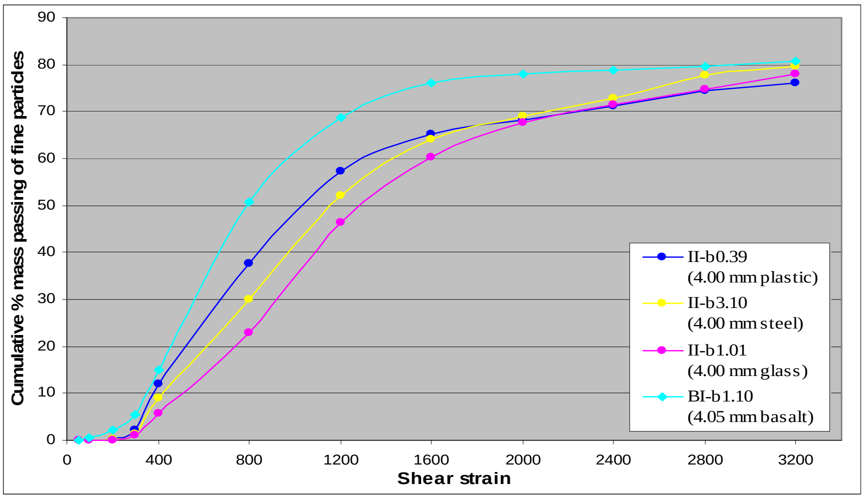


Figure 5.41: Mean shear strain versus cumulative % mass passing of fine particles (CPF) for the II and IB series. The bed-matrix is 15.75 mm glass sphere.

Alternatively, Bridgwater (1994) reported that for spherical particles (i.e., glass bead, plastic bead and steel sphere) an increase in percolating particle density gave a small increase in percolation rate. This assertion verified the small differences in CPF shown by the spherical denser particles than the less dense materials. For instance, the steel spheres ( $\rho_p / \rho_b$ =3.10) has the highest CPF of 79.64% follows by glass bead ( $\rho_p / \rho_b$ =1.01; 78.01%) and plastic beads ( $\rho_p / \rho_b$ =0.39; 76.10%) as illustrated in Figure 5.41. On contrary, the significantly higher CPF for 4.05 mm basalt aggregate ( $\rho_p / \rho_b$ =1.10) can also be correlated by series of particle density and shaped effect.

A third order polynomial fit of the II and BI series is presented in Figure 5.42. The graph represents plastic, steel, glass and basalt aggregate with a various particle densities ratio ( $\rho_p / \rho_b$ = 0.39; 3.10; 1.01; 1.10 respectively). Accordingly, a rapid increase (acceleration phase) in percolation were observed for each type of densities ratio between 100% $< \gamma_{total} <$ 1200%. After reaching the maxima, the attenuation phase began which suggests that a large percentage of spherical fines (i.e., plastic, steel and glass bead) may have sufficiently passed the void gaps. It is also postulated that during this stage, some of the fines began to accumulated and detained (or trapped) in the void gaps due to other effect such as particle shape and diameter ratio). During this phase, the fines percolation decreased.

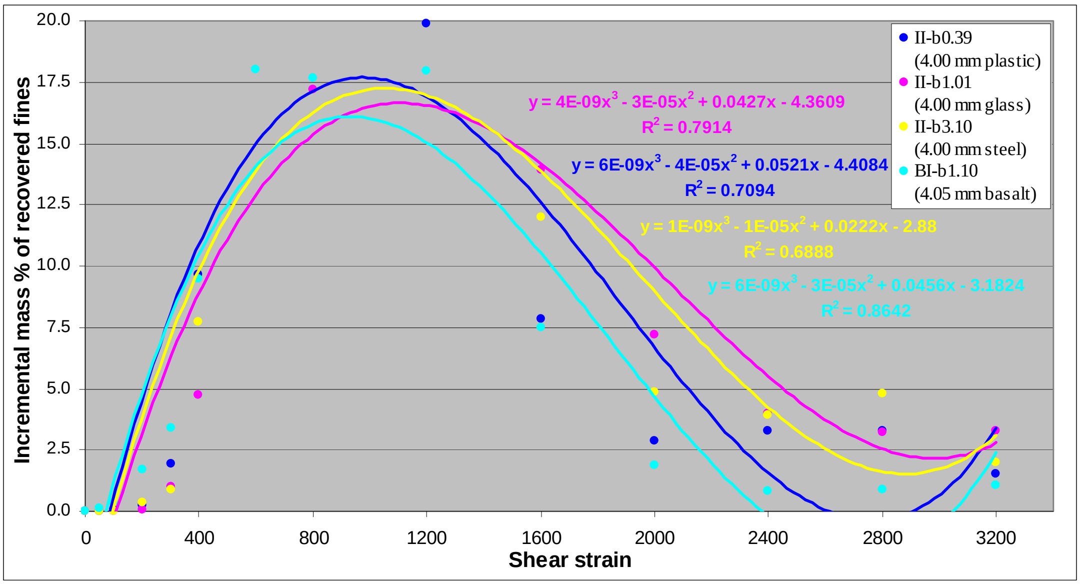


Figure 5.42: Shear strain versus incremental mass % of recovered fines (IMF) in II and BI series. Note that the equation and $R^2$ value denoted by the same colour while the bed-matrix is 15.75 mm glass sphere. The third order of polynomial fit was generated by the mean of three readings.

Nevertheless, at continuously higher shear strains (i.e., $\gamma_{total}$ >2800%), the acceleration stage was found to resume and it is postulated that some of trapped fines may sufficiently able to pass the void gaps. Implication to this shows that the effect of particle density is presumably smaller than the other effect (i.e., particle shape, diameter ratio).

### *5.5.4.3 Fines: Ideal media and crushed basalt; Bed-matrix: 13.20 mm crushed basalt (IB and BB series)*

Figure 5.43 illustrates the cumulative results of four different densities of percolating fine particles in the 13.20 mm coarse aggregate. Surprisingly, it is clearly observed that the plastic material ($\rho_p / \rho_b$ =0.35) percolated significantly faster than the other type of material such as glass sphere ($\rho_p / \rho_b$ =0.91), steel sphere ($\rho_p / \rho_b$ =2.80) and basalt aggregate ($\rho_p / \rho_b$ =0.99). This finding contradicts the observed density effect in the II and BI series (Section 5.5.4.2) and some previous work focusing on the use of mono-sized particles (glass sphere and/or sphere sand) i.e., Bridgwater et al. (1978) and Duffy and Puri (2002).

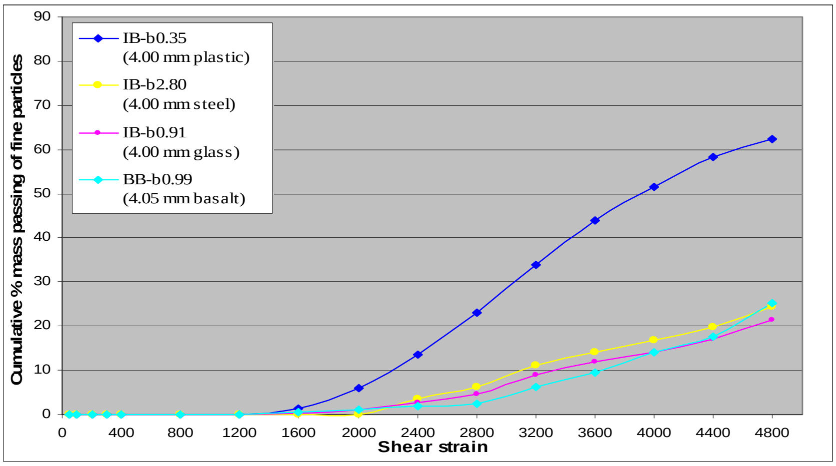


Figure 5.43: Mean shear strain versus cumulative % mass passing of fine particles (CPF) for the IB and BB series. The bed-matrix is 13.20 mm crushed basalt.

One plausible explanation to the higher CPF of the plastic material in the crushed aggregate media (13.20 mm basalt aggregate) may be related to the physical properties of plastic used in the test. In view on this line, Cooke et al. (1978) and Bridgwater et al. (1978) concluded that such soft material (i.e., teflon, plastic, rubber) may be squeezed through slightly smaller gaps during shearing as a result of small deformation by normal stress ($\sigma_n$) force and lower Young's modulus.

The above argument may be true for the plastic material used in the test since it is given the lowest approximate value in Young's modulus (2 GPa) compared to the other materials such as steel sphere (200 GPa), glass sphere (50 - 90 GPa) and basalt aggregate (50 - 100 GPa). It was also observed during the test that some of the plastic spheres were slightly deformed (Figure 5.44) probably as a result of abrasion and compaction by 13.20 mm basalt aggregate which generally consists of prismoidal particles with sharp edges (Section 4.4.3)

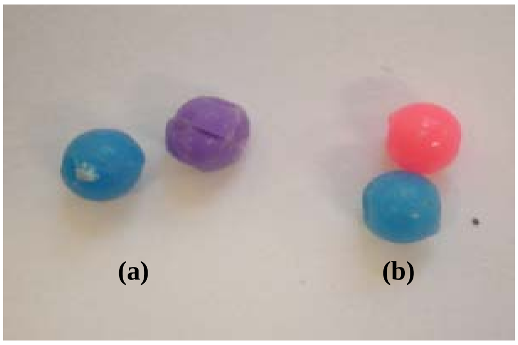


Figure 5.44: (a) Example of deformed plastic spheres collected as a result of abrasion and compaction by 13.20 mm basalt aggregate during the shearing test (b) Normal plastic spheres.

On the other hand, for the other types of densities (i.e., steel sphere, glass sphere and basalt aggregate), it was found to closely resemble CPF=24.37%, 25.01% and 25.29%; respectively. This close results suggested that the lower percolation results for IB and BB series are predominantly controlled by the type of bed-matrix used (angular shaped of 13.20 mm basalt aggregate).

In view of the slightly higher percentage of percolation between basalt aggregate (lighter particles) and steel sphere (denser particles), it was postulated that the series of shape and particle size (i.e., smaller equivalent spherical diameter, $D_s$ =3.94 mm) may significant have effect to this observation. Félix and Thomas (2004) commented that generally a difference of sizes has an equivalent effect on the particle coordination than a difference of density in which shown by the higher percolation of basalt aggregate than steel sphere.

Notably, the slightly higher percentage of percolation by basalt aggregate (lighter particles) than the steel sphere (denser particles) also proves that the “push-away” mechanism (Section 2.5.1) proposed by Tanaka (1971) which asserts that heavy and denser particles are able to force their way between lighter components is insignificant in this case.

Apparently, the percolation potential in the bed of coarse matrix (basalt aggregate) was significantly lower than that of the ideal media (glass sphere). Jha et al. (2008) noted that in the case of denser particles and larger void gaps, the percolation rate is generally higher. This assertion explained the significant lower percentage of percolation as shown in the IB and BB series which generally have lower void gap ratio than the spherical one (II and BI series).

In view of the above finding, Ridgway and Rupp (1970) used the superimposed layers of sand and measured the amount of mixing between the layers and concluded that the bulk density of a single flowing layer of particles is increased by increasing the particle shape coefficient. Ridgway and Rupp (1970) also reported that in general, the angularity of particle shape may cause the bed-matrix to effectively resist shearing. This finding suggests that angular shaped particles should lock together better than spherical shaped particles hence significantly reduce the void gaps and percolation potential.

Collectively, the significant higher value of percolated plastic sphere was also elucidated by the third order of polynomial fit as illustrates in Figure 5.45. It is obvious that for the plastic sphere particles, a rapid increment of polynomial fit (acceleration phase) were observed soon after its lap the interval phase. After reached its maxima at approximately $\gamma_{total}$ = 3600%, the plastic sphere particles began to entered the attenuation phase. It postulated that at this shear strain, most of the plastic spheres have passed through the bed-matrix in which it represented by the decreases in percolating fine particles distribution.

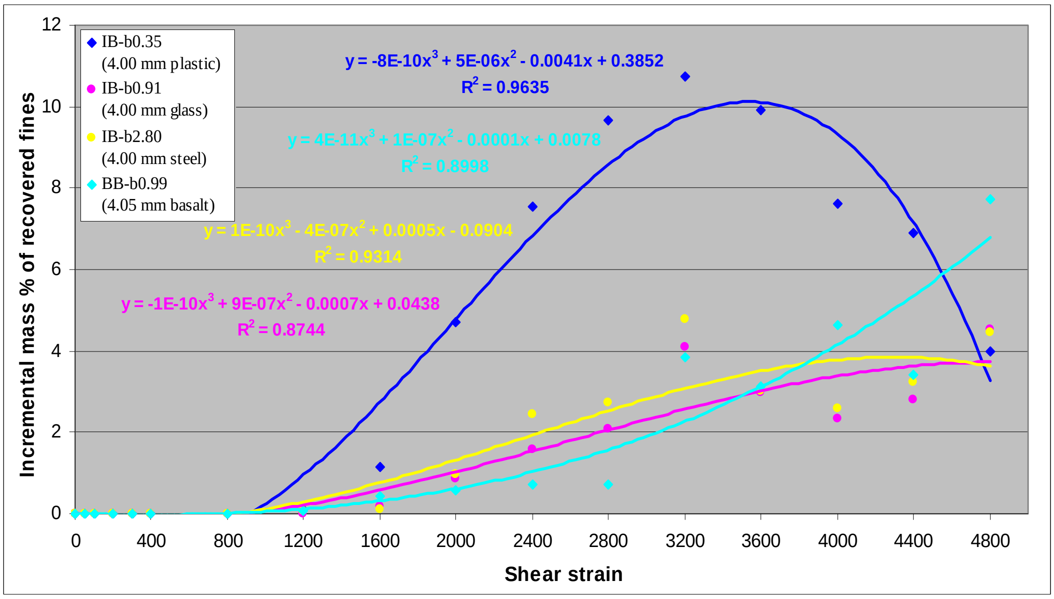


Figure 5.45: Shear strain versus incremental mass % of recovered fines (IMF) in IB and BB series. Note that the equation and $R^2$ value denoted by the same colour while the bed-matrix is 13.20 mm crushed basalt. The third order of polynomial fit was generated by the mean of three readings.

On the other hand, for other types of material, the acceleration phase progresses slowly after a longer interval phase (i.e., after $\gamma_{total}$ =1000%). However, it is observed that after $\gamma_{total}$ =3800% the percolation of basalt aggregate (BB-b0.99) rapidly increased and is significantly higher than that of the steel spheres (IB-b2.80) and glass spheres (IB-b0.91). This suggests that during this period, finer basalt aggregate has rearranged and oriented thus sufficiently pass through the bed-matrix of

13.20 mm basalt aggregate. Alternatively, within the test range the particle shape became the dominant factor that effecting the percolation than density.

#### *5.5.4.4 Summary*

In conclusion, the effect of particle density on percolation was small. This finding is true for the percolation of fine particles in both spherical and crushed aggregate bed matrices. On the other hand, the higher percolation for plastic materials may be related to the its lower Young's modulus (2 GPa) and the abrasion and compaction by 13.20 mm basalt aggregate during shearing. Therefore, these results indicate that the effect of particle density on percolation for denser ore (i.e., iron ore) and lighter ore (i.e., coal) in caving mine applications are smaller than other parameter such as shape and particle diameter ratio. These findings indicate a clear direction of future percolation studies for caving mine applications. Accordingly, attention may be focussed on the strain rate, particle diameter ratio and shape effect in order to better understanding on percolation phenomenon in caving mines.

## 5.6 DIMENSIONLESS PERCOLATION RATE (DPR)

Since experimental conditions differed substantially (i.e., effect of strain rate, particle diameter ratio, shape, density) it is useful to consider the results as dimensionless variables which take account the similarities and differences of all experiments. Accordingly, the concept of dimensionless percolation rate (DPR) ($u/\dot{\gamma}d_b$) by Bridgwater et al. 1978 was employed. DPR is defined as the measurement of the most probable distance in coarse bed particle diameters that an isolated percolating particle is expected to drop when subjected to shear strain, $\gamma$=100% or ($\gamma$=1.0) (Pierce 2004). For non-spherical particles, the equivalent spherical diameter method, $D_s$ is used (Scott and Bridgwater 1975) in which the effect of particle shape was adjusted into a dimensionless variable and provides the similarity of experiments parameters (i.e., $d_p/d_b$).

Measurement of the residence “travel time” were made by placing thirty percolating fine particles on the top of the matrix of coarse bed particles (approximately 220 mm height of the SCPG). Accordingly, the fines particles were initially positioned at the top-centre of shear cell as illustrated in Figure 5.46. A wooden plate with a 180 mm x 60 mm rectangle opening at the centre was used to produce a constant and standard configuration of the fine percolating particles/markers during loading (Section 5.2.2). The percolating particles were placed far enough apart not to interfere with one another in order to overcome interaction effects.

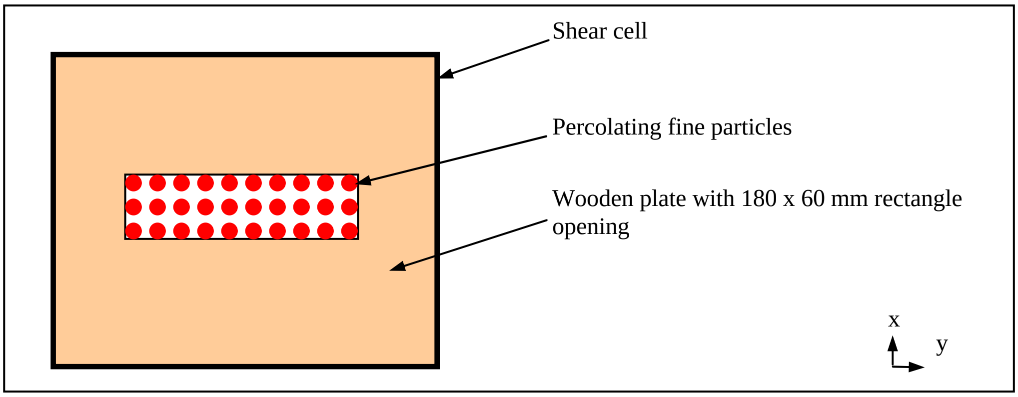


Figure 5.46: Configuration of thirty fine particles on the top of the matrix of coarse bed particles for measurement of residence “travel time”.

A 400 mm x 400 mm plastic container was placed under the shear cell and aligned to the SCPG centre to ensure all the particles will fall into the container and collected. The stop watch was set to the lap timer setting in which it can record a maximum of thirty residence times simultaneously and was started as the SCPG began the shearing.

When the particle fell out of the bottom of the SCPG, it struck the plastic container and a sound was produced and the residence time for the particle was recorded. The residence time travel for the fine particles were recorded until $\gamma_{total}$ =3200% (II and BI series) and $\gamma_{total}$ =4800% (IB and BB series). The operation was repeated for a new batch of fine particles and bed-matrix according to the designed parameters (strain rate, particle diameter ratio, shape, density effect) until the required number of readings was acquired.

A total of 100 readings of residence time were taken for each of designed parameters in the II and BI series. Less than 20% of the fine particles were collected in each operation for the IB and BB series owing to the reduced void gaps packing of bed-matrix at higher $\gamma_{total}$ and particle retention within the SCPG. For this reason, only 50 readings for each design parameters were collected for the IB and BB series due to experimental difficulty and time practicality.

Figure 5.47 compares the dimensionless percolation rate against the particle diameter ratio between the generalisation of SCPG tests and Bridgwater et al. (1978). It is worth noting that the Bridgwater's exponential plot used in Figure 5.47 is an estimate based on reproducing the closest arbitrary constants of $k_1$=20 and $k_2$=8 respectively (Equation 5.2) as reported by Pierce (2004, 2010) and Bridgwater et al. (1978) DPR plot at $\dot{\gamma}$=0.4 s$^{-1}$ thus the high value of $R^2$.

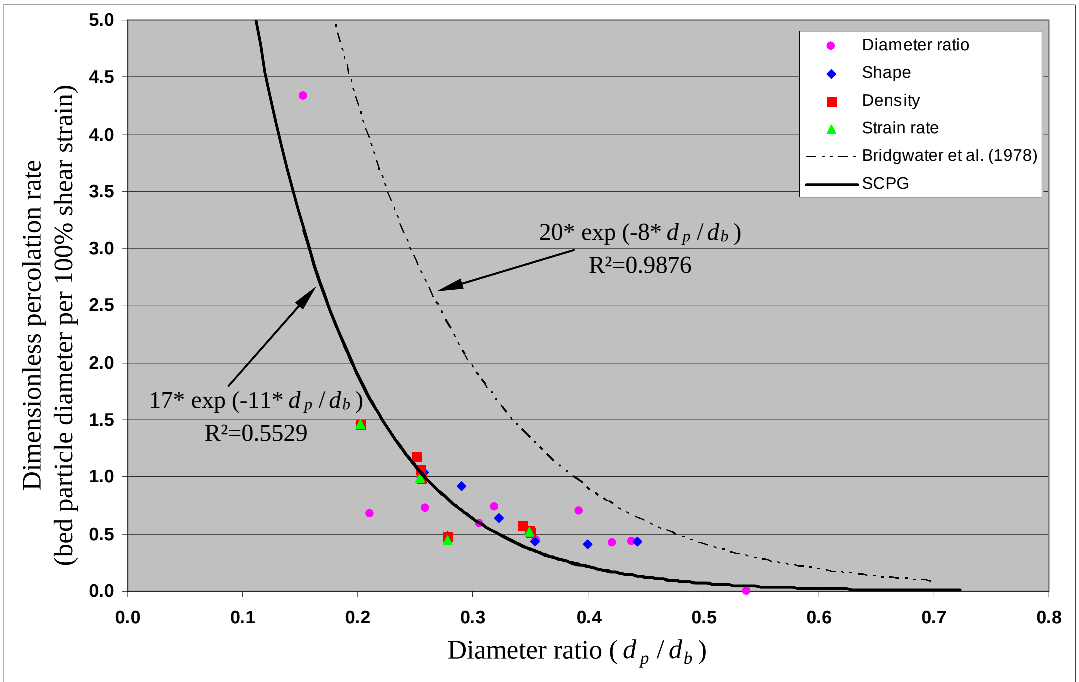


Figure 5.47: Comparison of dimensionless percolation rate (DPR) as a function of equivalent spherical diameter ( $D_s$ ) versus diameter ratio ( $d_p / d_b$ ) for the SCPG and Bridgwater et al. (1978).

Note: i) The Bridgwater et al. (1978) DPR graph is an estimate based on closest arbitrary constants of $k_1$ =20 and $k_2$ =8 at $\dot{\gamma}$ = 0.4 s$^{-1}$.

ii) The exponential plot for SCPG was based on the mean residence travel time of both ideal and crushed aggregate media for each of the designed parameters (particle diameter ratio, shape, density and strain rate effect) at $\dot{\gamma}$ = 0.04 s$^{-1}$.

iii) Both exponential graph were generated by various percolating and bed-matrix particles as a function of equivalent diameter ( $D_s$ ).

A key finding is that the constants $k_1$=17 and $k_2$=11 from the SCPG experiments varied from Bridgwater et al. (1978) due to the lower strain rate used in the SCPG ($\dot{\gamma}$=0.04 $s^{-1}$). Accordingly, Pierce (2004) noted that the negative exponential relation with diameter ratio indicates that as the size of the fine particles approaches that of the coarse particle, it takes an increasingly greater amount of shear strain for percolation to occur.

Nevertheless, it is concluded that generally, the exponential plot of SCPG has given a similar pattern to that of the Bridgwater et al. (1978). Bridgwater et al. (1978) compared two DPR exponential graphs carried out at $\dot{\gamma}$=0.21 $s^{-1}$ (Mark II/III shear cell apparatus) and $\dot{\gamma}$=0.4 $s^{-1}$ (Mark V) and found that generally both graphs produced similar pattern in which the Mark II/III percolation rates are slightly higher than Mark V. With regard to this, Bridgwater et al. (1978) commented that a plausible reason for the greater DPR shown by Mark II/III was due to the different strain rate employed by both shear cell apparatus thus verified the reliability of both plots and previous work carried out by his co-authors.

The exponential DPR plot generated from the physical model of SCPG will be extended in the numerical simulation of PFC3D™ software analysis in Chapter 6. In view of this, all physical properties of ideal and crushed aggregate media (e.g., particle density, size) and the experimental parameters (e.g., strain rate, normal stress) are used for comparison and verification of the numerical SCPG model. The calibrated numerical model is then used for development of a new numerical model focused on non-spherical shapes and sizes which more closely represent caved rock than that used for mono-sphere particles.

## 5.7 CONCLUSIONS

Despite the significant negative potential effects of fine particle percolation on ore recovery in the block caves, very little is known about the percolation of rock particles. Most existing work on percolation has emerged in chemical and/or powder applications which are far removed from caving mines. Moreover efforts to understand percolation mechanisms are made more difficult, since most previous studies considered only mono-size particles (i.e., glass sphere, sphere sand) or narrow size distributions.

The results in this section show that percolation in both ideal and angular bed-matrices is significantly influenced by the particle diameter ratio, particle shape, and strain rate. These results for both ideal and angular bed-matrices have similar trends with work by previous researchers on ideal materials. However, while these previous studies show that the effect of particle shape is small, they cover a limited range of shapes not relevant to block caving. In contrast, the results from this chapter show that for crushed aggregate, particle shape significantly effects percolation. This indicates that particle shape will also be significant for percolation in gravity flow in caving mines.

The effect of particle density on percolation was found to be small in bed-matrices of both ideal and crushed aggregate media. This finding is similar to previous work on ideal media. The significantly higher percolation observed for plastic fines is explained by its lower Young's modulus (Cooke et al. 1978) and also the abrasion and compaction induced by highly angular basalt aggregate during shearing. Accordingly, Cooke et al. (1978) asserts that for lower Young's modulus material (plastic fines) these soft materials may slightly deformed by the normal stress and may be squeezed through slightly smaller gaps than higher Young's modulus material.

It was also found that the cumulative percentage mass passing of fine particles (CPF) increased with shear strain and influence by the bed-matrix properties (i.e., particle shape and sizes). Alternatively, the fine percolation potential can be explained by the interval, acceleration and attenuation phases. Therefore, based on all the above findings it is concluded that since the results from ideal media do not agree with crushed aggregate media, the results from ideal media are not applicable to actual caved rock. In block caving, the caved rock consists of highly angular shaped particles and wide size distributions. The assumption that ideal media with equivalent spherical diameters similar to caved rock has the same percolation characteristics as caved rock appears to be incorrect.

Since the experimental parameters measured in this thesis are diverse, all data was integrated into a relation called the dimensionless percolation rate (DPR). Principally, DPR is defined as the measurement of the most probable distance in coarse bed particle diameters that an isolated percolating particle is expected to drop when subjected to shear strain at 100% or ($\gamma$=1.0).

It was clearly observed that when all parameters quantified through the experiments (i.e., effect of strain rate, particle diameter ratio, shape, density) are used to plot the DPR, a similar exponential relation to that of the Bridgwater et al. (1978) emerges. Alternatively, the DPR was found to be 17 exp[-11($d_p / d_b$)] which slightly lower than the Bridgwater et al. (1978) (e.g., 20 exp[-8($d_p / d_b$)]. This finding was reflected by the lower strain rate used in the SCPG ($\dot{\gamma}$=0.04 $s^{-1}$) compared to the Bridgwater et al. (1978) ($\dot{\gamma}$=0.4 $s^{-1}$). On the other hand, the lower $k_2$ value indicates that it takes an increasingly greater amount of shear strain for percolation to occur as the size of the fine particles approaches that of the coarse particle. Accordingly, the exponential DPR plot generated from the SCPG data is extended to calibrate and validate a numerical simulation using PFC3D™ in Chapter 6.

# CHAPTER 6: NUMERICAL SIMULATION: VALIDATION AND ANALYSIS

## 6.1 INTRODUCTION

It has been shown in the SCPG physical experiments (Chapter 5) that angular rock particles produce different percolation behaviour to smooth idealised particles. However this work was undertaken at 1:30 scale because full scale REV percolation test on caved rock are impractical. For instance, at 1:30 scale, the SCPG represents an actual volume with dimensions 10.65 m (length) x 10.65 m (width) x 7.5 m (height).

In the present conceptual numerical modelling study, four particles types were simulated resembling the fine percolating and bed-matrix of crushed basalt aggregates used in SCPG physical experiments. Alternatively the crushed basalt is represented by four different particle shapes as follows: spherical, cylindrical, cuboid and bi-conical. Each of the particle shape effect tests were simulated across four particle size ratios (0.21, 0.28, 0.36 and 0.42) for mono-size distributions. Alternatively, the selection of mono-size distributions in this chapter was in order to gain knowledge of the fundamental shape effects within the parameters range tested.

In regards to the limitations of full scale tests and physical models previously discussed in Chapter 2, the use of numerical modelling is perhaps the best method to explore fundamental mechanisms that are difficult or impossible to study at full scale. If it can be proven that the percolation mechanisms and parameters recorded in the SCPG experiments can be recovered adequately by DEM, it will be a step towards the numerical estimation of full scale REV problems in block caving. Moreover, these results can then be used in other codes such as REBOP, PCBC or CAVESIM to estimate mine scale dilution ingress. However, because of the lack of experimental data, numerical methods on percolation have not be validated or compared with actual experiments on rock particles.

The aim of this chapter therefore, is to firstly examine the scale effect on the dimensionless percolation rate (DPR) and to validate the numerical model through comparing and contrasting the DEM results to actual experiments. It is worth highlighting that the DEM simulations in this thesis aim to examine fundamental mechanisms across a wide range of parameters, rather than fully calibrated simulations with complete geometric similitude. It should be emphasised that due to the aims stated above, and the limitations of standard desktop computers, the DEM models similarly utilised a 1:30 scale model used in the SCPG experiments.

Notably the particle shape and diameter ratio ($d_p / d_b$) was found to be important parameters in the physical experiments (Chapter 5). Therefore, both parameters as stated above were simulated by the means of clump representations using the Particle Flow Code in Three Dimensions (PFC3D$^{TM}$). Based on the above approach, the second aim of this chapter is to test the hypothesis that clump representations of angular particles provide a better representation of percolation than spherical mono-size particles.

This chapter is divided into four sections. Section 6.2 discusses relevant applications and key features of PFC3D$^{TM}$. Sections 6.3 and 6.4 discuss model preparation and the simulation methods employed in the numerical study of percolation in caving mines. Section 6.5 details the simulation results. Finally, the overall findings and conclusions are presented in Section 6.6.

## 6.2 PARTICLE FLOW CODE IN THREE DIMENSIONS

It is generally agreed that in addition to physical testing, numerical models provide a powerful and versatile method for the investigation of granular flow (i.e., caved rock) (Campbell 1989; Savage and Dai 1993; Rosato and Kim 1994; Pierce et al. 2003). The strengths and limitations of numerical methods (i.e., continuum, discontinuum and hybrid continuum-discontinuum) for granular flow study were previously presented in Section 2.3.3.

Discontinuum methods such as Discrete Element Method (DEM) have received significant attention by previous researchers (Jing and Hudson 2002; Brown 2003; Pierce 2004; Ng 2005; Clearly 2008; Hadjigeorgiou and Lessard 2007; Li et al. 2010). The DEM approach (Cundall and Strack 1979; Guest and Cundall 1994) offers vast opportunities in visualizing and understanding the mechanisms of percolation as it provides insight into the microstructure of the granular material.

On the other hand, Particle Flow Code in three dimensions (PFC3D$^{TM}$) (Itasca 1999, 2005a, 2008b) which employed an explicit time-stepping algorithm is one of the finest examples of DEM models selected in this thesis due to several features as follow:

- ability to simulate a wide variety of caved rock situations, inter-body attraction laws and arbitrary geometries and allows a more detailed study of the micro-mechanics of the granular assemblies (Jing and Hudson 2002; Ng 2005); and
- flexibility in writing algorithms (in FISH language) for modelling complex geometries and problems (Itasca 2005b, 2008b).

It has been argued that modelling non-spherical shapes in DEM is essential for better understanding of granular materials (Powrie et al. 2005; Fraige et al. 2008). However, despite the fact that particle shape is known to affect the mechanical properties of granular materials, most DEM studies still represent grain shapes as discs in 2D or spheres in 3D (Sakakibara et al. 2008). The main reason for the ongoing use of discs and spheres is reduced simulation time and larger simulations. Run time is significantly shorter for discs and spherical particles, as compared to non-uniform particles (Fraige et al. 2008; Campbell 1990).

However, it was anticipated that at a micro-mechanical level, particle shape has been shown to have a very important effect on flow dynamics (Clearly 2008, Fu 2005). It is therefore the aim of this chapter to take steps towards an improved understanding of the impact of particle shape and size on percolation rate, through the application of DEM using PFC3D$^{TM}$ (i.e., clump logic).

### 6.2.1 Principle of PFC3D$^{TM}$

PFC3D$^{TM}$ is based on an explicit time-stepping method of calculation to simulate the dynamic behaviour of arbitrarily sized spherical particles (Itasca 2005b). By using microscopic input parameters for particle geometries in PFC3D$^{TM}$, the macroscopic behaviour of physical specimens can be represented. During the course of simulation, contacts are formed and broken automatically while micromechanical rules are repeatedly updated by a time-stepping algorithm. The force-displacement law updates contact forces according to the relative motion between particles and the contact constitutive model. Particle accelerations are computed according to the resultant force and the moment acting on the particle.

Potyondy and Cundall (2004) noted some of the basic assumptions in PFC:

- the particles are circular (in 2D) or spherical (in 3D) rigid bodies with a finite mass;
- the particles move independently of one another and can both translate and rotate;
- the particles interact only at contacts (i.e., this feature significantly reduces the calculation times). This is because the particles are circular or spherical in which a contact is comprised of exactly two particles;

- the particles are allowed to overlap one another and the force is given by this overlap. This overlap is much smaller in relation to the sizes of the interacting particles (i.e., at a point); and
- generalised force–displacement laws at each contact relate relative particle motion to force and moment at the contact.

### 6.2.2 Clump Particles

In PFC, non-spherical particles can be simulated by two approaches: the *cluster* (e.g., Jensen et al. 1999; Potyondy and Cundall 2004) and *clump logic* (e.g., Cho et al. 2007).

A cluster is created by several bonded particles in which elastic and strength properties are assigned to the intra-granular bonds and behave as one deformable particle and can break during the simulation (i.e., weak bond) (Li and Holt 2001). This method has been used to simulating particle crushing but limitations occur particularly when modelling large differences between the stiffness of the inter-granular and intra-granular bonds which results in numerical inefficiency (Li and Holt 2001).

On the other hand, clump logic provides a means to create and modify groups of slaved particles or clumps which behaves as a rigid body (i.e., the particles comprising the clump remain at fixed distance from each other) (Itasca 2005b, 2008b). Accordingly, clumped-particles (with a deformable boundary) will not break apart, regardless of the forces acting upon it (Itasca 2005b). Hence, clumped particles act like a single particle that has an irregular shape but move as a rigid body. This feature differed the clumped-particles from the clustered-particles. On the other hand, exceptionally high bond strength needs to be imposed by the clustered-particles for the particles to remain intact during the simulation (Lourel et al. 2006).

Alternatively, a clumped-particle can also be released and become several ordinary particles again during the simulation (i.e., modelling granular crushing). Accordingly, clump logic allows temporary or permanent rigid bonding between several spheres without detecting contacts or calculating contact forces between elements belonging to the same clump. Therefore, this approach is very efficient from a computational standpoint (Ashmawy et al. 2003). Nevertheless, the breakage of clumps has not been used in this thesis but may be taken into consideration for the future work in modelling of actual caved mines.

Clump logic provides some advantages in such a way that the contacts internal to the clump are skipped during the calculation cycle, resulting in reduced computational time compared to a similar calculations in which all contacts are active (i.e., clustered-particles) (Itasca 2008b). Some other advantages of clumped-particles over clustered-particles related to the particle rotation mechanism (Cho et al. 2007). Figure 6.1 shows that intra-cluster particles in clustered material have rotational velocities that significantly differ from clumped-particles assembly. Accordingly, a clump can have rotational velocity; hence reducing excessive particle rotation (Cho et al. 2007).

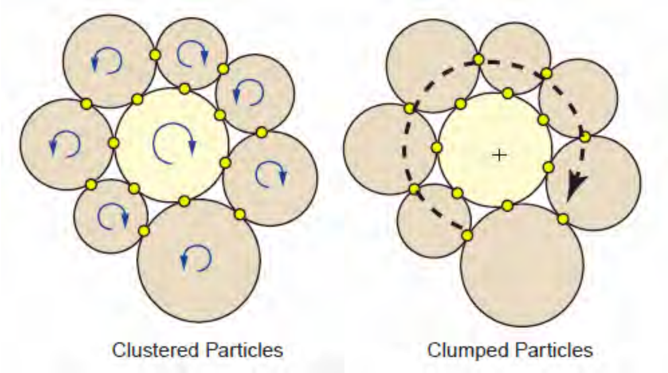


Figure 6.1: Particle rotation mechanisms in clustered and clumped particles (after Cho et al. 2007).

It is worth highlighting that both clusters and clumps experienced some limitations with regards to the execution difficulties as highlighted by Kazerani and Zhao (2010) and Kazerani et al. (2011). For instance, in simulating dynamic problems, clumps assume instantaneous action at a distance due to the lack of transmission of moments between particles in the clump.

Mass properties of a clump comprised of $N_p$ balls, in which of it has mass ($m^{[p]}$), radius ($R^{[p]}$) and centroid location ($x_i^{[p]}$) can be expressed as Equation 6.1, 6.2 and 6.3 respectively (Itasca 2005b, 2008b).

$$m = \sum_{p=1}^{N_p} m^{[p]} \quad \text{(Equation 6.1)}$$

$$x_i^{[G]} = \frac{1}{m}\sum_{p=1}^{N_p} m^{[p]} x_i^{[p]} \quad \text{(Equation 6.2)}$$

$$I_{ii} = \sum_{p=1}^{N_p}\left\{ m^{[p]}(x_j^{[p]} - x_j^{[G]})(x_j^{[p]} - x_j^{[G]}) + \frac{2}{5} m^{[p]} R^{[p]} R^{[p]} \right\} \quad \text{(Equation 6.3)}$$

$$I_{ij} = \sum_{p=1}^{N_p}\left\{ m^{[p]}(x_i^{[p]} - x_i^{[G]})(x_j^{[p]} - x_j^{[G]}) \right\} \ ; (j \neq i) \quad \text{(Equation 6.4)}$$

Where:

- $m$ refers to the total mass;
- $x_i^{[G]}$ refers to the location of the centre of mass; and
- $I_{ii}$ and $I_{ij}$ refers to the moments and products of inertia respectively.

It worth noting that both $I_{ii}$ and $I_{ij}$ are defined with respect to a reference frame that is attached to the clump at its centre of mass and aligned with the global axis system while generally there will be a non-principal set of axes (i.e., $I_{ij} \neq 0$).

On the other hand, the full equation of motion for a clump is determined by the resultant force and moment vector acting upon it and can be expressed in matrix form as Equation 6.4 (Itasca 2005b, 2008b):

$$[A]\left\{ x_i^{[p]} \right\} = \left\{ b \right\} \quad \text{(Equation 6.5)}$$

Where:

- $[A] = \begin{bmatrix} 1 & \omega_3 \Delta t/2 & -\omega_2 \Delta t/2 \\ -\omega_3 \Delta t/2 & 1 & \omega_1 \Delta t/2 \\ \omega_2 \Delta t/2 & -\omega_1 \Delta t/2 & 1 \end{bmatrix}$;
- $\left\{ b \right\} = \begin{Bmatrix} \dot{x}_1^{[G]} + \omega_2 (x_3^{[p]_b} - \bar{x}_3^{[G]}) - \omega_3 (x_2^{[p]_b} - \bar{x}_2^{[G]}) \\ \dot{x}_2^{[G]} + \omega_3 (x_1^{[p]_b} - \bar{x}_1^{[G]}) - \omega_1 (x_3^{[p]_b} - \bar{x}_3^{[G]}) \\ \dot{x}_3^{[G]} + \omega_1 (x_2^{[p]_b} - \bar{x}_2^{[G]}) - \omega_2 (x_1^{[p]_b} - \bar{x}_1^{[G]}) \end{Bmatrix}$;
- $\dot{x}_{i=1,2,3}^{[G]}$ refers to velocity of the translational motion of the centre of mass;

- $x_{i=1,2,3}^{[p]}$ denotes the position vector of particles [p] before the update;
- $\bar{x}_{i=1,2,3}^{[G]} = \dfrac{x_i^{[t+\Delta t)]} + x_i^{(t)}}{2}$ ;
- $\omega_{i=1,2,3}$ refers to angular velocity of the rotational motion of the clump; and
- $t$ and $\Delta t$ refers to time and timestep respectively.

Alternatively, clumps used in this thesis were created in such way that clump volume is automatically determined based on the positions and radii of its component particles. However, automatic volume computation (provided in PFC) is accurate only if all clump-overlap regions are defined by exactly two particles as illustrated by Figure 6.2a. During the generation of clump-particles, the balls in the range with arbitrary oriented clumps are replaced where clump particles have the same volume and centroidal position as the ball that it replaces.

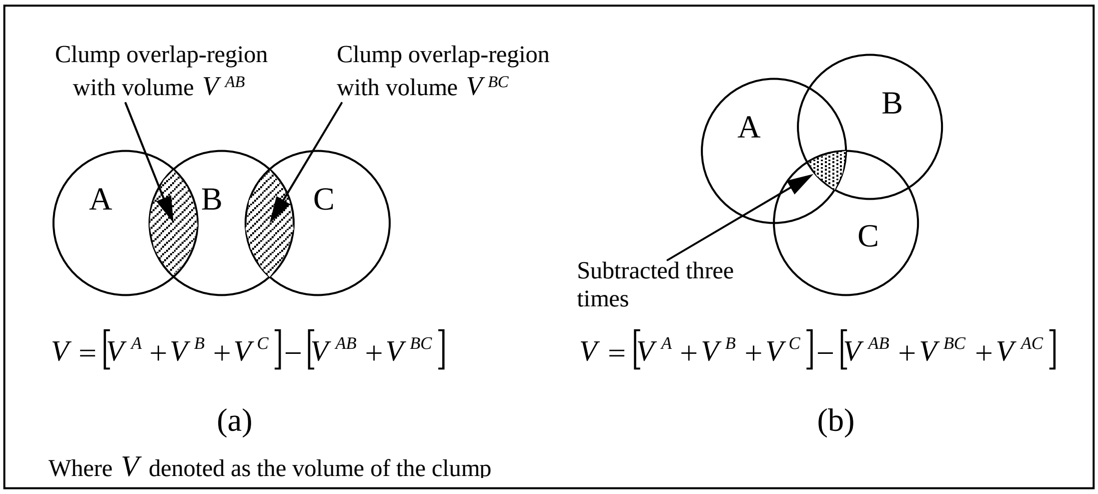


Figure 6.2: Illustration of when the automatic procedure to compute clump volume fails. Note that computed clump volume is correct for (a) and incorrect in (b) (after Itasca 2008b).

## 6.3 SIMULATION METHOD, PARTICLE AND WALL PARAMETERS

### 6.3.1 Simulation Method

The modelling philosophy was to undertake a numerical forward analysis based on keeping all numerical modelling parameters as close as possible to the SCPG physical and experimental parameters (e.g., SCPG length dimensions, strain rate, particle parameters). Accordingly, a simplified model of the experimental apparatus of SCPG physical experiment was constructed in PFC3D™. The modelling, was implemented using the algorithms and clump logic developed by Itasca (2008b). All algorithms written and clump logic templates for the numerical tests in this chapter are provided in Appendix D.

The model packing procedure is described as follows. The particles are randomly generated and oriented to 220 mm height in the SCPG, the initial porosity of the sample was then adjusted to represent the actual measured porosity. Thereafter, gravity and friction is applied. During this stage, the spheres are converted to clumps by replacing each particle with a clump of equivalent volume. The ball density is adjusted to achieve equal mass for both the single spherical particle and its equivalent clump. A rotational velocity was then applied to two moving walls to achieve a shear rate at 0.04 $s^{-1}$. The shearing direction is reversed after a shear strain of 50% from vertical (Figure 6.3). The model is then sheared until 400% strain (a complete cycle).

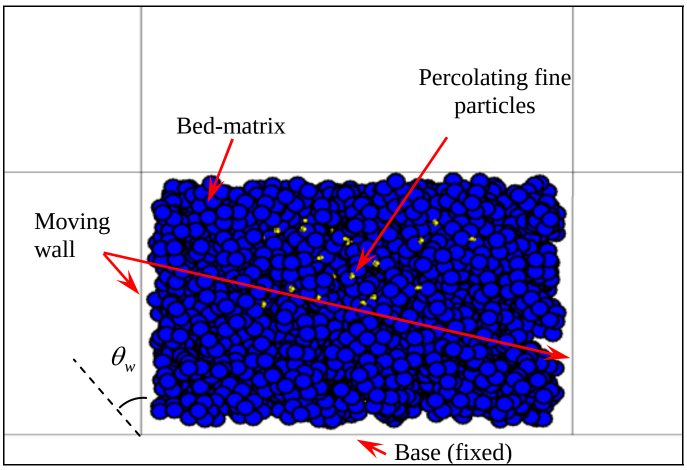


Figure 6.3: Vertical cross section through the shear cell showing coarse 4-particle clumps (blue) and fine particles (yellow) at $\gamma_{total}$ =200%. The remainder of bed-matrix particles near the wall have been hidden to provide clear view of wall vicinity. The fine particle is 4.97 mm while the bed-matrix is 17.75 mm ( $d_p / d_b$ =0.28). Model is 355 mm (length) x 355 mm (width) x 250 mm (height).

It is worth mentioning that in most tests, after $\gamma_{total}$ =400%, most of the fine particles (i.e., $d_p / d_b$ =0.21) are recovered, hence there is no requirement to run the experiment beyond this. Therefore, in order to provide a direct comparison of each parameter tested, $\gamma_{total}$ was set to maximum of 400%. In addition, this method provides standardisation in all numerical tests in which the mean of 400% shear strain was analysed and assessed. For that reason, the DPR of percolating fine particles was defined as the measurement of the most probable distance in coarser bed particle diameters that an isolated percolating particle is expected to drop when subjected to 100% shear strain (Pierce 2004, 2010).

Table 6.1 describes the parameters and permutations for the SCPG physical experiment and PFC3D™ numerical models. There are approximately 6,100 particles generated for the mono-sphere assemblies; 18,300 particles (cylindrical shaped); 24,400 particle (cuboid) and 36,600 particles (bi-conical) respectively. The use of a standard desktop computer employed in this thesis limited the ability to simulate a higher number of clump particles and as a result required long runtimes to simulate smaller particles.

Table 6.1: Parameters and model permutations for the PFC3D™ numerical model and SCPG physical experiment.

| Description | PFC3D™ numerical model | SCPG Physical Experiment |
|---|---|---|
| Cell dimensions (length x width x height) | 355 x 355 x 250 mm | 355 x 355 x 250 mm |
| Fine and bed-matrix particle density | 2540 kg/m³ (Ideal media);<br>2760 kg/m³ (Crushed basalt) | 2490 – 2540 kg/m³ (Glass sphere);<br>2730 – 2760 kg/m³ (Crushed basalt) |
| Percolating fine particle size (equivalent spherical diameter) | 3.65, 4.97, 6.39, 7.46 mm | 4.02, 5.03, 6.16 mm (Glass spheres);<br>2.41, 3.19, 4.08, 4.83 mm (Crushed basalts) |
| Coarse bed particle size (equivalent spherical diameter) | 17.75 mm | 15.78 mm (Glass sphere);<br>11.48 mm (Crushed basalt) |
| Fine-coarser particles diameter ratio | 0.21, 0.28, 0.36, 0.42 | 0.25, 0.32, 0.39 (Glass sphere);<br>0.21, 0.28, 0.36, 0.42 (Crushed basalts) |
| Shape | Spherical (Ideal media and crushed basalt);<br>Cylindrical (Crushed basalt);<br>Cuboid (Crushed basalt);<br>Bi-conical (Crushed basalt) | Spherical (Glass sphere);<br>Highly angular (Crushed basalt) |
| Size distribution | Mono-assemblies | Mono-assemblies (Glass sphere);<br>Wide range (Crushed basalt) |
| Strain rate | $0.04\ s^{-1}$ | $0.04\ s^{-1}$ |

The simulations were performed in two phases:

- simplification of particle shapes and size distributions, and SCPG physical experiment (Phase 1); and
- forward analysis of an ideal media and crushed basalt aggregates (Phase 2).

An attempt to test the scale effect was carried out by using fixed SCPG dimensions, with different particle sizes but identical $d_p/d_b$ as shown in Table 6.2. This is considered necessary in order to look into the possibility of using a smaller scale (i.e., larger particle size) which could be run at an appropriate simulation time. In addition, application of larger particle sizes significantly reduce the computational time required in Phase 1 and 2 respectively.

Table 6.2: Comparison of scale effect tests between 1:40, 1:35 and 1:30 scaled.

| Description | 1:40 scale | 1:35 scale | 1:30 scale |
|---|---|---|---|
| Percolating fine particle size (equivalent spherical diameter) | 2.75, 3.72, 4.79, 5.60 mm | 3.19, 4.26, 5.48, 6.39 mm | 3.65, 4.97, 6.39, 7.46 mm |
| Coarse bed particle size (equivalent spherical diameter) | 13.31 mm | 15.21 mm | 17.75 mm |
| Fine- bed matrix particles diameter ratio | 0.21, 0.28, 0.36, 0.42 | | |

The results of the scale effect tests are plotted in as the dimensionless percolation rate (DPR) illustrated in Figure 6.4. Over the range of parameters tested, it was found that the effect of scale on the DPR was minimal suggesting that a smaller scale (i.e., larger particle sizes) could be modelled using a standard desktop computer with appropriate computational time and limitations factored into the test. With regard to the above results, the 1:30 scaled model was chosen in the Phase 1 and 2 conceptual numerical studies. Simultaneously, at 1:30 scale, the numerical shear cell dimensions (355 mm length x 355 mm width x 250 mm height) represents 10.65 m (length) x 10.65 m (width) x 7.5 m (height) of an actual REV of caved rock. On the other hand, the coarse bed-matrix diameter was set to 17.75 mm to achieve a minimum REV=20$d_b$ (0.53 m actual rock fragmentation size at 1:30 scaled). Whilst, the $d_p/d_b$ of simulated fine-bed matrix particles were similar to that of the equivalent spherical diameter ($D_s$) (Nedderman 1992) of ideal and crushed aggregates media used in Chapter 5 (Table 6.1).

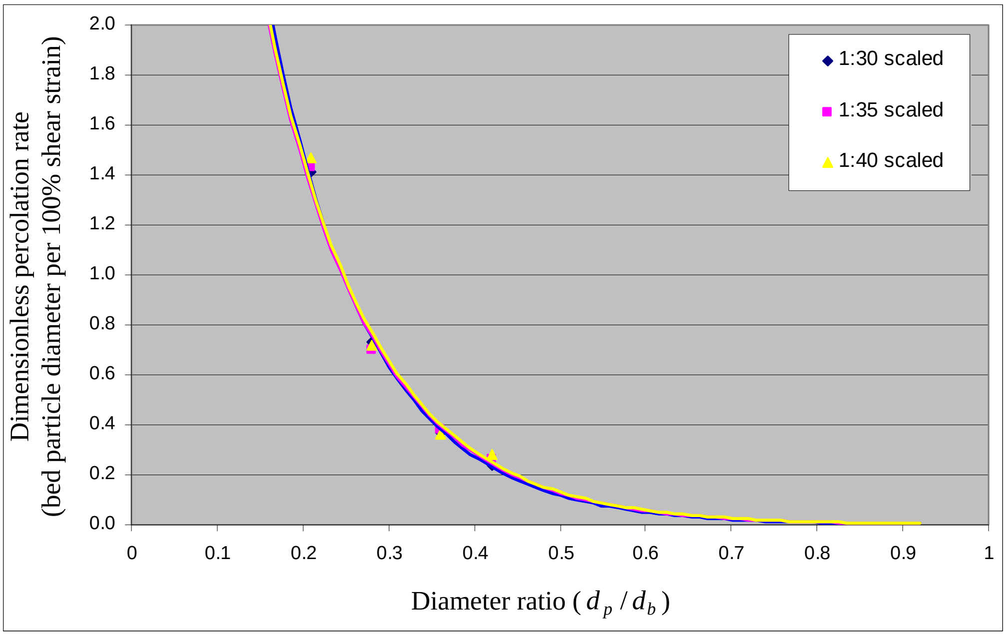


Figure 6.4: Comparison of diameter ratio versus dimensionless percolation rate (DPR) of PFC3D™ for various scale effect at $\dot{\gamma}$=0.04 s$^{-1}$. Note that the $d_p / d_b$ are similar in each scaled factors and define as a function of equivalent spherical diameter ($D_s$).

### 6.3.2 Particle and Wall Parameters

Table 6.3 summarises the properties of particle and wall used in the PFC3D$^{TM}$ numerical model. It is worth highlighting that since the DEM is a fully dynamic formulation, some form of damping is necessary to dissipate kinetic energy (Potyondy and Cundall 2004). For this purpose a damping coefficients of basalt aggregates (crushed aggregates media) was set to replicate the coefficient of restitution (COR) of 0.2, obtained from a pendulum test of basalt aggregate against rock (Iverson et al. 2003). On the other hand, the COR=0.84 obtained from drop tests carried out on glass (i.e., ideal media) (Bridgwater and Ingram 1971) was chosen for the ideal media.

Table 6.3: Particle and wall parameters used in PFC3D™ simulations.

| Description | Ideal Media (Glass sphere) | Crushed Basalt |
|---|---|---|
| Shape ( $d : d : d$ aspect ratio) | Single ball (1:1:1) | Single ball (1:1:1);<br>3-ball clumps (1:1:1.5);<br>4-ball clumps (1:1.5:2);<br>6-ball clumps (1.5:1.5:2) |
| Normal and shear stiffness of particles | 1.0 x $10^{7}$ N/m | 1.0 x $10^{7}$ N/m |
| Normal and shear stiffness of walls | 1.0 x $10^{7}$ N/m | 1.0 x $10^{7}$ N/m |
| Coefficient of friction | 0.25 | 0.40 |
| Coefficient of local damping | 0.84 | 0.20 |
| Time step | 1.0 x $10^{-6}$ s/step | 1.0 x $10^{-6}$ s/step |
| Particle contact modulus | 50 GPa | 50 GPa |
| Density | 2540 kg/m³ | 2760 kg/m³ |
| Initial porosity | 0.40 | 0.36 |
| Fine-bed matrix particles diameter ratio | 0.21, 0.28, 0.36, 0.42 | 0.21, 0.28, 0.36, 0.42 |

The particle tracking procedure used in the PFC3D™ shear cell simulations differs from that of Bridgwater's physical tests (Bridgwater et al. 1978). One difference relates to the position and tracking of the percolating fine particles. In the numerical simulations, a total of thirty fine particles were placed at the top of the coarse assembly (220 mm height) and the path travelled during shearing was tracked. An identical approach was adapted in the SCPG physical experiments in which thirty fine particles were simultaneously sheared in the DPR assessment as shown in Section 5.4. By contrast Bridgwater et al. (1978) and his co-authors added a single particle "one at a time" which passed through the entire bed.

The DPR for numerical tests is written as Equation 6.5 (Bridgwater et al. 1978).

$$\frac{\bar{y}}{\dot{\gamma} d_b} = k_1 \exp\left[-k_2 \frac{d_p}{d_b}\right] \qquad \text{(Equation 6.6)}$$

Where:

- $\bar{y}$ is defined as the mean percolation distance travelled by percolating particles at a given strain (mm);
- $k_1$ and $k_2$ are two arbitrary constants that were found to be equal to 17 and 11 respectively from the SCPG physical experiment (Chapter 5);
- $d_p / d_b$ is the ratio of percolating particle to coarser bed-matrix particle diameter or a measure of the utilisation of holes in the deforming large particles by small particles; and
- $\dot{\gamma}$ is denoted as the strain rate while $d_b$ refers to diameter of coarser bed particles; respectively.

It is noteworthy that interaction effects between wall and particles was identified in early physical experiments by Bridgwater et al. (1978). This problem was subsequently corrected through improvements to fine particle configuration during loading employed in SCPG physical experiment. Accordingly, in order to overcome interaction effects (i.e., particle-particle and wall-particle) during the simulation, particles were placed far enough apart not to interfere with one another (Pierce 2004, 2010; Hashim and Sharrock 2009).

In addition, only particles in the upper half of the shear cell at distances of approximately 100 mm from the wall edge were used for calculation of percolation distance. Since these simulations employ a higher number of clump particles than Pierce (2004, 2010) (i.e., two clump-particles) and Hashim and Sharrock (2009) (i.e., up to four clump-particles), it provided a better representation of angular rock particles compared to earlier models.

### 6.3.3 Simplification of Particle Shapes and Size Distributions, and SCPG

Due to the complex particle shapes and size distributions, model simplification is essential prior to forward analysis. As a result, a two stage process was adopted. The purpose of the first phase was to replicate and validate numerical SCPG model for the use in the forward analysis (second phase). The particle size distribution, shape and density are kept constant in each test (i.e., mono-size distribution of an ideal media).

The numerical model had identical dimensions as the SCPG model (355 mm length x 355 mm width x 250 mm height) employed in physical testing in Chapter 5. Simultaneously, the material properties of glass sphere (ideal media) were selected to closely represent the mono-sphere particles used in PFC3D™. Accordingly, the accuracy of the PFC3D™ model was verified through comparison of the DPR pattern with the SCPG physical experiment (Section 5.4). The calibrated PFC3D™ model was then used in the forward analysis of non-spherical shape and particle sizes distribution of basalt aggregates.

### 6.3.4 Simplification of Basalt Aggregate Tests

In order to investigate the effect of the shape of angular rock particle, the micro-properties of simulated particles were set to have similar properties to basalt aggregates used in the SCPG physical experiment (Table 6.1). Particularly, the validated PFC3D™ models in Section 6.3.3 were extended to more complex non-spherical particles with the use of clump logic. Three types of clump particles were generated and tested: cylinders (three-particle clumps), cuboids (four-particle clumps) and bi-cones (six-particle clumps). In addition, the spherical particles were also simulated to provide comparison between the sphere ball and clump particles.

Figure 6.5 illustrates the four shapes applied in the forward analysis of numerical SCPG model. Aspect ratios of 1:1:1, 1:1:1.5, 1:1.5:2 and 1.5:1.5:2 were selected to represents spherical, cylindrical, cuboidal and bi-conical shapes respectively.

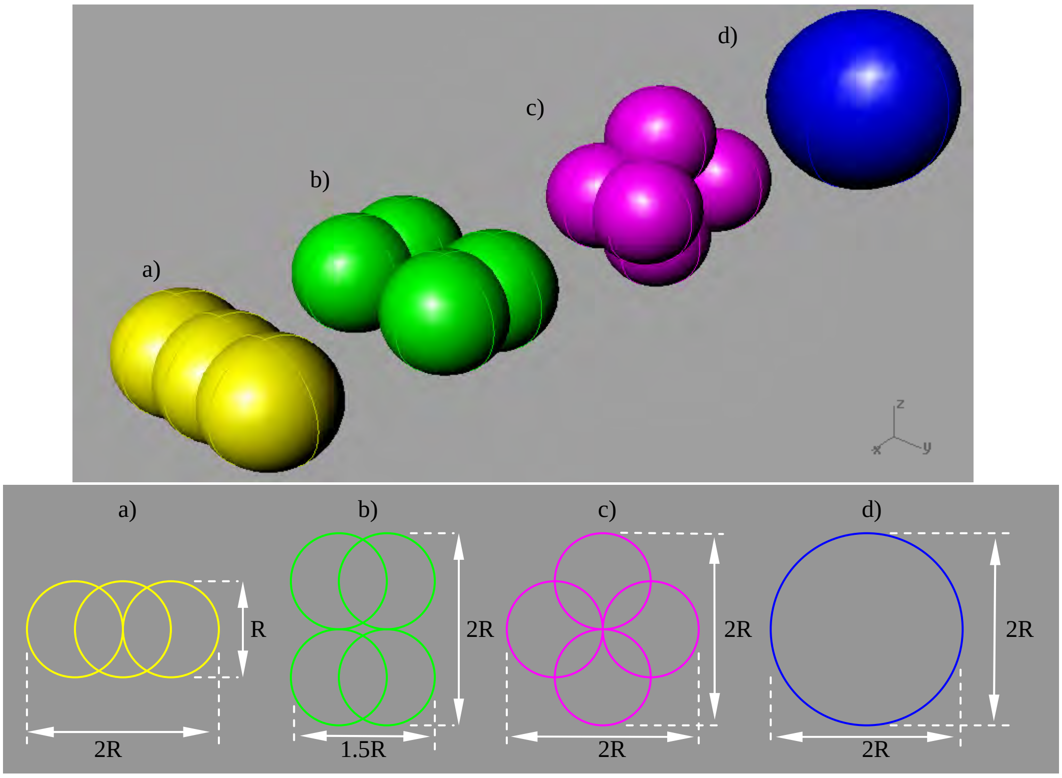


Figure 6.5: Non-spherical clump particles representing angular rock particles used in the PFC3D™ (drawn to scale) [top] and aspect ratio [bottom]. Note (a) Cylindrical (b) Cuboid (c) Bi-conical (d) Spherical.

The following parameters were kept constant in all tests on the effect of particle shape and size:

- particle diameter ratio( $d_p / d_b$ ) =0.21, 0.28, 0.36 and 0.42 respectively,
- normal stress ( $\sigma_n$ ) =0.9 kPa;
- shear strain ( $\gamma_{total}$ ) =400%;
- percolating fine and bed-matrix particle density ( $\rho$ ) =2760 kg/m³; and
- strain rate ( $\dot{\gamma}$ ) =0.04 $s^{-1}$.

## 6.4 RESULTS AND DISCUSSION

### 6.4.1 Ideal Media – Glass Sphere

Tests on ideal media (II series) were carried out on four different particle diameter ratios as follows: 0.21, 0.28, 0.36 and 0.42. Figure 6.6 illustrates the comparison of DPR plots against $d_p / d_b$ as a function of equivalent diameter ( $D_s$ ) for PFC3D™

idealised (sphere particle), generalisation of SCPG physical experiment and Bridgwater et al. (1978) physical tests respectively.

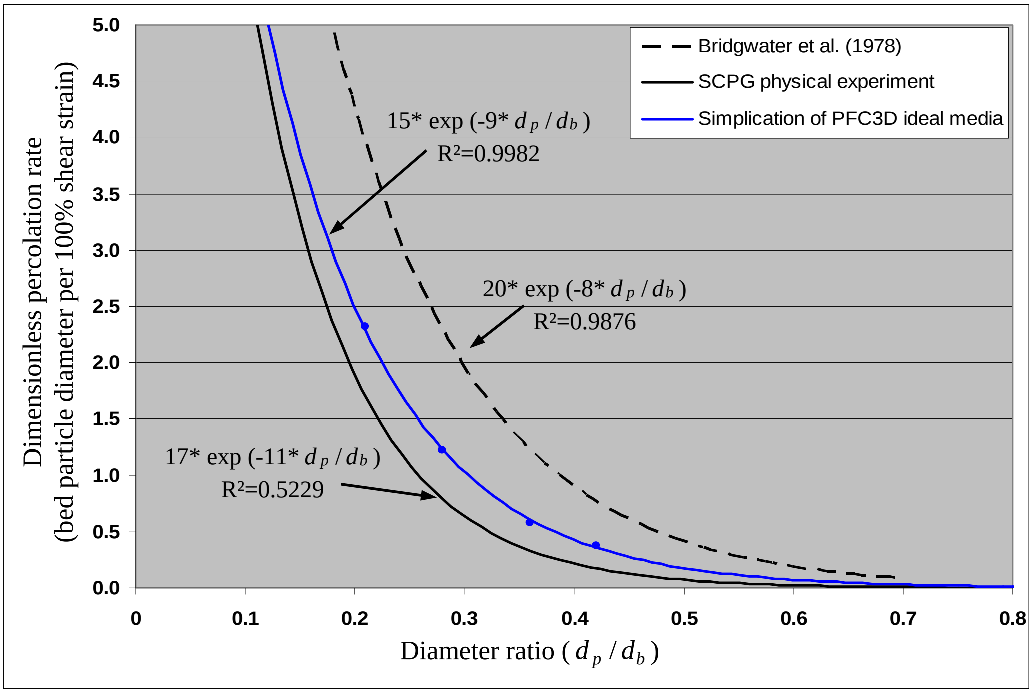


Figure 6.6: Comparison of diameter ratio versus dimensionless percolation rate (DPR) of PFC3D™ for ideal media and crushed basalt aggregates at $\dot{\gamma}$ =0.04 $s^{-1}$. Note that for Bridgwater et al. (1978) DPR plot at $\dot{\gamma}$ = 0.4 $s^{-1}$ while generalisation of SCPG physical experiment and PFC3D™ ideal media at $\dot{\gamma}$ = 0.04 $s^{-1}$ respectively. Diameter ratio is a function of equivalent spherical diameter ($D_s$).

The DPR simulation results for ideal media (glass spheres) generally has a similar exponential plot pattern with the SCPG physical experiments. However, Figure 6.6 shows that the PFC3D™ ideal media plot was slightly lower ($k_1$=15, $k_2$=9) than the SCPG physical experiment ($k_1$=17, $k_2$=11). One plausible reason for this difference relates to the parameters used in both tests. The SCPG plot was generated via a combination of various test parameters (i.e., $\dot{\gamma}$, $d_p/d_b$, density and shape effect) and represents a generalisation of the DPR plot while for the PFC3D™ idea media plot, it only considers spherical particles. In addition, the combination of test parameters used in the DPR plot of SCPG physical experiments explains the significantly lower $R^2$ value ($R^2 \approx 0.53$) compare to the PFC3D™ ideal media ($R^2$>0.98).

Apart from this, it is also postulated that the slightly higher $k_1$ and $k_2$ shown by the PFC3D™ ideal media than SCPG is related to the micro-properties of particles used in the simulation. For instance, the PFC3D$^{TM}$ applied ideal media properties (i.e., glass sphere) while the DPR plot of SCPG was generated by combining the data of both ideal (i.e., glass spheres) and crushed aggregates media (crushed basalt aggregates).

Conversely, the greater DPR plot shown by Bridgwater et al. (1978) compared to the PFC3D$^{TM}$ ideal media is related to the variation of strain rate employed in both tests. Bridgwater et al. (1978) carried out the percolation tests at $\dot{\gamma}$=0.4 $s^{-1}$ while a significantly lower strain rate of 0.04 $s^{-1}$ was used in the PFC3D$^{TM}$ ideal media. Nevertheless, it is concluded that the potential of DEM percolation simulations is demonstrated by the similarity of the DPR pattern with Bridgwater et al. (1978) work. In overview, the PFC3D$^{TM}$ ideal media tests indicates that PFC3D$^{TM}$ is capable of capturing key mechanisms involved in percolation studies on rock particles.

Following the validation studies on ideal media the forward analysis tests were undertaken to investigate the affect of angular particles using clump logic. Since the purpose of this chapter is to evaluate the DPR for non-spherical particle shapes, the grain size distribution and particle density are kept constant in all simulations (i.e., mono-size distribution). The tests were undertaken for four different mono-size assemblies of particles with the following shapes: spherical, bi-conical (six-particle clumps), cuboids (four-particle clumps) and cylinders (three-particle clumps) as presented in Section 6.4.2.

### 6.4.2 Forward Analysis – Crushed Basalt Aggregates

#### *6.4.2.1 Comparison of simplified particle shapes*

Following the exploration of the validity of PFC3D$^{TM}$ to recover the result of the SCPG physical experiments on ideal media (Section 6.4.1), an analysis of non-spherical shapes and particle sizes of basalt aggregates were undertaken. The complexity of particle shape was incrementally increased by changing the shape of the percolating particles from spheres to three-particle clumps (cylindrical shape), four-particle clumps (cuboids shape) and six-particle clumps (bi-conical shape). Overall, a total of 16 tests were performed (four tests for each particle shape at $d_p / d_b$=0.21, 0.28, 0.36 and 0.42 respectively).

The individual cylindrical, cuboids and bi-conical particles were modelled as clumps. The degree of particle rotation was observed to decrease significantly, with increasing aspect ratio. As a result, particles with high aspect ratio have lower DPR. Figure 6.7 illustrates that the DPR for bi-conical particles is the lowest compared to other shapes; this is related to the aspect ratio. For instance, the bi-conical particle has the highest aspect ratio (1.5:1.5:2) compared to cylinders (1:1:2), cuboids (1:1.5:2) and spheres (1:1:1). With regards to this, Abbaspour-Fard (2005) numerically investigated the role of particle shape in a silo and found that more arching occurred as the aspect ratio of particles increased thus verified the significant of aspect ratio in non-spherical particles.

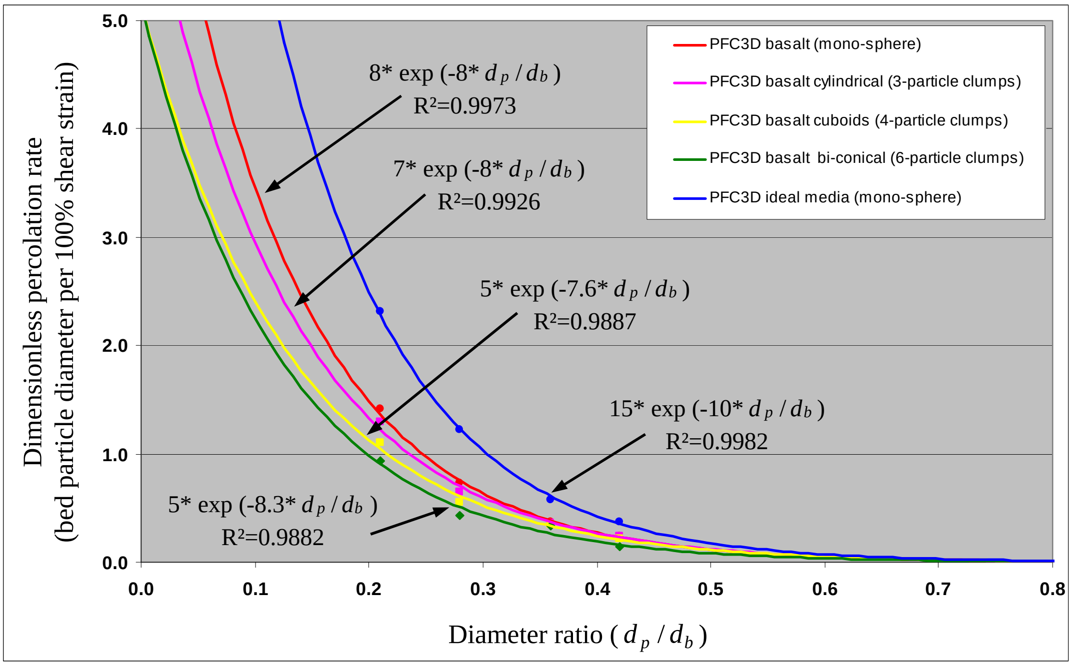


Figure 6.7: Comparison of diameter ratio versus dimensionless percolation rate (DPR) of PFC3D™ for ideal media and crushed basalt aggregates at $\dot{\gamma}$ =0.04 s$^{-1}$ . Note that the diameter ratio is a function of equivalent spherical diameter ( $D_s$ ).

The high aspect ratio of the six-particle clumps relative to the other bulk particle shapes also promotes greater interlocking and this significantly reduces the percolation rate. In addition, the particles with higher aspect ratios generally have greater resistance to shear or frictional forces. Jensen et al. (2001) used DEM to study the effect of particle shape on the interface behaviour of granular materials and found that as particles become more angular, they tend to interlock more and provide more resistance to shearing.

It was also found that the DPR of non-spherical shape particles decreased by up to 10% for the cylinders, 25% for the cuboids, and 40% for the bi-cones relative to spheres as illustrated in Figure 6.8. This finding broadly agrees with Cleary (1999) and Clearly and Sawley (2002) who reported that elongated particles can reduce percolation by up to 30% as compared to circular (in 2D) and spherical particles (in 3D). In addition, Cleary (1999) also found that the flow rates of particles decrease by up to 28% in highly blocky or highly angular particles and also have flow patterns that are quite different from the spherical particles.

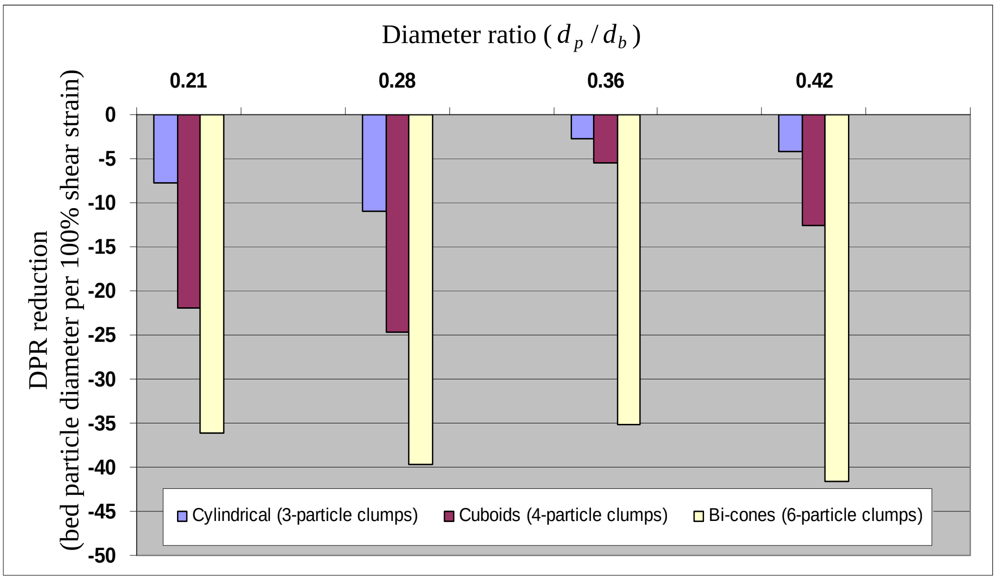


Figure 6.8: DPR reduction in clump particles against the mono-size spherical assemblies at $\dot{\gamma}$ =0.04 s$^{-1}$.

Hashim and Sharrock (2009) numerically replicated and validated Bridgwater et al. (1978) physical shear cell. Accordingly, the simulation works were extended using twice the shear cell dimensions and introduced non-spherical shape particle (i.e., three-particle clumps represent cylindrical shape and four-particle clumps represent cuboids shape). It was reported that the DPR of simulated shear cell is significantly affected by particle shape. In particular, percolation rates were most affected by the cuboid shape of bulk particles compared to the cylindrical and spheres. This suggests that for these assemblies and shear strain rates, the percolation rate is predominantly controlled by the shape factor.

Fraige et al. (2008) noted that compared to the rounded shapes, angular polygons potentially affect the mechanisms of packing and flow. As granular materials result from crushing or mining operations are generally highly angular (Campbell 1990), shape effects are significant and need to be considered in numerical and physical models. It is also noteworthy that compared to spheres the packing density of highly angular aggregates generated during crushing, minimizes void space. Changes in void space significantly affect the percolation rate especially to the lower diameter ratio of particles (i.e., $d_p / d_b$=0.21 and 0.28) where the void space is significantly lower, thus limiting the ability of fine particles to percolate through the bed-matrix.

The increased friction between the granular material (resulting from increased particle shape) and the bed comprised of highly non-spherical particles may also lead to a reduction in the percolation velocity and significantly affect the percolation rate. In contrast, spherical/circular particles (in 3D) or disk (in 2D) percolating in spherical/circular assemblies have lower friction and higher percolation velocities. As a result, the dimensionless percolation rate of mono-sphere particles was significantly higher compared to more complex shapes, in-terms of percolation velocity and percolation rate.

#### *6.4.2.2 Comparison of simplified particle shapes and physical experiments*

The DPR of the numerical analysis of basalt aggregates was compared to the SCPG physical experiments (Figure 6.9). It is observed that none of the mono-assemblies of spherical, cylindrical, cuboids or bi-conical particles used in the simulations could satisfactory reproduce the DPR plot of shape effect in SCPG physical experiment. One plausible reason relates to the type of coarse bed-matrix used in both the PFC3D™ and SCPG physical experiments. For instance, PFC3D™ simulated mono-sized assemblies while the SCPG physical experiment used wide size distributions (previously discussed in Section 4.4.1) as the coarse bed-matrix.

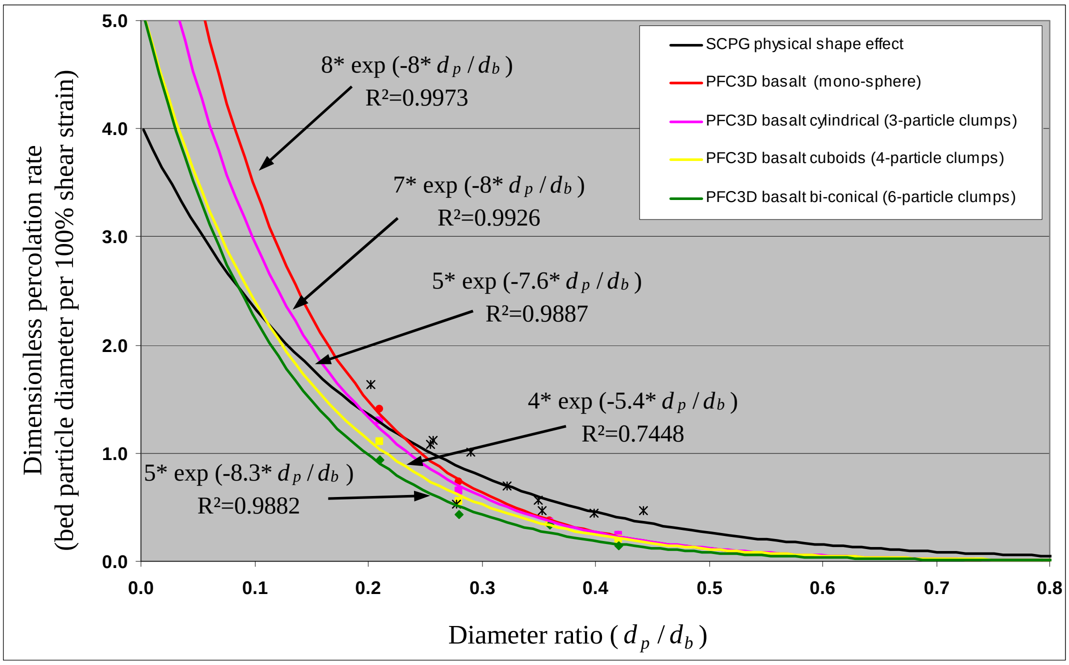


Figure 6.9: Comparison of diameter ratio versus dimensionless percolation rate (DPR) of shape effect for the PFC3D™ (basalt aggregates) and SCPG physical experiment at $\dot{\gamma}$ =0.04 s$^{-1}$. Note that the diameter ratio is a function of equivalent spherical diameter ( $D_s$ ).

With regard to the above argument, Pierce (2010) numerically demonstrated a series of size distribution in percolation which resulted in significantly lower percolation rates compared to the mono-sized assemblies. Pierce (2010) postulated that the much lower percolation rates of fines particles was due to the wide size distribution (i.e., mixture of fines to coarser particles) used in his study that restrict the ability of fines to percolate down though the column. Nevertheless, it can be argued that the use of non-spherical clump particles provides more reliable results than spherical particles. For instance, Figure 6.9 demonstrates that the DPR and SCPG physical experiments on angular rock are more closely represented by bi-cones (six-particle clumps) and cuboids (four-particle clumps) than spherical particles.

Accordingly, such findings suggest that in order to closely represent actual caved rock percolation, wider distributions of clumps than mono-size distributions are necessary. For example, mixtures of spherical, cylindrical, cuboids, bi-conical and others shapes should be created to closely resemble actual caved rock which is composed by highly angular shapes and a wide range of fragment sizes. Nonetheless, the effect of such mixtures requires extensive work in order to determine the appropriate proportion of non-spherical particles clumps is beyond the scope of this thesis.

## 6.5 CONCLUSIONS AND DISCUSSION

The used of DEM simulations in this chapter was aimed to examine fundamental mechanisms across a wide range of parameters, rather than fully calibrated simulations with complete geometric similitude. PFC3D$^{TM}$ ideal media tests were undertaken by the means of four particle size ratio as follows: 0.21, 0.28, 0.36 and 0.42. The accuracy of the model was compared to the DPR plots from the SCPG physical experiments. The results demonstrate the ability of PFC3D$^{TM}$ to model percolation in coarser bed-matrix particles during shearing.

The PFC3D$^{TM}$ model was extended to investigate the impact of particle shape which closely represents angular rock micro-properties (basalt aggregates). Four mono-size assemblies were tested with the following shapes: spheres, cylinders, cuboids and bi-cones. Accordingly, each of the particle shape effect tests were simulated on four different particle size ratio of 0.21, 0.28, 0.36 and 0.42 on mono-assemblies size distribution.

Over the range of particle sizes and shapes tested, it was found that dimensionless percolation rate (DPR) is predominantly affected by particle shape and size ratio of the fine and bed-matrix particles. It was also found that as the bed-matrix particle shape was varied from spheres to cylinders to cuboids to bi-cones, the DPR decreased. Accordingly, significant reduces of DPR by up to 10% for the cylinders, 25% for the cuboids, and 40% for the bi-cones relative to spheres were recorded. The implication for mining operations is that highly flaky or angular caved rock will have lower percolation rates than rounded boulders.

For experiments on mono-size assemblies of clumps representing angular rock fragments, it was observed that none of the mono-assemblies of spherical, cylindrical, cuboids or bi-conical particles used in the simulations could satisfactory reproduce the DPR plot of shape effect in SCPG physical experiment. Alternatively, the exponential plot of DPR was found to varies between 8*exp[-8($d_p / d_b$)] for the mono-sphere basalt to 5*exp[-8.3($d_p / d_b$)] for the six-particle clumps basalt. The results show that over the range of parameters tested, the numerical model still largely inadequate to replicate the SCPG physical model of 17*exp[-11($d_p / d_b$)]. Hence, it was demonstrated that more complex clump particles closely representing caved rock may be required before the numerical model could be carry out with confident. However, due to the limitations of standard desktop computer used in this thesis, the highly angular shaped of crushed basalt were only resembled by up to six-clump particles. This needs to be improved in future work.

Nevertheless, this conceptual study demonstrates the potential of DEM models of non-spherical particles to simulate percolation in block caving mines. Alternatively, the above study also proves that the hypothesis on discrete element models incorporating clump representations of angular particles provide better percolation estimates than spherical mono-size particles is true.

Further study is required to examine the range of strain rates, particle sizes distribution and shapes. Future models should consider more complex clump shapes hence better representing angular rock particles with more realistic size distributions (i.e., real caved rock fragmentation).

# CHAPTER 7:
# CONCLUSIONS AND RECOMMENDATIONS FOR FUTURE RESEARCH

## 7.1 AN OVERVIEW OF FINDINGS

This thesis has investigated the percolation of fine particles in a matrix of highly angular large/coarser aggregates under shearing and gravitation loading. Two approaches were adopted to study percolation: physical modelling and discrete element numerical simulation.

In the physical modelling, a Shear Cell for Percolation of Geomaterials (SCPG) was designed and fabricated while a Kvapil Type-A scaled models was used to access the magnitude of shear strain required for the percolation tests.

DEM simulations (using PFC3D$^{TM}$) were conducted in which particle shapes and size distributions were simplified, and numerical results were compared to the SCPG physical experiments. This was followed by a sensitivity analysis using clumps of various sizes to explore the impact of increasing the particle shape complexity for crushed basalt aggregate.

### 7.1.1 Physical Experiments

#### *7.1.1.1 Shear Cell for Percolation of Geomaterials (SCPG)*

Over the range of parameters tested, it is shown that percolation is significantly affected by the particle diameter ratio ($d_p / d_b$) and strain rate ($\dot{\gamma}$). By contrast, it was observed that the effect of particle density was small. Subsequently, these findings agree with the work of Bridgwater et al (1978), Cooke et al. (1978), Bridgwater et al. (1985a, 1985b) and Duffy and Puri (2002) on idealised media consisting of glass spheres and steel spheres.

On the other hand, although the effect of particle shape is generally postulated to be insignificant by many researchers for curved non-spherical media like pharmaceutical pills, this does not appear to be the case for angular rock fragments. The work presented in this thesis shows that for highly angular particles, particle shape influences percolation.

Since the experimental variables (i.e., effect of strain rate, particle diameter ratio, shape, density) in this thesis differed broadly, an attempt to take into account the similarity of all experimental parameters were taken by the mean of dimensionless percolation rate (DPR). Accordingly, the exponential plot of DPR was found to be 17*exp[-11($d_p / d_b$)] in which the lower $k_2$ value indicates that it takes an increasingly greater amount of shear strain for percolation to occur as the size of the fine particles approaches that of the coarse particle. Comparison between the SCPG physical experiments and Bridgwater et al. (1978) exponential plot of DPR shows a similar pattern.

#### *7.1.1.2 Shear strains assessment in a 1:100 scaled Kvapil Type-A model*

Research was conducted in a 1:100 scaled Kvapil Type-A physical model to assess the shear strain magnitude of a single isolated drawpoint in a block caving mine, using 13.20 mm basalt aggregate, identical to that used in the SCPG experiments.

The shear strains recorded were used for estimation of total shear strain and strain rate required in Chapter 5 and 6 respectively.

Apparently, there is no test documented or published with regards to the shear strain assessment on the block caving mines particularly due to several restrictions such as experimental difficulty and cost of construction for large scale models (i.e., 1:30 3D physical modelling). On the other hand, efforts to run full scale tests are even harder due to the nature of block caving mine relative to the time constraints, appropriate instrument apparatus and suitable markers.

Nevertheless, this assessment is significant in understanding and assessing the magnitude of shear strain in an isolated single drawpoint of block caving mine in which the results were used as the SCPG parameter. In order to describe the shape and magnitude of shear strain in a systematic way, each marker set was painted and numbered according to its initial position and digital images were taken after each draw and analysed using the Rhinoseros® computer aided drawing program. Typically, the markers were randomly selected in an attempt to minimise any bias in their flow. The results show a zone of high incremental shear strain on the edge of the movement zone, and indicate that the magnitude of shear strain along the central axis of the movement zone was lower compared to that of recorded within the IMZ and IEZ respectively.

### 7.1.2 Numerical Simulations with PFC3D™

Numerical modelling was conducted using a standard desktop computer in which the modelling philosophy was to keep all numerical modelling parameters as close as possible to the SCPG physical and experimental parameters. Subsequently, the DEM simulations in this thesis were aimed to examine fundamental mechanisms across a wide range of parameters, rather than fully calibrated simulations with complete geometric similitude. The numerical modelling comprised of two phases. The first phase involved the simplification of particle shapes and size distributions used in the SCPG physical experiment, by the means of mono-sized spherical particles resembling ideal media. To validate the effectiveness of the numerical model, a comparison between the DPR parameters for the numerical and experimental values was performed. The results show that PFC3D$^{TM}$ was able to capture the essential mechanisms involved in percolation of fine particles and gives a similar pattern to that of the generalised SCPG physical DPR plot.

The numerical models of the SCPG physical experiments were extended in the second phase, to explore more complex non-spherical shapes of crushed basalt aggregate. This was conducted using clump logic where up to six sphere balls were clumped together and behaved as a single bonding clumped particle. The micro-parameters for the clump-particles were similar to the measured properties used in the SCPG physical experiments.

The key findings are that percolation rates are predominantly affected by particle shape and size ratio (or diameter ratio) of the percolating and bed-matrix particles. It was also found that as the bed-matrix particle shape was varied from spheres to cylinders to cuboids to bi-cones, the DPR decreased by up to 10% for the cylinders, 25% for the cuboids, and 40% for the bi-cones relative to spheres.

However, the use of clumped-particles (up to six-clumped particles) employed in the numerical models still do not closely represent highly angular caved rock. Over the range of parameters tested, the exponential plot of DPR was found to varies between 8*exp[-8($d_p / d_b$)] for the mono-sphere basalt to 5*exp[-8.3($d_p / d_b$)] for the six-particle clumps basalt. Alternatively, these values were found to be lower than the DPR exponential plot of SCPG physical experiment. This finding is attributed to limitations on number of clump-particles used and computational limitations. Nevertheless, this study demonstrates that DEM models of non-spherical particles are different to the mono-spheres employed in previous studies and hence need to be considered in future percolation studies on caved rock.

## 7.2 A DISCUSSION ON HYPHOTHESES

An analysis of the hypotheses stated in the beginning of this thesis (Section 1.2) is presented in the following sections. Alternatively, both hypotheses were consolidated and evaluated according to the overall findings from Chapters 2-6.

### 7.2.1 Hypothesis One

The first hypothesis is restated as follows:

"*Particle shape and size significantly influence the percolation of fine particles in bed matrices of highly angular aggregates.*"

It is clearly demonstrated in the physical experiments in Chapter 5 that the effect of particle shape in both the percolating fine and coarser bed-matrix aggregates is significant. For example, under controlled experimental conditions, the comparison between the II and BI series evidently shows that the CPF of fine basalt aggregates was higher than the fine ideal media particles. Subsequently, for the ideal media, the effect of particle shape was significant as the shape varied from spheres to bi-cones to cylinders to cuboids in which the CPF decreased accordingly. Similar observations were found in the IB and BB series. These observations clearly confirm that the particle shape of fine and bed-matrix significantly impacts on the percolation rate of highly angular rock particles, similar to caved rock.

On the other hand, the effect of particle size was examined across fourteen different particle diameter ratios in the II, BI, IB and BB series. It was statistically verified that the larger the particle diameter ratio of the fine and bed-matrix particles, the lower the percolation rate. Considering the above findings, it is argued that, for the range of parameters tested in this thesis, hypothesis one is true.

### 7.2.2 Hypothesis Two

The second hypothesis is restated as follows:

"*Discrete element models incorporating clump representations of angular particles provide different percolation estimates than spherical mono-size particles*."

The above hypothesis is verified by the taking into consideration the numerical study presented in Chapter 6. The effect of clump particles was investigated in four different mono-size assemblies with the following shapes: spheres, bi-cones, cylinders and cuboids. Accordingly, each particle shape was simulated across four different particle diameter ratio: 0.21, 0.28, 0.36 and 0.42 respectively (Section 6.4.2).

Over the range of particle sizes and shapes tested, it was found that the DPR is predominantly affected by particle shape, and the size ratio of the percolating fine and bed-matrix particles. Additionally, the effect of particle size and shape were prominent as the matrix particle shape varied from spheres to cylinders to cuboids to bi-cones in which the DPR decreased accordingly. The implication for mining operations is that highly flaky or angular caved rock will have lower percolation rates than rounded boulders. For these reasons it is argued that, for the parametric ranges tested in this thesis, hypothesis two is true.

## 7.3 CONCLUSIONS

Although percolation studies have been undertaken for more than 50 years (mostly in chemical and powder applications), it was found that these studies focused only on the percolation of single particles and mono-size distributions (i.e., ideal media). The use of ideal media limits is far removed from the actual real world applications especially for the caving mining, civil engineering and mineral processing applications.

The shape effect has been shown to significantly influence percolation in both physical experiments and numerical simulations. Although crushed aggregate media is difficult to measure and characterise, the results offer a closer representation to caved rock.

Physical modelling of percolation is still relevant and the works in this thesis show that changes to industry assumptions, which are based on spherical particles are needed. Nevertheless, experience gained with the SCPG apparatus proves that it is reliable, reproducible and suitable for the study of angular rock fragments similar to caved rock.

Evidently, more complex distributions of non-spherical particles are required to confidently simulate highly angular particles representing caved rock. Given the computational limitations of standard desk-top computers used in this thesis, a greater and more powerful system (e.g., cluster processor) is necessary in order to simulate higher degree of clump-particles number. Nevertheless, it has been shown that the use of non-spherical particles provides closer agreement with the results of physical experiments than mono-spherical particles, but this came at the cost of longer run times and a reduction in the total number of particles. Significantly, the work in this thesis shows the potential of DEM in percolation studies on REV models of caved rock.

Whilst the results presented in this thesis are encouraging and added significantly to the understanding of percolation of fine particles in granular assemblies of angular rock, it is apparent that a number of key questions remain unanswered, and opportunities exist for further studies in appropriate scaled physical models, fully calibrated and validated numerical models and/or at full scale in block caving mines. Full scale tests are necessary to substantiate the results from physical modelling and/or calibrated numerical simulations in order to provide a meaningful and comprehensive knowledge of percolation in caving mines.

In conclusion, an improved knowledge of gravity flow of angular rock particles, especially percolation mechanisms, has general application in the caving mines (e.g., block caving, sub-level caving, back-fill method), minerals processing, geology, civil engineering and other fields such as chemical engineering (i.e., powder and pharmaceuticals).

## 7.4 RECOMMENDATIONS FOR FUTURE RESEARCH

It is shown in this thesis that the knowledge of percolation in angular rock assemblies is at an early stage of understanding. With regard to this statement, an outline of recommended future research is presented in following sections.

### 7.4.1 Physical Models

#### *7.4.1.1 Shear Cell for Percolation of Geomaterials (SCPG)*

In this present thesis, percolation of fine particles was studied for binary mixtures of fine and coarser bed-matrix particles (i.e., II, BI, IB and BB series). In order to more closely represent actual caved rock, it is recommended that more complex size distribution models such as tertiary or quaternary series should be tested. Nevertheless, it is worth highlighting that higher order mixtures may lead to experimental complexities and be extremely time consuming. However, it is suggested that the use of real caved rock fragmentation distributions should be taken into consideration in the future percolation studies.

Additionally, the development of cost-effective, reusable and individually identifiable “smart” markers for use as fine particles would provide insight of the fine percolating mechanisms. Ideally, the markers should be identically matched to the particle properties used in the test (e.g., density, size).

Finally, given that the SCPG apparatus designed for this thesis is believed to be the first apparatus that was designed and fabricated specially for the study of percolation on angular rock fragments, it is recommended that future research should focus on extending the following experimental parameters and apparatus designs:

- effect of sieve aperture size and shape;
- effect of moisture;
- effect of filling method in which the continuous fine particle filling is tested;
- effect of wall friction (or particle-wall friction);
- effect of the coarser bed-matrix height;
- effect of normal stress ($\sigma_n$);
- extension of larger particle diameter ratio (i.e., $d_p / d_b$>0.5);
- SCPG measurement system improvement in the way that the rock dust generated can be remove automatically thus provide better measurement control and significantly reduce experimental time;
- SCPG dimension upgrade in which larger volume, scale and particles size can be tested; and
- improvements in the timer setting system in which the fine marker residence time can be evaluate and recorded automatically thus increase the accuracy of the results.

#### *7.4.1.2 Shear strain assessment in a 1:100 scaled Kvapil Type-A model*

The preliminary shear strain assessments in this thesis are solely based on two dimensional modelling, and a three dimensional scaled model is recommended for future work. Although many physical modelling attempts have focused on the gravity flow of caved rock, no published work was discovered on the assessment of actual shear strains. Subsequently, it is also a prerequisite for scale modelling to be conducted in future work.

In addition, a better representation of particle size distributions more closely representing actual caved rock is required. Finally, similar to the application of cost-effective, reusable and individually identifiable marker in SCPG, the developments of cost effective and re-usable marker is strongly recommended. This is especially in 3D scaled model where the measurement and observation of the marker identification and coordination is difficult and time consuming.

### 7.4.2 Numerical Simulations

The discrete element method has proven to be a powerful and versatile method in the investigation of granular flows but for percolation studies is restricted by computational limits. Accordingly, the representation of large numbers of complex non-spherical shapes (and size distributions) of actual caved rock particularly restricts 3D modelling. One practical recommendation for future research to overcome this limitation may lie within the development of hybrid/coupled continuum-discontinuum.

The development of such hybrid/couple continuum-discontinuum provides complementary features for both input parameter of the particles, and continua. An accurately calibrated and validated hybrid/coupled codes is probably the best alternative to simulate percolation of fine and coarser aggregates of complex non-spherical shape and sizes at large scale of block caving mine. Alternatively, hybrid codes will run as a stand-alone computer codes with the possibility and flexibility of element transformation of granular (or continuum method) into discontinua (or discontinuum method) and vice versa.

# REFERENCES


Abbaspour-Fard, MH 2005, ‘Numerical simulations to investigate the role of particle shape on bulk behavior of particles in silos’, in E Oñate and DRJ Owen (eds), *Proceeding of VIII International Conference on Computational Plasticity (COMPLAS VIII)*, CIMNE, Barcelona, 4 p.

Abriak, NE and Caron, JF 2006, ‘Experimental study of shear in granular media’, *Advanced Powder Technology*, vol. 17, no. 3, pp. 297-318.

Akram, MS and Sharrock, GB 2009, ‘Physical and numerical investigation of a cemented granular assembly under uniaxial and triaxial compression’, in *43rd US Rock Mechanics Symposium and 4th U.S.-Canada Rock Mechanics Symposium*, 28 June-1 July 2009, Asheville, North Carolina, U.S., American Rock Mechanics Society (ARMA), North Carolina, ARMA09-024 (CD-ROM), paper no. 24.

Alvial, J 1992, ‘Analysis of the extraction at Teniente 4 Sur LHD’, in HW Glen (ed.), *Proceedings MassMin 1992*, Johannesburg, SAIMM, Johannesburg, pp. 233- 244.

Aranson, IS and Tsimring, LS 2001, ‘Continuum description of avalanches in granular media’, *Physical Review E*, vol. 64 - 020301(R), 4 p.

Arteaga, P and Tüzün, U 1990, ‘Flow of binary mixtures of equal-density granules in hoppers-size segregation, flowing density and discharges rates’, *Chemical Engineering Science*, vol. 45, pp. 205-223.

ASTM C125-03 2005, 'Standard terminology relating to concrete and concrete aggregate', in SJ Bailey et al. (eds), *Annual Book of ASTM Standards*, vol. 04.02, American Society of Testing Materials, Philadelphia, pp. 68-71.

ASTM Committee E-29 on Particle and Spray Characterization 1998, in LC Pope and CW Ward (eds), *Manual on test sieving methods: guidelines for establishing sieve analysis procedures*, 4th edn, American Society of Testing Materials, Mayfield, PA, United States.

ASTM D3080-98 2000, 'Standard test method for direct shear test of soils under consolidated drained conditions', *Annual Book of ASTM Standards*, vol. 04.08, American Society of Testing Materials, West Conshohocken, PA, United States, pp. 324-239.

ASTM D422-63 2007, 'Standard test method for particle size analysis of soils', *Annual Book of ASTM Standards*, vol. 04.08, American Society for Testing and Materials, Philadelphia, PA, United States.

ASTM D653-04 2005, 'Standard terminology relating to soil, rock, and contained fluids', in SJ Bailey et al. (eds), *Annual Book of ASTM Standards*, vol. 04.08, American Society of Testing Materials, Philadelphia pp. 46-79.

Ashmawy, AK, Sukumaran, B and Hoang, VV 2003, 'Evaluating the influence of particle shape on liquefaction behavior using discrete element modeling', in *Proceedings of the 13th International Offshore and Polar Engineering Conference*, Honolulu, Hawaii, USA, May 25-30, The International Society of Offshore and Polar Engineers, ISBN 1-880653-60-5, pp. 542-549.

Axe, DE 1995, 'Factors affecting uniformity of a mix', *Animal Feed Science and Technology*, vol. 53, no. 2, June 1995, pp. 211-220.

Bagster, DF and Kirk, R 1985, 'Computer generation of a model to simulate granular material behaviour', *Journal of Powder and Bulk Solids Technology*, vol. 9, no. 3, pp. 19-24.

Baiden, GR, Bissiri, Y and Saari, AV 2008, 'Real time sensing of rock flow in a block cave mine', in H Schunnesson and E Nordlund (eds), *Proceeding of*

*5th International Conference and Exhibition of Mass Mining*, 9-11 June 2008, Luleå University of Technology Press, Luleå, Sweden, pp. 993-1002.

Barker, GC 1994, 'Computer simulation of granular materials', in A Mehta (ed.), *Granular matter: an interdisciplinary approach*, Springer-Verlag Inc., New York, pp. 35-83.

Bathurst, RJ and Rothenburg, L 1989, 'Analytical study of induced anisotropy in idealized granular materials', *Geotechnique*, vol. 39, no. 4, pp. 601-614.

Baxter, GW and Behringer, RP 1991, 'Cellular automata models for the flow of granular materials', *Physica D (Nonlinear Phenomena)*, vol. 51, no. 1-3, pp. 465-471.

Bear, J 1972, *Dynamics of fluids in porous media*, American Elsevier Publishing Company, New York, re-edited by Dover Publications, Inc., New York.

Beus, M, Iverson, SR, Dreaschler, A and Scott, S 1999, 'Static and dynamic loads in ore and waste rock passes in underground mines', in B Amadei, RL Kranz, GA Scott and PH Smeallie (eds), *Rock Mechanics for Industries*, Balkema, Rotterdam, pp. 489-495.

Brady, BGH and Brown, ET 2004, *Rock Mechanics for Underground Mining*, 3rd edn, Kluwer Academic Publishers, Dordrecht, the Netherlands.

Bridgwater, J 1994, 'Mixing and segregation mechanisms in particle flow', in A Mehta (ed.), *Granular matter: an interdisciplinary approach*, Springer-Verlag Inc., New York, pp. 161-193.

Bridgwater, J 1995, 'Particle technology', *Chemical Engineering Science*, vol. 50, pp. 4081-4089.

Bridgwater, J and Ingram, ND 1971, 'Rate of spontaneous inter-particle percolation', *Transactions of the Institute of Chemical Engineers*, vol. 49, pp. 163-169.

Bridgwater, J, Cooke, MH and Scott, AM 1978, 'Inter-particle percolation: equipment development and mean percolation velocities', *Transactions of the Institute of Chemical Engineers*, vol. 56, pp. 157-167.

Bridgwater, J, Cooke, MH and Drahun, JA 1985a, 'Shear induced percolation', *Institute of Chemical Engineers Symposium Series 69*, pp. 171-191.

Bridgwater, J, Foo, WS and Stephens, DJ 1985b, 'Particle mixing and segregation in failure zones - theory and experiment', *Powder Technology*, vol. 41, pp. 147-158.

Bridgwater, J, Sharpe, NW and Stocker, DC 1969, 'Particle mixing by percolation', *Transactions of the Institute of Chemical Engineers*, vol. 47, pp. 114-119.

Brown, ET 2003, *Block caving geomechanics*, 1st edn, Julius Kruttschnitt Minerals Research Centre, The University of Queensland, Brisbane, pp. 245-292.

Brunton, ID 2008, 'The impact of blasting on sublevel caving material flow behaviour and recovery', PhD thesis, The University of Queensland, Brisbane.

Brunton, ID, Sharrock, GB and Lett, J 2012, 'Full scale near field material flow behaviour at the Ridgeway Deeps Block Cave operation', abstract submitted to the 6th International Conference on Mass Mining (MassMin 2012), 11-13 June 2012, Sudbury, Ontario, Canada.

BS EN 932-1:1997 1997, *Tests for general properties of aggregates - methods for sampling*, British Standards Institution, ISBN 0580268047.

Campbell, CS 1989, 'The stress tensor for simple shear flows of a granular material', *Journal of Fluid Mechanics*, vol. 203, pp. 449-473.

Campbell, AP and Bridgwater, J 1973, 'Mixing of dry solids by percolation', *Transactions of the Institute of Chemical Engineering*, vol. 51, no. 1, pp. 72-74.

Campbell, CS 1990, 'Rapid granular flows', *Annual Review Fluid Mechanics*, vol. 22, pp. 57-92.

Campbell, CS 2006, 'Granular material flows - an overview', *Powder Technology*, vol. 162, pp. 208-229.

Castro, RL 2003, ‘Report of similitude and scaling in rock flow models’, Julius Kruttschnitt Mineral Research Centre, The University of Queensland, Brisbane.

Castro, RL 2006, ‘Study of the mechanisms of gravity flow for block caving’, PhD thesis, The University of Queensland, Brisbane.

Castro, R, Trueman, R and Halim, A 2006, ‘A study of isolated draw zones in block caving mines by means of a large 3D physical model’, *International Journal of Rock Mechanics and Mining Sciences*, vol. 44, pp. 860–870.

Castro, R and Trueman, R 2008, ‘An experimental review and simulations of gravity flow in coarse materials for block/panel caving’, in H Schunnesson and E Nordlund (eds), *Proceeding of Fifth International Conference and Exhibition of Mass Mining*, 9-11 June 2008, Luleå University of Technology Press, Luleå, Sweden, pp. 1043-1051.

Chambers, D 2008, ‘Block Caving at Pebble - CSP2 Memo’, Centre for Science in Public Participation, Bozeman, MT, March 2008, accessed 9 January 2011, <http://www.csp2.org/reports/Block%20Caving%20at%20Pebble%20-%20CSP2%20Memo.pdf >.

Chen, G 1997, ‘Stochastic modelling of rock fragment flow under gravity’, *International Journal of Rock Mechanics and Mining Sciences*, vol. 34, no. 2, pp. 323-331.

Chen, J and Boshkov, SH 1981, ‘Recent developments and applications of bulk mining methods in the People Republic of China’, in DR Stewart (ed.), *Design and Operation of Caving and Sublevel Stoping Mines*, SME-AIME, New York, pp. 393-418.

Chitombo, GP 2010, ‘Cave mining - 16 years after Laubscher’s 1994 paper ‘Cave mining - state of the art’’, in Y. Potvin (ed.), *Proceeding of Second International Symposium on Block and Sublevel Caving*, 20-22 April 2010, Perth, Australian Centre for Geomechanics, Perth, pp. 45-61.

Cho, N, Martin, CD and Sego, DC 2007, ‘A clumped particle model for rock’, *International Journal of Rock Mechanics and Mining Sciences*, vol. 44, pp. 997-1010.

Christakis, N, Chapelle, P, Patel, MK, Wang, J, Cross, M, Baxter, J, Gröger, T, Abou-Chakra, H, Tüzün, U, Bridle, I and Leaper, MC 2002, 'Mathematical modelling of the behaviour of granular material in a computational fluid dynamics framework using micro-mechanical models', in HA Mang, FG Rammerstorfer and J Eberhardsteiner (eds), *Proceedings of the Fifth World Congress on Computational Mechanics*, July 2-12 2002, Vienna University of Technology, Vienna, Austria, 9 p.

Clark, NN and Meloy, TP 1988, 'Automated cascadography for particle sample shape description', *Powder Technology*, vol. 54, pp. 271-277.

Cleary, PW 1993, 'Design and loading of dragline buckets', *Proceeding Mathematics in Industry Study Group (MISG 1993)*, Melbourne, pp. 39-67.

Cleary, PW 1999, 'The effect of particle shape on hopper discharge', in *2nd International Conference on CFD in the Minerals and Process Industries*, CSIRO, Melbourne, Australia, 6-8 December 1999, Melbourne, pp. 71-76.

Clearly, PW 2008, 'The effect of particle shape on simple shear flows', *Powder Technology*, vol. 179, pp. 144-163.

Clearly, PW and Sawley, ML 2002, 'DEM modelling of industrial granular flows: 3D case studies and the effect of particle shape on hopper discharge', *Applied Mathematical Modelling*, vol. 26, pp. 89-111.

Cooke, MH, Bridgwater, J and Scott, AM 1978, 'Interparticle percolation: lateral and axial diffusion coefficients', *Powder Technology*, vol. 21, pp. 183-193.

Cooke, MH and Bridgwater, J 1979, 'Interparticle percolation: a statistical mechanical interpretation', *Industrial and Engineering Chemical Fundamental*, vol. 18, no. 1, pp. 25-27.

Cundall, PA 1974, 'Rational design of tunnel support: a computer model for rock mass behavior using interactive graphics for the input and out put of geometric data', Technical report MRD-2074, Missouri River Division, U.S. Army Corps of Engineers, The University of Minnesota.

Cundall, PA 1978, 'BALL-A Program to model granular media using the distinct element method', Technical note TN-LN-13, Advanced Technology Group, Dames & Moore, London.

Cundall, PA and Strack, ODL 1979a, 'A discrete numerical model for granular assemblies', Geotechnique, vol. 29, no. 1, pp. 47-65.

Cundall, PA and Strack, ODL 1979b, 'The distinct element method as a tool for research in granular media- Part II', Report to National Science Foundation, NSF Grant ENG76-20711, Department of Civil and Mineral Engineering, University of Minnesota.

Cundall, PA 1988, 'Formulation of a three dimensional distinct element model – Part I. A scheme to detect and represent contacts in a system composed of many polyhedral blocks', *International Journal of Rock Mechanics and Mining Science and Geomechanics Abstracts*, vol. 25, no. 3, pp. 107-116.

de Silva, S, Dyroy A and Enstad, GG 2000, 'Segregation mechanisms and their quantification using segregation testers', in AD Rosato and DL Blackmore (eds), *IUTAM Symposium on Segregation in Granular Flows*, Kluwer Academic Publishers, Boston, pp. 11-29.

Drahun, JA and Bridgwater, J 1983, 'The mechanism of free surface segregation', *Powder Technology*, vol. 36, pp. 39-53.

Duffy, SP 2001, 'A primary tester for size segregation analysis and development and validation of two mathematical models for percolation', PhD thesis, The Pennsylvania State University, University Park.

Duffy, SP and Puri, VM 2000, 'Measurement of percolation during shear', *American Society of Agricultural Engineers (ASAE)*, paper no. 00-4008, St. Joseph, Michigan.

Duffy, SP and Puri, VM 2002, 'Primary segregation shear cell for size-segregation analysis of binary mixtures', *KONA (Powder and Particle)*, vol. 20, pp. 196-207.

Elexon Electronics 2009, ‘How the smart marker system works’, accessed 28 January 2011, <http://www.elexonelectronics.com/sms/HowSmartMarkersWork.aspx>.

Enstad, GG 2001, ‘Segregation of powders - mechanisms, processes and counteraction’, *Handbook of Powder Technology*, vol. 10, pp. 589-602.

Erdoğan, ST 2003, ‘The effect of aggregates on the properties of concrete and proportioning methods’, M.S. thesis, The University of Texas at Austin, Texas.

Fabian, D, Cundall P, Billaux D and Groeger, T 2006, ‘Evaluation of damage-induced permeability using a three-dimensional Adaptive Continuum/ Discontinuum Code (AC/DC)’, *Physics and Chemistry of the Earth*, vol. 32, no. 8-14, pp. 681-690.

Félix, G and Thomas, N 2004, ‘Evidence of two effects in the size segregation process in dry granular media’, *Physical Review E*, vol. 70, pp. 051307 (1-16).

Foo, WS and Bridgwater, J 1983, ‘Particle migration’, *Powder Technology*, vol. 36, pp. 271-273.

Fraige, FY, Langston, PA and Chen, GZ 2008, ‘Distinct element modelling of cubic particle packing and flow’, *Powder Technology*, vol. 186, pp. 224-240.

Fu, Y 2005, ‘Experimental quantification and DEM simulation of micro-macro behaviors of granular materials using X-ray tomography imaging’, PhD thesis, Louisiana State University and Agricultural and Mechanical College

Furuuchi, M and Gotoh, K 1992, ‘Shape separation of particles’, *Powder Technology*, vol. 73, pp. 1-9.

Ghaboussi, J 1990, ‘Three dimensional discrete method for granular materials’, *International Journal for Numerical and Analytical Methods in Geomechanics*, vol. 14, pp. 451-472.

Gögüs, M, İpekci, ON and Kökpinar, MA 2001, ‘Effect of particle shape on fall velocity of angular particles’, *Journal of Hydraulic Engineering*, vol. 127, no. 10, pp. 860-869.

Goldhirsch, I 1999, ‘Scales and kinetics of granular flows’, *CHAOS*, vol. 9, no. 3, pp. 659-672.

Gray, JMNT and Thornton, AR 2005, ‘A theory for particle size segregation in shallow granular free-surface flows’, *Proceedings of the Royal Society A*, vol. 461, pp. 1447-1473.

Guest, AR 2007, ‘The difference between interaction and interactive draw’, in *First International Symposium on Block and Sublevel Caving*, V&A Waterfront, Cape Town, South Africa, The Southern African Institute of Mining and Metallurgy, pp. 123-132.

Guest, AR and Cundall, PA 1994, ‘A three-dimensional particles flow code for block cave modelling’, *The Application of Numerical Modeling in Geotechnical Engineering*, ISRM-SANG, Pretoria, pp. 15-18.

Gustafsson, P 1998, ‘Waste rock content variations during gravity flow in sublevel caving: analysis of full scale experiments and numerical simulations’, PhD thesis, Luleå University of Technology, Luleå, Sweden.

Hadjigeorgiou, J and Lessard, JF 2007, ‘Numerical investigations of ore pass hang-up phenomena’, *International Journal of Rock Mechanics and Mining Sciences*, vol. 44, pp. 820-834.

Hakuno, M and Yamamoto, T 1991, ‘Simulation analysis of dynamic nonlinear behavior of underground structures by the extended distinct element method’, in Beer et al. (eds), *Computer Methods and Advances in Geomechanics*, Balkema, pp. 481-486.

Halim, AE 2004, *3D large scale physical modelling for studying interactive drawing and drawpoint spacing in block caving mines*, Julius Kruttschnitt Mineral Research Centre, The University of Queensland, Brisbane.

Halim, AE 2006, ‘Study of the influence of interactive draw upon drawpoint spacing in block and sublevel caving mines’, PhD thesis, The University of Queensland, Brisbane.

Hamrin, H 2001, 'Underground mining methods and applications', in WA Hustrulid and RL Bullock (eds), *Underground mining methods: engineering fundamentals and international case histories*, Society for Mining, Metallurgy and Exploration, Littleton, Colorado, pp. 3-14.

Hancock, WR, Weatherley, DK and Chitombo, GP 2010, 'Large-scale simulations of gravity flow in block caving', in Y Potvin, *Caving 2010*, 20-22 April 2010, Perth, Australia, Australian Centre for Geomechanics, Perth, pp. 553- 566.

Hashim, MHM, Sharrock, GB and Saydam, S 2008, 'A review of particle percolation in mining', in Y Potvin, J Carter, A Dyskin and R Jeffrey (eds), *Proceeding First Southern Hemisphere International Rock Mechanics Symposium (SHIRMS)*, 16-19 September 2009, Perth, Australia, Australian Centre for Geomechanics, Perth, vol. 1, pp. 273-284.

Hashim, MHM and Sharrock, GB 2009, 'Numerical investigation of the effect of particle shape on percolation', in *43rd U.S. Rock Mechanics Symposium and 4th U.S.-Canada Rock Mechanics Symposium*, 28 June-1 July 2009, Asheville, North Carolina, U.S., American Rock Mechanics Society (ARMA), North Carolina, ARMA09-034 (CD-ROM), paper no. 34, 8 p.

Hashim, MHM and Sharrock, GB 2010, 'Quantification of shear-strains in a 2D block cave scaled physical model', in *ISRM International Symposium - 6th Asian Rock Mechanics Symposium*, 23-27 October 2010, New Delhi, India, Paper ARMS6-2010-025, New Delhi, CBIP-ISRM, 9 p., accessed 3 May 2011, <http://www.onepetro.org>.

Hashim, MHM and Sharrock, GB 2012, 'Effect of size distribution in percolation of fine particles', abstract submitted to the *6th International Conference and Exhibition on Mass Mining (MassMin 2012*), 11-13 June 2012, Sudbury, Canada.

Heslop, TG and Laubscher, DH, 1981, 'Draw control in caving operations on Southern African Chrysotile Asbestos Mines', in DR Stewart (ed.), *Design and operation of caving and sublevel stoping mines*, Society of Mining Engineers - AIME, New York, pp. 755-774.

Hill, JM, Zheng, XM 1994, 'Dynamical modelling of flowing granular materials', Post-doctoral report no. 1/94, University of Wollongong, Department of Mathematics, Wollongong.

Hoek, E and Bray, JW 1981, *Rock slope engineering*, 3rd edn, Taylor and Francis, New York.

Hogg, R 2003, 'Characterization of relative homogeneity in particulate solids', *International Journal Mineral Process*, vol. 72, pp. 477-487.

Hogg, R 2009, 'Mixing and segregation in powders: evaluation, mechanisms and processes', *KONA Powder and Particle Journal*, vol. 27, pp. 1-17.

Hogue, C and Newland, D 1993, 'Efficient computer simulation of moving granular particles', *Powder Technology*, vol. 78, pp. 51-66.

Horwitz, W 1990, 'Nomenclature for sampling in analytical chemistry (Recommendations 1990)', *Pure and Applied Chemistry*, vol. 62, no. 6, pp. 1193-1208.

Hollins, B and Tucker, J 2004, 'Draw point analysis using a marker trial at the Perseverance Nickel Mine, Leinster, Western Australia', in A Karzulovic and M Alvaro (eds), *Proceedings MassMin 2004*, Santiago, Instituto de Ingenieros de Chile, Santiago, pp. 498-502.

Hsiau, S and Shieh, Y 1999, 'Fluctuation and self-diffusion of sheared granular material flows', *Journal of Rheology*, vol. 43, no. 5, pp. 1049-1066.

Hu, J and Stroeven, P 2006, 'Shape characterization of concrete aggregate', *Image Analysis Stereology*, vol. 25, no. 1, pp. 43-53.

Hudson, RY, Herrman, FA Jr., Sagar, RA, Whalin, RW, Kenlegan, GH, Chathamm, CE Jr. and Hales, LZ 1979, 'Coastal hydraulic models', Special report no. 5, *U.S. Army Corps of Engineers*, Coastal Engineering Research Center, May 1979.

Hughes, SA 1993, 'Physical models and laboratory techniques in coastal engineering', *Advanced Series on Ocean Engineering*, vol. 7, World Scientific Publishing Co. Pte. Ltd., Singapore.

Hustrulid, AI 1997, 'Parallel implementation of the discrete element method', Report of Engineering Division, Colorado School of Mines, Golden, CO.

Hutter, K and Scheiwiller, T 1982, ‘Rapid plane flow of granular materials down a chute’, in Mechanics of granular materials, new models and constitutive relations, *Proceeding U.S./Japan Seminar on New Models and Constitutive Relations in the Mechanics of Granular Materials*, 23-27 August 1982, Ithaca, New York, USA, p. 283.

Hutter, K and Rajagopal, KR 1994, ‘On flows of granular materials’, *Continuum Mechanics and Thermodynamics*, vol. 6, pp. 81-139.

Itasca 1999, *PFC3D (Particle Flow Code in 3 Dimensions)*, ver. 2.0, Itasca Consulting Group, Inc., Minneapolis, Minnesota, USA.

Itasca 2003, *PFC3D (Particle Flow Code in 3 Dimensions)*, ver. 3.0, Itasca Consulting Group, Inc., Minneapolis, Minnesota, USA.

Itasca 2005a, *FLAC (Fast Lagrangian Analysis of Continua)*, ver. 5.0, Itasca Consulting Group, Inc., Minneapolis, Minnesota, USA.

Itasca 2005b, *PFC3D (Particle Flow Code in 3 Dimensions)*, ver. 3.1, Modelling software, Itasca Consulting Group, Inc., Minneapolis, Minnesota, USA.

Itasca 2008a, *PFC2D (Particle Flow Code in 2 Dimensions)*, ver. 4.0 - pre-release, Itasca Consulting Group, Inc., Minneapolis, Minnesota, USA.

Itasca 2008b, *PFC3D (Particle Flow Code in 3 Dimensions)*, ver. 4.0 - User’s Manual, Itasca Consulting Group, Inc., Minneapolis, Minnesota, USA.

Iverson, SR, Jung, SJ, Biswas, K 2003, ‘Comparison of ore pass computer simulations for design against dynamic load’, *SME Annual Meeting*, 24-26 Feb 2003, Cincinnati, USA, preprint 03-157, 11 p.

Jaeger, HM and Nagel, SR 1992, ‘Physics of the granular state’, *Science Magazine*, vol. 255, pp. 1523-1531, accessed 5 March 2009, <http://www.sciencemag.org/content/255/5051/1523.full.pdf>.

Jaeger, HM, Naegel, SR and Behringer, RP 1996, ‘Granular solids, liquids and gasses’, *Reviews of Modern Physics*, vol. 68, no. 4, pp. 1259-1273.

Janelid, I 1972, 'Study of the gravity flow process in sublevel caving', in *Proceedings of the International Sublevel Caving Symposium*, Atlas Copco, Stockholm.

Janelid, I and Kvapil, R 1966, 'Sublevel caving', *International Journal of Rock Mechanics and Mining Sciences*, vol. 3, pp. 129-153.

Jensen, RP, Bosscher, PJ, Plesha ME and Edil, TB 1999, 'DEM simulation of granular media structure interface: effects of surface roughness and particle shape', *International Journal for Numerical and Analytical Methods in Geomechanics*, vol. 23, pp. 531-547.

Jensen, RP, Edil, TB, Bosscher, PJ, Plesha, ME and Kahla, NB 2001, 'Effect of particle shape on interface behavior of DEM-simulated granular materials', *International Journal of Geomechanics*, vol. 1, no. 1, pp. 1-19.

Jha, AK, Gill, JS and Puri, VM 2008, 'Percolation segregation in binary size mixtures of spherical and angular-shaped particles of different densities', *Particulate Science and Technology*, vol. 26, no. 5, pp. 482-493.

Jha, AK and Puri, VM 2009, 'Percolation segregation of binary mixtures under periodic movement', *Powder Technology*, vol. 195, pp. 73-82.

Jha, AK and Puri, VM 2010, 'Percolation segregation of multi-size and multi-component particulate materials', *Powder Technology*, vol. 197, no. 3, pp. 274-282.

Jing, L and Hudson, JA 2002, 'Numerical methods in rock mechanics', *International Journal of Rock Mechanics and Mining Sciences*, vol. 39, pp. 409-427.

Johanson, JR 1996, 'Predicting segregation of bimodal particle mixtures using the flow properties of bulk solids,' *Pharmaceutical Technology Europe*, vol. 8, no. 1, pp. 38-44.

Johanson, K, Eckert, C, Ghose, D, Djomlija, M and Hubert, M, 2005, 'Quantitative measurement of particle segregation mechanisms', *Powder Technology*, vol. 159, pp. 1-12.

Just, GD and Free, GD 1971, ‘The gravity flow of material in the sublevel caving mining system’, in *Proceedings First Australia-New Zealand Conference on Geomechanics*, Melbourne, Institution of Engineers, Australia, pp. 88-97.

Just, GD 1981, ‘The significance of material flow in mine design and production’, in DR Stewart (ed.), *Design and Operation of Caving and Sublevel Stoping Mines*, SMEAIME, New York, pp. 715-728.

Kanit, T, Forest, S, Galliet, I, Mounoury, V and Jeulin, D 2003, ‘Determination of the size of the representative volume element for random composites: statistical and numerical approach’, *International Journal of Solids and Structures*, vol. 40, pp. 3647-3679.

Karlsson, T, Klisinski, M and Runesson, K 1999, ‘Finite element simulation of granular material flow in plane silos with complicated geometry’, *Powder Technology*, vol. 99, pp. 29-39.

Kazerani, T and Zhao, J 2010, ‘Micromechanical parameters in bonded particle method for modelling of brittle material failure’, *International Journal for Numerical and Analytical Methods in Geomechanics*, vol. 34, pp. 1877-1895.

Kazerani, T, Yang, ZY and Zhao, J 2011 ‘A discrete element model for predicting shear strength and degradation of rock joint by using compressive and tensile test data’, *Rock Mechanics and Rock Engineering* DOI 10.1007/s00603-011-0153-6, accessed 27 June 2011, <http://www.springerlink.com/content/x7h3100596t53733/fulltext.pdf>.

Ketterhagen, WR, Curtis, JS, Wassgren, CR and Hancock, BC 2008, ‘Modeling granular segregation in flow from quasi-three-dimensional, wedge-shape hoppers’, *Powder Technology*, vol. 179, pp.126-143.

Kwan, AKH and Mora, CF 2001, ‘Effects of various shape parameters on packing of aggregate particles’, *Magazine of Concrete Research*, vol. 53, no. 2, April 2001, pp. 91-100

Kvapil, R 1965a, ‘Gravity flow of granular material in hoppers and bins - Part I’, *International Journal of Rock Mechanics and Mining Sciences*, vol. 2, pp. 35-41.

Kvapil, R. 1965b, ‘Gravity flow of granular materials in hoppers and bins – Part II – coarse materials’, *International Journal of Rock Mechanics and Mining Sciences*, vol. 2, pp. 277-304.

Kvapil, R 1982, ‘The mechanics and design of sublevel caving systems’, in WA Hustrulid (ed.), *Underground mining methods handbook*, Society for Mining, Metallurgy and Exploration (SME), AIME, pp. 880 - 897.

Kvapil, R 1992, ‘Sublevel Caving’, in HL Hartman (ed.), *SME Mining Engineering Handbook*, 2nd edn, Society for Mining, Metallurgy and Exploration (SME), Littleton, Colorado, pp. 1789-1814.

Kvapil, R 2004, Gravity *flow in sublevel and panel caving-a common sense approach*, Luleå University of Technology Press, Luleå, Sweden.

Lamb, TW and Whitman, RV 1969, *Soil mechanics*, John Wiley & Sons, Inc., New York.

Langhaar, HL 1951, *Dimensional analysis and the theory of models*, Wiley, New York.

Laubscher, DH 1994, ‘Cave mining - the state of the art’, *Journal of the South African Institute of Mining and Metallurgy*, vol. 94, no. 10, pp. 279-293.

Laubscher, DH 2000, ‘Block caving manual’, Julius Kruttschnitt Mineral Research Centre, The University of Queensland, Brisbane, Australia and Itasca Consulting Group.

Lebron, I and Robinson, DA 2003, ‘Particle size segregation during hand packing of coarse granular materials and impacts on local pore-scale structure’, *Vadose Zone Journal*, vol. 2, pp. 330-337.

Lewis, RS and Clark, GB 1964, *Element of mining*, 3rd edition, John Wiley & Sons, Inc., New York.

Li, H 2005, Impact of cohesion forces on particle mixing and segregation’, PhD thesis, School of Engineering, University of Pittsburgh.

Li, J, Yu, AB, Bridgwater, J and Rough, SL 2010, 'Spontaneous inter-particle percolation: a kinematic simulation study', *Powder Technology*, vol. 203, pp. 397-403.

Li, L and Holt, RM 2001, 'Simulation of granular material using particle model with non-circularly shaped super-particles', in P Särkkä and P Eloranta (eds), *Rock mechanics: a challenge for society, Proceedings of the ISRM Regional Symposium Eurock 2001*, Espoo, Finland, 4-7 June 2001, International Society for Rock Mechanics, Swets & Zeitlinger Publishers, Lisse, The Netherlands, pp. 511-522

Lin, X and Ng, TT 1997 'A three-dimensional discrete element model using arrays of ellispoids', *Geotechnique*, vol. 47, no. 2, pp. 319-329.

Lourel, I, Wu, W and Morrison, DJ 2006, 'Experimental validation on the computational modelling of granular flow using the discrete element method (DEM)', *Asia-Pacific Bulk Materials Handling Conference (BULKEX 2006)*, Melbourne, Australia 25-27 September 2006, 14 p.

Makse, HA 1997, 'Stratification instability in granular flows', *Physical Review E*, vol. 56, no. 6, pp. 7008-7018.

Makse, HA 1999, 'Kinematic segregation of flowing grains in sandpiles', *European Physical Journal B*, vol. 7, pp. 271-276.

Marano, G 1980, 'The interaction between adjoining draw points in free flowing materials and its application to mining', *Chamber of Mines Journal*, Zimbabwe, pp. 25-32.

Marsal, RJ 1973, 'Mechanical properties of rockfill', in RC Hirschfeld and SJ Poulos (eds), *Embankment dam engineering- Casagrande volume*, John Wiley & Sons, Inc., New York, pp. 109-200.

Massol-Chaudeur, S, Berthiaux, H and Dodds, JA 2002, 'Experimental study of the mixing kinetics of binary pharmaceutical powder mixtures in a laboratory hoop mixer', *Chemical Engineering Science*, vol. 57, pp. 4053-4065.

Matveev, AV, Barysheva, LV, Koptyug, IV, Khanaev, VM and Noskov, AS 2006, ‘Investigation of fine granular material flow through a packed bed’, *Chemical Engineering Science*, vol. 61, pp. 2394-2405.

McMurray, DT 1976, ‘Sublevel caving at Shabanie mine, Rhodesia’, *Institution of Mining and Metallurgy*, October, pp. A136-A143.

McNearny, RL and Abel Jr, JF 1993, ‘Large-scale two-dimensional block caving model tests’, *International Journal of Rock Mechanics and Mining Sciences and Geomechanics Abstract*, vol. 30, no. 2, pp. 93-109.

McNearny, RL and Barker, KA 1998, ‘Numerical modelling of large-scale block cave physical models using PFC2D’, *Mining Engineering*, Technical paper, February 1998, pp. 72-75.

Melo, F, Vivanco, F, Fuentes, C and Apablaza, V 2006, ‘Kinematic model for quasi static granular displacement on block caving: dilatancy effect on drawbody shapes’, *preprint submitted to International Journal of Rock Mechanics and Mining Sciences*, 22 p.

Melo, F, Vivanco, F, Fuentes, C and Apablaza, V 2007, ‘On drawbody shapes: from Bergmark-Roos to kinematic models’, *International Journal of Rock Mechanics and Mining Sciences*, vol. 44, pp. 77-86.

Meloy, TP, Clark, NN, Durney, TE and Pitchumani, B 1985, ‘Measuring the particle shape mix in a powder with the cascadograph’, *Chemical Engineering Science*, vol. 40, pp. 1077-1084.

Mishra, BK and Rajamani, RK 1992 ‘Discrete element method in modelling ball mills’, *Journal of Applied Mathematical Modelling*, vol. 16, pp. 598-604.

Mosby, J, de Silva, SR and Enstad, GG 1996a, ‘Segregation of particulate materials-mechanisms and testers’, *KONA (Powder and Particle)*, vol. 14, pp. 31-42.

Mosby, J, de Silva, SR and Enstad, GG 1996b, ‘Segregation of sugar during flow’, *Transactions of ASAE*, vol. 41, no. 5, pp. 1469-1476.

Motion Technologies Pty. Ltd. 2010, *IJ SuperJack heavy duty industrial actuator series*, 4 p., accessed 3 Mac 2010, <www.motiontech.com.au/assets/pdf/IJ%20Superjack.pdf>.

Muller, D 1996 'Techniques informatiques efficaces pour la simulation de milieux granulaires par des methodes d'elements distincts'(in French), PhD Thesis, no. 1545, Dept. de mathematiques, École Polytechnique.

Nakao, T and Fityus, S 2008, 'Direct shear testing of a marginal material using a large shear box', *Geotechnical Testing Journal*, vol. 31, no. 5, Paper ID GTJ101237, 11 p.

Nedderman, RM 1992, *Statics and kinematics of granular materials*, Cambridge University Press, Cambridge.

Nedderman, RM 1995, 'The use of the kinematic model to predict the development of the stagnant zone boundary in the batch discharge of a bunker', *Chemical Engineering Science*, vol. 50, pp. 959-965.

Ng, TT 1989, 'Numerical simulation of granular soil under monotonic and cyclic loading: a particulate mechanics approach', PhD Thesis, Department of Civil Engineering, Renssler Ploytechnic Institute, Troy, New York.

Ng, TT and Dobry, R 1991, 'CONBAL- simulated granular material using quartz sphere with the discrete element method', Report to NSF, Rensseler Polytechnic Institute, Troy, New York.

Ng, T 2005, 'Behavior of gravity deposited granular material under different stress paths', *Canada Geotechnics Journal*, vol. 42, pp. 1644-1655.

Ng, BH, Ding, Y and Ghadiri, M 2008, 'Assessment of the kinetic–frictional model for dense granular flow', *Particuology*, vol. 6, no. 1, February 2008, pp. 50-58.

Ottino, JM and Khakhar, DV 2000, 'Mixing and segregation of granular materials', *Annual Review Fluid Mechanics*, vol. 32, pp. 55-91.

Pakalnis, R, Poulin, R and Vongpaisal, S 1995, 'Quantifying dilution for underground mine operations', *International Mining Trade Show and 97th Annual Meeting* *of the Canadian Institute of Mining, Metallurgy and Petroleum (CIM AGM)*, 15-18 May 1995, Halifax, Nova Scotia, Canada, paper no. 7.2.

Peters, DC 1984, 'Physical modeling of the draw behavior of broken rock in caving', *Quarterly of the Colorado School of Mines*, vol. 79, no. 1, pp. 1-60.

Pierce, ME, Cundall, PA, van Hout, GJ and Lorig, L 2003, 'PFC3D modeling of caved rock under draw', in H Konietzky (ed.), *Proceeding of the First International PFC Symposium: Numerical Modeling in Micromechanics via Particle Methods*, Gelsenkirchen, Germany, Balkema, Lisse, pp. 211-217.

Pierce, ME 2004, 'PFC3D modeling of inter-particles percolation in caved rock under draw', in Y Shimizu, R Hart and P Cundall (eds), *Numerical Modeling in Micromechanics via Particle Methods*, Taylor and Francis Group, London, pp. 149-156.

Pierce, ME 2010, 'A model for gravity flow of fragmented rock in block caving mines', PhD thesis, The University of Queensland, Brisbane.

Potyondy, DO and Cundall, PA 2004, 'A bonded-particle model for rock', *International Journal of Rock Mechanics and Mining Sciences*, vol. 41, no. 8, pp. 1329-1364

Pöschel, T, Saluena, C and Schwager, T 2001, 'Scaling properties of granular material', *Physical Review E*, vol. 64, no. 1, pp. 011308(1-4).

Power, GR 2004, 'Modelling granular flow in caving mines: large scale physical modelling and full scale experiments', PhD thesis, The University of Queensland, Brisbane.

Powrie, W, Ni, Q, Harkness, RM and Zhang, X 2005, 'Numerical modelling of plane strain tests on sands using a particulate approach', *Geotechnique*, vol. 55, no. 4, pp. 297-306.

Pretorius, D 2007, 'The effect of dilution on the underground block cave ore reserves at Palabora Mining Company', *Proceedings First International Symposium on Block and Sublevel Caving*, V&A Waterfront, Cape Town, South Africa, The Southern African Institute of Mining and Metallurgy, Johannesburg, South Africa, pp. 73-82.

Quinteiro, CR, Larsson, L and Hustrulid, WA 2001, ‘Theory and practice of very large scale sublevel caving’, in WA Hustrulid and RL Bullocks (eds), *Underground mining methods: engineering fundamentals and international case studies*, SME, Littleton, Colorado, pp. 381-394.

Ridgway, K and Rupp, R 1970, ‘The flow of granular material down chutes’, *Chemical and Process Engineering*, vol. 51, no 5, pp. 82-85.

Ridgway, K and Rupp, R 1971, ‘The mixing of powder layers on a chute: the effect of particle size and shape’, *Powder Technologies*, vol. 4, pp. 195-202.

Robinson, DA and Friedman, SP 2002, ‘Observations of the effects of particle shape and particle size distribution on avalanching of granular media’, *Physica A (Amsterdam)*, vol. 311, pp. 97-110.

Rosato, AD and Blackmore, DL 2000, *IUTAM symposium on segregation in granular flows*, Kluwer Academic Publishers, Dordrecht, The Netherlands.

Rosato, AD and Kim, H 1994, ‘Particle dynamics calculations of wall stresses and slip velocities for Couette flow of smooth inelastic spheres’, *Continuum Mechanics and Thermodynamics*, vol. 6, pp. 1-20.

Rothenburg, L and Bathurst, RJ 1991, ‘Numerical simulation of idealised granular assemblies with plane elliptical particles’, *Journal of Computers and Geotechnics*, vol. 11, pp. 315-329.

Rustan, A 2000, ‘Gravity flow of broken rock- what is known and unknown’, in *Proceeding MassMin 2000*, Brisbane, Australia, The Australasian Institute of Mining and Metallurgy, Brisbane, pp. 557-567.

Rycroft, CH, Kamrinc, K and Bazantd, MZ 2009, ‘Assessing continuum postulates in simulations of granular flow’, *Journal of the Mechanics and Physics of Solids*, vol. 57, no.5, pp. 828-839.

Saiang, D 2009, 'Stability analysis of the blast-induced damage zone by continuum and coupled continuum-discontinuum methods', *Engineering Geology*, DOI:10.1016/j.enggeo.2009.07.011.

Sakakibara, T, Kato, S, Shibuya, S and Chae, JG 2008, 'Effects of grain shape on mechanical behaviours and shear band of granular materials in DEM analysis', in R Hart et al. (eds), *Continuum and Distinct Element Numerical Modelling in Geo-Engineering*, Itasca Consulting Group Inc., Minneapolis, paper 08-08, 9 p.

Sandstrom, PO 1972, 'Application and optimization of sublevel caving techniques', *Engineering and Mining Journal*, June, pp.112-125.

Savage, SB 1987, 'Interparticle percolation and segregation in granular materials', in APS Selvadurai (ed.), *Developments in engineering mechanics*, Elsevier Science Publishers, Amsterdam, pp. 347-363.

Savage, SB and Dai, R 1993, 'Studies of shear flows, wall slip velocities, 'layering' and 'self-diffusion'', *Mechanics of Material*, vol. 16, pp. 225-238.

Schulze, D 2003, Frequently asked questions, accessed 3 February 2011, <http://www.dietmar-schulze.de/faqe.html>.

Schuring, DJ 1977, *Scale models in engineering: fundamental and applications*, Pergamon Press, New York.

Schwedes, J 2003, 'Review on testers for measuring flow properties of bulk solids', *Granular Matter*, vol. 5, pp. 1-43 , DOI 10.1007/s10035-002-0124-4.

Schwedes, J and Schulze, D 1990, 'Measurement of flow properties of bulk solids', *Powder Technology*, vol. 61, pp. 59-68.

Scott, AM and Bridgwater, J 1975, 'Interparticle percolation: a fundamental solids mixing mechanism', *Industrial and Engineering Chemistry Fundamentals*, vol. 14, no. 1, pp. 22-27.

Scott, AM and Bridgwater, J 1976, 'Self diffusion of spherical particles in a simple shear apparatus', *Powder Technology*, vol. 14, pp. 177-183.

Sharrock, GB 1999, 'Application of lattice grain cellular automata to sublevel caving', Technical notes on development of cellular automata theory.

Sharrock, GB 2003, 'Tool shearing of granular media', PhD thesis, The University of Queensland, Brisbane.

Sharrock, GB 2008, 'The isolated extraction zone in block caving - a review', in Y Potvin, J Carter, A Dyskin and R Jeffrey (eds), *Proceeding First Southern Hemisphere International Rock Mechanics Symposium (SHIRMS)*, 16-19 September 2009, Perth, Australia, Australian Centre for Geomechanics, Perth, vol. 1, pp. 255-271.

Sharrock, GB and Hashim, MHM 2009, 'Disturbed gravity flow in block caving', in *43rd US Rock Mechanics Symposium and Fourth U.S.-Canada Rock Mechanics Symposium (ARMA 2009)*, 28 June-1 July 2009, Asheville, North Carolina, U.S., American Rock Mechanics Society (ARMA), North Carolina, ARMA09-070 (CD-ROM), paper no. 70, 12 p.

Shi, GH 1988, 'Discontinous deformation analysis', PhD thesis, University of California, Berkeley, USA.

Shinohara, K, Shoji, K, Tanaka, T 1972, 'Mechanism of size segregation of particles in filling a hopper', *Industrial and Engineering Chemistry Process Design and Development*, vol. 11, no. 3, pp. 369-376.

Shinohara, K 1979, 'Mechanism of segregation of differently shaped particles in filling containers', *Industrial and Engineering Chemistry Process Design and Development*, vol. 18, no. 2, pp. 223-227.

Spencer, AJM 1980, *Continuum mechanics*, Longman Group Limited, New York.

Stephens, DJ and Bridgwater, J, 1978a, 'The mixing and segregation of cohesionless particulate materials part II: Microscopic mechanisms for particles differing in size', *Powder Technology*, vol. 21, pp. 29-36.

Stephens, DJ and Bridgwater, J 1978b, 'The mixing and segregation of cohesionless particulate materials - Part I: failure zone formation', *Powder Technology*, vol. 21, pp. 17-28.

Sterrett, SG 2002, ‘Physical models and fundamental laws: using one piece of the world to tell about another’, *Mind and Society 5*, vol. 3, pp. 51-66.

Tanaka, T 1971, ‘Segregation models of solid mixtures composed of different densities and particle sizes’, *Industrial and Engineering Chemistry Process Design and Development*, vol. 10, no. 3, pp. 332-340.

Tang, P 2004, ‘Percolation and sieving segregation patterns-quantification, mechanistic theory, model development and validation, and application’, PhD thesis, The Pennsylvania State University, University Park.

Tang, P and Puri, VM 2004, ‘Methods for minimizing segregation: a review’, *Particulate Science and Technology*, vol. 22, no. 4, pp. 321-337.

Tang, P and Puri, VM 2007, ‘Segregation quantification of two-component particulate mixtures: effect of particle size, density, shape and surface texture’, *Particulate Science and Technology*, vol. 25, no. 6, pp. 571-588.

Tang, P, Puri, VM and Patterson, PH 2003, ‘Design, development, and performance of second generation primary segregation shear cell for size-segregation’, Paper presented at Particulate Systems Analysis 2003, Sept. 10-12, Harrogate, U.K.

Tardos, GI 1997, ‘A fluid mechanistic approach to slow, frictional flow of powders’, *Powder Technology*, vol. 92, pp. 61-74.

Taylor, LM and Preece, DS 1989, ‘DMC- a rigid body motion code for determining the interaction of multiple spherical particles – Part 1’, Sandia National Laboratories, New Mexico, (Report SAND-88-3482).

Terzaghi, K, Peck, R and Mesri, G 1996, *Soil mechanics in engineering practice*, John Wiley & Sons, Inc., New York.

Ting, JM, Corkum, BT, Kauffman, CR and Greco, C 1989, ‘Discrete numerical model for soil mechanics’, *Journal of Geotechnical and Geoenvironmental Engineering – ASCE*, vol. 115, no. 3, pp. 379-398.

Trueman, R, Castro, R, and Halim, A 2008, ‘Study of multiple draw-zone interaction in block caving mines by means of a large 3D physical model’, *International Journal of Rock Mechanics and Mining Sciences*, vol. 45, pp. 1044-1051.

U.S. Pharmacopeia n.d., *General chapter: 1174 – powder flow*, accessed 25 January 2011, < http://www.pharmacopeia.cn/v29240/usp29nf24s0_c1174.html>.

Vallance, JW and Savage, SB 2000, 'Particle segregation in granular flows down chutes', in AD Rosato and DL Blackmore (eds), *IUTAM Symposium on Segregation in Granular Flows*, Kluwer Academic Publishers, Boston, pp. 31-51.

Walton, OR, Braun, RG, Mallon, DM and Cervelli, DM 1988, 'Particle dynamic calculations of gravity flow inelastic fractional spheres', in M Satake and JT Jenkins (eds), *Micromechanics of granular media*, Elsevier Science Publishers, Amsterdam, pp. 153-161.

Weatherley, D 2009, 'ESyS-Particle: HPC Discrete Element Modelling Software', accessed 1 January 2011, <https://launchpad.net/esys-particle>.

Wellmer, FW, Dalheimer, D and Wagner, M 2008, *Economic evaluations in exploration*, 2nd edn, Springer Berlin Heidelberg, New York

White, HE and Walton, SF 1937, 'Particle packing and particle shape', *Journal of the American Ceramic Society*, vol. 20, no. 1-12, pp. 155-166.

Williams, JC 1976, 'The segregation of particulate materials: a review', *Powder Technology*, vol. 15, pp. 245-251.

Williams, JR and Pentland, AP 1989, 'Superquadratics and modal dynamics for discrete elements in concurrent design', in GGW Mustoe, M Henriksen and HP Huttelmaier, *Proceding of First U.S. Conference on Discrete Element Methods*, October 1989, Golden, Colorado, Colorado School of Mines Press, Colorado, pp. 19-35.

Wyllie, DC 1999, *Foundation on rock*, 2nd edn, E&FN Spon, London.

Xu, BH and Yu, AB 1997, 'Numerical simulation of the gas-solid flow in a fluidised bed by combining discrete particle method with computational fluid dynamics', *Journal of Chemical Engineering Science*, vol. 52, no.16, pp. 2785-2809.

Yenge, LI 1980, 'Analysis of bulk flow of materials under gravity caving processes. Part 1: sublevel caving in relation to flow in bins and bunkers', *Quarterly of Colorado School of Mines*, vol. 75, no. 4.

Yi, H, Li, F, Mittal, B, Puri, VM and Mancino, CF 2001, 'Measurement of bulk mechanical properties and modeling the load-response of root zone sands. Part 1: Round and angular monosize and binary mixtures', *Particulate Science and Technology*, vol. 19, no. 2, pp. 145-173.

# APPENDICES

# APPENDIX A: SIGNIFICANT MODELLING STUDIES ON THE ISOLATED EXTRACTION ZONE

Table A1: Significant modelling studies on the IEZ (after Sharrock 2008)

| Authors/Year/Model description | Remarks and conclusions |
|---|---|
| Lehman (1916)<br>Scale: 1:60<br>Model Size: (w:d:h): (0.76:0.51:64) m<br>Prototype Size (w:d:h): (46:31:38) m<br>Medium: Crusher ore and waste<br>Mine: Inspiration (BC) | Aim: Investigate the rate of dilution entry for waste rock placed above ore.<br>Method: 16 experiments were run, and results reported for a range of size fractions.<br>Results: (1) The less distance between chute centres, the greater the extraction; (2) The higher the ore column, the greater the extraction; (3) The less the amount draw at a time from each chute, uniformly, the great the extraction of clean ore before the capping(waste) appeared; (4) The coarser the ore and capping without fines, the greater the extraction; (5) The higher the grade of ore, the greater the extract, when a uniform limit of grade is allowed at the end of the chute drawing. |
| McNicholas et al. (1946)<br>No markers placed in model | Aim: Studied ore recovery in Miami copper, and Climax Molybdenum mines (USA).<br>Results: Commented on higher potential for arching at drawpoints for coarse fragmentation, as compared to fine fragmentation. |
| Redaelli (1963)<br>Scale: 1:50<br>Medium: Sand | Scale modelling was used to help design the layout for Koskullskulle sub-level cave. |
| Kvapil (1965a)<br>Medium: Sand<br>Mine/Context: Flow in Bins | First quantitative attempt to understand mechanisms controlling gravity flow. Developed ellipsoidal theory, postulated IEZ width increases with particle size. Marker system proposed. Commented that exact shape of extraction zone could only be found using full scale tests. |
| Kvapil (1965b) | Extension of Kvapil (1965a) to coarse materials. Mentions particle rotation and translation. |
| Airey (1965)<br>Scale: 1:50<br>Mine: Mufalira (SLC) | Two models were presented for the design of Mufulira mine: (1) SLC: determined angle of draw and ore recovery from dead zone between drawpoints; (2) Section through SLC "trial" mining area on a ring by ring basis. |
| Janelid and Kvapil (1966) | Applied Kvapil (1965a; 1965b) to sub-level caving. Noted importance of particle size of ore relative to waste. Proposed design rules for the planning of sub-level caving layouts. |
| McCormick (1968) | Commented that an ellipse does not accurately represent the shape of the IEZ for broken rock.<br>Results: at high values of draw height, the extraction is approximated by a cylinder with a conical base, and hemispherical top, rather than an ellipse. |
| Haglund (1968) | Reported Ahlin's work on experiments at 1:10, 1:50 and 1:100 scale.<br>Results: each scale were not convertible. According to Halim (2006) results were based on limited data set. |

| | |
|---|---|
| Gardner (1966) | 2D experimental work on flow in bins and hoppers.<br>Results: (1) Mathematical model forecasting shape of dead zones as function of angle of internal friction. (2) considered density changes in model resulting from loading procedure. (3) walls of model had layer of granular media. Level of media in model kept constant. |
| Free (1970); Just and Free (1971)<br>Scale: 1:60<br>Model size (w:d:h): (0.76:0.51:64) m<br>Prototype size (w:d:h): (46:31:38) m | Found ellipse theory is a good fit for a range of material types using a 2D Model.<br>Found that for glass beads IEZ width increases with particle diameter (three sizes considered) which supports Kvapil (1965a).<br>Mine: 2D Longitudinal and Transverse SLC Layout.<br>Medium: Glass Beads (3, 5, 8) Gravel (1.6, 7.9) mm |
| Janelid (1972) | Compared Grangesberg full scale SLC experiments with 1:20 model, and found good agreement.<br>Results: scale model tests give a higher and narrower drawzone, since the model material is less packed and has higher mobility than the prototype. Friction angle has an effect on draw width – greater friction angle results in greater draw width. |
| Sandstrom (1972) | SLC Model examining 3D modelling and similitude requirements such as media mass, consolidation and friction. Tests with crushed ore give qualitative quantitative results that are useful. Recommended wall of model be roughened to represent particle internal friction angle. |
| Janelid (1972) | Commented that an ellipse does not accurately represent the shape of the IEZ or IMZ for broken rock at high values of IEZ height. |
| McMurray (1976)<br>Model size (w:d:h): (0.76:0.76:2.4) m | Documents modelling work at Shabanie SLC asbestos mine. Heslop and Laubscher (1981) report some details on model. |
| Panczakiewicz (1977) | 1:50 scale 2D and 3D experiments on SLC layout. Investigated effect of vertical compaction of media though the use of a custom designed compactor. Did not relate modelled compaction to prototype. Presented description of mechanisms influencing gravity flow. |
| Marano (1980)<br>Scale: 1:80<br>Model size (w:d:h): (0.76:0.76:2.40) m<br>Prototype size (w:d:h): (60:60:192) m | Used a 1:80 scale sand model to examine interactive draw in block caving. Commented that at high values of draw height, the extraction zone is approximated by a cylinder with a conical base, and hemispherical top. This supports McCormick (1968). Commented on interaction theory, and that in multiple drawpoint scenarios, application of ellipse theory was incorrect.<br>Medium: Sand ($p_{50}$ = 0.7 mm). |
| Chen and Boshkov (1981) | Full scale SLC test at He-Pei (China). Markers used to determine IEZ. |
| Yenge (1980; 1981) | 2D models at Colorado School of Mines, examined the influence of selected parameters on the gravity flow of gravel. Used marker system, and repeated experiments 7 to 14 times. Refilled model. Based on Gardner (1966) and Sandstrom (1972) used nails through glass panel to roughen the model wall to represent particle internal friction angle. Found that for small column heights ellipse theory is a good representation of IEZ (i.e. SLC mines). |

| | |
|---|---|
| Heslop and Laubscher (1981)<br>Scale: 1:80<br>Model size (w:d:h): (0.76:0.76:2.40) m<br>Prototype size (w:d:h): (60:60:192) m<br>Medium: Sand ($p_{50}$=0.7 mm) | Interpreted and documents McMurray (1976). Used scale modelling and observations to establish basic mechanics of gravity flow for block caving mines. Commented on interaction theory, and that in multiple drawpoint scenarios, application of ellipse theory was incorrect. Measured IDZ width as 108 mm.<br>Mine/Context: (BC). |
| Peters (1984)<br>Scale: 1:50<br>Model size (w:d:h):<br>(0.5:3.6:4.5) m<br>Prototype size (w:d:h): n/a<br>Medium: Gravel (12, 25, 38) mm | Investigated the effect of particle size and drawpoint width on the extraction zone size and shape. layers of markers. Concluded that size has minimal influence on drawzone width. Power (2004) notes that the model width was restricted relative to height, hence results cannot be applied in 3D. For small column heights ellipse theory is a good representation of IEZ (i.e. SLC mines). Found no interaction at drawpoint spacing of 1.14 times the width of the IEZ. Markers used. |
| Alvial (1992) | Full scale BC tests at El Teniente mine Chile. A single layer of "tyres" used as markers. 19 were recovered over a 10 years period. Data could not be used to define the IEZ geometry. |
| McNearny and Abel (1993)<br>Model size (w:d:h):<br>(0.9:4.6:6.1) m<br>Prototype size (w:d:h): (60:60:192) m<br>Medium: Bricks (w:d:h): (53:95:95) mm | Large scale 2D tests using bricks<br>Aim: to measure and compare movement zones with UDEC simulations.<br>Results: shape of drawzone (inverted cone) is substantially different to the draw envelope produced by 1 inch nominal gravel (ellipse). The distribution of stress controls drawing behaviour. |
| Gustafsson (1998) | Full scale SLC tests at Kiruna (Sweden). |
| Sharrock (1999) | Developed 3D cellular automata for granular flow, which was later used to recover IEZ width data. |
| Hollins and Tucker (2004); Szwedzicki and Cooper (2007) | Full scale SLC tests at Perseverence mine Leinster (Australia). Developed IEZ geometric parameters for a range of blasting and recovery scenarios. Results linked to mass drawn, each bucket load was "laid out". |
| Lowther (pers. comm., 2008) | Full scale SLC marker trial at Ridgway mine (Australia). Over 50 rings were tested, and results continue to be compiled to 2008. Key results included quantification of IEZ width, and height, and associated ore recovery. |
| Pierce et al. (2003) | PFC3D numerical models of particle friction, size and shape for isolated draw column, approximately 30 m high. Models were developed for the ICS and were used in conjunction with Power (2004) scale physical model, to calibrate REBOP. |
| Sharrock (2003)<br>Scale: 1:100<br>Medium: Gravel (5, 15) mm | 2D scaled physical model for investigation of particle micro-mechanics.<br>Aim: to exam shear banding in granular media, through a simple glass sided window.<br>Mine: Perseverance – Leinster |

| | |
|---|---|
| Pierce and Hakan (2004) | Development of REBOP (Rapid Emulator based on PFC3D). Encodes algorithms describing erosion and collapse, and in particular the relation between particle size and IEZ transient geometry, derived from Power (2004). |
| Power (2004)<br>Scale: 1:30<br>Model size (w:d:h):<br>(2.1:2.2:3.3) m<br>Prototype size m (w:d:h):<br>(63:66:99) m | Found a weak correlation between particle size and IEZ width for 5, 7 and 14 mm gravel based on one repetition of experiments. Found no similar relation between 14 and 20 mm gravel.<br>Marker Pattern: 100 mm spacing (actual 3 m).<br>Mine: drawbell based on Palabora. Concluded that an ellipsoid is a good model for the IEZ up to draw height of 100 m. |
| Halim (2004) | Compared results from Power (2004), Chen and Boshkov (1981) and JKMRC (2003), against Kvapil (1965a). Concluded that the curves provided in Kvapil (1965a) give poor estimates of IEZ width for a given IEZ height for three brief case studies. |
| Pretorius (2006)<br>Scale: 1:100 | Key aim was to determine dilution entry point. Waste was introduced into the top of the model as glass beads. Percolation was tracked. Ore flow tracked by position markers. More details are required to fully understand this model, but it appears to represent a slice through the orebody, with a window to observe flow.<br>Mine: Palabora (BC). |
| Castro et al. (2006)<br>Scale: 1:100<br>Model size (w:d:h):<br>(2.1:2.2:3.3) m<br>Actual size (w:d:h):<br>(210:220:330) m<br>Medium: Gravel (8,18) mm | Examined the effect of particle size and height of draw has on the isolated extraction and movement zone geometries. Results: main variables affecting IEZ are mass drawn and the height of draw. Particle size has minimal influence on IEZ and IMZ width. Contradicts previous study by Power (2004) undertaken with the same model, (but at 1:30 scale). Also found no significant distortion between 1:30 and 1:100 scale. Implies it is possible to extrapolate results from model scale to full scale. |
| Brunton (2008) | Aim: Study blasting effects in sub level caving at Ridgeway mine, Australia. |
| Trueman et al. (2008)<br>Model: Same as Castro et al. (2006)<br>Medium: Gravel (8) mm | Aim: to study interaction of MZ’s, for a large number of drawpoints. Four experiments were undertaken. The first two assessed the IMZ dimensions for isolated draw: found similar results to Castro et al. (2006). The other experiments studied MZ’s associated with nine drawpoints spaced 780 mm apart. Results showed no interaction at 1.2 times the IDZ width or greater. By contrast Heslop and Laubscher (1981) recorded interaction at values less than 1.5 times the IDZ width. |
| Sharrock et al. (2008)<br>Scale: 1:100<br>Model size (w:d:h):<br>(1.5:1.5:2.5) m<br>Actual size m (w:d:h):<br>(150:150:250) m<br>Medium: Gravel (5) mm | Detailed investigation of IEZ for three interrelated parameters: stress on major, minor apex, and IEZ/IMZ boundaries. Detailed particle scale examination of the isolated extraction zone geometry, and movement zone. Experiments were repeated size times at high resolution. Variance in IEZ geometry was categorised.<br>Marker Pattern: 10 mm spacing (actual 1 m). |

| | |
|---|---|
| Hashim and Sharrock (2009)<br>Scale: 1:100<br>Model size (w:d:h):<br>(1.0:1.0:0.13) m<br>Actual size (w:d:h):<br>(100:100:13) m<br>Medium: Gravel ($p_{50}$=13.20) mm | A 1:100 scaled 2D Kvapil's Type-A Model using gravel aggregate as a medium was employed to assess the shear strain experienced in an isolated drawpoint, representing a block caving mine. Shear strain ($\gamma$) was found to have magnitude of $\gamma \leq 0.05$ per draw event along the central axis of the movement zone. By contrast, a significantly higher magnitude of $0.01 \leq \gamma \leq 0.10$ per draw event was recorded off-axis, in the IMZ and IEZ respectively.<br>Marker Pattern: A set of four markers in a rectangle pattern at approximately 50 mm spacing (actual 5 m). Each set were divided into six horizontal levels and were positioned at approximately at a row spacing of 150 mm and column spacing of 100 mm respectively |

# APPENDIX B: PHYSICAL MODELLING – MATERIAL PROPERTIES AND CHARACTERISATION

Table B1: Particle shape test, density, volume, porosity and voids ratio for the 13.20 mm basalt aggregates.

| Particle | Length, $l$ (mm) | Width, $w$ (mm) | Depth, $d$ (mm) | $d_m$ (mm) | $l/w$ | $l/d$ | $d/d_m$ | $r_v$ | $D_s$ (mm) | Weight in air (gram) | Weight in water (gram) | Volume ($cm^3$) | $\rho_s$ ($g/cm^3$) | $\rho_b$ ($g/cm^3$) | Porosity ($\eta$) | Void ratio ($\varepsilon$) |
|---|---|---|---|---|---|---|---|---|---|---|---|---|---|---|---|---|
| 1 | 15.41 | 13.24 | 9.24 | 12.63 | 1.16 | 1.67 | 0.73 | 0.70 | 11.20 | 2.04 | 1.30 | 0.74 | 2.77 | 1.77 | 0.36 | 0.56 |
| 2 | 14.32 | 10.12 | 8.42 | 10.95 | 1.42 | 1.70 | 0.77 | 0.69 | 9.69 | 1.31 | 0.83 | 0.48 | 2.75 | 1.75 | 0.36 | 0.57 |
| 3 | 15.57 | 12.58 | 10.38 | 12.84 | 1.24 | 1.50 | 0.81 | 0.68 | 11.29 | 2.06 | 1.31 | 0.75 | 2.74 | 1.74 | 0.37 | 0.58 |
| 4 | 16.57 | 14.04 | 10.58 | 13.73 | 1.18 | 1.57 | 0.77 | 0.64 | 11.86 | 2.43 | 1.56 | 0.87 | 2.79 | 1.79 | 0.36 | 0.56 |
| 5 | 19.02 | 15.56 | 11.56 | 15.38 | 1.22 | 1.65 | 0.75 | 0.83 | 14.44 | 4.36 | 2.78 | 1.58 | 2.76 | 1.76 | 0.36 | 0.57 |
| 6 | 15.25 | 12.65 | 9.59 | 12.50 | 1.21 | 1.59 | 0.77 | 0.72 | 11.22 | 2.05 | 1.32 | 0.74 | 2.78 | 1.78 | 0.36 | 0.56 |
| 7 | 14.28 | 12.03 | 10.21 | 12.17 | 1.19 | 1.40 | 0.84 | 0.71 | 10.84 | 1.87 | 1.20 | 0.67 | 2.79 | 1.79 | 0.36 | 0.56 |
| 8 | 13.05 | 10.90 | 6.98 | 10.31 | 1.20 | 1.87 | 0.68 | 0.81 | 9.60 | 1.28 | 0.82 | 0.46 | 2.76 | 1.76 | 0.36 | 0.57 |
| 9 | 16.12 | 14.85 | 9.32 | 13.43 | 1.09 | 1.73 | 0.69 | 0.69 | 11.85 | 2.41 | 1.54 | 0.87 | 2.76 | 1.76 | 0.36 | 0.57 |
| 10 | 14.01 | 12.36 | 8.54 | 11.64 | 1.13 | 1.64 | 0.73 | 0.68 | 10.23 | 1.56 | 1.00 | 0.56 | 2.78 | 1.78 | 0.36 | 0.56 |
| 11 | 11.46 | 10.23 | 8.89 | 10.19 | 1.12 | 1.29 | 0.87 | 0.85 | 9.66 | 1.27 | 0.80 | 0.47 | 2.70 | 1.70 | 0.37 | 0.59 |
| 12 | 13.56 | 11.42 | 9.98 | 11.65 | 1.19 | 1.36 | 0.86 | 0.70 | 10.35 | 1.60 | 1.02 | 0.58 | 2.76 | 1.76 | 0.36 | 0.57 |
| 13 | 11.58 | 8.91 | 6.02 | 8.84 | 1.30 | 1.92 | 0.68 | 0.81 | 8.23 | 0.80 | 0.51 | 0.29 | 2.74 | 1.74 | 0.36 | 0.57 |
| 14 | 15.04 | 12.35 | 9.23 | 12.21 | 1.22 | 1.63 | 0.76 | 0.80 | 11.35 | 2.08 | 1.32 | 0.76 | 2.72 | 1.72 | 0.37 | 0.58 |
| 15 | 12.78 | 10.01 | 5.98 | 9.59 | 1.28 | 2.14 | 0.62 | 0.82 | 8.99 | 1.05 | 0.67 | 0.38 | 2.77 | 1.77 | 0.36 | 0.56 |
| 16 | 10.03 | 8.65 | 6.87 | 8.52 | 1.16 | 1.46 | 0.81 | 0.82 | 7.97 | 0.72 | 0.46 | 0.27 | 2.73 | 1.73 | 0.37 | 0.58 |
| 17 | 14.33 | 12.65 | 8.65 | 11.88 | 1.13 | 1.66 | 0.73 | 0.67 | 10.39 | 1.59 | 1.00 | 0.59 | 2.71 | 1.71 | 0.37 | 0.58 |
| 18 | 19.03 | 15.23 | 12.55 | 15.60 | 1.25 | 1.52 | 0.80 | 0.78 | 14.38 | 4.27 | 2.71 | 1.56 | 2.74 | 1.74 | 0.36 | 0.57 |
| 19 | 17.56 | 15.21 | 12.86 | 15.21 | 1.15 | 1.37 | 0.85 | 0.80 | 14.11 | 4.09 | 2.62 | 1.47 | 2.78 | 1.78 | 0.36 | 0.56 |
| 20 | 15.68 | 13.84 | 10.50 | 13.34 | 1.13 | 1.49 | 0.79 | 0.82 | 12.48 | 2.80 | 1.79 | 1.02 | 2.76 | 1.76 | 0.36 | 0.57 |
| 21 | 13.47 | 12.56 | 9.51 | 11.85 | 1.07 | 1.42 | 0.80 | 0.80 | 10.98 | 1.87 | 1.18 | 0.69 | 2.71 | 1.71 | 0.37 | 0.59 |
| 22 | 14.00 | 12.32 | 8.98 | 11.77 | 1.14 | 1.56 | 0.76 | 0.74 | 10.66 | 1.73 | 1.09 | 0.64 | 2.72 | 1.72 | 0.37 | 0.58 |
| 23 | 18.98 | 15.83 | 10.64 | 15.15 | 1.20 | 1.78 | 0.70 | 0.82 | 14.18 | 4.05 | 2.56 | 1.49 | 2.71 | 1.71 | 0.37 | 0.58 |
| 24 | 12.56 | 11.24 | 8.33 | 10.71 | 1.12 | 1.51 | 0.78 | 0.84 | 10.10 | 1.45 | 0.91 | 0.54 | 2.70 | 1.70 | 0.37 | 0.59 |
| 25 | 13.02 | 10.65 | 6.95 | 10.21 | 1.22 | 1.87 | 0.68 | 0.85 | 9.65 | 1.29 | 0.82 | 0.47 | 2.74 | 1.74 | 0.37 | 0.57 |
| 26 | 13.56 | 11.02 | 8.65 | 11.08 | 1.23 | 1.57 | 0.78 | 0.74 | 10.03 | 1.48 | 0.95 | 0.53 | 2.79 | 1.79 | 0.36 | 0.56 |
| 27 | 18.75 | 15.54 | 12.12 | 15.47 | 1.21 | 1.55 | 0.78 | 0.77 | 14.17 | 4.14 | 2.65 | 1.49 | 2.78 | 1.78 | 0.36 | 0.56 |
| 28 | 17.69 | 15.23 | 11.69 | 14.87 | 1.16 | 1.51 | 0.79 | 0.76 | 13.55 | 3.60 | 2.30 | 1.30 | 2.76 | 1.76 | 0.36 | 0.57 |
| 29 | 14.59 | 12.10 | 5.97 | 10.89 | 1.21 | 2.44 | 0.55 | 0.74 | 9.84 | 1.38 | 0.89 | 0.50 | 2.77 | 1.77 | 0.36 | 0.56 |
| 30 | 19.98 | 17.87 | 10.14 | 16.00 | 1.12 | 1.97 | 0.63 | 0.81 | 14.91 | 4.84 | 3.10 | 1.74 | 2.79 | 1.79 | 0.36 | 0.56 |
| 31 | 11.85 | 9.24 | 7.24 | 9.44 | 1.28 | 1.64 | 0.77 | 0.75 | 8.60 | 0.90 | 0.57 | 0.33 | 2.71 | 1.71 | 0.37 | 0.59 |
| 32 | 15.06 | 12.20 | 9.61 | 12.29 | 1.23 | 1.57 | 0.78 | 0.78 | 11.30 | 2.08 | 1.32 | 0.76 | 2.75 | 1.75 | 0.36 | 0.57 |
| 33 | 18.54 | 15.42 | 13.63 | 15.86 | 1.20 | 1.36 | 0.86 | 0.79 | 14.68 | 4.52 | 2.86 | 1.66 | 2.73 | 1.73 | 0.37 | 0.58 |
| 34 | 17.55 | 14.37 | 11.45 | 14.46 | 1.22 | 1.53 | 0.79 | 0.78 | 13.32 | 3.45 | 2.21 | 1.24 | 2.79 | 1.79 | 0.36 | 0.56 |

| | | | | | | | | | | | | | | | | |
|---|---|---|---|---|---|---|---|---|---|---|---|---|---|---|---|---|
| 35 | 18.26 | 15.03 | 12.60 | 15.30 | 1.21 | 1.45 | 0.82 | 0.82 | 14.32 | 4.18 | 2.64 | 1.54 | 2.72 | 1.72 | 0.37 | 0.58 |
| 36 | 14.38 | 11.09 | 8.02 | 11.16 | 1.30 | 1.79 | 0.72 | 0.75 | 10.16 | 1.52 | 0.97 | 0.55 | 2.77 | 1.77 | 0.36 | 0.57 |
| 37 | 16.50 | 13.89 | 11.25 | 13.88 | 1.19 | 1.47 | 0.81 | 0.76 | 12.65 | 2.93 | 1.87 | 1.06 | 2.77 | 1.77 | 0.36 | 0.57 |
| 38 | 19.06 | 15.15 | 10.56 | 14.92 | 1.26 | 1.80 | 0.71 | 0.75 | 13.56 | 3.55 | 2.24 | 1.31 | 2.72 | 1.72 | 0.37 | 0.58 |
| 39 | 18.05 | 15.13 | 12.09 | 15.09 | 1.19 | 1.49 | 0.80 | 0.84 | 14.26 | 4.10 | 2.58 | 1.52 | 2.70 | 1.70 | 0.37 | 0.59 |
| 40 | 16.98 | 14.02 | 11.37 | 14.12 | 1.21 | 1.49 | 0.81 | 0.81 | 13.16 | 3.28 | 2.09 | 1.19 | 2.75 | 1.75 | 0.36 | 0.57 |
| 41 | 17.23 | 14.21 | 12.51 | 14.65 | 1.21 | 1.38 | 0.85 | 0.75 | 13.28 | 3.41 | 2.19 | 1.23 | 2.78 | 1.78 | 0.36 | 0.56 |
| 42 | 19.86 | 17.65 | 12.16 | 16.56 | 1.13 | 1.63 | 0.73 | 0.81 | 15.42 | 5.24 | 3.32 | 1.92 | 2.73 | 1.73 | 0.37 | 0.58 |
| 43 | 18.54 | 15.42 | 11.38 | 15.11 | 1.20 | 1.63 | 0.75 | 0.81 | 14.09 | 4.01 | 2.55 | 1.46 | 2.74 | 1.74 | 0.37 | 0.57 |
| 44 | 17.22 | 13.29 | 12.65 | 14.39 | 1.30 | 1.36 | 0.88 | 0.78 | 13.25 | 3.39 | 2.17 | 1.22 | 2.78 | 1.78 | 0.36 | 0.56 |
| 45 | 17.68 | 13.58 | 12.76 | 14.67 | 1.30 | 1.39 | 0.87 | 0.76 | 13.39 | 3.43 | 2.18 | 1.26 | 2.73 | 1.73 | 0.37 | 0.58 |
| 46 | 14.90 | 12.50 | 8.03 | 11.81 | 1.19 | 1.86 | 0.68 | 0.70 | 10.48 | 1.65 | 1.05 | 0.60 | 2.75 | 1.75 | 0.36 | 0.57 |
| 47 | 15.45 | 10.42 | 8.01 | 11.29 | 1.48 | 1.93 | 0.71 | 0.76 | 10.31 | 1.58 | 1.01 | 0.57 | 2.75 | 1.75 | 0.36 | 0.57 |
| 48 | 16.58 | 15.69 | 11.23 | 14.50 | 1.06 | 1.48 | 0.77 | 0.76 | 13.25 | 3.39 | 2.17 | 1.22 | 2.78 | 1.78 | 0.36 | 0.56 |
| 49 | 17.59 | 16.01 | 10.25 | 14.62 | 1.10 | 1.72 | 0.70 | 0.75 | 13.26 | 3.39 | 2.17 | 1.22 | 2.78 | 1.78 | 0.36 | 0.56 |
| 50 | 20.51 | 17.51 | 13.66 | 17.23 | 1.17 | 1.50 | 0.79 | 0.78 | 15.83 | 5.69 | 3.61 | 2.08 | 2.74 | 1.74 | 0.37 | 0.58 |
| 51 | 17.55 | 16.22 | 11.61 | 15.13 | 1.08 | 1.51 | 0.77 | 0.84 | 14.30 | 4.13 | 2.60 | 1.53 | 2.70 | 1.70 | 0.37 | 0.59 |
| 52 | 19.27 | 15.08 | 10.15 | 14.83 | 1.28 | 1.90 | 0.68 | 0.73 | 13.34 | 3.37 | 2.13 | 1.24 | 2.71 | 1.71 | 0.37 | 0.58 |
| 53 | 13.61 | 11.13 | 8.87 | 11.20 | 1.22 | 1.53 | 0.79 | 0.75 | 10.20 | 1.54 | 0.98 | 0.56 | 2.77 | 1.77 | 0.36 | 0.56 |
| 54 | 15.34 | 13.26 | 10.26 | 12.95 | 1.16 | 1.50 | 0.79 | 0.70 | 11.50 | 2.20 | 1.41 | 0.80 | 2.77 | 1.77 | 0.36 | 0.57 |
| 55 | 14.88 | 10.84 | 8.54 | 11.42 | 1.37 | 1.74 | 0.75 | 0.74 | 10.33 | 1.61 | 1.03 | 0.58 | 2.78 | 1.78 | 0.36 | 0.56 |
| 56 | 14.68 | 10.45 | 8.35 | 11.16 | 1.40 | 1.76 | 0.75 | 0.75 | 10.13 | 1.52 | 0.97 | 0.54 | 2.78 | 1.78 | 0.36 | 0.56 |
| 57 | 12.12 | 9.20 | 7.99 | 9.77 | 1.32 | 1.52 | 0.82 | 0.83 | 9.19 | 1.12 | 0.71 | 0.41 | 2.75 | 1.75 | 0.36 | 0.57 |
| 58 | 16.55 | 14.32 | 12.21 | 14.36 | 1.16 | 1.36 | 0.85 | 0.81 | 13.36 | 3.37 | 2.12 | 1.25 | 2.70 | 1.70 | 0.37 | 0.59 |
| 59 | 14.36 | 12.84 | 10.41 | 12.54 | 1.12 | 1.38 | 0.83 | 0.76 | 11.47 | 2.17 | 1.39 | 0.79 | 2.76 | 1.76 | 0.36 | 0.57 |
| 60 | 18.56 | 15.61 | 11.81 | 15.33 | 1.19 | 1.57 | 0.77 | 0.84 | 14.47 | 4.41 | 2.83 | 1.59 | 2.78 | 1.78 | 0.36 | 0.56 |
| mean | 15.51 | 13.25 | 10.18 | 12.90 | 1.20 | 1.56 | 0.79 | 0.77 | 11.48 | 2.19 | 1.40 | 0.79 | 2.76 | 1.76 | 0.36 | 0.57 |
| st. dev | 2.46 | 2.30 | 1.98 | 2.14 | 0.08 | 0.21 | 0.93 | 0.05 | 2.02 | 1.27 | 0.81 | 0.47 | 0.03 | 0.03 | 0.00 | 0.01 |
| max | 20.51 | 17.87 | 13.66 | 17.23 | 1.48 | 2.44 | 0.79 | 0.85 | 15.83 | 5.68 | 3.61 | 2.08 | 2.80 | 1.79 | 0.37 | 0.59 |
| min | 10.03 | 8.65 | 5.97 | 8.52 | 1.06 | 1.29 | 0.70 | 0.64 | 7.97 | 0.72 | 0.46 | 0.27 | 2.70 | 1.70 | 0.36 | 0.56 |

Table B2: Particle shape test, density, volume, porosity and voids ratio for the 6.18 mm basalt aggregates.

| Particle | Length, $l$ (mm) | Width, $w$ (mm) | Depth, $d$ (mm) | $d_m$ (mm) | $l/w$ | $l/d$ | $d/d_m$ | $r_v$ | $D_s$ (mm) | Weight in air (gram) | Weight in water (gram) | Volume ($cm^3$) | $\rho_s$ ($g/cm^3$) | $\rho_b$ ($g/cm^3$) | Porosity ($\eta$) | Void ratio ($\varepsilon$) |
|---|---|---|---|---|---|---|---|---|---|---|---|---|---|---|---|---|
| 1 | 5.86 | 4.45 | 4.15 | 4.82 | 1.32 | 1.41 | 0.86 | 0.84 | 4.55 | 0.14 | 0.09 | 0.05 | 2.75 | 1.75 | 0.36 | 0.57 |
| 2 | 6.01 | 4.82 | 4.17 | 5.00 | 1.25 | 1.44 | 0.83 | 0.84 | 4.72 | 0.15 | 0.10 | 0.06 | 2.74 | 1.74 | 0.36 | 0.57 |
| 3 | 6.01 | 4.84 | 4.62 | 5.16 | 1.24 | 1.30 | 0.90 | 0.83 | 4.84 | 0.16 | 0.10 | 0.06 | 2.71 | 1.71 | 0.37 | 0.58 |
| 4 | 6.34 | 5.22 | 3.99 | 5.18 | 1.21 | 1.59 | 0.77 | 0.84 | 4.89 | 0.17 | 0.11 | 0.06 | 2.75 | 1.75 | 0.36 | 0.57 |
| 5 | 6.36 | 4.35 | 3.67 | 4.79 | 1.46 | 1.73 | 0.77 | 0.83 | 4.51 | 0.13 | 0.08 | 0.05 | 2.71 | 1.71 | 0.37 | 0.58 |
| 6 | 5.94 | 4.92 | 3.85 | 4.90 | 1.21 | 1.54 | 0.79 | 0.84 | 4.62 | 0.14 | 0.09 | 0.05 | 2.75 | 1.75 | 0.36 | 0.57 |
| 7 | 6.98 | 5.65 | 4.94 | 5.86 | 1.24 | 1.41 | 0.84 | 0.85 | 5.54 | 0.24 | 0.15 | 0.09 | 2.73 | 1.73 | 0.37 | 0.58 |
| 8 | 5.91 | 4.76 | 4.33 | 5.00 | 1.24 | 1.36 | 0.87 | 0.84 | 4.72 | 0.15 | 0.10 | 0.06 | 2.74 | 1.74 | 0.36 | 0.57 |
| 9 | 6.32 | 5.81 | 5.03 | 5.72 | 1.09 | 1.26 | 0.88 | 0.84 | 5.39 | 0.23 | 0.14 | 0.08 | 2.75 | 1.75 | 0.36 | 0.57 |
| 10 | 5.75 | 4.93 | 4.35 | 5.01 | 1.17 | 1.32 | 0.87 | 0.83 | 4.71 | 0.15 | 0.09 | 0.05 | 2.73 | 1.73 | 0.37 | 0.58 |
| 11 | 6.12 | 5.34 | 4.25 | 5.24 | 1.15 | 1.44 | 0.81 | 0.84 | 4.93 | 0.17 | 0.11 | 0.06 | 2.76 | 1.76 | 0.36 | 0.57 |
| 12 | 6.05 | 5.63 | 4.54 | 5.41 | 1.07 | 1.33 | 0.84 | 0.84 | 5.10 | 0.19 | 0.12 | 0.07 | 2.75 | 1.75 | 0.36 | 0.57 |
| 13 | 6.34 | 4.77 | 4.01 | 5.04 | 1.33 | 1.58 | 0.80 | 0.85 | 4.78 | 0.15 | 0.10 | 0.06 | 2.70 | 1.70 | 0.37 | 0.59 |
| 14 | 6.02 | 4.85 | 3.89 | 4.92 | 1.24 | 1.55 | 0.79 | 0.85 | 4.65 | 0.14 | 0.09 | 0.05 | 2.72 | 1.72 | 0.37 | 0.58 |
| 15 | 5.11 | 4.81 | 4.37 | 4.76 | 1.06 | 1.17 | 0.92 | 0.84 | 4.49 | 0.13 | 0.08 | 0.05 | 2.75 | 1.75 | 0.36 | 0.57 |
| 16 | 6.45 | 5.91 | 4.86 | 5.74 | 1.09 | 1.33 | 0.85 | 0.84 | 5.41 | 0.23 | 0.15 | 0.08 | 2.75 | 1.75 | 0.36 | 0.57 |
| 17 | 6.13 | 4.97 | 3.73 | 4.94 | 1.23 | 1.64 | 0.75 | 0.83 | 4.65 | 0.15 | 0.09 | 0.05 | 2.76 | 1.76 | 0.36 | 0.57 |
| 18 | 7.49 | 6.08 | 4.92 | 6.16 | 1.23 | 1.52 | 0.80 | 0.84 | 5.81 | 0.28 | 0.18 | 0.10 | 2.74 | 1.74 | 0.36 | 0.57 |
| 19 | 6.78 | 5.95 | 5.37 | 6.03 | 1.14 | 1.26 | 0.89 | 0.84 | 5.69 | 0.26 | 0.17 | 0.10 | 2.75 | 1.75 | 0.36 | 0.57 |
| 20 | 6.55 | 5.29 | 4.79 | 5.54 | 1.24 | 1.37 | 0.86 | 0.85 | 5.25 | 0.21 | 0.13 | 0.08 | 2.72 | 1.72 | 0.37 | 0.58 |
| 21 | 6.43 | 5.93 | 5.09 | 5.82 | 1.08 | 1.26 | 0.88 | 0.84 | 5.49 | 0.24 | 0.15 | 0.09 | 2.74 | 1.74 | 0.36 | 0.57 |
| 22 | 7.12 | 5.87 | 4.61 | 5.87 | 1.21 | 1.54 | 0.79 | 0.82 | 5.49 | 0.24 | 0.15 | 0.09 | 2.79 | 1.79 | 0.36 | 0.56 |
| 23 | 5.89 | 5.14 | 4.41 | 5.15 | 1.15 | 1.34 | 0.86 | 0.84 | 4.85 | 0.16 | 0.10 | 0.06 | 2.74 | 1.74 | 0.36 | 0.57 |
| 24 | 6.35 | 5.32 | 4.02 | 5.23 | 1.19 | 1.58 | 0.77 | 0.84 | 4.93 | 0.17 | 0.11 | 0.06 | 2.75 | 1.75 | 0.36 | 0.57 |
| 25 | 6.73 | 4.96 | 3.83 | 5.17 | 1.36 | 1.76 | 0.74 | 0.85 | 4.89 | 0.17 | 0.11 | 0.06 | 2.73 | 1.73 | 0.37 | 0.58 |
| 26 | 6.63 | 4.93 | 3.57 | 5.04 | 1.34 | 1.86 | 0.71 | 0.85 | 4.78 | 0.16 | 0.10 | 0.06 | 2.72 | 1.72 | 0.37 | 0.58 |
| 27 | 5.99 | 4.62 | 3.89 | 4.83 | 1.30 | 1.54 | 0.80 | 0.84 | 4.56 | 0.14 | 0.09 | 0.05 | 2.75 | 1.75 | 0.36 | 0.57 |
| 28 | 6.70 | 5.94 | 4.87 | 5.84 | 1.13 | 1.38 | 0.83 | 0.81 | 5.44 | 0.23 | 0.15 | 0.08 | 2.72 | 1.72 | 0.37 | 0.58 |
| 29 | 6.13 | 5.35 | 3.93 | 5.14 | 1.15 | 1.56 | 0.77 | 0.83 | 4.82 | 0.16 | 0.10 | 0.06 | 2.76 | 1.76 | 0.36 | 0.57 |
| 30 | 5.89 | 4.84 | 3.98 | 4.90 | 1.22 | 1.48 | 0.81 | 0.84 | 4.62 | 0.14 | 0.09 | 0.05 | 2.75 | 1.75 | 0.36 | 0.57 |
| 31 | 6.57 | 5.64 | 4.14 | 5.45 | 1.16 | 1.59 | 0.76 | 0.85 | 5.16 | 0.20 | 0.12 | 0.07 | 2.71 | 1.71 | 0.37 | 0.59 |
| 32 | 5.59 | 4.49 | 4.15 | 4.74 | 1.24 | 1.35 | 0.87 | 0.89 | 4.56 | 0.14 | 0.09 | 0.05 | 2.79 | 1.79 | 0.36 | 0.56 |
| 33 | 6.56 | 5.21 | 4.51 | 5.43 | 1.26 | 1.45 | 0.83 | 0.84 | 5.12 | 0.19 | 0.12 | 0.07 | 2.75 | 1.75 | 0.36 | 0.57 |
| 34 | 6.75 | 5.43 | 4.69 | 5.62 | 1.24 | 1.44 | 0.83 | 0.84 | 5.30 | 0.21 | 0.14 | 0.08 | 2.74 | 1.74 | 0.36 | 0.57 |
| 35 | 6.14 | 5.14 | 3.91 | 5.06 | 1.19 | 1.57 | 0.77 | 0.85 | 4.81 | 0.16 | 0.10 | 0.06 | 2.70 | 1.70 | 0.37 | 0.59 |
| 36 | 6.41 | 4.32 | 3.54 | 4.76 | 1.48 | 1.81 | 0.74 | 0.84 | 4.49 | 0.13 | 0.08 | 0.05 | 2.74 | 1.74 | 0.36 | 0.57 |
| 37 | 6.11 | 3.99 | 2.86 | 4.32 | 1.53 | 2.14 | 0.66 | 0.81 | 4.03 | 0.10 | 0.06 | 0.03 | 2.77 | 1.77 | 0.36 | 0.57 |

| | | | | | | | | | | | | | | | |
|---|---|---|---|---|---|---|---|---|---|---|---|---|---|---|---|
| 38 | 6.23 | 4.95 | 3.98 | 5.05 | 1.26 | 1.57 | 0.79 | 0.81 | 4.71 | 0.15 | 0.10 | 0.05 | 2.77 | 1.77 | 0.36 | 0.56 |
| 39 | 5.67 | 4.61 | 3.83 | 4.70 | 1.23 | 1.48 | 0.81 | 0.84 | 4.43 | 0.13 | 0.08 | 0.05 | 2.75 | 1.75 | 0.36 | 0.57 |
| 40 | 6.23 | 5.88 | 5.31 | 5.81 | 1.06 | 1.17 | 0.91 | 0.85 | 5.50 | 0.24 | 0.15 | 0.09 | 2.73 | 1.73 | 0.37 | 0.58 |
| 41 | 6.78 | 4.75 | 4.65 | 5.39 | 1.43 | 1.46 | 0.86 | 0.84 | 5.09 | 0.19 | 0.12 | 0.07 | 2.75 | 1.75 | 0.36 | 0.57 |
| 42 | 6.23 | 5.31 | 4.67 | 5.40 | 1.17 | 1.33 | 0.86 | 0.85 | 5.12 | 0.19 | 0.12 | 0.07 | 2.77 | 1.77 | 0.36 | 0.57 |
| 43 | 7.21 | 6.69 | 5.89 | 6.60 | 1.08 | 1.22 | 0.89 | 0.84 | 6.22 | 0.35 | 0.22 | 0.13 | 2.75 | 1.75 | 0.36 | 0.57 |
| 44 | 6.43 | 4.53 | 4.84 | 5.27 | 1.42 | 1.33 | 0.92 | 0.84 | 4.97 | 0.18 | 0.11 | 0.06 | 2.74 | 1.74 | 0.36 | 0.57 |
| 45 | 5.17 | 4.12 | 3.87 | 4.39 | 1.25 | 1.34 | 0.88 | 0.88 | 4.21 | 0.11 | 0.07 | 0.04 | 2.71 | 1.71 | 0.37 | 0.59 |
| 46 | 6.67 | 4.47 | 3.67 | 4.94 | 1.49 | 1.82 | 0.74 | 0.84 | 4.66 | 0.15 | 0.09 | 0.05 | 2.74 | 1.74 | 0.36 | 0.57 |
| 47 | 6.42 | 5.11 | 3.65 | 5.06 | 1.26 | 1.76 | 0.72 | 0.85 | 4.80 | 0.16 | 0.10 | 0.06 | 2.71 | 1.71 | 0.37 | 0.58 |
| 48 | 6.11 | 5.66 | 4.89 | 5.55 | 1.08 | 1.25 | 0.88 | 0.81 | 5.17 | 0.20 | 0.12 | 0.07 | 2.72 | 1.72 | 0.37 | 0.58 |
| 49 | 6.03 | 4.72 | 4.23 | 4.99 | 1.28 | 1.43 | 0.85 | 0.84 | 4.71 | 0.15 | 0.10 | 0.05 | 2.75 | 1.75 | 0.36 | 0.57 |
| 50 | 6.28 | 4.96 | 4.37 | 5.20 | 1.27 | 1.44 | 0.84 | 0.80 | 4.82 | 0.16 | 0.10 | 0.06 | 2.70 | 1.70 | 0.37 | 0.59 |
| mean | 6.26 | 4.97 | 4.24 | 5.15 | 1.23 | 1.44 | 0.83 | 0.84 | 0.06 | 2.74 | 1.74 | 6.26 | 4.97 | 4.24 | 0.36 | 0.57 |
| st. dev | 0.46 | 0.57 | 0.56 | 0.45 | 0.12 | 0.19 | 0.06 | 0.02 | 0.02 | 0.02 | 0.02 | 0.46 | 0.57 | 0.56 | 0.00 | 0.01 |
| max | 7.49 | 6.69 | 5.89 | 6.60 | 1.53 | 2.14 | 0.92 | 0.89 | 0.13 | 2.79 | 1.79 | 7.49 | 6.69 | 5.89 | 0.37 | 0.59 |
| min | 5.11 | 3.99 | 2.86 | 4.32 | 1.06 | 1.17 | 0.66 | 0.80 | 0.03 | 2.70 | 1.70 | 5.11 | 3.99 | 2.86 | 0.36 | 0.56 |

Table B3: Particle shape test, density, volume, porosity and voids ratio for the 5.21 mm basalt aggregates.

| Particle | Length, $l$ (mm) | Width, $w$ (mm) | Depth, $d$ (mm) | $d_m$ (mm) | $l/w$ | $l/d$ | $d/d_m$ | $r_v$ | $D_s$ (mm) | Weight in air (gram) | Weight in water (gram) | Volume (cm³) | $\rho_s$ (g/cm³) | $\rho_b$ (g/cm³) | Porosity ($\eta$) | Void ratio ($\varepsilon$) |
|---|---|---|---|---|---|---|---|---|---|---|---|---|---|---|---|---|
| 1 | 1 | 5.79 | 4.38 | 3.85 | 4.67 | 1.32 | 1.50 | 0.82 | 0.82 | 4.38 | 0.12 | 0.08 | 0.04 | 2.70 | 1.72 | 0.57 |
| 2 | 2 | 6.08 | 4.02 | 3.88 | 4.66 | 1.51 | 1.57 | 0.83 | 0.82 | 4.36 | 0.12 | 0.07 | 0.04 | 2.71 | 1.71 | 0.59 |
| 3 | 3 | 5.06 | 4.75 | 4.23 | 4.68 | 1.07 | 1.20 | 0.90 | 0.81 | 4.36 | 0.12 | 0.08 | 0.04 | 2.74 | 1.74 | 0.57 |
| 4 | 4 | 5.94 | 4.36 | 3.47 | 4.59 | 1.36 | 1.71 | 0.76 | 0.82 | 4.30 | 0.11 | 0.07 | 0.04 | 2.71 | 1.71 | 0.59 |
| 5 | 5 | 4.13 | 3.16 | 2.45 | 3.25 | 1.31 | 1.69 | 0.75 | 0.95 | 3.19 | 0.05 | 0.03 | 0.02 | 2.71 | 1.71 | 0.58 |
| 6 | 6 | 5.26 | 3.51 | 3.01 | 3.93 | 1.50 | 1.75 | 0.77 | 0.79 | 3.64 | 0.07 | 0.05 | 0.03 | 2.79 | 1.79 | 0.56 |
| 7 | 7 | 4.99 | 3.86 | 3.44 | 4.10 | 1.29 | 1.45 | 0.84 | 0.81 | 3.82 | 0.08 | 0.05 | 0.03 | 2.73 | 1.73 | 0.58 |
| 8 | 8 | 5.69 | 3.98 | 3.29 | 4.32 | 1.43 | 1.73 | 0.76 | 0.81 | 4.03 | 0.09 | 0.06 | 0.03 | 2.74 | 1.74 | 0.58 |
| 9 | 9 | 5.42 | 4.66 | 3.81 | 4.63 | 1.16 | 1.42 | 0.82 | 0.81 | 4.32 | 0.12 | 0.07 | 0.04 | 2.74 | 1.74 | 0.58 |
| 10 | 10 | 5.44 | 4.76 | 3.62 | 4.61 | 1.14 | 1.50 | 0.79 | 0.79 | 4.27 | 0.11 | 0.07 | 0.04 | 2.79 | 1.79 | 0.56 |
| 11 | 11 | 5.13 | 4.61 | 2.71 | 4.15 | 1.11 | 1.89 | 0.65 | 0.81 | 3.87 | 0.08 | 0.05 | 0.03 | 2.73 | 1.73 | 0.58 |
| 12 | 12 | 4.93 | 4.56 | 3.61 | 4.37 | 1.08 | 1.37 | 0.83 | 0.81 | 4.07 | 0.10 | 0.06 | 0.04 | 2.74 | 1.74 | 0.57 |
| 13 | 13 | 5.84 | 4.49 | 3.25 | 4.53 | 1.30 | 1.80 | 0.72 | 0.82 | 4.23 | 0.11 | 0.07 | 0.04 | 2.72 | 1.72 | 0.58 |
| 14 | 14 | 5.39 | 3.82 | 2.21 | 3.81 | 1.41 | 2.44 | 0.58 | 0.82 | 3.56 | 0.06 | 0.04 | 0.02 | 2.70 | 1.70 | 0.59 |
| 15 | 15 | 5.32 | 4.43 | 3.39 | 4.38 | 1.20 | 1.57 | 0.77 | 0.81 | 4.08 | 0.10 | 0.06 | 0.04 | 2.75 | 1.75 | 0.57 |
| 16 | 16 | 5.58 | 4.54 | 3.14 | 4.42 | 1.23 | 1.78 | 0.71 | 0.81 | 4.12 | 0.10 | 0.06 | 0.04 | 2.73 | 1.73 | 0.58 |
| 17 | 17 | 5.30 | 4.39 | 3.46 | 4.38 | 1.21 | 1.53 | 0.79 | 0.82 | 4.10 | 0.10 | 0.06 | 0.04 | 2.71 | 1.71 | 0.58 |
| 18 | 18 | 4.50 | 3.66 | 3.17 | 3.78 | 1.23 | 1.42 | 0.84 | 0.81 | 3.51 | 0.06 | 0.04 | 0.02 | 2.75 | 1.75 | 0.57 |
| 19 | 19 | 5.68 | 4.95 | 3.81 | 4.81 | 1.15 | 1.49 | 0.79 | 0.81 | 4.48 | 0.13 | 0.08 | 0.05 | 2.74 | 1.74 | 0.57 |
| 20 | 20 | 5.39 | 4.25 | 3.42 | 4.35 | 1.27 | 1.58 | 0.79 | 0.80 | 4.03 | 0.10 | 0.06 | 0.03 | 2.79 | 1.79 | 0.56 |
| 21 | 21 | 6.59 | 4.91 | 3.68 | 5.06 | 1.34 | 1.79 | 0.73 | 0.81 | 4.72 | 0.15 | 0.10 | 0.06 | 2.73 | 1.73 | 0.58 |
| 22 | 22 | 5.97 | 4.96 | 3.37 | 4.77 | 1.20 | 1.77 | 0.71 | 0.82 | 4.45 | 0.13 | 0.08 | 0.05 | 2.72 | 1.72 | 0.58 |
| 23 | 23 | 5.76 | 4.39 | 2.97 | 4.37 | 1.31 | 1.94 | 0.68 | 0.80 | 4.05 | 0.10 | 0.06 | 0.03 | 2.79 | 1.79 | 0.56 |
| 24 | 24 | 5.66 | 4.61 | 3.90 | 4.72 | 1.23 | 1.45 | 0.83 | 0.80 | 4.39 | 0.12 | 0.08 | 0.04 | 2.75 | 1.75 | 0.57 |
| 25 | 25 | 6.27 | 4.89 | 2.93 | 4.70 | 1.28 | 2.14 | 0.62 | 0.82 | 4.39 | 0.12 | 0.08 | 0.04 | 2.71 | 1.71 | 0.58 |
| 26 | 26 | 5.18 | 4.33 | 3.55 | 4.35 | 1.20 | 1.46 | 0.82 | 0.82 | 4.07 | 0.10 | 0.06 | 0.04 | 2.71 | 1.71 | 0.59 |
| 27 | 27 | 5.59 | 3.99 | 3.19 | 4.26 | 1.40 | 1.75 | 0.75 | 0.82 | 3.99 | 0.09 | 0.06 | 0.03 | 2.70 | 1.70 | 0.59 |
| 28 | 28 | 5.92 | 4.31 | 3.28 | 4.50 | 1.37 | 1.81 | 0.73 | 0.81 | 4.19 | 0.11 | 0.07 | 0.04 | 2.75 | 1.75 | 0.57 |
| 29 | 29 | 5.83 | 4.06 | 2.85 | 4.25 | 1.44 | 2.05 | 0.67 | 0.82 | 3.98 | 0.09 | 0.06 | 0.03 | 2.70 | 1.70 | 0.59 |
| 30 | 30 | 5.27 | 3.89 | 3.29 | 4.15 | 1.36 | 1.60 | 0.79 | 0.81 | 3.87 | 0.08 | 0.05 | 0.03 | 2.76 | 1.76 | 0.57 |
| 31 | 31 | 6.01 | 5.31 | 4.78 | 5.37 | 1.13 | 1.26 | 0.89 | 0.81 | 5.00 | 0.18 | 0.11 | 0.07 | 2.72 | 1.72 | 0.58 |
| 32 | 32 | 5.23 | 3.86 | 3.48 | 4.19 | 1.35 | 1.50 | 0.83 | 0.81 | 3.90 | 0.09 | 0.05 | 0.03 | 2.74 | 1.74 | 0.57 |
| 33 | 33 | 4.92 | 4.55 | 3.71 | 4.39 | 1.08 | 1.33 | 0.84 | 0.81 | 4.10 | 0.10 | 0.06 | 0.04 | 2.72 | 1.72 | 0.58 |
| 34 | 34 | 4.73 | 4.32 | 3.58 | 4.21 | 1.10 | 1.32 | 0.85 | 0.82 | 3.93 | 0.09 | 0.05 | 0.03 | 2.72 | 1.72 | 0.58 |
| 35 | 35 | 5.61 | 4.89 | 3.62 | 4.71 | 1.15 | 1.55 | 0.77 | 0.82 | 4.40 | 0.12 | 0.08 | 0.04 | 2.72 | 1.72 | 0.58 |
| 36 | 36 | 5.17 | 4.17 | 3.24 | 4.19 | 1.24 | 1.60 | 0.77 | 0.80 | 3.90 | 0.09 | 0.05 | 0.03 | 2.75 | 1.75 | 0.57 |
| 37 | 37 | 5.11 | 4.25 | 3.34 | 4.23 | 1.20 | 1.53 | 0.79 | 0.82 | 3.96 | 0.09 | 0.06 | 0.03 | 2.72 | 1.72 | 0.58 |

| | | | | | | | | | | | | | | | | |
|---|---|---|---|---|---|---|---|---|---|---|---|---|---|---|---|---|
| 38 | 38 | 5.36 | 3.97 | 3.51 | 4.28 | 1.35 | 1.53 | 0.82 | 0.80 | 3.98 | 0.09 | 0.06 | 0.03 | 2.74 | 1.74 | 0.57 |
| 39 | 39 | 5.09 | 3.35 | 2.67 | 3.70 | 1.52 | 1.90 | 0.72 | 0.81 | 3.46 | 0.06 | 0.04 | 0.02 | 2.70 | 1.70 | 0.59 |
| 40 | 40 | 4.32 | 3.42 | 2.85 | 3.53 | 1.26 | 1.51 | 0.81 | 0.80 | 3.28 | 0.05 | 0.03 | 0.02 | 2.76 | 1.76 | 0.57 |
| 41 | 41 | 5.45 | 4.27 | 3.57 | 4.43 | 1.28 | 1.53 | 0.81 | 0.82 | 4.14 | 0.10 | 0.06 | 0.04 | 2.70 | 1.70 | 0.59 |
| 42 | 42 | 5.18 | 3.98 | 2.90 | 4.02 | 1.30 | 1.79 | 0.72 | 0.80 | 3.73 | 0.08 | 0.05 | 0.03 | 2.76 | 1.76 | 0.57 |
| 43 | 43 | 6.33 | 4.71 | 3.86 | 4.97 | 1.34 | 1.64 | 0.78 | 0.82 | 4.64 | 0.14 | 0.09 | 0.05 | 2.71 | 1.71 | 0.58 |
| 44 | 44 | 5.73 | 4.76 | 4.25 | 4.91 | 1.20 | 1.35 | 0.87 | 0.81 | 4.58 | 0.14 | 0.09 | 0.05 | 2.74 | 1.74 | 0.58 |
| 45 | 45 | 5.53 | 4.42 | 3.97 | 4.64 | 1.25 | 1.39 | 0.86 | 0.83 | 4.35 | 0.12 | 0.07 | 0.04 | 2.70 | 1.70 | 0.59 |
| 46 | 46 | 5.43 | 4.43 | 3.21 | 4.36 | 1.23 | 1.69 | 0.74 | 0.81 | 4.06 | 0.10 | 0.06 | 0.04 | 2.74 | 1.74 | 0.57 |
| 47 | 47 | 6.01 | 4.76 | 3.43 | 4.73 | 1.26 | 1.75 | 0.72 | 0.82 | 4.43 | 0.12 | 0.08 | 0.05 | 2.71 | 1.71 | 0.58 |
| 48 | 48 | 4.98 | 3.87 | 2.67 | 3.84 | 1.29 | 1.86 | 0.70 | 0.81 | 3.58 | 0.07 | 0.04 | 0.02 | 2.72 | 1.72 | 0.58 |
| 49 | 49 | 5.36 | 4.13 | 3.54 | 4.34 | 1.30 | 1.52 | 0.81 | 0.80 | 4.03 | 0.10 | 0.06 | 0.03 | 2.79 | 1.79 | 0.56 |
| 50 | 50 | 5.69 | 4.53 | 3.78 | 4.67 | 1.26 | 1.50 | 0.81 | 0.81 | 4.34 | 0.12 | 0.07 | 0.04 | 2.74 | 1.74 | 0.58 |
| mean | mean | 5.43 | 4.37 | 3.44 | 4.38 | 1.27 | 1.57 | 0.79 | 0.81 | 4.08 | 0.10 | 0.06 | 0.04 | 2.73 | 1.73 | 0.58 |
| st. dev | st. dev | 0.49 | 0.46 | 0.47 | 0.39 | 0.11 | 0.23 | 0.07 | 0.02 | 0.36 | 0.03 | 0.02 | 0.01 | 0.03 | 0.03 | 0.01 |
| max | max | 6.59 | 5.31 | 4.78 | 5.37 | 1.52 | 2.44 | 0.90 | 0.95 | 5.00 | 0.18 | 0.11 | 0.07 | 2.79 | 1.79 | 0.59 |
| min | min | 4.13 | 3.16 | 2.21 | 3.25 | 1.07 | 1.20 | 0.58 | 0.79 | 3.19 | 0.05 | 0.03 | 0.02 | 2.70 | 1.70 | 0.56 |

Table B4: Particle shape test, density, volume, porosity and voids ratio for the 4.05 mm basalt aggregates.

| Particle | Length, $l$ (mm) | Width, $w$ (mm) | Depth, $d$ (mm) | $d_m$ (mm) | $l/w$ | $l/d$ | $d/d_m$ | $r_v$ | $D_s$ (mm) | Weight in air (gram) | Weight in water (gram) | Volume ($cm^3$) | $\rho_s$ ($g/cm^3$) | $\rho_b$ ($g/cm^3$) | Porosity ($\eta$) | Void ratio ($\varepsilon$) |
|---|---|---|---|---|---|---|---|---|---|---|---|---|---|---|---|---|
| 1 | 4.26 | 3.36 | 3.15 | 3.59 | 1.27 | 1.35 | 0.88 | 0.80 | 3.33 | 0.05 | 0.03 | 0.02 | 2.77 | 1.77 | 0.36 | 0.57 |
| 2 | 3.91 | 3.29 | 2.63 | 3.28 | 1.19 | 1.49 | 0.80 | 0.81 | 3.05 | 0.04 | 0.03 | 0.01 | 2.75 | 1.75 | 0.36 | 0.57 |
| 3 | 3.86 | 3.44 | 3.32 | 3.54 | 1.12 | 1.16 | 0.94 | 0.83 | 3.32 | 0.05 | 0.03 | 0.02 | 2.71 | 1.71 | 0.37 | 0.58 |
| 4 | 5.07 | 4.37 | 3.05 | 4.16 | 1.16 | 1.66 | 0.73 | 0.81 | 3.88 | 0.08 | 0.05 | 0.03 | 2.76 | 1.76 | 0.36 | 0.57 |
| 5 | 4.26 | 3.67 | 3.42 | 3.78 | 1.16 | 1.25 | 0.90 | 0.81 | 3.53 | 0.06 | 0.04 | 0.02 | 2.74 | 1.74 | 0.36 | 0.57 |
| 6 | 3.75 | 3.19 | 2.62 | 3.19 | 1.18 | 1.43 | 0.82 | 0.80 | 2.96 | 0.04 | 0.02 | 0.01 | 2.76 | 1.76 | 0.36 | 0.57 |
| 7 | 4.54 | 3.96 | 3.71 | 4.07 | 1.15 | 1.22 | 0.91 | 0.82 | 3.81 | 0.08 | 0.05 | 0.03 | 2.72 | 1.72 | 0.37 | 0.58 |
| 8 | 4.33 | 3.67 | 3.34 | 3.78 | 1.18 | 1.30 | 0.88 | 0.87 | 3.61 | 0.07 | 0.04 | 0.02 | 2.70 | 1.70 | 0.37 | 0.59 |
| 9 | 4.69 | 3.40 | 2.88 | 3.66 | 1.38 | 1.63 | 0.79 | 0.81 | 3.41 | 0.06 | 0.04 | 0.02 | 2.75 | 1.75 | 0.36 | 0.57 |
| 10 | 4.34 | 3.06 | 2.86 | 3.42 | 1.42 | 1.52 | 0.84 | 0.82 | 3.20 | 0.05 | 0.03 | 0.02 | 2.72 | 1.72 | 0.37 | 0.58 |
| 11 | 4.05 | 3.56 | 3.16 | 3.59 | 1.14 | 1.28 | 0.88 | 0.80 | 3.33 | 0.05 | 0.03 | 0.02 | 2.78 | 1.78 | 0.36 | 0.56 |
| 12 | 3.92 | 3.05 | 2.77 | 3.25 | 1.29 | 1.42 | 0.85 | 0.86 | 3.09 | 0.04 | 0.03 | 0.02 | 2.72 | 1.72 | 0.37 | 0.58 |
| 13 | 3.97 | 3.24 | 2.96 | 3.39 | 1.23 | 1.34 | 0.87 | 0.77 | 3.11 | 0.04 | 0.03 | 0.02 | 2.73 | 1.73 | 0.37 | 0.58 |
| 14 | 4.42 | 3.05 | 2.86 | 3.44 | 1.45 | 1.55 | 0.83 | 0.83 | 3.24 | 0.05 | 0.03 | 0.02 | 2.75 | 1.75 | 0.36 | 0.57 |
| 15 | 3.81 | 1.97 | 1.56 | 2.45 | 1.93 | 2.44 | 0.64 | 0.91 | 2.37 | 0.02 | 0.01 | 0.01 | 2.73 | 1.73 | 0.37 | 0.58 |
| 16 | 4.49 | 3.07 | 2.65 | 3.40 | 1.46 | 1.69 | 0.78 | 0.82 | 3.18 | 0.05 | 0.03 | 0.02 | 2.73 | 1.73 | 0.37 | 0.58 |
| 17 | 3.92 | 3.69 | 2.46 | 3.36 | 1.06 | 1.59 | 0.73 | 0.82 | 3.15 | 0.04 | 0.03 | 0.02 | 2.71 | 1.71 | 0.37 | 0.58 |
| 18 | 3.92 | 2.87 | 2.63 | 3.14 | 1.37 | 1.49 | 0.84 | 0.81 | 2.93 | 0.04 | 0.02 | 0.01 | 2.75 | 1.75 | 0.36 | 0.57 |
| 19 | 3.56 | 3.00 | 2.26 | 2.94 | 1.19 | 1.58 | 0.77 | 0.81 | 2.74 | 0.03 | 0.02 | 0.01 | 2.74 | 1.74 | 0.36 | 0.57 |
| 20 | 4.21 | 3.12 | 2.67 | 3.33 | 1.35 | 1.58 | 0.80 | 0.85 | 3.16 | 0.05 | 0.03 | 0.02 | 2.75 | 1.75 | 0.36 | 0.57 |
| 21 | 4.16 | 3.65 | 2.99 | 3.60 | 1.14 | 1.39 | 0.83 | 0.80 | 3.35 | 0.05 | 0.03 | 0.02 | 2.76 | 1.76 | 0.36 | 0.57 |
| 22 | 5.01 | 4.25 | 3.67 | 4.31 | 1.18 | 1.37 | 0.85 | 0.81 | 4.02 | 0.09 | 0.06 | 0.03 | 2.75 | 1.75 | 0.36 | 0.57 |
| 23 | 4.48 | 3.87 | 3.12 | 3.82 | 1.16 | 1.44 | 0.82 | 0.82 | 3.58 | 0.07 | 0.04 | 0.02 | 2.71 | 1.71 | 0.37 | 0.58 |
| 24 | 4.19 | 3.67 | 3.23 | 3.70 | 1.14 | 1.30 | 0.87 | 0.82 | 3.47 | 0.06 | 0.04 | 0.02 | 2.71 | 1.71 | 0.37 | 0.58 |
| 25 | 3.77 | 3.43 | 3.15 | 3.45 | 1.10 | 1.20 | 0.91 | 0.80 | 3.21 | 0.05 | 0.03 | 0.02 | 2.77 | 1.77 | 0.36 | 0.57 |
| 26 | 4.75 | 3.49 | 2.72 | 3.65 | 1.36 | 1.75 | 0.74 | 0.80 | 3.39 | 0.06 | 0.04 | 0.02 | 2.75 | 1.75 | 0.36 | 0.57 |
| 27 | 4.65 | 3.65 | 2.93 | 3.74 | 1.27 | 1.59 | 0.78 | 0.81 | 3.49 | 0.06 | 0.04 | 0.02 | 2.74 | 1.74 | 0.37 | 0.58 |
| 28 | 3.91 | 3.35 | 2.86 | 3.37 | 1.17 | 1.37 | 0.85 | 0.80 | 3.13 | 0.04 | 0.03 | 0.02 | 2.75 | 1.75 | 0.36 | 0.57 |
| 29 | 4.54 | 3.98 | 3.81 | 4.11 | 1.14 | 1.19 | 0.93 | 0.83 | 3.85 | 0.08 | 0.05 | 0.03 | 2.71 | 1.71 | 0.37 | 0.58 |
| 30 | 4.23 | 3.12 | 2.89 | 3.41 | 1.36 | 1.46 | 0.85 | 0.81 | 3.18 | 0.05 | 0.03 | 0.02 | 2.76 | 1.76 | 0.36 | 0.57 |
| 31 | 4.22 | 3.25 | 3.12 | 3.53 | 1.30 | 1.35 | 0.88 | 0.83 | 3.32 | 0.05 | 0.03 | 0.02 | 2.71 | 1.71 | 0.37 | 0.59 |
| 32 | 4.13 | 3.67 | 3.52 | 3.77 | 1.13 | 1.17 | 0.93 | 0.80 | 3.51 | 0.06 | 0.04 | 0.02 | 2.74 | 1.74 | 0.36 | 0.57 |
| 33 | 3.93 | 3.21 | 2.65 | 3.26 | 1.22 | 1.48 | 0.81 | 0.81 | 3.04 | 0.04 | 0.03 | 0.01 | 2.73 | 1.73 | 0.37 | 0.58 |
| 34 | 3.81 | 2.96 | 2.69 | 3.15 | 1.29 | 1.42 | 0.85 | 0.80 | 2.93 | 0.04 | 0.02 | 0.01 | 2.73 | 1.73 | 0.37 | 0.58 |
| 35 | 3.97 | 3.04 | 2.87 | 3.29 | 1.31 | 1.38 | 0.87 | 0.81 | 3.07 | 0.04 | 0.03 | 0.02 | 2.73 | 1.73 | 0.37 | 0.58 |
| 36 | 4.29 | 2.96 | 2.77 | 3.34 | 1.45 | 1.55 | 0.83 | 0.81 | 3.12 | 0.04 | 0.03 | 0.02 | 2.75 | 1.75 | 0.36 | 0.57 |
| 37 | 3.89 | 1.91 | 1.69 | 2.50 | 2.04 | 2.30 | 0.68 | 0.81 | 2.33 | 0.02 | 0.01 | 0.01 | 2.76 | 1.76 | 0.36 | 0.57 |

| | | | | | | | | | | | | | | | | |
|---|---|---|---|---|---|---|---|---|---|---|---|---|---|---|---|---|
| 38 | 4.36 | 2.98 | 2.57 | 3.30 | 1.46 | 1.70 | 0.78 | 0.83 | 3.11 | 0.04 | 0.03 | 0.02 | 2.77 | 1.77 | 0.36 | 0.56 |
| 39 | 3.89 | 3.28 | 3.02 | 3.40 | 1.19 | 1.29 | 0.89 | 0.81 | 3.16 | 0.05 | 0.03 | 0.02 | 2.72 | 1.72 | 0.37 | 0.58 |
| 40 | 4.80 | 2.79 | 2.55 | 3.38 | 1.72 | 1.88 | 0.75 | 0.83 | 3.17 | 0.05 | 0.03 | 0.02 | 2.71 | 1.71 | 0.37 | 0.59 |
| 41 | 3.45 | 2.91 | 2.26 | 2.87 | 1.19 | 1.53 | 0.79 | 0.80 | 2.67 | 0.03 | 0.02 | 0.01 | 2.74 | 1.74 | 0.36 | 0.57 |
| 42 | 4.11 | 3.03 | 2.59 | 3.24 | 1.36 | 1.59 | 0.80 | 0.81 | 3.02 | 0.04 | 0.03 | 0.01 | 2.74 | 1.74 | 0.36 | 0.57 |
| 43 | 4.06 | 3.55 | 2.90 | 3.50 | 1.14 | 1.40 | 0.83 | 0.81 | 3.26 | 0.05 | 0.03 | 0.02 | 2.75 | 1.75 | 0.36 | 0.57 |
| 44 | 4.86 | 4.32 | 3.56 | 4.25 | 1.13 | 1.37 | 0.84 | 0.82 | 3.97 | 0.09 | 0.06 | 0.03 | 2.73 | 1.73 | 0.37 | 0.58 |
| 45 | 4.24 | 3.75 | 3.03 | 3.67 | 1.13 | 1.40 | 0.82 | 0.79 | 3.40 | 0.06 | 0.04 | 0.02 | 2.79 | 1.79 | 0.36 | 0.56 |
| 46 | 4.05 | 3.56 | 3.13 | 3.58 | 1.14 | 1.29 | 0.87 | 0.82 | 3.35 | 0.05 | 0.03 | 0.02 | 2.72 | 1.72 | 0.37 | 0.58 |
| 47 | 3.66 | 3.33 | 3.07 | 3.35 | 1.10 | 1.19 | 0.92 | 0.82 | 3.13 | 0.04 | 0.03 | 0.02 | 2.75 | 1.75 | 0.36 | 0.57 |
| 48 | 4.61 | 3.38 | 2.85 | 3.61 | 1.36 | 1.62 | 0.79 | 0.83 | 3.39 | 0.06 | 0.04 | 0.02 | 2.75 | 1.75 | 0.36 | 0.57 |
| 49 | 4.41 | 3.57 | 2.79 | 3.59 | 1.24 | 1.58 | 0.78 | 0.85 | 3.41 | 0.06 | 0.04 | 0.02 | 2.77 | 1.77 | 0.36 | 0.56 |
| 50 | 3.79 | 3.24 | 2.77 | 3.27 | 1.17 | 1.37 | 0.85 | 0.83 | 3.07 | 0.04 | 0.03 | 0.02 | 2.74 | 1.74 | 0.37 | 0.58 |
| mean | 4.18 | 3.34 | 2.88 | 3.43 | 1.19 | 1.42 | 0.83 | 0.81 | 3.21 | 0.05 | 0.03 | 0.02 | 2.74 | 1.74 | 0.36 | 0.57 |
| st. dev | 0.37 | 0.47 | 0.43 | 0.37 | 0.20 | 0.25 | 0.06 | 0.02 | 0.34 | 0.02 | 0.01 | 0.01 | 0.02 | 0.02 | 0.00 | 0.01 |
| max | 5.07 | 4.37 | 3.81 | 4.31 | 2.04 | 2.44 | 0.94 | 0.91 | 4.02 | 0.09 | 0.06 | 0.03 | 2.79 | 1.79 | 0.37 | 0.59 |
| min | 3.45 | 1.91 | 1.56 | 2.45 | 1.06 | 1.16 | 0.64 | 0.77 | 2.33 | 0.02 | 0.01 | 0.01 | 2.70 | 1.70 | 0.36 | 0.56 |

Table B5: Particle shape test, density, volume, porosity and voids ratio for the 2.86 mm basalt aggregates.

| Particle | Length, $l$ (mm) | Width, $w$ (mm) | Depth, $d$ (mm) | $d_m$ (mm) | $l/w$ | $l/d$ | $d/d_m$ | $r_v$ | $D_s$ (mm) | Weight in air (gram) | Weight in water (gram) | Volume ($cm^3$) | $\rho_s$ ($g/cm^3$) | $\rho_b$ ($g/cm^3$) | Porosity ($\eta$) | Void ratio ($\varepsilon$) |
|---|---|---|---|---|---|---|---|---|---|---|---|---|---|---|---|---|
| 1 | 2.85 | 2.21 | 1.94 | 2.33 | 1.29 | 1.47 | 0.83 | 0.83 | 2.19 | 0.02 | 0.01 | 0.01 | 2.76 | 1.76 | 0.36 | 0.57 |
| 2 | 3.59 | 2.82 | 2.42 | 2.94 | 1.27 | 1.48 | 0.82 | 0.82 | 2.75 | 0.03 | 0.02 | 0.01 | 2.71 | 1.71 | 0.37 | 0.59 |
| 3 | 2.96 | 2.06 | 1.68 | 2.23 | 1.44 | 1.76 | 0.75 | 0.79 | 2.06 | 0.01 | 0.01 | 0.00 | 2.74 | 1.74 | 0.37 | 0.58 |
| 4 | 3.25 | 1.98 | 1.54 | 2.26 | 1.64 | 2.11 | 0.68 | 0.81 | 2.11 | 0.01 | 0.01 | 0.00 | 2.73 | 1.73 | 0.37 | 0.58 |
| 5 | 3.26 | 2.65 | 2.20 | 2.70 | 1.23 | 1.48 | 0.81 | 0.81 | 2.52 | 0.02 | 0.01 | 0.01 | 2.75 | 1.75 | 0.36 | 0.57 |
| 6 | 3.11 | 1.99 | 1.37 | 2.16 | 1.56 | 2.27 | 0.64 | 0.80 | 2.00 | 0.01 | 0.01 | 0.00 | 2.71 | 1.71 | 0.37 | 0.58 |
| 7 | 3.26 | 2.89 | 2.65 | 2.93 | 1.13 | 1.23 | 0.90 | 0.82 | 2.75 | 0.03 | 0.02 | 0.01 | 2.71 | 1.71 | 0.37 | 0.59 |
| 8 | 3.81 | 2.94 | 2.61 | 3.12 | 1.30 | 1.46 | 0.84 | 0.82 | 2.92 | 0.04 | 0.02 | 0.01 | 2.72 | 1.72 | 0.37 | 0.58 |
| 9 | 3.59 | 3.15 | 2.06 | 2.93 | 1.14 | 1.74 | 0.70 | 0.83 | 2.76 | 0.03 | 0.02 | 0.01 | 2.69 | 1.69 | 0.37 | 0.59 |
| 10 | 3.48 | 3.11 | 2.86 | 3.15 | 1.12 | 1.22 | 0.91 | 0.82 | 2.95 | 0.04 | 0.02 | 0.01 | 2.72 | 1.72 | 0.37 | 0.58 |
| 11 | 3.34 | 3.05 | 1.54 | 2.64 | 1.10 | 2.17 | 0.58 | 0.81 | 2.46 | 0.02 | 0.01 | 0.01 | 2.76 | 1.76 | 0.36 | 0.57 |
| 12 | 3.23 | 2.89 | 1.98 | 2.70 | 1.12 | 1.63 | 0.73 | 0.84 | 2.55 | 0.02 | 0.01 | 0.01 | 2.71 | 1.71 | 0.37 | 0.58 |
| 13 | 3.91 | 3.03 | 2.33 | 3.09 | 1.29 | 1.68 | 0.75 | 0.82 | 2.89 | 0.03 | 0.02 | 0.01 | 2.72 | 1.72 | 0.37 | 0.58 |
| 14 | 3.16 | 2.11 | 1.69 | 2.32 | 1.50 | 1.87 | 0.73 | 0.78 | 2.14 | 0.01 | 0.01 | 0.01 | 2.78 | 1.78 | 0.36 | 0.56 |
| 15 | 3.43 | 2.41 | 1.17 | 2.34 | 1.42 | 2.93 | 0.50 | 0.85 | 2.22 | 0.02 | 0.01 | 0.01 | 2.77 | 1.77 | 0.36 | 0.56 |
| 16 | 3.21 | 2.19 | 1.89 | 2.43 | 1.47 | 1.70 | 0.78 | 0.81 | 2.27 | 0.02 | 0.01 | 0.01 | 2.70 | 1.70 | 0.37 | 0.59 |
| 17 | 2.66 | 1.97 | 1.45 | 2.03 | 1.35 | 1.83 | 0.72 | 0.83 | 1.90 | 0.01 | 0.01 | 0.00 | 2.75 | 1.75 | 0.36 | 0.57 |
| 18 | 3.10 | 2.75 | 2.03 | 2.63 | 1.13 | 1.53 | 0.77 | 0.84 | 2.48 | 0.02 | 0.01 | 0.01 | 2.68 | 1.68 | 0.37 | 0.60 |
| 19 | 2.54 | 2.14 | 1.60 | 2.09 | 1.19 | 1.59 | 0.76 | 0.81 | 1.95 | 0.01 | 0.01 | 0.00 | 2.74 | 1.74 | 0.36 | 0.57 |
| 20 | 3.22 | 2.23 | 1.91 | 2.45 | 1.44 | 1.69 | 0.78 | 0.83 | 2.30 | 0.02 | 0.01 | 0.01 | 2.69 | 1.69 | 0.37 | 0.59 |
| 21 | 2.97 | 1.89 | 1.45 | 2.10 | 1.57 | 2.05 | 0.69 | 0.84 | 1.99 | 0.01 | 0.01 | 0.00 | 2.73 | 1.73 | 0.37 | 0.58 |
| 22 | 2.88 | 1.67 | 1.19 | 1.91 | 1.72 | 2.42 | 0.62 | 0.85 | 1.81 | 0.01 | 0.01 | 0.00 | 2.74 | 1.74 | 0.36 | 0.57 |
| 23 | 3.21 | 2.76 | 2.11 | 2.69 | 1.16 | 1.52 | 0.78 | 0.79 | 2.49 | 0.02 | 0.01 | 0.01 | 2.79 | 1.79 | 0.36 | 0.56 |
| 24 | 3.71 | 2.99 | 2.14 | 2.95 | 1.24 | 1.73 | 0.73 | 0.82 | 2.76 | 0.03 | 0.02 | 0.01 | 2.70 | 1.70 | 0.37 | 0.59 |
| 25 | 2.69 | 2.45 | 1.76 | 2.30 | 1.10 | 1.53 | 0.77 | 0.82 | 2.15 | 0.01 | 0.01 | 0.01 | 2.73 | 1.73 | 0.37 | 0.58 |
| 26 | 3.57 | 3.21 | 1.94 | 2.91 | 1.11 | 1.84 | 0.67 | 0.80 | 2.70 | 0.03 | 0.02 | 0.01 | 2.78 | 1.78 | 0.36 | 0.56 |
| 27 | 3.39 | 2.61 | 2.09 | 2.70 | 1.30 | 1.62 | 0.78 | 0.80 | 2.50 | 0.02 | 0.01 | 0.01 | 2.76 | 1.76 | 0.36 | 0.57 |
| 28 | 2.79 | 2.37 | 2.04 | 2.40 | 1.18 | 1.37 | 0.85 | 0.83 | 2.25 | 0.02 | 0.01 | 0.01 | 2.72 | 1.72 | 0.37 | 0.58 |
| 29 | 2.96 | 2.13 | 2.01 | 2.37 | 1.39 | 1.47 | 0.85 | 0.81 | 2.20 | 0.02 | 0.01 | 0.01 | 2.77 | 1.77 | 0.36 | 0.57 |
| 30 | 3.32 | 3.12 | 2.62 | 3.02 | 1.06 | 1.27 | 0.87 | 0.80 | 2.81 | 0.03 | 0.02 | 0.01 | 2.77 | 1.77 | 0.36 | 0.57 |
| 31 | 3.21 | 2.28 | 1.55 | 2.35 | 1.41 | 2.07 | 0.66 | 0.83 | 2.20 | 0.02 | 0.01 | 0.01 | 2.71 | 1.71 | 0.37 | 0.58 |
| 32 | 3.27 | 3.07 | 2.63 | 2.99 | 1.07 | 1.24 | 0.88 | 0.81 | 2.79 | 0.03 | 0.02 | 0.01 | 2.74 | 1.74 | 0.37 | 0.58 |
| 33 | 3.55 | 2.87 | 2.34 | 2.92 | 1.24 | 1.52 | 0.80 | 0.83 | 2.74 | 0.03 | 0.02 | 0.01 | 2.71 | 1.71 | 0.37 | 0.58 |
| 34 | 3.09 | 2.01 | 1.78 | 2.29 | 1.54 | 1.74 | 0.78 | 0.81 | 2.14 | 0.01 | 0.01 | 0.01 | 2.76 | 1.76 | 0.36 | 0.57 |
| 35 | 2.99 | 2.27 | 1.23 | 2.16 | 1.32 | 2.43 | 0.57 | 0.81 | 2.02 | 0.01 | 0.01 | 0.00 | 2.74 | 1.74 | 0.36 | 0.57 |
| 36 | 3.32 | 3.15 | 2.91 | 3.13 | 1.05 | 1.14 | 0.93 | 0.81 | 2.92 | 0.04 | 0.02 | 0.01 | 2.74 | 1.74 | 0.37 | 0.58 |
| 37 | 3.53 | 2.98 | 1.65 | 2.72 | 1.18 | 2.14 | 0.61 | 0.82 | 2.54 | 0.02 | 0.01 | 0.01 | 2.72 | 1.72 | 0.37 | 0.58 |

| | | | | | | | | | | | | | | | |
|---|---|---|---|---|---|---|---|---|---|---|---|---|---|---|---|
| 38 | 3.16 | 2.47 | 1.79 | 2.47 | 1.28 | 1.77 | 0.72 | 0.80 | 2.29 | 0.02 | 0.01 | 0.01 | 2.76 | 1.76 | 0.36 | 0.57 |
| 39 | 3.70 | 3.14 | 2.89 | 3.24 | 1.18 | 1.28 | 0.89 | 0.81 | 3.03 | 0.04 | 0.03 | 0.01 | 2.73 | 1.73 | 0.37 | 0.58 |
| 40 | 2.56 | 2.37 | 1.81 | 2.25 | 1.08 | 1.41 | 0.81 | 0.83 | 2.11 | 0.01 | 0.01 | 0.00 | 2.76 | 1.76 | 0.36 | 0.57 |
| 41 | 2.65 | 2.12 | 1.78 | 2.18 | 1.25 | 1.49 | 0.82 | 0.83 | 2.05 | 0.01 | 0.01 | 0.00 | 2.76 | 1.76 | 0.36 | 0.57 |
| 42 | 3.23 | 2.74 | 2.47 | 2.81 | 1.18 | 1.31 | 0.88 | 0.82 | 2.64 | 0.03 | 0.02 | 0.01 | 2.76 | 1.76 | 0.36 | 0.57 |
| 43 | 3.39 | 3.06 | 2.76 | 3.07 | 1.11 | 1.23 | 0.90 | 0.81 | 2.86 | 0.03 | 0.02 | 0.01 | 2.72 | 1.72 | 0.37 | 0.58 |
| 44 | 3.32 | 2.21 | 1.31 | 2.28 | 1.50 | 2.53 | 0.57 | 0.77 | 2.09 | 0.01 | 0.01 | 0.00 | 2.79 | 1.79 | 0.36 | 0.56 |
| 45 | 3.19 | 2.41 | 1.96 | 2.52 | 1.32 | 1.63 | 0.78 | 0.79 | 2.33 | 0.02 | 0.01 | 0.01 | 2.79 | 1.79 | 0.36 | 0.56 |
| 46 | 3.05 | 2.93 | 2.79 | 2.92 | 1.04 | 1.09 | 0.95 | 0.83 | 2.74 | 0.03 | 0.02 | 0.01 | 2.71 | 1.71 | 0.37 | 0.58 |
| 47 | 2.89 | 2.10 | 1.74 | 2.24 | 1.38 | 1.66 | 0.78 | 0.83 | 2.11 | 0.01 | 0.01 | 0.00 | 2.76 | 1.76 | 0.36 | 0.57 |
| 48 | 3.07 | 2.51 | 2.15 | 2.58 | 1.22 | 1.43 | 0.83 | 0.83 | 2.42 | 0.02 | 0.01 | 0.01 | 2.72 | 1.72 | 0.37 | 0.58 |
| 49 | 2.97 | 2.67 | 1.89 | 2.51 | 1.11 | 1.57 | 0.75 | 0.82 | 2.35 | 0.02 | 0.01 | 0.01 | 2.72 | 1.72 | 0.37 | 0.58 |
| 50 | 3.38 | 2.88 | 2.42 | 2.89 | 1.17 | 1.40 | 0.84 | 0.82 | 2.71 | 0.03 | 0.02 | 0.01 | 2.75 | 1.75 | 0.36 | 0.57 |
| mean | 3.22 | 2.56 | 1.95 | 2.55 | 1.24 | 1.60 | 0.78 | 0.82 | 2.38 | 0.02 | 0.01 | 0.01 | 2.74 | 1.74 | 0.37 | 0.58 |
| st. dev | 0.32 | 0.43 | 0.47 | 0.35 | 0.17 | 0.39 | 0.10 | 0.02 | 0.33 | 0.01 | 0.01 | 0.00 | 0.03 | 0.03 | 0.00 | 0.01 |
| max | 3.91 | 3.21 | 2.91 | 3.24 | 1.72 | 2.93 | 0.95 | 0.85 | 3.03 | 0.04 | 0.03 | 0.01 | 2.79 | 1.79 | 0.37 | 0.60 |
| min | 2.54 | 1.67 | 1.17 | 1.91 | 1.04 | 1.09 | 0.50 | 0.77 | 1.81 | 0.01 | 0.01 | 0.00 | 2.68 | 1.68 | 0.36 | 0.56 |

Table B6: Particle shape test, density, volume, porosity and voids ratio for the 15.75 mm glass bead.

| Particle | Length, $l$ (mm) | Width, $w$ (mm) | Depth, $d$ (mm) | $d_m$ (mm) | $l/w$ | $l/d$ | $d/d_m$ | $r_v$ | $D_s$ (mm) | Weight in air (gram) | Weight in water (gram) | Volume (cm³) | $\rho_s$ (g/cm³) | $\rho_b$ (g/cm³) | Porosity ($\eta$) | Void ratio ($\varepsilon$) |
|---|---|---|---|---|---|---|---|---|---|---|---|---|---|---|---|---|
| 1 | 15.77 | 15.75 | 15.75 | 15.76 | 1.00 | 1.00 | 1.00 | 1.01 | 15.80 | 5.14 | 3.07 | 2.06 | 2.49 | 1.49 | 0.40 | 0.67 |
| 2 | 15.85 | 15.82 | 15.81 | 15.83 | 1.00 | 1.00 | 1.00 | 0.99 | 15.79 | 5.14 | 3.07 | 2.06 | 2.49 | 1.49 | 0.40 | 0.67 |
| 3 | 15.76 | 15.75 | 15.74 | 15.75 | 1.00 | 1.00 | 1.00 | 1.01 | 15.78 | 5.14 | 3.08 | 2.06 | 2.50 | 1.50 | 0.40 | 0.67 |
| 4 | 15.65 | 15.63 | 15.62 | 15.63 | 1.00 | 1.00 | 1.00 | 1.03 | 15.81 | 5.14 | 3.07 | 2.07 | 2.48 | 1.48 | 0.40 | 0.67 |
| 5 | 15.76 | 15.75 | 15.75 | 15.75 | 1.00 | 1.00 | 1.00 | 1.00 | 15.77 | 5.13 | 3.08 | 2.05 | 2.50 | 1.50 | 0.40 | 0.67 |
| 6 | 15.75 | 15.75 | 15.70 | 15.73 | 1.00 | 1.00 | 1.00 | 1.01 | 15.80 | 5.14 | 3.07 | 2.06 | 2.49 | 1.49 | 0.40 | 0.67 |
| 7 | 15.76 | 15.74 | 15.71 | 15.74 | 1.00 | 1.00 | 1.00 | 1.00 | 15.74 | 5.12 | 3.07 | 2.04 | 2.51 | 1.51 | 0.40 | 0.66 |
| 8 | 15.76 | 15.76 | 15.69 | 15.74 | 1.00 | 1.00 | 1.00 | 1.00 | 15.75 | 5.13 | 3.08 | 2.05 | 2.51 | 1.51 | 0.40 | 0.66 |
| 9 | 15.73 | 15.72 | 15.71 | 15.72 | 1.00 | 1.00 | 1.00 | 1.01 | 15.79 | 5.13 | 3.07 | 2.06 | 2.49 | 1.49 | 0.40 | 0.67 |
| 10 | 15.74 | 15.73 | 15.71 | 15.73 | 1.00 | 1.00 | 1.00 | 1.00 | 15.74 | 5.12 | 3.07 | 2.04 | 2.50 | 1.50 | 0.40 | 0.66 |
| 11 | 15.75 | 15.74 | 15.74 | 15.74 | 1.00 | 1.00 | 1.00 | 1.00 | 15.74 | 5.13 | 3.08 | 2.04 | 2.51 | 1.51 | 0.40 | 0.66 |
| 12 | 15.76 | 15.70 | 15.70 | 15.72 | 1.00 | 1.00 | 1.00 | 1.01 | 15.77 | 5.13 | 3.07 | 2.05 | 2.50 | 1.50 | 0.40 | 0.67 |
| 13 | 15.75 | 15.73 | 15.72 | 15.73 | 1.00 | 1.00 | 1.00 | 1.02 | 15.82 | 5.14 | 3.06 | 2.07 | 2.48 | 1.48 | 0.40 | 0.68 |
| 14 | 15.89 | 15.78 | 15.81 | 15.83 | 1.01 | 1.01 | 1.00 | 0.99 | 15.80 | 5.14 | 3.07 | 2.06 | 2.49 | 1.49 | 0.40 | 0.67 |
| 15 | 15.67 | 15.64 | 15.62 | 15.64 | 1.00 | 1.00 | 1.00 | 1.04 | 15.85 | 5.15 | 3.06 | 2.08 | 2.47 | 1.47 | 0.40 | 0.68 |
| 16 | 15.54 | 15.53 | 15.31 | 15.46 | 1.00 | 1.02 | 0.99 | 1.06 | 15.74 | 5.12 | 3.07 | 2.04 | 2.50 | 1.50 | 0.40 | 0.66 |
| 17 | 15.76 | 15.71 | 15.69 | 15.72 | 1.00 | 1.00 | 1.00 | 1.01 | 15.80 | 5.14 | 3.07 | 2.06 | 2.49 | 1.49 | 0.40 | 0.67 |
| 18 | 15.76 | 15.69 | 15.65 | 15.70 | 1.00 | 1.01 | 1.00 | 1.02 | 15.80 | 5.13 | 3.06 | 2.06 | 2.48 | 1.48 | 0.40 | 0.67 |
| 19 | 15.75 | 15.73 | 15.73 | 15.74 | 1.00 | 1.00 | 1.00 | 1.02 | 15.82 | 5.15 | 3.08 | 2.07 | 2.48 | 1.48 | 0.40 | 0.67 |
| 20 | 15.75 | 15.75 | 15.74 | 15.75 | 1.00 | 1.00 | 1.00 | 1.01 | 15.80 | 5.13 | 3.07 | 2.06 | 2.49 | 1.49 | 0.40 | 0.67 |
| 21 | 15.75 | 15.75 | 15.73 | 15.74 | 1.00 | 1.00 | 1.00 | 1.02 | 15.85 | 5.14 | 3.05 | 2.08 | 2.46 | 1.46 | 0.41 | 0.68 |
| 22 | 15.81 | 15.79 | 15.78 | 15.79 | 1.00 | 1.00 | 1.00 | 0.99 | 15.74 | 5.12 | 3.07 | 2.04 | 2.51 | 1.51 | 0.40 | 0.66 |
| 23 | 15.76 | 15.76 | 15.74 | 15.75 | 1.00 | 1.00 | 1.00 | 1.00 | 15.75 | 5.13 | 3.08 | 2.05 | 2.51 | 1.51 | 0.40 | 0.66 |
| 24 | 15.76 | 15.72 | 15.72 | 15.73 | 1.00 | 1.00 | 1.00 | 1.01 | 15.76 | 5.14 | 3.09 | 2.05 | 2.51 | 1.51 | 0.40 | 0.66 |
| 25 | 15.75 | 15.74 | 15.71 | 15.73 | 1.00 | 1.00 | 1.00 | 1.01 | 15.77 | 5.13 | 3.08 | 2.05 | 2.50 | 1.50 | 0.40 | 0.67 |
| 26 | 15.76 | 15.75 | 15.74 | 15.75 | 1.00 | 1.00 | 1.00 | 1.00 | 15.77 | 5.12 | 3.06 | 2.05 | 2.49 | 1.49 | 0.40 | 0.67 |
| 27 | 15.80 | 15.80 | 15.78 | 15.79 | 1.00 | 1.00 | 1.00 | 1.00 | 15.79 | 5.14 | 3.07 | 2.06 | 2.49 | 1.49 | 0.40 | 0.67 |
| 28 | 15.76 | 15.76 | 15.73 | 15.75 | 1.00 | 1.00 | 1.00 | 1.00 | 15.72 | 5.13 | 3.09 | 2.04 | 2.52 | 1.52 | 0.40 | 0.66 |
| 29 | 15.75 | 15.71 | 15.69 | 15.72 | 1.00 | 1.00 | 1.00 | 1.02 | 15.81 | 5.14 | 3.07 | 2.07 | 2.48 | 1.48 | 0.40 | 0.67 |
| 30 | 15.75 | 15.75 | 15.74 | 15.75 | 1.00 | 1.00 | 1.00 | 0.99 | 15.72 | 5.13 | 3.10 | 2.03 | 2.52 | 1.52 | 0.40 | 0.66 |
| mean | 15.76 | 15.75 | 15.73 | 15.74 | 1.00 | 1.00 | 1.00 | 1.01 | 15.78 | 5.13 | 3.07 | 2.06 | 2.49 | 1.49 | 0.40 | 0.67 |
| st. dev | 0.06 | 0.05 | 0.09 | 0.06 | 0.00 | 0.00 | 0.00 | 0.01 | 0.03 | 0.01 | 0.01 | 0.01 | 0.01 | 0.01 | 0.00 | 0.01 |
| max | 15.89 | 15.82 | 15.81 | 15.83 | 1.01 | 1.02 | 1.00 | 1.06 | 15.85 | 5.15 | 3.10 | 2.08 | 2.52 | 1.52 | 0.41 | 0.68 |
| min | 15.54 | 15.53 | 15.31 | 15.46 | 1.00 | 1.00 | 0.99 | 0.99 | 15.72 | 5.12 | 3.05 | 2.03 | 2.46 | 1.46 | 0.40 | 0.66 |

Table B7: Particle shape test, density, volume, porosity and voids ratio for the 6.00 mm glass bead.

| Particle | Length, $l$ (mm) | Width, $w$ (mm) | Depth, $d$ (mm) | $d_m$ (mm) | $l/w$ | $l/d$ | $d/d_m$ | $r_v$ | $D_s$ (mm) | Weight in air (gram) | Weight in water (gram) | Volume ($cm^3$) | $\rho_s$ ($g/cm^3$) | $\rho_b$ ($g/cm^3$) | Porosity ($\eta$) | Void ratio ($\varepsilon$) |
|---|---|---|---|---|---|---|---|---|---|---|---|---|---|---|---|---|
| 1 | 6.15 | 6.12 | 6.07 | 6.11 | 1.00 | 1.01 | 0.99 | 1.03 | 6.17 | 0.31 | 0.19 | 0.12 | 2.50 | 1.50 | 0.40 | 0.66 |
| 2 | 6.11 | 6.00 | 5.98 | 6.03 | 1.02 | 1.02 | 0.99 | 1.03 | 6.09 | 0.30 | 0.18 | 0.12 | 2.56 | 1.56 | 0.39 | 0.64 |
| 3 | 6.25 | 6.07 | 6.03 | 6.12 | 1.03 | 1.04 | 0.99 | 0.99 | 6.09 | 0.30 | 0.18 | 0.12 | 2.54 | 1.54 | 0.39 | 0.65 |
| 4 | 6.02 | 6.02 | 5.83 | 5.96 | 1.00 | 1.03 | 0.98 | 1.09 | 6.13 | 0.30 | 0.18 | 0.12 | 2.52 | 1.52 | 0.40 | 0.66 |
| 5 | 6.10 | 6.04 | 6.07 | 6.07 | 1.01 | 1.00 | 1.00 | 1.05 | 6.17 | 0.31 | 0.19 | 0.12 | 2.53 | 1.53 | 0.40 | 0.66 |
| 6 | 5.86 | 5.79 | 5.66 | 5.77 | 1.01 | 1.04 | 0.98 | 1.08 | 5.91 | 0.28 | 0.17 | 0.11 | 2.59 | 1.59 | 0.39 | 0.63 |
| 7 | 6.23 | 6.08 | 5.90 | 6.07 | 1.02 | 1.06 | 0.97 | 1.07 | 6.21 | 0.31 | 0.19 | 0.13 | 2.51 | 1.51 | 0.40 | 0.66 |
| 8 | 6.14 | 6.04 | 5.77 | 5.98 | 1.02 | 1.06 | 0.96 | 1.03 | 6.04 | 0.30 | 0.18 | 0.12 | 2.56 | 1.56 | 0.39 | 0.64 |
| 9 | 6.27 | 6.14 | 6.05 | 6.15 | 1.02 | 1.04 | 0.98 | 1.10 | 6.34 | 0.34 | 0.20 | 0.13 | 2.53 | 1.53 | 0.40 | 0.66 |
| 10 | 6.11 | 6.01 | 5.84 | 5.99 | 1.02 | 1.05 | 0.98 | 1.05 | 6.09 | 0.30 | 0.18 | 0.12 | 2.53 | 1.53 | 0.39 | 0.65 |
| 11 | 5.81 | 6.05 | 6.13 | 6.00 | 0.96 | 0.95 | 1.02 | 1.05 | 6.10 | 0.30 | 0.18 | 0.12 | 2.53 | 1.53 | 0.39 | 0.65 |
| 12 | 6.15 | 5.99 | 5.89 | 6.01 | 1.03 | 1.04 | 0.98 | 1.07 | 6.15 | 0.30 | 0.18 | 0.12 | 2.48 | 1.48 | 0.40 | 0.68 |
| 13 | 6.05 | 6.04 | 5.98 | 6.02 | 1.00 | 1.01 | 0.99 | 1.13 | 6.27 | 0.32 | 0.19 | 0.13 | 2.51 | 1.51 | 0.40 | 0.66 |
| 14 | 6.14 | 6.13 | 6.00 | 6.09 | 1.00 | 1.02 | 0.99 | 1.07 | 6.22 | 0.32 | 0.19 | 0.13 | 2.50 | 1.50 | 0.40 | 0.67 |
| 15 | 6.26 | 6.25 | 6.12 | 6.21 | 1.00 | 1.02 | 0.99 | 1.05 | 6.32 | 0.34 | 0.20 | 0.13 | 2.55 | 1.55 | 0.39 | 0.65 |
| 16 | 6.13 | 6.12 | 6.07 | 6.11 | 1.00 | 1.01 | 0.99 | 1.03 | 6.16 | 0.30 | 0.18 | 0.12 | 2.47 | 1.47 | 0.40 | 0.68 |
| 17 | 6.12 | 6.00 | 5.98 | 6.03 | 1.02 | 1.02 | 0.99 | 1.09 | 6.21 | 0.31 | 0.19 | 0.13 | 2.49 | 1.49 | 0.40 | 0.67 |
| 18 | 6.09 | 6.07 | 6.03 | 6.06 | 1.00 | 1.01 | 0.99 | 1.10 | 6.26 | 0.31 | 0.18 | 0.13 | 2.42 | 1.42 | 0.41 | 0.70 |
| 19 | 6.07 | 6.03 | 5.98 | 6.03 | 1.01 | 1.02 | 0.99 | 1.07 | 6.17 | 0.30 | 0.18 | 0.12 | 2.48 | 1.48 | 0.40 | 0.68 |
| 20 | 6.12 | 6.07 | 6.04 | 6.08 | 1.01 | 1.01 | 0.99 | 1.09 | 6.25 | 0.32 | 0.19 | 0.13 | 2.50 | 1.50 | 0.40 | 0.67 |
| 21 | 6.02 | 6.12 | 6.07 | 6.07 | 0.98 | 0.99 | 1.00 | 1.09 | 6.25 | 0.32 | 0.20 | 0.13 | 2.53 | 1.53 | 0.39 | 0.65 |
| 22 | 5.98 | 5.97 | 5.93 | 5.96 | 1.00 | 1.01 | 0.99 | 1.10 | 6.16 | 0.31 | 0.19 | 0.12 | 2.54 | 1.54 | 0.39 | 0.65 |
| 23 | 6.07 | 6.05 | 6.03 | 6.05 | 1.00 | 1.01 | 1.00 | 1.11 | 6.26 | 0.32 | 0.19 | 0.13 | 2.50 | 1.50 | 0.40 | 0.67 |
| 24 | 6.03 | 6.02 | 6.02 | 6.02 | 1.00 | 1.00 | 1.00 | 1.10 | 6.21 | 0.32 | 0.20 | 0.13 | 2.59 | 1.59 | 0.39 | 0.63 |
| 25 | 6.10 | 6.07 | 6.04 | 6.07 | 1.00 | 1.01 | 1.00 | 1.03 | 6.14 | 0.31 | 0.19 | 0.12 | 2.56 | 1.56 | 0.39 | 0.64 |
| 26 | 6.12 | 6.10 | 6.07 | 6.10 | 1.00 | 1.01 | 1.00 | 1.03 | 6.16 | 0.31 | 0.19 | 0.12 | 2.55 | 1.55 | 0.39 | 0.64 |
| 27 | 6.02 | 6.00 | 5.98 | 6.00 | 1.00 | 1.01 | 1.00 | 1.07 | 6.13 | 0.30 | 0.18 | 0.12 | 2.51 | 1.51 | 0.40 | 0.66 |
| 28 | 6.05 | 6.02 | 6.03 | 6.03 | 1.00 | 1.00 | 1.00 | 1.03 | 6.09 | 0.30 | 0.18 | 0.12 | 2.54 | 1.54 | 0.39 | 0.65 |
| 29 | 6.06 | 6.04 | 6.03 | 6.04 | 1.00 | 1.00 | 1.00 | 1.04 | 6.12 | 0.30 | 0.18 | 0.12 | 2.51 | 1.51 | 0.40 | 0.66 |
| 30 | 6.07 | 6.04 | 6.01 | 6.04 | 1.00 | 1.01 | 1.00 | 1.05 | 6.14 | 0.31 | 0.19 | 0.12 | 2.57 | 1.57 | 0.39 | 0.64 |
| mean | 6.10 | 6.04 | 6.03 | 6.04 | 1.00 | 1.01 | 0.99 | 1.07 | 6.16 | 0.31 | 0.19 | 0.12 | 2.53 | 1.53 | 0.40 | 0.66 |
| st. dev | 0.10 | 0.08 | 0.10 | 0.08 | 0.01 | 0.02 | 0.01 | 0.03 | 0.09 | 0.01 | 0.01 | 0.01 | 0.04 | 0.04 | 0.01 | 0.02 |
| max | 6.27 | 6.25 | 6.13 | 6.21 | 1.03 | 1.06 | 1.02 | 1.13 | 6.34 | 0.34 | 0.20 | 0.13 | 2.59 | 1.59 | 0.41 | 0.70 |
| min | 5.81 | 5.79 | 5.66 | 5.77 | 0.96 | 0.95 | 0.96 | 0.99 | 5.91 | 0.28 | 0.17 | 0.11 | 2.42 | 1.42 | 0.39 | 0.63 |

Table B8: Particle shape test, density, volume, porosity and voids ratio for the 5.00 mm glass bead.

| Particle | Length, $l$ (mm) | Width, $w$ (mm) | Depth, $d$ (mm) | $d_m$ (mm) | $l/w$ | $l/d$ | $d/d_m$ | $r_v$ | $D_s$ (mm) | Weight in air (gram) | Weight in water (gram) | Volume (cm³) | $\rho_s$ (g/cm³) | $\rho_b$ (g/cm³) | Porosity ($\eta$) | Void ratio ($\varepsilon$) |
|---|---|---|---|---|---|---|---|---|---|---|---|---|---|---|---|---|
| 1 | 5.26 | 5.19 | 5.06 | 5.17 | 1.01 | 1.04 | 0.98 | 1.00 | 5.18 | 0.18 | 0.11 | 0.07 | 2.51 | 1.51 | 0.40 | 0.66 |
| 2 | 5.22 | 5.05 | 4.85 | 5.04 | 1.03 | 1.08 | 0.96 | 0.99 | 5.02 | 0.17 | 0.10 | 0.07 | 2.50 | 1.50 | 0.40 | 0.67 |
| 3 | 5.30 | 5.15 | 5.03 | 5.16 | 1.03 | 1.05 | 0.97 | 0.98 | 5.13 | 0.18 | 0.11 | 0.07 | 2.52 | 1.52 | 0.40 | 0.66 |
| 4 | 5.11 | 5.06 | 5.04 | 5.07 | 1.01 | 1.01 | 0.99 | 0.96 | 5.00 | 0.17 | 0.10 | 0.07 | 2.57 | 1.57 | 0.39 | 0.64 |
| 5 | 5.20 | 5.16 | 5.15 | 5.17 | 1.01 | 1.01 | 1.00 | 1.02 | 5.20 | 0.18 | 0.11 | 0.07 | 2.48 | 1.48 | 0.40 | 0.68 |
| 6 | 5.12 | 5.09 | 5.04 | 5.08 | 1.01 | 1.02 | 0.99 | 0.99 | 5.07 | 0.18 | 0.11 | 0.07 | 2.58 | 1.58 | 0.39 | 0.63 |
| 7 | 4.81 | 4.77 | 4.76 | 4.78 | 1.01 | 1.01 | 1.00 | 1.14 | 4.99 | 0.17 | 0.10 | 0.07 | 2.55 | 1.55 | 0.39 | 0.64 |
| 8 | 5.12 | 4.89 | 5.02 | 5.01 | 1.05 | 1.02 | 1.00 | 0.92 | 4.88 | 0.16 | 0.10 | 0.06 | 2.57 | 1.57 | 0.39 | 0.63 |
| 9 | 5.08 | 5.05 | 4.94 | 5.02 | 1.01 | 1.03 | 0.98 | 0.94 | 4.92 | 0.16 | 0.09 | 0.06 | 2.52 | 1.52 | 0.40 | 0.66 |
| 10 | 5.04 | 4.98 | 4.90 | 4.97 | 1.01 | 1.03 | 0.99 | 1.09 | 5.13 | 0.18 | 0.11 | 0.07 | 2.51 | 1.51 | 0.40 | 0.66 |
| 11 | 5.10 | 5.03 | 4.98 | 5.04 | 1.01 | 1.02 | 0.99 | 0.98 | 5.00 | 0.17 | 0.10 | 0.07 | 2.56 | 1.56 | 0.39 | 0.64 |
| 12 | 5.11 | 5.04 | 5.02 | 5.06 | 1.01 | 1.02 | 0.99 | 1.01 | 5.08 | 0.18 | 0.11 | 0.07 | 2.59 | 1.59 | 0.39 | 0.63 |
| 13 | 5.21 | 5.11 | 5.13 | 5.15 | 1.02 | 1.02 | 1.00 | 0.96 | 5.08 | 0.18 | 0.11 | 0.07 | 2.59 | 1.59 | 0.39 | 0.63 |
| 14 | 4.95 | 4.93 | 4.93 | 4.94 | 1.00 | 1.00 | 1.00 | 1.05 | 5.01 | 0.17 | 0.10 | 0.07 | 2.55 | 1.55 | 0.39 | 0.64 |
| 15 | 5.12 | 5.07 | 5.02 | 5.07 | 1.01 | 1.02 | 0.99 | 0.85 | 4.79 | 0.15 | 0.09 | 0.06 | 2.57 | 1.57 | 0.39 | 0.64 |
| 16 | 5.09 | 5.08 | 5.02 | 5.06 | 1.00 | 1.01 | 0.99 | 1.02 | 5.10 | 0.18 | 0.11 | 0.07 | 2.57 | 1.57 | 0.39 | 0.64 |
| 17 | 5.12 | 5.08 | 5.07 | 5.09 | 1.01 | 1.01 | 1.00 | 1.02 | 5.12 | 0.18 | 0.11 | 0.07 | 2.54 | 1.54 | 0.39 | 0.65 |
| 18 | 5.03 | 4.96 | 4.84 | 4.94 | 1.01 | 1.04 | 0.98 | 1.05 | 5.02 | 0.17 | 0.10 | 0.07 | 2.55 | 1.55 | 0.39 | 0.64 |
| 19 | 5.13 | 5.09 | 4.97 | 5.06 | 1.01 | 1.03 | 0.98 | 1.03 | 5.11 | 0.18 | 0.11 | 0.07 | 2.56 | 1.56 | 0.39 | 0.64 |
| 20 | 4.97 | 4.94 | 4.90 | 4.94 | 1.01 | 1.01 | 0.99 | 1.01 | 4.96 | 0.16 | 0.10 | 0.06 | 2.50 | 1.50 | 0.40 | 0.67 |
| 21 | 5.11 | 5.02 | 5.02 | 5.05 | 1.02 | 1.02 | 0.99 | 1.00 | 5.06 | 0.17 | 0.10 | 0.07 | 2.51 | 1.51 | 0.40 | 0.66 |
| 22 | 5.07 | 5.01 | 4.98 | 5.02 | 1.01 | 1.02 | 0.99 | 0.94 | 4.92 | 0.16 | 0.10 | 0.06 | 2.55 | 1.55 | 0.39 | 0.65 |
| 23 | 5.12 | 5.06 | 5.02 | 5.07 | 1.01 | 1.02 | 0.99 | 0.99 | 5.04 | 0.17 | 0.10 | 0.07 | 2.52 | 1.52 | 0.40 | 0.66 |
| 24 | 5.11 | 5.03 | 5.01 | 5.05 | 1.02 | 1.02 | 0.99 | 1.05 | 5.14 | 0.18 | 0.11 | 0.07 | 2.52 | 1.52 | 0.40 | 0.66 |
| 25 | 5.26 | 5.10 | 5.05 | 5.14 | 1.03 | 1.04 | 0.98 | 1.00 | 5.13 | 0.18 | 0.11 | 0.07 | 2.53 | 1.53 | 0.39 | 0.65 |
| 26 | 4.87 | 4.85 | 4.65 | 4.79 | 1.00 | 1.05 | 0.97 | 1.10 | 4.94 | 0.16 | 0.10 | 0.06 | 2.53 | 1.53 | 0.40 | 0.65 |
| 27 | 5.07 | 5.01 | 5.00 | 5.03 | 1.01 | 1.01 | 0.99 | 1.07 | 5.14 | 0.18 | 0.11 | 0.07 | 2.53 | 1.53 | 0.39 | 0.65 |
| 28 | 5.21 | 5.13 | 5.07 | 5.14 | 1.02 | 1.03 | 0.99 | 0.88 | 4.92 | 0.16 | 0.10 | 0.06 | 2.57 | 1.57 | 0.39 | 0.64 |
| 29 | 5.05 | 5.05 | 4.99 | 5.03 | 1.00 | 1.01 | 0.99 | 0.99 | 5.02 | 0.17 | 0.10 | 0.07 | 2.57 | 1.57 | 0.39 | 0.63 |
| 30 | 5.12 | 5.02 | 4.98 | 5.04 | 1.02 | 1.03 | 0.99 | 0.95 | 4.96 | 0.16 | 0.10 | 0.06 | 2.52 | 1.52 | 0.40 | 0.66 |
| mean | 5.11 | 5.05 | 5.02 | 5.05 | 1.01 | 1.02 | 0.99 | 1.00 | 5.03 | 0.17 | 0.10 | 0.07 | 2.54 | 1.54 | 0.39 | 0.65 |
| st. dev | 0.11 | 0.09 | 0.10 | 0.09 | 0.01 | 0.02 | 0.01 | 0.06 | 0.10 | 0.01 | 0.01 | 0.00 | 0.03 | 0.03 | 0.00 | 0.01 |
| max | 5.30 | 5.19 | 5.15 | 5.17 | 1.05 | 1.08 | 1.00 | 1.14 | 5.20 | 0.18 | 0.11 | 0.07 | 2.59 | 1.59 | 0.40 | 0.68 |
| min | 4.81 | 4.77 | 4.65 | 4.78 | 1.00 | 1.00 | 0.96 | 0.85 | 4.79 | 0.15 | 0.09 | 0.06 | 2.48 | 1.48 | 0.39 | 0.63 |

Table B9: Particle shape test, density, volume, porosity and voids ratio for the 4.00 mm glass bead.

| Particle | Length, $l$ (mm) | Width, $w$ (mm) | Depth, $d$ (mm) | $d_m$ (mm) | $l/w$ | $l/d$ | $d/d_m$ | $r_v$ | $D_s$ (mm) | Weight in air (gram) | Weight in water (gram) | Volume (cm$^3$) | $\rho_s$ (g/cm$^3$) | $\rho_b$ (g/cm$^3$) | Porosity ($\eta$) | Void ratio ($\varepsilon$) |
|---|---|---|---|---|---|---|---|---|---|---|---|---|---|---|---|---|
| 1 | 4.06 | 4.03 | 4.00 | 4.03 | 1.01 | 1.02 | 0.99 | 0.97 | 3.99 | 0.08 | 0.05 | 0.033 | 2.48 | 1.48 | 0.40 | 0.68 |
| 2 | 4.12 | 4.08 | 4.06 | 4.09 | 1.01 | 1.01 | 0.99 | 0.88 | 3.92 | 0.08 | 0.05 | 0.032 | 2.55 | 1.55 | 0.39 | 0.65 |
| 3 | 4.03 | 4.00 | 3.99 | 4.01 | 1.01 | 1.01 | 1.00 | 1.06 | 4.09 | 0.09 | 0.05 | 0.036 | 2.50 | 1.50 | 0.40 | 0.67 |
| 4 | 4.12 | 4.05 | 4.02 | 4.06 | 1.02 | 1.02 | 0.99 | 0.97 | 4.02 | 0.09 | 0.05 | 0.034 | 2.51 | 1.51 | 0.40 | 0.66 |
| 5 | 4.09 | 4.05 | 3.98 | 4.04 | 1.01 | 1.03 | 0.99 | 0.93 | 3.95 | 0.08 | 0.05 | 0.032 | 2.52 | 1.52 | 0.40 | 0.66 |
| 6 | 4.10 | 4.05 | 4.04 | 4.06 | 1.01 | 1.01 | 0.99 | 0.96 | 4.02 | 0.08 | 0.05 | 0.034 | 2.49 | 1.49 | 0.40 | 0.67 |
| 7 | 4.13 | 4.12 | 4.09 | 4.11 | 1.00 | 1.01 | 0.99 | 0.93 | 4.01 | 0.08 | 0.05 | 0.034 | 2.51 | 1.51 | 0.40 | 0.66 |
| 8 | 4.09 | 4.07 | 3.95 | 4.04 | 1.00 | 1.04 | 0.98 | 0.85 | 3.82 | 0.07 | 0.04 | 0.029 | 2.53 | 1.53 | 0.39 | 0.65 |
| 9 | 4.13 | 4.02 | 3.98 | 4.04 | 1.03 | 1.04 | 0.98 | 0.91 | 3.91 | 0.08 | 0.05 | 0.031 | 2.56 | 1.56 | 0.39 | 0.64 |
| 10 | 4.09 | 4.06 | 3.69 | 3.95 | 1.01 | 1.11 | 0.93 | 0.98 | 3.92 | 0.08 | 0.05 | 0.032 | 2.49 | 1.49 | 0.40 | 0.67 |
| 11 | 4.17 | 3.79 | 3.65 | 3.87 | 1.10 | 1.14 | 0.94 | 1.11 | 4.01 | 0.09 | 0.05 | 0.034 | 2.55 | 1.55 | 0.39 | 0.64 |
| 12 | 4.12 | 4.06 | 4.02 | 4.07 | 1.01 | 1.02 | 0.99 | 0.99 | 4.05 | 0.09 | 0.06 | 0.035 | 2.59 | 1.59 | 0.39 | 0.63 |
| 13 | 4.11 | 4.11 | 4.04 | 4.09 | 1.00 | 1.02 | 0.99 | 0.95 | 4.02 | 0.09 | 0.05 | 0.034 | 2.54 | 1.54 | 0.39 | 0.65 |
| 14 | 4.12 | 4.09 | 3.87 | 4.03 | 1.01 | 1.06 | 0.96 | 1.03 | 4.07 | 0.09 | 0.05 | 0.035 | 2.47 | 1.47 | 0.41 | 0.68 |
| 15 | 4.13 | 4.10 | 4.01 | 4.08 | 1.01 | 1.03 | 0.98 | 0.97 | 4.03 | 0.09 | 0.05 | 0.034 | 2.54 | 1.54 | 0.39 | 0.65 |
| 16 | 4.14 | 4.00 | 4.00 | 4.05 | 1.04 | 1.04 | 0.99 | 0.99 | 4.04 | 0.09 | 0.05 | 0.035 | 2.53 | 1.53 | 0.39 | 0.65 |
| 17 | 4.07 | 3.99 | 3.89 | 3.98 | 1.02 | 1.05 | 0.98 | 1.02 | 4.01 | 0.09 | 0.05 | 0.034 | 2.55 | 1.55 | 0.39 | 0.65 |
| 18 | 4.16 | 4.09 | 4.08 | 4.11 | 1.02 | 1.02 | 0.99 | 0.84 | 3.88 | 0.08 | 0.05 | 0.030 | 2.51 | 1.51 | 0.40 | 0.66 |
| 19 | 4.20 | 4.04 | 4.02 | 4.09 | 1.04 | 1.04 | 0.98 | 0.96 | 4.03 | 0.09 | 0.05 | 0.034 | 2.54 | 1.54 | 0.39 | 0.65 |
| 20 | 4.22 | 4.21 | 4.19 | 4.21 | 1.00 | 1.01 | 1.00 | 0.88 | 4.03 | 0.09 | 0.05 | 0.034 | 2.51 | 1.51 | 0.40 | 0.66 |
| 21 | 4.19 | 4.11 | 4.08 | 4.13 | 1.02 | 1.03 | 0.99 | 0.93 | 4.03 | 0.09 | 0.05 | 0.034 | 2.55 | 1.55 | 0.39 | 0.65 |
| 22 | 4.35 | 4.11 | 4.11 | 4.19 | 1.06 | 1.06 | 0.98 | 0.91 | 4.06 | 0.09 | 0.05 | 0.035 | 2.51 | 1.51 | 0.40 | 0.66 |
| 23 | 4.21 | 4.04 | 4.01 | 4.09 | 1.04 | 1.05 | 0.98 | 0.75 | 3.71 | 0.07 | 0.04 | 0.027 | 2.53 | 1.53 | 0.39 | 0.65 |
| 24 | 4.15 | 4.03 | 4.00 | 4.06 | 1.03 | 1.04 | 0.99 | 0.99 | 4.04 | 0.09 | 0.05 | 0.035 | 2.55 | 1.55 | 0.39 | 0.64 |
| 25 | 4.43 | 3.99 | 3.89 | 4.10 | 1.11 | 1.14 | 0.95 | 0.97 | 4.06 | 0.09 | 0.05 | 0.035 | 2.52 | 1.52 | 0.40 | 0.66 |
| 26 | 4.13 | 4.06 | 3.96 | 4.05 | 1.02 | 1.04 | 0.98 | 1.01 | 4.07 | 0.09 | 0.05 | 0.035 | 2.51 | 1.51 | 0.40 | 0.66 |
| 27 | 3.97 | 3.97 | 3.90 | 3.95 | 1.00 | 1.02 | 0.99 | 1.10 | 4.08 | 0.09 | 0.05 | 0.035 | 2.51 | 1.51 | 0.40 | 0.66 |
| 28 | 4.06 | 4.04 | 4.01 | 4.04 | 1.01 | 1.01 | 0.99 | 1.03 | 4.08 | 0.09 | 0.05 | 0.036 | 2.51 | 1.51 | 0.40 | 0.66 |
| 29 | 4.14 | 4.12 | 3.98 | 4.08 | 1.00 | 1.04 | 0.98 | 0.87 | 3.89 | 0.08 | 0.05 | 0.031 | 2.59 | 1.59 | 0.39 | 0.63 |
| 30 | 4.05 | 4.01 | 3.89 | 3.98 | 1.01 | 1.04 | 0.98 | 1.15 | 4.17 | 0.09 | 0.05 | 0.038 | 2.37 | 1.37 | 0.42 | 0.73 |
| mean | 4.12 | 4.05 | 4.00 | 4.06 | 1.01 | 1.03 | 0.99 | 0.97 | 4.02 | 0.09 | 0.05 | 0.03 | 2.52 | 1.52 | 0.40 | 0.66 |
| st. dev | 0.09 | 0.07 | 0.11 | 0.07 | 0.03 | 0.03 | 0.02 | 0.08 | 0.09 | 0.01 | 0.00 | 0.00 | 0.04 | 0.04 | 0.01 | 0.02 |
| max | 4.43 | 4.21 | 4.19 | 4.21 | 1.11 | 1.14 | 1.00 | 1.15 | 4.17 | 0.09 | 0.06 | 0.04 | 2.59 | 1.59 | 0.42 | 0.73 |
| min | 3.97 | 3.79 | 3.65 | 3.87 | 1.00 | 1.01 | 0.93 | 0.75 | 3.71 | 0.07 | 0.04 | 0.03 | 2.37 | 1.37 | 0.39 | 0.63 |

Table B10: Particle shape test, density, volume, porosity and voids ratio for the 4.00 mm steel sphere.

| Particle | Length, $l$ (mm) | Width, $w$ (mm) | Depth, $d$ (mm) | $d_m$ (mm) | $l/w$ | $l/d$ | $d/d_m$ | $r_v$ | $D_s$ (mm) | Weight in air (gram) | Weight in water (gram) | Volume ($cm^3$) | $\rho_s$ ($g/cm^3$) | $\rho_b$ ($g/cm^3$) | Porosity ($\eta$) | Void ratio ($\varepsilon$) |
|---|---|---|---|---|---|---|---|---|---|---|---|---|---|---|---|---|
| 1 | 4.00 | 4.00 | 3.99 | 4.00 | 1.00 | 1.00 | 1.00 | 1.00 | 4.00 | 0.26 | 0.23 | 0.03 | 7.73 | 6.73 | 0.13 | 0.15 |
| 2 | 4.00 | 4.00 | 4.00 | 4.00 | 1.00 | 1.00 | 1.00 | 1.00 | 4.00 | 0.26 | 0.23 | 0.03 | 7.72 | 6.72 | 0.13 | 0.15 |
| 3 | 4.00 | 4.00 | 4.00 | 4.00 | 1.00 | 1.00 | 1.00 | 1.00 | 4.00 | 0.26 | 0.23 | 0.03 | 7.72 | 6.72 | 0.13 | 0.15 |
| 4 | 4.00 | 4.00 | 4.00 | 4.00 | 1.00 | 1.00 | 1.00 | 1.00 | 4.00 | 0.26 | 0.23 | 0.03 | 7.72 | 6.72 | 0.13 | 0.15 |
| 5 | 4.00 | 4.00 | 4.00 | 4.00 | 1.00 | 1.00 | 1.00 | 1.00 | 4.00 | 0.26 | 0.23 | 0.03 | 7.72 | 6.72 | 0.13 | 0.15 |
| 6 | 4.00 | 4.00 | 4.00 | 4.00 | 1.00 | 1.00 | 1.00 | 1.00 | 4.00 | 0.26 | 0.23 | 0.03 | 7.72 | 6.72 | 0.13 | 0.15 |
| 7 | 4.00 | 4.00 | 4.00 | 4.00 | 1.00 | 1.00 | 1.00 | 1.00 | 4.00 | 0.26 | 0.23 | 0.03 | 7.72 | 6.72 | 0.13 | 0.15 |
| 8 | 4.00 | 4.00 | 4.00 | 4.00 | 1.00 | 1.00 | 1.00 | 1.00 | 4.00 | 0.26 | 0.23 | 0.03 | 7.72 | 6.72 | 0.13 | 0.15 |
| 9 | 4.00 | 4.00 | 4.00 | 4.00 | 1.00 | 1.00 | 1.00 | 1.00 | 4.00 | 0.26 | 0.23 | 0.03 | 7.72 | 6.72 | 0.13 | 0.15 |
| 10 | 4.00 | 4.00 | 4.00 | 4.00 | 1.00 | 1.00 | 1.00 | 1.00 | 4.00 | 0.26 | 0.23 | 0.03 | 7.72 | 6.72 | 0.13 | 0.15 |
| 11 | 4.00 | 4.00 | 4.00 | 4.00 | 1.00 | 1.00 | 1.00 | 1.00 | 4.00 | 0.26 | 0.23 | 0.03 | 7.72 | 6.72 | 0.13 | 0.15 |
| 12 | 4.00 | 3.99 | 4.00 | 4.00 | 1.00 | 1.00 | 1.00 | 1.00 | 4.00 | 0.26 | 0.23 | 0.03 | 7.73 | 6.73 | 0.13 | 0.15 |
| 13 | 4.00 | 4.00 | 4.00 | 4.00 | 1.00 | 1.00 | 1.00 | 1.00 | 4.00 | 0.26 | 0.23 | 0.03 | 7.72 | 6.72 | 0.13 | 0.15 |
| 14 | 4.00 | 4.00 | 4.00 | 4.00 | 1.00 | 1.00 | 1.00 | 1.00 | 4.00 | 0.26 | 0.23 | 0.03 | 7.72 | 6.72 | 0.13 | 0.15 |
| 15 | 4.00 | 4.00 | 4.00 | 4.00 | 1.00 | 1.00 | 1.00 | 1.00 | 4.00 | 0.26 | 0.23 | 0.03 | 7.72 | 6.72 | 0.13 | 0.15 |
| 16 | 4.00 | 4.00 | 4.00 | 4.00 | 1.00 | 1.00 | 1.00 | 1.00 | 4.00 | 0.26 | 0.23 | 0.03 | 7.72 | 6.72 | 0.13 | 0.15 |
| 17 | 4.00 | 4.00 | 4.00 | 4.00 | 1.00 | 1.00 | 1.00 | 1.00 | 4.00 | 0.26 | 0.23 | 0.03 | 7.72 | 6.72 | 0.13 | 0.15 |
| 18 | 4.00 | 4.00 | 4.00 | 4.00 | 1.00 | 1.00 | 1.00 | 1.00 | 4.00 | 0.26 | 0.23 | 0.03 | 7.72 | 6.72 | 0.13 | 0.15 |
| 19 | 4.00 | 4.00 | 4.00 | 4.00 | 1.00 | 1.00 | 1.00 | 1.00 | 4.00 | 0.26 | 0.23 | 0.03 | 7.72 | 6.72 | 0.13 | 0.15 |
| 20 | 4.00 | 4.00 | 4.00 | 4.00 | 1.00 | 1.00 | 1.00 | 1.00 | 4.00 | 0.26 | 0.23 | 0.03 | 7.72 | 6.72 | 0.13 | 0.15 |
| 21 | 4.00 | 4.00 | 4.00 | 4.00 | 1.00 | 1.00 | 1.00 | 1.00 | 4.00 | 0.26 | 0.23 | 0.03 | 7.72 | 6.72 | 0.13 | 0.15 |
| 22 | 4.00 | 4.00 | 4.00 | 4.00 | 1.00 | 1.00 | 1.00 | 1.00 | 4.00 | 0.26 | 0.23 | 0.03 | 7.72 | 6.72 | 0.13 | 0.15 |
| 23 | 4.00 | 4.00 | 4.00 | 4.00 | 1.00 | 1.00 | 1.00 | 1.00 | 4.00 | 0.26 | 0.23 | 0.03 | 7.72 | 6.72 | 0.13 | 0.15 |
| 24 | 4.00 | 4.00 | 4.00 | 4.00 | 1.00 | 1.00 | 1.00 | 1.00 | 4.00 | 0.26 | 0.23 | 0.03 | 7.72 | 6.72 | 0.13 | 0.15 |
| 25 | 4.00 | 4.00 | 4.00 | 4.00 | 1.00 | 1.00 | 1.00 | 1.00 | 4.00 | 0.26 | 0.23 | 0.03 | 7.72 | 6.72 | 0.13 | 0.15 |
| 26 | 4.00 | 4.00 | 4.00 | 4.00 | 1.00 | 1.00 | 1.00 | 1.00 | 4.00 | 0.26 | 0.23 | 0.03 | 7.72 | 6.72 | 0.13 | 0.15 |
| 27 | 4.00 | 4.00 | 4.00 | 4.00 | 1.00 | 1.00 | 1.00 | 1.00 | 4.00 | 0.26 | 0.23 | 0.03 | 7.72 | 6.72 | 0.13 | 0.15 |
| 28 | 4.00 | 4.00 | 4.00 | 4.00 | 1.00 | 1.00 | 1.00 | 1.00 | 4.00 | 0.26 | 0.23 | 0.03 | 7.72 | 6.72 | 0.13 | 0.15 |
| 29 | 4.00 | 4.00 | 4.00 | 4.00 | 1.00 | 1.00 | 1.00 | 1.00 | 4.00 | 0.26 | 0.23 | 0.03 | 7.72 | 6.72 | 0.13 | 0.15 |
| 30 | 4.00 | 4.00 | 4.00 | 4.00 | 1.00 | 1.00 | 1.00 | 1.00 | 4.00 | 0.26 | 0.23 | 0.03 | 7.72 | 6.72 | 0.13 | 0.15 |
| mean | 4.00 | 4.00 | 4.00 | 4.00 | 1.00 | 1.00 | 1.00 | 1.00 | 4.00 | 0.26 | 0.23 | 0.03 | 7.72 | 6.72 | 0.13 | 0.15 |
| st. dev | 0.00 | 0.00 | 0.00 | 0.00 | 0.00 | 0.00 | 0.00 | 0.00 | 0.00 | 0.00 | 0.00 | 0.00 | 0.00 | 0.00 | 0.00 | 0.00 |
| max | 4.00 | 4.00 | 4.00 | 4.00 | 1.00 | 1.00 | 1.00 | 1.00 | 4.00 | 0.26 | 0.23 | 0.03 | 7.73 | 6.73 | 0.13 | 0.15 |
| min | 4.00 | 3.99 | 3.99 | 4.00 | 1.00 | 1.00 | 1.00 | 1.00 | 4.00 | 0.26 | 0.23 | 0.03 | 7.72 | 6.72 | 0.13 | 0.15 |

Table B11: Particle shape test, density, volume, porosity and voids ratio for the 4.00 mm cubical glass.

| Particle | Length, $l$ (mm) | Width, $w$ (mm) | Depth, $d$ (mm) | $d_m$ (mm) | $l/w$ | $l/d$ | $d/d_m$ | $r_v$ | $D_s$ (mm) | Weight in air (gram) | Weight in water (gram) | Volume ($cm^3$) | $\rho_s$ ($g/cm^3$) | $\rho_b$ ($g/cm^3$) | Porosity ($\eta$) | Void ratio ($\varepsilon$) |
|---|---|---|---|---|---|---|---|---|---|---|---|---|---|---|---|---|
| 1 | 4.20 | 4.13 | 4.00 | 4.11 | 1.02 | 1.05 | 0.97 | 2.00 | 5.18 | 0.18 | 0.11 | 0.07 | 2.51 | 1.51 | 0.40 | 0.66 |
| 2 | 4.22 | 4.20 | 4.05 | 4.16 | 1.00 | 1.04 | 0.97 | 1.76 | 5.02 | 0.17 | 0.10 | 0.07 | 2.50 | 1.50 | 0.40 | 0.67 |
| 3 | 4.25 | 4.20 | 4.10 | 4.18 | 1.01 | 1.04 | 0.98 | 1.89 | 5.18 | 0.18 | 0.11 | 0.07 | 2.45 | 1.45 | 0.41 | 0.69 |
| 4 | 4.22 | 4.15 | 4.15 | 4.17 | 1.02 | 1.02 | 0.99 | 1.77 | 5.05 | 0.17 | 0.10 | 0.07 | 2.50 | 1.50 | 0.40 | 0.67 |
| 5 | 4.20 | 4.15 | 4.12 | 4.16 | 1.01 | 1.02 | 0.99 | 1.95 | 5.20 | 0.18 | 0.11 | 0.07 | 2.48 | 1.48 | 0.40 | 0.68 |
| 6 | 4.22 | 4.20 | 4.20 | 4.21 | 1.00 | 1.00 | 1.00 | 1.80 | 5.12 | 0.18 | 0.11 | 0.07 | 2.51 | 1.51 | 0.40 | 0.66 |
| 7 | 4.21 | 4.15 | 4.14 | 4.17 | 1.01 | 1.02 | 0.99 | 1.76 | 5.03 | 0.17 | 0.10 | 0.07 | 2.50 | 1.50 | 0.40 | 0.67 |
| 8 | 4.20 | 4.20 | 4.15 | 4.18 | 1.00 | 1.01 | 0.99 | 1.64 | 4.93 | 0.16 | 0.09 | 0.06 | 2.49 | 1.49 | 0.40 | 0.67 |
| 9 | 4.25 | 4.20 | 4.20 | 4.22 | 1.01 | 1.01 | 1.00 | 1.59 | 4.92 | 0.16 | 0.09 | 0.06 | 2.52 | 1.52 | 0.40 | 0.66 |
| 10 | 4.13 | 4.10 | 4.08 | 4.10 | 1.01 | 1.01 | 0.99 | 1.95 | 5.13 | 0.18 | 0.11 | 0.07 | 2.51 | 1.51 | 0.40 | 0.66 |
| 11 | 4.33 | 4.12 | 4.10 | 4.18 | 1.05 | 1.06 | 0.98 | 1.79 | 5.07 | 0.17 | 0.10 | 0.07 | 2.45 | 1.45 | 0.41 | 0.69 |
| 12 | 4.21 | 4.15 | 4.13 | 4.16 | 1.01 | 1.02 | 0.99 | 1.89 | 5.15 | 0.18 | 0.11 | 0.07 | 2.51 | 1.51 | 0.40 | 0.66 |
| 13 | 4.29 | 4.20 | 4.15 | 4.21 | 1.02 | 1.03 | 0.98 | 1.82 | 5.15 | 0.18 | 0.11 | 0.07 | 2.49 | 1.49 | 0.40 | 0.67 |
| 14 | 4.18 | 4.15 | 4.15 | 4.16 | 1.01 | 1.01 | 1.00 | 1.80 | 5.06 | 0.17 | 0.10 | 0.07 | 2.48 | 1.48 | 0.40 | 0.68 |
| 15 | 4.24 | 4.15 | 4.12 | 4.17 | 1.02 | 1.03 | 0.99 | 1.57 | 4.85 | 0.15 | 0.09 | 0.06 | 2.49 | 1.49 | 0.40 | 0.67 |
| 16 | 4.18 | 4.14 | 4.10 | 4.14 | 1.01 | 1.02 | 0.99 | 1.93 | 5.15 | 0.18 | 0.11 | 0.07 | 2.50 | 1.50 | 0.40 | 0.67 |
| 17 | 4.13 | 4.08 | 4.06 | 4.09 | 1.01 | 1.02 | 0.99 | 2.02 | 5.17 | 0.18 | 0.11 | 0.07 | 2.47 | 1.47 | 0.40 | 0.68 |
| 18 | 4.29 | 4.25 | 4.22 | 4.25 | 1.01 | 1.02 | 0.99 | 1.69 | 5.07 | 0.17 | 0.10 | 0.07 | 2.48 | 1.48 | 0.40 | 0.68 |
| 19 | 4.24 | 4.20 | 4.10 | 4.18 | 1.01 | 1.03 | 0.98 | 1.91 | 5.19 | 0.18 | 0.11 | 0.07 | 2.45 | 1.45 | 0.41 | 0.69 |
| 20 | 4.32 | 4.20 | 4.15 | 4.22 | 1.03 | 1.04 | 0.98 | 1.65 | 4.99 | 0.16 | 0.09 | 0.06 | 2.46 | 1.46 | 0.41 | 0.69 |
| 21 | 4.34 | 4.24 | 4.25 | 4.28 | 1.02 | 1.02 | 0.99 | 1.68 | 5.08 | 0.17 | 0.10 | 0.07 | 2.47 | 1.47 | 0.40 | 0.68 |
| 22 | 4.25 | 4.12 | 4.10 | 4.16 | 1.03 | 1.04 | 0.99 | 1.74 | 5.00 | 0.16 | 0.09 | 0.07 | 2.43 | 1.43 | 0.41 | 0.70 |
| 23 | 4.18 | 4.18 | 4.07 | 4.14 | 1.00 | 1.03 | 0.98 | 1.83 | 5.07 | 0.17 | 0.10 | 0.07 | 2.48 | 1.48 | 0.40 | 0.68 |
| 24 | 4.21 | 4.10 | 4.10 | 4.14 | 1.03 | 1.03 | 0.99 | 1.97 | 5.19 | 0.18 | 0.11 | 0.07 | 2.45 | 1.45 | 0.41 | 0.69 |
| 25 | 4.23 | 4.05 | 4.05 | 4.11 | 1.04 | 1.04 | 0.99 | 2.03 | 5.21 | 0.18 | 0.11 | 0.07 | 2.43 | 1.43 | 0.41 | 0.70 |
| 26 | 4.10 | 4.10 | 4.05 | 4.08 | 1.00 | 1.01 | 0.99 | 1.84 | 5.01 | 0.16 | 0.09 | 0.07 | 2.43 | 1.43 | 0.41 | 0.70 |
| 27 | 4.25 | 4.18 | 4.15 | 4.19 | 1.02 | 1.02 | 0.99 | 1.91 | 5.20 | 0.18 | 0.11 | 0.07 | 2.45 | 1.45 | 0.41 | 0.69 |
| 28 | 4.14 | 4.10 | 4.04 | 4.09 | 1.01 | 1.02 | 0.99 | 1.79 | 4.97 | 0.16 | 0.10 | 0.06 | 2.49 | 1.49 | 0.40 | 0.67 |
| 29 | 4.30 | 4.20 | 4.20 | 4.23 | 1.02 | 1.02 | 0.99 | 1.74 | 5.09 | 0.17 | 0.10 | 0.07 | 2.46 | 1.46 | 0.41 | 0.68 |
| 30 | 4.24 | 4.15 | 4.10 | 4.16 | 1.02 | 1.03 | 0.98 | 1.73 | 5.00 | 0.16 | 0.10 | 0.07 | 2.46 | 1.46 | 0.41 | 0.69 |
| mean | 4.22 | 4.15 | 4.11 | 4.17 | 1.01 | 1.02 | 0.99 | 1.80 | 5.08 | 0.17 | 0.10 | 0.07 | 2.48 | 1.48 | 0.40 | 0.68 |
| st. dev | 0.06 | 0.05 | 0.06 | 0.05 | 0.01 | 0.01 | 0.01 | 0.13 | 0.09 | 0.01 | 0.01 | 0.00 | 0.03 | 0.03 | 0.00 | 0.01 |
| max | 4.34 | 4.25 | 4.25 | 4.28 | 1.05 | 1.06 | 1.00 | 2.03 | 5.21 | 0.18 | 0.11 | 0.07 | 2.52 | 1.52 | 0.41 | 0.70 |
| min | 4.10 | 4.05 | 4.00 | 4.08 | 1.00 | 1.00 | 0.97 | 1.57 | 4.85 | 0.15 | 0.09 | 0.06 | 2.43 | 1.43 | 0.40 | 0.66 |

Table B12: Particle shape test, density, volume, porosity and voids ratio for the 4.00 mm cylindrical glass.

| Particle | Length, $l$ (mm) | Width, $w$ (mm) | Depth, $d$ (mm) | $d_m$ (mm) | $l/w$ | $l/d$ | $d/d_m$ | $r_v$ | $D_s$ (mm) | Weight in air (gram) | Weight in water (gram) | Volume (cm³) | $\rho_s$ (g/cm³) | $\rho_b$ (g/cm³) | Porosity ($\eta$) | Void ratio ($\varepsilon$) |
|---|---|---|---|---|---|---|---|---|---|---|---|---|---|---|---|---|
| 1 | 4.20 | 4.10 | 4.10 | 4.13 | 1.02 | 1.02 | 0.99 | 1.35 | 4.56 | 0.12 | 0.07 | 0.05 | 2.41 | 1.41 | 0.41 | 0.71 |
| 2 | 4.20 | 4.15 | 4.10 | 4.15 | 1.01 | 1.02 | 0.99 | 1.33 | 4.57 | 0.12 | 0.07 | 0.05 | 2.42 | 1.42 | 0.41 | 0.70 |
| 3 | 4.20 | 4.20 | 4.20 | 4.20 | 1.00 | 1.00 | 1.00 | 1.33 | 4.62 | 0.12 | 0.07 | 0.05 | 2.37 | 1.37 | 0.42 | 0.73 |
| 4 | 4.10 | 4.00 | 4.00 | 4.03 | 1.03 | 1.03 | 0.99 | 1.37 | 4.48 | 0.12 | 0.07 | 0.05 | 2.49 | 1.49 | 0.40 | 0.67 |
| 5 | 4.22 | 4.20 | 4.15 | 4.19 | 1.00 | 1.02 | 0.99 | 1.33 | 4.61 | 0.12 | 0.07 | 0.05 | 2.38 | 1.38 | 0.42 | 0.72 |
| 6 | 4.05 | 4.05 | 4.05 | 4.05 | 1.00 | 1.00 | 1.00 | 1.37 | 4.50 | 0.12 | 0.07 | 0.05 | 2.47 | 1.47 | 0.40 | 0.68 |
| 7 | 4.25 | 4.20 | 4.20 | 4.22 | 1.01 | 1.01 | 1.00 | 1.33 | 4.64 | 0.12 | 0.07 | 0.05 | 2.35 | 1.35 | 0.43 | 0.74 |
| 8 | 4.24 | 4.21 | 4.20 | 4.22 | 1.01 | 1.01 | 1.00 | 1.32 | 4.62 | 0.12 | 0.07 | 0.05 | 2.37 | 1.37 | 0.42 | 0.73 |
| 9 | 4.18 | 4.15 | 4.14 | 4.16 | 1.01 | 1.01 | 1.00 | 1.34 | 4.58 | 0.12 | 0.07 | 0.05 | 2.40 | 1.40 | 0.42 | 0.72 |
| 10 | 4.12 | 4.10 | 4.10 | 4.11 | 1.00 | 1.00 | 1.00 | 1.34 | 4.53 | 0.12 | 0.07 | 0.05 | 2.45 | 1.45 | 0.41 | 0.69 |
| 11 | 4.10 | 4.05 | 4.05 | 4.07 | 1.01 | 1.01 | 1.00 | 1.39 | 4.54 | 0.12 | 0.07 | 0.05 | 2.42 | 1.42 | 0.41 | 0.71 |
| 12 | 4.15 | 4.10 | 4.10 | 4.12 | 1.01 | 1.01 | 1.00 | 1.35 | 4.56 | 0.12 | 0.07 | 0.05 | 2.42 | 1.42 | 0.41 | 0.70 |
| 13 | 4.06 | 4.05 | 4.05 | 4.05 | 1.00 | 1.00 | 1.00 | 1.36 | 4.49 | 0.12 | 0.07 | 0.05 | 2.49 | 1.49 | 0.40 | 0.67 |
| 14 | 4.10 | 4.04 | 4.04 | 4.06 | 1.01 | 1.01 | 1.00 | 1.40 | 4.54 | 0.12 | 0.07 | 0.05 | 2.40 | 1.40 | 0.42 | 0.71 |
| 15 | 4.21 | 4.15 | 4.15 | 4.17 | 1.01 | 1.01 | 1.00 | 1.34 | 4.60 | 0.12 | 0.07 | 0.05 | 2.39 | 1.39 | 0.42 | 0.72 |
| 16 | 4.26 | 4.20 | 4.20 | 4.22 | 1.01 | 1.01 | 1.00 | 1.34 | 4.65 | 0.12 | 0.07 | 0.05 | 2.33 | 1.33 | 0.43 | 0.75 |
| 17 | 4.25 | 4.20 | 4.20 | 4.22 | 1.01 | 1.01 | 1.00 | 1.33 | 4.64 | 0.12 | 0.07 | 0.05 | 2.35 | 1.35 | 0.43 | 0.74 |
| 18 | 4.24 | 4.15 | 4.15 | 4.18 | 1.02 | 1.02 | 0.99 | 1.32 | 4.59 | 0.12 | 0.07 | 0.05 | 2.40 | 1.40 | 0.42 | 0.71 |
| 19 | 4.23 | 4.20 | 4.20 | 4.21 | 1.01 | 1.01 | 1.00 | 1.33 | 4.63 | 0.12 | 0.07 | 0.05 | 2.35 | 1.35 | 0.42 | 0.74 |
| 20 | 4.15 | 4.12 | 4.12 | 4.13 | 1.01 | 1.01 | 1.00 | 1.35 | 4.56 | 0.12 | 0.07 | 0.05 | 2.42 | 1.42 | 0.41 | 0.70 |
| 21 | 4.15 | 4.10 | 4.10 | 4.12 | 1.01 | 1.01 | 1.00 | 1.36 | 4.56 | 0.12 | 0.07 | 0.05 | 2.42 | 1.42 | 0.41 | 0.71 |
| 22 | 4.24 | 4.15 | 4.15 | 4.18 | 1.02 | 1.02 | 0.99 | 1.32 | 4.59 | 0.12 | 0.07 | 0.05 | 2.40 | 1.40 | 0.42 | 0.71 |
| 23 | 4.22 | 4.15 | 4.15 | 4.17 | 1.02 | 1.02 | 0.99 | 1.34 | 4.60 | 0.12 | 0.07 | 0.05 | 2.38 | 1.38 | 0.42 | 0.72 |
| 24 | 4.25 | 4.20 | 4.20 | 4.22 | 1.01 | 1.01 | 1.00 | 1.31 | 4.61 | 0.12 | 0.07 | 0.05 | 2.39 | 1.39 | 0.42 | 0.72 |
| 25 | 4.20 | 4.20 | 4.20 | 4.20 | 1.00 | 1.00 | 1.00 | 1.33 | 4.62 | 0.12 | 0.07 | 0.05 | 2.36 | 1.36 | 0.42 | 0.73 |
| 26 | 4.16 | 4.15 | 4.15 | 4.15 | 1.00 | 1.00 | 1.00 | 1.34 | 4.58 | 0.12 | 0.07 | 0.05 | 2.40 | 1.40 | 0.42 | 0.71 |
| 27 | 4.23 | 4.16 | 4.20 | 4.20 | 1.02 | 1.01 | 1.00 | 1.33 | 4.61 | 0.12 | 0.07 | 0.05 | 2.38 | 1.38 | 0.42 | 0.72 |
| 28 | 4.16 | 4.10 | 4.10 | 4.12 | 1.01 | 1.01 | 1.00 | 1.34 | 4.54 | 0.12 | 0.07 | 0.05 | 2.44 | 1.44 | 0.41 | 0.69 |
| 29 | 4.09 | 4.05 | 4.05 | 4.06 | 1.01 | 1.01 | 1.00 | 1.39 | 4.53 | 0.12 | 0.07 | 0.05 | 2.43 | 1.43 | 0.41 | 0.70 |
| 30 | 4.15 | 4.12 | 4.10 | 4.12 | 1.01 | 1.01 | 0.99 | 1.33 | 4.54 | 0.12 | 0.07 | 0.05 | 2.45 | 1.45 | 0.41 | 0.69 |
| mean | 4.20 | 4.15 | 4.15 | 4.16 | 1.01 | 1.01 | 1.00 | 1.34 | 4.58 | 0.12 | 0.07 | 0.05 | 2.40 | 1.40 | 0.42 | 0.71 |
| st. dev | 0.06 | 0.06 | 0.06 | 0.06 | 0.01 | 0.01 | 0.00 | 0.02 | 0.05 | 0.00 | 0.00 | 0.00 | 0.04 | 0.04 | 0.01 | 0.02 |
| max | 4.26 | 4.21 | 4.20 | 4.22 | 1.03 | 1.03 | 1.00 | 1.40 | 4.65 | 0.12 | 0.07 | 0.05 | 2.49 | 1.49 | 0.43 | 0.75 |
| min | 4.05 | 4.00 | 4.00 | 4.03 | 1.00 | 1.00 | 0.99 | 1.31 | 4.48 | 0.12 | 0.07 | 0.05 | 2.33 | 1.33 | 0.40 | 0.67 |

Table B13: Particle shape test, density, volume, porosity and voids ratio for the 4.00 mm bi-conical glass.

| Particle | Length, $l$ (mm) | Width, $w$ (mm) | Depth, $d$ (mm) | $d_m$ (mm) | $l/w$ | $l/d$ | $d/d_m$ | $r_v$ | $D_s$ (mm) | Weight in air (gram) | Weight in water (gram) | Volume ($cm^3$) | $\rho_s$ ($g/cm^3$) | $\rho_b$ ($g/cm^3$) | Porosity ($\eta$) | Void ratio ($\varepsilon$) |
|---|---|---|---|---|---|---|---|---|---|---|---|---|---|---|---|---|
| 1 | 4.21 | 4.21 | 3.95 | 4.12 | 1.00 | 1.07 | 0.96 | 0.95 | 4.06 | 0.09 | 0.05 | 0.04 | 2.45 | 1.45 | 0.41 | 0.69 |
| 2 | 4.24 | 4.14 | 4.00 | 4.13 | 1.02 | 1.06 | 0.97 | 0.96 | 4.07 | 0.09 | 0.05 | 0.04 | 2.44 | 1.44 | 0.41 | 0.69 |
| 3 | 4.35 | 4.25 | 3.95 | 4.18 | 1.02 | 1.10 | 0.94 | 0.94 | 4.10 | 0.09 | 0.05 | 0.04 | 2.44 | 1.44 | 0.41 | 0.69 |
| 4 | 4.20 | 4.12 | 4.00 | 4.11 | 1.02 | 1.05 | 0.97 | 0.96 | 4.05 | 0.09 | 0.05 | 0.03 | 2.46 | 1.46 | 0.41 | 0.68 |
| 5 | 4.40 | 4.20 | 4.01 | 4.20 | 1.05 | 1.10 | 0.95 | 0.95 | 4.13 | 0.09 | 0.05 | 0.04 | 2.42 | 1.42 | 0.41 | 0.71 |
| 6 | 4.16 | 4.15 | 3.95 | 4.09 | 1.00 | 1.05 | 0.97 | 0.94 | 4.00 | 0.08 | 0.05 | 0.03 | 2.48 | 1.48 | 0.40 | 0.68 |
| 7 | 4.18 | 4.15 | 4.00 | 4.11 | 1.01 | 1.05 | 0.97 | 0.95 | 4.05 | 0.08 | 0.05 | 0.03 | 2.42 | 1.42 | 0.41 | 0.71 |
| 8 | 4.21 | 4.13 | 4.00 | 4.11 | 1.02 | 1.05 | 0.97 | 0.96 | 4.06 | 0.09 | 0.05 | 0.04 | 2.45 | 1.45 | 0.41 | 0.69 |
| 9 | 4.16 | 4.15 | 3.95 | 4.09 | 1.00 | 1.05 | 0.97 | 0.97 | 4.04 | 0.08 | 0.05 | 0.03 | 2.43 | 1.43 | 0.41 | 0.70 |
| 10 | 4.18 | 4.12 | 4.00 | 4.10 | 1.01 | 1.05 | 0.98 | 0.94 | 4.02 | 0.09 | 0.05 | 0.03 | 2.49 | 1.49 | 0.40 | 0.67 |
| 11 | 4.32 | 4.20 | 4.01 | 4.18 | 1.03 | 1.08 | 0.96 | 0.94 | 4.10 | 0.09 | 0.05 | 0.04 | 2.44 | 1.44 | 0.41 | 0.69 |
| 12 | 4.20 | 4.18 | 4.03 | 4.14 | 1.00 | 1.04 | 0.97 | 0.94 | 4.06 | 0.09 | 0.05 | 0.04 | 2.45 | 1.45 | 0.41 | 0.69 |
| 13 | 4.35 | 4.20 | 4.00 | 4.18 | 1.04 | 1.09 | 0.96 | 0.94 | 4.10 | 0.09 | 0.05 | 0.04 | 2.44 | 1.44 | 0.41 | 0.69 |
| 14 | 4.15 | 4.15 | 4.00 | 4.10 | 1.00 | 1.04 | 0.98 | 0.95 | 4.03 | 0.09 | 0.05 | 0.03 | 2.48 | 1.48 | 0.40 | 0.68 |
| 15 | 4.20 | 4.14 | 3.97 | 4.10 | 1.01 | 1.06 | 0.97 | 0.97 | 4.06 | 0.09 | 0.05 | 0.04 | 2.45 | 1.45 | 0.41 | 0.69 |
| 16 | 4.15 | 4.05 | 3.97 | 4.06 | 1.02 | 1.05 | 0.98 | 0.98 | 4.03 | 0.09 | 0.05 | 0.03 | 2.48 | 1.48 | 0.40 | 0.68 |
| 17 | 4.20 | 4.20 | 4.10 | 4.17 | 1.00 | 1.02 | 0.98 | 0.92 | 4.06 | 0.09 | 0.05 | 0.04 | 2.45 | 1.45 | 0.41 | 0.69 |
| 18 | 4.15 | 4.14 | 4.00 | 4.10 | 1.00 | 1.04 | 0.98 | 0.95 | 4.03 | 0.09 | 0.05 | 0.03 | 2.49 | 1.49 | 0.40 | 0.67 |
| 19 | 4.25 | 4.21 | 4.05 | 4.17 | 1.01 | 1.05 | 0.97 | 0.91 | 4.04 | 0.09 | 0.05 | 0.03 | 2.48 | 1.48 | 0.40 | 0.68 |
| 20 | 4.15 | 4.12 | 4.00 | 4.09 | 1.01 | 1.04 | 0.98 | 0.97 | 4.05 | 0.08 | 0.05 | 0.03 | 2.43 | 1.43 | 0.41 | 0.70 |
| 21 | 4.22 | 4.15 | 4.02 | 4.13 | 1.02 | 1.05 | 0.97 | 0.95 | 4.06 | 0.08 | 0.05 | 0.04 | 2.42 | 1.42 | 0.41 | 0.70 |
| 22 | 4.25 | 4.20 | 3.99 | 4.15 | 1.01 | 1.07 | 0.96 | 0.96 | 4.10 | 0.09 | 0.05 | 0.04 | 2.41 | 1.41 | 0.41 | 0.71 |
| 23 | 4.26 | 4.23 | 4.00 | 4.16 | 1.01 | 1.07 | 0.96 | 0.95 | 4.10 | 0.09 | 0.05 | 0.04 | 2.41 | 1.41 | 0.41 | 0.71 |
| 24 | 4.10 | 4.10 | 4.00 | 4.07 | 1.00 | 1.03 | 0.98 | 0.98 | 4.04 | 0.08 | 0.05 | 0.03 | 2.45 | 1.45 | 0.41 | 0.69 |
| 25 | 4.15 | 4.12 | 4.02 | 4.10 | 1.01 | 1.03 | 0.98 | 0.96 | 4.05 | 0.09 | 0.05 | 0.03 | 2.47 | 1.47 | 0.41 | 0.68 |
| 26 | 4.20 | 4.05 | 4.00 | 4.08 | 1.04 | 1.05 | 0.98 | 0.97 | 4.04 | 0.09 | 0.05 | 0.03 | 2.47 | 1.47 | 0.40 | 0.68 |
| 27 | 4.16 | 4.12 | 4.04 | 4.11 | 1.01 | 1.03 | 0.98 | 0.96 | 4.05 | 0.09 | 0.05 | 0.03 | 2.46 | 1.46 | 0.41 | 0.68 |
| 28 | 4.20 | 4.15 | 4.00 | 4.12 | 1.01 | 1.05 | 0.97 | 0.97 | 4.08 | 0.09 | 0.05 | 0.04 | 2.43 | 1.43 | 0.41 | 0.70 |
| 29 | 4.25 | 4.16 | 4.03 | 4.15 | 1.02 | 1.05 | 0.97 | 0.94 | 4.07 | 0.09 | 0.05 | 0.04 | 2.45 | 1.45 | 0.41 | 0.69 |
| 30 | 4.25 | 4.21 | 4.05 | 4.17 | 1.01 | 1.05 | 0.97 | 0.92 | 4.06 | 0.09 | 0.05 | 0.04 | 2.45 | 1.45 | 0.41 | 0.69 |
| mean | 4.20 | 4.15 | 4.00 | 4.12 | 1.01 | 1.05 | 0.97 | 0.95 | 4.06 | 0.09 | 0.05 | 0.04 | 2.45 | 1.45 | 0.41 | 0.69 |
| st. dev | 0.07 | 0.05 | 0.03 | 0.04 | 0.01 | 0.02 | 0.01 | 0.02 | 0.03 | 0.00 | 0.00 | 0.00 | 0.02 | 0.02 | 0.00 | 0.01 |
| max | 4.40 | 4.25 | 4.10 | 4.20 | 1.05 | 1.10 | 0.98 | 0.98 | 4.13 | 0.09 | 0.05 | 0.04 | 2.49 | 1.49 | 0.41 | 0.71 |
| min | 4.10 | 4.05 | 3.95 | 4.06 | 1.00 | 1.02 | 0.94 | 0.91 | 4.00 | 0.08 | 0.05 | 0.03 | 2.41 | 1.41 | 0.40 | 0.67 |

Table B14: Particle shape test, density, volume, porosity and voids ratio for the 4.00 mm plastic bead.

| Particle | Length, $l$ (mm) | Width, $w$ (mm) | Depth, $d$ (mm) | $d_m$ (mm) | $l / w$ | $l / d$ | $d / d_m$ | $r_v$ | $D_s$ (mm) | Weight in air (gram) | Weight in water (gram) | Volume (cm³) | $\rho_s$ (g/cm³) |
|---|---|---|---|---|---|---|---|---|---|---|---|---|---|
| 1 | 4.00 | 4.00 | 3.98 | 3.99 | 1.00 | 1.01 | 1.00 | 1.00 | 3.99 | 0.03 | 0.00 | 0.03 | 0.97 |
| 2 | 3.99 | 3.99 | 3.99 | 3.99 | 1.00 | 1.00 | 1.00 | 1.00 | 3.99 | 0.03 | 0.00 | 0.03 | 0.97 |
| 3 | 4.01 | 4.01 | 3.98 | 4.00 | 1.00 | 1.01 | 1.00 | 1.00 | 4.00 | 0.03 | 0.00 | 0.03 | 0.97 |
| 4 | 4.00 | 4.00 | 3.97 | 3.99 | 1.00 | 1.01 | 0.99 | 1.00 | 3.99 | 0.03 | 0.00 | 0.03 | 0.97 |
| 5 | 4.00 | 4.01 | 3.96 | 3.99 | 1.00 | 1.01 | 0.99 | 1.00 | 3.99 | 0.03 | 0.00 | 0.03 | 0.97 |
| 6 | 4.00 | 4.00 | 3.95 | 3.98 | 1.00 | 1.01 | 0.99 | 1.00 | 3.98 | 0.03 | 0.00 | 0.03 | 0.97 |
| 7 | 4.00 | 4.00 | 3.95 | 3.98 | 1.00 | 1.01 | 0.99 | 1.00 | 3.98 | 0.03 | 0.00 | 0.03 | 0.97 |
| 8 | 4.00 | 4.00 | 3.96 | 3.99 | 1.00 | 1.01 | 0.99 | 1.00 | 3.99 | 0.03 | 0.00 | 0.03 | 0.97 |
| 9 | 4.00 | 4.00 | 3.97 | 3.99 | 1.00 | 1.01 | 0.99 | 1.00 | 3.99 | 0.03 | 0.00 | 0.03 | 0.97 |
| 10 | 3.99 | 4.00 | 3.98 | 3.99 | 1.00 | 1.00 | 1.00 | 1.00 | 3.99 | 0.03 | 0.00 | 0.03 | 0.97 |
| 11 | 4.00 | 4.00 | 3.98 | 3.99 | 1.00 | 1.01 | 1.00 | 1.00 | 3.99 | 0.03 | 0.00 | 0.03 | 0.96 |
| 12 | 4.01 | 4.01 | 3.97 | 4.00 | 1.00 | 1.01 | 0.99 | 1.00 | 4.00 | 0.03 | 0.00 | 0.03 | 0.96 |
| 13 | 4.00 | 3.99 | 3.96 | 3.98 | 1.00 | 1.01 | 0.99 | 1.00 | 3.98 | 0.03 | 0.00 | 0.03 | 0.97 |
| 14 | 4.00 | 3.99 | 3.96 | 3.98 | 1.00 | 1.01 | 0.99 | 1.00 | 3.98 | 0.03 | 0.00 | 0.03 | 0.97 |
| 15 | 4.00 | 3.99 | 3.96 | 3.98 | 1.00 | 1.01 | 0.99 | 1.00 | 3.98 | 0.03 | 0.00 | 0.03 | 0.97 |
| 16 | 4.00 | 4.00 | 3.97 | 3.99 | 1.00 | 1.01 | 0.99 | 1.00 | 3.99 | 0.03 | 0.00 | 0.03 | 0.97 |
| 17 | 4.00 | 4.00 | 3.98 | 3.99 | 1.00 | 1.01 | 1.00 | 1.00 | 3.99 | 0.03 | 0.00 | 0.03 | 0.96 |
| 18 | 4.01 | 4.00 | 3.99 | 4.00 | 1.00 | 1.01 | 1.00 | 1.00 | 4.00 | 0.03 | 0.00 | 0.03 | 0.96 |
| 19 | 4.00 | 4.00 | 3.98 | 3.99 | 1.00 | 1.01 | 1.00 | 1.00 | 3.99 | 0.03 | 0.00 | 0.03 | 0.96 |
| 20 | 4.00 | 4.00 | 3.99 | 4.00 | 1.00 | 1.00 | 1.00 | 1.00 | 4.00 | 0.03 | 0.00 | 0.03 | 0.96 |
| 21 | 4.01 | 4.00 | 3.96 | 3.99 | 1.00 | 1.01 | 0.99 | 1.00 | 3.99 | 0.03 | 0.00 | 0.03 | 0.97 |
| 22 | 4.01 | 4.01 | 3.95 | 3.99 | 1.00 | 1.02 | 0.99 | 1.00 | 3.99 | 0.03 | 0.00 | 0.03 | 0.97 |
| 23 | 4.00 | 3.99 | 3.98 | 3.99 | 1.00 | 1.01 | 1.00 | 1.00 | 3.99 | 0.03 | 0.00 | 0.03 | 0.97 |
| 24 | 4.00 | 4.00 | 3.97 | 3.99 | 1.00 | 1.01 | 0.99 | 1.00 | 3.99 | 0.03 | 0.00 | 0.03 | 0.97 |
| 25 | 4.00 | 4.00 | 3.99 | 4.00 | 1.00 | 1.00 | 1.00 | 1.00 | 4.00 | 0.03 | 0.00 | 0.03 | 0.96 |
| 26 | 4.00 | 4.00 | 3.99 | 4.00 | 1.00 | 1.00 | 1.00 | 1.00 | 4.00 | 0.03 | 0.00 | 0.03 | 0.96 |
| 27 | 4.00 | 4.00 | 3.98 | 3.99 | 1.00 | 1.01 | 1.00 | 1.00 | 3.99 | 0.03 | 0.00 | 0.03 | 0.96 |
| 28 | 4.00 | 4.00 | 3.97 | 3.99 | 1.00 | 1.01 | 0.99 | 1.00 | 3.99 | 0.03 | 0.00 | 0.03 | 0.97 |
| 29 | 4.00 | 4.00 | 3.95 | 3.98 | 1.00 | 1.01 | 0.99 | 1.00 | 3.98 | 0.03 | 0.00 | 0.03 | 0.97 |
| 30 | 4.00 | 4.00 | 3.97 | 3.99 | 1.00 | 1.01 | 0.99 | 1.00 | 3.99 | 0.03 | 0.00 | 0.03 | 0.97 |
| mean | 4.00 | 4.00 | 3.97 | 3.99 | 1.00 | 1.01 | 0.99 | 1.00 | 3.99 | 0.03 | 0.00 | 0.03 | 0.97 |
| st. dev | 0.00 | 0.01 | 0.01 | 0.00 | 0.00 | 0.00 | 0.00 | 0.00 | 0.00 | 0.03 | 0.00 | 0.00 | 0.00 |
| max | 4.01 | 4.01 | 3.99 | 4.00 | 1.00 | 1.02 | 1.00 | 1.00 | 4.00 | 0.03 | 0.00 | 0.03 | 0.97 |
| min | 3.99 | 3.99 | 3.95 | 3.98 | 1.00 | 1.00 | 0.99 | 1.00 | 3.98 | 0.03 | 0.00 | 0.03 | 0.96 |

# APPENDIX C: SCPG PHYSICAL MODEL RESULTS

## C1 Effect of Strain Rate

Table C1.1: Fine (4.00 mm glass bead); Bed-matrix (15.75 mm glass bead); $\dot{\gamma}$ =0.01 $s^{-1}$ .

| $\gamma_{total}$ | Test 1 | | Test 2 | | Test 3 | | Mean | | Std. dev. | |
|---|---|---|---|---|---|---|---|---|---|---|
| | CPF (%) | IMF (%) | CPF (%) | IMF (%) | CPF (%) | IMF (%) | CPF (%) | IMF (%) | CPF (%) | IMF (%) |
| 0 | 0.00 | 0.00 | 0.00 | 0.00 | 0.00 | 0.00 | 0.00 | 0.00 | 0.00 | 0.00 |
| 50 | 0.00 | 0.00 | 0.00 | 0.00 | 0.00 | 0.00 | 0.00 | 0.00 | 0.00 | 0.00 |
| 100 | 0.00 | 0.00 | 0.00 | 0.00 | 0.00 | 0.00 | 0.00 | 0.00 | 0.00 | 0.00 |
| 200 | 0.00 | 0.00 | 0.00 | 0.00 | 0.00 | 0.00 | 0.00 | 0.00 | 0.00 | 0.00 |
| 400 | 1.87 | 1.87 | 1.03 | 1.03 | 1.66 | 1.66 | 1.52 | 1.52 | 0.44 | 0.44 |
| 800 | 15.95 | 14.08 | 15.00 | 13.97 | 14.13 | 12.47 | 15.03 | 13.51 | 0.91 | 0.90 |
| 1200 | 33.54 | 17.59 | 31.15 | 16.15 | 29.82 | 15.69 | 31.50 | 16.48 | 1.89 | 0.99 |
| 1600 | 41.50 | 7.96 | 40.69 | 9.54 | 43.27 | 13.45 | 41.82 | 10.32 | 1.32 | 2.83 |
| 2000 | 51.22 | 9.72 | 53.25 | 12.56 | 53.52 | 10.25 | 52.66 | 10.84 | 1.26 | 1.51 |
| 2400 | 54.06 | 2.84 | 55.84 | 2.59 | 56.42 | 2.90 | 55.44 | 2.78 | 1.23 | 0.16 |
| 2800 | 56.17 | 2.11 | 57.82 | 1.98 | 59.27 | 2.85 | 57.75 | 2.31 | 1.55 | 0.47 |
| 3200 | 58.28 | 2.11 | 59.97 | 2.15 | 61.47 | 2.20 | 59.91 | 2.15 | 1.60 | 0.05 |

Table C1.2: Fine (4.00 mm glass bead); Bed-matrix (15.75 mm glass bead); $\dot{\gamma}$ =0.02 $s^{-1}$ .

| $\gamma_{total}$ | Test 1 | | Test 2 | | Test 3 | | Mean | | Std. dev. | |
|---|---|---|---|---|---|---|---|---|---|---|
| | CPF (%) | IMF (%) | CPF (%) | IMF (%) | CPF (%) | IMF (%) | CPF (%) | IMF (%) | CPF (%) | IMF (%) |
| 0 | 0.00 | 0.00 | 0.00 | 0.00 | 0.00 | 0.00 | 0.00 | 0.00 | 0.00 | 0.00 |
| 50 | 0.00 | 0.00 | 0.00 | 0.00 | 0.00 | 0.00 | 0.00 | 0.00 | 0.00 | 0.00 |
| 100 | 0.00 | 0.00 | 0.00 | 0.00 | 0.00 | 0.00 | 0.00 | 0.00 | 0.00 | 0.00 |
| 200 | 0.00 | 0.00 | 0.00 | 0.00 | 0.00 | 0.00 | 0.00 | 0.00 | 0.00 | 0.00 |
| 400 | 5.37 | 5.37 | 4.70 | 4.70 | 4.30 | 4.30 | 4.79 | 4.79 | 0.54 | 0.54 |
| 800 | 21.90 | 16.53 | 16.44 | 11.74 | 18.14 | 13.84 | 18.83 | 14.04 | 2.79 | 2.40 |
| 1200 | 34.99 | 13.09 | 33.23 | 16.79 | 33.99 | 15.85 | 34.07 | 15.24 | 0.88 | 1.92 |
| 1600 | 45.55 | 10.56 | 48.08 | 14.85 | 49.49 | 15.50 | 47.71 | 13.64 | 2.00 | 2.68 |
| 2000 | 54.98 | 9.43 | 52.75 | 4.67 | 55.78 | 6.29 | 54.50 | 6.80 | 1.57 | 2.42 |
| 2400 | 58.11 | 3.13 | 61.15 | 8.40 | 62.15 | 6.37 | 60.47 | 5.97 | 2.10 | 2.66 |
| 2800 | 60.26 | 2.15 | 62.72 | 1.57 | 65.09 | 2.94 | 62.69 | 2.22 | 2.42 | 0.69 |
| 3200 | 62.19 | 1.93 | 64.49 | 1.77 | 67.95 | 2.86 | 64.88 | 2.19 | 2.90 | 0.59 |

Table C1.3: Fine (4.00 mm glass bead); Bed-matrix (15.75 mm glass bead); $\dot{\gamma}$ =0.03 $s^{-1}$ .

| $\gamma_{total}$ | Test 1 | | Test 2 | | Test 3 | | Mean | | Std. dev. | |
|---|---|---|---|---|---|---|---|---|---|---|
| | CPF (%) | IMF (%) | CPF (%) | IMF (%) | CPF (%) | IMF (%) | CPF (%) | IMF (%) | CPF (%) | IMF (%) |
| 0 | 0.00 | 0.00 | 0.00 | 0.00 | 0.00 | 0.00 | 0.00 | 0.00 | 0.00 | 0.00 |
| 50 | 0.00 | 0.00 | 0.00 | 0.00 | 0.00 | 0.00 | 0.00 | 0.00 | 0.00 | 0.00 |
| 100 | 0.00 | 0.00 | 0.00 | 0.00 | 0.00 | 0.00 | 0.00 | 0.00 | 0.00 | 0.00 |
| 200 | 0.00 | 0.00 | 0.00 | 0.00 | 0.00 | 0.00 | 0.00 | 0.00 | 0.00 | 0.00 |
| 400 | 3.81 | 3.81 | 3.99 | 3.99 | 5.18 | 5.18 | 4.33 | 4.33 | 0.74 | 0.74 |
| 800 | 17.08 | 13.27 | 19.06 | 15.07 | 22.07 | 16.89 | 19.40 | 15.08 | 2.51 | 1.81 |
| 1200 | 39.99 | 22.91 | 38.13 | 19.07 | 40.62 | 18.55 | 39.58 | 20.18 | 1.29 | 2.38 |
| 1600 | 56.72 | 16.73 | 55.69 | 17.56 | 58.77 | 18.15 | 57.06 | 17.48 | 1.57 | 0.71 |
| 2000 | 63.22 | 6.50 | 61.51 | 5.82 | 65.17 | 6.40 | 63.30 | 6.24 | 1.83 | 0.37 |
| 2400 | 67.51 | 4.29 | 64.03 | 2.52 | 66.90 | 1.73 | 66.15 | 2.85 | 1.86 | 1.31 |
| 2800 | 69.37 | 1.86 | 67.03 | 3.00 | 68.33 | 1.43 | 68.24 | 2.10 | 1.17 | 0.81 |
| 3200 | 71.07 | 1.70 | 68.87 | 1.84 | 73.01 | 4.68 | 70.98 | 2.74 | 2.07 | 1.68 |

Table C1.4: Fine 4.00 mm glass bead); Bed-matrix (15.75 mm glass bead); $\dot{\gamma}$ =0.04 $s^{-1}$.

| $\gamma_{total}$ | Test 1 | | Test 2 | | Test 3 | | Mean | | Std. dev. | |
|---|---|---|---|---|---|---|---|---|---|---|
| | CPF (%) | IMF (%) | CPF (%) | IMF (%) | CPF (%) | IMF (%) | CPF (%) | IMF (%) | CPF (%) | IMF (%) |
| 0 | 0.00 | 0.00 | 0.00 | 0.00 | 0.00 | 0.00 | 0.00 | 0.00 | 0.00 | 0.00 |
| 50 | 0.00 | 0.00 | 0.00 | 0.00 | 0.00 | 0.00 | 0.00 | 0.00 | 0.00 | 0.00 |
| 100 | 0.00 | 0.00 | 0.00 | 0.00 | 0.00 | 0.00 | 0.00 | 0.00 | 0.00 | 0.00 |
| 200 | 0.00 | 0.00 | 0.09 | 0.09 | 0.12 | 0.12 | 0.07 | 0.07 | 0.06 | 0.06 |
| 400 | 4.78 | 4.78 | 6.23 | 6.14 | 6.37 | 6.25 | 5.79 | 5.72 | 0.88 | 0.82 |
| 800 | 20.92 | 16.14 | 26.32 | 20.09 | 21.72 | 15.35 | 22.99 | 17.19 | 2.91 | 2.54 |
| 1200 | 46.00 | 25.08 | 49.45 | 23.13 | 43.87 | 22.15 | 46.44 | 23.45 | 2.82 | 1.49 |
| 1600 | 60.77 | 14.77 | 62.21 | 12.76 | 58.04 | 14.17 | 60.34 | 13.90 | 2.12 | 1.03 |
| 2000 | 70.39 | 9.62 | 68.98 | 6.77 | 63.20 | 5.16 | 67.52 | 7.18 | 3.81 | 2.26 |
| 2400 | 74.54 | 4.15 | 71.58 | 2.60 | 68.39 | 5.19 | 71.50 | 3.98 | 3.08 | 1.30 |
| 2800 | 78.28 | 3.74 | 73.74 | 2.16 | 72.15 | 3.76 | 74.72 | 3.22 | 3.18 | 0.92 |
| 3200 | 78.92 | 0.64 | 77.37 | 3.63 | 77.75 | 5.60 | 78.01 | 3.29 | 0.81 | 2.50 |

Table C1.5: Fine (4.05 mm crushed basalt); Bed-matrix (15.75 mm glass bead); $\dot{\gamma}$ =0.01 $s^{-1}$.

| $\gamma_{total}$ | Test 1 | | Test 2 | | Test 3 | | Mean | | Std. dev. | |
|---|---|---|---|---|---|---|---|---|---|---|
| | CPF (%) | IMF (%) | CPF (%) | IMF (%) | CPF (%) | IMF (%) | CPF (%) | IMF (%) | CPF (%) | IMF (%) |
| 0 | 0.00 | 0.00 | 0.00 | 0.00 | 0.00 | 0.00 | 0.00 | 0.00 | 0.00 | 0.00 |
| 50 | 0.00 | 0.00 | 0.00 | 0.00 | 0.00 | 0.00 | 0.00 | 0.00 | 0.00 | 0.00 |
| 100 | 0.00 | 0.00 | 0.00 | 0.00 | 0.00 | 0.00 | 0.00 | 0.00 | 0.00 | 0.00 |
| 200 | 0.00 | 0.00 | 0.00 | 0.00 | 0.00 | 0.00 | 0.00 | 0.00 | 0.00 | 0.00 |
| 400 | 9.54 | 9.54 | 12.28 | 12.28 | 9.44 | 9.44 | 10.42 | 10.42 | 1.61 | 1.61 |
| 800 | 38.23 | 28.69 | 40.76 | 28.48 | 39.21 | 29.77 | 39.40 | 28.98 | 0.69 | 0.69 |
| 1200 | 50.08 | 11.85 | 47.49 | 6.73 | 47.09 | 7.88 | 48.22 | 8.82 | 1.62 | 2.69 |
| 1600 | 59.60 | 9.52 | 55.58 | 8.09 | 55.17 | 8.08 | 56.78 | 8.56 | 2.45 | 0.83 |
| 2000 | 63.89 | 4.29 | 62.41 | 6.83 | 59.22 | 4.05 | 61.84 | 5.06 | 2.39 | 1.54 |
| 2400 | 65.62 | 1.73 | 63.63 | 1.22 | 62.57 | 3.35 | 63.94 | 2.10 | 1.55 | 1.11 |
| 2800 | 67.03 | 1.41 | 66.15 | 2.52 | 64.70 | 2.13 | 65.96 | 2.02 | 1.18 | 0.56 |
| 3200 | 68.04 | 1.01 | 66.83 | 0.68 | 65.18 | 0.48 | 66.68 | 0.72 | 1.44 | 0.27 |

Table C1.6: Fine (4.05 mm crushed basalt); Bed-matrix (15.75 mm glass bead); $\dot{\gamma}$ =0.02 $s^{-1}$.

| $\gamma_{total}$ | Test 1 | | Test 2 | | Test 3 | | Mean | | Std. dev. | |
|---|---|---|---|---|---|---|---|---|---|---|
| | CPF (%) | IMF (%) | CPF (%) | IMF (%) | CPF (%) | IMF (%) | CPF (%) | IMF (%) | CPF (%) | IMF (%) |
| 0 | 0.00 | 0.00 | 0.00 | 0.00 | 0.00 | 0.00 | 0.00 | 0.00 | 0.00 | 0.00 |
| 50 | 0.00 | 0.00 | 0.00 | 0.00 | 0.00 | 0.00 | 0.00 | 0.00 | 0.00 | 0.00 |
| 100 | 0.00 | 0.00 | 0.00 | 0.00 | 0.00 | 0.00 | 0.00 | 0.00 | 0.00 | 0.00 |
| 200 | 0.00 | 0.00 | 0.00 | 0.00 | 0.00 | 0.00 | 0.00 | 0.00 | 0.00 | 0.00 |
| 400 | 10.49 | 10.49 | 9.67 | 9.67 | 9.13 | 9.13 | 9.76 | 9.76 | 0.68 | 0.68 |
| 800 | 39.88 | 29.39 | 38.18 | 28.51 | 36.35 | 27.22 | 38.14 | 28.37 | 1.09 | 1.09 |
| 1200 | 51.11 | 11.23 | 53.64 | 15.46 | 51.10 | 14.75 | 51.95 | 13.81 | 1.46 | 2.27 |
| 1600 | 61.78 | 10.67 | 61.17 | 7.53 | 59.20 | 8.10 | 60.72 | 8.77 | 1.35 | 1.67 |
| 2000 | 67.15 | 5.37 | 66.87 | 5.70 | 63.87 | 4.67 | 65.96 | 5.25 | 1.82 | 0.53 |
| 2400 | 69.37 | 2.22 | 68.96 | 2.09 | 65.79 | 1.92 | 68.04 | 2.08 | 1.96 | 0.15 |
| 2800 | 72.30 | 2.93 | 71.70 | 2.74 | 68.40 | 2.61 | 70.80 | 2.76 | 2.10 | 0.16 |
| 3200 | 74.50 | 2.20 | 72.69 | 0.99 | 70.40 | 2.00 | 72.53 | 1.73 | 2.05 | 0.65 |

Table C1.7: Fine (4.05 mm crushed basalt); Bed-matrix (15.75 mm glass bead); $\dot{\gamma}$ =0.03 s $^{-1}$.

| $\gamma_{total}$ | Test 1 | | Test 2 | | Test 3 | | Mean | | Std. dev. | |
|---|---|---|---|---|---|---|---|---|---|---|
| | CPF (%) | IMF (%) | CPF (%) | IMF (%) | CPF (%) | IMF (%) | CPF (%) | IMF (%) | CPF (%) | IMF (%) |
| 0 | 0.00 | 0.00 | 0.00 | 0.00 | 0.00 | 0.00 | 0.00 | 0.00 | 0.00 | 0.00 |
| 50 | 0.00 | 0.00 | 0.00 | 0.00 | 0.00 | 0.00 | 0.00 | 0.00 | 0.00 | 0.00 |
| 100 | 0.00 | 0.00 | 0.00 | 0.00 | 0.00 | 0.00 | 0.00 | 0.00 | 0.00 | 0.00 |
| 200 | 2.06 | 2.06 | 1.33 | 1.33 | 1.61 | 1.61 | 1.67 | 1.67 | 0.37 | 0.37 |
| 400 | 9.89 | 7.83 | 8.02 | 6.69 | 8.95 | 7.34 | 8.95 | 7.29 | 0.57 | 0.57 |
| 800 | 35.42 | 25.53 | 38.93 | 30.91 | 37.97 | 29.02 | 37.44 | 28.49 | 2.73 | 2.73 |
| 1200 | 56.09 | 20.67 | 57.72 | 18.79 | 53.54 | 15.57 | 55.78 | 18.34 | 2.11 | 2.58 |
| 1600 | 63.64 | 7.55 | 66.60 | 8.88 | 63.57 | 10.03 | 64.60 | 8.82 | 1.73 | 1.24 |
| 2000 | 74.96 | 11.32 | 73.74 | 7.14 | 71.04 | 7.47 | 73.25 | 8.64 | 2.01 | 2.32 |
| 2400 | 77.45 | 2.49 | 76.05 | 2.31 | 71.52 | 0.48 | 75.01 | 1.76 | 3.10 | 1.11 |
| 2800 | 77.78 | 0.33 | 79.63 | 3.58 | 74.54 | 3.02 | 77.32 | 2.31 | 2.58 | 1.74 |
| 3200 | 78.86 | 1.08 | 80.16 | 0.53 | 74.79 | 0.25 | 77.94 | 0.62 | 2.80 | 0.42 |

Table C1.8: Fine (4.05 mm crushed basalt); Bed-matrix (15.75 mm glass bead); $\dot{\gamma}$ =0.04 s $^{-1}$.

| $\gamma_{total}$ | Test 1 | | Test 2 | | Test 3 | | Mean | | Std. dev. | |
|---|---|---|---|---|---|---|---|---|---|---|
| | CPF (%) | IMF (%) | CPF (%) | IMF (%) | CPF (%) | IMF (%) | CPF (%) | IMF (%) | CPF (%) | IMF (%) |
| 0 | 0.00 | 0.00 | 0.00 | 0.00 | 0.00 | 0.00 | 0.00 | 0.00 | 0.00 | 0.00 |
| 50 | 0.12 | 0.12 | 0.24 | 0.24 | 0.00 | 0.00 | 0.12 | 0.12 | 0.12 | 0.12 |
| 100 | 0.53 | 0.41 | 0.90 | 0.66 | 0.67 | 0.69 | 0.70 | 0.59 | 0.15 | 0.15 |
| 200 | 3.56 | 3.03 | 2.94 | 2.04 | 3.61 | 3.24 | 3.37 | 2.77 | 0.64 | 0.64 |
| 400 | 16.32 | 12.76 | 17.45 | 14.51 | 14.53 | 10.92 | 16.10 | 12.73 | 1.80 | 1.80 |
| 800 | 51.75 | 35.43 | 53.83 | 36.38 | 46.43 | 31.90 | 50.67 | 34.57 | 2.36 | 2.36 |
| 1200 | 68.20 | 16.45 | 71.76 | 17.93 | 65.86 | 19.43 | 68.61 | 17.94 | 2.97 | 1.49 |
| 1600 | 75.75 | 7.55 | 78.41 | 6.65 | 74.04 | 8.18 | 76.07 | 7.46 | 2.20 | 0.77 |
| 2000 | 76.47 | 0.72 | 80.87 | 2.46 | 76.57 | 2.53 | 77.97 | 1.90 | 2.51 | 1.03 |
| 2400 | 77.05 | 0.58 | 81.83 | 0.96 | 77.42 | 0.85 | 78.77 | 0.80 | 2.66 | 0.20 |
| 2800 | 78.29 | 1.24 | 82.05 | 0.22 | 78.63 | 1.21 | 79.66 | 0.89 | 2.08 | 0.58 |
| 3200 | 78.30 | 0.01 | 83.06 | 1.01 | 80.82 | 2.19 | 80.73 | 1.07 | 2.38 | 1.09 |

Table C1.9: Fine (4.00 mm glass bead); Bed-matrix (13.20 mm crushed basalt); $\dot{\gamma}$ =0.01 s $^{-1}$.

| $\gamma_{total}$ | Test 1 | | Test 2 | | Test 3 | | Mean | | Std. dev. | |
|---|---|---|---|---|---|---|---|---|---|---|
| | CPF (%) | IMF (%) | CPF (%) | IMF (%) | CPF (%) | IMF (%) | CPF (%) | IMF (%) | CPF (%) | IMF (%) |
| 0 | 0.00 | 0.00 | 0.00 | 0.00 | 0.00 | 0.00 | 0.00 | 0.00 | 0.00 | 0.00 |
| 50 | 0.00 | 0.00 | 0.00 | 0.00 | 0.00 | 0.00 | 0.00 | 0.00 | 0.00 | 0.00 |
| 100 | 0.00 | 0.00 | 0.00 | 0.00 | 0.00 | 0.00 | 0.00 | 0.00 | 0.00 | 0.00 |
| 200 | 0.00 | 0.00 | 0.00 | 0.00 | 0.00 | 0.00 | 0.00 | 0.00 | 0.00 | 0.00 |
| 400 | 0.00 | 0.00 | 0.00 | 0.00 | 0.00 | 0.00 | 0.00 | 0.00 | 0.00 | 0.00 |
| 800 | 0.00 | 0.00 | 0.00 | 0.00 | 0.00 | 0.00 | 0.00 | 0.00 | 0.00 | 0.00 |
| 1200 | 0.00 | 0.00 | 0.00 | 0.00 | 0.00 | 0.00 | 0.00 | 0.00 | 0.00 | 0.00 |
| 1600 | 0.00 | 0.00 | 0.00 | 0.00 | 0.00 | 0.00 | 0.00 | 0.00 | 0.00 | 0.00 |
| 2000 | 0.00 | 0.00 | 0.00 | 0.00 | 0.00 | 0.00 | 0.00 | 0.00 | 0.00 | 0.00 |
| 2400 | 0.00 | 0.00 | 0.00 | 0.00 | 0.00 | 0.00 | 0.00 | 0.00 | 0.00 | 0.00 |
| 2800 | 0.00 | 0.00 | 0.24 | 0.24 | 0.00 | 0.00 | 0.08 | 0.08 | 0.14 | 0.14 |
| 3200 | 0.47 | 0.47 | 0.47 | 0.23 | 0.48 | 0.48 | 0.47 | 0.39 | 0.01 | 0.14 |
| 3600 | 1.87 | 1.40 | 2.56 | 2.09 | 3.04 | 2.56 | 2.49 | 2.02 | 0.59 | 0.58 |
| 4000 | 3.63 | 1.76 | 4.50 | 1.94 | 5.33 | 2.29 | 4.49 | 2.00 | 0.85 | 0.27 |
| 4400 | 4.86 | 1.23 | 5.85 | 1.35 | 7.00 | 1.67 | 5.90 | 1.42 | 1.07 | 0.23 |
| 4800 | 7.71 | 2.85 | 10.35 | 4.50 | 10.62 | 3.62 | 9.56 | 3.66 | 1.61 | 0.83 |

Table C1.10: Fine (4.00 mm glass bead); Bed-matrix (13.20 mm crushed basalt); $\dot{\gamma}$ =0.02 $s^{-1}$.

| $\gamma_{total}$ | Test 1 | | Test 2 | | Test 3 | | Mean | | Std. dev. | |
|---|---|---|---|---|---|---|---|---|---|---|
| | CPF (%) | IMF (%) | CPF (%) | IMF (%) | CPF (%) | IMF (%) | CPF (%) | IMF (%) | CPF (%) | IMF (%) |
| 0 | 0.00 | 0.00 | 0.00 | 0.00 | 0.00 | 0.00 | 0.00 | 0.00 | 0.00 | 0.00 |
| 50 | 0.00 | 0.00 | 0.00 | 0.00 | 0.00 | 0.00 | 0.00 | 0.00 | 0.00 | 0.00 |
| 100 | 0.00 | 0.00 | 0.00 | 0.00 | 0.00 | 0.00 | 0.00 | 0.00 | 0.00 | 0.00 |
| 200 | 0.00 | 0.00 | 0.00 | 0.00 | 0.00 | 0.00 | 0.00 | 0.00 | 0.00 | 0.00 |
| 400 | 0.00 | 0.00 | 0.00 | 0.00 | 0.00 | 0.00 | 0.00 | 0.00 | 0.00 | 0.00 |
| 800 | 0.00 | 0.00 | 0.00 | 0.00 | 0.00 | 0.00 | 0.00 | 0.00 | 0.00 | 0.00 |
| 1200 | 0.00 | 0.00 | 0.00 | 0.00 | 0.00 | 0.00 | 0.00 | 0.00 | 0.00 | 0.00 |
| 1600 | 0.00 | 0.00 | 0.00 | 0.00 | 0.00 | 0.00 | 0.00 | 0.00 | 0.00 | 0.00 |
| 2000 | 0.00 | 0.00 | 0.00 | 0.00 | 0.00 | 0.00 | 0.00 | 0.00 | 0.00 | 0.00 |
| 2400 | 0.19 | 0.19 | 0.28 | 0.28 | 0.27 | 0.27 | 0.25 | 0.25 | 0.05 | 0.05 |
| 2800 | 0.50 | 0.31 | 0.57 | 0.29 | 0.52 | 0.25 | 0.53 | 0.28 | 0.04 | 0.03 |
| 3200 | 2.19 | 1.69 | 1.85 | 1.28 | 3.08 | 2.56 | 2.37 | 1.84 | 0.64 | 0.65 |
| 3600 | 3.90 | 1.71 | 3.77 | 1.92 | 5.20 | 2.12 | 4.29 | 1.92 | 0.79 | 0.21 |
| 4000 | 5.06 | 1.16 | 4.75 | 0.98 | 6.35 | 1.15 | 5.39 | 1.10 | 0.85 | 0.10 |
| 4400 | 8.57 | 3.51 | 9.23 | 4.48 | 11.94 | 5.59 | 9.91 | 4.53 | 1.79 | 1.04 |
| 4800 | 10.84 | 2.27 | 11.73 | 2.50 | 14.89 | 2.95 | 12.49 | 2.57 | 2.13 | 0.35 |

Table C1.11: Fine (4.00 mm glass bead); Bed-matrix (13.20 mm crushed basalt); $\dot{\gamma}$ =0.03 $s^{-1}$.

| $\gamma_{total}$ | Test 1 | | Test 2 | | Test 3 | | Mean | | Std. dev. | |
|---|---|---|---|---|---|---|---|---|---|---|
| | CPF (%) | IMF (%) | CPF (%) | IMF (%) | CPF (%) | IMF (%) | CPF (%) | IMF (%) | CPF (%) | IMF (%) |
| 0 | 0.00 | 0.00 | 0.00 | 0.00 | 0.00 | 0.00 | 0.00 | 0.00 | 0.00 | 0.00 |
| 50 | 0.00 | 0.00 | 0.00 | 0.00 | 0.00 | 0.00 | 0.00 | 0.00 | 0.00 | 0.00 |
| 100 | 0.00 | 0.00 | 0.00 | 0.00 | 0.00 | 0.00 | 0.00 | 0.00 | 0.00 | 0.00 |
| 200 | 0.00 | 0.00 | 0.00 | 0.00 | 0.00 | 0.00 | 0.00 | 0.00 | 0.00 | 0.00 |
| 400 | 0.00 | 0.00 | 0.00 | 0.00 | 0.00 | 0.00 | 0.00 | 0.00 | 0.00 | 0.00 |
| 800 | 0.00 | 0.00 | 0.00 | 0.00 | 0.00 | 0.00 | 0.00 | 0.00 | 0.00 | 0.00 |
| 1200 | 0.00 | 0.00 | 0.00 | 0.00 | 0.00 | 0.00 | 0.00 | 0.00 | 0.00 | 0.00 |
| 1600 | 0.00 | 0.00 | 0.00 | 0.00 | 0.00 | 0.00 | 0.00 | 0.00 | 0.00 | 0.00 |
| 2000 | 0.19 | 0.19 | 0.00 | 0.00 | 0.15 | 0.15 | 0.11 | 0.11 | 0.10 | 0.10 |
| 2400 | 0.79 | 0.60 | 0.60 | 0.60 | 0.66 | 0.51 | 0.68 | 0.57 | 0.10 | 0.05 |
| 2800 | 2.44 | 1.65 | 2.47 | 1.87 | 2.23 | 1.57 | 2.38 | 1.70 | 0.13 | 0.16 |
| 3200 | 5.62 | 3.18 | 6.50 | 4.03 | 4.97 | 2.74 | 5.70 | 3.32 | 0.77 | 0.66 |
| 3600 | 6.94 | 1.32 | 8.43 | 1.93 | 6.58 | 1.61 | 7.32 | 1.62 | 0.98 | 0.31 |
| 4000 | 10.66 | 3.72 | 11.64 | 3.21 | 9.93 | 3.35 | 10.74 | 3.43 | 0.86 | 0.26 |
| 4400 | 14.45 | 3.79 | 13.70 | 2.06 | 11.16 | 1.23 | 13.10 | 2.36 | 1.72 | 1.31 |
| 4800 | 16.74 | 2.29 | 17.61 | 3.91 | 14.85 | 3.69 | 16.40 | 3.30 | 1.41 | 0.88 |

Table C1.12: Fine (4.00 mm glass bead); Bed-matrix (13.20 mm crushed basalt); $\dot{\gamma}$ =0.04 $s^{-1}$.

| $\gamma_{total}$ | Test 1 | | Test 2 | | Test 3 | | Mean | | Std. dev. | |
|---|---|---|---|---|---|---|---|---|---|---|
| | CPF (%) | IMF (%) | CPF (%) | IMF (%) | CPF (%) | IMF (%) | CPF (%) | IMF (%) | CPF (%) | IMF (%) |
| 0 | 0.00 | 0.00 | 0.00 | 0.00 | 0.00 | 0.00 | 0.00 | 0.00 | 0.00 | 0.00 |
| 50 | 0.00 | 0.00 | 0.00 | 0.00 | 0.00 | 0.00 | 0.00 | 0.00 | 0.00 | 0.00 |
| 100 | 0.00 | 0.00 | 0.00 | 0.00 | 0.00 | 0.00 | 0.00 | 0.00 | 0.00 | 0.00 |
| 200 | 0.00 | 0.00 | 0.00 | 0.00 | 0.00 | 0.00 | 0.00 | 0.00 | 0.00 | 0.00 |
| 400 | 0.00 | 0.00 | 0.00 | 0.00 | 0.00 | 0.00 | 0.00 | 0.00 | 0.00 | 0.00 |
| 800 | 0.00 | 0.00 | 0.00 | 0.00 | 0.00 | 0.00 | 0.00 | 0.00 | 0.00 | 0.00 |
| 1200 | 0.00 | 0.00 | 0.00 | 0.00 | 0.00 | 0.00 | 0.00 | 0.00 | 0.00 | 0.00 |
| 1600 | 0.25 | 0.25 | 0.30 | 0.30 | 0.00 | 0.00 | 0.18 | 0.18 | 0.16 | 0.16 |
| 2000 | 0.62 | 0.37 | 1.58 | 1.28 | 0.97 | 0.97 | 1.06 | 0.87 | 0.49 | 0.46 |
| 2400 | 1.23 | 0.61 | 3.75 | 2.17 | 2.96 | 1.99 | 2.65 | 1.59 | 1.29 | 0.85 |
| 2800 | 3.10 | 1.87 | 5.86 | 2.11 | 5.23 | 2.27 | 4.73 | 2.08 | 1.45 | 0.20 |
| 3200 | 7.65 | 4.55 | 10.36 | 4.50 | 8.48 | 3.25 | 8.83 | 4.10 | 1.39 | 0.74 |
| 3600 | 9.56 | 1.91 | 13.66 | 3.30 | 12.21 | 3.73 | 11.81 | 2.98 | 2.08 | 0.95 |
| 4000 | 12.17 | 2.61 | 15.16 | 1.50 | 15.13 | 2.92 | 14.15 | 2.34 | 1.72 | 0.75 |
| 4400 | 15.89 | 3.72 | 17.13 | 1.97 | 17.88 | 2.75 | 16.97 | 2.81 | 1.01 | 0.88 |
| 4800 | 21.11 | 5.22 | 22.80 | 5.67 | 20.60 | 2.72 | 21.50 | 4.54 | 1.15 | 1.59 |

Table C1.13: Fine (4.05 mm crushed basalt); Bed-matrix (13.20 mm crushed basalt); $\dot{\gamma}$ =0.01 s$^{-1}$.

| $\gamma_{total}$ | Test 1 | | Test 2 | | Test 3 | | Mean | | Std. dev. | |
|---|---|---|---|---|---|---|---|---|---|---|
| | CPF (%) | IMF (%) | CPF (%) | IMF (%) | CPF (%) | IMF (%) | CPF (%) | IMF (%) | CPF (%) | IMF (%) |
| 0 | 0.00 | 0.00 | 0.00 | 0.00 | 0.00 | 0.00 | 0.00 | 0.00 | 0.00 | 0.00 |
| 50 | 0.00 | 0.00 | 0.00 | 0.00 | 0.00 | 0.00 | 0.00 | 0.00 | 0.00 | 0.00 |
| 100 | 0.00 | 0.00 | 0.00 | 0.00 | 0.00 | 0.00 | 0.00 | 0.00 | 0.00 | 0.00 |
| 200 | 0.00 | 0.00 | 0.00 | 0.00 | 0.00 | 0.00 | 0.00 | 0.00 | 0.00 | 0.00 |
| 400 | 0.00 | 0.00 | 0.00 | 0.00 | 0.00 | 0.00 | 0.00 | 0.00 | 0.00 | 0.00 |
| 800 | 0.00 | 0.00 | 0.00 | 0.00 | 0.00 | 0.00 | 0.00 | 0.00 | 0.00 | 0.00 |
| 1200 | 0.00 | 0.00 | 0.00 | 0.00 | 0.00 | 0.00 | 0.00 | 0.00 | 0.00 | 0.00 |
| 1600 | 0.00 | 0.00 | 0.00 | 0.00 | 0.00 | 0.00 | 0.00 | 0.00 | 0.00 | 0.00 |
| 2000 | 0.00 | 0.00 | 0.00 | 0.00 | 0.00 | 0.00 | 0.00 | 0.00 | 0.00 | 0.00 |
| 2400 | 0.17 | 0.17 | 0.17 | 0.17 | 0.40 | 0.40 | 0.25 | 0.25 | 0.13 | 0.13 |
| 2800 | 0.34 | 0.17 | 0.38 | 0.21 | 0.65 | 0.25 | 0.46 | 0.21 | 0.04 | 0.04 |
| 3200 | 1.49 | 1.15 | 1.88 | 1.50 | 2.13 | 1.48 | 1.83 | 1.38 | 0.32 | 0.20 |
| 3600 | 3.14 | 1.65 | 5.65 | 3.77 | 3.96 | 1.83 | 4.25 | 2.42 | 1.28 | 1.18 |
| 4000 | 4.07 | 0.93 | 6.04 | 0.39 | 4.48 | 0.52 | 4.86 | 0.61 | 1.04 | 0.28 |
| 4400 | 7.16 | 3.09 | 8.55 | 2.51 | 7.42 | 2.94 | 7.71 | 2.85 | 0.74 | 0.30 |
| 4800 | 11.43 | 4.27 | 13.26 | 4.71 | 11.30 | 3.88 | 12.00 | 4.29 | 1.10 | 0.42 |

Table C1.14: Fine (4.00 mm crushed basalt); Bed-matrix (13.20 mm crushed basalt); $\dot{\gamma}$ =0.02 s$^{-1}$.

| $\gamma_{total}$ | Test 1 | | Test 2 | | Test 3 | | Mean | | Std. dev. | |
|---|---|---|---|---|---|---|---|---|---|---|
| | CPF (%) | IMF (%) | CPF (%) | IMF (%) | CPF (%) | IMF (%) | CPF (%) | IMF (%) | CPF (%) | IMF (%) |
| 0 | 0.00 | 0.00 | 0.00 | 0.00 | 0.00 | 0.00 | 0.00 | 0.00 | 0.00 | 0.00 |
| 50 | 0.00 | 0.00 | 0.00 | 0.00 | 0.00 | 0.00 | 0.00 | 0.00 | 0.00 | 0.00 |
| 100 | 0.00 | 0.00 | 0.00 | 0.00 | 0.00 | 0.00 | 0.00 | 0.00 | 0.00 | 0.00 |
| 200 | 0.00 | 0.00 | 0.00 | 0.00 | 0.00 | 0.00 | 0.00 | 0.00 | 0.00 | 0.00 |
| 400 | 0.00 | 0.00 | 0.00 | 0.00 | 0.00 | 0.00 | 0.00 | 0.00 | 0.00 | 0.00 |
| 800 | 0.00 | 0.00 | 0.00 | 0.00 | 0.00 | 0.00 | 0.00 | 0.00 | 0.00 | 0.00 |
| 1200 | 0.00 | 0.00 | 0.00 | 0.00 | 0.00 | 0.00 | 0.00 | 0.00 | 0.00 | 0.00 |
| 1600 | 0.00 | 0.00 | 0.00 | 0.00 | 0.00 | 0.00 | 0.00 | 0.00 | 0.00 | 0.00 |
| 2000 | 0.00 | 0.00 | 0.00 | 0.00 | 0.00 | 0.00 | 0.00 | 0.00 | 0.00 | 0.00 |
| 2400 | 0.63 | 0.63 | 0.43 | 0.43 | 0.93 | 0.93 | 0.66 | 0.66 | 0.25 | 0.25 |
| 2800 | 1.39 | 0.76 | 1.40 | 0.97 | 1.82 | 0.89 | 1.54 | 0.87 | 0.25 | 0.11 |
| 3200 | 2.94 | 1.55 | 3.03 | 1.63 | 2.76 | 0.94 | 2.91 | 1.37 | 0.14 | 0.38 |
| 3600 | 6.26 | 3.32 | 7.85 | 4.82 | 7.37 | 4.61 | 7.16 | 4.25 | 0.82 | 0.81 |
| 4000 | 8.46 | 2.20 | 10.09 | 2.24 | 10.41 | 3.04 | 9.65 | 2.49 | 1.05 | 0.47 |
| 4400 | 13.69 | 5.23 | 14.82 | 4.73 | 14.23 | 3.82 | 14.25 | 4.59 | 0.57 | 0.71 |
| 4800 | 16.18 | 2.49 | 18.78 | 3.96 | 17.56 | 3.33 | 17.51 | 3.26 | 1.30 | 0.74 |

Table C1.15: Fine (4.00 mm crushed basalt); Bed-matrix (13.20 mm crushed basalt); $\dot{\gamma}$ =0.03 s$^{-1}$.

| $\gamma_{total}$ | Test 1 | | Test 2 | | Test 3 | | Mean | | Std. dev. | |
|---|---|---|---|---|---|---|---|---|---|---|
| | CPF (%) | IMF (%) | CPF (%) | IMF (%) | CPF (%) | IMF (%) | CPF (%) | IMF (%) | CPF (%) | IMF (%) |
| 0 | 0.00 | 0.00 | 0.00 | 0.00 | 0.00 | 0.00 | 0.00 | 0.00 | 0.00 | 0.00 |
| 50 | 0.00 | 0.00 | 0.00 | 0.00 | 0.00 | 0.00 | 0.00 | 0.00 | 0.00 | 0.00 |
| 100 | 0.00 | 0.00 | 0.00 | 0.00 | 0.00 | 0.00 | 0.00 | 0.00 | 0.00 | 0.00 |
| 200 | 0.00 | 0.00 | 0.00 | 0.00 | 0.00 | 0.00 | 0.00 | 0.00 | 0.00 | 0.00 |
| 400 | 0.00 | 0.00 | 0.00 | 0.00 | 0.00 | 0.00 | 0.00 | 0.00 | 0.00 | 0.00 |
| 800 | 0.00 | 0.00 | 0.00 | 0.00 | 0.00 | 0.00 | 0.00 | 0.00 | 0.00 | 0.00 |
| 1200 | 0.00 | 0.00 | 0.00 | 0.00 | 0.00 | 0.00 | 0.00 | 0.00 | 0.00 | 0.00 |
| 1600 | 0.00 | 0.00 | 0.00 | 0.00 | 0.00 | 0.00 | 0.00 | 0.00 | 0.00 | 0.00 |
| 2000 | 0.18 | 0.18 | 0.25 | 0.25 | 0.19 | 0.19 | 0.21 | 0.21 | 0.04 | 0.04 |
| 2400 | 0.92 | 0.74 | 1.13 | 0.88 | 0.80 | 0.61 | 0.95 | 0.74 | 0.17 | 0.14 |
| 2800 | 2.22 | 1.30 | 2.66 | 1.53 | 2.13 | 1.33 | 2.34 | 1.39 | 0.28 | 0.13 |
| 3200 | 4.78 | 2.56 | 4.73 | 2.07 | 4.86 | 2.73 | 4.79 | 2.45 | 0.07 | 0.34 |
| 3600 | 7.75 | 2.97 | 9.35 | 4.62 | 7.70 | 2.84 | 8.27 | 3.48 | 0.94 | 0.99 |
| 4000 | 11.98 | 4.23 | 13.96 | 4.61 | 12.59 | 4.89 | 12.84 | 4.58 | 1.01 | 0.33 |
| 4400 | 14.91 | 2.93 | 17.17 | 3.21 | 15.85 | 3.26 | 15.98 | 3.13 | 1.14 | 0.18 |
| 4800 | 19.53 | 4.62 | 20.76 | 3.59 | 20.91 | 5.06 | 20.40 | 4.42 | 0.76 | 0.75 |

Table C1.16: Fine (4.05 mm crushed basalt); Bed-matrix (13.20 mm crushed basalt); $\dot{\gamma}$ =0.04 s $^{-1}$ .

| $\gamma_{total}$ | Test 1 | | Test 2 | | Test 3 | | Mean | | Std. dev. | |
|---|---|---|---|---|---|---|---|---|---|---|
| | CPF (%) | IMF (%) | CPF (%) | IMF (%) | CPF (%) | IMF (%) | CPF (%) | IMF (%) | CPF (%) | IMF (%) |
| 0 | 0.00 | 0.00 | 0.00 | 0.00 | 0.00 | 0.00 | 0.00 | 0.00 | 0.00 | 0.00 |
| 50 | 0.00 | 0.00 | 0.00 | 0.00 | 0.00 | 0.00 | 0.00 | 0.00 | 0.00 | 0.00 |
| 100 | 0.00 | 0.00 | 0.00 | 0.00 | 0.00 | 0.00 | 0.00 | 0.00 | 0.00 | 0.00 |
| 200 | 0.00 | 0.00 | 0.00 | 0.00 | 0.00 | 0.00 | 0.00 | 0.00 | 0.00 | 0.00 |
| 400 | 0.00 | 0.00 | 0.00 | 0.00 | 0.00 | 0.00 | 0.00 | 0.00 | 0.00 | 0.00 |
| 800 | 0.00 | 0.00 | 0.00 | 0.00 | 0.00 | 0.00 | 0.00 | 0.00 | 0.00 | 0.00 |
| 1200 | 0.00 | 0.00 | 0.17 | 0.17 | 0.00 | 0.00 | 0.06 | 0.06 | 0.10 | 0.10 |
| 1600 | 0.35 | 0.35 | 0.43 | 0.26 | 0.71 | 0.71 | 0.50 | 0.44 | 0.19 | 0.24 |
| 2000 | 0.71 | 0.36 | 0.62 | 0.19 | 1.91 | 1.20 | 1.08 | 0.58 | 0.72 | 0.54 |
| 2400 | 1.49 | 0.78 | 1.35 | 0.73 | 2.57 | 0.66 | 1.80 | 0.72 | 0.67 | 0.06 |
| 2800 | 2.46 | 0.97 | 1.94 | 0.59 | 3.16 | 0.59 | 2.52 | 0.72 | 0.61 | 0.22 |
| 3200 | 6.38 | 3.92 | 5.62 | 3.68 | 7.06 | 3.90 | 6.35 | 3.83 | 0.72 | 0.13 |
| 3600 | 9.55 | 3.17 | 8.48 | 2.86 | 10.45 | 3.39 | 9.49 | 3.14 | 0.99 | 0.27 |
| 4000 | 13.90 | 4.35 | 13.16 | 4.68 | 15.32 | 4.87 | 14.13 | 4.63 | 1.10 | 0.26 |
| 4400 | 17.85 | 3.95 | 15.71 | 2.55 | 19.11 | 3.79 | 17.56 | 3.43 | 1.72 | 0.77 |
| 4800 | 25.06 | 7.21 | 22.44 | 6.73 | 28.36 | 9.25 | 25.29 | 7.73 | 2.97 | 1.34 |

## C2 Effect of Particle Diameter Ratio

Table C2.1: Fine (4.00 mm glass bead); Bed-matrix (15.75 mm glass bead); $\dot{\gamma}$ =0.04 s $^{-1}$ .

| $\gamma_{total}$ | Test 1 | | Test 2 | | Test 3 | | Mean | | Std. dev. | |
|---|---|---|---|---|---|---|---|---|---|---|
| | CPF (%) | IMF (%) | CPF (%) | IMF (%) | CPF (%) | IMF (%) | CPF (%) | IMF (%) | CPF (%) | IMF (%) |
| 0 | 0.00 | 0.00 | 0.00 | 0.00 | 0.00 | 0.00 | 0.00 | 0.00 | 0.00 | 0.00 |
| 50 | 0.00 | 0.00 | 0.00 | 0.00 | 0.00 | 0.00 | 0.00 | 0.00 | 0.00 | 0.00 |
| 100 | 0.00 | 0.00 | 0.00 | 0.00 | 0.00 | 0.00 | 0.00 | 0.00 | 0.00 | 0.00 |
| 200 | 0.00 | 0.00 | 0.09 | 0.09 | 0.12 | 0.12 | 0.07 | 0.07 | 0.06 | 0.06 |
| 400 | 4.78 | 4.78 | 6.23 | 6.14 | 6.37 | 6.25 | 5.79 | 5.72 | 0.88 | 0.82 |
| 800 | 20.92 | 16.14 | 26.32 | 20.09 | 21.72 | 15.35 | 22.99 | 17.19 | 2.91 | 2.54 |
| 1200 | 46.00 | 25.08 | 49.45 | 23.13 | 43.87 | 22.15 | 46.44 | 23.45 | 2.82 | 1.49 |
| 1600 | 60.77 | 14.77 | 62.21 | 12.76 | 54.04 | 10.17 | 59.01 | 12.57 | 4.36 | 2.31 |
| 2000 | 70.39 | 9.62 | 68.98 | 6.77 | 63.20 | 9.16 | 67.52 | 8.52 | 3.81 | 1.53 |
| 2400 | 74.54 | 4.15 | 71.58 | 2.60 | 68.39 | 5.19 | 71.50 | 3.98 | 3.08 | 1.30 |
| 2800 | 78.28 | 3.74 | 73.74 | 2.16 | 72.15 | 3.76 | 74.72 | 3.22 | 3.18 | 0.92 |
| 3200 | 78.92 | 0.64 | 77.37 | 3.63 | 77.75 | 5.60 | 78.01 | 3.29 | 0.81 | 2.50 |

Table C2.2: Fine (5.00 mm glass bead); Bed-matrix (15.75 mm glass bead); $\dot{\gamma}$ =0.04 s $^{-1}$ .

| $\gamma_{total}$ | Test 1 | | Test 2 | | Test 3 | | Mean | | Std. dev. | |
|---|---|---|---|---|---|---|---|---|---|---|
| | CPF (%) | IMF (%) | CPF (%) | IMF (%) | CPF (%) | IMF (%) | CPF (%) | IMF (%) | CPF (%) | IMF (%) |
| 0 | 0.00 | 0.00 | 0.00 | 0.00 | 0.00 | 0.00 | 0.00 | 0.00 | 0.00 | 0.00 |
| 50 | 0.00 | 0.00 | 0.00 | 0.00 | 0.00 | 0.00 | 0.00 | 0.00 | 0.00 | 0.00 |
| 100 | 0.00 | 0.00 | 0.00 | 0.00 | 0.00 | 0.00 | 0.00 | 0.00 | 0.00 | 0.00 |
| 200 | 0.00 | 0.00 | 0.00 | 0.00 | 0.00 | 0.00 | 0.00 | 0.00 | 0.00 | 0.00 |
| 400 | 0.00 | 0.00 | 0.00 | 0.00 | 1.17 | 1.17 | 0.39 | 0.39 | 0.68 | 0.68 |
| 800 | 4.68 | 4.68 | 4.35 | 4.35 | 3.79 | 2.62 | 4.27 | 3.88 | 0.45 | 1.11 |
| 1200 | 10.39 | 5.71 | 10.27 | 5.92 | 12.13 | 8.34 | 10.93 | 6.66 | 1.04 | 1.46 |
| 1600 | 20.10 | 9.71 | 22.41 | 12.14 | 24.84 | 12.71 | 22.45 | 11.52 | 2.37 | 1.59 |
| 2000 | 26.61 | 6.51 | 27.60 | 5.19 | 30.83 | 5.99 | 28.35 | 5.90 | 2.21 | 0.66 |
| 2400 | 34.21 | 7.60 | 33.46 | 5.86 | 36.31 | 5.48 | 34.66 | 6.31 | 1.48 | 1.13 |
| 2800 | 39.58 | 5.37 | 41.76 | 8.30 | 45.17 | 8.86 | 42.17 | 7.51 | 2.82 | 1.87 |
| 3200 | 40.76 | 1.18 | 42.92 | 1.16 | 46.97 | 1.80 | 43.55 | 1.38 | 3.15 | 0.36 |

Table C2.3: Fine (6.00 mm glass bead); Bed-matrix (15.75 mm glass bead); $\dot{\gamma}$ =0.04 s $^{-1}$ .

| $\gamma_{total}$ | Test 1 | | Test 2 | | Test 3 | | Mean | | Std. dev. | |
|---|---|---|---|---|---|---|---|---|---|---|
| | CPF (%) | IMF (%) | CPF (%) | IMF (%) | CPF (%) | IMF (%) | CPF (%) | IMF (%) | CPF (%) | IMF (%) |
| 0 | 0.00 | 0.00 | 0.00 | 0.00 | 0.00 | 0.00 | 0.00 | 0.00 | 0.00 | 0.00 |
| 50 | 0.00 | 0.00 | 0.00 | 0.00 | 0.00 | 0.00 | 0.00 | 0.00 | 0.00 | 0.00 |
| 100 | 0.00 | 0.00 | 0.00 | 0.00 | 0.00 | 0.00 | 0.00 | 0.00 | 0.00 | 0.00 |
| 200 | 0.00 | 0.00 | 0.00 | 0.00 | 0.00 | 0.00 | 0.00 | 0.00 | 0.00 | 0.00 |
| 400 | 0.00 | 0.00 | 0.00 | 0.00 | 0.00 | 0.00 | 0.00 | 0.00 | 0.00 | 0.00 |
| 800 | 0.00 | 0.00 | 0.00 | 0.00 | 0.00 | 0.00 | 0.00 | 0.00 | 0.00 | 0.00 |
| 1200 | 0.54 | 0.54 | 0.00 | 0.00 | 1.03 | 1.03 | 0.52 | 0.52 | 0.52 | 0.52 |
| 1600 | 2.50 | 1.96 | 1.69 | 1.69 | 3.20 | 2.17 | 2.46 | 1.94 | 0.76 | 0.24 |
| 2000 | 3.73 | 1.23 | 4.51 | 2.82 | 8.63 | 5.43 | 5.62 | 3.16 | 2.63 | 2.12 |
| 2400 | 3.73 | 0.00 | 5.41 | 0.90 | 9.66 | 1.03 | 6.27 | 0.64 | 3.06 | 0.56 |
| 2800 | 5.43 | 1.70 | 6.69 | 1.28 | 9.66 | 0.00 | 7.26 | 0.99 | 2.17 | 0.89 |
| 3200 | 5.43 | 0.00 | 6.69 | 0.00 | 9.66 | 0.00 | 7.26 | 0.00 | 2.17 | 0.00 |

Table C2.4: Fine (2.86 mm crushed basalt); Bed-matrix (15.75 mm glass bead); $\dot{\gamma}$ =0.04 s $^{-1}$.

| $\gamma_{total}$ | Test 1 | | Test 2 | | Test 3 | | Mean | | Std. dev. | |
|---|---|---|---|---|---|---|---|---|---|---|
| | CPF (%) | IMF (%) | CPF (%) | IMF (%) | CPF (%) | IMF (%) | CPF (%) | IMF (%) | CPF (%) | IMF (%) |
| 0 | 0.00 | 0.00 | 0.00 | 0.00 | 0.00 | 0.00 | 0.00 | 0.00 | 0.00 | 0.00 |
| 50 | 11.23 | 11.23 | 11.92 | 11.92 | 10.53 | 10.53 | 11.23 | 11.23 | 0.70 | 0.70 |
| 100 | 23.62 | 12.39 | 24.80 | 12.88 | 22.87 | 12.34 | 23.76 | 12.54 | 0.30 | 0.30 |
| 200 | 43.56 | 19.94 | 43.95 | 19.15 | 42.20 | 19.33 | 43.24 | 19.47 | 0.41 | 0.41 |
| 400 | 82.74 | 39.18 | 84.06 | 40.11 | 81.38 | 39.18 | 82.73 | 39.49 | 0.54 | 0.54 |
| 800 | 95.67 | 12.93 | 96.74 | 12.68 | 95.13 | 13.75 | 95.85 | 13.12 | 0.56 | 0.56 |
| 1200 | 97.81 | 2.14 | 98.52 | 1.78 | 97.51 | 2.38 | 97.95 | 2.10 | 0.52 | 0.30 |
| 1600 | 98.27 | 0.46 | 98.87 | 0.35 | 97.85 | 0.34 | 98.33 | 0.38 | 0.51 | 0.07 |
| 2000 | 98.45 | 0.18 | 99.02 | 0.15 | 97.97 | 0.12 | 98.48 | 0.15 | 0.53 | 0.03 |
| 2400 | 98.70 | 0.25 | 99.20 | 0.18 | 98.14 | 0.17 | 98.68 | 0.20 | 0.53 | 0.04 |
| 2800 | 98.96 | 0.26 | 99.26 | 0.06 | 98.25 | 0.11 | 98.82 | 0.14 | 0.52 | 0.10 |
| 3200 | 99.20 | 0.24 | 99.26 | 0.00 | 98.48 | 0.23 | 98.98 | 0.16 | 0.43 | 0.14 |

Table C2.5: Fine (4.05 crushed basalt); Bed-matrix (15.75 mm glass bead); $\dot{\gamma}$ =0.04 s $^{-1}$.

| $\gamma_{total}$ | Test 1 | | Test 2 | | Test 3 | | Mean | | Std. dev. | |
|---|---|---|---|---|---|---|---|---|---|---|
| | CPF (%) | IMF (%) | CPF (%) | IMF (%) | CPF (%) | IMF (%) | CPF (%) | IMF (%) | CPF (%) | IMF (%) |
| 0 | 0.00 | 0.00 | 0.00 | 0.00 | 0.00 | 0.00 | 0.00 | 0.00 | 0.00 | 0.00 |
| 50 | 0.12 | 0.12 | 0.24 | 0.24 | 0.00 | 0.00 | 0.12 | 0.12 | 0.12 | 0.12 |
| 100 | 0.53 | 0.41 | 0.90 | 0.66 | 0.67 | 0.69 | 0.70 | 0.59 | 0.15 | 0.15 |
| 200 | 3.56 | 3.03 | 2.94 | 2.04 | 3.61 | 3.24 | 3.37 | 2.77 | 0.64 | 0.64 |
| 400 | 16.32 | 12.76 | 17.45 | 14.51 | 14.53 | 10.92 | 16.10 | 12.73 | 1.80 | 1.80 |
| 800 | 51.75 | 35.43 | 53.83 | 36.38 | 46.43 | 31.90 | 50.67 | 34.57 | 2.36 | 2.36 |
| 1200 | 68.20 | 16.45 | 71.76 | 17.93 | 65.86 | 19.43 | 68.61 | 17.94 | 2.97 | 1.49 |
| 1600 | 75.75 | 7.55 | 78.41 | 6.65 | 74.04 | 8.18 | 76.07 | 7.46 | 2.20 | 0.77 |
| 2000 | 76.47 | 0.72 | 80.87 | 2.46 | 76.57 | 2.53 | 77.97 | 1.90 | 2.51 | 1.03 |
| 2400 | 77.05 | 0.58 | 81.83 | 0.96 | 77.42 | 0.85 | 78.77 | 0.80 | 2.66 | 0.20 |
| 2800 | 78.29 | 1.24 | 82.05 | 0.22 | 78.63 | 1.21 | 79.66 | 0.89 | 2.08 | 0.58 |
| 3200 | 78.30 | 0.01 | 83.06 | 1.01 | 80.82 | 2.19 | 80.73 | 1.07 | 2.38 | 1.09 |

Table C2.6: Fine (5.21 mm crushed basalt); Bed-matrix (15.75 mm glass bead); $\dot{\gamma}$ =0.04 s $^{-1}$.

| $\gamma_{total}$ | Test 1 | | Test 2 | | Test 3 | | Mean | | Std. dev. | |
|---|---|---|---|---|---|---|---|---|---|---|
| | CPF (%) | IMF (%) | CPF (%) | IMF (%) | CPF (%) | IMF (%) | CPF (%) | IMF (%) | CPF (%) | IMF (%) |
| 0 | 0.00 | 0.00 | 0.00 | 0.00 | 0.00 | 0.00 | 0.00 | 0.00 | 0.00 | 0.00 |
| 50 | 0.00 | 0.00 | 0.00 | 0.00 | 0.00 | 0.00 | 0.00 | 0.00 | 0.00 | 0.00 |
| 100 | 0.00 | 0.00 | 0.00 | 0.00 | 0.00 | 0.00 | 0.00 | 0.00 | 0.00 | 0.00 |
| 200 | 0.00 | 0.00 | 0.00 | 0.00 | 0.00 | 0.00 | 0.00 | 0.00 | 0.00 | 0.00 |
| 400 | 1.68 | 1.68 | 1.48 | 1.48 | 2.16 | 2.16 | 1.77 | 1.77 | 0.35 | 0.35 |
| 800 | 4.42 | 2.74 | 5.99 | 4.51 | 6.70 | 4.54 | 5.70 | 3.93 | 1.03 | 1.03 |
| 1200 | 13.56 | 9.14 | 16.69 | 10.70 | 14.87 | 8.17 | 15.04 | 9.34 | 1.57 | 1.28 |
| 1600 | 18.62 | 5.06 | 25.40 | 8.71 | 21.11 | 6.24 | 21.71 | 6.67 | 3.43 | 1.86 |
| 2000 | 28.22 | 9.60 | 37.48 | 12.08 | 32.59 | 11.48 | 32.76 | 11.05 | 4.63 | 1.29 |
| 2400 | 34.18 | 5.96 | 46.26 | 8.78 | 36.62 | 4.03 | 39.02 | 6.26 | 6.39 | 2.39 |
| 2800 | 40.86 | 6.68 | 49.95 | 3.69 | 44.59 | 7.97 | 45.13 | 6.11 | 4.57 | 2.20 |
| 3200 | 43.61 | 2.75 | 57.02 | 7.07 | 48.22 | 3.63 | 49.62 | 4.48 | 6.81 | 2.28 |

Table C2.7: Fine (6.18 mm crushed basalt); Bed-matrix (15.75 mm glass bead); $\dot{\gamma}$ =0.04 s $^{-1}$ .

| $\gamma_{total}$ | Test 1 | | Test 2 | | Test 3 | | Mean | | Std. dev. | |
|---|---|---|---|---|---|---|---|---|---|---|
| | CPF (%) | IMF (%) | CPF (%) | IMF (%) | CPF (%) | IMF (%) | CPF (%) | IMF (%) | CPF (%) | IMF (%) |
| 0 | 0.00 | 0.00 | 0.00 | 0.00 | 0.00 | 0.00 | 0.00 | 0.00 | 0.00 | 0.00 |
| 50 | 0.00 | 0.00 | 0.00 | 0.00 | 0.00 | 0.00 | 0.00 | 0.00 | 0.00 | 0.00 |
| 100 | 0.00 | 0.00 | 0.00 | 0.00 | 0.00 | 0.00 | 0.00 | 0.00 | 0.00 | 0.00 |
| 200 | 0.00 | 0.00 | 0.00 | 0.00 | 0.00 | 0.00 | 0.00 | 0.00 | 0.00 | 0.00 |
| 400 | 0.00 | 0.00 | 0.00 | 0.00 | 0.00 | 0.00 | 0.00 | 0.00 | 0.00 | 0.00 |
| 800 | 0.00 | 0.00 | 0.00 | 0.00 | 0.00 | 0.00 | 0.00 | 0.00 | 0.00 | 0.00 |
| 1200 | 0.60 | 0.60 | 0.00 | 0.00 | 1.70 | 1.70 | 0.77 | 0.77 | 0.86 | 0.86 |
| 1600 | 1.03 | 0.43 | 1.55 | 1.55 | 2.94 | 1.24 | 1.84 | 1.07 | 0.99 | 0.58 |
| 2000 | 4.22 | 3.19 | 5.45 | 3.90 | 6.20 | 3.26 | 5.29 | 3.45 | 1.00 | 0.39 |
| 2400 | 8.89 | 4.67 | 10.01 | 4.56 | 11.03 | 4.83 | 9.98 | 4.69 | 1.07 | 0.14 |
| 2800 | 10.74 | 1.85 | 11.83 | 1.82 | 12.10 | 1.07 | 11.56 | 1.58 | 0.72 | 0.44 |
| 3200 | 14.32 | 3.58 | 13.30 | 1.47 | 13.63 | 1.53 | 13.75 | 2.19 | 0.52 | 1.20 |

Table C2.8: Fine (4.00 mm glass bead); Bed-matrix (13.20 mm crushed basalt); $\dot{\gamma}$ =0.04 s $^{-1}$ .

| $\gamma_{total}$ | Test 1 | | Test 2 | | Test 3 | | Mean | | Std. dev. | |
|---|---|---|---|---|---|---|---|---|---|---|
| | CPF (%) | IMF (%) | CPF (%) | IMF (%) | CPF (%) | IMF (%) | CPF (%) | IMF (%) | CPF (%) | IMF (%) |
| 0 | 0.00 | 0.00 | 0.00 | 0.00 | 0.00 | 0.00 | 0.00 | 0.00 | 0.00 | 0.00 |
| 50 | 0.00 | 0.00 | 0.00 | 0.00 | 0.00 | 0.00 | 0.00 | 0.00 | 0.00 | 0.00 |
| 100 | 0.00 | 0.00 | 0.00 | 0.00 | 0.00 | 0.00 | 0.00 | 0.00 | 0.00 | 0.00 |
| 200 | 0.00 | 0.00 | 0.00 | 0.00 | 0.00 | 0.00 | 0.00 | 0.00 | 0.00 | 0.00 |
| 400 | 0.00 | 0.00 | 0.00 | 0.00 | 0.00 | 0.00 | 0.00 | 0.00 | 0.00 | 0.00 |
| 800 | 0.00 | 0.00 | 0.00 | 0.00 | 0.00 | 0.00 | 0.00 | 0.00 | 0.00 | 0.00 |
| 1200 | 0.00 | 0.00 | 0.00 | 0.00 | 0.00 | 0.00 | 0.00 | 0.00 | 0.00 | 0.00 |
| 1600 | 0.25 | 0.25 | 0.30 | 0.30 | 0.00 | 0.00 | 0.18 | 0.18 | 0.16 | 0.16 |
| 2000 | 0.62 | 0.37 | 1.58 | 1.28 | 0.97 | 0.97 | 1.06 | 0.87 | 0.46 | 0.46 |
| 2400 | 1.23 | 0.61 | 3.75 | 2.17 | 2.96 | 1.99 | 2.65 | 1.59 | 0.85 | 0.85 |
| 2800 | 3.10 | 1.87 | 5.86 | 2.11 | 5.23 | 2.27 | 4.73 | 2.08 | 0.20 | 0.20 |
| 3200 | 7.65 | 4.55 | 10.36 | 4.50 | 8.48 | 3.25 | 8.83 | 4.10 | 1.39 | 0.74 |
| 3600 | 9.56 | 1.91 | 13.66 | 3.30 | 12.21 | 3.73 | 11.81 | 2.98 | 2.08 | 0.95 |
| 4000 | 12.17 | 2.61 | 15.16 | 1.50 | 15.13 | 2.92 | 14.15 | 2.34 | 1.72 | 0.75 |
| 4400 | 15.89 | 3.72 | 17.13 | 1.97 | 17.88 | 2.75 | 16.97 | 2.81 | 1.01 | 0.88 |
| 4800 | 21.11 | 5.22 | 22.80 | 5.67 | 20.60 | 2.72 | 21.50 | 4.54 | 1.15 | 1.59 |

Table C2.9: Fine (5.00 mm glass bead); Bed-matrix (13.20 mm crushed basalt); $\dot{\gamma}$ =0.04 s $^{-1}$ .

| $\gamma_{total}$ | Test 1 | | Test 2 | | Test 3 | | Mean | | Std. dev. | |
|---|---|---|---|---|---|---|---|---|---|---|
| | CPF (%) | IMF (%) | CPF (%) | IMF (%) | CPF (%) | IMF (%) | CPF (%) | IMF (%) | CPF (%) | IMF (%) |
| 0 | 0.00 | 0.00 | 0.00 | 0.00 | 0.00 | 0.00 | 0.00 | 0.00 | 0.00 | 0.00 |
| 50 | 0.00 | 0.00 | 0.00 | 0.00 | 0.00 | 0.00 | 0.00 | 0.00 | 0.00 | 0.00 |
| 100 | 0.00 | 0.00 | 0.00 | 0.00 | 0.00 | 0.00 | 0.00 | 0.00 | 0.00 | 0.00 |
| 200 | 0.00 | 0.00 | 0.00 | 0.00 | 0.00 | 0.00 | 0.00 | 0.00 | 0.00 | 0.00 |
| 400 | 0.00 | 0.00 | 0.00 | 0.00 | 0.00 | 0.00 | 0.00 | 0.00 | 0.00 | 0.00 |
| 800 | 0.00 | 0.00 | 0.00 | 0.00 | 0.00 | 0.00 | 0.00 | 0.00 | 0.00 | 0.00 |
| 1200 | 0.00 | 0.00 | 0.00 | 0.00 | 0.00 | 0.00 | 0.00 | 0.00 | 0.00 | 0.00 |
| 1600 | 0.00 | 0.00 | 0.00 | 0.00 | 0.00 | 0.00 | 0.00 | 0.00 | 0.00 | 0.00 |
| 2000 | 0.00 | 0.00 | 0.00 | 0.00 | 0.00 | 0.00 | 0.00 | 0.00 | 0.00 | 0.00 |
| 2400 | 0.00 | 0.00 | 0.00 | 0.00 | 0.00 | 0.00 | 0.00 | 0.00 | 0.00 | 0.00 |
| 2800 | 0.00 | 0.00 | 0.00 | 0.00 | 0.00 | 0.00 | 0.00 | 0.00 | 0.00 | 0.00 |
| 3200 | 0.00 | 0.00 | 0.44 | 0.44 | 0.34 | 0.34 | 0.26 | 0.26 | 0.23 | 0.23 |
| 3600 | 0.44 | 0.44 | 1.05 | 0.61 | 1.04 | 0.70 | 0.84 | 0.58 | 0.35 | 0.13 |
| 4000 | 0.93 | 0.49 | 1.05 | 0.00 | 2.17 | 1.13 | 1.38 | 0.54 | 0.68 | 0.57 |
| 4400 | 3.78 | 2.85 | 4.39 | 3.34 | 4.33 | 2.16 | 4.17 | 2.78 | 0.34 | 0.59 |
| 4800 | 5.83 | 2.05 | 5.44 | 1.05 | 5.19 | 0.86 | 5.49 | 1.32 | 0.32 | 0.64 |

Table C2.10: Fine (6.00 mm glass bead); Bed-matrix (13.20 mm crushed basalt); $\dot{\gamma}$ =0.04 s $^{-1}$.

| $\gamma_{total}$ | Test 1 | | Test 2 | | Test 3 | | Mean | | Std. dev. | |
|---|---|---|---|---|---|---|---|---|---|---|
| | CPF (%) | IMF (%) | CPF (%) | IMF (%) | CPF (%) | IMF (%) | CPF (%) | IMF (%) | CPF (%) | IMF (%) |
| 0 | 0.00 | 0.00 | 0.00 | 0.00 | 0.00 | 0.00 | 0.00 | 0.00 | 0.00 | 0.00 |
| 50 | 0.00 | 0.00 | 0.00 | 0.00 | 0.00 | 0.00 | 0.00 | 0.00 | 0.00 | 0.00 |
| 100 | 0.00 | 0.00 | 0.00 | 0.00 | 0.00 | 0.00 | 0.00 | 0.00 | 0.00 | 0.00 |
| 200 | 0.00 | 0.00 | 0.00 | 0.00 | 0.00 | 0.00 | 0.00 | 0.00 | 0.00 | 0.00 |
| 400 | 0.00 | 0.00 | 0.00 | 0.00 | 0.00 | 0.00 | 0.00 | 0.00 | 0.00 | 0.00 |
| 800 | 0.00 | 0.00 | 0.00 | 0.00 | 0.00 | 0.00 | 0.00 | 0.00 | 0.00 | 0.00 |
| 1200 | 0.00 | 0.00 | 0.00 | 0.00 | 0.00 | 0.00 | 0.00 | 0.00 | 0.00 | 0.00 |
| 1600 | 0.00 | 0.00 | 0.00 | 0.00 | 0.00 | 0.00 | 0.00 | 0.00 | 0.00 | 0.00 |
| 2000 | 0.00 | 0.00 | 0.00 | 0.00 | 0.00 | 0.00 | 0.00 | 0.00 | 0.00 | 0.00 |
| 2400 | 0.00 | 0.00 | 0.00 | 0.00 | 0.00 | 0.00 | 0.00 | 0.00 | 0.00 | 0.00 |
| 2800 | 0.00 | 0.00 | 0.00 | 0.00 | 0.00 | 0.00 | 0.00 | 0.00 | 0.00 | 0.00 |
| 3200 | 0.00 | 0.00 | 0.00 | 0.00 | 0.00 | 0.00 | 0.00 | 0.00 | 0.00 | 0.00 |
| 3600 | 0.00 | 0.00 | 0.00 | 0.00 | 0.00 | 0.00 | 0.00 | 0.00 | 0.00 | 0.00 |
| 4000 | 0.00 | 0.00 | 0.00 | 0.00 | 0.00 | 0.00 | 0.00 | 0.00 | 0.00 | 0.00 |
| 4400 | 0.00 | 0.00 | 0.00 | 0.00 | 0.00 | 0.00 | 0.00 | 0.00 | 0.00 | 0.00 |
| 4800 | 0.00 | 0.00 | 0.00 | 0.00 | 0.00 | 0.00 | 0.00 | 0.00 | 0.00 | 0.00 |

Table C2.11: Fine (2.86 mm crushed basalt); Bed-matrix (13.20 mm crushed basalt); $\dot{\gamma}$ =0.04 s $^{-1}$.

| $\gamma_{total}$ | Test 1 | | Test 2 | | Test 3 | | Mean | | Std. dev. | |
|---|---|---|---|---|---|---|---|---|---|---|
| | CPF (%) | IMF (%) | CPF (%) | IMF (%) | CPF (%) | IMF (%) | CPF (%) | IMF (%) | CPF (%) | IMF (%) |
| 0 | 0.00 | 0.00 | 0.00 | 0.00 | 0.00 | 0.00 | 0.00 | 0.00 | 0.00 | 0.00 |
| 50 | 0.00 | 0.00 | 0.00 | 0.00 | 0.00 | 0.00 | 0.00 | 0.00 | 0.00 | 0.00 |
| 100 | 0.00 | 0.00 | 0.00 | 0.00 | 0.00 | 0.00 | 0.00 | 0.00 | 0.00 | 0.00 |
| 200 | 0.00 | 0.00 | 0.00 | 0.00 | 0.00 | 0.00 | 0.00 | 0.00 | 0.00 | 0.00 |
| 400 | 0.00 | 0.00 | 0.00 | 0.00 | 0.00 | 0.00 | 0.00 | 0.00 | 0.00 | 0.00 |
| 800 | 0.26 | 0.26 | 0.58 | 0.58 | 0.53 | 0.53 | 0.46 | 0.46 | 0.17 | 0.17 |
| 1200 | 2.77 | 2.51 | 3.43 | 2.85 | 3.12 | 2.59 | 3.11 | 2.65 | 0.18 | 0.18 |
| 1600 | 9.22 | 6.45 | 8.74 | 5.31 | 9.07 | 5.95 | 9.01 | 5.90 | 0.57 | 0.57 |
| 2000 | 23.26 | 14.04 | 22.08 | 13.34 | 19.79 | 10.72 | 21.71 | 12.70 | 1.75 | 1.75 |
| 2400 | 39.68 | 16.42 | 36.22 | 14.14 | 38.25 | 18.46 | 38.05 | 16.34 | 2.16 | 2.16 |
| 2800 | 50.02 | 10.34 | 48.25 | 12.03 | 53.40 | 15.15 | 50.56 | 12.51 | 2.44 | 2.44 |
| 3200 | 58.97 | 8.95 | 57.66 | 9.41 | 62.88 | 9.48 | 59.84 | 9.28 | 2.72 | 0.29 |
| 3600 | 65.20 | 6.23 | 62.75 | 5.09 | 65.43 | 2.55 | 64.46 | 4.62 | 1.49 | 1.88 |
| 4000 | 70.34 | 5.14 | 69.81 | 7.06 | 74.90 | 9.47 | 71.68 | 7.22 | 2.80 | 2.17 |
| 4400 | 75.94 | 5.60 | 74.83 | 5.02 | 78.16 | 3.26 | 76.31 | 4.63 | 1.70 | 1.22 |
| 4800 | 79.91 | 3.97 | 77.64 | 2.81 | 81.33 | 3.17 | 79.63 | 3.32 | 1.86 | 0.59 |

Table C2.12: Fine (4.05 mm crushed basalt); Bed-matrix (13.20 mm crushed basalt); $\dot{\gamma}$ =0.04 s $^{-1}$.

| $\gamma_{total}$ | Test 1 | | Test 2 | | Test 3 | | Mean | | Std. dev. | |
|---|---|---|---|---|---|---|---|---|---|---|
| | CPF (%) | IMF (%) | CPF (%) | IMF (%) | CPF (%) | IMF (%) | CPF (%) | IMF (%) | CPF (%) | IMF (%) |
| 0 | 0.00 | 0.00 | 0.00 | 0.00 | 0.00 | 0.00 | 0.00 | 0.00 | 0.00 | 0.00 |
| 50 | 0.00 | 0.00 | 0.00 | 0.00 | 0.00 | 0.00 | 0.00 | 0.00 | 0.00 | 0.00 |
| 100 | 0.00 | 0.00 | 0.00 | 0.00 | 0.00 | 0.00 | 0.00 | 0.00 | 0.00 | 0.00 |
| 200 | 0.00 | 0.00 | 0.00 | 0.00 | 0.00 | 0.00 | 0.00 | 0.00 | 0.00 | 0.00 |
| 400 | 0.00 | 0.00 | 0.00 | 0.00 | 0.00 | 0.00 | 0.00 | 0.00 | 0.00 | 0.00 |
| 800 | 0.00 | 0.00 | 0.00 | 0.00 | 0.00 | 0.00 | 0.00 | 0.00 | 0.00 | 0.00 |
| 1200 | 0.00 | 0.00 | 0.17 | 0.17 | 0.00 | 0.00 | 0.06 | 0.06 | 0.10 | 0.10 |
| 1600 | 0.35 | 0.35 | 0.43 | 0.26 | 0.71 | 0.71 | 0.50 | 0.44 | 0.24 | 0.24 |
| 2000 | 0.71 | 0.36 | 0.62 | 0.19 | 1.91 | 1.20 | 1.08 | 0.58 | 0.54 | 0.54 |
| 2400 | 1.49 | 0.78 | 1.35 | 0.73 | 2.57 | 0.66 | 1.80 | 0.72 | 0.06 | 0.06 |
| 2800 | 2.46 | 0.97 | 1.94 | 0.59 | 3.16 | 0.59 | 2.52 | 0.72 | 0.61 | 0.22 |
| 3200 | 6.38 | 3.92 | 5.62 | 3.68 | 7.06 | 3.90 | 6.35 | 3.83 | 0.72 | 0.13 |
| 3600 | 9.55 | 3.17 | 8.48 | 2.86 | 10.45 | 3.39 | 9.49 | 3.14 | 0.99 | 0.27 |
| 4000 | 13.90 | 4.35 | 13.16 | 4.68 | 15.32 | 4.87 | 14.13 | 4.63 | 1.10 | 0.26 |
| 4400 | 17.85 | 3.95 | 15.71 | 2.55 | 19.11 | 3.79 | 17.56 | 3.43 | 1.72 | 0.77 |
| 4800 | 25.06 | 7.21 | 22.44 | 6.73 | 28.36 | 9.25 | 25.29 | 7.73 | 2.97 | 1.34 |

Table C2.13: Fine (5.21 mm crushed basalt); Bed-matrix (13.20 mm crushed basalt); $\dot{\gamma}$ =0.04 s $^{-1}$ .

| $\gamma_{total}$ | Test 1 | | Test 2 | | Test 3 | | Mean | | Std. dev. | |
|---|---|---|---|---|---|---|---|---|---|---|
| | CPF (%) | IMF (%) | CPF (%) | IMF (%) | CPF (%) | IMF (%) | CPF (%) | IMF (%) | CPF (%) | IMF (%) |
| 0 | 0.00 | 0.00 | 0.00 | 0.00 | 0.00 | 0.00 | 0.00 | 0.00 | 0.00 | 0.00 |
| 50 | 0.00 | 0.00 | 0.00 | 0.00 | 0.00 | 0.00 | 0.00 | 0.00 | 0.00 | 0.00 |
| 100 | 0.00 | 0.00 | 0.00 | 0.00 | 0.00 | 0.00 | 0.00 | 0.00 | 0.00 | 0.00 |
| 200 | 0.00 | 0.00 | 0.00 | 0.00 | 0.00 | 0.00 | 0.00 | 0.00 | 0.00 | 0.00 |
| 400 | 0.00 | 0.00 | 0.00 | 0.00 | 0.00 | 0.00 | 0.00 | 0.00 | 0.00 | 0.00 |
| 800 | 0.00 | 0.00 | 0.00 | 0.00 | 0.00 | 0.00 | 0.00 | 0.00 | 0.00 | 0.00 |
| 1200 | 0.00 | 0.00 | 0.00 | 0.00 | 0.00 | 0.00 | 0.00 | 0.00 | 0.00 | 0.00 |
| 1600 | 0.00 | 0.00 | 0.00 | 0.00 | 0.00 | 0.00 | 0.00 | 0.00 | 0.00 | 0.00 |
| 2000 | 0.00 | 0.00 | 0.00 | 0.00 | 0.00 | 0.00 | 0.00 | 0.00 | 0.00 | 0.00 |
| 2400 | 0.00 | 0.00 | 0.00 | 0.00 | 0.00 | 0.00 | 0.00 | 0.00 | 0.00 | 0.00 |
| 2800 | 0.00 | 0.00 | 0.00 | 0.00 | 0.00 | 0.00 | 0.00 | 0.00 | 0.00 | 0.00 |
| 3200 | 0.45 | 0.45 | 0.48 | 0.48 | 0.47 | 0.47 | 0.47 | 0.47 | 0.02 | 0.02 |
| 3600 | 1.00 | 0.55 | 1.07 | 0.59 | 1.06 | 0.59 | 1.04 | 0.58 | 0.04 | 0.02 |
| 4000 | 2.37 | 1.37 | 3.42 | 2.35 | 3.40 | 2.34 | 3.06 | 2.02 | 0.60 | 0.56 |
| 4400 | 3.28 | 0.91 | 4.61 | 1.19 | 3.40 | 0.00 | 3.76 | 0.70 | 0.74 | 0.62 |
| 4800 | 5.38 | 2.10 | 6.55 | 1.94 | 6.13 | 2.73 | 6.02 | 2.26 | 0.59 | 0.42 |

Table C2.14: Fine (6.18 mm crushed basalt); Bed-matrix (13.20 mm crushed basalt); $\dot{\gamma}$ =0.04 s $^{-1}$ .

| $\gamma_{total}$ | Test 1 | | Test 2 | | Test 3 | | Mean | | Std. dev. | |
|---|---|---|---|---|---|---|---|---|---|---|
| | CPF (%) | IMF (%) | CPF (%) | IMF (%) | CPF (%) | IMF (%) | CPF (%) | IMF (%) | CPF (%) | IMF (%) |
| 0 | 0.00 | 0.00 | 0.00 | 0.00 | 0.00 | 0.00 | 0.00 | 0.00 | 0.00 | 0.00 |
| 50 | 0.00 | 0.00 | 0.00 | 0.00 | 0.00 | 0.00 | 0.00 | 0.00 | 0.00 | 0.00 |
| 100 | 0.00 | 0.00 | 0.00 | 0.00 | 0.00 | 0.00 | 0.00 | 0.00 | 0.00 | 0.00 |
| 200 | 0.00 | 0.00 | 0.00 | 0.00 | 0.00 | 0.00 | 0.00 | 0.00 | 0.00 | 0.00 |
| 400 | 0.00 | 0.00 | 0.00 | 0.00 | 0.00 | 0.00 | 0.00 | 0.00 | 0.00 | 0.00 |
| 800 | 0.00 | 0.00 | 0.00 | 0.00 | 0.00 | 0.00 | 0.00 | 0.00 | 0.00 | 0.00 |
| 1200 | 0.00 | 0.00 | 0.00 | 0.00 | 0.00 | 0.00 | 0.00 | 0.00 | 0.00 | 0.00 |
| 1600 | 0.00 | 0.00 | 0.00 | 0.00 | 0.00 | 0.00 | 0.00 | 0.00 | 0.00 | 0.00 |
| 2000 | 0.00 | 0.00 | 0.00 | 0.00 | 0.00 | 0.00 | 0.00 | 0.00 | 0.00 | 0.00 |
| 2400 | 0.00 | 0.00 | 0.00 | 0.00 | 0.00 | 0.00 | 0.00 | 0.00 | 0.00 | 0.00 |
| 2800 | 0.00 | 0.00 | 0.00 | 0.00 | 0.00 | 0.00 | 0.00 | 0.00 | 0.00 | 0.00 |
| 3200 | 0.00 | 0.00 | 0.00 | 0.00 | 0.00 | 0.00 | 0.00 | 0.00 | 0.00 | 0.00 |
| 3600 | 0.00 | 0.00 | 0.00 | 0.00 | 0.00 | 0.00 | 0.00 | 0.00 | 0.00 | 0.00 |
| 4000 | 0.00 | 0.00 | 0.67 | 0.67 | 0.00 | 0.00 | 0.22 | 0.22 | 0.39 | 0.39 |
| 4400 | 0.72 | 0.72 | 1.37 | 0.70 | 0.77 | 0.77 | 0.95 | 0.73 | 0.36 | 0.04 |
| 4800 | 1.51 | 0.79 | 2.22 | 0.85 | 1.62 | 0.85 | 1.78 | 0.83 | 0.38 | 0.03 |

## C3 Effect of Particle Shape

Table C3.1: Fine (4.00 mm cubical glass); Bed-matrix (15.75 mm glass bead); $\dot{\gamma}$ =0.04 s $^{-1}$.

| $\gamma_{total}$ | Test 1 | | Test 2 | | Test 3 | | Mean | | Std. dev. | |
|---|---|---|---|---|---|---|---|---|---|---|
| | CPF (%) | IMF (%) | CPF (%) | IMF (%) | CPF (%) | IMF (%) | CPF (%) | IMF (%) | CPF (%) | IMF (%) |
| 0 | 0.00 | 0.00 | 0.00 | 0.00 | 0.00 | 0.00 | 0.00 | 0.00 | 0.00 | 0.00 |
| 50 | 0.00 | 0.00 | 0.00 | 0.00 | 0.00 | 0.00 | 0.00 | 0.00 | 0.00 | 0.00 |
| 100 | 0.00 | 0.00 | 0.00 | 0.00 | 0.00 | 0.00 | 0.00 | 0.00 | 0.00 | 0.00 |
| 200 | 0.00 | 0.00 | 0.00 | 0.00 | 0.00 | 0.00 | 0.00 | 0.00 | 0.00 | 0.00 |
| 400 | 0.00 | 0.00 | 0.00 | 0.00 | 0.00 | 0.00 | 0.00 | 0.00 | 0.00 | 0.00 |
| 800 | 2.10 | 2.10 | 0.00 | 0.00 | 0.00 | 0.00 | 0.70 | 0.70 | 1.21 | 1.21 |
| 1200 | 4.16 | 2.06 | 1.99 | 1.99 | 1.94 | 1.94 | 2.70 | 2.00 | 1.27 | 0.06 |
| 1600 | 19.06 | 14.90 | 22.62 | 20.63 | 21.56 | 19.62 | 21.08 | 18.38 | 1.83 | 3.06 |
| 2000 | 29.86 | 10.80 | 33.18 | 10.56 | 32.28 | 10.72 | 31.77 | 10.69 | 1.72 | 0.12 |
| 2400 | 44.72 | 14.86 | 42.97 | 9.79 | 43.14 | 10.86 | 43.61 | 11.84 | 0.97 | 2.67 |
| 2800 | 56.41 | 11.69 | 57.88 | 14.91 | 60.58 | 17.44 | 58.29 | 14.68 | 2.12 | 2.88 |
| 3200 | 59.73 | 3.32 | 62.30 | 4.42 | 63.65 | 3.07 | 61.89 | 3.60 | 1.99 | 0.72 |

Table C3.2: Fine (4.00 mm cylindrical glass); Bed-matrix (15.75 mm glass bead); $\dot{\gamma}$ =0.04 s $^{-1}$.

| $\gamma_{total}$ | Test 1 | | Test 2 | | Test 3 | | Mean | | Std. dev. | |
|---|---|---|---|---|---|---|---|---|---|---|
| | CPF (%) | IMF (%) | CPF (%) | IMF (%) | CPF (%) | IMF (%) | CPF (%) | IMF (%) | CPF (%) | IMF (%) |
| 0 | 0.00 | 0.00 | 0.00 | 0.00 | 0.00 | 0.00 | 0.00 | 0.00 | 0.00 | 0.00 |
| 50 | 0.00 | 0.00 | 0.00 | 0.00 | 0.00 | 0.00 | 0.00 | 0.00 | 0.00 | 0.00 |
| 100 | 0.00 | 0.00 | 0.00 | 0.00 | 0.00 | 0.00 | 0.00 | 0.00 | 0.00 | 0.00 |
| 200 | 0.00 | 0.00 | 0.00 | 0.00 | 0.00 | 0.00 | 0.00 | 0.00 | 0.00 | 0.00 |
| 400 | 2.65 | 2.65 | 2.23 | 2.23 | 2.63 | 2.63 | 2.50 | 2.50 | 0.24 | 0.24 |
| 800 | 17.61 | 14.96 | 16.96 | 14.73 | 20.41 | 17.78 | 18.33 | 15.82 | 1.83 | 1.70 |
| 1200 | 36.11 | 18.50 | 32.53 | 15.57 | 35.50 | 15.09 | 34.71 | 16.39 | 1.92 | 1.85 |
| 1600 | 47.43 | 11.32 | 43.51 | 10.98 | 46.25 | 10.75 | 45.73 | 11.02 | 2.01 | 0.29 |
| 2000 | 59.49 | 12.06 | 56.41 | 12.90 | 58.53 | 12.28 | 58.14 | 12.41 | 1.58 | 0.44 |
| 2400 | 69.21 | 9.72 | 65.27 | 8.86 | 66.55 | 8.02 | 67.01 | 8.87 | 2.01 | 0.85 |
| 2800 | 71.01 | 1.80 | 66.57 | 1.30 | 68.24 | 1.69 | 68.61 | 1.60 | 2.24 | 0.26 |
| 3200 | 71.77 | 0.76 | 69.04 | 2.47 | 68.81 | 0.57 | 69.87 | 1.27 | 1.65 | 1.05 |

Table C3.3: Fine (4.00 mm bi-conical glass); Bed-matrix (15.75 mm glass bead); $\dot{\gamma}$ =0.04 s $^{-1}$.

| $\gamma_{total}$ | Test 1 | | Test 2 | | Test 3 | | Mean | | Std. dev. | |
|---|---|---|---|---|---|---|---|---|---|---|
| | CPF (%) | IMF (%) | CPF (%) | IMF (%) | CPF (%) | IMF (%) | CPF (%) | IMF (%) | CPF (%) | IMF (%) |
| 0 | 0.00 | 0.00 | 0.00 | 0.00 | 0.00 | 0.00 | 0.00 | 0.00 | 0.00 | 0.00 |
| 50 | 0.00 | 0.00 | 0.00 | 0.00 | 0.00 | 0.00 | 0.00 | 0.00 | 0.00 | 0.00 |
| 100 | 0.00 | 0.00 | 0.00 | 0.00 | 0.00 | 0.00 | 0.00 | 0.00 | 0.00 | 0.00 |
| 200 | 0.00 | 0.00 | 0.00 | 0.00 | 0.00 | 0.00 | 0.00 | 0.00 | 0.00 | 0.00 |
| 400 | 4.36 | 4.36 | 3.13 | 3.13 | 4.02 | 4.02 | 3.84 | 3.84 | 0.64 | 0.64 |
| 800 | 27.71 | 23.35 | 30.78 | 27.65 | 32.70 | 28.68 | 30.40 | 26.56 | 2.52 | 2.83 |
| 1200 | 39.54 | 11.83 | 43.51 | 12.73 | 42.59 | 9.89 | 41.88 | 11.48 | 2.08 | 1.45 |
| 1600 | 50.29 | 10.75 | 57.29 | 13.78 | 54.66 | 12.07 | 54.08 | 12.20 | 3.54 | 1.52 |
| 2000 | 61.00 | 10.71 | 62.89 | 5.60 | 63.75 | 9.09 | 62.55 | 8.47 | 1.41 | 2.61 |
| 2400 | 66.76 | 5.76 | 65.24 | 2.35 | 69.44 | 5.69 | 67.15 | 4.60 | 2.13 | 1.95 |
| 2800 | 66.76 | 0.00 | 67.72 | 2.48 | 71.48 | 2.04 | 68.65 | 1.51 | 2.49 | 1.32 |
| 3200 | 68.27 | 1.51 | 70.89 | 3.17 | 76.64 | 5.16 | 71.93 | 3.28 | 4.28 | 1.83 |

Table C3.4: Fine (4.00 mm sphere glass); Bed-matrix (15.75 mm glass bead); $\dot{\gamma}$ =0.04 s $^{-1}$.

| $\gamma_{total}$ | Test 1 | | Test 2 | | Test 3 | | Mean | | Std. dev. | |
|---|---|---|---|---|---|---|---|---|---|---|
| | CPF (%) | IMF (%) | CPF (%) | IMF (%) | CPF (%) | IMF (%) | CPF (%) | IMF (%) | CPF (%) | IMF (%) |
| 0 | 0.00 | 0.00 | 0.00 | 0.00 | 0.00 | 0.00 | 0.00 | 0.00 | 0.00 | 0.00 |
| 50 | 0.00 | 0.00 | 0.00 | 0.00 | 0.00 | 0.00 | 0.00 | 0.00 | 0.00 | 0.00 |
| 100 | 0.00 | 0.00 | 0.00 | 0.00 | 0.00 | 0.00 | 0.00 | 0.00 | 0.00 | 0.00 |
| 200 | 0.00 | 0.00 | 0.09 | 0.09 | 0.12 | 0.12 | 0.07 | 0.07 | 0.06 | 0.06 |
| 400 | 2.03 | 2.03 | 0.61 | 0.52 | 0.56 | 0.44 | 1.07 | 1.00 | 0.90 | 0.90 |
| 800 | 4.78 | 2.75 | 6.23 | 5.62 | 6.37 | 5.81 | 5.79 | 4.73 | 0.88 | 1.71 |
| 1200 | 20.92 | 16.14 | 26.32 | 20.09 | 21.72 | 15.35 | 22.99 | 17.19 | 2.91 | 2.54 |
| 1600 | 46.00 | 25.08 | 49.45 | 23.13 | 43.87 | 22.15 | 46.44 | 23.45 | 2.82 | 1.49 |
| 2000 | 60.77 | 14.77 | 62.21 | 12.76 | 58.04 | 14.17 | 60.34 | 13.90 | 2.12 | 1.03 |
| 2400 | 70.39 | 9.62 | 68.98 | 6.77 | 63.20 | 5.16 | 67.52 | 7.18 | 3.81 | 2.26 |
| 2800 | 74.54 | 4.15 | 71.58 | 2.60 | 68.39 | 5.19 | 71.50 | 3.98 | 3.08 | 1.30 |
| 3200 | 78.28 | 3.74 | 73.74 | 2.16 | 72.15 | 3.76 | 74.72 | 3.22 | 3.18 | 0.92 |

Table C3.5: Fine (4.05 mm angular crushed basalt); Bed-matrix (15.75 mm glass bead); $\dot{\gamma}$ =0.04 s $^{-1}$.

| $\gamma_{total}$ | Test 1 | | Test 2 | | Test 3 | | Mean | | Std. dev. | |
|---|---|---|---|---|---|---|---|---|---|---|
| | CPF (%) | IMF (%) | CPF (%) | IMF (%) | CPF (%) | IMF (%) | CPF (%) | IMF (%) | CPF (%) | IMF (%) |
| 0 | 0.00 | 0.00 | 0.00 | 0.00 | 0.00 | 0.00 | 0.00 | 0.00 | 0.00 | 0.00 |
| 50 | 0.12 | 0.12 | 0.24 | 0.24 | 0.00 | 0.00 | 0.12 | 0.12 | 0.12 | 0.12 |
| 100 | 0.53 | 0.41 | 0.90 | 0.66 | 0.67 | 0.69 | 0.70 | 0.59 | 0.15 | 0.15 |
| 200 | 3.56 | 3.03 | 2.94 | 2.04 | 3.61 | 3.24 | 3.37 | 2.77 | 0.64 | 0.64 |
| 400 | 16.32 | 12.76 | 17.45 | 14.51 | 14.53 | 10.92 | 16.10 | 12.73 | 1.80 | 1.80 |
| 800 | 51.75 | 35.43 | 53.83 | 36.38 | 46.43 | 31.90 | 50.67 | 34.57 | 2.36 | 2.36 |
| 1200 | 68.20 | 16.45 | 71.76 | 17.93 | 65.86 | 19.43 | 68.61 | 17.94 | 2.97 | 1.49 |
| 1600 | 75.75 | 7.55 | 78.41 | 6.65 | 74.04 | 8.18 | 76.07 | 7.46 | 2.20 | 0.77 |
| 2000 | 76.47 | 0.72 | 80.87 | 2.46 | 76.57 | 2.53 | 77.97 | 1.90 | 2.51 | 1.03 |
| 2400 | 77.05 | 0.58 | 81.83 | 0.96 | 77.42 | 0.85 | 78.77 | 0.80 | 2.66 | 0.20 |
| 2800 | 78.29 | 1.24 | 82.05 | 0.22 | 78.63 | 1.21 | 79.66 | 0.89 | 2.08 | 0.58 |
| 3200 | 78.30 | 0.01 | 83.06 | 1.01 | 80.82 | 2.19 | 80.73 | 1.07 | 2.38 | 1.09 |

Table D3.6: Fine (4.00 mm cubical glass); Bed-matrix (13.20 mm crushed basalt); $\dot{\gamma}$ =0.04 s $^{-1}$.

| $\gamma_{total}$ | Test 1 | | Test 2 | | Test 3 | | Mean | | Std. dev. | |
|---|---|---|---|---|---|---|---|---|---|---|
| | CPF (%) | IMF (%) | CPF (%) | IMF (%) | CPF (%) | IMF (%) | CPF (%) | IMF (%) | CPF (%) | IMF (%) |
| 0 | 0.00 | 0.00 | 0.00 | 0.00 | 0.00 | 0.00 | 0.00 | 0.00 | 0.00 | 0.00 |
| 50 | 0.00 | 0.00 | 0.00 | 0.00 | 0.00 | 0.00 | 0.00 | 0.00 | 0.00 | 0.00 |
| 100 | 0.00 | 0.00 | 0.00 | 0.00 | 0.00 | 0.00 | 0.00 | 0.00 | 0.00 | 0.00 |
| 200 | 0.00 | 0.00 | 0.00 | 0.00 | 0.00 | 0.00 | 0.00 | 0.00 | 0.00 | 0.00 |
| 400 | 0.00 | 0.00 | 0.00 | 0.00 | 0.00 | 0.00 | 0.00 | 0.00 | 0.00 | 0.00 |
| 800 | 0.00 | 0.00 | 0.00 | 0.00 | 0.00 | 0.00 | 0.00 | 0.00 | 0.00 | 0.00 |
| 1200 | 0.00 | 0.00 | 0.00 | 0.00 | 0.00 | 0.00 | 0.00 | 0.00 | 0.00 | 0.00 |
| 1600 | 0.00 | 0.00 | 0.00 | 0.00 | 0.00 | 0.00 | 0.00 | 0.00 | 0.00 | 0.00 |
| 2000 | 0.00 | 0.00 | 0.00 | 0.00 | 0.00 | 0.00 | 0.00 | 0.00 | 0.00 | 0.00 |
| 2400 | 0.00 | 0.00 | 0.00 | 0.00 | 0.00 | 0.00 | 0.00 | 0.00 | 0.00 | 0.00 |
| 2800 | 0.00 | 0.00 | 0.00 | 0.00 | 0.00 | 0.00 | 0.00 | 0.00 | 0.00 | 0.00 |
| 3200 | 1.21 | 1.21 | 1.20 | 1.20 | 1.18 | 1.18 | 1.20 | 1.20 | 0.02 | 0.02 |
| 3600 | 1.21 | 0.00 | 2.44 | 1.24 | 2.38 | 1.20 | 2.01 | 0.81 | 0.69 | 0.70 |
| 4000 | 3.39 | 2.18 | 3.42 | 0.98 | 3.32 | 0.94 | 3.38 | 1.37 | 0.05 | 0.70 |
| 4400 | 4.56 | 1.17 | 4.64 | 1.22 | 4.75 | 1.43 | 4.65 | 1.27 | 0.10 | 0.14 |
| 4800 | 5.55 | 0.99 | 7.26 | 2.62 | 6.54 | 1.79 | 6.45 | 1.80 | 0.86 | 0.82 |

Table C3.7: Fine (4.00 mm cylindrical glass); Bed-matrix (13.20 mm crushed basalt); $\dot{\gamma}$ =0.04 s $^{-1}$.

| $\gamma_{total}$ | Test 1 | | Test 2 | | Test 3 | | Mean | | Std. dev. | |
|---|---|---|---|---|---|---|---|---|---|---|
| | CPF (%) | IMF (%) | CPF (%) | IMF (%) | CPF (%) | IMF (%) | CPF (%) | IMF (%) | CPF (%) | IMF (%) |
| 0 | 0.00 | 0.00 | 0.00 | 0.00 | 0.00 | 0.00 | 0.00 | 0.00 | 0.00 | 0.00 |
| 50 | 0.00 | 0.00 | 0.00 | 0.00 | 0.00 | 0.00 | 0.00 | 0.00 | 0.00 | 0.00 |
| 100 | 0.00 | 0.00 | 0.00 | 0.00 | 0.00 | 0.00 | 0.00 | 0.00 | 0.00 | 0.00 |
| 200 | 0.00 | 0.00 | 0.00 | 0.00 | 0.00 | 0.00 | 0.00 | 0.00 | 0.00 | 0.00 |
| 400 | 0.00 | 0.00 | 0.00 | 0.00 | 0.00 | 0.00 | 0.00 | 0.00 | 0.00 | 0.00 |
| 800 | 0.00 | 0.00 | 0.00 | 0.00 | 0.00 | 0.00 | 0.00 | 0.00 | 0.00 | 0.00 |
| 1200 | 0.00 | 0.00 | 0.00 | 0.00 | 0.00 | 0.00 | 0.00 | 0.00 | 0.00 | 0.00 |
| 1600 | 0.00 | 0.00 | 0.00 | 0.00 | 0.00 | 0.00 | 0.00 | 0.00 | 0.00 | 0.00 |
| 2000 | 0.00 | 0.00 | 0.00 | 0.00 | 0.00 | 0.00 | 0.00 | 0.00 | 0.00 | 0.00 |
| 2400 | 0.00 | 0.00 | 0.00 | 0.00 | 0.00 | 0.00 | 0.00 | 0.00 | 0.00 | 0.00 |
| 2800 | 0.00 | 0.00 | 0.85 | 0.85 | 0.00 | 0.00 | 0.28 | 0.28 | 0.49 | 0.49 |
| 3200 | 0.89 | 0.89 | 1.76 | 0.91 | 0.88 | 0.88 | 1.18 | 0.89 | 0.51 | 0.02 |
| 3600 | 2.65 | 1.76 | 2.63 | 0.87 | 2.71 | 1.83 | 2.66 | 1.49 | 0.04 | 0.54 |
| 4000 | 4.98 | 2.33 | 5.37 | 2.74 | 5.30 | 2.59 | 5.22 | 2.55 | 0.21 | 0.21 |
| 4400 | 10.88 | 5.90 | 14.29 | 8.92 | 13.43 | 8.13 | 12.87 | 7.65 | 1.77 | 1.57 |
| 4800 | 19.74 | 8.86 | 22.01 | 7.72 | 20.74 | 7.31 | 20.83 | 7.96 | 1.14 | 0.80 |

Table C3.8: Fine (4.00 mm bi-conical glass); Bed-matrix (13.20 mm crushed basalt); $\dot{\gamma}$ =0.04 s $^{-1}$.

| $\gamma_{total}$ | Test 1 | | Test 2 | | Test 3 | | Mean | | Std. dev. | |
|---|---|---|---|---|---|---|---|---|---|---|
| | CPF (%) | IMF (%) | CPF (%) | IMF (%) | CPF (%) | IMF (%) | CPF (%) | IMF (%) | CPF (%) | IMF (%) |
| 0 | 0.00 | 0.00 | 0.00 | 0.00 | 0.00 | 0.00 | 0.00 | 0.00 | 0.00 | 0.00 |
| 50 | 0.00 | 0.00 | 0.00 | 0.00 | 0.00 | 0.00 | 0.00 | 0.00 | 0.00 | 0.00 |
| 100 | 0.00 | 0.00 | 0.00 | 0.00 | 0.00 | 0.00 | 0.00 | 0.00 | 0.00 | 0.00 |
| 200 | 0.00 | 0.00 | 0.00 | 0.00 | 0.00 | 0.00 | 0.00 | 0.00 | 0.00 | 0.00 |
| 400 | 0.00 | 0.00 | 0.00 | 0.00 | 0.00 | 0.00 | 0.00 | 0.00 | 0.00 | 0.00 |
| 800 | 0.00 | 0.00 | 0.00 | 0.00 | 0.00 | 0.00 | 0.00 | 0.00 | 0.00 | 0.00 |
| 1200 | 0.00 | 0.00 | 0.00 | 0.00 | 0.00 | 0.00 | 0.00 | 0.00 | 0.00 | 0.00 |
| 1600 | 0.00 | 0.00 | 0.00 | 0.00 | 0.00 | 0.00 | 0.00 | 0.00 | 0.00 | 0.00 |
| 2000 | 0.00 | 0.00 | 0.00 | 0.00 | 0.00 | 0.00 | 0.00 | 0.00 | 0.00 | 0.00 |
| 2400 | 0.00 | 0.00 | 0.94 | 0.94 | 0.00 | 0.00 | 0.31 | 0.31 | 0.54 | 0.54 |
| 2800 | 1.65 | 1.65 | 2.86 | 1.92 | 1.59 | 1.59 | 2.03 | 1.72 | 0.72 | 0.18 |
| 3200 | 4.32 | 2.67 | 5.61 | 2.75 | 4.89 | 3.30 | 4.94 | 2.91 | 0.65 | 0.34 |
| 3600 | 6.68 | 2.36 | 8.97 | 3.36 | 7.11 | 2.22 | 7.59 | 2.65 | 1.22 | 0.62 |
| 4000 | 10.96 | 4.28 | 12.58 | 3.61 | 10.82 | 3.71 | 11.45 | 3.87 | 0.98 | 0.36 |
| 4400 | 13.91 | 2.95 | 18.05 | 5.47 | 14.06 | 3.24 | 15.34 | 3.89 | 2.35 | 1.38 |
| 4800 | 19.64 | 5.73 | 21.50 | 3.45 | 22.23 | 8.17 | 21.12 | 5.78 | 1.34 | 2.36 |

Table C3.9: Fine (4.00 sphere glass); Bed-matrix (13.20 mm crushed basalt); $\dot{\gamma}$ =0.04 s $^{-1}$.

| $\gamma_{total}$ | Test 1 | | Test 2 | | Test 3 | | Mean | | Std. dev. | |
|---|---|---|---|---|---|---|---|---|---|---|
| | CPF (%) | IMF (%) | CPF (%) | IMF (%) | CPF (%) | IMF (%) | CPF (%) | IMF (%) | CPF (%) | IMF (%) |
| 0 | 0.00 | 0.00 | 0.00 | 0.00 | 0.00 | 0.00 | 0.00 | 0.00 | 0.00 | 0.00 |
| 50 | 0.00 | 0.00 | 0.00 | 0.00 | 0.00 | 0.00 | 0.00 | 0.00 | 0.00 | 0.00 |
| 100 | 0.00 | 0.00 | 0.00 | 0.00 | 0.00 | 0.00 | 0.00 | 0.00 | 0.00 | 0.00 |
| 200 | 0.00 | 0.00 | 0.00 | 0.00 | 0.00 | 0.00 | 0.00 | 0.00 | 0.00 | 0.00 |
| 400 | 0.00 | 0.00 | 0.00 | 0.00 | 0.00 | 0.00 | 0.00 | 0.00 | 0.00 | 0.00 |
| 800 | 0.00 | 0.00 | 0.00 | 0.00 | 0.00 | 0.00 | 0.00 | 0.00 | 0.00 | 0.00 |
| 1200 | 0.00 | 0.00 | 0.00 | 0.00 | 0.00 | 0.00 | 0.00 | 0.00 | 0.00 | 0.00 |
| 1600 | 0.25 | 0.25 | 0.30 | 0.30 | 0.00 | 0.00 | 0.18 | 0.18 | 0.16 | 0.16 |
| 2000 | 0.62 | 0.37 | 1.58 | 1.28 | 0.97 | 0.97 | 1.06 | 0.87 | 0.46 | 0.46 |
| 2400 | 1.23 | 0.61 | 3.75 | 2.17 | 2.96 | 1.99 | 2.65 | 1.59 | 0.85 | 0.85 |
| 2800 | 3.10 | 1.87 | 5.86 | 2.11 | 5.23 | 2.27 | 4.73 | 2.08 | 0.20 | 0.20 |
| 3200 | 7.65 | 4.55 | 10.36 | 4.50 | 8.48 | 3.25 | 8.83 | 4.10 | 1.39 | 0.74 |
| 3600 | 9.56 | 1.91 | 13.66 | 3.30 | 12.21 | 3.73 | 11.81 | 2.98 | 2.08 | 0.95 |
| 4000 | 12.17 | 2.61 | 15.16 | 1.50 | 15.13 | 2.92 | 14.15 | 2.34 | 1.72 | 0.75 |
| 4400 | 15.89 | 3.72 | 17.13 | 1.97 | 17.88 | 2.75 | 16.97 | 2.81 | 1.01 | 0.88 |
| 4800 | 21.11 | 5.22 | 22.80 | 5.67 | 20.60 | 2.72 | 21.50 | 4.54 | 1.15 | 1.59 |

Table C3.10: Fine (4.05 mm angular crushed basalt); Bed-matrix (13.20 mm crushed basalt); $\dot{\gamma}$ =0.04 $s^{-1}$.

| $\gamma_{total}$ | Test 1 | | Test 2 | | Test 3 | | Mean | | Std. dev. | |
|---|---|---|---|---|---|---|---|---|---|---|
| | CPF (%) | IMF (%) | CPF (%) | IMF (%) | CPF (%) | IMF (%) | CPF (%) | IMF (%) | CPF (%) | IMF (%) |
| 0 | 0.00 | 0.00 | 0.00 | 0.00 | 0.00 | 0.00 | 0.00 | 0.00 | 0.00 | 0.00 |
| 50 | 0.00 | 0.00 | 0.00 | 0.00 | 0.00 | 0.00 | 0.00 | 0.00 | 0.00 | 0.00 |
| 100 | 0.00 | 0.00 | 0.00 | 0.00 | 0.00 | 0.00 | 0.00 | 0.00 | 0.00 | 0.00 |
| 200 | 0.00 | 0.00 | 0.00 | 0.00 | 0.00 | 0.00 | 0.00 | 0.00 | 0.00 | 0.00 |
| 400 | 0.00 | 0.00 | 0.00 | 0.00 | 0.00 | 0.00 | 0.00 | 0.00 | 0.00 | 0.00 |
| 800 | 0.00 | 0.00 | 0.00 | 0.00 | 0.00 | 0.00 | 0.00 | 0.00 | 0.00 | 0.00 |
| 1200 | 0.00 | 0.00 | 0.17 | 0.17 | 0.00 | 0.00 | 0.06 | 0.06 | 0.10 | 0.10 |
| 1600 | 0.35 | 0.35 | 0.43 | 0.26 | 0.71 | 0.71 | 0.50 | 0.44 | 0.19 | 0.24 |
| 2000 | 0.71 | 0.36 | 0.62 | 0.19 | 1.91 | 1.20 | 1.08 | 0.58 | 0.72 | 0.54 |
| 2400 | 1.49 | 0.78 | 1.35 | 0.73 | 2.57 | 0.66 | 1.80 | 0.72 | 0.67 | 0.06 |
| 2800 | 2.46 | 0.97 | 1.94 | 0.59 | 3.16 | 0.59 | 2.52 | 0.72 | 0.61 | 0.22 |
| 3200 | 6.38 | 3.92 | 5.62 | 3.68 | 7.06 | 3.90 | 6.35 | 3.83 | 0.72 | 0.13 |
| 3600 | 9.55 | 3.17 | 8.48 | 2.86 | 10.45 | 3.39 | 9.49 | 3.14 | 0.99 | 0.27 |
| 4000 | 13.90 | 4.35 | 13.16 | 4.68 | 15.32 | 4.87 | 14.13 | 4.63 | 1.10 | 0.26 |
| 4400 | 17.85 | 3.95 | 15.71 | 2.55 | 19.11 | 3.79 | 17.56 | 3.43 | 1.72 | 0.77 |
| 4800 | 25.06 | 7.21 | 22.44 | 6.73 | 28.36 | 9.25 | 25.29 | 7.73 | 2.97 | 1.34 |

## C4 Effect of Particle Density

Table C4.1: Fine (4.00 mm plastic bead); Bed-matrix (15.75 mm glass bead); $\dot{\gamma}$=0.04 $s^{-1}$; $\rho_p / \rho_b$ =0.39.

| $\gamma_{total}$ | Test 1 | | Test 2 | | Test 3 | | Mean | | Std. dev. | |
|---|---|---|---|---|---|---|---|---|---|---|
| | CPF (%) | IMF (%) | CPF (%) | IMF (%) | CPF (%) | IMF (%) | CPF (%) | IMF (%) | CPF (%) | IMF (%) |
| 0 | 0.00 | 0.00 | 0.00 | 0.00 | 0.00 | 0.00 | 0.00 | 0.00 | 0.00 | 0.00 |
| 50 | 0.00 | 0.00 | 0.00 | 0.00 | 0.00 | 0.00 | 0.00 | 0.00 | 0.00 | 0.00 |
| 100 | 0.23 | 0.23 | 0.00 | 0.00 | 0.00 | 0.00 | 0.08 | 0.08 | 0.13 | 0.13 |
| 200 | 0.69 | 0.46 | 0.23 | 0.23 | 0.00 | 0.00 | 0.31 | 0.23 | 0.23 | 0.23 |
| 400 | 11.78 | 11.09 | 10.26 | 10.03 | 13.69 | 13.69 | 11.91 | 11.60 | 1.88 | 1.88 |
| 800 | 37.64 | 25.86 | 36.60 | 26.34 | 38.28 | 24.59 | 37.51 | 25.60 | 0.90 | 0.90 |
| 1200 | 57.28 | 19.64 | 55.48 | 18.88 | 59.40 | 21.12 | 57.39 | 19.88 | 1.96 | 1.14 |
| 1600 | 64.90 | 7.62 | 63.40 | 7.92 | 67.29 | 7.89 | 65.20 | 7.81 | 1.96 | 0.17 |
| 2000 | 67.67 | 2.77 | 66.43 | 3.03 | 70.07 | 2.78 | 68.06 | 2.86 | 1.85 | 0.15 |
| 2400 | 71.59 | 3.92 | 70.40 | 3.97 | 71.93 | 1.86 | 71.31 | 3.25 | 0.80 | 1.20 |
| 2800 | 75.75 | 4.16 | 73.66 | 3.26 | 74.25 | 2.32 | 74.55 | 3.25 | 1.08 | 0.92 |
| 3200 | 75.98 | 0.23 | 75.29 | 1.63 | 77.03 | 2.78 | 76.10 | 1.55 | 0.88 | 1.28 |

Table C4.2: Fine (4.00 mm glass bead); Bed-matrix (15.75 mm glass bead); $\dot{\gamma}$=0.04 $s^{-1}$; $\rho_p / \rho_b$ =1.01.

| $\gamma_{total}$ | Test 1 | | Test 2 | | Test 3 | | Mean | | Std. dev. | |
|---|---|---|---|---|---|---|---|---|---|---|
| | CPF (%) | IMF (%) | CPF (%) | IMF (%) | CPF (%) | IMF (%) | CPF (%) | IMF (%) | CPF (%) | IMF (%) |
| 0 | 0.00 | 0.00 | 0.00 | 0.00 | 0.00 | 0.00 | 0.00 | 0.00 | 0.00 | 0.00 |
| 50 | 0.00 | 0.00 | 0.00 | 0.00 | 0.00 | 0.00 | 0.00 | 0.00 | 0.00 | 0.00 |
| 100 | 0.00 | 0.00 | 0.00 | 0.00 | 0.00 | 0.00 | 0.00 | 0.00 | 0.00 | 0.00 |
| 200 | 0.00 | 0.00 | 0.09 | 0.09 | 0.12 | 0.12 | 0.07 | 0.07 | 0.06 | 0.06 |
| 400 | 2.03 | 2.03 | 0.61 | 0.52 | 0.56 | 0.44 | 1.07 | 1.00 | 0.90 | 0.90 |
| 800 | 4.78 | 2.75 | 6.23 | 5.62 | 6.37 | 5.81 | 5.79 | 4.73 | 0.88 | 1.71 |
| 1200 | 20.92 | 16.14 | 26.32 | 20.09 | 21.72 | 15.35 | 22.99 | 17.19 | 2.91 | 2.54 |
| 1600 | 46.00 | 25.08 | 49.45 | 23.13 | 43.87 | 22.15 | 46.44 | 23.45 | 2.82 | 1.49 |
| 2000 | 60.77 | 14.77 | 62.21 | 12.76 | 58.04 | 14.17 | 60.34 | 13.90 | 2.12 | 1.03 |
| 2400 | 70.39 | 9.62 | 68.98 | 6.77 | 63.20 | 5.16 | 67.52 | 7.18 | 3.81 | 2.26 |
| 2800 | 74.54 | 4.15 | 71.58 | 2.60 | 68.39 | 5.19 | 71.50 | 3.98 | 3.08 | 1.30 |
| 3200 | 78.28 | 3.74 | 73.74 | 2.16 | 72.15 | 3.76 | 74.72 | 3.22 | 3.18 | 0.92 |

Table C4.3: Fine (4.00 mm steel sphere); Bed-matrix (15.75 mm glass bead); $\dot{\gamma}$=0.04 $s^{-1}$; $\rho_p / \rho_b$ =3.10.

| $\gamma_{total}$ | Test 1 | | Test 2 | | Test 3 | | Mean | | Std. dev. | |
|---|---|---|---|---|---|---|---|---|---|---|
| | CPF (%) | IMF (%) | CPF (%) | IMF (%) | CPF (%) | IMF (%) | CPF (%) | IMF (%) | CPF (%) | IMF (%) |
| 0 | 0.00 | 0.00 | 0.00 | 0.00 | 0.00 | 0.00 | 0.00 | 0.00 | 0.00 | 0.00 |
| 50 | 0.00 | 0.00 | 0.00 | 0.00 | 0.00 | 0.00 | 0.00 | 0.00 | 0.00 | 0.00 |
| 100 | 0.00 | 0.00 | 0.00 | 0.00 | 0.00 | 0.00 | 0.00 | 0.00 | 0.00 | 0.00 |
| 200 | 0.91 | 0.91 | 0.00 | 0.00 | 0.21 | 0.21 | 0.37 | 0.37 | 0.48 | 0.48 |
| 400 | 9.87 | 8.96 | 8.79 | 8.79 | 8.25 | 8.04 | 8.97 | 8.60 | 0.49 | 0.49 |
| 800 | 30.40 | 20.53 | 28.45 | 19.66 | 31.55 | 23.30 | 30.13 | 21.16 | 1.57 | 1.90 |
| 1200 | 50.02 | 19.62 | 52.93 | 24.48 | 53.20 | 21.65 | 52.05 | 21.92 | 1.76 | 2.44 |
| 1600 | 62.95 | 12.93 | 63.45 | 10.52 | 65.77 | 12.57 | 64.06 | 12.01 | 1.50 | 1.30 |
| 2000 | 67.60 | 4.65 | 68.62 | 5.17 | 70.52 | 4.75 | 68.91 | 4.86 | 1.48 | 0.28 |
| 2400 | 71.23 | 3.63 | 72.59 | 3.97 | 74.64 | 4.12 | 72.82 | 3.91 | 1.72 | 0.25 |
| 2800 | 76.33 | 5.10 | 78.62 | 6.03 | 77.94 | 3.30 | 77.63 | 4.81 | 1.18 | 1.39 |
| 3200 | 79.17 | 2.84 | 80.17 | 1.55 | 79.59 | 1.65 | 79.64 | 2.01 | 0.50 | 0.72 |

Table C4.4: Fine (4.05 mm crushed basalt); Bed-matrix (15.75 mm glass bead); $\dot{\gamma}$ =0.04 $s^{-1}$; $\rho_p / \rho_b$ =1.10.

| $\gamma_{total}$ | Test 1 | | Test 2 | | Test 3 | | Mean | | Std. dev. | |
|---|---|---|---|---|---|---|---|---|---|---|
| | CPF (%) | IMF (%) | CPF (%) | IMF (%) | CPF (%) | IMF (%) | CPF (%) | IMF (%) | CPF (%) | IMF (%) |
| 0 | 0.00 | 0.00 | 0.00 | 0.00 | 0.00 | 0.00 | 0.00 | 0.00 | 0.00 | 0.00 |
| 50 | 0.12 | 0.12 | 0.24 | 0.24 | 0.00 | 0.00 | 0.12 | 0.12 | 0.12 | 0.12 |
| 100 | 0.53 | 0.41 | 0.90 | 0.66 | 0.67 | 0.69 | 0.70 | 0.59 | 0.15 | 0.15 |
| 200 | 3.56 | 3.03 | 2.94 | 2.04 | 3.61 | 3.24 | 3.37 | 2.77 | 0.64 | 0.64 |
| 400 | 16.32 | 12.76 | 17.45 | 14.51 | 14.53 | 10.92 | 16.10 | 12.73 | 1.80 | 1.80 |
| 800 | 51.75 | 35.43 | 53.83 | 36.38 | 46.43 | 31.90 | 50.67 | 34.57 | 2.36 | 2.36 |
| 1200 | 68.20 | 16.45 | 71.76 | 17.93 | 65.86 | 19.43 | 68.61 | 17.94 | 2.97 | 1.49 |
| 1600 | 75.75 | 7.55 | 78.41 | 6.65 | 74.04 | 8.18 | 76.07 | 7.46 | 2.20 | 0.77 |
| 2000 | 76.47 | 0.72 | 80.87 | 2.46 | 76.57 | 2.53 | 77.97 | 1.90 | 2.51 | 1.03 |
| 2400 | 77.05 | 0.58 | 81.83 | 0.96 | 77.42 | 0.85 | 78.77 | 0.80 | 2.66 | 0.20 |
| 2800 | 78.29 | 1.24 | 82.05 | 0.22 | 78.63 | 1.21 | 79.66 | 0.89 | 2.08 | 0.58 |
| 3200 | 78.30 | 0.01 | 83.06 | 1.01 | 80.82 | 2.19 | 80.73 | 1.07 | 2.38 | 1.09 |

Table C4.5: Fine (4.00 mm plastic bead); Bed-matrix (13.20 mm crushed basalt); $\dot{\gamma}$ =0.04 $s^{-1}$; $\rho_p / \rho_b$ =0.35.

| $\gamma_{total}$ | Test 1 | | Test 2 | | Test 3 | | Mean | | Std. dev. | |
|---|---|---|---|---|---|---|---|---|---|---|
| | CPF (%) | IMF (%) | CPF (%) | IMF (%) | CPF (%) | IMF (%) | CPF (%) | IMF (%) | CPF (%) | IMF (%) |
| 0 | 0.00 | 0.00 | 0.00 | 0.00 | 0.00 | 0.00 | 0.00 | 0.00 | 0.00 | 0.00 |
| 50 | 0.00 | 0.00 | 0.00 | 0.00 | 0.00 | 0.00 | 0.00 | 0.00 | 0.00 | 0.00 |
| 100 | 0.00 | 0.00 | 0.00 | 0.00 | 0.00 | 0.00 | 0.00 | 0.00 | 0.00 | 0.00 |
| 200 | 0.00 | 0.00 | 0.00 | 0.00 | 0.00 | 0.00 | 0.00 | 0.00 | 0.00 | 0.00 |
| 400 | 0.00 | 0.00 | 0.00 | 0.00 | 0.00 | 0.00 | 0.00 | 0.00 | 0.00 | 0.00 |
| 800 | 0.00 | 0.00 | 0.00 | 0.00 | 0.00 | 0.00 | 0.00 | 0.00 | 0.00 | 0.00 |
| 1200 | 0.29 | 0.29 | 0.00 | 0.00 | 0.00 | 0.00 | 0.10 | 0.10 | 0.17 | 0.17 |
| 1600 | 0.73 | 0.44 | 1.97 | 1.97 | 1.02 | 1.02 | 1.24 | 1.14 | 0.77 | 0.77 |
| 2000 | 4.16 | 3.43 | 7.00 | 5.03 | 6.69 | 5.67 | 5.95 | 4.71 | 1.15 | 1.15 |
| 2400 | 12.76 | 8.60 | 15.30 | 8.30 | 12.43 | 5.74 | 13.50 | 7.55 | 1.57 | 1.57 |
| 2800 | 21.15 | 8.39 | 27.02 | 11.72 | 21.36 | 8.93 | 23.18 | 9.68 | 1.79 | 1.79 |
| 3200 | 33.37 | 12.22 | 35.20 | 8.18 | 33.20 | 11.84 | 33.92 | 10.75 | 1.11 | 2.23 |
| 3600 | 44.48 | 11.11 | 43.51 | 8.31 | 43.56 | 10.36 | 43.85 | 9.93 | 0.55 | 1.45 |
| 4000 | 51.48 | 7.00 | 49.68 | 6.17 | 53.23 | 9.67 | 51.46 | 7.61 | 1.78 | 1.83 |
| 4400 | 58.36 | 6.88 | 57.15 | 7.47 | 59.61 | 6.38 | 58.37 | 6.91 | 1.23 | 0.55 |
| 4800 | 62.73 | 4.37 | 61.03 | 3.88 | 63.37 | 3.76 | 62.38 | 4.00 | 1.21 | 0.32 |

Table C4.6: Fine (4.00 mm glass bead); Bed-matrix (13.20 mm crushed basalt); $\dot{\gamma}$ =0.04 $s^{-1}$; $\rho_p / \rho_b$ =0.91.

| $\gamma_{total}$ | Test 1 | | Test 2 | | Test 3 | | Mean | | Std. dev. | |
|---|---|---|---|---|---|---|---|---|---|---|
| | CPF (%) | IMF (%) | CPF (%) | IMF (%) | CPF (%) | IMF (%) | CPF (%) | IMF (%) | CPF (%) | IMF (%) |
| 0 | 0.00 | 0.00 | 0.00 | 0.00 | 0.00 | 0.00 | 0.00 | 0.00 | 0.00 | 0.00 |
| 50 | 0.00 | 0.00 | 0.00 | 0.00 | 0.00 | 0.00 | 0.00 | 0.00 | 0.00 | 0.00 |
| 100 | 0.00 | 0.00 | 0.00 | 0.00 | 0.00 | 0.00 | 0.00 | 0.00 | 0.00 | 0.00 |
| 200 | 0.00 | 0.00 | 0.00 | 0.00 | 0.00 | 0.00 | 0.00 | 0.00 | 0.00 | 0.00 |
| 400 | 0.00 | 0.00 | 0.00 | 0.00 | 0.00 | 0.00 | 0.00 | 0.00 | 0.00 | 0.00 |
| 800 | 0.00 | 0.00 | 0.00 | 0.00 | 0.00 | 0.00 | 0.00 | 0.00 | 0.00 | 0.00 |
| 1200 | 0.00 | 0.00 | 0.00 | 0.00 | 0.00 | 0.00 | 0.00 | 0.00 | 0.00 | 0.00 |
| 1600 | 0.25 | 0.25 | 0.30 | 0.30 | 0.00 | 0.00 | 0.18 | 0.18 | 0.16 | 0.16 |
| 2000 | 0.62 | 0.37 | 1.58 | 1.28 | 0.97 | 0.97 | 1.06 | 0.87 | 0.46 | 0.46 |
| 2400 | 1.23 | 0.61 | 3.75 | 2.17 | 2.96 | 1.99 | 2.65 | 1.59 | 0.85 | 0.85 |
| 2800 | 3.10 | 1.87 | 5.86 | 2.11 | 5.23 | 2.27 | 4.73 | 2.08 | 0.20 | 0.20 |
| 3200 | 7.65 | 4.55 | 10.36 | 4.50 | 8.48 | 3.25 | 8.83 | 4.10 | 1.39 | 0.74 |
| 3600 | 9.56 | 1.91 | 13.66 | 3.30 | 12.21 | 3.73 | 11.81 | 2.98 | 2.08 | 0.95 |
| 4000 | 12.17 | 2.61 | 15.16 | 1.50 | 15.13 | 2.92 | 14.15 | 2.34 | 1.72 | 0.75 |
| 4400 | 15.89 | 3.72 | 17.13 | 1.97 | 17.88 | 2.75 | 16.97 | 2.81 | 1.01 | 0.88 |
| 4800 | 21.11 | 5.22 | 22.80 | 5.67 | 20.60 | 2.72 | 21.50 | 4.54 | 1.15 | 1.59 |

Table C4.7: Fine (4.00 mm steel sphere); Bed-matrix (13.20 mm crushed basalt); $\dot{\gamma}$=0.04 $s^{-1}$; $\rho_p / \rho_b$ =2.80.

| $\gamma_{total}$ | Test 1 | | Test 2 | | Test 3 | | Mean | | Std. dev. | |
|---|---|---|---|---|---|---|---|---|---|---|
| | CPF (%) | IMF (%) | CPF (%) | IMF (%) | CPF (%) | IMF (%) | CPF (%) | IMF (%) | CPF (%) | IMF (%) |
| 0 | 0.00 | 0.00 | 0.00 | 0.00 | 0.00 | 0.00 | 0.00 | 0.00 | 0.00 | 0.00 |
| 50 | 0.00 | 0.00 | 0.00 | 0.00 | 0.00 | 0.00 | 0.00 | 0.00 | 0.00 | 0.00 |
| 100 | 0.00 | 0.00 | 0.00 | 0.00 | 0.00 | 0.00 | 0.00 | 0.00 | 0.00 | 0.00 |
| 200 | 0.00 | 0.00 | 0.00 | 0.00 | 0.00 | 0.00 | 0.00 | 0.00 | 0.00 | 0.00 |
| 400 | 0.00 | 0.00 | 0.00 | 0.00 | 0.00 | 0.00 | 0.00 | 0.00 | 0.00 | 0.00 |
| 800 | 0.00 | 0.00 | 0.00 | 0.00 | 0.00 | 0.00 | 0.00 | 0.00 | 0.00 | 0.00 |
| 1200 | 0.00 | 0.00 | 0.17 | 0.17 | 0.00 | 0.00 | 0.06 | 0.06 | 0.10 | 0.10 |
| 1600 | 0.13 | 0.13 | 0.17 | 0.00 | 0.21 | 0.21 | 0.17 | 0.11 | 0.11 | 0.11 |
| 2000 | 1.20 | 1.07 | 1.03 | 0.86 | 1.24 | 1.03 | 1.16 | 0.99 | 0.11 | 0.11 |
| 2400 | 3.20 | 2.00 | 3.25 | 2.22 | 4.33 | 3.09 | 3.59 | 2.44 | 0.58 | 0.58 |
| 2800 | 5.87 | 2.67 | 7.35 | 4.10 | 5.77 | 1.44 | 6.33 | 2.74 | 0.88 | 1.33 |
| 3200 | 11.33 | 5.46 | 11.45 | 4.10 | 10.52 | 4.75 | 11.10 | 4.77 | 0.51 | 0.68 |
| 3600 | 14.00 | 2.67 | 14.53 | 3.08 | 13.81 | 3.29 | 14.11 | 3.01 | 0.37 | 0.32 |
| 4000 | 16.13 | 2.13 | 17.27 | 2.74 | 16.70 | 2.89 | 16.70 | 2.59 | 0.57 | 0.40 |
| 4400 | 19.60 | 3.47 | 20.17 | 2.90 | 20.00 | 3.30 | 19.92 | 3.22 | 0.29 | 0.29 |
| 4800 | 24.40 | 4.80 | 23.76 | 3.59 | 24.95 | 4.95 | 24.37 | 4.45 | 0.60 | 0.75 |

Table C4.8: Fine (4.05 mm crushed basalt); Bed-matrix (13.20 mm crushed basalt); $\dot{\gamma}$=0.04 $s^{-1}$; $\rho_p / \rho_b$ =0.99.

| $\gamma_{total}$ | Test 1 | | Test 2 | | Test 3 | | Mean | | Std. dev. | |
|---|---|---|---|---|---|---|---|---|---|---|
| | CPF (%) | IMF (%) | CPF (%) | IMF (%) | CPF (%) | IMF (%) | CPF (%) | IMF (%) | CPF (%) | IMF (%) |
| 0 | 0.00 | 0.00 | 0.00 | 0.00 | 0.00 | 0.00 | 0.00 | 0.00 | 0.00 | 0.00 |
| 50 | 0.00 | 0.00 | 0.00 | 0.00 | 0.00 | 0.00 | 0.00 | 0.00 | 0.00 | 0.00 |
| 100 | 0.00 | 0.00 | 0.00 | 0.00 | 0.00 | 0.00 | 0.00 | 0.00 | 0.00 | 0.00 |
| 200 | 0.00 | 0.00 | 0.00 | 0.00 | 0.00 | 0.00 | 0.00 | 0.00 | 0.00 | 0.00 |
| 400 | 0.00 | 0.00 | 0.00 | 0.00 | 0.00 | 0.00 | 0.00 | 0.00 | 0.00 | 0.00 |
| 800 | 0.00 | 0.00 | 0.00 | 0.00 | 0.00 | 0.00 | 0.00 | 0.00 | 0.00 | 0.00 |
| 1200 | 0.00 | 0.00 | 0.17 | 0.17 | 0.00 | 0.00 | 0.06 | 0.06 | 0.10 | 0.10 |
| 1600 | 0.35 | 0.35 | 0.43 | 0.26 | 0.71 | 0.71 | 0.50 | 0.44 | 0.19 | 0.24 |
| 2000 | 0.71 | 0.36 | 0.62 | 0.19 | 1.91 | 1.20 | 1.08 | 0.58 | 0.72 | 0.54 |
| 2400 | 1.49 | 0.78 | 1.35 | 0.73 | 2.57 | 0.66 | 1.80 | 0.72 | 0.67 | 0.06 |
| 2800 | 2.46 | 0.97 | 1.94 | 0.59 | 3.16 | 0.59 | 2.52 | 0.72 | 0.61 | 0.22 |
| 3200 | 6.38 | 3.92 | 5.62 | 3.68 | 7.06 | 3.90 | 6.35 | 3.83 | 0.72 | 0.13 |
| 3600 | 9.55 | 3.17 | 8.48 | 2.86 | 10.45 | 3.39 | 9.49 | 3.14 | 0.99 | 0.27 |
| 4000 | 13.90 | 4.35 | 13.16 | 4.68 | 15.32 | 4.87 | 14.13 | 4.63 | 1.10 | 0.26 |
| 4400 | 17.85 | 3.95 | 15.71 | 2.55 | 19.11 | 3.79 | 17.56 | 3.43 | 1.72 | 0.77 |
| 4800 | 25.06 | 7.21 | 22.44 | 6.73 | 28.36 | 9.25 | 25.29 | 7.73 | 2.97 | 1.34 |

# APPENDIX D: FISH ALGORITHMS FOR PFC3D

## D1 Numerical SCPG Modelling

```
;;;===========================================
;;        Numerical SCPG modelling
;;;===========================================

New
set random  ; reset random-number generator
set gen_error off
set max_balls 3000000
macro big 'id 1,100000'
macro small 'id 1000001,1000050'


set dt auto
set safety_fac 0.8
def wfric
  wfric = 0.69
  pfric = 0.25
  nkn = 1e7
  sks = 1e7
  y_rotation = 0
end

wfric

;;;===========================================
;;;======== wall-generation procedure ========
;;;===========================================

;  east wall (drive wall)
wall id=1 ks 1e7 kn 1e7 fric wfric face (0.354,0.0,0.0) & (0.354,0.0,0.446) & (0.354,0.355,0.446)
                                                      & (0.354,0.355,0.0)
                                                      & x 0.354 y 0.1775 z 0.0 ys y_rotation

;  north wall (side wall)
wall id=2 ks 1e7 kn 1e7 fric wfric face (-0.3,0.355,0.0) & (0.654,0.355,0.0) & (0.654,0.355,0.246)
                                                      & (-0.3,0.355,0.246)

;  west wall (drive wall)
wall id=3 ks 1e7 kn 1e7 fric wfric face (0.0,0.0,0.0) & (0.0,0.355,0.0) & (0.0,0.355,0.446)
                                                      & (0.0,0.0,0.446)
                                                      & x 0.0 y 0.1775 z 0.0 ys y_rotation

;  south wall(side wall)
wall id=4 ks 1e7 kn 1e7 fric wfric face (-0.3,0.0,0.0) & (-0.3,0.0,0.246) & (0.654,0.0,0.246)
                                                      & (0.654,0.0,0.0)

;  crown wall
wall id=5 ks 1e7 kn 1e7 fric wfric face (-0.3,0.0,0.246) & (-0.3,0.355,0.246) & (0.654,0.355,0.246)
                                                      & (0.654,0.0,0.246)

;  floor wall
wall id=6 ks 1e7 kn 1e7 fric wfric face (0.0,0.0,0.0) & (0.354,0.0,0.0) & (0.354,0.355,0.0)
                                                      & (0.0,0.355,0.0)



;;;===========================================
;;;======== ball-generation procedure ========
;;;===== Works for both PFC2D and PFC3D ======
;;;===========================================


def bg_fillbox
;
; ----- Implements the ball-generation algorithm.
;
; INPUT: bg_h   - height of sample
;        bg_w   - width of sample
```

```
;       bg_l   - length of sample (PFC3D only)
;       bg_n   - final porosity of sample
;       bg_rmin - minimum ball radius
;       bg_rmax - maximum ball radius
;
 if dim = 2 then
   _bg_makewalls2d
 else
   _bg_makewalls3d
 end_if

; --- Compute number of balls to generate
;     using the expression:
;          N = A(1 - n) / (pi*Rbar^2)     (PFC2D)
;          N = 3V(1 - n) / (4*pi*Rbar^3)  (PFC3D)
;
  _rbar = 0.5*( bg_rmin + bg_rmax )
  if dim = 2 then
   _numballs = bg_h*bg_w*( 1.0 - bg_n ) / (pi*_rbar^2)
  else
    _numballs = 3.0*bg_h*bg_w*bg_l*( 1.0 - bg_n ) / (4.0*pi*_rbar^3)
  end_if
  _rlo = 0.5 * bg_rmin
  _rhi = 0.5 * bg_rmax
  if dim = 2 then
    _xl = 0.0
    _xu = bg_w
    _yl = 0.0
    _yu = bg_h
    command
      GENERATE x=(_xl,_xu) y=(_yl,_yu) &
           rad=(_rlo,_rhi)        &
           id=(1,_numballs)
    end_command
  else
    _xl = 0.0
    _xu = bg_w
    _yl = 0.0
    _yu = bg_l
    _zl = 0.0
    _zu = bg_h


    command
     GENERATE x=(_xl,_xu) y=(_yl,_yu) z=(_zl,_zu) &
           rad=(_rlo,_rhi)        &
           id=(1,_numballs)
           prop ks bg_ks kn bg_kn dens bg_dens fric bg_fric
                                & shear bg_shear damp bg_damp
    end_command
  end_if

; --- Determine radius multiplier, [_m], so that we
;     achieve desired porosity, [bg_n].

 _n0 = bg_poros
 if dim = 2 then
   _m = ( (1.0 - bg_n) / (1.0 - _n0) )^(1.0/2.0)
 else
   _m = ( (1.0 - bg_n) / (1.0 - _n0) )^(1.0/3.0)
 end_if
 command
   change rad mult _m
 end_command
end
; ==============================================================

def bg_poros ; ----- Return the porosity of the current model.
 _totval = 0.0
 bp = ball_head
 loop while bp # null
   if dim = 2 then
     _totval = _totval + pi*b_rad(bp)^2
   else
     _totval = _totval + (4.0/3.0)*pi*b_rad(bp)^3
```

```
    end_if
    bp = b_next(bp)
  end_loop

  if dim = 2 then
    _boxval = bg_h * bg_w
  else
    _boxval = bg_h * bg_w * bg_l
  end_if
  bg_poros = 1.0 - ( _totval / _boxval )
end
; ================================================================
def bg_setballprops
  bg_shear = bg_shear
  bg_dens = bg_dens
  bg_kn = bg_kn
  bg_ks = bg_ks
  bg_fric = bg_fric
  bg_damp  = bg_damp
  command
    prop dens=bg_dens kn=bg_kn ks=bg_ks fric=bg_fric damp=bg_damp
  end_command
end
; ================================================================
def _bg_makewalls2d  ; --- Generate the four bounding walls
   _x0 = 0.0
   _y0 = 0.0
   _x1 = bg_w
   _y1 = 0.0
  command
    wall id=1 fric=0.0 kn=1e8 ks=1e8 &
                   nodes (_x0,_y0) (_x1,_y1)
  end_command
   _x0 = bg_w
   _y0 = 0.0
   _x1 = bg_w
   _y1 = bg_h
  command
    wall id=2 fric=0.0 kn=1e8 ks=1e8 &
                   nodes (_x0,_y0) (_x1,_y1)
  end_command
   _x0 = bg_w
   _y0 = bg_h
   _x1 = 0.0
   _y1 = bg_h
  command
    wall id=3 fric=0.0 kn=1e8 ks=1e8 &
                   nodes (_x0,_y0) (_x1,_y1)
  end_command
   _x0 = 0.0
   _y0 = bg_h
   _x1 = 0.0
   _y1 = 0.0
  command
    wall id=4 fric=0.0 kn=1e8 ks=1e8 &
                   nodes (_x0,_y0) (_x1,_y1)
  end_command
end
; ================================================================


def _bg_makewalls3d
  command
    wall id=1 ks 1e7 kn 1e7 fric wfric face (0.354,0.0,0.0) & (0.354,0.0,0.446) & (0.354,0.355,0.446)
                                                             & (0.354,0.355,0.0)
  end_command

     ;  north wall
  command
     wall id=2 ks 1e7 kn 1e7 fric wfric face (-0.3,0.355,0) & (0.654,0.355,0.0) & (0.654,0.355,0.246)
                                                             & (-0.3,0.355,0.246)
  end_command

     ;  west wall
  command
```

```
    wall id=3 ks 1e7 kn 1e7 fric wfric face (0.0,0.0,0.0) & (0.0,0.355,0.0) & (0.0,0.355,0.446)
                                                                        & (0.0,0.0,0.446)
  end_command

     ;  south wall
  command
     wall id=4 ks 1e7 kn 1e7 fric wfric face (-0.3,0.0,0.0) & (-0.3,0.0,0.246) & (0.654,0.0,0.246)
                                                                        & (0.654,0.0,0.0)
  end_command

     ;  crown wall
  command
    wall id=5 ks 1e7 kn 1e7 fric wfric face (-0.3,0.0,0.246) & (-0.3,0.355,0.246) & (0.654,0.355,0.246)
                                                                        & (0.654,0.0,0.246)
  end_command

     ;  floor wall
  command
    wall id=6 ks 1e7 kn 1e7 fric wfric face (0.0,0.0,0.0) & (0.354,0.0,0.0) & (0.354,0.355,0.0)
                                                                        & (0.0,0.355,0.0)
  end_command
end

 SET bg_w=0.354 bg_l=0.355 bg_h=0.220 bg_n=0.4 bg_rmin=0.008875 bg_rmax=0.008875   ;3D

bg_fillbox

 SET bg_dens=2540 bg_kn=1e7 bg_ks=1e7 bg_fric=0.25 bg_shear= 50e9 bg_damp=0.84
bg_setballprops

plot create footing
plot add ball blue  red yellow lgreen wall white   ; Separation of specimen into discrete colour layers
plot add wall white
plot set mag 2.50
plot add s yellow
plot show

delete ball range z 0.355 2.00

plot show

;;;================================================================================
;;;======== create percolating fine particles and applied micro-properties ========
;;;================================================================================
def small_p
   small_p_min = small_p_min_0
   small_p_max = small_p_max_0
   y_min       = y_min_0
   y_max       = y_max_0
   z_min       = z_min_0
   z_max       = z_max_0
   dens        = dens_0
   damping     = damp_0
   shear       = shear_0
   zforce      = zforce_0
   ks          = ks_0
   kn          = kn_0
   p_fric      = pfric_0
   tries       = tries_0
   x1          = x1_0
   x2          = x2_0
   y1          = y1_0
   y2          = y2_0
   z1          = z1_0
   z2          = z2_0
end

SET small_p_min_0 = 0.00320 small_p_max_0 = 0.00320 y_min_0 =0.10 y_max_0 = 0.25 z_min_0 = 0.220
z_max_0 = 0.220 tries_0 = 3000000
SET kn_0 = 1e7 ks_0 = 1e7 dens_0 = 2540 pfric_0 = 0.25 shear_0 = 50e9 damp_0 = 0.84


small_p
```

gen small id=1000001,1000001   rad small_p_min_0,small_p_max_0 x=0.1003,0.1003 y=y_min_0,y_max_0 z=z_min_0,z_max_0   tries tries_0
 prop ks ks_0 kn kn_0 dens dens_0 fric pfric_0 shear = shear_0 damping = damp_0 range x=0,0.354 y=0,0.355 z=0.0,0.246

gen small id=1000002,1000002   rad small_p_min_0,small_p_max_0 x=0.1121,0.1121 y=y_min_0,y_max_0 z=z_min_0,z_max_0   tries tries_0
 prop ks ks_0 kn kn_0 dens dens_0 fric pfric_0 shear = shear_0 damping = damp_0 range x=0,0.354 y=0,0.355 z=0.0,0.246

gen small id=1000003,1000003   rad small_p_min_0,small_p_max_0 x=0.1239,0.1239 y=y_min_0,y_max_0 z=z_min_0,z_max_0   tries tries_0
 prop ks ks_0 kn kn_0 dens dens_0 fric pfric_0 shear = shear_0 damping = damp_0 range x=0,0.354 y=0,0.355 z=0.0,0.246

gen small id=1000004,1000004   rad small_p_min_0,small_p_max_0 x=0.1357,0.1357 y=y_min_0,y_max_0 z=z_min_0,z_max_0   tries tries_0
 prop ks ks_0 kn kn_0 dens dens_0 fric pfric_0 shear = shear_0 damping = damp_0 range x=0,0.354 y=0,0.355 z=0.0,0.246

gen small id=1000005,1000005   rad small_p_min_0,small_p_max_0 x=0.1475,0.1475 y=y_min_0,y_max_0 z=z_min_0,z_max_0   tries tries_0
 prop ks ks_0 kn kn_0 dens dens_0 fric pfric_0 shear = shear_0 damping = damp_0 range x=0,0.354 y=0,0.355 z=0.0,0.246

gen small id=1000006,1000006   rad small_p_min_0,small_p_max_0 x=0.1593,0.1593 y=y_min_0,y_max_0 z=z_min_0,z_max_0   tries tries_0
 prop ks ks_0 kn kn_0 dens dens_0 fric pfric_0 shear = shear_0 damping = damp_0 range x=0,0.354 y=0,0.355 z=0.0,0.246

gen small id=1000007,1000007   rad small_p_min_0,small_p_max_0 x=0.1711,0.1711 y=y_min_0,y_max_0 z=z_min_0,z_max_0   tries tries_0
 prop ks ks_0 kn kn_0 dens dens_0 fric pfric_0 shear = shear_0 damping = damp_0 range x=0,0.354 y=0,0.355 z=0.0,0.246

gen small id=1000008,1000008   rad small_p_min_0,small_p_max_0 x=0.1829,0.1829 y=y_min_0,y_max_0 z=z_min_0,z_max_0   tries tries_0
 prop ks ks_0 kn kn_0 dens dens_0 fric pfric_0 shear = shear_0 damping = damp_0 range x=0,0.354 y=0,0.355 z=0.0,0.246

gen small id=1000009,1000009   rad small_p_min_0,small_p_max_0 x=0.1003,0.1003 y=y_min_0,y_max_0 z=z_min_0,z_max_0   tries tries_0
 prop ks ks_0 kn kn_0 dens dens_0 fric pfric_0 shear = shear_0 damping = damp_0 range x=0,0.354 y=0,0.355 z=0.0,0.246

gen small id=1000010,1000010   rad small_p_min_0,small_p_max_0 x=0.1121,0.1121 y=y_min_0,y_max_0 z=z_min_0,z_max_0   tries tries_0
 prop ks ks_0 kn kn_0 dens dens_0 fric pfric_0 shear = shear_0 damping = damp_0 range x=0,0.354 y=0,0.355 z=0.0,0.246

gen small id=1000011,1000011   rad small_p_min_0,small_p_max_0 x=0.1239,0.1239 y=y_min_0,y_max_0 z=z_min_0,z_max_0   tries tries_0
 prop ks ks_0 kn kn_0 dens dens_0 fric pfric_0 shear = shear_0 damping = damp_0 range x=0,0.354 y=0,0.355 z=0.0,0.246

gen small id=1000012,1000012   rad small_p_min_0,small_p_max_0 x=0.1357,0.1357 y=y_min_0,y_max_0 z=z_min_0,z_max_0   tries tries_0
 prop ks ks_0 kn kn_0 dens dens_0 fric pfric_0 shear = shear_0 damping = damp_0 range x=0,0.354 y=0,0.355 z=0.0,0.246

gen small id=1000013,1000013   rad small_p_min_0,small_p_max_0 x=0.1475,0.1475 y=y_min_0,y_max_0 z=z_min_0,z_max_0   tries tries_0
 prop ks ks_0 kn kn_0 dens dens_0 fric pfric_0 shear = shear_0 damping = damp_0 range x=0,0.354 y=0,0.355 z=0.0,0.246

gen small id=1000014,1000014   rad small_p_min_0,small_p_max_0 x=0.1593,0.1593 y=y_min_0,y_max_0 z=z_min_0,z_max_0   tries tries_0
 prop ks ks_0 kn kn_0 dens dens_0 fric pfric_0 shear = shear_0 damping = damp_0 range x=0,0.354 y=0,0.355 z=0.0,0.246

gen small id=1000015,1000015   rad small_p_min_0,small_p_max_0 x=0.1711,0.1711 y=y_min_0,y_max_0 z=z_min_0,z_max_0   tries tries_0
 prop ks ks_0 kn kn_0 dens dens_0 fric pfric_0 shear = shear_0 damping = damp_0 range x=0,0.354 y=0,0.355 z=0.0,0.246

```
gen small id=1000016,1000016   rad small_p_min_0,small_p_max_0 x=0.1829,0.1829 y=y_min_0,y_max_0
z=z_min_0,z_max_0   tries tries_0
 prop ks ks_0 kn kn_0 dens dens_0 fric pfric_0 shear = shear_0 damping = damp_0 range x=0,0.354 y=0,0.355
z=0.0,0.246

gen small id=1000017,1000017   rad small_p_min_0,small_p_max_0 x=0.1947,0.1947 y=y_min_0,y_max_0
z=z_min_0,z_max_0   tries tries_0
 prop ks ks_0 kn kn_0 dens dens_0 fric pfric_0 shear = shear_0 damping = damp_0 range x=0,0.354 y=0,0.355
z=0.0,0.246

gen small id=1000018,1000018   rad small_p_min_0,small_p_max_0 x=0.2065,0.2065 y=y_min_0,y_max_0
z=z_min_0,z_max_0   tries tries_0
 prop ks ks_0 kn kn_0 dens dens_0 fric pfric_0 shear = shear_0 damping = damp_0 range x=0,0.354 y=0,0.355
z=0.0,0.246

gen small id=1000019,1000019   rad small_p_min_0,small_p_max_0 x=0.2183,0.2183 y=y_min_0,y_max_0
z=z_min_0,z_max_0   tries tries_0
 prop ks ks_0 kn kn_0 dens dens_0 fric pfric_0 shear = shear_0 damping = damp_0 range x=0,0.354 y=0,0.355
z=0.0,0.246

gen small id=1000020,1000020   rad small_p_min_0,small_p_max_0 x=0.2301,0.2301 y=y_min_0,y_max_0
z=z_min_0,z_max_0   tries tries_0
 prop ks ks_0 kn kn_0 dens dens_0 fric pfric_0 shear = shear_0 damping = damp_0 range x=0,0.354 y=0,0.355
z=0.0,0.246

gen small id=1000021,1000021   rad small_p_min_0,small_p_max_0 x=0.2419,0.2419 y=y_min_0,y_max_0
z=z_min_0,z_max_0   tries tries_0
 prop ks ks_0 kn kn_0 dens dens_0 fric pfric_0 shear = shear_0 damping = damp_0 range x=0,0.354 y=0,0.355
z=0.0,0.246

gen small id=1000022,1000022   rad small_p_min_0,small_p_max_0 x=0.2537,0.2537 y=y_min_0,y_max_0
z=z_min_0,z_max_0   tries tries_0
 prop ks ks_0 kn kn_0 dens dens_0 fric pfric_0 shear = shear_0 damping = damp_0 range x=0,0.354 y=0,0.355
z=0.0,0.246

gen small id=1000023,1000023   rad small_p_min_0,small_p_max_0 x=0.1711,0.1711 y=y_min_0,y_max_0
z=z_min_0,z_max_0   tries tries_0
 prop ks ks_0 kn kn_0 dens dens_0 fric pfric_0 shear = shear_0 damping = damp_0 range x=0,0.354 y=0,0.355
z=0.0,0.246

gen small id=1000024,1000024   rad small_p_min_0,small_p_max_0 x=0.1829,0.1829 y=y_min_0,y_max_0
z=z_min_0,z_max_0   tries tries_0
 prop ks ks_0 kn kn_0 dens dens_0 fric pfric_0 shear = shear_0 damping = damp_0 range x=0,0.354 y=0,0.355
z=0.0,0.246

gen small id=1000025,1000025   rad small_p_min_0,small_p_max_0 x=0.1947,0.1947 y=y_min_0,y_max_0
z=z_min_0,z_max_0   tries tries_0
 prop ks ks_0 kn kn_0 dens dens_0 fric pfric_0 shear = shear_0 damping = damp_0 range x=0,0.354 y=0,0.355
z=0.0,0.246

gen small id=1000026,1000026   rad small_p_min_0,small_p_max_0 x=0.2065,0.2065 y=y_min_0,y_max_0
z=z_min_0,z_max_0   tries tries_0
 prop ks ks_0 kn kn_0 dens dens_0 fric pfric_0 shear = shear_0 damping = damp_0 range x=0,0.354 y=0,0.355
z=0.0,0.246

gen small id=1000027,1000027   rad small_p_min_0,small_p_max_0 x=0.2183,0.2183 y=y_min_0,y_max_0
z=z_min_0,z_max_0   tries tries_0
 prop ks ks_0 kn kn_0 dens dens_0 fric pfric_0 shear = shear_0 range x=0,0.354 y=0,0.355 z=0.0,0.246

gen small id=1000028,1000028   rad small_p_min_0,small_p_max_0 x=0.2301,0.2301 y=y_min_0,y_max_0
z=z_min_0,z_max_0   tries tries_0
 prop ks ks_0 kn kn_0 dens dens_0 fric pfric_0 shear = shear_0 range x=0,0.354 y=0,0.355 z=0.0,0.246

gen small id=1000029,1000029   rad small_p_min_0,small_p_max_0 x=0.2419,0.2419 y=y_min_0,y_max_0
z=z_min_0,z_max_0   tries tries_0
 prop ks ks_0 kn kn_0 dens dens_0 fric pfric_0 shear = shear_0 range x=0,0.354 y=0,0.355 z=0.0,0.246

gen small id=1000030,1000030   rad small_p_min_0,small_p_max_0 x=0.2537,0.2537 y=y_min_0,y_max_0
z=z_min_0,z_max_0   tries tries_0
 prop ks ks_0 kn kn_0 dens dens_0 fric pfric_0 shear = shear_0 range x=0,0.354 y=0,0.355 z=0.0,0.246


set gravity 0 0 -9.81
plot ball active on id off range small wall wire on
plot add dis yellow range small
```

```
property c_index 3 range small
plot set foreground black
plot set color on
plot set 3d on
plot set perspective on
plot create assembly
plot create view
plot disp black
plot set animate on


DEF set_time
tim0  = clock
_dummy=out('timer has been reset...')
END

;;================================================================
DEF get_time
  _tim_s   = (clock - tim0)/100   ; this is to express it in seconds...
  _tim_m   = _tim_s/60
  _tim_h   = _tim_m/60
  _out     = string ('delta_t since last reset [sec] = ' + string(_tim_s))
  _dummy   = out(_out)
  _out     = string ('delta_t since last reset [min] = ' + string(_tim_m))
  _dummy   = out(_out)
  _out     = string ('delta_t since last reset [hour] = ' + string(_tim_h))
  _dummy   = out(_out)
  get_time = clock - tim0
END

set_time = 0
get_time

set logfile II0.36_DPDB_begin.log
set log on
print ball pos range small
set log off

hist get_time            ;(his 1)
hist ball zp id 1000001  ;(his 2)
hist ball zp id 1000003  ;(his 3)
hist ball zp id 1000006  ;(his 4)
hist ball zp id 1000009  ;(his 5)
hist ball zp id 1000012  ;(his 6)
hist ball zp id 1000015  ;(his 7)
hist ball zp id 1000018  ;(his 8)
hist ball zp id 1000021  ;(his 9)
hist ball zp id 1000022  ;(his 10)
hist ball zp id 1000026  ;(his 11)
hist ball zp id 1000030  ;(his 12)
hist ball zp id 1000023  ;(his 13)
hist diagnostic muf      ;(his 14)
;;;====== apply shearing ======

def cycle_shear
  cycle_0        = cycle_0
  cycle_1        = cycle_1
  n_stress       = n_stress_0
end

SET cycle_0 = 68600 cycle_1 = 66800 n_stress_0 = -0.9e3
cycle_shear

;;;==========================================================
;;;======== positive direction 1 (50% shear-strain)=========
;;;==========================================================

ini xv 0 yv 0 zv 0 range small
ini xv 0 yv 0 zv 0 range big
fix z range big
ini zforce n_stress_0 range small   ;;======= for fine particles ======
ini zforce n_stress_0 range big     ;;======= for bulk particles ======

set y_rotation = 3.15 ; 0.04 s-1
print y_rotation
```

```
wall id 3 ys y_rotation  range x 0,0.354 y 0,0.355 z 0,0.355
wall id 1 ys  y_rotation range x 0,0.354 y 0,0.355 z 0,0.355

cycle cycle_0

;;;==========================================================
;;;======== initial direction 1 (100% shear-strain) ========
;;;==========================================================

ini xv 0 yv 0 zv 0 range small
ini xv 0 yv 0 zv 0 range big
fix z range big
ini zforce n_stress_0 range small   ;;======= for fine particles ======
ini zforce n_stress_0 range big     ;;======= for bulk particles ======

set y_rotation_1 = -3.15
print y_rotation_1

wall id 3 yspin y_rotation_1 range x 0,0.354 y 0,0.355 z 0,0.355
wall id 1 yspin y_rotation_1 range x 0,0.354 y 0,0.355 z 0,0.355

cycle cycle_1
delete ball range z 0.246 5.00

;;;==========================================================
;;;======== negative direction 1 (150% shear-strain)========
;;;==========================================================

ini xv 0 yv 0 zv 0 range small
ini xv 0 yv 0 zv 0 range big
fix z range big
ini zforce n_stress_0 range small   ;;======= for fine particles ======
ini zforce n_stress_0 range big     ;;======= for bulk particles ======

set y_rotation_2 = -3.15
print y_rotation_2

wall id 3 yspin y_rotation_2 range x 0,0.354 y 0,0.355 z 0,0.355
wall id 1 yspin y_rotation_2 range x 0,0.354 y 0,0.355 z 0,0.355

cycle cycle_1
delete ball range z 0.246 5.00
plot show

;;;==========================================================
;;;======== positive direction 1 (200% shear-strain)========
;;;==========================================================

ini xv 0 yv 0 zv 0 range small
ini xv 0 yv 0 zv 0 range big
fix z range big
ini zforce n_stress_0 range small   ;;======= for fine particles ======
ini zforce n_stress_0 range big     ;;======= for bulk particles ======

set y_rotation = 3.15
print y_rotation

wall id 3 ys y_rotation  range x 0,0.354 y 0,0.355 z 0,0.355
wall id 1 ys  y_rotation range x 0,0.354 y 0,0.355 z 0,0.355

cycle cycle_0

;;;==========================================================
;;;======== positive direction 1 (250% shear-strain)========
;;;==========================================================

ini xv 0 yv 0 zv 0 range small
ini xv 0 yv 0 zv 0 range big
ini zforce n_stress_0 range small   ;;======= for fine particles ======
ini zforce n_stress_0 range big     ;;======= for bulk particles ======

set y_rotation = 3.15
print y_rotation
```

```
wall id 3 ys y_rotation  range x 0,0.354 y 0,0.355 z 0,0.355
wall id 1 ys  y_rotation range x 0,0.354 y 0,0.355 z 0,0.355

cycle cycle_0

;;;=========================================================
;;;======== initial direction 1 (300% shear-strain) ========
;;;=========================================================

ini xv 0 yv 0 zv 0 range small
ini xv 0 yv 0 zv 0 range big
fix z range big
ini zforce n_stress_0 range small   ;;======= for fine particles ======
ini zforce n_stress_0 range big     ;;======= for bulk particles ======

set y_rotation_1 = -3.15
print y_rotation_1

wall id 3 yspin y_rotation_1 range x 0,0.354 y 0,0.355 z 0,0.355
wall id 1 yspin y_rotation_1 range x 0,0.354 y 0,0.355 z 0,0.355

cycle cycle_1
delete ball range z 0.246 5.00

;;;==========================================================
;;;======== negative direction 1 (350% shear-strain)=========
;;;==========================================================

ini xv 0 yv 0 zv 0 range small
ini xv 0 yv 0 zv 0 range big
fix z range big
ini zforce n_stress_0 range small   ;;======= for fine particles ======
ini zforce n_stress_0 range big     ;;======= for bulk particles ======

set y_rotation_2 = -3.15
print y_rotation_2

wall id 3 yspin y_rotation_2 range x 0,0.354 y 0,0.355 z 0,0.355
wall id 1 yspin y_rotation_2 range x 0,0.354 y 0,0.355 z 0,0.355

cycle cycle_1
delete ball range z 0.246 5.00
plot show

;;;=========================================================
;;;======== positive direction 1 (400% shear-strain)========
;;;=========================================================

ini xv 0 yv 0 zv 0 range small
ini xv 0 yv 0 zv 0 range big
fix z range big
ini zforce n_stress_0 range small   ;;======= for fine particles ======
ini zforce n_stress_0 range big     ;;======= for bulk particles ======

set y_rotation = 3.15
print y_rotation

wall id 3 ys y_rotation  range x 0,0.354 y 0,0.355 z 0,0.355
wall id 1 ys  y_rotation range x 0,0.354 y 0,0.355 z 0,0.355

cycle cycle_0




;;;========================================================================
;;;======== recording of history variables in vertical displacement ===========
;;;==============  for selected percolating fine particles ===============
;;;========================================================================

plot add his 2 3 4 5 6 7 8 9 10 12 13  vs  1 black blue red green cyan yellow lgreen lblue magenta orange cyan lred
plot his 2 3 4 5 6 7 8 9 10 12 13 vs 1 ymax 0.4
```

```
;plot show

set logfile II0.36_DPDB_end.log
set log on
print ball pos range small
set log off

return  ; test complete
```

## D2 Clump Logic Templates

```
;;;==========================================
;;  TEMPLATE FOR CLUMP-PARTICLES GENERATION
;;;==========================================



;;;================================================
;;;======== Bi-conical (six-particle clumps) =======
;;;================================================

clump template make rock 6 &
     radii 1.0  1.0  1.0  1.0  1.0  1.0  &
     pos (-1.0,0.0,0.0) (1.0,0.0,0.0) (0.0,0.0,1.0) (0.0,0.0,-1.0) (0.0,1.0,0.0) (0.0,-1.0,0.0)


clump replace 6 rock 0.2 rock 0.2 rock 0.2 rock 0.2 rock 0.1 rock 0.1

clump property full on
clump property permanent
plot add clump



;;;=============================================
;;;======== Cuboid (four-particle clumps) =======
;;;=============================================

clump template make cuboid 4 &
     radii 1.0 1.0  1.0  1.0     &
     pos (-1.0,0.0,0.0) (1.0,0.0,0.0) (0.0,0.0,1.0) (0.0,0.0,-1.0)


clump replace 4 cuboid 0.25 cuboid 0.25 cuboid 0.25 cuboid 0.25

clump property full on
clump property permanent
plot add clump



;;;===================================================
;;;======== Cylindrical (three-particle clumps) =======
;;;===================================================

clump template make peanut 3 &
     radii 1.0  1.0  1.0 &
     pos (0.0,0.0,0.0) (-1.0,0.0,0.0) (1.0,0.0,0.0)


clump replace 3 peanut 0.34 peanut 0.33 peanut 0.33

clump property full on
clump property permanent
plot add clump
```